

(NASA-CP-2405) TURBINE ENGINE HOT SECTION  
TECHNOLOGY, 1985 (NASA) 443 p Avail: NTIS  
HC A19/NP A01 CSCL 20R

W88-11140:

--THRU--

W88-11185

Unclas

81/39 0102788

*NASA Conference Publication 2405*

# Turbine Engine Hot Section Technology 1985

*Proceedings of a conference  
sponsored by NASA Lewis Research Center  
Cleveland, Ohio  
October 22 and 23, 1985*

**NASA**

National Aeronautics  
and Space Administration

Scientific and Technical  
Information Branch

1985

## FOREWORD

Aircraft gas-turbine engine designs have been pushed to ever higher levels of performance, primarily due to competition and the need for improved fuel efficiency. Such improved performance is possible primarily due to higher operating pressures and temperatures. The effect, however, has been a decrease in engine durability. In hot-section components - the combustor and turbine - the more hostile environments have accelerated damage and wear of parts, with associated dramatically increased maintenance costs. In the past, minimal efforts have been made to assure required durability due to technology advances being directed primarily toward improving performance.

The activities of the NASA Turbine Engine Hot Section Technology (HOST) Project are directed toward durability needs, as defined by industry, and a more balanced approach to engine design. The HOST efforts will improve the understanding and prediction of thermal environments, thermal loads, structural responses, and life by focused experimental and analytical research activities. The overall approach is to assess existing analysis methods for strengths and deficiencies, to conduct supporting analytical and experimental research to rectify these deficiencies, to incorporate state-of-the-art improvements into the analysis methods, and finally to verify the improvements by bench-mark quality experiments. The research is supported by the HOST Project with contracts, grants, and Lewis in-house activities.

To provide representatives from industry, academia, and government with the latest findings and progress toward improved aircraft turbine engine durability, a two-day workshop was held in October 1985. This publication contains the papers presented at the workshop.

Daniel E. Sokolowski  
Manager, HOST Project Office

PRECEDING PAGE BLANK NOT FILMED

## CONTENTS

### OVERVIEWS

Turbine Engine Hot Section Technology (HOST) Project Daniel E. Sokolowski and C. Robert Ensign, NASA Lewis Research Center . . . . .	1
HOST Instrumentation R&D Program Overview D.R. Englund, NASA Lewis Research Center . . . . .	7
HOST Combustion R&T Overview Raymond E. Gaugler, NASA Lewis Research Center . . . . .	9
HOST Turbine Heat Transfer R&T Overview Robert J. Simoneau, NASA Lewis Research Center . . . . .	11
HOST Structural Analysis Program Overview R.L. Thompson, NASA Lewis Research Center . . . . .	17
HOST Fatigue and Fracture R&T Overview G.R. Halford, NASA Lewis Research Center . . . . .	23
HOST Surface Protection R&T Overview Carl A. Stearns, NASA Lewis Research Center . . . . .	27

### INSTRUMENTATION

Further Development of the Dynamic Gas Temperature Measurement System D.L. Elmore, W.W. Robinson, and W.B. Watkins, Pratt & Whitney Engineering Division . . . . .	37
The Development of A High Temperature Static Strain Gage System Charles O. Hulse and Richard S. Bailey, United Technologies Research Center . . . . .	45
Development of Heat Flux Sensors for Turbine Airfoils William H. Atkinson, Marcia A. Cyr, and Richard R. Strange, United Technologies Corporation, Pratt & Whitney . . . . .	51
Elevated Temperature Strain Gages J.O. Brittain, D. Geslin, and J.F. Lei, Northwestern University . . . . .	59
The Four Spot Time-of-Flight Laser Anemometer Mark P. Wernet, NASA Lewis Research Center . . . . .	67

PRECEDING PAGE BLANK NOT FILMED

The Lewis Strain Gauge Laboratory - Status and Plans Howard F. Hobart and Herbert A. Will, NASA Lewis Research Center . . . . .	77
---	----

Correlation of Velocity and Velocity-Density Turbulence in the Exhaust of an Atmospheric Burner Gustave C. Fralick, NASA Lewis Research Center . . . . .	81
--	----

## COMBUSTION

Improved Numerical Methods for Turbulent Viscous Recirculating Flows - A Progress Report A. Turan, Avco Everett Research Laboratory, Inc. . . . .	87
---	----

Aerothermal Modeling Program - Phase II H.C. Mongia, S.V. Patankar, S.N.B. Murthy, J.P. Sullivan, and G.S. Samuelsen, Allison Gas Turbine Division, General Motors Corporation . . . . .	89
---	----

Fuel-Injector/Air-Swirl Characterization J.B. McVey and J.B. Kennedy, United Technologies Research Center, and J.C. Bennett, University of Connecticut . . . . .	109
--	-----

Efficient Numerical Techniques for Complex Fluid Flows Suhas V. Patankar, University of Minnesota . . . . .	119
--	-----

Combustor-Diffuser Interaction Program R. Srinivasan and C. White, Garrett Turbine Engine Company . . . . .	121
--	-----

Dilution Jet Mixing Program - Phase III R. Srinivasan, G. Myers, and C. White, Garrett Turbine Engine Company . . . . .	127
---	-----

On the Mixing of a Row of Jets with a Confined Crossflow J.D. Holdeman, NASA Lewis Research Center . . . . .	133
---	-----

## TURBINE HEAT TRANSFER

Heat Transfer in a Real Engine Environment Herbert J. Gladden, NASA Lewis Research Center . . . . .	139
--	-----

Film Cooling Heat Transfer on a Turbine Airfoil Larry D. Hylton, Allison Gas Turbine Division . . . . .	151
--	-----

Flow Field Measurements in a 90 Degree Turning Duct Roger A. Crawford and Carroll E. Peters, The University of Tennessee Space Institute . . . . .	161
--	-----

Measurement of Airfoil Heat Transfer Coefficients on a Turbine Stage Robert P. Dring, Michael F. Blair, and H. David Joslyn, United Technologies Research Center . . . . .	165
--	-----

Heat Transfer in the Tip Region of a Rotor Blade Simulator D.E. Metzger, M.K. Chyu, and H.K. Moon, Mechanical and Aerospace Engineering Department, Arizona State University . . . . .	175
Coolant Passage Heat Transfer With Rotation T.J. Hajek and A.W. Higgins, United Technologies Corporation, Pratt & Whitney . . . . .	187
Heat Transfer With Very High Free-Stream Turbulence Robert J. Moffat and Paul K. Maciejewski, Stanford University . . . . .	203
Prediction of Turbine Blade Heat Transfer Suhas V. Patankar, University of Minnesota . . . . .	217
Flow in a Model Turbine Stator R.C. Buggeln, S.J. Shamroth, and W.R. Briley, Scientific Research Associates . . . . .	221

## STRUCTURES

3D Inelastic Analysis Methods for Hot Section Components L.T. Dame, P.C. Chen, M.S. Hartle, and H.T. Huang, General Electric Company . . . . .	227
3-D Inelastic Analysis Methods for Hot Section Components E.S. Todd, United Technologies Corporation, Pratt & Whitney . . . . .	239
Component Specific Modeling R.L. McKnight and M.T. Tipton, General Electric Company . . . . .	245
Experimental Determination of Flow Potential Surfaces Supporting A Multiaxial Formulation of Viscoplasticity J.R. Ellis and D.N. Robinson, The University of Akron . . . . .	259
Constitutive Modeling for Single Crystal Superalloys Donald C. Stouffer, L. Thomas Dame, and N. Jayaraman, University of Cincinnati and General Electric Company . . . . .	271
Constitutive Modeling of Superalloy Single Crystals with Verification Testing Eric Jordan, University of Connecticut, and Kevin P. Walker, Engineering Science Software, Inc. . . . .	277
High Temperature Stress-Strain Analysis Robert L. Thompson, NASA Lewis Research Center . . . . .	287

## FATIGUE

Constitutive Modeling for Isotropic Materials Ulric S. Lindholm, Southwest Research Institute . . . . .	303
--	-----

Constitutive Modeling for Isotropic Materials V.G. Ramaswamy, R.H. Van Stone, L.T. Dame, and J.H. Laflen, General Electric Company . . . . .	307
Creep Fatigue Life Prediction for Engine Hot Section Materials (Isotropic) - Third Year Progress Review Richard S. Nelson and John F. Schoendorf, United Technologies Corporation . . . . .	321
Elevated Temperature Crack Growth S.N. Malik, R.H. Van Stone, K.S. Kim, J.H. Laflen, General Electric Company . . . . .	329
Life Prediction and Constitutive Models for Engine Hot Section Anisotropic Materials Program G.A. Swanson, United Technologies Corporation, Pratt & Whitney . . . . .	341
Creep-Fatigue Behavior of NiCoCrAlY Coated PWA 1480 Superalloy Single Crystals R.V. Miner, J. Gayda, and M.G. Hebsur, NASA Lewis Research Center . . . . .	351
Lewis' Enhanced Laboratory for Research into the Fatigue and Constitutive Behavior of High Temperature Materials Michael A. McGaw, NASA Lewis Research Center . . . . .	361

#### SURFACE PROTECTION

Turbine Airfoil Deposition Models and Their Hot Corrosion Implications D.E. Rosner and R. Nagarajan, Yale University . . . . .	373
Experimental Verification of Vapor Deposition Rate Theory in High Velocity Burner Rigs Suleyman A. Gokoglu, Case Western Reserve University, and Gilbert J. Santoro, NASA Lewis Research Center . . . . .	383
Effects of Surface Chemistry on Hot Corrosion Life R.E. Fryxell, General Electric Company, and G.E. Leese, TRW Inc. . . . .	391
Coating Life Prediction James A. Nesbitt and Michael A. Gedwill, NASA Lewis Research Center . . . . .	397
Thermal Expansion Mismatch and Oxidation in Thermal Barrier Coatings G.C. Chang, W. Phucharoen, Cleveland State University, and R.A. Miller, NASA Lewis Research Center . . . . .	405
Thermal Barrier Coating Life Prediction Model Development T.E. Strangman, J.F. Neumann, and A. Tasooji, Garrett Turbine Engine Company . . . . .	427
Thermal Barrier Coating Life Prediction Model Development R.V. Hillery, B.H. Pilsner, and E.C. Duderstadt, General Electric . . . . .	433

Thermal Barrier Coating Life Prediction Model Development J.T. DeMasi, and K.D. Sheffler, United Technologies Corporation, Pratt & Whitney . . . . .	445
Concluding Remarks: Fourth Annual Workshop for the HOST Project Daniel E. Sokolowski, NASA Lewis Research Center . . . . .	457

## **TURBINE ENGINE HOT SECTION TECHNOLOGY (HOST) PROJECT**

**Daniel E. Sokolowski and C. Robert Ensign  
NASA Lewis Research Center  
Cleveland, Ohio**

The Hot Section Technology (HOST) Project is a NASA-sponsored endeavor to improve the durability of advanced gas turbine engines for commercial and military aircraft. Through improvements in the analytical models and life prediction systems, designs for future turbine-engine hot section components - the combustor and turbine - will be analyzed more accurately and will incorporate features required for longer life in the more hostile operating environment of high performance engines.

Started in fiscal year 1981, the HOST Project has activities planned through 1989 with an estimated total cost of over \$44 million. While the Project's focused research activities are necessarily analytical in nature, significant experimental testing is required for benchmark quality assessments as well as for model validations. The efforts are being conducted in-house at the NASA Lewis Research Center, under contracts with major domestic turbine engine manufacturers, and under grants to qualified universities. The contract and grant funding total equals 50 percent of the total budget for fiscal year 1986.

At NASA Lewis the HOST Project Office serves as the focal point for advocacy, funding, technical coordination, and information exchange. This workshop serves as the primary vehicle for this last function; that is, to disseminate information and elicit the exchange of ideas among participants.

Activities of the HOST Project are categorized under six disciplines: (1) instrumentation, (2) combustion, (3) turbine heat transfer, (4) structural analysis, (5) fatigue and fracture, and (6) surface protection. Management of the project uses the matrix approach, as shown in figure 1. A subproject manager is responsible for each discipline and reports to the manager of the HOST Project Office.

To further understand the organization of the project and, more importantly, the reasons for its activities, it is useful to review the critical steps leading to life prediction. The flow diagram in figure 2 shows such critical steps and may be used for any hot section subcomponent, for example, liners, blades, or vanes. The first series of steps (see fig. 2) defines the engine subcomponent geometry, material, and operating requirements. As shown in figure 3 the next step (see arrow) is to characterize the hot section environment around the subcomponent. Activities in the HOST project which support improvements to this characterization are listed and grouped according to responsible discipline; that is, instrumentation and combustion. Next, the characterization of thermomechanical loads on the subcomponent is being improved by activities listed in figure 4 under the above two disciplines plus turbine heat transfer. The next step (fig. 5) is to determine the material behavior and structural response due to imposed loads. Activities aimed at improving this determination are, again, in instrumentation but include broad efforts in structural analysis. Finally, prediction of subcomponent life is being improved by activities shown in figure 6 in the disciplines of fatigue and fracture as well as surface protection.

To summarize the activities supported by the HOST project and reported herein, instrumentation is being developed to obtain high-temperature, benchmark-quality data to develop and verify analysis methods. These include flow sensors (LDV), heat flux sensors (thin film), strain sensors (1800 °F static thin film), gas temperature sensors (frequency compensated), and hot-section optical viewing systems. Combustion work includes aerothermal model assessment and development, dilution jet modeling, high-pressure flame radiation/heat flux testing, and the development of a thermal structural cyclic test facility. Turbine heat transfer is studying two- and three-dimensional flow and heat transfer on airfoil external boundaries, emphasizing boundary-layer transition and viscous modeling. It also investigates coolant-passage heat transfer, including midchord jet impingement cooling and rotational passage effects. Structural analysis includes research into thermal mechanical load models, component geometry specific models, and three-dimensional inelastic analysis methods development. Fatigue and fracture includes constitutive model development for both isotropic and anisotropic materials, for both single-crystal and directionally solidified forms. It also includes research in life-prediction methods for creep-fatigue interactions and elastoplastic crack propagation. The surface protection research includes studies of corrosion and oxidation phenomena, environmental mechanics models, and metallic and thermal barrier coating analysis method developments.

Workshop publications and most contractor final reports carry the label "For Early Domestic Dissemination" (FEDD) to protect national interests and, thus, are available only to qualified U.S. citizens. Although contractor final reports have been published, they often represent initial phases of multiphased work. Thus, this annual workshop report is the primary document for reporting technical results for the entire project.

# ORGANIZATION: HOT SECTION TECHNOLOGY (HOST) PROJECT

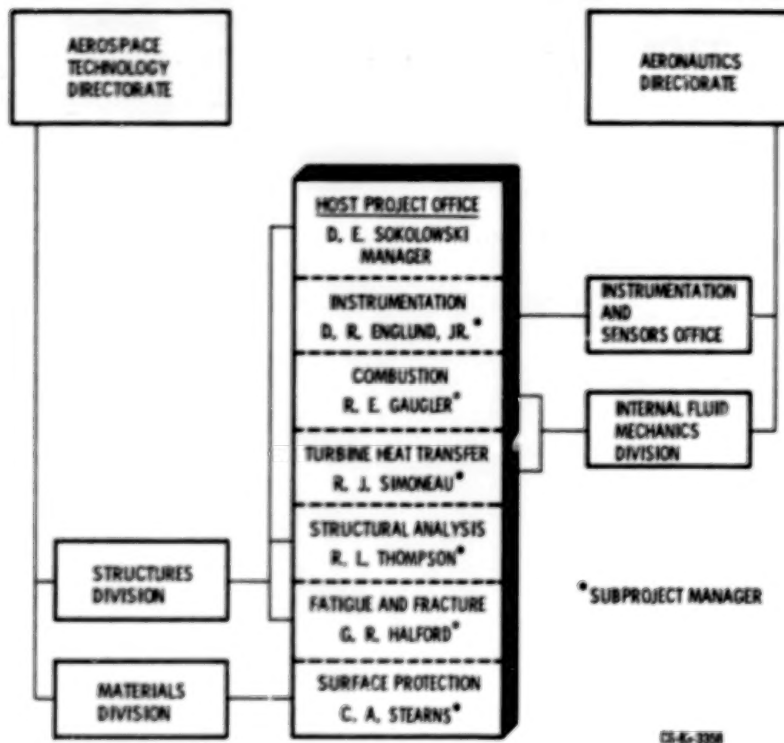


Figure 1

## INTEGRATION OF ANALYTICAL ANALYSES LEADS TO LIFE PREDICTION

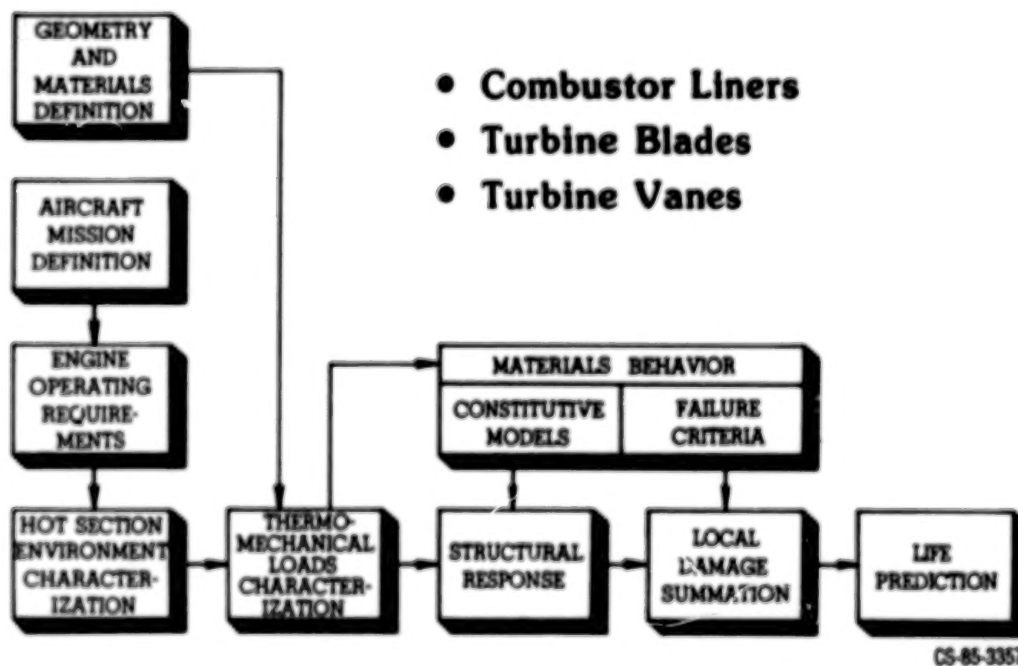
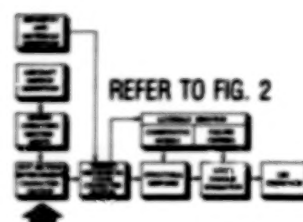


Figure 2

## IMPROVING THE CHARACTERIZATION OF THE HOT SECTION ENVIRONMENT



### ADVANCED INSTRUMENTATION

HOT-SECTION VIEWING SYSTEM	UTRC	0
DYNAMIC GAS TEMPERATURE MEASURING SYSTEM	P&W	0
LASER ANEMOMETRY FOR HOT SECTION APPLICATIONS	NASA	0

### COMBUSTOR AEROTHERMAL MODELING

ASSESSMENT OF AEROTHERMAL MODELS	GE/GTEC/P&W	0
IMPROVEMENT OF AEROTHERMAL MODELS	AGTD/AVCO/UTRC/U. MINN.	0
DIFFUSER/COMBUSTOR MODEL	GTEC	0
DILUTION JET MIXING STUDIES	GTEC/OKAL. ST./NASA	0

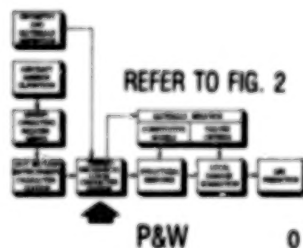
0 IN PROGRESS

● COMPLETED

CS-85-3356

Figure 3

## IMPROVING THE CHARACTERIZATION OF THERMOMECHANICAL LOADS



### ADVANCED INSTRUMENTATION

TURBINE HEAT FLUX SENSORS	P&W	0
---------------------------	-----	---

### COMBUSTOR HEAT TRANSFER

FLAME RADIATION STUDIES	NASA	0
-------------------------	------	---

### TURBINE HEAT TRANSFER

3D VISCOUS FLOW AND HEAT TRANSFER	UTSI	0
2D HEAT TRANSFER WITH FILM COOLING	AGTD	0
IMPINGEMENT HEAT TRANSFER	ASU	0
EFFECTS OF TURBULENCE ON HEAT TRANSFER	STANFORD	0
MEASUREMENT OF AIRFOIL HEAT-TRANSFER COEF.	UTRC	0
ASSESSMENT OF 3D B.L. CODE FOR HEAT TRANSFER	UTRC	0
COOLANT-SIDE HEAT TRANSFER WITH ROTATION	P&W	0
TIP REGION HEAT TRANSFER	ASU	0
ANALYTICAL FLOW AND HEAT TRANSFER	SRA	0
COMPUTATION OF TURBINE BLADE HEAT TRANSFER	U. MINN.	0
WARM TURBINE FLOW MAPPING W/L.A. SYSTEM	NASA	0
REAL-ENGINE TYPE TESTING	NASA	0

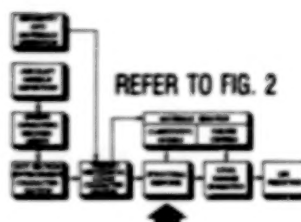
0 IN PROGRESS

● COMPLETED

CS-85-3353

Figure 4

## IMPROVING THE PREDICTION OF STRUCTURAL RESPONSE



### ADVANCED INSTRUMENTATION

HIGH TEMPERATURE STRAIN GAGE MATERIALS  
TURBINE STATIC STRAIN GAGE  
LASER SPECKLE STRAIN MEASUREMENT

NW UNIV. 0  
UTRC 0  
UTRC 0

### STRUCTURAL ANALYSIS

CONSTITUTIVE MODEL DEVELOPMENT  
CONSTITUTIVE MODELS-ISOTROPIC MATERIALS  
CONSTITUTIVE MODELS-ANISOTROPIC MATERIALS  
3D INELASTIC ANALYSIS METHODS  
COMPONENT SPECIFIC MODELING  
THERMAL/STRUCTURAL LOADS TRANSFER MODULE  
STRUCTURAL COMPONENTS RESPONSE  
HIGH TEMPERATURE STRUCTURES RESEARCH

NASA 0  
GE/SWRI 0  
U. CINN./U. CONN. 0  
GE/P&W 0  
GE 0  
GE 0  
NASA 0  
NASA 0

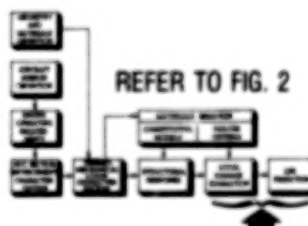
o IN PROGRESS

● COMPLETED

CS-85-3355

Figure 5

## IMPROVING LIFE PREDICTION



### FATIGUE AND FRACTURE

CREEP-FATIGUE LIFE PREDICTION FOR ISOTROPIC MAT'LS.  
ELEVATED TEMPERATURE CRACK PROPAGATION  
ANALYSIS OF FATIGUE CRACK GROWTH  
LIFE PREDICTION/MAT'LS. BEHAVIOR FOR ANISOTROPIC MAT'LS.  
FATIGUE LAB VITALIZATION

P&W 0  
GE 0  
SYRACUSE 0  
P&W 0  
NASA 0

### SURFACE PROTECTION

AIRFOIL DEPOSITION MODEL  
DEPOSITION MODEL VERIFICATION  
EFFECTS OF SURFACE CHEMISTRY - CORROSION  
THERMAL BARRIER COATING LIFE PREDICTION  
MECHANICAL BEHAVIOR OF TBC  
TBC RiG/ENGINE CORRELATION

YALE 0  
NASA 0  
GE 0  
GE/GTEC/UTRC 0  
CSU 0  
NASA 0

o IN PROGRESS

● COMPLETED

CS-85-3354

Figure 6

## HOST INSTRUMENTATION R&D PROGRAM OVERVIEW

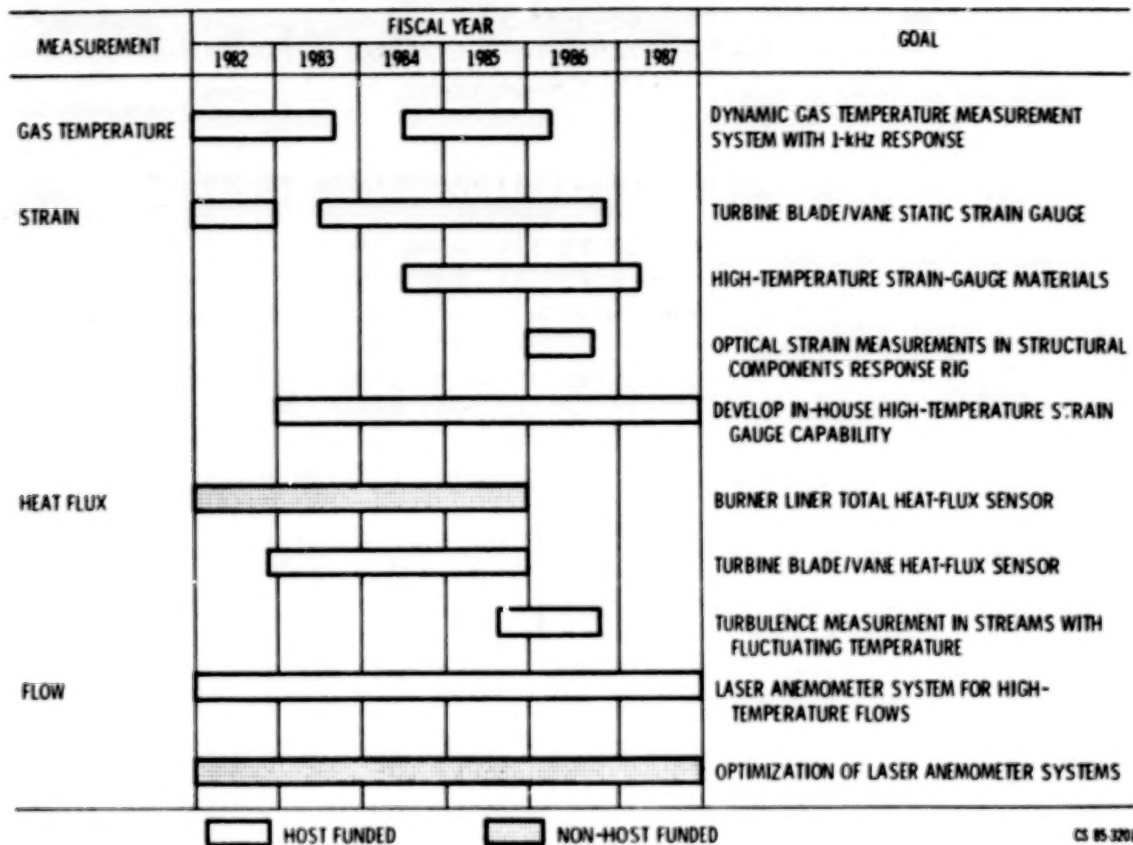
D.R. Englund  
NASA Lewis Research Center  
Cleveland, Ohio

The HOST Instrumentation R&D program is directed at the development of two categories of instrumentation. One is instrumentation capable of characterizing the environment imposed on turbine engine hot-section components. This category includes instruments for the measurements of gas flow, gas temperature, and heat flux. The second category is instrumentation to measure the effect of the environment on the hot-section components. This category includes strain measuring instruments and an optical system capable of providing interior views of a burner liner during operation. The program was formulated to concentrate on critical measurements that could not be made with available instruments or with instruments under development via NASA- or DOD-funded programs or via IR&D programs.

The schedule for the HOST Instrumentation R&D program is shown in the accompanying figure. This schedule shows contract, grant, and in-house work funded by HOST and, in addition, two non-HOST funded efforts that have HOST-related goals. One effort on previous versions of this figure has been omitted this year: The combustor viewing system. The development work on this system was completed last year, and the system was used at Lewis in the last test of the hot section facility combustor. Future uses of this system are at the Naval Air Propulsion Center (on a temporary loan basis) and for a series of tests to demonstrate the capability to "see through" a luminous flame. Two new efforts are also in this program: optical strain measurements on the structural component response rig and a turbulence measurement experiment. The first of these will demonstrate the capability of the laser speckle photogrammetry technique to measure high-temperature two-dimensional strain on burner-liner structures subjected to thermal cycling. In this test, the burner liner will be viewed through air at atmospheric pressure. This should eliminate the problem encountered in a previous test of this technique in a high-pressure burner rig, that is, of speckle pattern distortion due to density gradients in the high-pressure air within the viewing path. The objective of the turbulence measurement experiment is to explore how turbulence should be measured or specified for convective heat-transfer experiments in flow streams in which there is an appreciable fluctuation in both density and velocity. We are making measurements with the laser anemometer and the dynamic gas temperature probe in the exhaust stream of an atmospheric burner, and we will be comparing the turbulence expressed in velocity terms only with that derived from the density-velocity product.

PRECEDING PAGE BLANK NOT FILMED

# HOST INSTRUMENTATION R & D PROGRAM



CS 85-3201

## HOST COMBUSTION R&T OVERVIEW

Raymond E. Gaugler  
NASA Lewis Research Center  
Cleveland, Ohio

The overall objective of the Turbine Engine Hot Section Technology Combustion Project is to develop and verify improved and more accurate analysis methods for increasing the ability to design with confidence combustion systems for advanced aircraft turbine engines.

This project's approach was to first assess and evaluate existing combustor aerothermal analysis models by means of a contracted effort initiated during fiscal year 1982. This effort has quantified the strengths and deficiencies of existing models. The results of this assessment were summarized at last year's HOST Workshop.

A program is now being conducted to support, focus, and accelerate the development of new methods to more accurately predict and model the physical phenomena occurring within the combustor. This program includes both analytical and experimental research efforts in the area of aerothermal modeling.

During fiscal year 1984, phase II of the aerothermal modeling program was initiated, which consisted of contracted model development efforts in the areas of improved numerical methods for turbulent viscous flows, flow interactions, and fuel-spray flow-field interactions. The first progress reports on these efforts will be presented at this meeting.

A Phase III effort will begin in fiscal year 1987. That phase will involve a characterization of the thermal loads to the combustor structure.

## COMBUSTION

PROGRAM ELEMENT	FISCAL YEAR									EXPECTED RESULT
	81	82	83	84	85	86	87	88	89	
AEROTHERMAL MODELING ASSESSMENT, PHASE I:										
GARRETT										IDENTIFY MODEL AND BENCHMARK DATA DEFICIENCIES
GENERAL ELECTRIC										
PRATT AND WHITNEY										
LATERAL JET INJECTION (OKLAHOMA STATE U.)										3D FLOW MEASUREMENTS
AEROTHERMAL MODEL DEVELOPMENT, PHASE II										
MASS & MOMENTUM TRANSFER (P&W)										NEW PHYSICAL MODEL AND COMPUTING METHODS
NUMERICAL METHODS (ALLISON, AVCO EVERETT)										
FLOW INTERACTION (ALLISON)										
FUEL SPRAY-FLOWFIELD INTERACTIONS (ALLISON, UTRC)										
NUMERICAL METHODS (U. MINNESOTA)										
MULTIPLE JET DILUTION MIXING (GARRETT)										
FLAME RADIATION/HEAT FLUX										EXIT TEMPERATURE PROFILE
DILUTION JET ANALYSIS										HIGH PRESSURE FLAME RADIATION
DIFFUSER STUDIES (GARRETT) (JOINT WITH AIR FORCE)										JET MIXING MODEL
AEROTHERMAL MODEL DEVELOPMENT, PHASE III										IMPROVED COMBUSTOR-DIFFUSER INTERACTION MODEL
										THERMAL LOADS CHARACTERIZATION

CS 85-3200

## HOST TURBINE HEAT TRANSFER R&T OVERVIEW

Robert J. Simoneau  
NASA Lewis Research Center  
Cleveland, Ohio

As of this reporting the HOST Turbine Heat Transfer Project is in full bloom. Most, if not all, programs are in place and many are bearing fruit. The output, which had begun to mature at the 1984 HOST Workshop, is developing rapidly, as will be seen at the present workshop. The experimental output is leading the analyses slightly, particularly in the nonrotating area (figs. 1 and 2). This situation is somewhat by tradition and somewhat by design.

The experimental part of the turbine heat transfer subproject consists of six large experiments, which will be highlighted in this overview, and three of somewhat more modest scope. Three of the large experiments were conducted in the stationary frame of reference and are at or near completion. One of the first programs was the vane airfoil heat-transfer program being conducted at Allison Gas-Turbine Division in the cascade shown in figure 3. The convectively cooled and shower-head film-cooled data have already been reported and the gill-region film-cooling testing contract is underway. The investigation of secondary flows in a 90° curved duct is underway at the University of Tennessee Space Institute in the rig shown in figure 4. The first phase is complete, and a report is expected soon; the second, higher turbulence phase, is fully operational. Two experiments have been conducted at Lewis in the high-pressure facility (fig. 5). One examined full-coverage film-cooled vanes, and the other advanced instrumentation. Reports on some of the results were published this past year.

Two of the rotating frame experiments are in full production. An experiment to obtain gas-path airfoil heat-transfer coefficients in a rotating machine are underway at United Technologies Research Center in its large, low-speed turbine (fig. 6). The single-stage data with both high- and low-inlet turbulence are nearly complete. In the second phase the turbine will be one and one-half stages, and the focus will be on the second vane row.

Coolant passage data in a rotating frame are being obtained at Pratt & Whitney/United Technologies Research Center in the rig shown in figure 7. The smooth wall data have been obtained, and the turbulator experiments will begin soon.

The final large experiment will be conducted at Lewis in the warm-core turbine shown in figure 8. The turbine, which fully scales a modern turbine stage, is being modified for laser anemometry access to the vane and blade passages. Research will begin in 1987. Once intended to be a step on the way to the high pressure turbine, this rig is now the main verification rig in the turbine heat transfer subproject.

The three smaller and somewhat more fundamental experiments are directed at important mechanisms. Two are at Arizona State University. The first, on impingement cooling, is complete. The second, on tip region simulation, is just beginning. An experiment on the heat-transfer effects of large scale - high-intensity turbulence, similar to that found at combustor exits, is underway at Stanford University.

The analytic efforts in the turbine heat transfer subproject are characterized by efforts to adapt existing codes and analyses to turbine heat transfer. In general these codes and analyses were well established before HOST became involved; however, the applications were not for turbine heat transfer, and extensive work has often been required. In many cases the analytic and experimental work were part of the same contract. Modifications to the well-known STAN5 boundary-layer code were performed at Allison Gas Turbine Division to adjust starting points and transition to accommodate their data both with and without film cooling.

United Technologies Research Center assessed its three-dimensional boundary layer code and modified it to allow for easier application of turbine type inviscid edge conditions. (The report was published this year.) The same code is being modified for use as a two-dimensional unsteady code in order to analyze the rotor-stator interaction data.

The also well-known three-dimensional Navier-Stokes TEACH code has been modified by Pratt & Whitney to incorporate rotational terms. The modified code has been delivered to NASA Lewis and work has begun on it here.

A fully elliptic three-dimensional Navier-Stokes code has been under development at Scientific Research Associates (SRA) for many years. It was primarily directed at inlets and nozzles. SRA, first as subcontractors to Allison Gas Turbine Division and now as a prime contractor, has been modifying the code for turbine applications. This includes grid work for turbine airfoils, improved coding, and improved user friendliness. The code has been installed on the Lewis Cray 1S and a first report on its use for turbine heat-transfer was published this year.

Finally, a fundamental study on numerical turbulence modeling, directed specifically at the airfoil in the turbine environment, is underway at the University of Minnesota.

### TURBINE HEAT TRANSFER SUBPROJECT (1)

EXPERIMENTS	FY										EXPECTED RESULTS
	81	82	83	84	85	86	87	88	89		
NONROTATING:											PROVIDE FUNDAMENTAL EXPERIMENTAL DATA BASES WITH FOCUS ON -
AIRFOIL WITH FILM COOLING <sup>a</sup>											FILM COOLING
CURVED DUCT											SECONDARY FLOWS
IMPINGEMENT COOLING											IMPINGEMENT PATTERN CORRELATIONS
LARGE-SCALE, HIGH-INTENSITY TURBULENCE											COMBUSTOR EXIT SIMULATION
REAL ENGINE ENVIRONMENT											THE REAL ENVIRONMENT
ROTATING:											
LARGE LOW-SPEED TURBINE <sup>a</sup>											ROTOR-STATOR INTERACTION
ROTATING COOLANT PASSAGE <sup>a</sup>											CORIOLIS AND BUOYANCY EFFECTS
TIP REGION SIMULATOR											FLOW ACROSS MOVING AIRFOIL TIP
WARM CORE TURBINE											VANE AND BLADE PASSAGE FLOW MAP FULLY SCALED

<sup>a</sup>EXPERIMENT AND ANALYSIS IN THE SAME CONTRACT

CS-85-3159

Figure 1

### TURBINE HEAT TRANSFER SUBPROJECT (2)

ELEMENT	FY										EXPECTED RESULTS
	81	82	83	84	85	86	87	88	89		
ANALYSES:											ENHANCE ANALYTIC TOOLS FOR TURBINE APPLICATION 1/M
STANS MODIFICATIONS <sup>a</sup>											ADAPT BOUNDARY LAYER CODE TO CURRENT AIRFOIL DATA
3-D BOUNDARY LAYER											ZOOM FOCUS ON 3-D REGIONS
UNSTEADY BOUNDARY LAYER <sup>a</sup>											ACCOUNT FOR ROTOR-STATOR INTERACTION EFFECTS
TEACH CODE WITH ROTATION <sup>a</sup>											3-D NAVIER-STOKES WITH ROTATION TERMS
LOW REYNOLDS NUMBER TURBULENCE MODELING											DEVELOP TURBINE AIRFOIL SPECIFIC TURBULENCE MODEL
MINT CODE <sup>b</sup>											3-D NAVIER-STOKES APPLIED TO TURBINE AIRFOIL GEOMETRY

<sup>a</sup>EXPERIMENT AND ANALYSIS IN THE SAME CONTRACT

<sup>b</sup>WORK DONE UNDER TWO SEPARATE CONTRACTS

CS-85-3160

Figure 2

# **TURBINE VANE HEAT-TRANSFER CASCADE**

(ALLISON GAS TURBINE DIVISION)

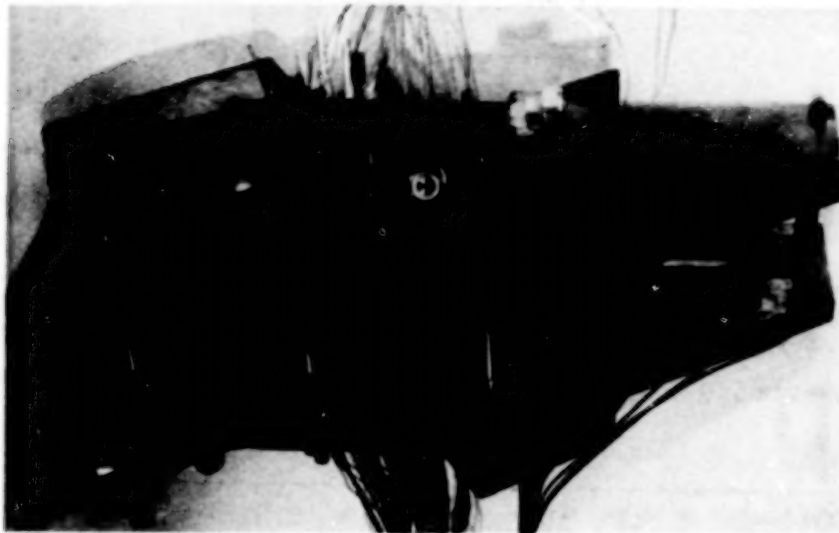


**Figure 3**

# **90° CURVED DUCT FLOW FACILITY**

(UNIVERSITY OF TENNESSEE SPACE INSTITUTE)



**Figure 4**

# HIGH-PRESSURE TURBINE (NASA LEWIS RESEARCH CENTER)

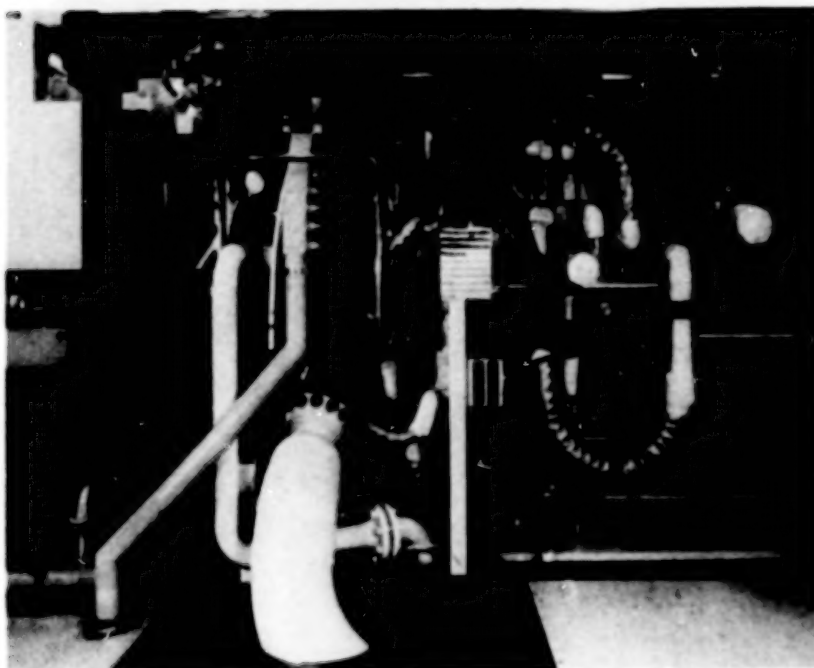


Figure 5

# LARGE LOW-SPEED TURBINE (UNITED TECHNOLOGIES RESEARCH CENTER)



Figure 6

# INTERNAL COOLANT PASSAGE ROTATING RIG

(UNITED TECHNOLOGIES RESEARCH CENTER)

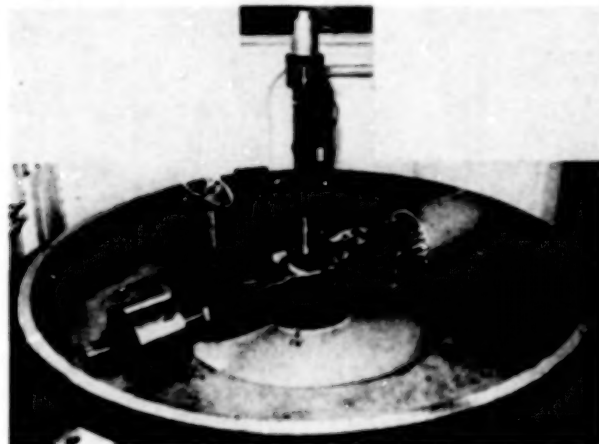


Figure 7

# WARM CORE TURBINE

(NASA LEWIS RESEARCH CENTER)

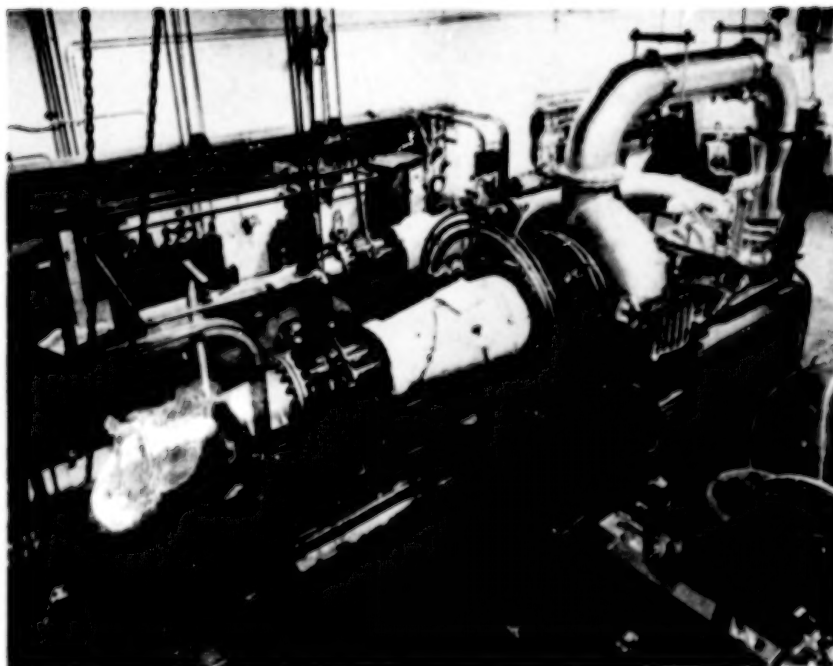


Figure 8

## HOST STRUCTURAL ANALYSIS PROGRAM OVERVIEW

R.L. Thompson  
NASA Lewis Research Center  
Cleveland, Ohio

Hot-section components of aircraft gas-turbine engines are subjected to severe thermal-structural loading conditions, especially during the startup and takeoff portions of the engine cycle. The most severe and damaging stresses and strains are those induced by the steep thermal gradients induced during the startup transient. These transient stresses and strains are also the most difficult to predict, in part because the temperature gradients and distributions are not well known or readily predictable and, in part, because the cyclic elastic-viscoplastic behavior of the materials at these extremes of temperature and strain are not well known or readily predictable.

A broad spectrum of structures-related technology programs is underway to address these deficiencies at the basic as well as the applied level, with participation by industry, and universities, as well as in-house at NASA Lewis. In addition to the HOST structural analysis program, some related program elements are being supported through our base research and technology program. The three key program elements in the HOST structural analysis program are computations, constitutive modeling, and experimentation. These elements are shown in the accompanying schedule and figures.

The computations element of the structures program focuses on developing improved time-varying thermal-mechanical load models for the entire engine mission cycle, from startup to shutdown. The thermal model refinements will be consistent with those required by the structural code, including considerations of mesh-point density, strain concentrations, and thermal gradients. Models will be developed for the burner liner, turbine vane, and turbine blade. One recently developed aspect of this part of the program is a thermal data transfer module which automates the transfer of temperatures from available heat-transfer codes or experimental data sets to the structural analysis code.

Another part of this element is an automated component-specific geometric modeling capability, which will produce three-dimensional finite-element models of the components. Self-adaptive solution strategies will be developed and included to facilitate the selection of appropriate elements, mesh sizes, etc. The development of new and improved, nonlinear, three-dimensional finite elements and associated structural analysis programs, including the development of temporal elements with time-dependent properties to account for creep effects in the materials and component, is another major part of this element.

The second element of the structures program is constitutive modeling. Improved constitutive modeling methods to improve the prediction of cyclic thermomechanical viscoplastic material behavior are being developed for both isotropic and anisotropic materials. The models are then being incorporated in nonlinear, finite-element structural analysis computer programs.

The third element of the structures program is experimentation. Experimental facilities to aid in developing and verifying theories and models as well as to aid in evaluating advanced instrumentation are currently being constructed at Lewis. These include the high temperature structures laboratory for testing tubular specimens and the structural component response test facility for testing plates, cylinders, and combustor liner segments.

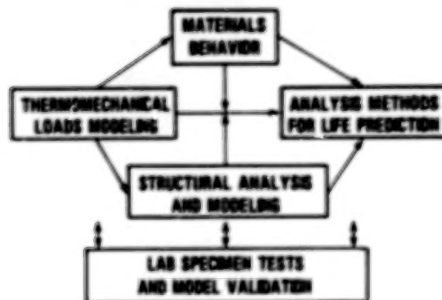
Further explanation and details about the three elements in the structures program mentioned above are given in the Structural Analysis section of this publication.

# STRUCTURAL ANALYSIS...IT'S ROLE IN HOST

## GOAL:

TO DEVELOP AND VALIDATE INTEGRATED TIME-VARYING THERMAL/MECHANICAL LOAD MODELS, COMPONENT-SPECIFIC AUTOMATED GEOMETRIC MODELING AND SOLUTION STRATEGY CAPABILITIES, AND ADVANCED INELASTIC ANALYSIS METHODS AND CONSTITUTIVE MODELS, INCLUDING PLASTICITY AND CREEP EFFECTS, FOR NONLINEAR, ANISOTROPIC, FINITE ELEMENT STRUCTURAL ANALYSIS AND DESIGN COMPUTER CODES.

## PROGRAM INTEGRATION



## PROGRAM ELEMENTS:

- THERMAL/STRUCTURAL DATA TRANSFER MODULE
- THERMAL/MECHANICAL LOAD/MISSION AND COMPONENT-SPECIFIC STRUCTURAL MODELS
- 3-D INELASTIC ANALYSIS METHODS
- CONSTITUTIVE MODELING
- STRUCTURAL COMPONENT RESPONSE RIG
- HIGH TEMPERATURE STRUCTURES LABORATORY

CS-85-3781

Figure 1

## STRUCTURAL ANALYSIS

PROGRAM ELEMENT	FISCAL YEAR							EXPECTED RESULT
	82	83	84	85	86	87	88	
THERMAL DATA TRANSFER	(C)							COMPUTER MODULE LINKING THERMAL AND STRUCTURAL ANALYSES
COMPONENT SPECIFIC MODELING		(C)						COMPONENT-RELATED, TIME VARYING, THERMAL-MECHANICAL LOAD HISTORY AND GEOMETRIC MODELS
3-D INELASTIC ANALYSIS		(C)						ADVANCED 3-D INELASTIC STRUCTURAL STRESS ANALYSIS METHODS AND SOLUTION STRATEGIES
STRUCTURAL COMPONENT RESPONSE	(H)							BURNER STRUCTURAL LIFE EXPERIMENTS
HIGH-TEMPERATURE STRUCTURES LAB		(H)						INTEGRATED EXPERIMENTAL AND ANALYTICAL RESEARCH
MATERIAL BEHAVIOR TECHNOLOGY	(H)							CONSTITUTIVE THEORY AND MODELING METHODS

CS-85-3781

Figure 2

## HOT SECTION COMPONENTS REQUIRING 3-D INELASTIC ANALYSIS

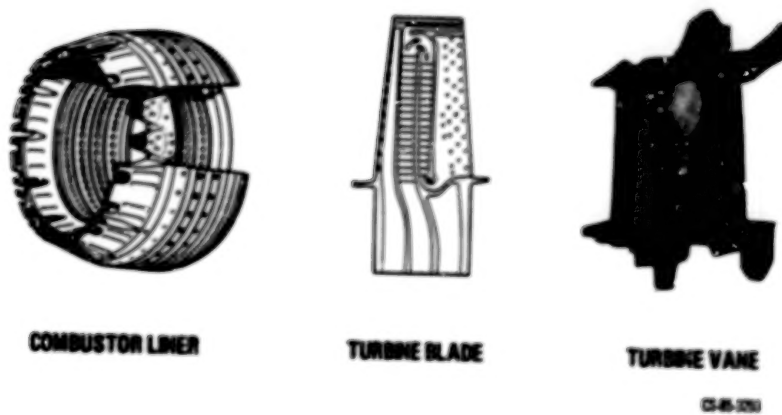


Figure 3

## COMPONENT—SPECIFIC MODELING (HOST)

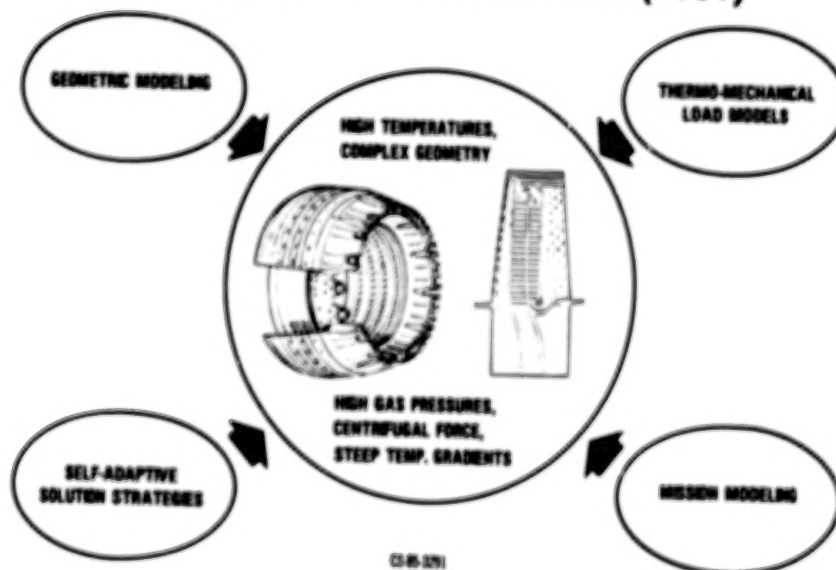


Figure 4

### 3-D INELASTIC ANALYSIS (HOST)

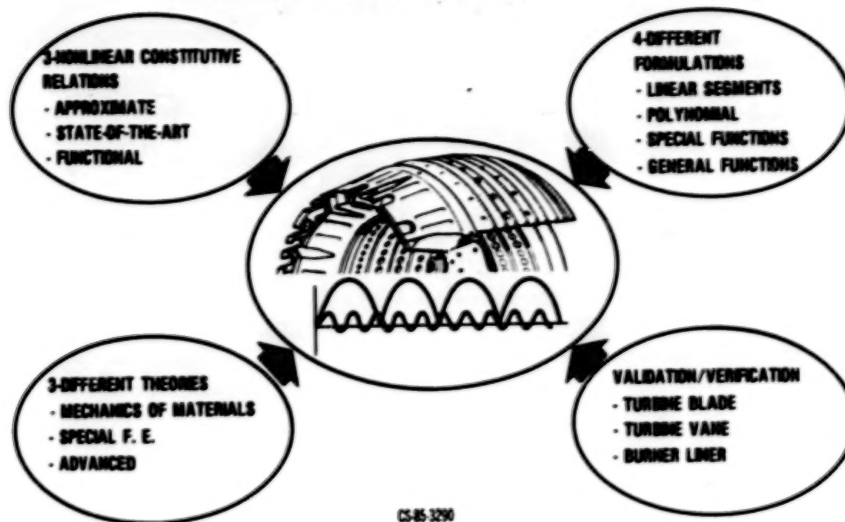


Figure 5

### AUTOMATED HIGH TEMPERATURE STRUCTURES RESEARCH LABORATORY

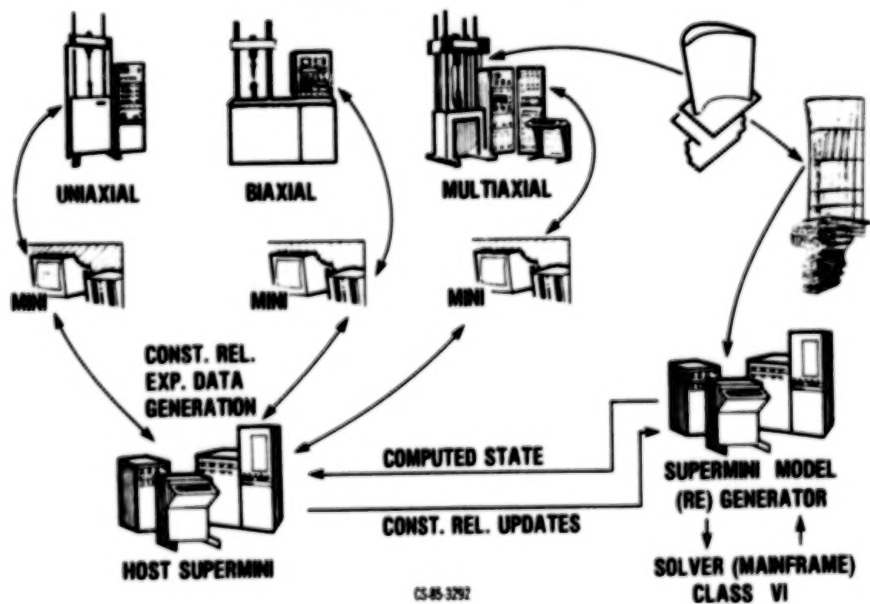


Figure 6

# OVERALL PROGRAM SCHEMATIC FOR 3-DIMENSIONAL TRANCITS (HOST)

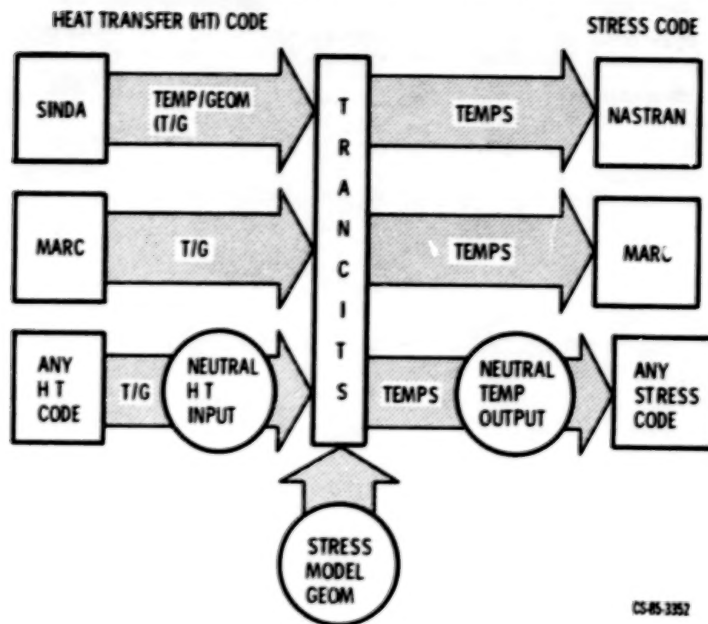


Figure 7

## HOST FATIGUE AND FRACTURE R&T OVERVIEW

G.R. Halford  
NASA Lewis Research Center  
Cleveland, Ohio

All of the contractual, grant, and in-house research programs in the fatigue and fracture discipline of the HOST Project are now producing important new results. Details of the individual efforts will be conveyed by the responsible principal investigators in the fatigue and fracture section of this proceedings. At this point, I would like to give a brief overview of the status of these programs.

The programs involve the development of appropriate analytic material models for cyclic stress-strain-temperature-time behavior and cyclic crack initiation and propagation. It was convenient to divide the research efforts into two camps, depending upon the nominally isotropic or anisotropic mechanical response of the materials. Five industrial contracts with three different research organizations, one university grant, and two in-house programs round out the overall effort.

Figures 1 to 6 are block flow diagrams of the activities within the various programs. The dashed lines drawn through the diagrams indicate the degree of completion of the technical efforts.

I want to emphasize for the fourth year in a row, the underlying thrust of these programs: the development and verification of WORKABLE engineering methods for the calculation, in advance of service, of the local cyclic stress-strain response at the critical life governing location in hot section components and the resultant cyclic crack initiation and crack growth lifetimes.

## FATIGUE & FRACTURE ... IT'S ROLE IN HOST

**GOAL:** DEVELOP AND VERIFY ANALYTIC ENGINEERING MODELS THAT CAN BE USED ON A ROUTINE DESIGN BASIS FOR THE PREDICTION OF CYCLIC STRESS-STRAIN-TEMPERATURE-TIME RESPONSE (I.e., CONSTITUTIVE RESPONSE) AND FATIGUE CRACK INITIATION AND PROPAGATION LIFETIMES OF TURBINE ENGINE HOT SECTION COMPONENTS MADE OF ISOTROPIC OR ANISOTROPIC ALLOYS

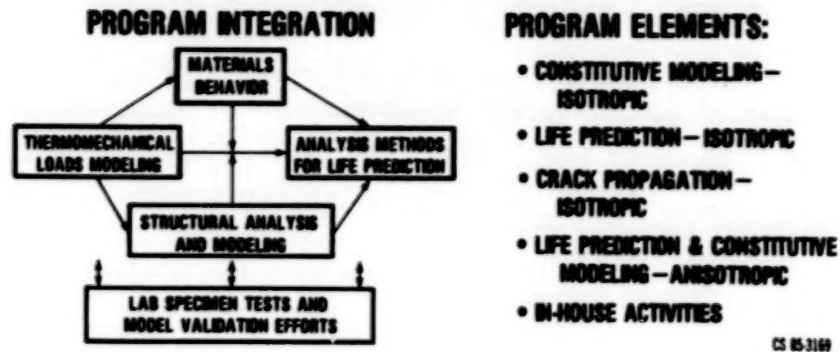


Figure 1

## CONSTITUTIVE MODELING—ISOTROPIC MATERIAL

SOUTHWEST RESEARCH, LINDHOLM; AND GENERAL ELECTRIC, LAFLIN

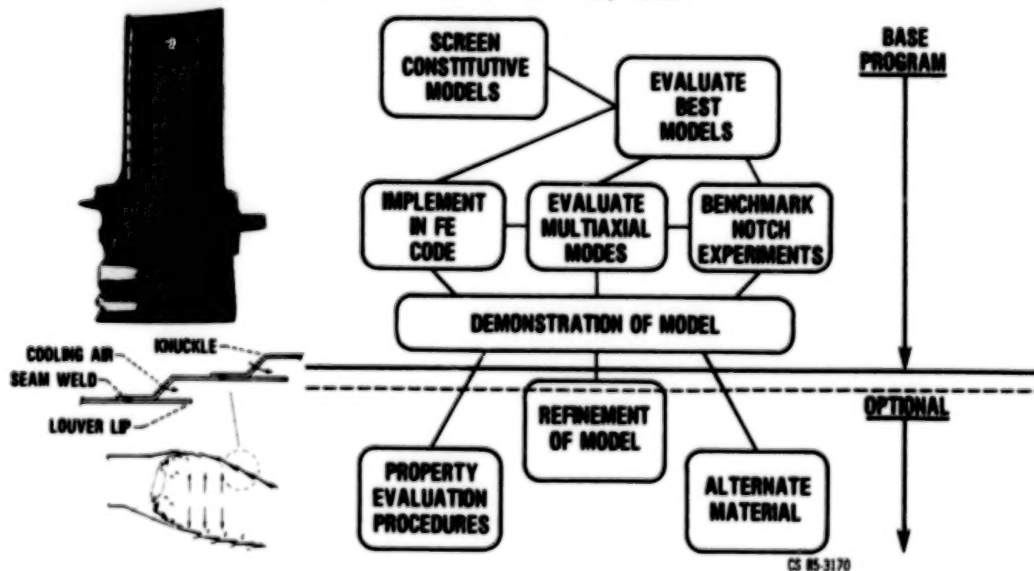


Figure 2

## LIFE PREDICTION—ISOTROPIC MATERIAL

PRATT AND WHITNEY, NELSON

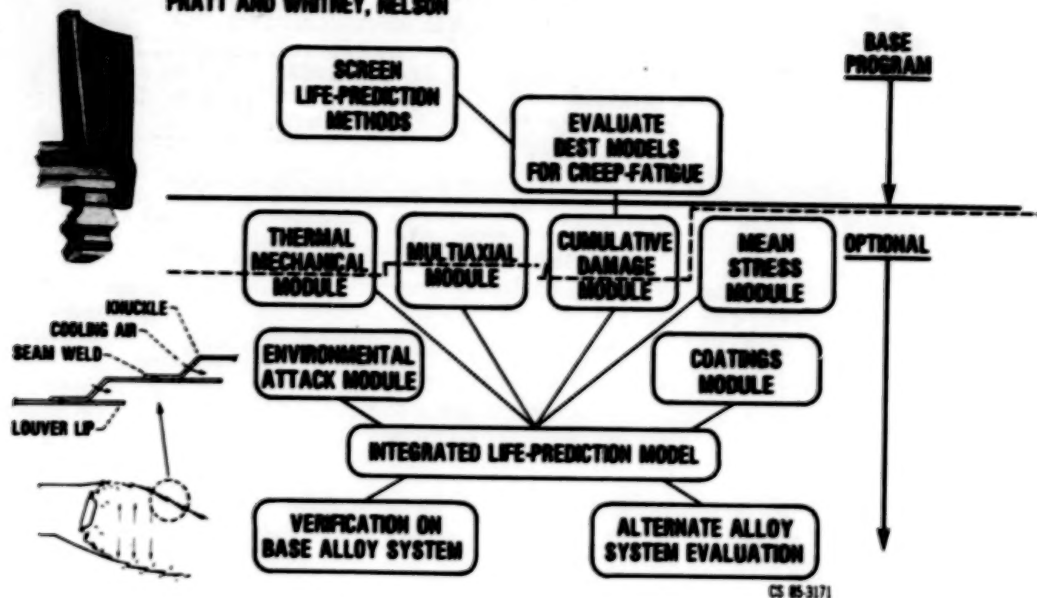


Figure 3

## CRACK PROPAGATION—ISOTROPIC MATERIAL

GENERAL ELECTRIC, LAFLEN

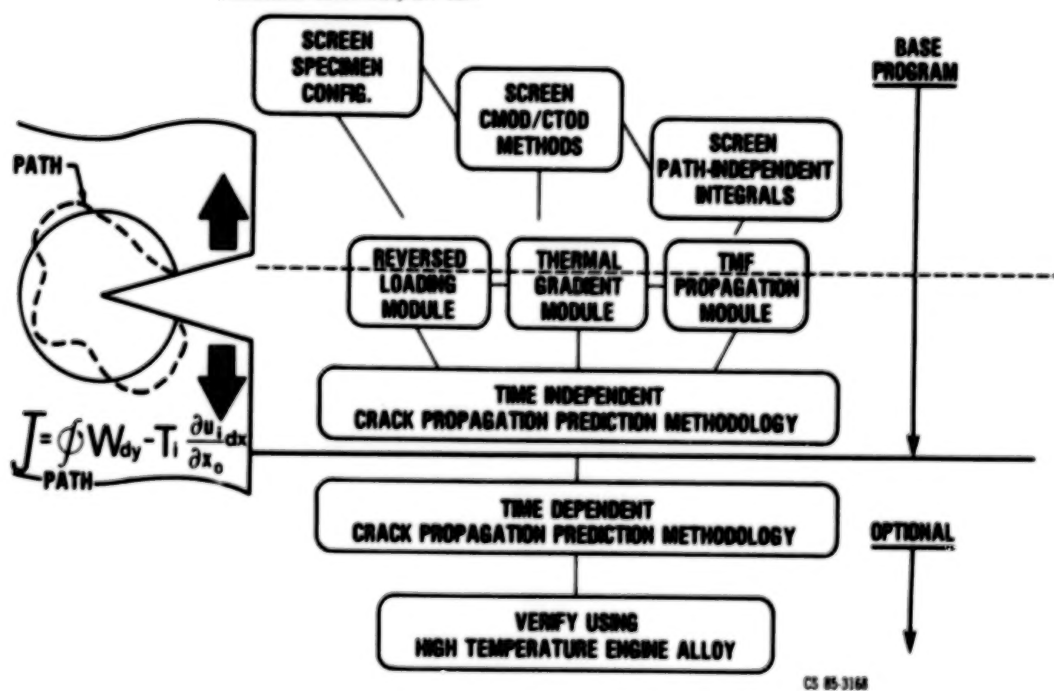


Figure 4

## LIFE PREDICTION & CONSTITUTIVE MODELING-- ANISOTROPIC MATERIAL

PRATT AND WHITNEY, SWANSON

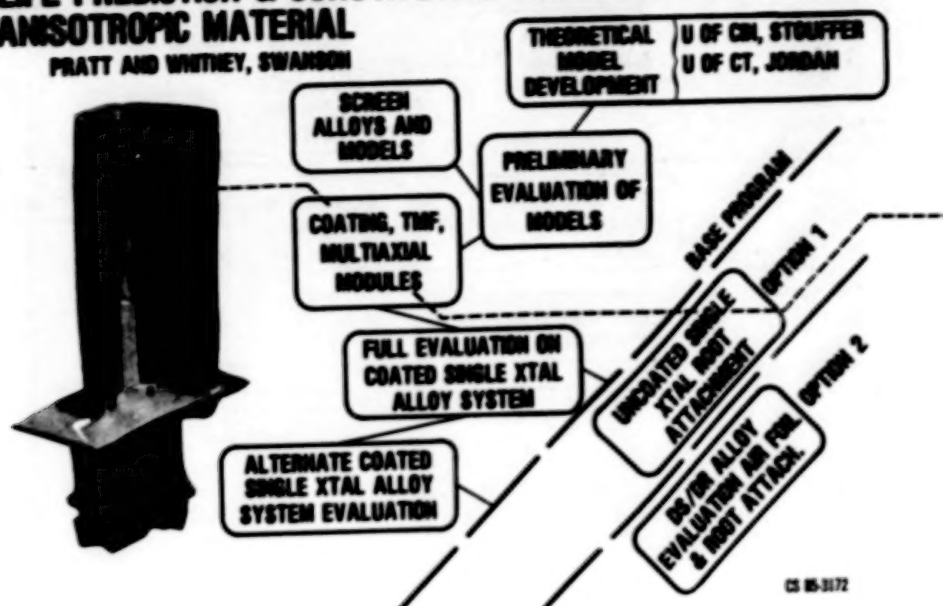


Figure 5

## LEWIS ACTIVITIES

### UPGRADE FATIGUE LABORATORY

McGAW

- HOST/SATELLITE COMPUTER SYSTEM
- EXPANDED HYDRAULIC SYSTEM
- EXPANDED TEST CELL AREA
- CENTRALIZED CONTROL ROOM
- TENSION/TORSION BIAXIAL FATIGUE MACHINES
- HCF/LCF MACHINES FOR CUMULATIVE DAMAGE

• TMF MACHINES

### SINGLE-CRYSTAL/COATING THERMAL MECHANICAL FATIGUE PROGRAM

MIDNER, GAYDA, HALFORD

- PWA 1480 BARE AND COATED
- STAND ALONE COATING
- ISOTHERMAL, [H]THERMAL, THERMOMECHANICAL TESTING
- FUNDAMENTAL APPROACH TO UNDERSTANDING OF CYCLIC FLOW AND CRACKING BEHAVIOR OF COMPLEX ALLOY/COATING SYSTEM

CS 85-3167

Figure 6

## HOST SURFACE PROTECTION R&T OVERVIEW

Carl A. Stearns  
NASA Lewis Research Center  
Cleveland, Ohio 44135

### INTRODUCTION

The hot section of aircraft combustion turbine engines presents a severe chemical environment because of the presence of available oxygen and the favorable kinetics resulting from the high temperatures involved. In addition, the occasional presence of certain air-borne and fuel-borne impurities can contribute further to the severity by being the source of particularly corrosive salt deposits which can produce accelerated and/or catastrophic attack. Such attack degrades system efficiency and reduces component life. A consequence of severe attack is illustrated in figure 1. Obviously, then, one must consider such phenomena as oxidation and corrosion in addition to creep and fatigue responses imposed by mechanical and thermal loads. The interplay of chemical and mechanical response must be understood to adequately design system components. Thus, the goal of the surface protection subproject has been to develop an integrated environmental-attack life-prediction methodology for metal and ceramic hot-section components.

The approach followed considers environmental-attack life-prediction as well as the effects of environment and coatings on mechanical response. As illustrated in figure 2, thermal and mechanical loads are inputs, and the analysis methods result from studies of material behavior in laboratory and engine tests. The major thrusts of the surface protection effort are listed in figure 3 together with the expected results and the anticipated time frame. As a result of the HOST reassessment, the first two thrusts will be terminated in fiscal year 1986. The airfoil deposition model is near completion, and it is expected to predict the location and potential severity of high-temperature corrosion attack. The metallic coating-life prediction effort has made significant progress, but it is not nearly complete or at the goal of being able to predict metallic coating life or the effects of environment and coatings on mechanical response.

The thermal barrier coating (TBC) thrust will continue under HOST as shown in figure 3. This thrust is rapidly progressing, and the effort will yield life-prediction tools to permit use of TBC's in the primary reliant mode. Aggressive use of TBC's places the burden for component integrity on the life of the coating; therefore, the progress of this technology is certainly life-prediction-capability critical. Figure 4 presents further details for each thrust. Note that some elements of the airfoil deposition model will be continued but not under HOST auspices. These elements are critical to the Materials Division's mission; therefore, they will be supported as part of the base R&T effort.

### AIRFOIL DEPOSITION MODEL

The goal, approach, and status of the airfoil deposition model thrust are set forth in figures 5 and 6. Air- and fuel-borne impurities can be collected on stationary or rotating airfoils by vapor deposition and particle impaction

mechanisms. Such salt deposits can be depleted by evaporation, shedding, or molten salt flow. The purpose of the deposition model is to account for the local temporal inventory of molten salt as an input to the coating life-prediction model. The airfoil deposition model is being developed, via grant, by Professor Dan Rosner and coworkers at Yale. Model verification is being carried out at Lewis in Mach 0.3 burner rig tests and ultimately in a high-pressure burner rig. This effort is supported by the work of Dr. S. Gökoglu at Lewis. In parallel with the model development, Lewis' burner rig facilities are being modernized in support of this and other HOST activities.

To date, the works of Rosner and Gökoglu, and their coworkers have been documented by numerous publications in the open literature (refer to their workshop papers for references) which describe the initial airfoil deposition model and its verification.

As shown in figure 7, a key feature of the surface protection subproject is to verify the airfoil deposition model and there thermal barrier coating failure mechanism and life-prediction models in a simulated engine environment. This will be accomplished in the high-pressure burner rig facility at Lewis. Key features of this facility are described in figure 8. This rig is very nearly operational and should be available for testing in the near future. Of course, some initial effort will have to be expended to determine the magnitude of heat flux available.

#### METALLIC COATING LIFE PREDICTION

As shown schematically in figure 9, metallic coatings protect structural alloys from the environment by providing a reservoir of a protective oxide-scale-forming element, for example, an aluminum bearing alloy which is selectively oxidized to form aluminum oxide. Aluminum is depleted by oxidation and thermal-cycle-induced oxide-scale spallation. Aluminum is also diluted by interdiffusion with the substrate. Exposure to corrosive salts may lead to hot-corrosion attack of the oxide scale and coating. Finally, the coating must withstand thermal-mechanical loads without degrading system mechanical response.

The metallic coating-life prediction thrust deals with both the chemical and mechanical aspects of the problem. The goal, approach, and status for this thrust are presented in figures 9 and 10. An oxidation/diffusion life model is being developed at Lewis by building on existing interdiffusion and cyclic oxidation/spalling models developed for special alloy systems. This task has proven more difficult than envisioned due to spall measurement problems. The hot corrosion efforts, one in-house and one via contract with General Electric, were initiated in fiscal year 1983. All three efforts were scheduled to culminate in a contractual life-prediction integration and verification effort, but the HOST reassessment has resulted in their termination in fiscal year 1986.

The roles of the environment and coatings on the mechanical responses of isotropic and anisotropic materials are being addressed by our support of contract efforts managed through the fatigue and fracture subproject.

#### THERMAL BARRIER COATING LIFE PREDICTION

Thermal barrier coatings are finding increasing use in noncritical gas-turbine applications to extend component life. Present coatings suffer from limited coating

life and inadequate design capability when considered for more critical applications such as turbine airfoils. As illustrated in figure 11, both life prediction and advanced coatings are vital to the future use of TBC on airfoils for large improvement in system performance. The TBC life prediction thrust has become the major thrust of the surface protection subproject. The goal, approach, and status are described in figures 12 and 13.

The mechanical behavior effort is a grant with Professor George Chang at Cleveland State University. The core effort involves parallel, complementary contracts with Garrett Turbine Engine Company, General Electric, and Pratt & Whitney Aircraft. These contracted efforts build on our research and technology base failure mechanisms research and are supported by parallel in-house high-heat-flux tests. All three contractors are investigating their current advanced plasma-sprayed TBC, which consists of a low-pressure plasma-sprayed MCrAlY bond coat and an air-plasma-sprayed yttria partially stabilized zirconia ceramic layer. In addition, Garrett is conducting a parallel effort involving a vapor-deposited zirconia layer.

#### CONCLUDING REMARKS

The past year has been one of considerable progress for the HOST surface protection subproject and some major accomplishments are listed in figure 14. Deposition theory has really matured and many valuable insights have derived from the theoretical effort. Verification of the vapor-deposition theory in burner rigs has provided a new tool and certainly better understanding of burner-rig hot-corrosion testing. Metallic coating life-prediction efforts have succeeded in modeling cyclic furnace oxidation degradation of overlay coatings. Finally, the role of oxidation in TBC life is becoming understood, and preliminary life models are evolving. Details of the surface protection program are contained in the papers covering each major program element.

## HIGH TEMPERATURE ENVIRONMENTAL ATTACK



- REDUCES EFFICIENCY
- LIMITS LIFE
- COSTS \$

Figure 1

## SURFACE PROTECTION ... IT'S ROLE IN HOST

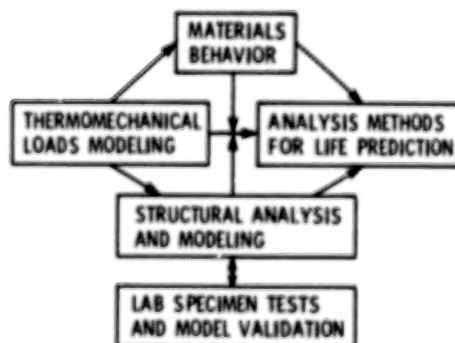
### GOAL

DEVELOP AN INTEGRATED ENVIRONMENTAL  
ATTACK LIFE PREDICTION METHODOLOGY  
FOR METAL AND CERAMIC COATED HOT  
SECTION COMPONENTS

### PROGRAM ELEMENTS

- AIRFOIL DEPOSITION MODEL
  - MODEL
  - MODEL VERIFICATION
  - RIG/ENGINE CORRELATION
  - BURNER RIG MODERNIZATION
- METALLIC COATING LIFE PREDICTION
  - ENVIRONMENT/MECH. PROP. INTERACTIONS
  - OXIDATION/DIFFUSION
  - HOT CORROSION SURFACE CHEMISTRY
  - OXIDATION/CORROSION ATTACK
  - LIFE PREDICTION VERIFICATION
- THERMAL BARRIER COATINGS
  - LIFE PREDICTION
  - MECHANICAL BEHAVIOR
  - RIG/ENGINE CORRELATION

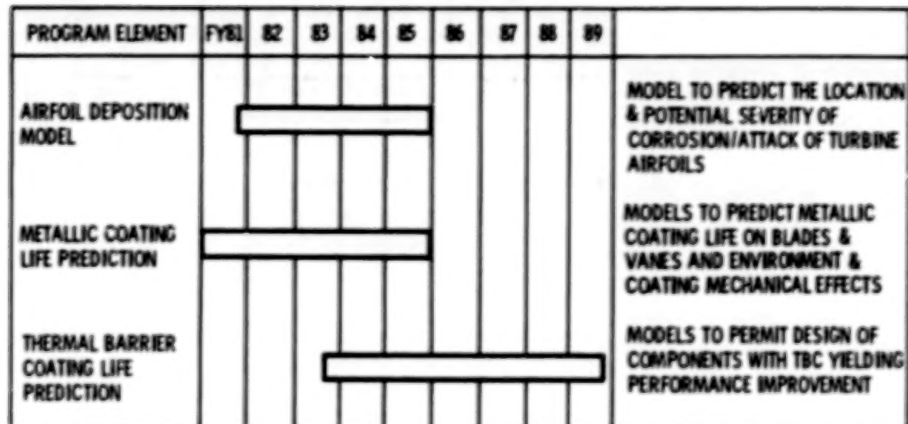
### PROGRAM INTEGRATION



CS 85-3186

Figure 2

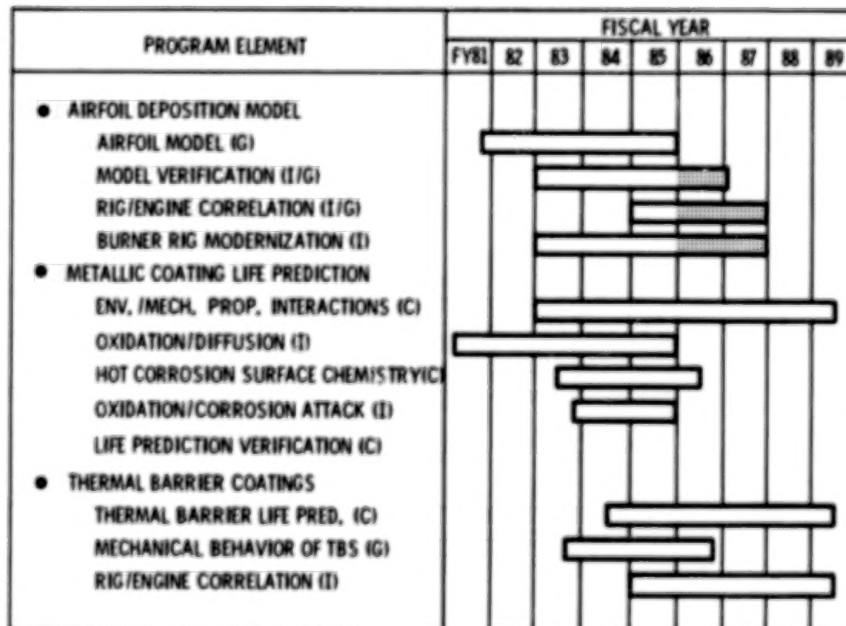
## SURFACE PROTECTION



CS 85-3175

Figure 3

## SURFACE PROTECTION



CS 85-3177

Figure 4

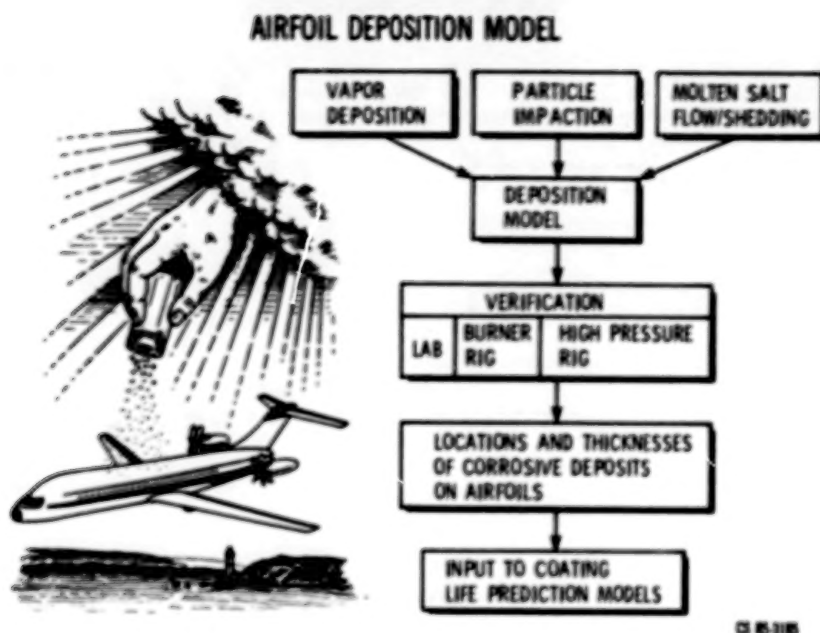


Figure 5

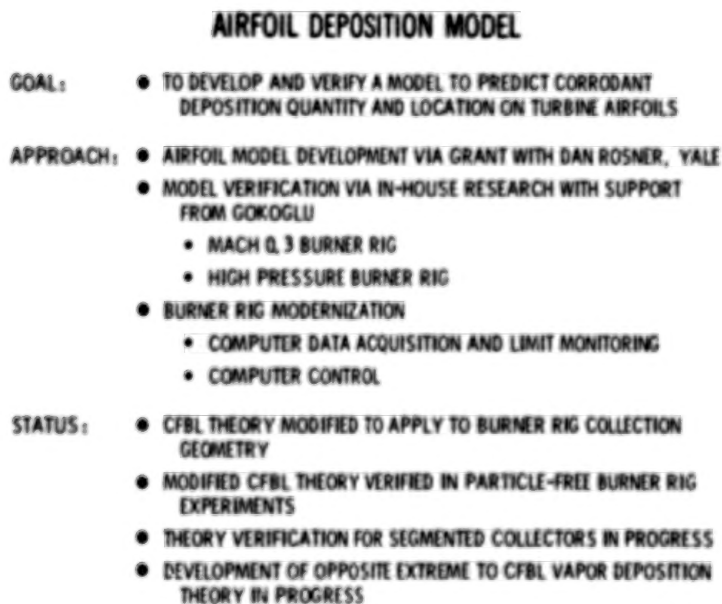


Figure 6

## RIG/ENGINE CORRELATION

**GOAL:** PROVIDE A UNIQUE AND RELATIVELY INEXPENSIVE LABORATORY TO AID IN THE DEVELOPMENT OF ENVIRONMENTAL ATTACK LIFE PREDICTION TOOLS FOR HOT SECTION MATERIALS

**APPROACH:** VERIFY ADVANCES MADE IN THE LIFE PREDICTION OF HOT SECTION MATERIALS AT PRESSURE LEVELS ENCOUNTERED IN GAS TURBINE ENGINES

- VERIFY DEPOSITION THEORY AND DEW POINT EFFECT IN THE DEPOSITION OF  $H_2SO_4$  CORRODANT AT ELEVATED PRESSURES
- DETERMINE THE EFFECT OF HIGH HEAT FLUXES ON THE LIFE OF THERMAL BARRIER COATINGS

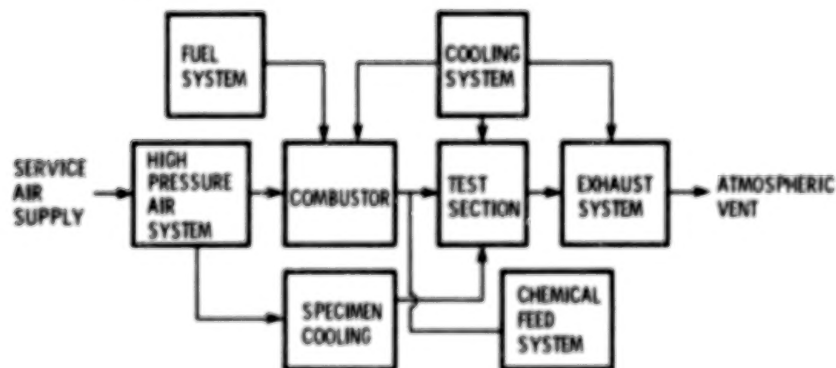
**STATUS:** CHECKOUT COMPLETE  
OPERATIONAL ENVELOPE BEING ESTABLISHED AND SYSTEM "BUGS" BEING ELIMINATED

CS 85-2182

Figure 7

## HIGH PRESSURE BURNER RIG FACILITY

### BLOCK FLOW DIAGRAM



### TEST SECTION SPECIFICATIONS

- SAMPLE TEMPERATURES TO 3000 °F
- PRESSURES TO 50 ATM
- VELOCITIES TO >MACH 2.0
- CYCLIC CAPABILITY
- INDEPENDENT SAMPLE TEMPERATURE CONTROL
- MASS FLOW TO 2 lb/sec

CS 85-2181

Figure 8

## METALLIC COATING LIFE PREDICTION

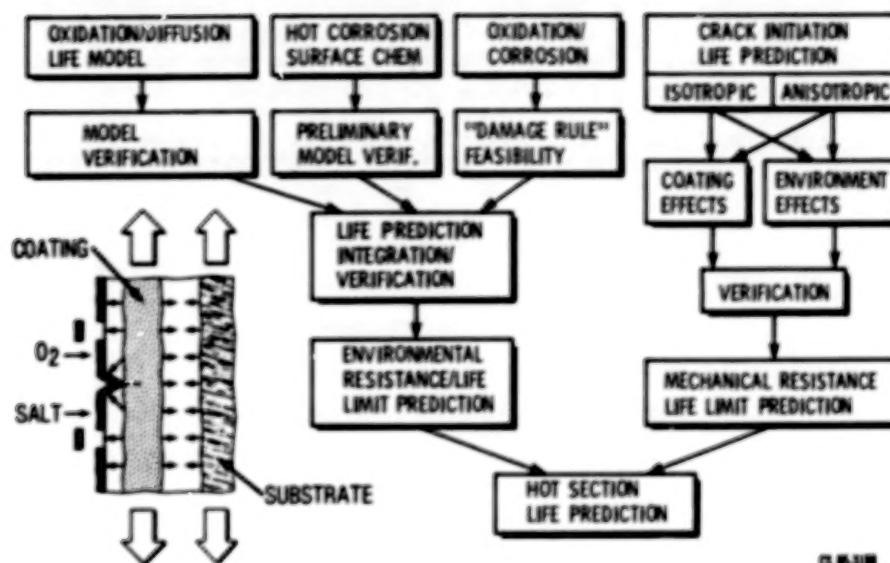


Figure 9

## METALLIC COATING LIFE PREDICTION

- GOAL:**
- TO DEVELOP A COATING LIFE MODEL FOR OXIDATION, SPALLING, HOT CORROSION, AND COATING/SUBSTRATE DIFFUSION AND ACCOUNT FOR ENVIRONMENTAL AND COATING EFFECTS ON MECHANICAL RESPONSE
- APPROACH:**
- ENVIRONMENT/MECHANICAL PROPERTY INTERACTIONS
    - SUPPORT CONTRACT EFFORTS MANAGED BY FATIGUE AND FRACTURE SUBPROJECT
  - OXIDATION/DIFFUSION LIFE PREDICTION (IH)
    - INTEGRATE CYCLIC OXIDATION SPALLING PREDICTION AND COATING/SUBSTRATE INTERDIFFUSION MODELS FOR COATED SUPERALLOY AND VERIFY
  - HOT CORROSION SURFACE CHEMISTRY (IG/TRW)
    - ASSESS EFFECTS OF AGING ENVIRONMENT AND HOT CORROSION LIFE FOR VARIOUS COATING/ALLOY SYSTEMS AS A BASIS FOR PROPOSING AND VERIFYING A LIFE MODEL
  - OXIDATION/HOT CORROSION DUAL CYCLE ATTACK (IH)
    - DETERMINE FEASIBILITY OF AN EMPIRICAL LINEAR DAMAGE MODEL FOR OXIDATION/MILD HOT CORROSION ATTACK OF COATED SUPERALLOY
  - LIFE PREDICTION VERIFICATION (IC)
    - INTEGRATE RESULTS INTO A MISSION SIMULATION PREDICTION MODEL AND VERIFY
- STATUS:**
- ISOTHERMAL AND CYCLIC FURNACE OXIDATION OF ALUMINUM AND LPPS NiCoCrAlY COATED U-700 COMPLETED
  - OVERLAY COATING DEGRADATION DURING CYCLIC FURNACE OXIDATION SUCCESSFULLY MODELED

Figure 10

## STRONG HOST SUPPORT VITAL TO TBC PROGRESS

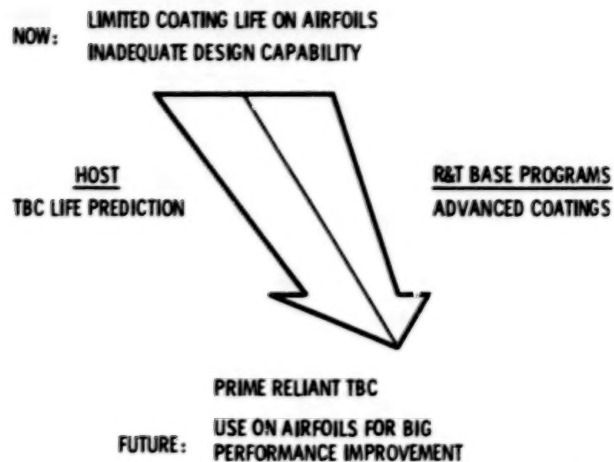


Figure 11

## THERMAL BARRIER COATING LIFE PREDICTION

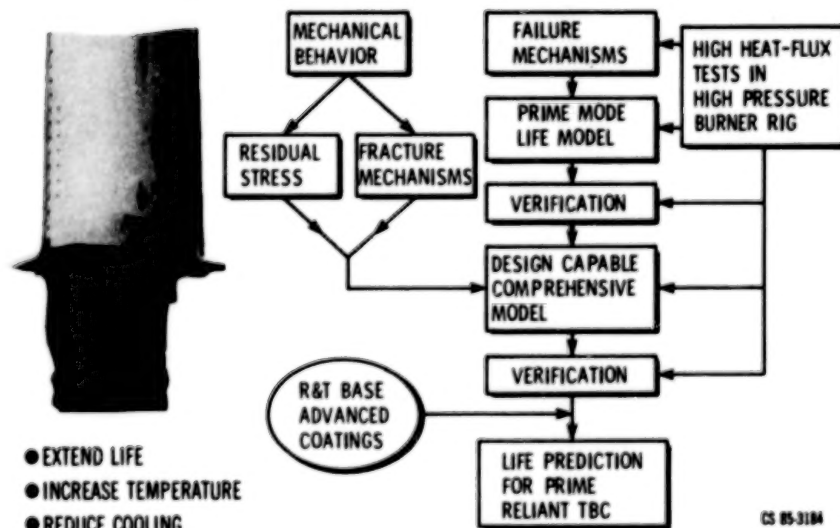


Figure 12

## THERMAL-BARRIER-COATING LIFE PREDICTION

GOAL: TO DEVELOP AND VERIFY LIFE PREDICTION METHODOLOGIES  
FOR THERMAL BARRIER COATINGS (TBC)

APPROACH: TBC LIFE PREDICTION MODEL DEVELOPMENT (C)

- PHASE I: FAILURE ANALYSIS AND PRELIMINARY  
MODEL (MULTIPLE CONTRACTS)
- PHASE II: DESIGN CAPABLE MODELS (TBD)

MECHANICAL BEHAVIOR OF TBC (G-JIAPP/CSU)

- FRACTURE MECHANISMS (C. BERNDT, ON-SITE)
- RESIDUAL STRESS MODELING (G. CHANG, CSU)
- RIG AND ENGINE CORRELATION (I) - HIGH-HEAT-  
FLUX TESTS IN HIGH-PRESSURE BURNER RIG TO  
COMPLEMENT CONTRACT EFFORT
- FAILURE MECHANISMS
- MODEL VERIFICATION

STATUS: PRELIMINARY LIFE MODEL UNDER DEVELOPMENT

CS 85-3181

Figure 13

## SURFACE PROTECTION FY85 ACCOMPLISHMENTS

- CFBL VAPOR DEPOSITION THEORY HAS BEEN VERIFIED IN  
STANDARD BURNER RIG TESTING
- TURBINE AIRFOIL DEPOSITION MODELS HAVE BEEN DEVELOPED  
AND THEIR HOT-CORROSION IMPLICATIONS HAVE BEEN  
DETAILED
- THE HIGH-PRESSURE-BURNER-RIG FACILITY HAS BEEN COM-  
PLETED
- BURNER-RIG MODERNIZATION HAS BEEN PROTOTYPED
- OVERLAY COATING DEGRADATION DURING CYCLIC FURNACE  
OXIDATION HAS BEEN MODELED
- ROLE OF OXIDATION IN TBC LIFE HAS BEEN ELUCIDATED
- INITIAL LIFE MODELING FOR TBC'S HAS BEEN POSTULATED

CS 85-3179

Figure 14

## Further Development of The Dynamic Gas Temperature Measurement System\*

D. L. Elmore, W. W. Robinson, W. B. Watkins  
Pratt and Whitney Engineering Division  
West Palm Beach, Florida 33402

### SUMMARY

Two experiments for verifying the frequency response of a previously-developed dynamic gas temperature measurement system have been performed. The first involves a rotating wheel and gas manifolds alternately introducing heated and ambient air to the sensors. The second involves a high-temperature atmospheric pressure burner which produces a wide band temperature spectrum. In both experiments, fine-wire resistance temperature sensors were used as standards, and the compensated dynamic temperature sensor data will be compared with the standards to verify the compensation method. In the rotating wheel experiment, knowledge of the air supply temperatures and repetition frequency provides an additional check on the compensated data. In the burner experiment redundant sensors were employed, and uncompensated data from different combinations of sensors will be used in the compensation algorithm. The two experiments are described in detail. A short description of the numerical compensation method and software revisions in the past year are described.

### INTRODUCTION

The measurement system developed in reference 1 uses a compensated two-element thermocouple probe. The compensation technique uses the ratio of signal amplitudes from the two thermocouples' passive responses to gas temperature variations. Comparisons with a numerical heat transfer model allow compensation of temperature fluctuations to above 1KHz. Two-element sensors were used in atmospheric pressure burners and gas turbine engines in reference 1, and demonstrated durability required for these test environments. In addition, compensated data were generated.

The objectives of the present program are to: 1) verify experimentally the frequency response of the dynamic gas temperature measurement system; 2) optimize the computer compensation method for execution speed; and 3)

\* Work performed under NASA Contract NAS3-24228

to implement the reference 1 computer code in Fortran IV for use on generally available computers.

The program is organized into four basic tasks including (1) frequency response experimental verification; (2) compensation code execution streamlining; (3) implementation of the compensation code in Fortran IV; and (4) data acquisition at NASA Lewis Research Center. This progress report will describe progress since the October 1984 HOST meeting (reference 2). Efforts in tasks 2 and 3 are complete. The experiments of task 1 have been performed and data analysis is underway. The numerical compensation method has been streamlined for execution on an IBM3081 computer in Fortran.

#### FREQUENCY RESPONSE VERIFICATION EXPERIMENTS

Reference 2 describes twelve conceptual experiments for verifying the measurement system compensation system. From the twelve, two were selected for detailed design, fabrication and execution. Both set-ups have capability to generate minimum peak-to-peak fluctuations of 278K (500°F) at Mach numbers greater than 0.1 and frequency content to 250Hz. The experiments are described in detail below.

##### Rotating Wheel

The rotating wheel experiment consists of a hot gas manifold supplying 568K (563°F) air, a cold gas manifold supplying ambient air at 291K (63°F), a wheel with eight holes in the periphery, a bifurcated collection manifold, and the dynamic temperature sensor (Figure 1). The wheel is driven by an electric motor at rotation rate  $N$  revolutions per second. The hot gas and adjacent ambient air manifolds exhaust into the plane of the wheel such that one opens into a hole on the wheel and the gas is collected by one leg of the collection duct as the other manifold and collection duct leg are blocked. Then, as the hole rotates beneath the adjacent manifold, its gas flows to the second leg of the bifurcation duct, and the first gas supply is blocked. The common leg of the collection duct in turn exhausts alternate hot and ambient air streams onto the dynamic temperature sensor. The resultant flow generated consists of an approximate square wave pulse train of frequencies from 20Hz to 250Hz and peak to peak amplitude of the hot air supply temperature minus the ambient air supply temperature.

The dynamic temperature sensor and a fine-wire anemometer resistance thermometer are mounted in the collection duct discharge stream. The fine wire anemometer is used as a temperature measurement standard. Uncompensated frequency response of the fine wire thermometer was computed from a

theoretical model, the probe geometry, and the gas path parameters to be approximately 350Hz (1st order response). An existing Pratt and Whitney-designed analog compensation amplifier was set up to provide the inverse function (1st order RC high pass filter with  $F_c = 350\text{Hz}$ ) for use in extending the frequency roll-off of the sensor. Dynamic temperature sensor and fine wire thermometer data were recorded on FM tape. The dynamic temperature sensor data will then be compensated using the method described in reference 1. Comparison between the fine wire resistance signals, known frequency and amplitude inputs generated by the apparatus, and the compensated dynamic temperature sensor signals will then be made.

Figures 2 through 4 show three views of the experiment. Figure 5 shows the two-wire dynamic temperature sensor used in these experiments. The two-wire sensor consists of two thermocouple elements constructed using Type K material. The junctions were formed using a technique that produces no bead and thus a uniform cylindrical cross section, which simplifies the analysis and compensation. The two elements were fabricated using  $76\text{ }\mu\text{m}$  (.003 inch) and  $254\text{ }\mu\text{m}$  (.010 inch) diameter wire. The support wires are  $381\text{ }\mu\text{m}$  (.015 inch) and  $508\text{ }\mu\text{m}$  (.020 inch) in diameter. The probe was inspected prior to testing to determine actual dimensions and the results are presented in Figure 6.

#### Atmospheric Pressure Burner

Measurements taken under the previous contract (reference 1) characterized the atmospheric burner flowfield as having large ( $> 500^\circ\text{F}$  p-p) temperature fluctuations. Verification of the compensation algorithm using burner data by compensating both small ( $76\text{ }\mu\text{m}$ ) and large ( $254\text{ }\mu\text{m}$ ) thermocouple signals and comparing results was done. This comparison is to be extended under this effort by adding an intermediate size thermoelement ( $127\text{ }\mu\text{m}$ ) and a fine-wire resistance thermometer. Compensations then may be done with three combinations of thermocouples:  $76\text{ }\mu\text{m}$ - $254\text{ }\mu\text{m}$ ;  $76\text{ }\mu\text{m}$ - $127\text{ }\mu\text{m}$ ; and  $127\text{ }\mu\text{m}$ - $254\text{ }\mu\text{m}$ . Compensated spectra for the three pairs may also be compared with the fine-wire resistance thermometer.

The dynamic temperature sensors shown in Figure 7 consist of one probe with  $127\text{ }\mu\text{m}$  (.005 inch) and  $254\text{ }\mu\text{m}$  (.010 inch) diameter elements and another probe with a single  $76\text{ }\mu\text{m}$  (.003 inch) diameter element. The elements were constructed with Type B thermocouple material and have beadless junctions. The probes tested were inspected and the results are shown in Figure 8. The fine-wire resistance thermometer was fabricated using  $8.3\text{ }\mu\text{m}$  (.00025 inch) and  $12.7\text{ }\mu\text{m}$  (.0005 inch) diameter elements.

Figure 9 is a diagram of the burner setup. The dynamic temperature sensors, a fine wire resistance thermometer, and a total pressure impact tube were mounted together to obtain a close spatial relationship as shown in Figure 10. The sensors were then mounted downstream of the burner which was run at the minimum operating combustion temperature due to the structural limits of the fine-wire thermometer sensor. Figure 11 is a photograph of the experiment with approximately 1367K (2000°F) flowfield. The sensors were located approximately 28 cm (11 inches) from the burner nozzle exit plane.

#### COMPUTER CODE OPTIMIZATION

Task 2, involving compensation code execution streamlining, and Task 3, involving implementation of the compensation code in Fortran, are both complete. The reference 1 numerical method calculates thermocouple response at several frequencies, and the compensation spectrum is obtained by cumulating results of several calculations (Figure 12). This approach was originally implemented on a Hewlett-Packard 5451C Fourier Analyzer, and reprogramming into Fortran and optimization for execution time was required for practical, repeated use. The reference 1 approach was retained in the reprogramming software. Execution time for a typical data set was reduced to about 3 minutes of IBM 3081 computer time as compared with about 2 hours on the HP5451C. The upgraded compensation software is now in routine use, and will be used to compensate data from the previously described experiments.

#### DATA ANALYSIS

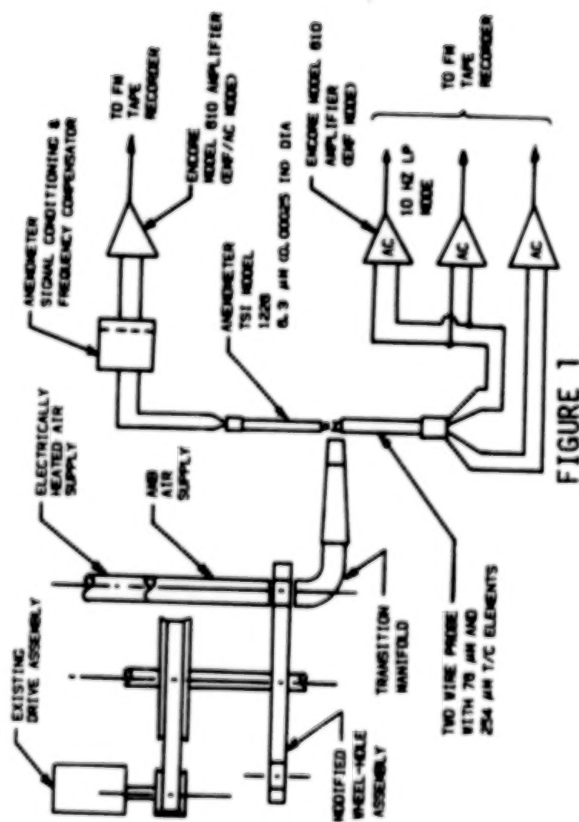
Data taken in the two experiments described above will be analyzed and results will be presented at the next HOST meeting.

#### REFERENCES

1. Elmore, D.L., Robinson, W.W., and Watkins, W.B., "Dynamic Gas Temperature Measurement System", NASA CR-168207 (May, 1983). This work is summarized in ISA Transactions 24, No. 2, P. 73-82.
2. Elmore, D.L., Robinson, W.W., and Watkins, W.B., "Further Development of the Dynamic Gas Temperature Measurement System", in Turbine Engine Hot Section Technology, NASA CP-2339 (October, 1984).

## ROTATING WHEEL EXPERIMENT

### Test Configuration



## ROTATING WHEEL EXPERIMENT

### Test Apparatus - Wheel/Manifold Detail



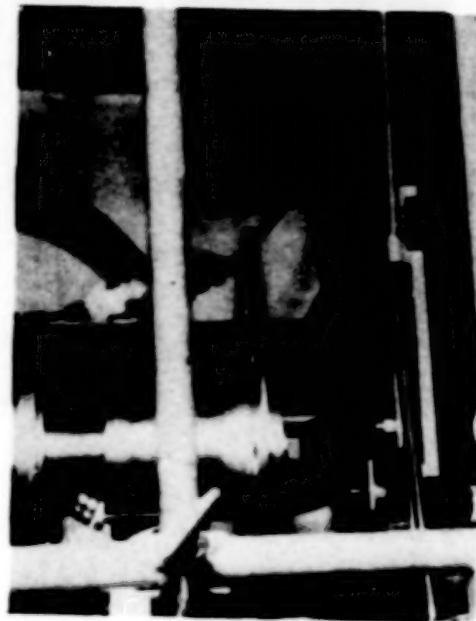
## ROTATING WHEEL EXPERIMENT

**Test Apparatus - Overall View**



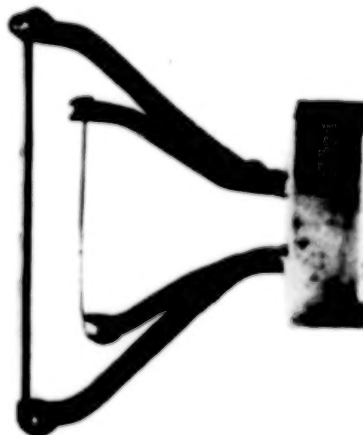
## ROTATING WHEEL EXPERIMENT

### Test Apparatus - Probe Detail



# ROTATING WHEEL EXPERIMENT PROBE

As Fabricated

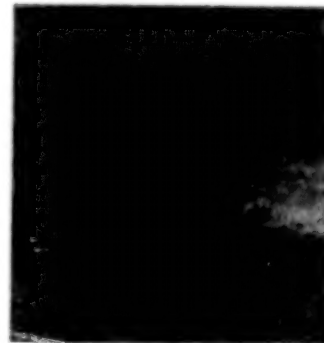


ORIGINAL PAGE IS  
OF POOR QUALITY

FIGURE 5

## LABORATORY BURNER PROBE

SINGLE WIRE ASSEMBLY  
AS FABRICATED



TWO WIRE ASSEMBLY  
AS FABRICATED

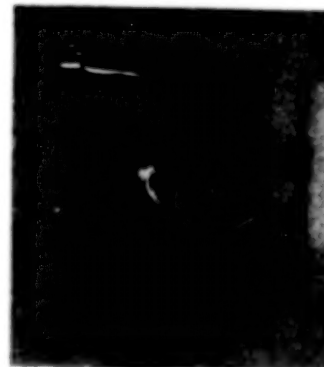


FIGURE 7

## PROBE PRE-TEST INSPECTION SUMMARY

Rotating Wheel Experiment

DIM	PRINT μm (IN)	MEASURED μm (IN)
A	76.2 (0.003)	71.78 (0.0028260)
B	254 (0.010)	245.92 (0.0096425)
C	4572 (0.180)	4826 (0.190)
D	5842 (0.230)	6604 (0.260)
E	3810 (0.150)	3810 (0.150)
F	7620 (0.300)	7620 (0.300)
G	508 (0.020)	508 (0.020)
H	381 (0.015)	381 (0.015)

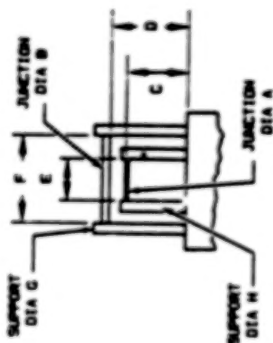


FIGURE 6

## PROBE PRE-TEST INSPECTION SUMMARY

Laboratory Burner Experiment

DIM	PRINT μm (IN)	MEASURED μm (IN)
A	76.2 (0.003)	732 (0.0029)
B	127 (0.005)	1236 (0.0049)
C	254 (0.010)	2491 (0.0098)
D	2540 (0.100)	3574 (0.1407)
E	3810 (0.150)	3709 (0.146)
F	5080 (0.200)	5055 (0.199)
G	2286 (0.090)	2591 (0.102)
H	3556 (0.140)	3556 (0.140)
I	5080 (0.200)	5131 (0.202)
J	381 (0.015)	381 (0.015)
K	381 (0.015)	381 (0.015)
L	508 (0.020)	508 (0.020)

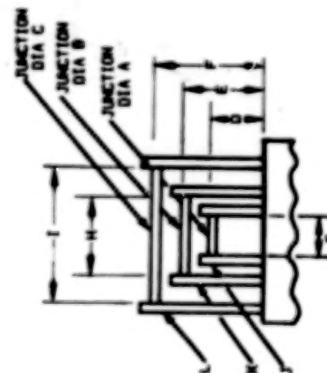


FIGURE 8

# LABORATORY BURNER EXPERIMENT

Test Configuration

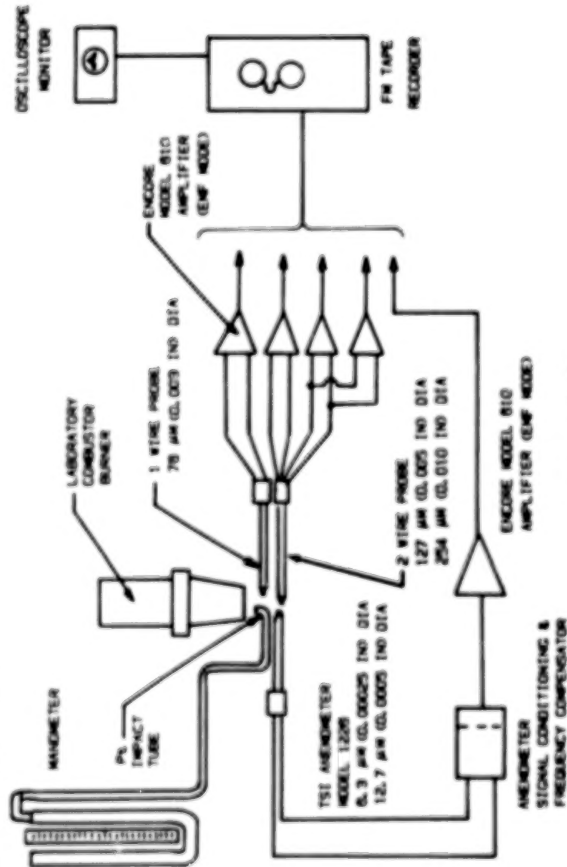


FIGURE 9

# LABORATORY BURNER EXPERIMENT

Test Firing

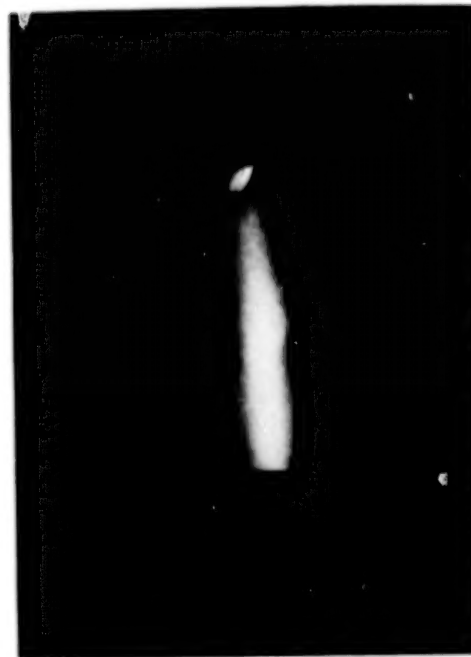


FIGURE 11

# LABORATORY BURNER EXPERIMENT

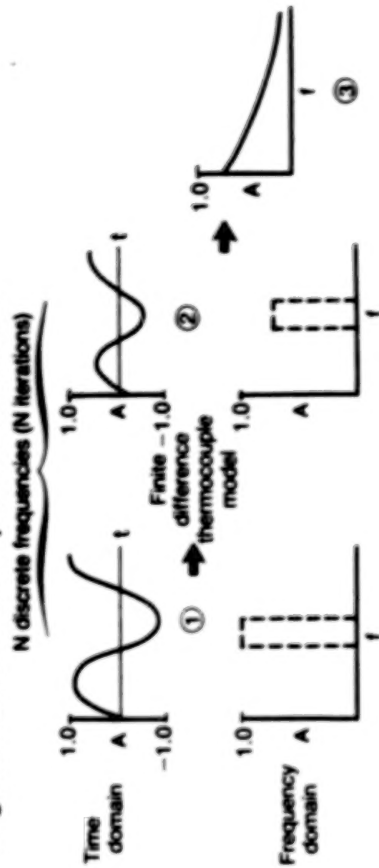
Test Probe Set-Up



FIGURE 10

# COMPUTER CODE OPTIMIZATION

Original numerical compensation method



- Individual frequencies input to finite difference T/C models
- Output from model complex added to yield compensation spectrum

FIGURE 12

# THE DEVELOPMENT OF A HIGH TEMPERATURE STATIC STRAIN GAGE SYSTEM\*

Charles O. Hulse and Richard S. Bailey  
United Technologies Research Center

and  
Howard P. Grant  
Pratt and Whitney

N88-11142

The objective of this program is to develop electrical resistance strain gages which will permit the measurement of static strains on nickel and cobalt superalloy parts inside gas turbine engines running on a test stand. The ability to make measurements of this type is essential to the goals of the HOST program because, without reliable knowledge of the stresses and strains which exist in specific components during engine operation, it will be difficult to effectively determine where improvements in design and materials can be implemented.

The specific goal of this work is to develop a complete system able to make strain measurements up to  $\pm 2,000$   $\mu$ strain with a total error of no more than  $\pm 10\%$  over a 50 hour period at 1250K. In addition to simple survival and stability, attaining a low thermal coefficient of resistivity, of the order of 100 ppm/K or less, is a major goal. This need results from the presently unavoidable uncertainties in measurements of the exact temperatures inside gas turbines. The initial part of this work consisted of a strain gage alloy development effort in which a variety of alloys were evaluated after being prepared by drop-casting or splat cooling.

The thermal cycling apparatus shown in figure 1 was used to make resistivity measurements up to 1250K at heating and cooling rates as high as 250K/min. The sample was positioned axially in the center of a split metal tube heater which could be cycled or held at a constant temperature under program control. Platinum leads for use in a four wire resistance circuit and a thermocouple at the center of the sample were attached by spot welding. The heating system also included an external plenum, not shown in figure 1, to permit cooling gases to be introduced at lower temperatures for better temperature control. A variety of circuit and computer program changes have been made to improve the accuracy of the data.

Our previous work (ref. 1) on the properties of various metal alloys prepared by drop casting resulted in the identification of two candidates from two different alloy systems. The first candidate was a FeCrAl alloy called Mod 3 of composition Fe-11.9Al-10.6Al, in weight percent. The effects of a whole series of alloying additions to this candidate were evaluated without discovering any which resulted in significant improvements. This alloy shows a resistivity versus temperature behavior which is very similar to that of the Chinese FeCrAl-base alloy recently described by Hobart (ref. 2), with the difference that it appears able to be used to a higher temperature.

\*Work done under NASA Contract NAS3-23722.

It was subsequently observed, however, as shown in figure 2, that the resistivity versus temperature curves for this alloy does show a gradual change with increasing times of exposure to 1250K in air. Because of this effect and concern over the oxidation of this alloy, work on this system was discontinued in favor of work on the second alloy candidate.

The best PdCr alloy candidate identified in this second alloy system was Pd-13Cr, in weight percent. The ultimate strength and the 0.02 percent off-set yield strengths determined on bulk samples as a function of temperature are shown in figure 3. The gage factor of this alloy determined at room temperatures using commercial strain gages was 1.78. These properties may be different when evaluated for thin sputtered films which are in intimate contact on both sides with oxides. Although it is more sensitive to temperature than the FeCrAl Mod 3 alloy, the response of the Pd-13Cr alloy to temperature, as shown in figure 4, is linear which indicates that no internal microstructural changes which could be time dependent are taking place. It was decided that this stability was most important for a static gage system and that thermal compensation by the incorporation of a small second grid of a pure precious metal would be the optimum way to proceed. This will be developed in Task 5 of the program.

As a final step in the alloy development process, sputtered films of Pd-13Cr have been prepared on Hastelloy-X substrates. Although the initial plans were to form sputtered films approximately 30 microns (30 micrometers) thick, problems encountered in the removal of the masks after sputtering limited the maximum thicknesses to approximately 6.5 microns. Results to date indicate that the as-sputtered films are very well bonded to the substrate. When these sputtered films are subsequently exposed to air at elevated temperatures, they develop a coating of chromium oxide,  $\text{Cr}_2\text{O}_3$ , which is also extremely adherent. It is difficult even with grit blasting to remove the oxide to expose the underlying metal in order to make electrical contacts.

The measured thermal sensitivities of the resistances of these films after oxidation are approximately ten times higher than for the original as-sputtered alloy because most of the chromium in the alloy has been consumed in order to make the protective oxide coating. Moreover, the observed rates of electrical drift at 1250K suggest that, at this small a dimension, the  $\text{Cr}_2\text{O}_3$  coating does not provide a sufficient level of stability and protection from oxidation. Experiments to recrystallize the sputtered nodules and thus to remove the enhanced diffusion paths provided by the boundaries between the nodules were successful, but unacceptable levels of drift still remained. These results indicate that the use of an additional overcoating system will be necessary. Current effort on this problem involves sputtering a coating of aluminum on top of the  $\text{Cr}_2\text{O}_3$  which can then be oxidized in place to form a tight overcoating of  $\text{Al}_2\text{O}_3$  which should be much more protective. The subject of overcoating will also be examined in a later task of the program (Task 5).

#### REFERENCES

1. Hulse, C. O.; Bailey, R. S.; Lemkey, F. D.: "High Temperature Static Strain Gage Alloy Development Program," UTRC Report No. R85-915952-13, NASA Lewis Research Center, CR-174833, Contract NAS3-23169.
2. Hobart, H. F.: "Evaluation Results of the 700°C Chinese Strain Gages," NASA Conference Publication 2339, Turbine Engine Hot Section Technology 1984, NASA Lewis Research Center.

# HIGH SPEED THERMAL CYCLE/RESISTIVITY MEASUREMENT APPARATUS

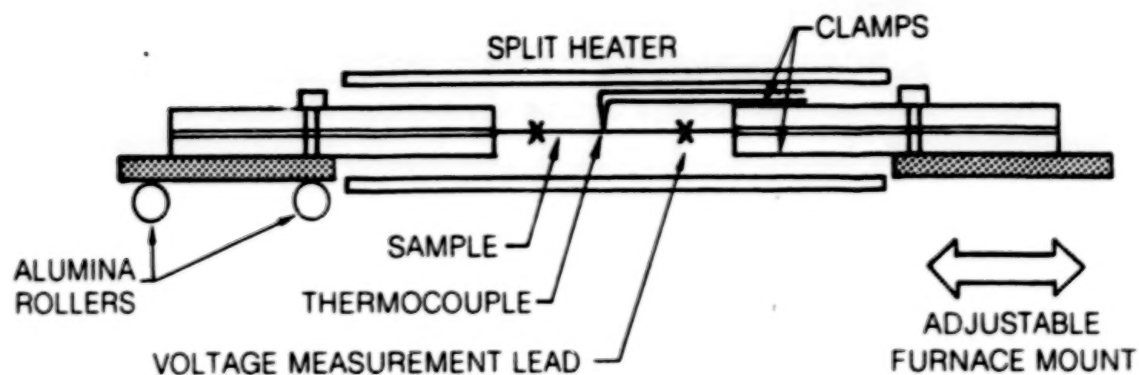


FIGURE 1

## CHANGE IN MOD 3 FeCrAl ALLOY RESISTANCE VS TEMPERATURE AFTER DIFFERENT SOAK TIMES AT 1250K

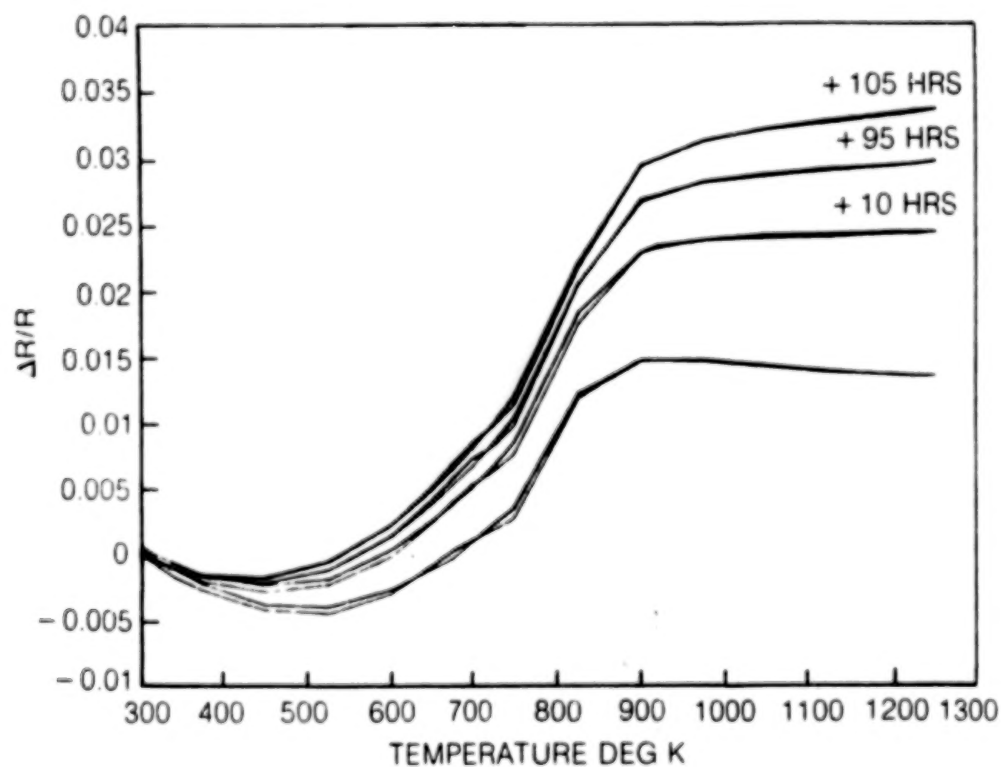


FIGURE 2

# STRENGTH VS TEMPERATURE OF DROP-CAST Pd-13 Wt % Cr

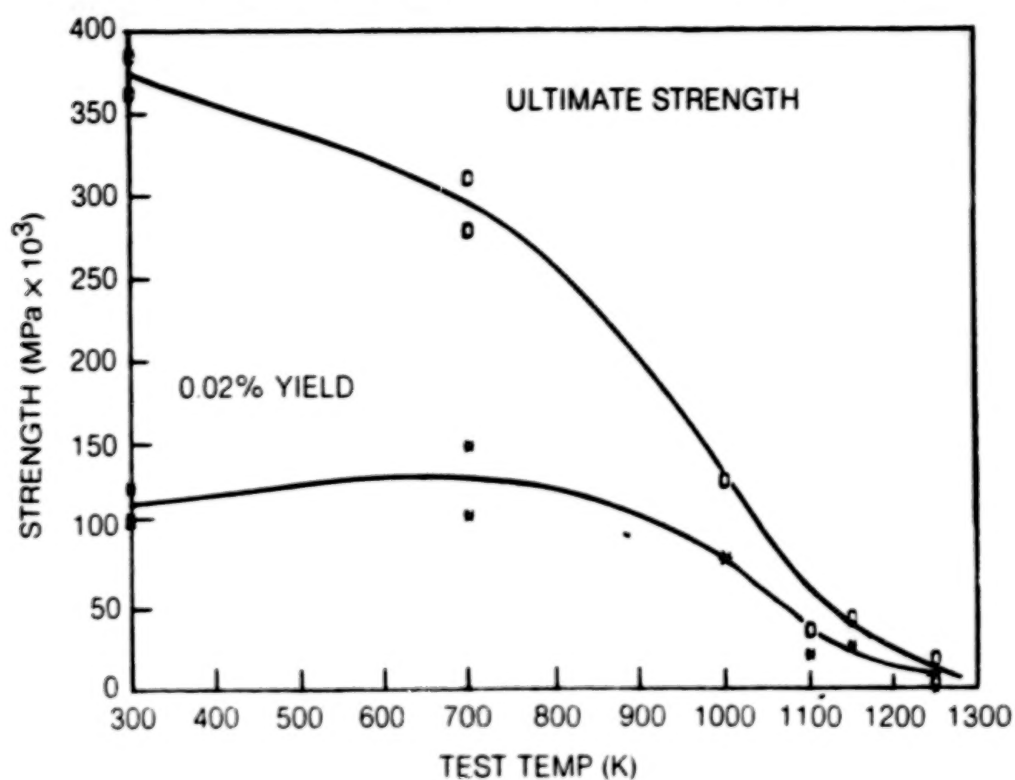


FIGURE 3

# RESISTANCE VS TEMPERATURE AT 50 DEG K/MIN (Pd-13 Wt % Cr)

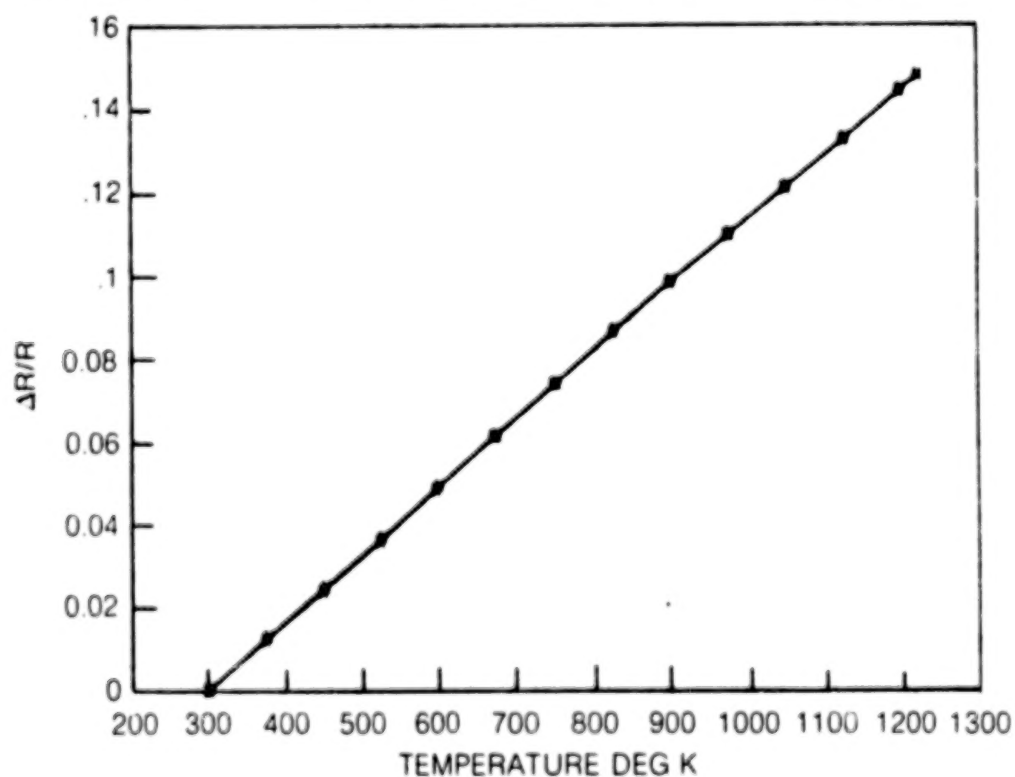


FIGURE 4

DEVELOPMENT OF HEAT FLUX SENSORS FOR  
TURBINE AIRFOILS<sup>1</sup>

William H. Atkinson, Marcia A. Cyr and Richard R. Strange  
United Technologies Corporation  
Pratt & Whitney

## INTRODUCTION

The objectives of this program are to develop heat flux sensors suitable for installation in hot section airfoils of advanced aircraft turbine engines and to experimentally verify the operation of these heat flux sensors in a cylinder in cross flow experiment. During the first phase of the program, embedded thermocouple and Gardon gauge sensors were developed and fabricated into both blades and vanes. They were then calibrated using a quartz lamp bank heat source and finally subjected to thermal cycle and thermal soak testing. This work has been reported in Reference 1. In the second phase of the program, these sensors were fabricated into cylindrical test pieces and tested in a burner exhaust to verify the heat flux measurements produced by these sensors. This paper describes the results of the cylinder in cross flow tests and reviews the conclusions and recommendations resulting from the test program.

## DESCRIPTION OF THE TEST PIECES

Two test pieces were fabricated from Hastelloy-X tubing 1.6 cm. in diameter with a wall thickness of 0.15 cm. An embedded thermocouple sensor, a Gardon gauge sensor and a slug calorimeter were fabricated into each test piece spaced 5 cm. apart. Figure 1 shows the sensor locations in one of the cylinders. Design details of the test pieces and fabrication of the sensors are given in References 2 and 3. Steady state heat flux measurements were made with the embedded thermocouple and Gardon gauge sensors and transient heat flux measurements with the Gardon gauge sensor and slug calorimeter. These sensors were calibrated using a quartz lamp bank as a heat source and a commercially available heat flux sensor as a transfer standard. Two other test pieces, fabricated from 1.6 cm. diameter NiCoCrAlY tubes having a wall thickness of 0.48 centimeters, were instrumented with an array of sputtered thermocouples to measure the fluctuating metal surface temperature. This information, in conjunction with fluctuating gas temperature measurements made with the dynamic temperature probe developed under contract NAS3-23154 (Ref.4), was to be used to calculate the heat transfer coefficient.

## DESCRIPTION OF THE TEST PROGRAM

Tests were run in the exhaust of a Becon type atmospheric pressure combustor with a 5 cm. diameter exhaust nozzle. The cylinders were positioned downstream of the nozzle and mounted on a traverse can capable of both linear and rotational movement. Prior to running the tests with the cylinders, a series of tests was conducted to characterize the exit gas temperature and pressure profiles from the burner, using an aspirating thermocouple probe and a pressure probe. Data were obtained at temperatures from 1500 to 1760K and Mach numbers from .42 to .74. The aspirating thermocouple probe was used throughout the test program to set the burner

<sup>1</sup> NASA Contract NAS3-23529

conditions. The test setup is shown in Figure 2. For the steady state points, the burner conditions were stabilized and the internally cooled cylinder was traversed into position in the gas stream to make the measurements. The transient tests were run with the uncooled cylinder initially out of the gas stream to maintain a uniform temperature and then shuttled rapidly into the gas stream to start the transient.

## TEST RESULTS

Figures 3 and 4 show typical pressure and temperature profiles in the combustor exit. Based on the profile data generated in these tests, as well as laser doppler velocimetry (LDV) data obtained on a similar combustor at NASA Lewis, the primary location for data acquisition was selected at a distance of 5 cm. behind the nozzle. Data from the steady state sensors on both cylinders at the stagnation point plotted as a function of Mach number is shown in fig. 5. The data from the two embedded thermocouple sensors show reasonable agreement, while the data from the two Gardon gauge sensors show a wide variation which is believed to be due to the placement of the junctions internal to the Gardon gauges. To confirm this, the cylinders were rotated to acquire data around the circumference of the cylinder. Figure 6 shows the variation in heat transfer coefficient around the cylinder measured with the two embedded thermocouple sensors. These match the profiles widely reported in the literature. Figure 7 shows similar data as acquired from the two Gardon gauge sensors. These data seem to indicate that the two sensors were built with the junctions located off the stagnation point in opposite directions, and that the circumferential temperature gradients in the cylinders may be causing significant differences in the outputs. A finite difference thermal analysis was run, which confirmed that the observed output can be predicted based on the location of the thermocouple junctions. The data from the transient sensors at the stagnation point plotted as a function of Mach number are shown in fig. 8. This data is well behaved and indicate an increase in the heat transfer coefficient as the Mach number is increased.

Figure 9 shows a plot of the ratio of the measured heat transfer coefficient to the calculated heat transfer coefficient plotted against Mach number for both the transient and steady state sensors. The calculated heat transfer coefficient is based on zero turbulence. The NASA LDV data indicates a turbulence level of about 10% could be expected, hence, the ratio should be significantly greater than 1. The transient sensors yield a ratio that is about 10% greater, while the steady state sensors generally yield a ratio that is up to 70% greater than 1. This difference is consistent between sensors and between runs and is currently unexplained.

All the sensors were operational at the end of the test program. A recalibration of the sensors was performed which revealed the sensors outputs were within 3% of the pretest values, indicating there were no shifts in output or degradation of the sensors during the test program.

The test program on the cylinders with sputtered thermocouples yielded heat transfer coefficients that were an order of magnitude higher than those measured with the other cylinders. Inspection of the data revealed that the dynamic temperature probe performed properly and that the temperature fluctuations measured with the sputtered thermocouples were unrealistically high. A post-test examination of the cylinders revealed that the sputtered thermocouples developed shorts to ground as the cylinder temperature was raised. The sputtered thermocouples also exhibited adherence problems and most of the films had lifted by the end of the

test. The unrealistically high output from the sputtered thermocouples is believed to be due to ground loops, ion effects from the flame, or undesired thermoelectric effects from the NiCoCrAlY. It is planned to install new sputtered thermocouples on the cylinders and rerun tests to obtain valid data.

#### CONCLUSIONS AND RECOMMENDATIONS

In general, the steady state sensors produced heat transfer coefficient measurements that were up to 70% higher than theoretical predictions for zero turbulence. This would be anticipated from the approximately 10% turbulence reported from the LDV results. There is a systematic bias between the steady state measurements and the transient measurements. The transient measurements produced heat transfer coefficients only up to 10% higher than the theoretical predictions for zero turbulence which are lower than would be anticipated with the 10% turbulence levels. All repeat points on the sensors were within 10% and some of this variation may be due to repositioning the cylinder in the gas stream. The post-test calibration values were within 3% of the pre-test values, indicating that the sensor outputs were stable and the environmental conditions did not cause shifts in the sensor outputs. The dynamic temperature probe gave good results throughout the test, but the durability and performance of the sputtered thermocouples was very poor.

The following recommendations are offered in light of the experience gained from this test program:

1. Use of sensors in hot section airfoils should be limited to areas that approximate flat plate geometries and where temperature gradients are minimal.
2. Use of embedded thermocouple sensors instead of Gardon gauge sensors should be favored in areas with moderate thermal gradients.
3. Develop methods of calibrating heat flux sensors in areas of sharp curvature and large temperature gradients.
4. Improve the durability of the sputtered thermocouples and conduct a test program to evaluate the use of sputtered sensors within a flame.

#### REFERENCES

1. Atkinson, W. H.; Cyr, M. A.; and Strange, R. R.: Turbine Blade and Vane Heat Flux Sensor Development. Phase 1 Final Report NASA CR-168297, August 1984.
2. Atkinson, W. H.; Cyr, M. A.; and Strange, R. R.: Turbine Blade and Vane Heat Flux Sensor Development. Phase 2 Final Report NASA CR-174995, 1985.
3. Atkinson, W. H.; and Strange, R. R.: Development of Heat Flux Sensors in Turbine Airfoils. NASA Conference Publication 2339, October 1984.
4. Elmore, D. L.; Robinson, W. W.; and Watkins, W. B.: Dynamic Gas Temperature Measurement System. Final Report NASA CR-168167, May 1983.

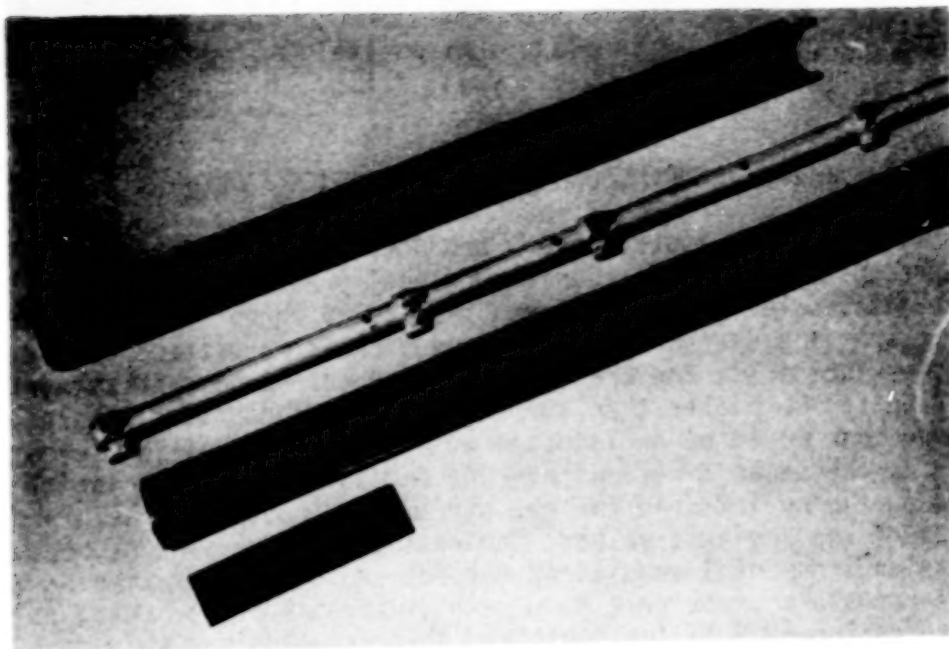


Figure 1 Test Piece During Fabrication Showing Sensor Locations



Figure 2 Cylinder in Cross Flow Test Setup

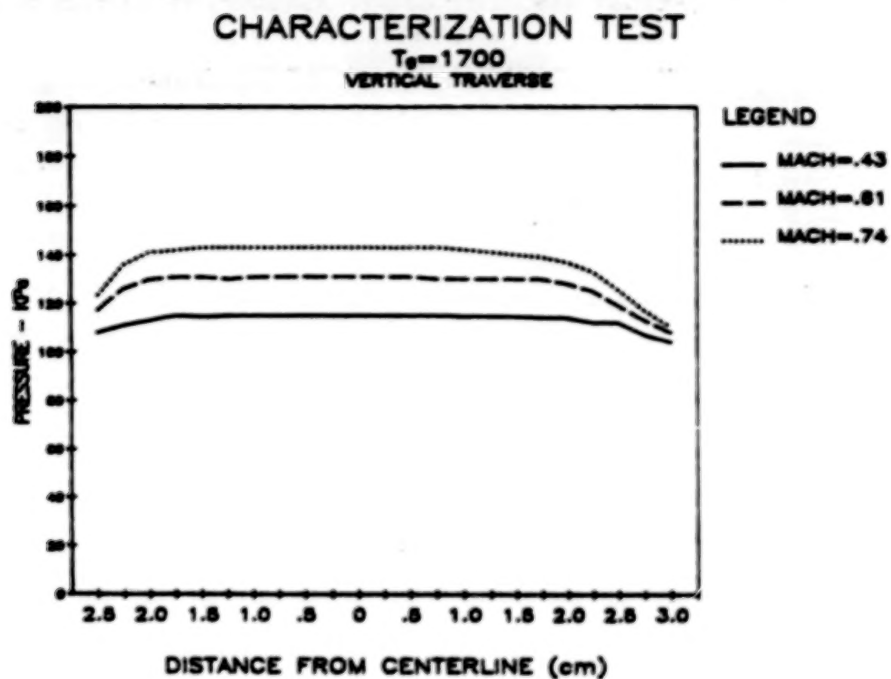


Figure 3 Pressure Profile Across the Burner Exhaust

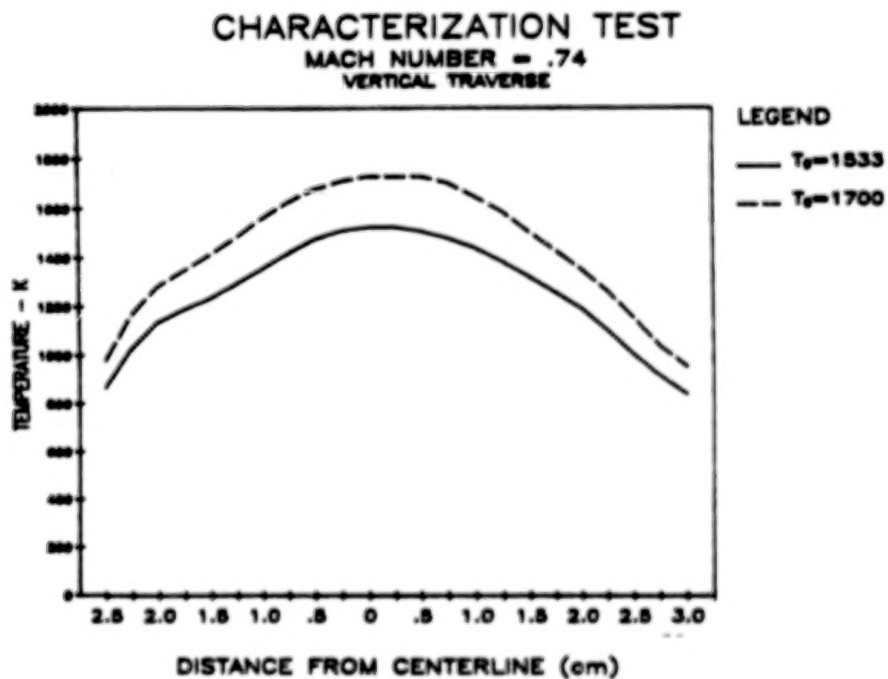


Figure 4 Temperature Profile Across the Burner Exhaust

# STEADY STATE SENSOR COMPARISONS T=1700 K

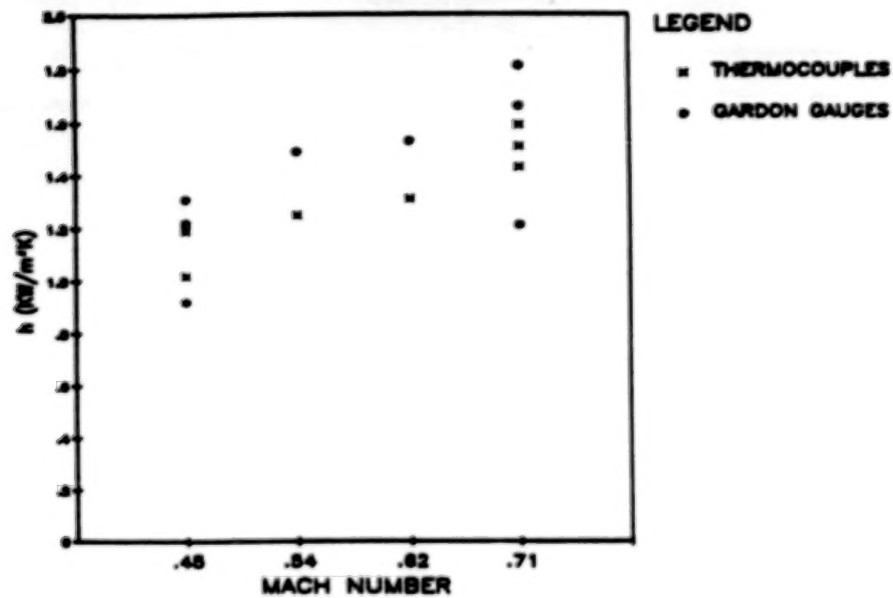


Figure 5 Steady State Heat Flux Sensor Data

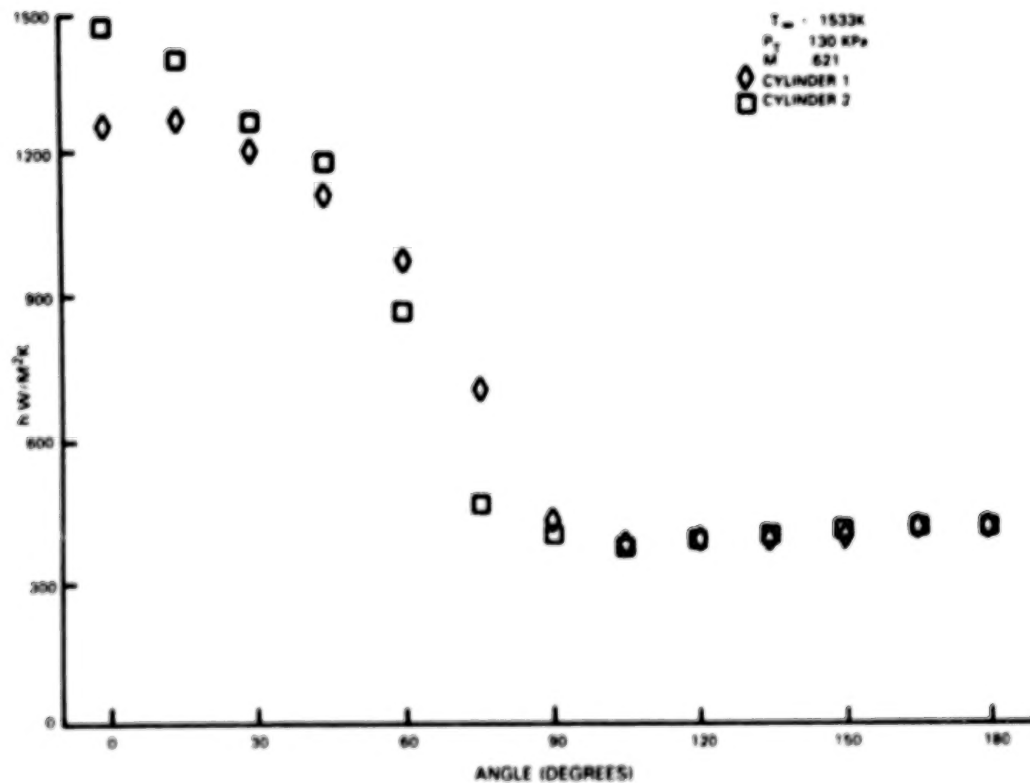


Figure 6 Heat Transfer Coefficient Variation Around the Cylinder As Measured with the Embedded Thermocouple Sensors

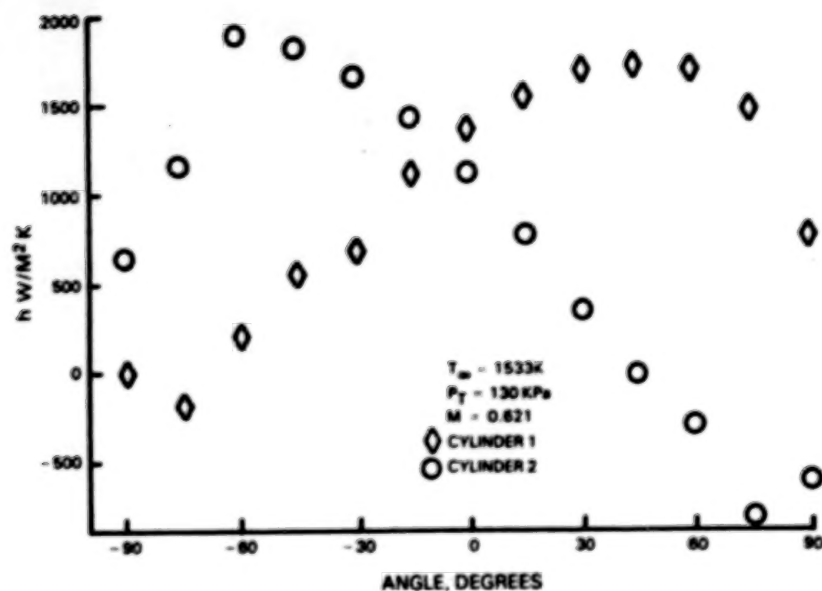


Figure 7 Heat Transfer Coefficient Variation Around the Cylinder As Measured with the Gardon Gauge Sensors

### TRANSIENT SENSOR COMPARISON $T=1533 K$

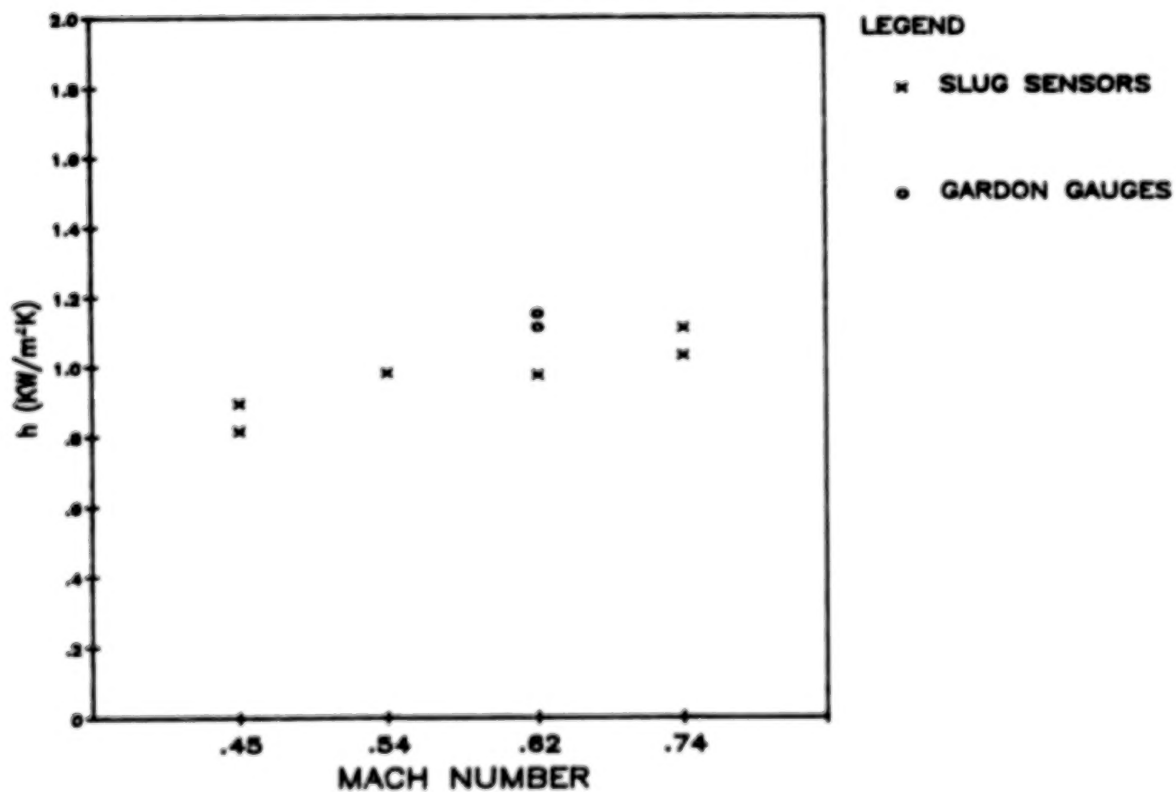


Figure 8 Transient Heat Flux Sensor Results

# SENSOR COMPARISONS T=1700 K

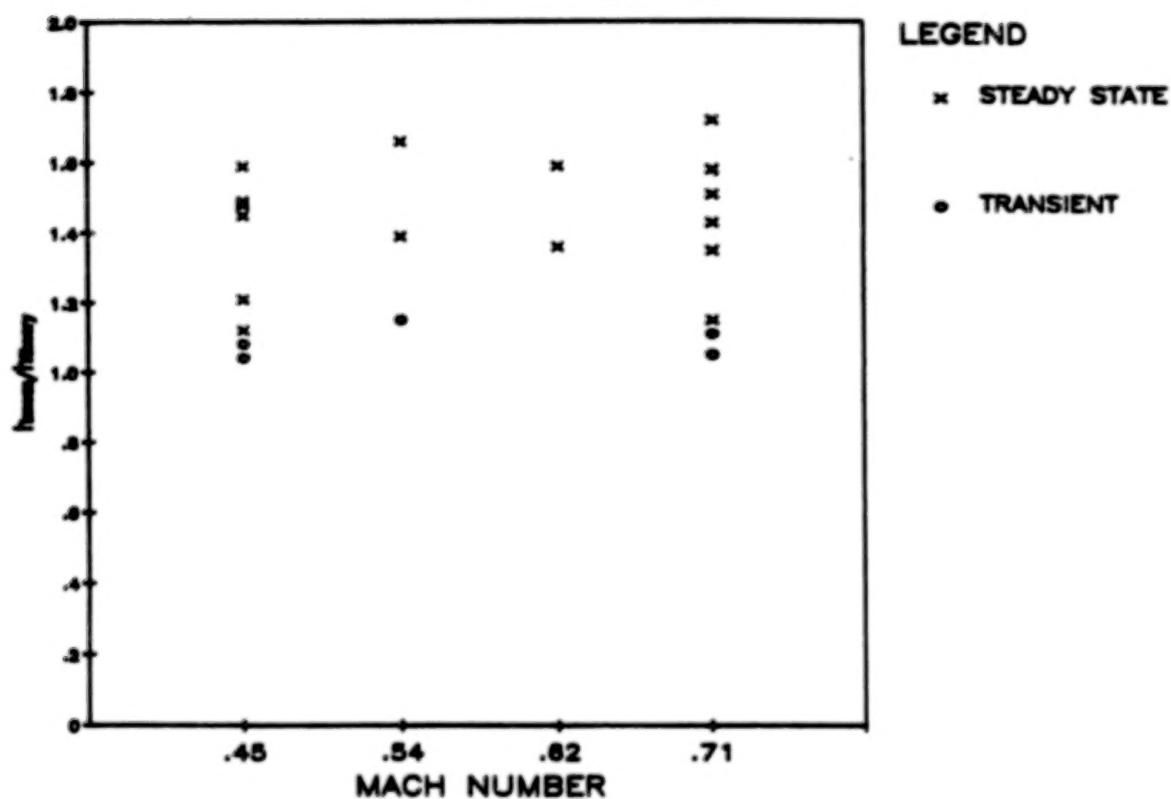


Figure 9 Comparison of Measured Heat Transfer Coefficients with Theoretical Predictions

## ELEVATED TEMPERATURE STRAIN GAGES\*

J. O. Brittain, D. Geslin and J. F. Lei  
Northwestern University

The Host Program has as one of its goals the development of electrical resistance strain gages for static strain measurements at temperatures  $\geq 1273^{\circ}\text{K}$ . In order to attain this goal strain gage materials must have a characteristic response to strain, temperature and time that is reproducible or that varies in a predictable manner within specified limits. The principal contributions to the relative change in resistance are (1) the change in resistance with strain, (2) the change in resistance with temperature (coefficient of thermal resistance) and (3) time dependent changes in resistance due to chemical changes (e.g., oxidation) and dimensional changes (creep) (ref. 1). These then are the principal parameters to be considered in the selection of materials for strain gage elements. However, in order to proceed with the development of such gages the selection of material for the gage elements, consideration must be given to material parameters that effect electrical resistance. The material factors are: phase, magnetic and order-disorder transitions, short range ordering, clustering, plastic deformation and chemical changes associated with material reactions with an elevated temperature environment. These material parameters are interrelated and their effects on elevated temperature electrical resistance are both temperature and time dependent (refs. 2 and 3).

Prior to the selection of a list of materials for potential strain gage applications, we set out to establish the criteria to be used in the selection of material for evaluation. Phase diagrams of binary alloys were utilized as the first step in the selection of materials that have sufficiently high melting temperature, do not undergo a phase transformation or a magnetic transition. Since phase diagrams usually provide no information on structural changes associated with order-disorder transitions or clustering, we made use of thermodynamic data when available to select ideal solid solution alloys. Alloys that are ideal solutions should not undergo transitions such as clustering, order-disorder, etc. The basis for classifying an alloy as an ideal solution is that the activity coefficient is equal to one. Alloy compositions with activity coefficients of the two components within about 15% of one were selected, see Table I. Several qualitative criteria have evolved to aid in the selection process when quantitative activity data did not exist. These qualitative rules suggest that alloys tend to form ideal solutions when the molar volume of the two components are equal and when the electronegativity of the two components are similar (refs. 4 and 5). In addition several alloys that have a linear electrical resistivity-temperature relation were included in the initial list of materials for evaluation (ref. 5). The list of binary alloys for the first phase of the investigation is listed in Table I.

In addition to the metallic alloys, evaluation of a series of transition metal carbides, nitrides and silicides, Table I, is also in progress. These materials were selected based upon the following: (1) high melting temperature, (2) good mechanical strength at elevated temperature, (3) low and metallic like resistivities, (4) the absence of phase transitions within the  $0^{\circ} - 1000^{\circ}\text{C}$  temperature range,

\*Work done under NASA Grant NAG3-501.

(5) good oxidation resistance and (6) thin films can be etched for pattern geometry (ref. 6). In addition to the six compounds (TiC, TiN, ZrC, ZrN, TaSi<sub>2</sub> and TiSi<sub>2</sub>) selected as most promising for evaluation, interest in SiC has evolved. This semiconducting compound is of interest because of its stable physical characteristics, similar to those described above for the transition metal compounds, at temperatures up to 1200°C, as well as the observation that efforts to develop SiC elevated temperature gages are in progress in Russia (ref. 7).

#### MATERIAL PREPARATION AND PROCESSING

The alloys listed in Table I are being prepared by arc melting in the usual manner. The homogenized ingots were processed into specimens by electric discharge machining or slicing with a diamond wheel. Specimens of CrV were 25 x 2.1 x .406 mm, Al-V 12 x 1.8 x 1.5 mm. Specimens have also been prepared by means of drawing the molten alloy into a quartz tube connected to a vacuum. This latter technique produced longer wire specimens. So far our efforts to produce specimens of MoRe and MoW by the quartz tube technique have not been successful.

Samples of SiC, TiN, TiC in thin film form have been obtained from several sources. These samples were prepared by sputtering or by CVD techniques. Specimens of SiC on a Al<sub>2</sub>O<sub>3</sub> substrate were cut to 13 x 1.2 mm and 2500 Å thick.

The electrical resistance of the specimens was measured via a four probe technique using Pt leads and pressure contacts. The contacts were checked and found to be ohmic at all temperatures. Measurements were conducted in a quartz evacuated tube that contained an Al<sub>2</sub>O<sub>3</sub> specimen holder with a metal tube envelope surrounding the quartz tube. The vacuum was better than 10<sup>-5</sup> Torr and the temperature gradient was found to vary by about 2 - 10°C along the specimen holder, with a temperature variation over the length of the specimen of ~ 2-4°C at the elevated temperatures.

#### RESULTS

The resistance-temperature data was obtained with a heating rate of ~ 1.25°C/min. and a cooling rate of ~ 0.6°C/min. The resistance data is an average of approximately 8 measurements that were made after a sojourn of about 30 minutes at the temperature of interest. Thermal EMF's were eliminated by changing the current direction. Figure 1 is a plot of resistance vs temperature for a nominal 69.1 w/o (70 a/o) V-Cr alloy. The resistance varied linearly with temperature, with a slope of ~ 2.68 x 10<sup>-3</sup> mΩ/C, there is good agreement for the two cycles shown, furthermore the drift at 1000°C after 15 hrs. was relatively small. Figure 2 shows the resistance drift as a function of time, the drift after 900 minutes was ~1.7 %. Table II relates the resistance drift for short times at intermediate temperatures. From figure 1, the thermal coefficient of resistance at 1000°C was found to be ~ 5.6 x 10<sup>-4</sup>/°C.

The resistance-temperature data for the 81.6 w/o (70 a/o) V-Al alloy is shown in figure 3. After the first heating cycle, the resistance varied reproducibly with temperature. The origin of the initial high resistance from room temperature to ~ 500°C is unknown. The decrease in resistance with temperature suggests that we repeat these measurements to insure that they are not due to a fault in the measuring technique. If repeated measurements produce the same temperature dependence, that would indicate semiconducting electronic behavior.

Figure 4 shows the resistance-temperature data for SiC sputtered film on an  $\text{Al}_2\text{O}_3$  substrate. The specimen was initially conditioned by heating and cooling from  $1000^\circ\text{C}$ . The resistance drift at  $1000^\circ\text{C}$  during the first heating cycle was associated with a 17 hr. sojourn at  $1000^\circ\text{C}$ . After the first heating cycle, there is some indication that the resistance-temperature relation is constant. However, as indicated in figure 5, the resistance showed a positive drift with time at 840 and  $900^\circ\text{C}$ , while a negative drift was observed at 949 and  $1000^\circ\text{C}$ . Inasmuch as we observed extensive contact reactions between the Pt wire and SiC, the present data is suspect and we are in the process of examining other probe materials.

#### REFERENCES

1. Sharpe, W. N. Jr.: Strain Gages for Long Term High Temperature Strain Measurements. *Experimental Mechanics*.
2. Ochiai, Y. and Brittain, J. O.: Anomalous Electrical Resistivity in CoGa Intermetallic Compounds. *Phys. Letters.*, vol. 72A, 1979, pp. 347-49.
3. Ochiai, Y. and Brittain, J. O.: Negative Temperature Coefficient of Resistivity in  $\beta\text{-Co}_{52}\text{Ga}_{48}$ . *J. Phys. F: Metal Physics*, Vol. 10, 1980, pp. 1183-93.
4. Kubashevski, O., Evans, E. L. and Alcock: Metallurgical Thermodynamics. Pergamon, N. Y., 1967, p. 76.
5. Cahn, R. W. Haasen, P.: Physical Metallurgy. American Elsevier, N. Y., 1983, p. 176.
6. Schröder, Klaus: Handbook of Electrical Resistivities of Binary Metallic Alloys. CRC Press, 1983.
7. Drennen, D. C. et al.: LMFBR Instrumentation-Strain Gages, Phase I High Temperature Strain Gage Development Program: Battelle Memorial Institute, 1970.
8. Rapatskaya, V. and Rudashevskii, G. E.: Silicon  $\alpha$ -Carbide Strain Transducers. *Measurement Techniques* 1968, pp. 771-772. Translated from *Izmeritel'naya Tekhnika*, 6, 1968, pp. 117-123.

TABLE I  
MATERIALS SELECTED FOR EVALUATION

Material	Basis for Selection
Pd-Ag	1
Al-V	1
Nb-V	2
Mo-W	2
Hf-Zr	2
Pd-Rh	2
Cr-V	3
Ta-W	3
Mo-Re	3
TiC	4
TiN	4
TiSi <sub>2</sub>	4
ZrC	4
ZrN	4
TaSi <sub>2</sub>	4
SiC	4

1. Ideal solution, thermodynamic data.
2. Qualitative parameters, tendency to form ideal solutions.
3. Resistance-temperature data.
4. Refractory compounds, high melting temperature, structural stability, oxidation resistance.

TABLE II  
RESISTANCE DRIFT FOR CrV ALLOY, m $\Omega$

	TIME	0	1/2 h	1 h
TEMPERATURE (°C)				
429.9		3.376		
428.78			3.392	3.283
581.75		3.749		3.755
586			3.743	
703		4.179		4.081
705.5			4.084	
845		4.481		4.486
850			4.484	

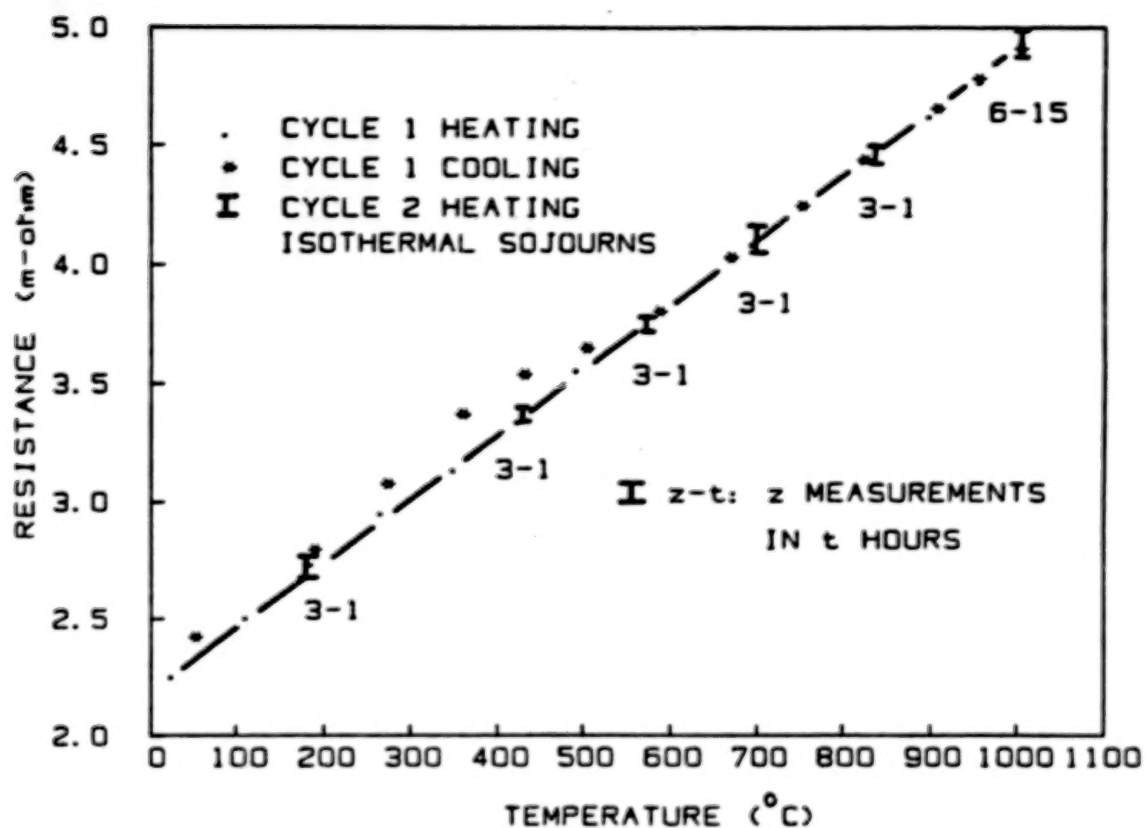


FIGURE 1 RESISTANCE Vs. TEMPERATURE OF Cr-V

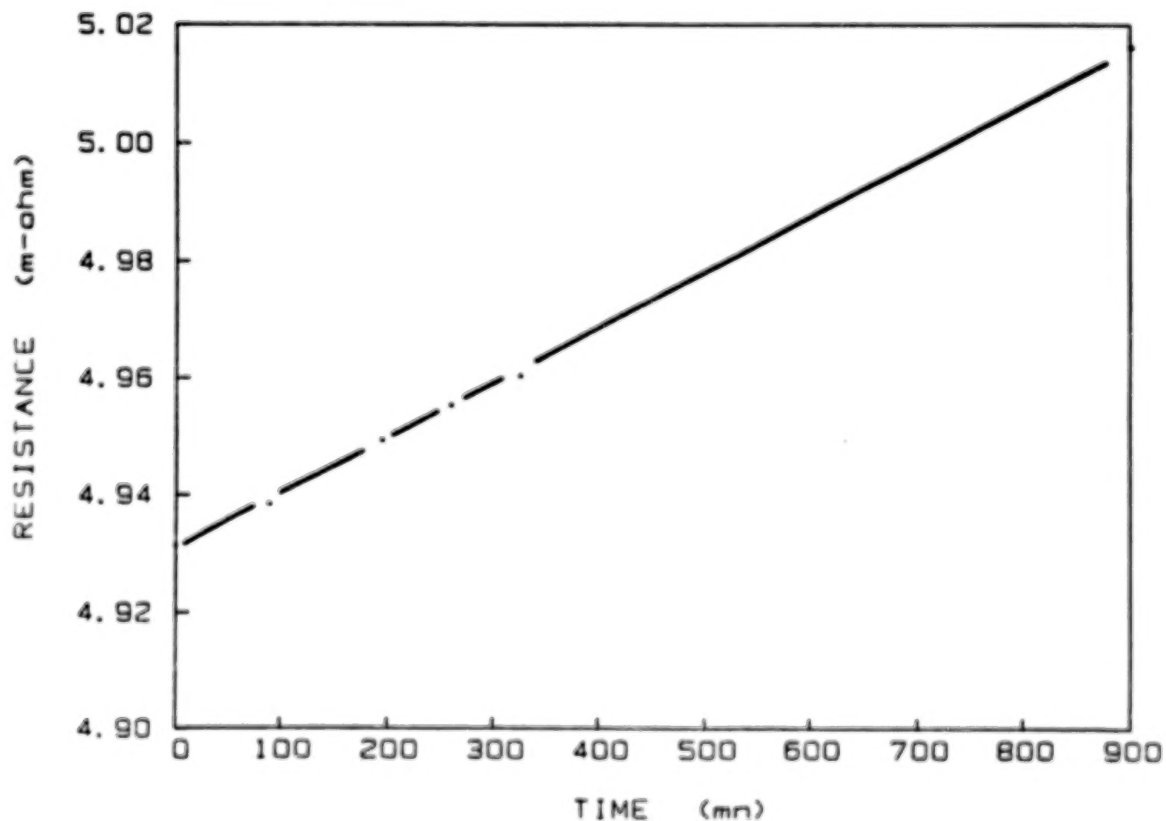


FIGURE 2 RESISTANCE DRIFT Vs. TIME at  $1002.5^{\circ}\text{C}$  OF Cr-V

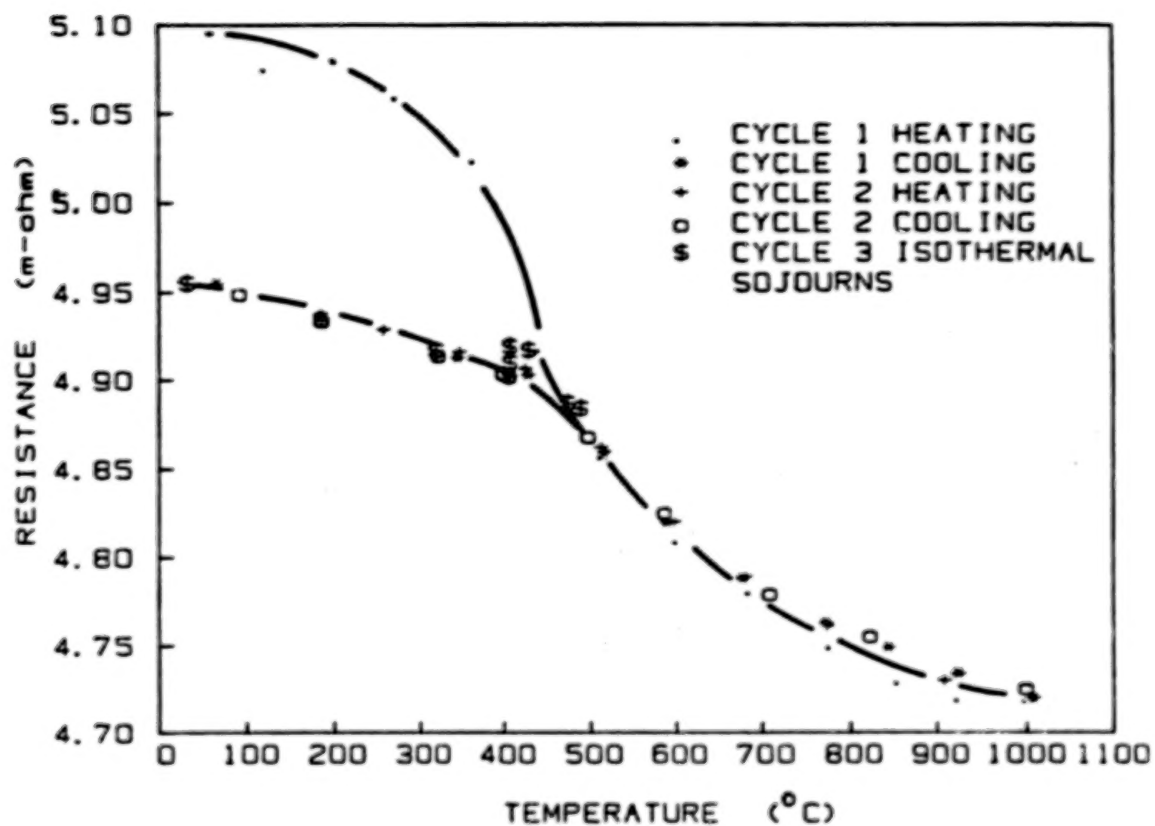


FIGURE 3 RESISTANCE V<sub>s</sub>. TEMPERATURE OF AlV

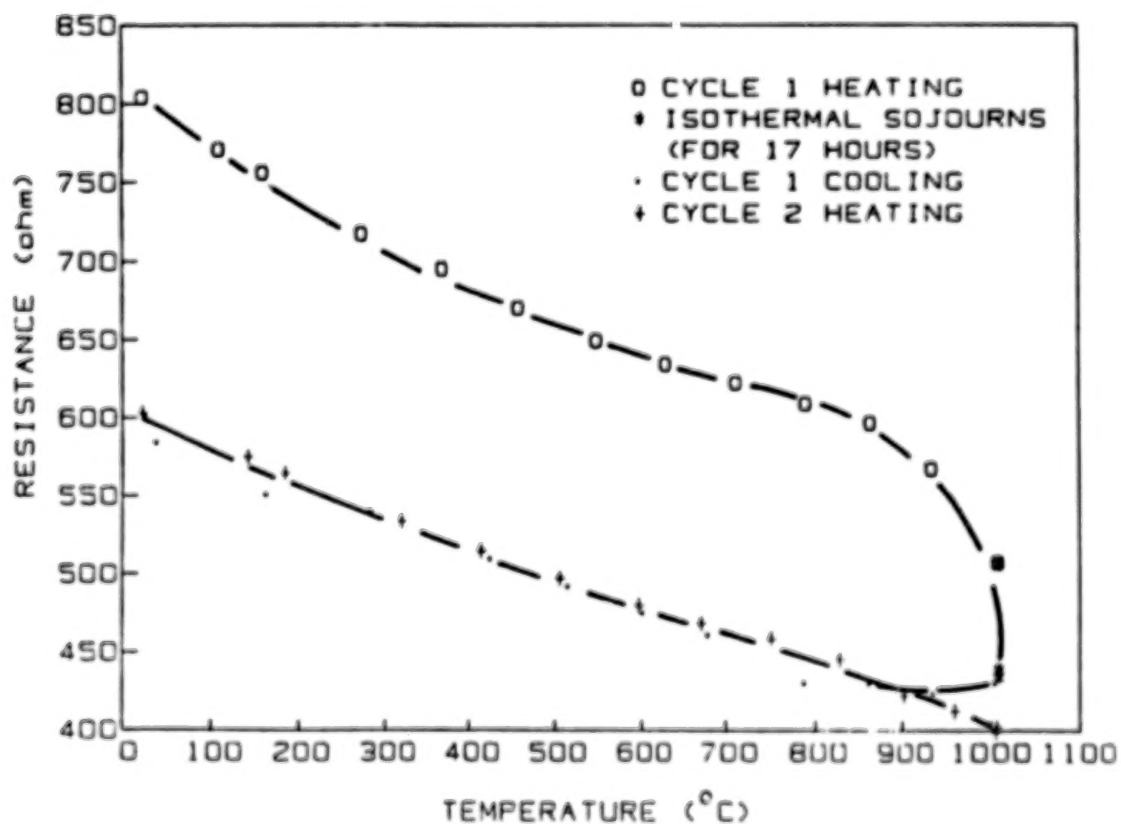


FIGURE 4 RESISTANCE V<sub>s</sub>. TEMPERATURE OF SiC

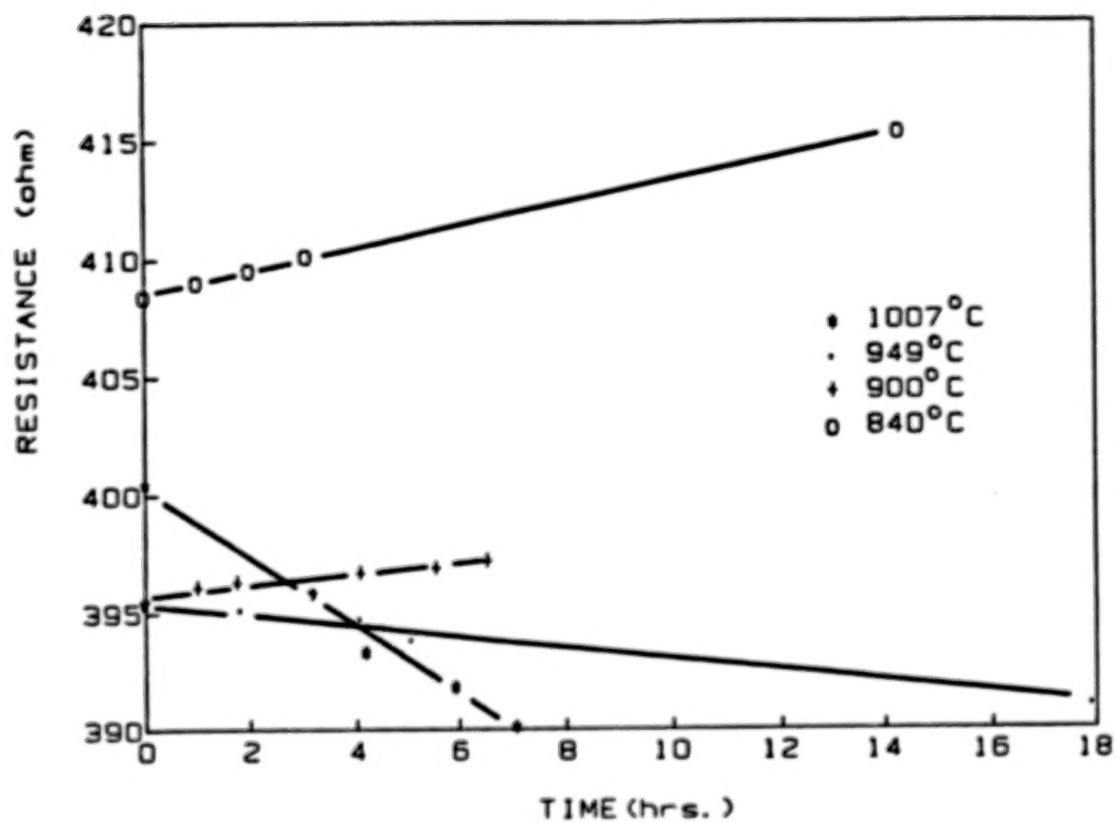


FIGURE 5 RESISTANCE DRIFT Vs. TIME OF SiC

## THE FOUR SPOT TIME-OF-FLIGHT LASER ANEMOMETER

Mark P. Wernet  
NASA Lewis Research Center  
Cleveland, Ohio

## INTRODUCTION

A new time-of-flight laser anemometer system utilizing a spatial lead-lag filter for bipolar pulse generation has been constructed, and initial testing has been initiated. This new TOF has been modified to enable measurements high velocity, turbulent gas flows near walls. Good results have been obtained to 75  $\mu\text{m}$  normal to the surface, with an F number 2.5 collecting lens. Further testing of the new system will be conducted in open jet burner facility in CE-13 to evaluate its suitability for use in hot section flow experiments.

A laser anemometer offers a nonintrusive method for obtaining flow-field information. Particles entrained in the flow provide scattering centers for the incident light. Two common techniques for optically coding the measurement region exist. The laser fringe anemometer (LFA) employs a sinusoidally varying fringe pattern. Knowledge of the fringe spacing and the detected frequency of particles traversing the measurement region permits the determination of the velocity component normal to the fringes. Another technique for encoding the measurement region uses two closely spaced spots, where the flow velocity component parallel to the axis of the spots is obtained from the time-of-flight of particles traversing the two spots.

The motivation for this work was the desire for an anemometer capable of measurements near walls in turbulent flows. This requires a laser anemometer with special qualities. The optimum anemometer would have a wide acceptance angle, to enable measurements of wide flow angle variations, and also have a high spatial selectivity, to limit unwanted flare light scattered from surfaces from reaching the detector. The LFA typically has a wider acceptance angle than a conventional time-of-flight (TOF) system (ref. 1). The lower acceptance angle reduces the utility of TOF systems in turbulent flows. However, the TOF receiver can have much better spatial resolution than the LFA for the same f/number system.

In this work we describe a new, modified TOF system that has been constructed and tested for turbulent flow measurements near walls. The new TOF system uses elliptical spots to increase the flow acceptance angle to be comparable with that of an LFA. Also, the new TOF uses an optical code that vastly simplifies the pulse-detection processor. A simple electronic pulse position technique was used instead of the more complex correlation techniques (refs. 2 to 4).

## THEORY

The electronic signal obtained from a normal two-spot TOF system consists of two noisy gaussian shaped pulses separated by the transit time of a particle traversing the two light spots in the measurement region. An estimate of the peak to peak time of flight and knowledge of the spot spacing then yields the particle velocity component along the axis of the two spots. The inherent noise on any type of photon-

detection system decreases the ability of the signal processor to determine the exact time-of-occurrence of a pulse. The particle's time of flight can be obtained more accurately by transforming the unipolar pulse into a bipolar pulse. The zero crossings of the bipolar pulses yield the estimated time of flight. The transformation from a unipolar to a bipolar pulse should not introduce additional noise to the signal. Lading (ref. 1) analyzed the performance of three methods for generating bipolar pulses: the derivative operator, Hilbert transforms, and the spatial lead-lag filter. He found that the Hilbert transform and spatial lead-lag filters were less sensitive to the signal bandwidth. The derivative operator yielded optimum performance when the filter bandwidth was equal to the signal bandwidth. He suggested that an advantage could be obtained by implementing the lead-lag filter spatially, before photon detection. The advantage of the spatial lead-lag filter is that the dimensions are fixed in space, but the temporal scale of the signal depends on the velocity. Thus, a spatial implementation will behave as an adaptive temporal lead-lag operator. The transformation to a bipolar pulse is thus made without adding noise to the signal and in a robust manner that does not depend on electronic delays. The TOF system described herein has a spatial lead-lag filter.

#### IMPLEMENTATION

The new TOF system uses two pairs of elliptical spots in the measurement region. These two pairs of spots, labeled A to D, are separated by a distance  $X_0$  and orthogonally polarized and partially overlapping (fig. 1). The use of elliptical spots increases the acceptance angle of the measurement region, comparable with that of a laser fringe anemometer.

The transmitting section of the system contains two quarter-wave plate/Wollaston prism pairs (fig. 2). The input light is linearly polarized. A cylindrical lens transforms the circular input beam into an elliptical beam. The first quarter-wave plate/Wollaston prism pair  $Q_1/W_1$  generates two angularly diverging, orthogonally polarized beams. These plane, polarized beams are imaged by  $L_2$  and  $L_3$  onto the second pair  $Q_2/W_2$ . The first pair  $Q_1/W_1$  must be at the back focal plane of  $L_2$ , and  $Q_2/W_2$  must be at the front focal plane of  $L_3$  to maintain the sharpness of the imaged spots. Emerging from the  $Q_2/W_2$  pair are four consecutively, orthogonally polarized beams. The angular divergence of these beams is transformed into a spatial separation by the lens  $L_4$ . The angular divergence imparted by the  $Q_1/W_1$  pair creates the spatial separation  $X_0$ . The angular divergence imparted by  $Q_2/W_2$  creates the partially overlapping spots in the measurement region.

The measurement region geometry is controlled by the input beam diameter, by the angular divergences of  $W_1$  and  $W_2$ , and by the focal length of  $L_4$ . The position of  $L_4$  is the most critical adjustment in the transmitter. A very smooth, linear positioning translator is required to position  $L_4$  such that the  $Q_2/W_2$  pair is at the back focal plane. This critical adjustment determines the sharpness of the spots at the focal plane and their relative separation. To generate pulses of roughly equal amplitude, the quarter-wave plate/Wollaston prism pairs will each have to be adjusted to equalize the intensities of the four spots.

The backscatter system configuration collects the scattered light from the measurement region back along the axis of the transmitted beam. The use of the two elevation mirrors  $M_1$  and  $M_2$  allows this coaxial configuration. The received image is magnified by the image pair  $L_4$  and  $L_7$ . The rectangular mirror  $M_2$  acts as a vertical spatial filter mask in the receiver. The received light is recombined into two pairs of totally overlapping spots by a third Wollaston prism,

$W_3$  which has the same angular split as  $W_2$ . These two spots are imaged onto the receiver mask consisting of two precision air slits. The two totally overlapping pairs of spots are separated by a polarization-selective beam-splitting cube. Two right-angle prisms are used to separate the spot pairs into four individual signals. The separated signals are detected by four RCA 8645 photomultiplier tubes.

The receiver system shares the image pair  $L_5$  and  $L_6$  with the transmitter. Lenses  $L_5$  and  $L_6$  are 100 mm in diameter and have focal lengths of 500 and 250 mm, respectively. The receiver system is sensitive to the position of lens  $L_4$ . The use of  $L_4$  as a common lens focuses both the transmitter and receiver simultaneously. No extensive amount of flare light has been observed from this configuration.

A dove prism image rotator has been incorporated into the new TOF system. The image rotator is common to both the transmitter and receiver. The image rotator permits two-dimensional velocity scans by taking measurements at several angular orientations of the measurement volume.

A prototype system has been constructed and tested in cooperation with Dr. R.V. Edwards at Case Western Reserve University. The second-generation system has been constructed at Lewis from optical erector components (figs. 3 and 4). An argon-ion laser source, operating at 300 mW and 514.5 nm, was used. The specifications of the critical optical components used are

$$W_1 = 5 \text{ mrad}$$

$$W_2 = W_3 = 250 \text{ } \mu\text{rad}$$

$$L_4 = 80 \text{ mm}$$

The resulting measurement region geometry was

Elliptical spot width, $\mu\text{m}$ . . . . .	20
Elliptical spot height, $\mu\text{m}$ . . . . .	280
Spot overlap, $\mu\text{m}$ . . . . .	12
Spot pair spacing, $\mu\text{m}$ . . . . .	200
Acceptance angle, . . . . .	$\pm 50^\circ$

#### OPERATION

The temporal separation of the bipolar pulses is detected by a zero crossing detection circuit. Figure 5 shows the signal processing electronics. There are six input signals to the pulse detection circuit: the A, D, A + B, A - B, C + D, and C - D signals. The circuit uses the A and D signals to determine the direction of the detected particle. The A + B and C + D signals are used to enable comparators to search for the zero crossings of the A - B and C - D signals, respectively. The amplitude where either the A + B or the C + D signal enables the comparator is the threshold level. A particle traversing from the left, through the AB and then CD spot pairs yields an A + B signal, which enables the A + B comparator. The circuit finds the A - B zero crossing and then disables the A + B comparator until either the particle is detected at C + D or the time window expires. The time window is set as the maximum time the processor will wait for a signal from the CD spot pair, that is, the slowest expected velocity, before resetting the circuit. The analogous process occurs for a particle traversing from the opposite direction, first enabling C + D. The circuit now searches for the C - D

zero crossing and then disables the C + D comparator until either a particle is detected at A + B or, again, until the time window expires. This technique yields the flow direction and minimizes the number of false counts due to simultaneous particles in the measurement region and/or particles traversing only one of the spot pairs.

The zero crossing detection circuit outputs start and stop pulses, which are fed into a time analyzer. The start and stop pulses correspond to a particle traversing the two pairs of spots in the measurement region, that is, the time of flight. The time analyzer generates a voltage pulse (0 to 10 V) that is proportional in amplitude to the time difference between the start-stop pulses. These voltage pulses are sent to a pulse height analyzer, which sorts the voltage pulses and makes a histogram of their amplitude. The pulse-height analyzer uses 1024 bins to display the time-of-flight probability distribution (TPD) on an internal cathode ray tube (CRT). The TPD's were transferred to a personal computer, via an RS-232 interface, for analysis. The future data acquisition system will use the time analyzer output and an analog to digital converter to convert the time-of-flight into digital words. The digital data will be sent to a TSI Model 1998 master interface and then to a PDP 11/44 computer for analysis.

#### EXPERIMENT

The ability to discriminate against light not originating at the focii of the TOP beams is a very important characteristic of a practical laser anemometer. Particles traveling at a different velocity than particles at the focal plane, that is when a velocity gradient exists across the measurement volume, may scatter light which is detected by the system. Thus a spread of velocities will be measured. One wishes to minimize this spread. Shot noise from light scattered from walls decreases the signal-to-noise ratio and requires a higher threshold level for optimum signal processing. Hence, this shot noise caused from flare light is the limiting factor in how close to a wall one can get and obtain a measurement of the flow velocity.

A practical test of an anemometer's spatial selectivity is obtained by operating the system in a flow near a wall. A boundary-layer flow field would supply the necessary measurement environment. The boundary-layer thickness  $\delta(x)$  was defined as the distance from the surface where the velocity reached 99 percent of the free-stream velocity. Two experimental setups were used. A rectangular nozzle (6 by 12 mm) with an access window provided an environment similar to that encountered in a windowed engine casing. Measurements were made in the boundary layer that formed off the back wall of the nozzle. The back wall was painted black to reduce the amount of flare light. The second setup consisted of a low-velocity circular nozzle. A flat plate was placed parallel to the flow at the nozzle exit and perpendicular to the incoming light. The flat plate had a smooth polished surface. These two setups yielded a measure of how close to a wall measurements can be obtained.

The time probability distributions were converted to velocity probability distributions (VPD) using the known spot spacing. The velocity distributions were measured at various points along a line perpendicular to the plane of the surface. The variance of the VPD gives an estimate of the range of velocities present across the length of the sample volume. The mean velocities at each measurement position were fit to a cubic polynomial describing the boundary-layer velocity profile. The variances of the VPD's were plotted versus distance from the surface.

The results of these boundary-layer profiles are shown in figures 6 to 9. Figure 6 shows the mean velocity versus distance from the surface for the windowed nozzle flow. Measurements were obtained to 100  $\mu\text{m}$  from the surface for this setup. Figure 7 shows the velocity variance versus position for the profile of figure 6. The threshold level in the signal processor was adjusted at each measurement position to minimize the background noise. This accounts for the variation in the measured velocity variances in this figure.

Figures 8 and 9 show the mean velocity and velocity variance versus position for the flat-plate configuration, respectively. The profile was made 1 cm from the leading edge of the plate. Measurements were obtained 75  $\mu\text{m}$  from the surface of the plate. The threshold level was held constant for the entire profile. Figure 9 shows the expected behavior of increasing velocity variance inside the boundary layer as the magnitude of the velocity gradient increases.

The contraction nozzles used to supply the flow fields were driven by the building service air. The low-velocity limit restricts the pressure drop across the nozzle to approximately 0.1 psia. Fluctuations in the service air cause perturbations in the flow field. Some of the structures observed in these boundary-layer profiles may be artifacts of the service air fluctuations.

This second-generation four-spot TOF system uses a new prototype zero crossing detection circuit. The prototype signal processor uses the more robust processing scheme described above. The upper bandwidth limit on the prototype signal processor limits the maximum measurable velocity at approximately 40 m/sec. A new high-speed ECL version is under construction.

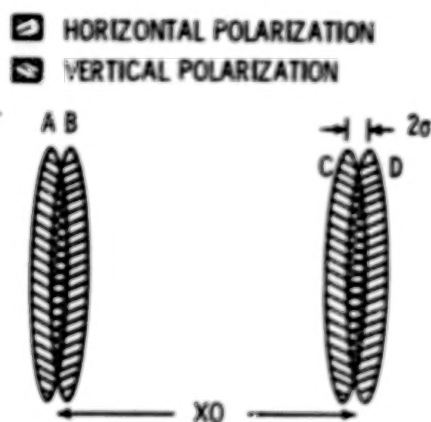
#### CONCLUSIONS

The newly constructed, four-spot anemometer has been shown to perform as predicted. The new anemometer's measurement region has the required characteristics: wide acceptance angle and high spatial selectivity to permit measurements in turbulent, hostile environments.

#### REFERENCES

1. L. Lading; "Estimating Time and Time Lag in Time-of-Flight Velocimetry," Appl. Opt. 22, 3637-3643, 1983.
2. M.J. Fisher and F.R. Krause; The Crossed-Beam Correlation Technique, J. Fluid Mech. 28, 705-717, 1967.
3. W. Matthes, W. Riebold, and E. de Cooman; Measurement of Gas Bubbles in Water by a Correlation Method, Rev. Sci. Instr. 41, 843-845, 1970.
4. T.S. Durrani and C.A. Greated; Spectral Analysis and Cross-Correlation Techniques for Photon Counting Measurements in Fluid Flows, Appl. Opt. 14, 778-786, 1975.
5. L. Lading; Comparing a Laser Doppler Anemometer with a Laser Correlation Anemometer, "Conference on the Engineering Uses of Coherent Optics," Glasgow, 493-510, Cambridge University Press, 1975.

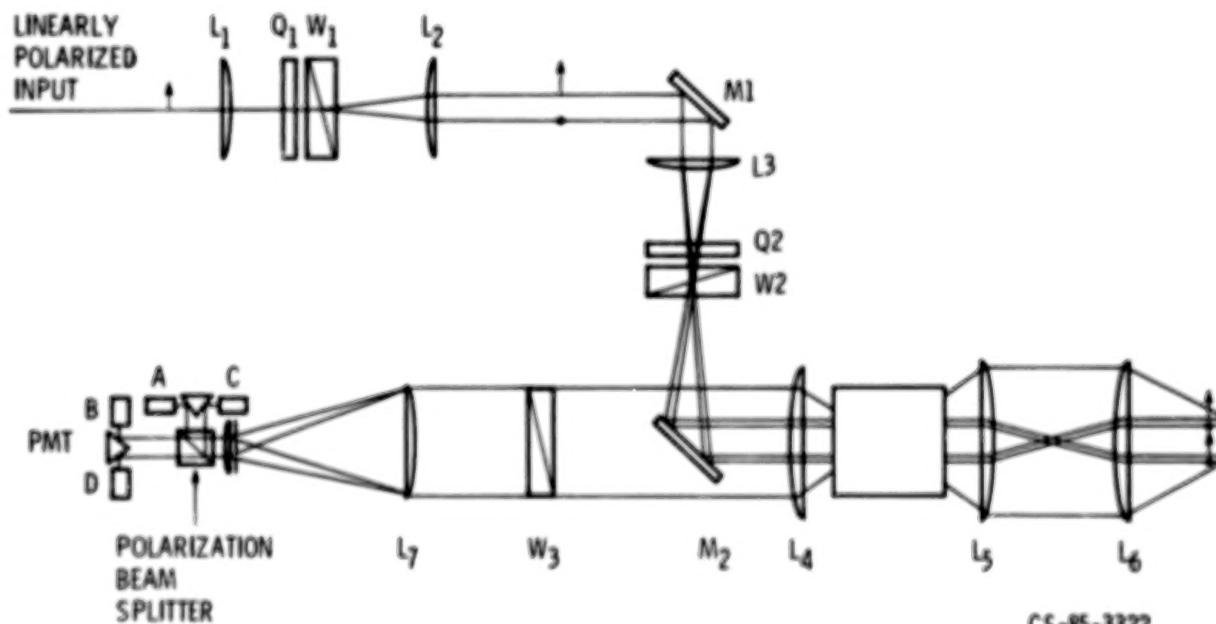
# FOUR-SPOT ANEMOMETER MEASUREMENT VOLUME GEOMETRY



CS-85-3324

Figure 1

# FOUR-SPOT ANEMOMETER OPTICAL COMPONENT LAYOUT



CS-85-3322

Figure 2

# FOUR-SPOT ANEMOMETER CONSTRUCTED FROM OPTICAL ERECTOR COMPONENTS

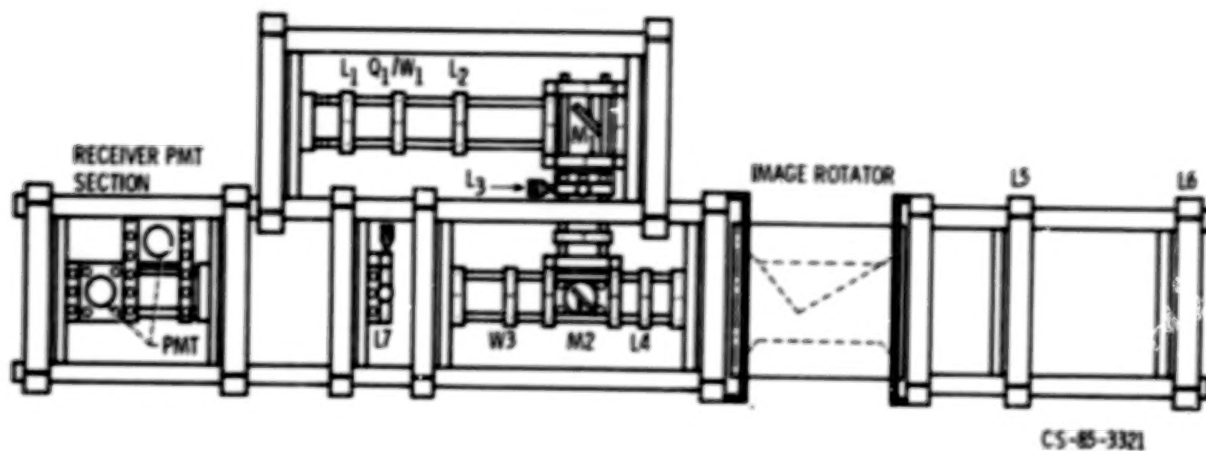


Figure 3

## FOUR-SPOT ANEMOMETER PHOTOGRAPH

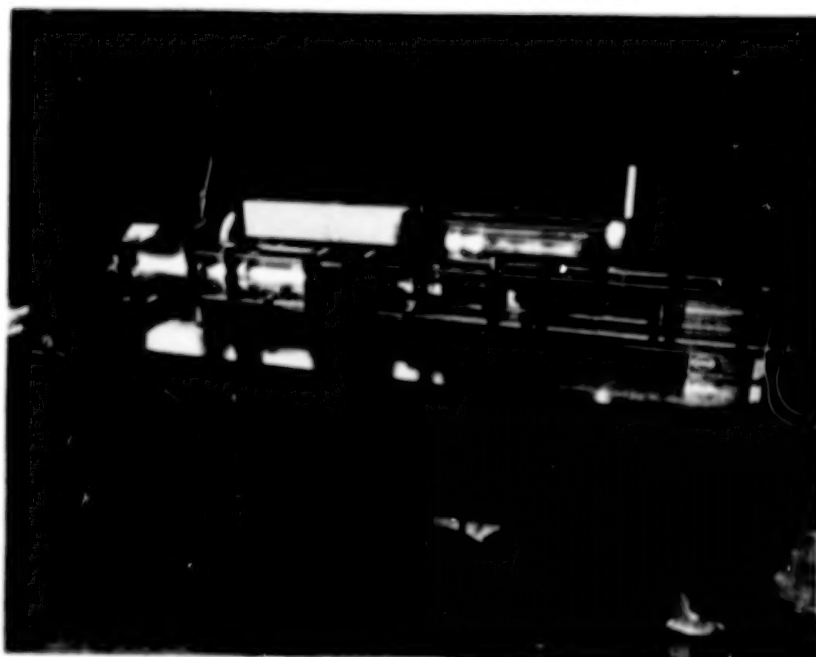
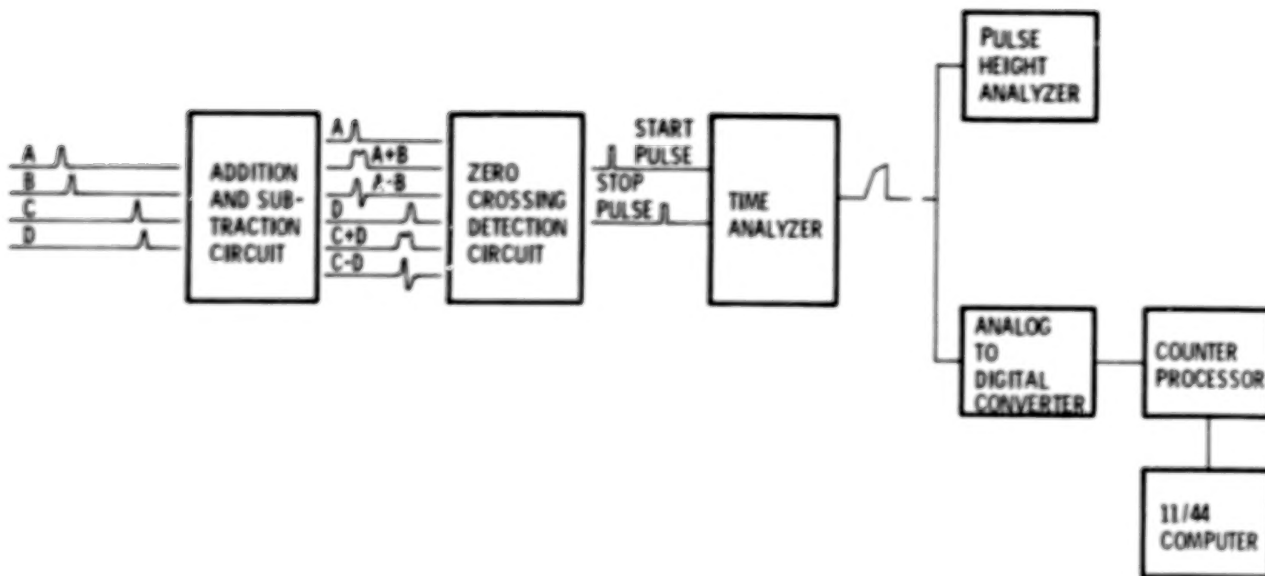


Figure 4

# SIGNAL PROCESSING FLOW CHART

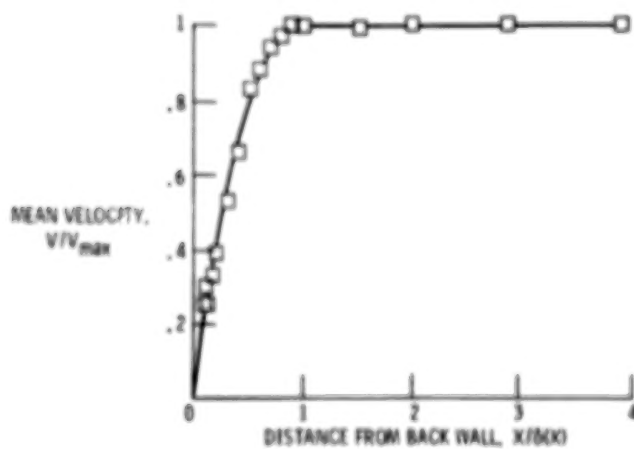


CS-85-3323

Figure 5

## WINDOWED NOZZLE BOUNDARY LAYER FLOW

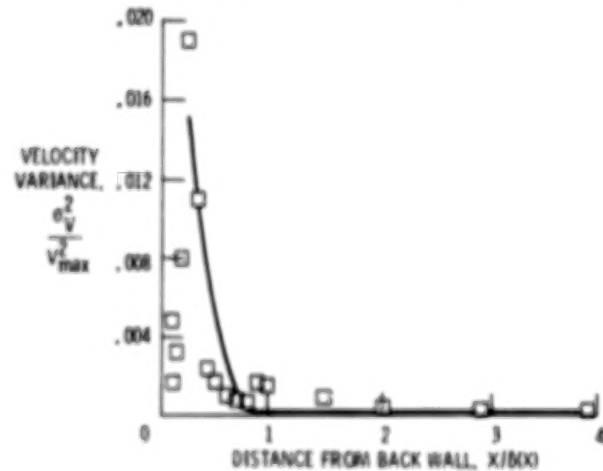
$V_{max} = 16.9 \text{ m/sec}$ ,  $\delta(x) = 1050 \mu\text{m}$ ,  $x_{min} = 100 \mu\text{m}$



CS-85-3326

Figure 6

## VELOCITY VARIANCE VS POSITION FOR WINDOWED NOZZLE BOUNDARY LAYER FLOW



CS-85-3327

Figure 7

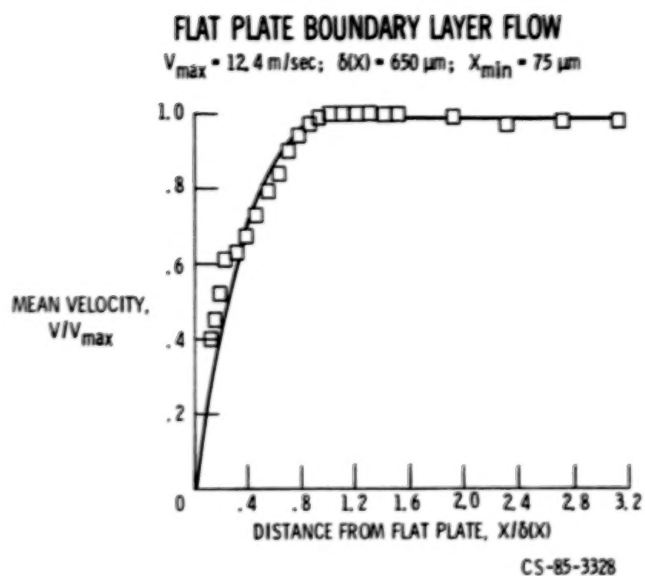


Figure 8

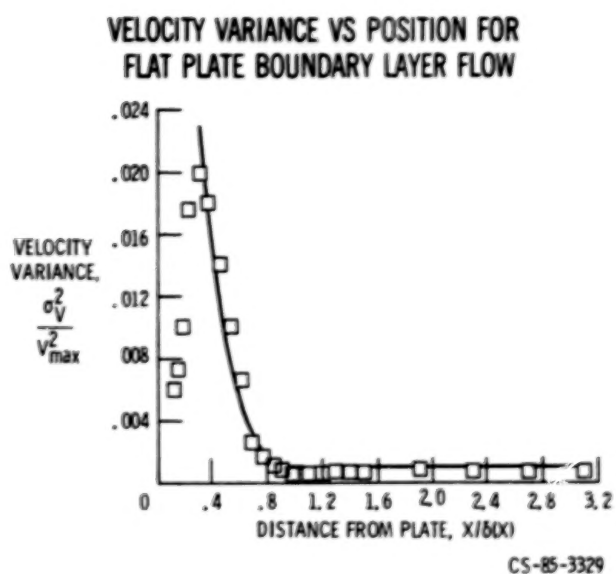


Figure 9

## THE LEWIS STRAIN GAUGE LABORATORY - STATUS AND PLANS

Howard F. Hobart and Herbert A. Will  
NASA Lewis Research Center  
Cleveland, Ohio

Several recent and ongoing HOST programs have the goal of developing electrical resistance strain gauge systems for measuring static strain in the hot-section components (combustors and turbine blades and vanes) of gas-turbine engines. A typical goal is to be able to measure static strain up to  $\pm 2000$  microstrain to within  $\pm 10$  percent at temperatures to 1250 K over a 50-hr period.

The approach to the problem has been to first develop an alloy with suitable high-temperature characteristics. Once a suitable alloy has been identified, gauges made of sputtered thin films or small diameter (0.025 mm) wire will be fabricated and evaluated.

The ongoing HOST programs are a combination of parallel in-house and contract work to achieve these goals. An in-house lab has been established for developing, testing, and evaluating high-temperature strain gauges and to aid in in-house applications of high-temperature strain instrumentation. To accomplish these tasks, data must be taken over a wide range of temperatures, times, and strain levels. If done manually, this becomes a very labor-intensive effort; therefore, the lab is automated to provide computer control of oven temperatures, imposed strain, and data sampling.

#### Test Apparatus

The basic equipment of the lab consists of two ovens, a test fixture for holding a constant strain beam, an actuator for deflecting the beam, and a computer controller and data system. One oven is dedicated to the test fixture. The computer-controlled actuator is mounted at the rear of the oven and deflects the beam via an extension rod. This system allows determination of gauge factor at various strain levels and temperatures all under computer control. The second oven is presently set up with a holding-cooling fixture to support an in-house experiment in the burner cyclic rig (ref. 1). Both ovens have been modified by the addition of an air mixer to eliminate temperature gradients.

#### Computer Controller and Data System

A standard IBM PC is set up as a system controller and data collector for the testing of high-temperature strain gauges. A block diagram of the strain gauge testing system is shown in figure 1.

The testing system consists of a 10-channel digital thermometer, a 2-channel digital-to-analog converter in programming the oven temperatures, a digital multimeter for measuring strain gauge resistance, a single-axis linear actuator for mechanically bending the strain gauge beam, and a 10-channel strain gauge bridge for measuring strain directly. The computer communicates with the strain gauge instrumentation by means of an IEEE-488 bus and an RS-232 serial interface.

The computer program (written in Fortran 77) is a very versatile time-sequencing controller. The operator can control each instrument by putting a series of times and commands in a dataset. The computer program then controls the instruments according to this series of commands. Commands are written in any order in an easy to understand English language format.

Currently, the program records data from the instruments and prints it out on a sheet of paper. In the future the data will be recorded on a floppy disk for analysis by other computer programs.

#### Lab Status and Future Plans

Today the strain gauge laboratory, is nearly operational. The computer control program is operational, with only a few minor bugs.

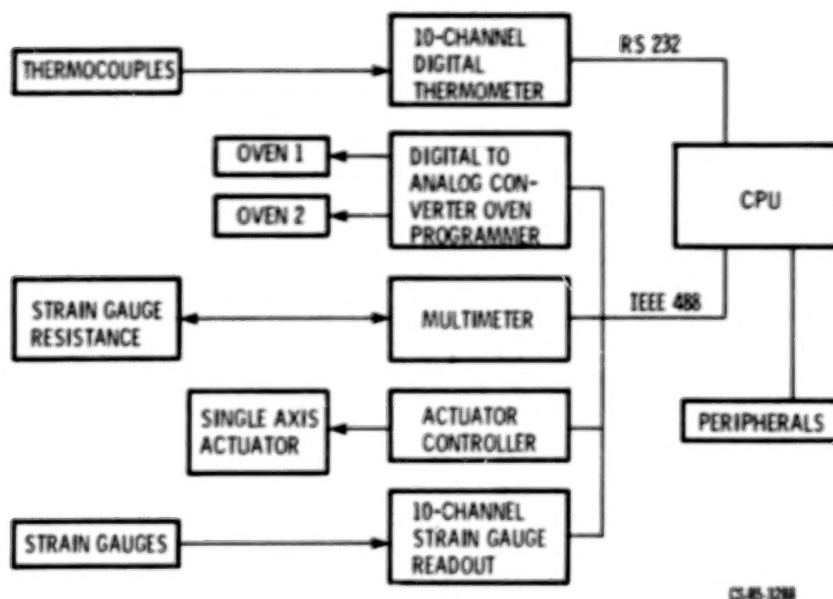
Several tests will be conducted in the near future. One involves characterizing strain gauges mounted on a Hastelloy X plate. Four Chinese-type gauges (ref. 2) and four Kanthal A-1 wire gauges (ref. 3) will be used in this in-house experiment on combustor simulation. The other test is related to a contractor effort to develop gauge systems from a palladium - 13-weight-percent-chromium alloy (ref. 4); NASA has ordered 0.025-mm-diameter wire for winding gauges of this material. Also, a sputtering target of Pd-Cr is in use to develop in-house expertise in the thin film sputtering area.

The strain gauge laboratory as designed is expected to perform these types of automated tests to yield maximum data with minimum manpower expended.

#### REFERENCES

1. Thompson, Robert L.: High Temperature Stress-Strain Analysis. Turbine Engine Hot Section Technology 1984, NASA CP-2339, 1984, pp. 259-272.
2. Hobart, Howard F.: Evaluation Results of the 700 °C Chinese Strain Gages. Turbine Engine Hot Section Technology 1984, NASA CP-2339, 1984, pp. 77-84.
3. Grant, Howard P.; Anderson, Wilbur L.: Demonstration Test of Burner Liner Strain Measurements Using Resistance Strain Gages. Turbine Engine Hot Section Technology 1984, NASA CP-2339, 1984, pp. 85-100.
4. Hulse, Charles; Bailey, Richard; Grant, Howard: High Temperature Static Strain Gage Program. Turbine Engine Hot Section Technology 1984, NASA CP-2339, 1984, pp. 71-76.

# STRAIN GAUGE TESTING SYSTEM



CS-85-3286

Figure 1

CORRELATION OF VELOCITY AND VELOCITY-DENSITY TURBULENCE IN THE EXHAUST  
OF AN ATMOSPHERIC BURNER

Gustave C. Fralick  
NASA Lewis Research Center  
Cleveland, Ohio

Laser doppler anemometers are by now widely used to measure the turbulence properties of moving fluids. Their nonintrusive nature makes their use very attractive. By the nature of the measurement process, the turbulence parameters such as turbulence intensity and turbulence scale are based strictly on velocity measurements. However, if one is interested in convective heat transfer and if the gas stream has appreciable density fluctuations (which are equivalent to temperature fluctuations if the static pressure is constant), the turbulence should probably be based on the density-velocity product. Hot-wire anemometers, for instance, give results based on the product of density and velocity, and the operation of a hot-wire anemometer depends on the flow of heat away from the wire. Hot-wire anemometry though, is not practical in high-temperature or high-velocity flows.

In the experiment to be described herein, temperature (density) and velocity are measured separately but simultaneously as functions of time so that it is possible to determine the relationships among velocity, density, and the product of density and velocity.

DESCRIPTION OF EXPERIMENT

An atmospheric burner rig was used to provide the flow for this experiment. Data were taken at various flow conditions, at mean temperatures ranging from 740 to 1620 °F, Mach numbers from 0.26 to 0.38, and values of Reynolds number divided by characteristic length in the range 33 000 to 64 000 in<sup>-1</sup>. Temperature fluctuations as great as ±500 °F were measured in a similar burner, so compensated temperature fluctuations are expected to be in this range. This level of temperature fluctuation implies a density fluctuation of approximately 17 percent; previous measurements of velocity fluctuation in this rig were in the range of 5 to 10 percent.

Temperatures were measured with a dual-wire thermocouple probe (fig. 1) which is part of the dynamic gas temperature measurement system (ref. 1). The probe consists of two platinum-rhodium thermocouples located in close proximity to each other. The wires are of different diameters, 3 and 10 mils, respectively, in this case. By comparing the signals from the two thermocouples at different frequencies, it is possible to generate a compensation spectrum and thus to determine temperature fluctuations at frequencies up to 1 kHz.

Velocity data were supplied by a fringe-type laser-doppler anemometer (ref. 2), with sampling volume location varied from 0.2 to 2.5 mm upstream of the thermocouples. Data rates varied from 400 Hz for unseeded flow to 15 kHz for fully seeded flow.

Figure 2 shows the setup of the probe in the flow stream of the burner and the crossing laser beams which form the sampling volume just in front of the probe.

The signals from the thermocouples and the laser were recorded on FM magnetic tape for later processing. The quantities stored are the ac-coupled voltages from both thermocouples, which will permit frequency compensation of the temperature data, the dc-coupled signal from the large thermocouple, which provides the mean temperature, and the laser doppler signal, from which both mean and instantaneous velocity can be extracted.

#### PRELIMINARY RESULTS

For turbulence measurements the quantities of interest are  $v_{rms}/\bar{v}$ ,  $(\rho Z)_{rms}/\rho\bar{v}$ , and their autocorrelations to provide a measure of turbulence intensity and turbulence scale. The cross correlations are also of interest; they will answer questions such as whether the velocity peaks are related to the hotter combustion products or to the cooler, denser filaments of dilution air. Figure 3 is the cross correlation of the velocity and the temperature signal from the 3-mil thermocouple; figure 4 is the cross correlation of the same signal from the 10-mil thermocouple. The correlations were calculated at a 5-kHz sampling rate. Both figures relate to the same flow;  $M = 0.28$ ,  $Re/L = 32\,000\text{ in}^{-1}$ ,  $T = 1581^\circ\text{F}$ . In both cases, the temperature signals were uncompensated for the frequency response of the thermocouples. When the temperature signals are compensated, the shape of the cross correlation curves may change, but it can be seen that the two quantities, velocity, and density are correlated; they show a characteristic cross correlation peak. A distinctive characteristic of the curves is the delay between the velocity and density. This was seen in all the data, for 13 different flow conditions, with seeded or unseeded flow. The delay was consistently greater for the larger thermocouple, but as yet, we are unable to relate the delay to the time constant of the thermocouples.

#### FUTURE EFFORTS

Future efforts will proceed in several areas. One will be further analysis on the effect of sensor time constant on correlation delay. The above described correlations will also be repeated after the temperature signals are compensated for. The density-velocity product as a function of time must also be generated; it will then be possible to compare turbulence based on velocity with that based on the density-velocity product. Having done that, the experiments will be rerun with heat-flux instrumentation in the flow field. This will permit relating the convective heat-transfer coefficient to both the velocity and velocity-density turbulence.

#### REFERENCES

1. Elmore, D.L.; Robinson, W.W.; Watkins, W.B.: Dynamic Gas Temperature Measurement System. NASA CR-168267.
2. Seasholtz, R.G.; Oberle, L.G.; Weikle, D.H.: Laser Anemometry for Hot Section Applications Turbine Engine Hot Section Technology-1983. NASA CP-2289, 1983, pp. 57-68.

# DUAL WIRE THERMOCOUPLE PROBE



Figure 1

# DUAL WIRE THERMOCOUPLE AND LDA SAMPLING VOLUME IN EXHAUST OF ATMOSPHERIC BURNER

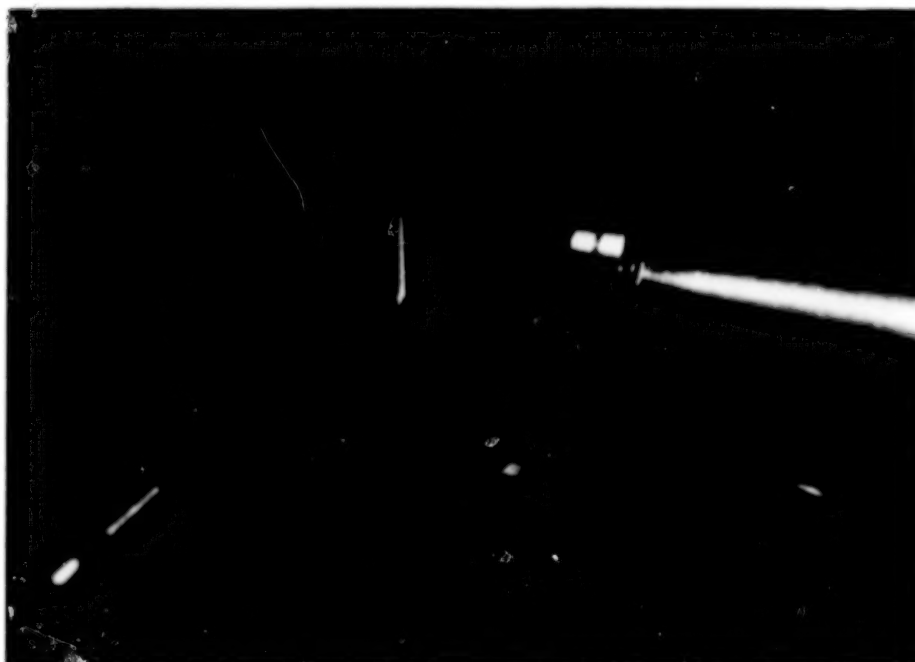
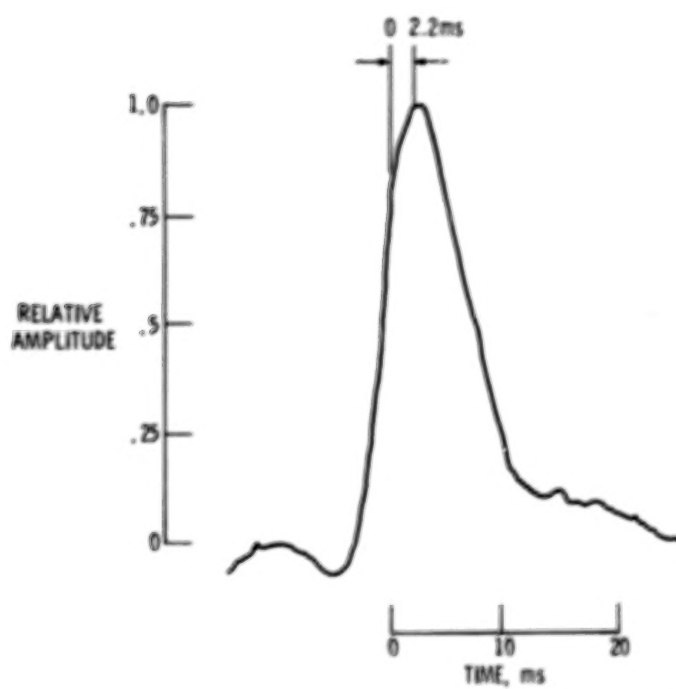


Figure 2

### VELOCITY-TEMPERATURE CROSS CORRELATION

3-mil THERMOCOUPLE;  $\bar{V} = 187$  m/sec;  $\bar{T} = 158$  °F

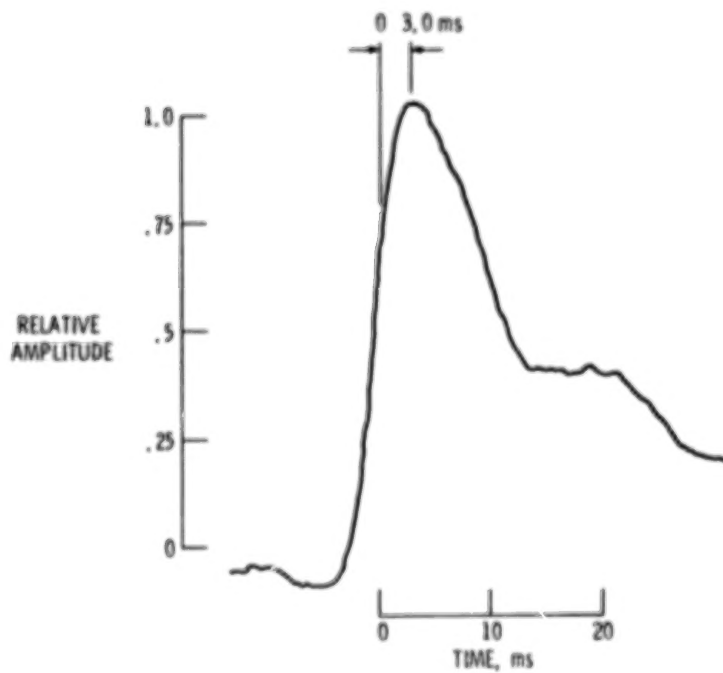


CS-85-3404

Figure 3

### VELOCITY-TEMPERATURE CROSS CORRELATION

10-mil THERMOCOUPLE;  $\bar{V} = 187$  m/sec;  $\bar{T} = 158$  °F



CS-85-3403

Figure 4

## IMPROVED NUMERICAL METHODS FOR TURBULENT VISCOUS RECIRCULATING FLOWS\*

## A PROGRESS REPORT

A. Turan

Avco Everett Research Laboratory, Inc.

The hybrid-upwind finite difference schemes employed in generally available combustor codes possess excessive numerical diffusion errors which preclude accurate quantitative calculations. The present study has as its primary objective, the identification and assessment of improved solution algorithm as well as discretization schemes applicable to analysis of turbulent viscous recirculating flows. The assessment is to be carried primarily in two dimensional/axisymmetric geometries with a view to identifying an appropriate technique to be incorporated in a three-dimensional code.

To accomplish the above objective, a semi-exhaustive survey was carried out of the relevant literature for computing turbulent viscous recirculating (incompressible) flows. The following techniques were identified as candidates offering the best compromise between accuracy and boundedness and hence were selected for further evaluation (quantitatively) in two-dimensional problems.

- a) Second Order Upwind Differencing
- b) Modified Skew Upwind Differencing
- c) Operator Compact Implicit Differencing
- d) Various Advanced Solvers

Item d encompasses a myriad of solvers including the strongly implicit scheme (SIP) and incomplete Cholesky (IC) as base solvers, accelerated by a variety of techniques. These accelerators include conjugate gradient (CG), multi-grid (MG) and block correction (BC) algorithms.

Second order upwind differencing yielded minor oscillations when applied to the test problem for the convection-diffusion of a scalar for various inlet angles. The same behavior was also observed in the driven cavity problem for some of the high Reynolds number cases considered.

Bounded skew upwind differencing including streamwise source corrections (necessitated by the poor performance of the original skew scheme in the driven cavity problem) is currently being evaluated for select test problems. To overcome the arbitrariness and limitations introduced by the particular bounding scheme, work on a further alternative including a novel, mass-based formulation incorporating an optimized interpolator is in progress. This has been shown to provide more

\*This paper briefly describes the work performed under contract NAS3-24351.

accurate and bounded predictions than previous applications of skew upwind differencing.

Operator compact implicit differencing with a formal accuracy of fourth order in smooth flow regions, has been formulated in a finite difference framework and select examples will be discussed that highlight accuracy and boundness issues. Work is also in progress to reformulate the scheme in a conservative, flux-based finite volume manner incorporating boundness at the expense of accuracy in high Peclet number regions of the flow.

In incompressible flow predictions utilizing the segregated SIMPLE derivative algorithms, most of the effort goes to satisfying the incompressibility constraint, i.e., the pressure/correction equation. The advanced solvers considered for this effort are designed to provide faster convergence rates for this "Poisson-like" equation as well as being inherently more suited for solving extended node cluster formulations arising either due to the particular differencing scheme and/or the increase in the dimensionality of the problem. Studies aimed at assessing the performance of these solvers for the linearized pressure/correction equation in various test problems have identified a group of optimum base solvers and accelerators. These include SIP-MG, SIP-BC and IC-MG. Issues related to non-linear applications including 3-D problems will be discussed.

Select results from all phases of the work (where available) will be presented and the relevant issues will be discussed in detail.

## AEROTHERMAL MODELING PROGRAM - PHASE II\*

H.C. Mongia, S.V. Patankar<sup>†</sup>, S.N.B. Murthy,<sup>‡</sup> J.P. Sullivan,<sup>‡</sup>  
and G.S. Samuelsen<sup>§</sup>

Allison Gas Turbine Division, General Motors Corporation

The main objectives of the NASA-sponsored Aerothermal Modeling Program, Phase II are:

- o to develop an improved numerical scheme for incorporation in a 3-D combustor flow model
- o to conduct a benchmark quality experiment to study interaction of primary jet with a confined swirling crossflow and to assess current and advanced turbulence and scalar transport models
- o to conduct experimental evaluation of the air swirler interaction with fuel injector, assessment of the current two-phase models, and verification of the improved spray evaporation/dispersion models

To improve predictive capabilities of current combustor aerothermal models, improvements are needed in numerical schemes, modeling of turbulence and scalar transport processes, and spray modeling of interaction with turbulent recirculating swirling flows. To assess current models and help the development of advanced models, detailed and accurate experimental data are needed for well defined test configurations. The main objective of the NASA Aerothermal Program is to provide the gas turbine combustion community with benchmark quality data and significantly improved numerical scheme, turbulence, scalar, and spray transport models..

There are three elements of the Aerothermal Modeling program--Phase II. They are:

Element A - Improved Numerical Methods for Turbulent Viscous Recirculating Flows

Element B - Flow Interaction Experiment

Element C - Fuel injector - Air Swirl Characterization

Each element will be briefly described.

#### I. IMPROVED NUMERICAL METHODS FOR TURBULENT VISCOUS RECIRCULATING FLOWS

The advanced numerics effort consists of the following three technical tasks. Task 1 has been completed and Task 2 is under progress.

##### Task 1. Numerical Methods Selection

The first phase of Task 1 involved the selection of at least six numerical techniques. These techniques were evaluated in the second phase of Task 1. Based on this preliminary evaluation four techniques were chosen for detailed evaluation under Task 2. The selected schemes had to be more accurate than the conventional upwind differencing (UD) and hybrid schemes; in particular the numerical schemes had to minimize the numerical diffusion encountered in UD and hybrid schemes for grid Peclet numbers greater than two. In addition, the schemes had to be stable, bounded, and computationally efficient for a wide range of Peclet numbers and a broad class of problems.

<sup>†</sup>University of Minnesota

<sup>‡</sup>Purdue University

<sup>§</sup>University of California at Irvine

\*Work done under NASA Contract NAS3-24350.

Among the techniques chosen for preliminary evaluation were the finite element scheme of Baliga and Patankar, the cubic-spline method, the skew upwind differencing scheme (SUDS), the quadratic upwind differencing scheme (QUDS or QUICK), the flux-blended versions of SUDS and QUDS, the Agarwal fourth order scheme, the exponential (tabulated) scheme, and Patankar's flux-spline schemes. As a first step an extensive literature survey was conducted, firstly, to derive conclusions regarding the relative merits of the various schemes based on comparative studies reported in the literature and secondly, to identify new schemes or techniques to modify existing schemes. The survey showed that while many of the schemes are considerably more accurate than the hybrid scheme for specific test cases, no second order scheme is currently available that is unconditionally stable, bounded, and conservative. Therefore, an effort was initiated to focus on modifying an existing scheme and/or developing a new scheme that would meet the objectives of the program. In addition, the task of identifying the most promising techniques among those listed continued with the application of the various techniques to test problems. The result of these two efforts are summarized in the following paragraphs.

A number of test problems were chosen and solved by different numerical schemes. Of all the schemes studied the flux-spline scheme (and its variants) and the quadratic upwind scheme (QUICK) seemed to perform significantly better than the other schemes. The basic flux-spline scheme assumes that the total flux  $J$  (convection + diffusion) of the dependent scalar variable  $\phi$ , varies linearly with distance over each control volume. Two versions of the scheme result from the assumption of a stepwise and piecewise linear velocity distribution, respectively, for the underlying convection field. The improved flux-spline scheme is based on a cubic variation of the total flux  $J$  as well as the underlying velocity. The QUICK (or QUDS) scheme seemed to show the best performance among the schemes studied under the NASA Error Reduction Program at Pratt and Whitney, (see reference 1) although the stability and means of improving the solution technique for the scheme were vastly unexplored. In particular, the flux-blending scheme, to keep the solution bounded, was not incorporated in the QUDS scheme for various reasons. Therefore, the bounded QUICK scheme is considered to merit further exploration in the present study.

Efforts to develop a new second order scheme resulted in the controlled numerical diffusion with internal feedback (CONDIF) scheme (developed by Runchal), which is a modified central differencing scheme (CDS). CONDIF recasts the centered-difference equation in a form that leads to unconditional stability and low numerical diffusion. Results for sample test problems show improved accuracy over those for the hybrid scheme, especially at high Peclet numbers. CONDIF retains the second order accuracy of CDS, but unlike CDS is unconditionally stable and devoid of over and under-shoots in the solution of the dependent variable.

Another aspect of Task 1 concerns the selection of a suitable solution algorithm for the flow field. The momentum and continuity equations represent a nonlinear coupled set that must be solved to get a prediction for the flow field. Iterative methods such as SIMPLE and SIMPLER have been developed to solve the flow equations. These methods, although quite successful, have proved to be slowly converging and hence time consuming. Their success also depends on the proper choice of under-relaxation factors. An alternative to these iterative methods is the direct solution of the whole set of momentum and continuity equations. This alternate method uses the D'Yakonov iteration scheme and the Yale University Sparse Matrix Package. Preliminary investigation of two schemes based on the direct solution method showed that the schemes converged considerably faster than SIMPLE AND SIMPLER.

Based on the findings under Task 1, the following four techniques were selected for further evaluation Task 2:

1. Flux-spline scheme and its variants
2. CONDIFF scheme
3. Bounded QUICK scheme
4. Direct solution methods

#### Task 2--Technique Evaluation

Under Task 2, the techniques selected in Task 1 will be tested extensively in terms of accuracy, stability, and computational efficiency. The techniques will be used to calculate a variety of test cases including 2-D recirculating flows-turbulent and non-turbulent, with and without swirl. The first step, which is currently under progress, is to identify the test cases for which accurate numerical or analytical solutions or detailed experimental data exist. The techniques will be used to calculate the selected test cases and the technique showing the best performance will be incorporated in Task 3.

#### Task 3--3-D Computation Evaluation

An existing NASA Lewis 3-D elliptic code (COM3D) will be modified to incorporate the "best" advanced numerical scheme identified in Task 2. A test case will be selected including the geometry, experimental data, and computational details. This case will be run to assess the performance of the advanced numerical scheme including accuracy, stability, convergence rate, and computational time.

## II. FLOW INTERACTION EXPERIMENT

This element consists of both experimental and numerical investigations that include five major technical tasks as discussed in the following:

#### Task 1--Experimental Configuration

This task involved preliminary design of the test section, its detailed design for fabrication and the experimental plan for data acquisition. A layout for the test section geometry is shown in Figure 1 with photographs shown in Figure 2. The 30-in. long test section made of plexiglass to facilitate optical access for the LDV has rectangular cross-section (15 in. x 3 in.) The main flow is established using five swirlers and the primary jets are injected in cross-flow as shown in the figure. Under this task, two similar rigs - one using air for LDV measurements and the other using water for flow visualization have been designed.

The detailed test matrix for the Flow Interaction program is given in Figure 3 and the corresponding flow configurations are shown in Figure 4. The configuration changes are made in both the air and water rigs with interchangeable upper and lower plates.

The first two tests have no fluid entering through the primary jets. Test 1 admits nonswirling fluid through five annular jets while Test 2 uses 60 deg flat vane swirlers. Tests 3 through 6 involve the interaction of swirling flow with the flow from two primary jets. The mass flow ratio and the downstream distance is the same for these cases with the cross-channel location and the stagger of the jets varying as shown in Figures 4A through 4D. The effect of downstream location of the two primary jets is investigated in Tests 9 and 10 and the effect of mass flow ratio

in Tests 14 and 15. A similar set of experiments involving four primary jets per swirler is scheduled in Tests 7, 8, 11, 12, 16 and 17. The four jet configurations are shown in Figures 4E and 4F.

### Task 2--Modeling

This task involved the selection of a 3-D flow code and simulation of different flow configurations using the current turbulence model ( $\kappa$ - $\epsilon$ ) for a preliminary study of the flow fields. The main importance of the task has been in highlighting different vortical regions in the flow field that would be taken into account during LDV measurements so as to resolve these regions of steep velocity gradients. For the purpose of numerical simulation, the COM3D computer code was selected. Each flow configuration was computed using a  $35 \times 25 \times 25$  grid that was uniform in the y-z plane and nonuniform along the x-direction (the main flow direction). The solution convergence was typically obtained in about 200 iterations.

The results of computing the chosen basic flow configurations (See Figure 4) indicate that these configurations indeed offer interesting flow fields for the final verification/validation of the model against the data base. For example, some results for configuration B are shown in Figures 5 and 6. A complex interaction between the swirling flow and the jets in cross-flow is clearly seen. For  $X_j/H = 0.5$ , Figure 5C shows two concentrated vortices, one at the upper right-hand corner and the other at the lower left-hand corner. In these regions the primary jets are aiding the angular momentum of the swirling flow. With the reduced swirl downstream at  $X_j/H = 1.0$ , the interaction with the jets results in larger vortical regions in the cross-plane as shown in Figure 6.

### Task 3--Measurements

Two test rigs and various test configurations have been fabricated under Task 3. The test rigs along with the associated instrumentation have been assembled and initial checkout runs have been made to ensure that the rig, instrumentation, and data reduction software are performing well.

The flow visualization rig will be used to establish flow characteristics and define regions of interest for conducting detailed single-point measurements.

For the flow configurations identified in Task 1, measurements will be made to obtain the following:

- o detailed wall static pressure distribution
- o mean velocity and Reynolds stress components
- o fluctuating and mean concentration measurements for assessing scalar transport models

Velocity measurements are made with a two-color, two-component LDV system, shown in Figure 7, is mounted on a computer-controlled table that along with computer control of the field lens allows movement of the probe volume in three dimensions.

The data acquisition system consists of TSI counter type processors interfaced to a DEC 11/23 computer (See Figure 8). The hardware interface contains a resettable 10 MHz clock for measuring the time of arrival of a valid LDV signal. The simultaneous arrival of signals from the two components is determined in software by requiring that the respective clock signals are within 1-microsecond of each other.

The DEC 11/23 also controls the x-y-z position of the probe volume through a stepper motor controller.

The three beam optical arrangement allows measurements to be made close to a wall. By rotating the optics package about the optical axis, measurements near the end-wall, top wall, and bottom wall are possible.

Detailed velocity measurements are underway and the results will be presented during the meeting.

#### Task 4--Results and Analysis

Under this task, measurements of velocity and smoke concentration will be analyzed to determine the probability density function and auto- and cross-correlations.

#### Task 5--Model Improvement

This task involves the development and use of improved turbulence and scalar transport models for complex swirling flows.

### III. FUEL INJECTOR--AIR SWIRL CHARACTERIZATION

This element, which covers both experimental and numerical research on two-phase flow interactions to support analytical modeling of the dome region of the combustor, consists of five major tasks. Tasks 1 and 2 have been completed. A brief description of the five tasks is given in the following paragraphs.

#### Task 1--Experimental Configuration

This task involves preliminary design of the test section, its detailed design for fabrication, and the experimental plan for data acquisition.

The proposed experiment will consist of a fuel injector and a swirler typical of current use in aircraft turbine engines (See Figure 9). The fuel nozzle and swirler combination will be run at both free of confinement and confined conditions (6-in. duct). The experimental plan will cover a wide range of tests that could be staged in complexity, with the constituent flows measured separately and then in combination. The duct is designed in such a way to enable the required measurements to be taken at the inlet plane and at seven axial locations downstream of the swirler-fuel injector combination. The measurements will include the following quantities: the three components of mean and root mean square (rms) gas velocity as well as Reynolds stresses, the three components of mean and rms droplet velocity, Sauter mean diameter, droplet size distribution, spatial distribution of droplets, cone angle, fraction of liquid evaporated in the duct (vapor concentration), the static pressure along the wall of the duct, and the inlet air temperature.

All the test configurations (See Figure 10) will first be operated free of injected particles (except for the Laser anemometer seed), second with injected monodisperse solid particles (30-micron glass beads), then with injected multi-sized solid particles (30, 50, and 100  $\mu$ m glass beads), and finally with a fuel spray (methanol).

## Task 2--Modeling Sensitivity Analysis

Allison had run its 2-D codes (parabolic and elliptic) to predict the distribution of the flow field variables for all proposed flow and geometry test conditions of the experimental test matrix. The main purpose of this task is to determine if the planned experiment is sensitive to the significant variables and which variables and boundary conditions are necessary to measure.

As proposed in Allison EDR 11754, the COMDISP code (the modified version of the OCG-2 computer code of Brigham Young group) has been run to predict the test plan cases. Two cases will be demonstrated. The first case represents single-phase flow (no injected particles) through the primary tube and air swirler of 60 deg in a 6-in. duct. Figure 11 shows that the main flow is attached to the wall (first radially outward then axially forward). This finding is in complete agreement with the simple flow visualization studies done at Purdue University under Element B of the HOST program. To get a good flow pattern in the duct, it has been suggested that the swirler be recessed into the head plate by 1/4-in. for the test matrices of both Elements B and C of the HOST program.

The second case represents a fuel nozzle centered in 1.5-ft duct to simulate a free of confinement conditions thus allowing the spray to be characterized in the absence of wall effects. A low stream of air through the duct will be used to suppress recirculation and the subsequent accumulation of aerosol. Even with this low stream (.5 m/s) a weak recirculation bubble has been formed near the wall but farther downstream from the exit plane (See Figure 12). In this case, the problem can not be predicted using a parabolic code that does not consider the wall effects. This turns down the main function of the big duct. Accordingly, Allison has suggested to replace the 1.5-ft plexiglass duct by a screen enclosure. The screen will allow the necessary air, demanded by the jet entrainment, to enter the chamber and thereby preclude wall recirculations.

## Task 3--Measurements

The efforts of the first year have been directed to (1) the design, fabrication, and testing of the facility, (2) the preliminary verification of the laser interferometer diagnostics (See Figure 13), and (3) the acquisition of test data in the spray chamber.

In the present program, the utility, applicability, and accuracy of phase Doppler has been tested in a series of experiments in which pitch diameter (PD) has been compared to visibility/intensity validation and laser diffraction using a Malvern, (See References 2 and 3). Basically, two comparisons are considered: radial variation in SMD and composite weight distributions, both at selected axial locations in a air assist nozzle operating on water as the liquid.

The radial variation of the spatial SMD of the spray is depicted in Figure 14 for axial positions of 30-mm and 50-mm. In each case, the single line-of-sight Malvern measurement (from both the Rosin Rammler and Model Independent Analyses) is also illustrated. The correspondence between the two interferometric measurements is very good at both axial stations. Differences that surface are realistic in light of the relative limitations of the instruments. The phase Doppler was configured to measure diameters as small as 1-micron, whereas the V/IV was configured to measure diameters as small as 6-microns. The large sizes typical of the outer regions of the spray, require a change in the V/IV optics and concomitant splicing of data. For example, at 30-mm the outer two data points are each composites of two separate

measurements; at 50-mm the outer three points are composites of eight data runs, splicing different size windows and frequency bands. In addition to being somewhat tedious, the required splicing of data sets introduces potential error in that the method of splicing data points is uncertain. Note that, at 50-mm, there is a shift in the data as the spliced sets are encountered.

Comparing the point measurements to the single line of sight measurement is encouraging. Both interference techniques give plausible radial profiles of SMD in light of the diffraction measurement.

At 30-mm PD yields a composite SMD of 31.8-microns (weighted in addition by the radial growth of the effective probe volume); V/IV measures 28.9-microns. The Malvern yields values of 19.5-microns (Rosin Rammler) and 28.3-microns (Model Independent). At 50-mm the PD composite value of 29.4-microns; that of V/IV is 31.9-microns. The Malvern yields values of 24.4-microns (Rosin Rammler) and 30.7-microns (Model Independent). At both locations the correspondence between point measurements and the Model Independent analyses of diffraction data is excellent. The Rosin Rammler value is typically low, suggesting it does not adequately fit the diffraction data.

In Figure 15, the same data sets are examined in terms of their distribution of liquid weight. Distributions from the point measurements are composites, generated in a manner consistent with the composite SMD formulation. The Rosin-Rammler distributions are plotted on the same scale as the Model Independent distributions (15 parameter curve fit) for the same data. The size intervals represented by each point vary in accordance with the size and radial position of elements of the focal plane detector. Although both the Rosin-Rammler and Model Independent distributions compare favorably at this axial location, the point measurements agree better with the Model Independent treatment of the diffraction data in locating the distribution's peak. The apparent divergence of the diffraction data at large drop sizes is an artifact of plotting the data in the size intervals of the Model Independent algorithm (the resolution of the distribution model decreases in inverse proportion to drop size).

#### Task 4--Results and Analysis

Experimental data of Task 3 will be reduced and presented in a format suitable to make direct comparison with model predictions and to quantify the effects of the flow and geometric variables in various transport processes.

#### Task 5--Model Improvement

An advanced spray/flow interaction model will be validated under this effort. The model will include improved submodels of turbulence, spray injection, trajectory, evaporation, particle dispersion, and scalar transport processes.

#### REFERENCES

1. Syed, S.A., Chiapetta, L.M., and Gosman, A.D., Error Reduction Program, Final Report, NASA CR-174776, January 1985.
2. Jackson, T.A., and Samuelsen, G.S. "Spatially Resolved Droplet Size Measurements," ASME 85-GT-038, ASME Gas Turbine Conference, Houston, TX (Accepted for publication in Journal of Engineering for Gas Turbines and Power). 1985.

3. Jackson, T.A., and Samuelsen, G.S. "Performance Comparison of Two Interferometric Droplet Sizing Techniques," SPIE 573-09, Society of Photo-Optical Instrumentation Engineers 29th Annual International Technical Symposium, San Diego, CA. 1985.

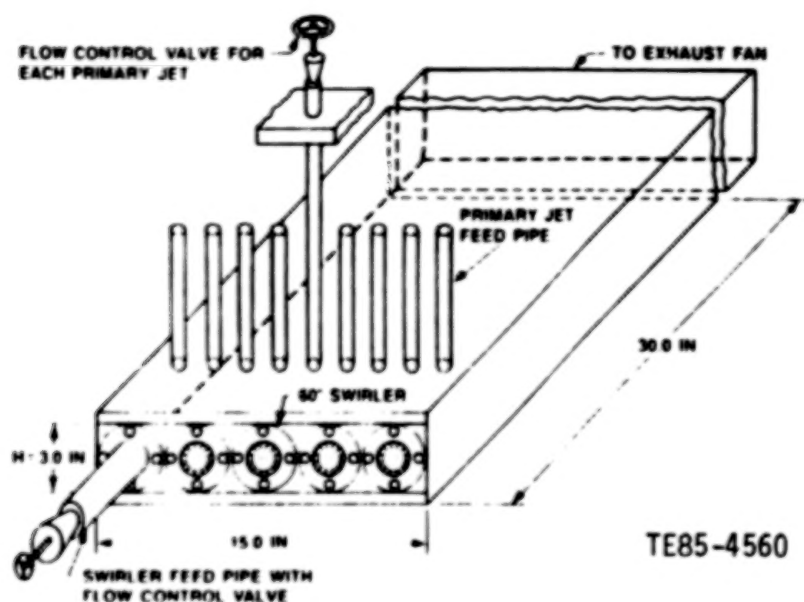
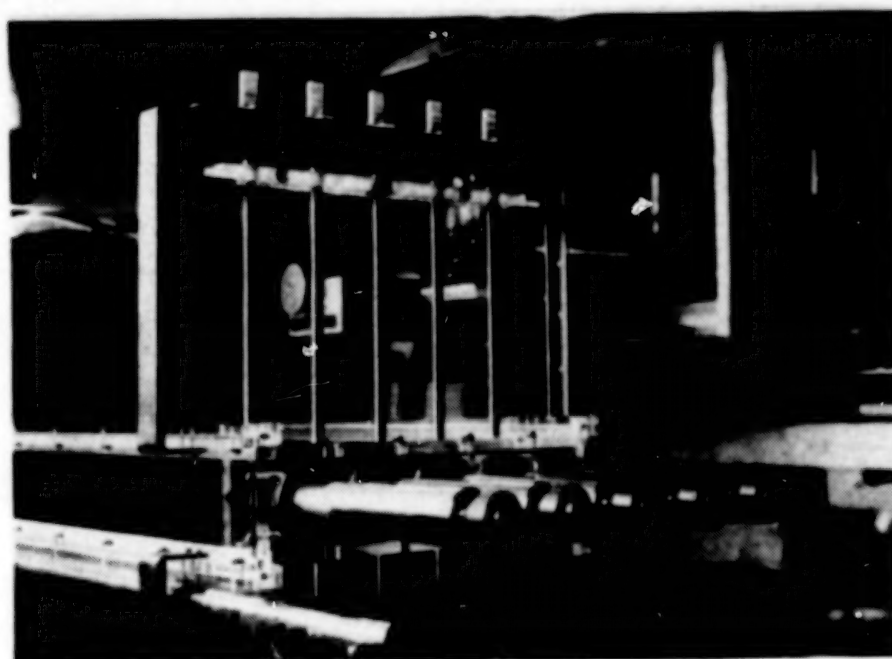
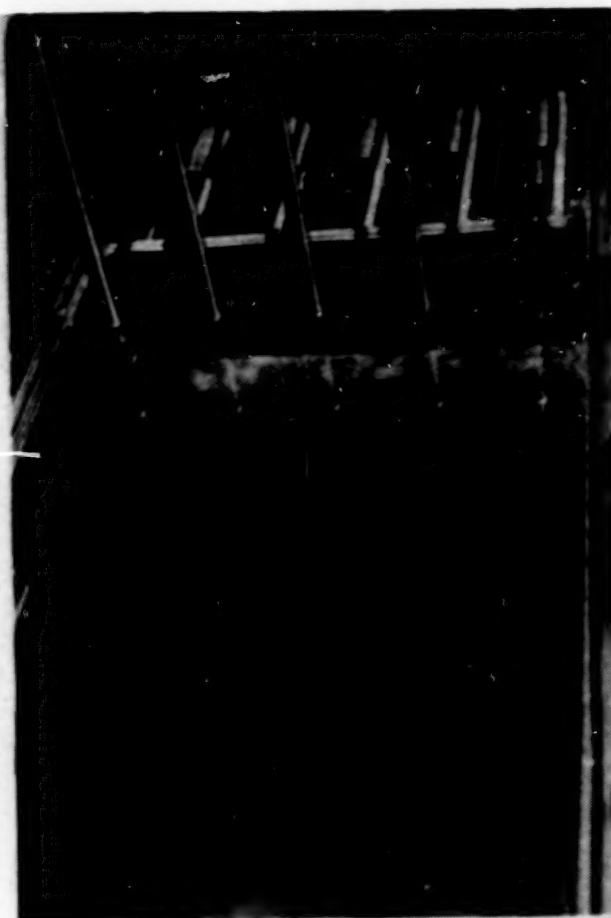
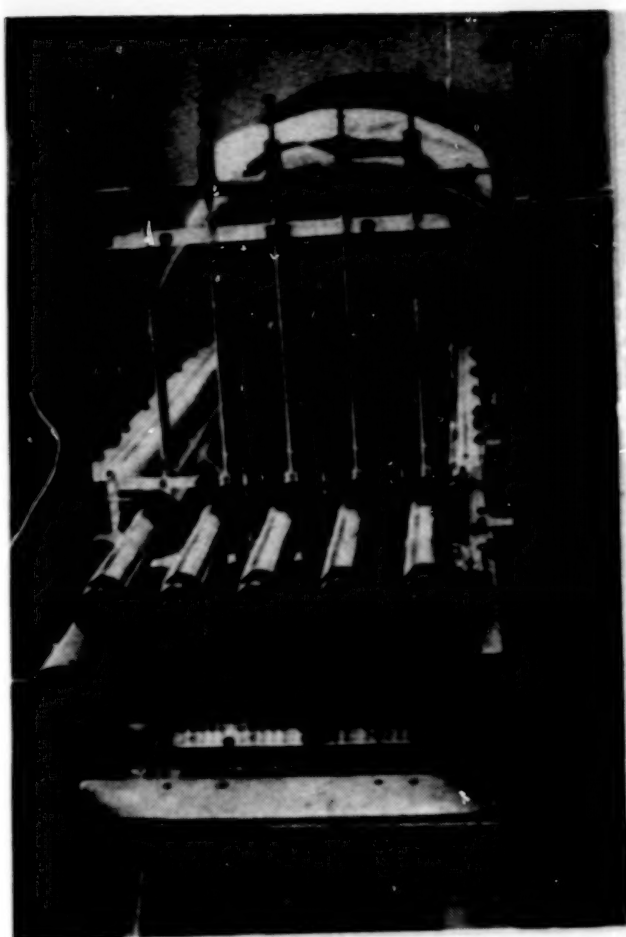


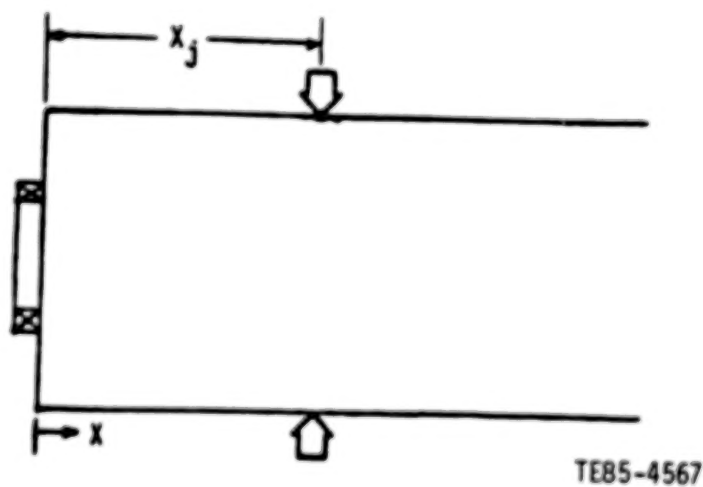
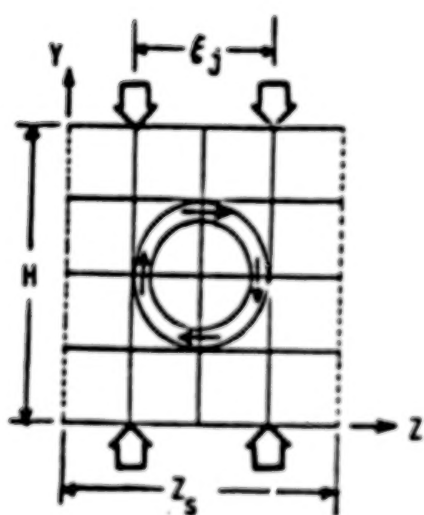
Figure 1. Test section geometry.



TE85-4561

Figure 2. Flow interaction experiment - air rig.

Test No.	Configuration	$\xi_j/H$	$X_j/H$	$M_j/M_s$	Tracer	Jets/swirler
1	BC1	-	-	-	No	-
2	BC2	-	-	-	No	-
3	A	1.0	0.5	0.75	No	2
4	B	1.0	0.5	0.75	No	2
5	C	1.0	0.5	0.75	No	2
6	D	1.0	0.5	0.75	No	2
7	E	0.5	0.5	1.50	No	4
8	F	0.5	0.5	1.50	No	4
9	A	1.0	1.0	0.75	No	2
10	B	1.0	1.0	0.75	No	2
11	E	0.5	1.0	1.50	No	4
12	F	0.5	1.0	1.50	No	4
13	A	1.0	0.5	1.50	No	2
14	A	1.0	0.5	0.75	Yes	2
15	B	1.0	0.5	0.75	Yes	2
16	E	0.5	0.5	1.50	Yes	4
17	F	0.5	0.5	1.50	Yes	4



TE85-4567

Figure 3. Text matrix.

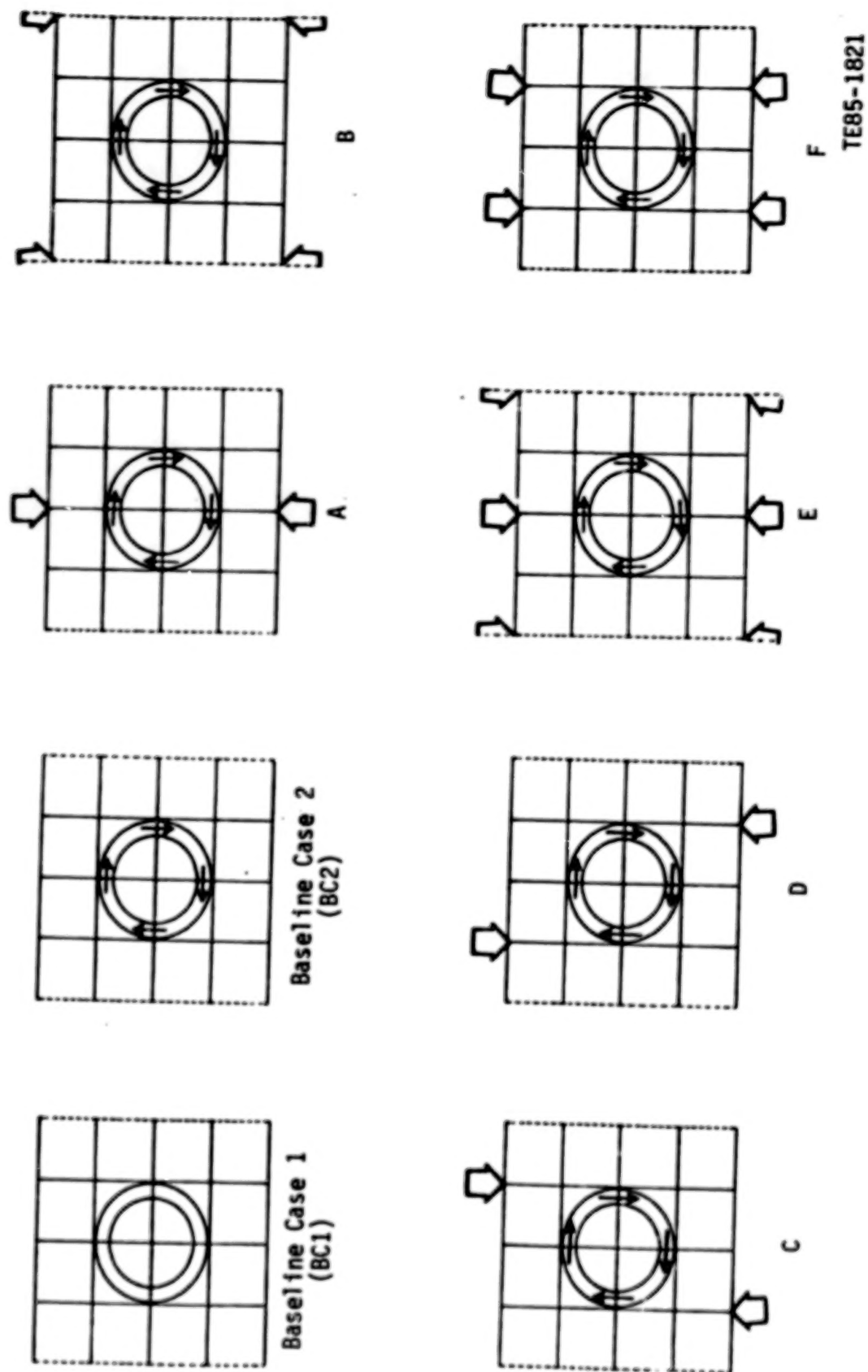
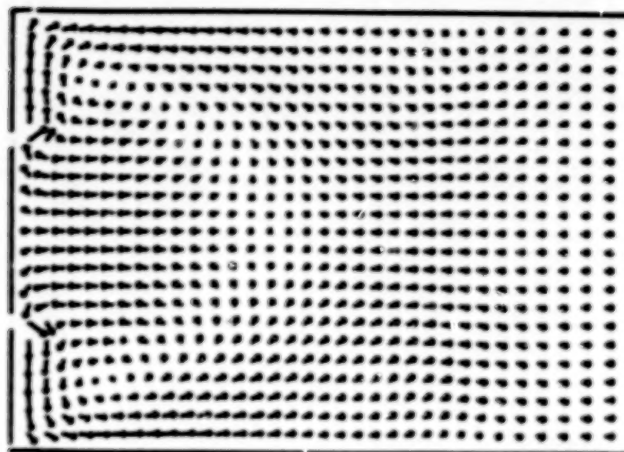
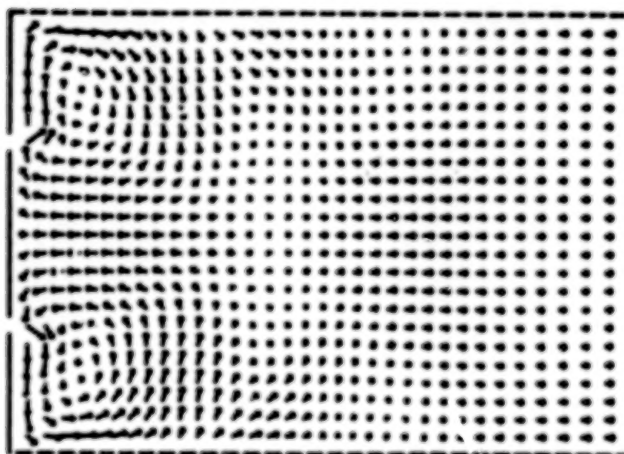


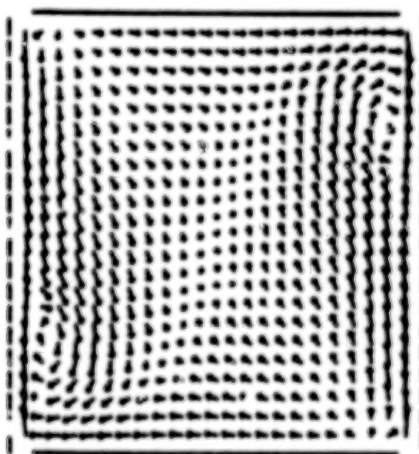
Figure 4. Basic flow configuration.



a. Midswirler plane (X-Y)



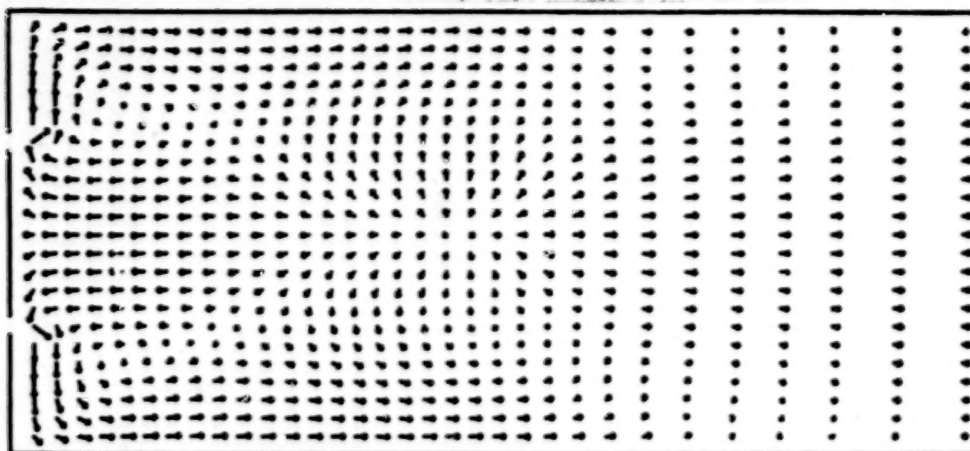
b. Midswirler plane (X-Z)



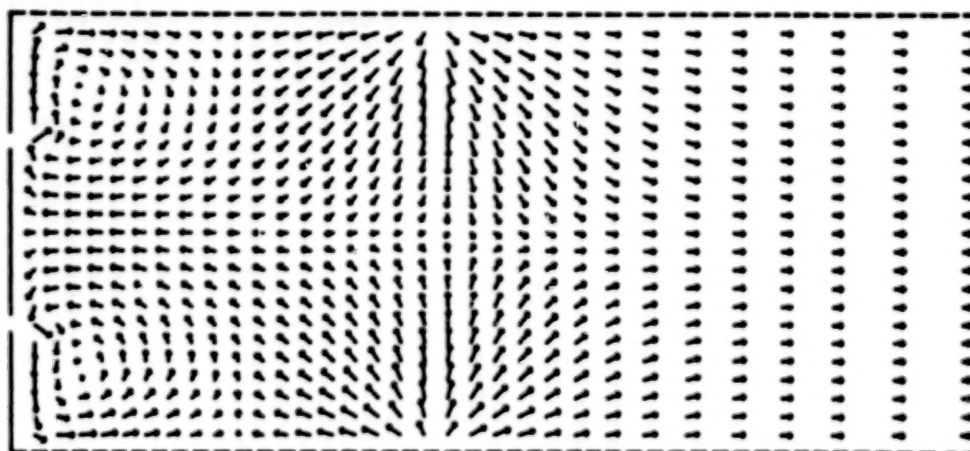
c. Transverse plane (Y-Z) through jet axes

TE85-1983

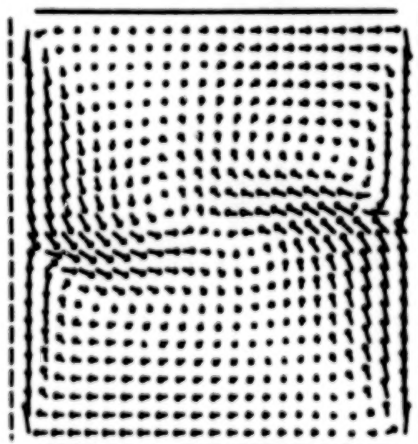
Figure 5. Velocity fields for configuration B;  $X_j/H=0.5$ .



a. Midswirler plane (X-Y)



b. Midswirler plane (X-Z)



c. Transverse plane (Y-Z) through jet axes

TE85-1984

Figure 6. Velocity fields for configuration B;  $X_j/H=1.0$ .

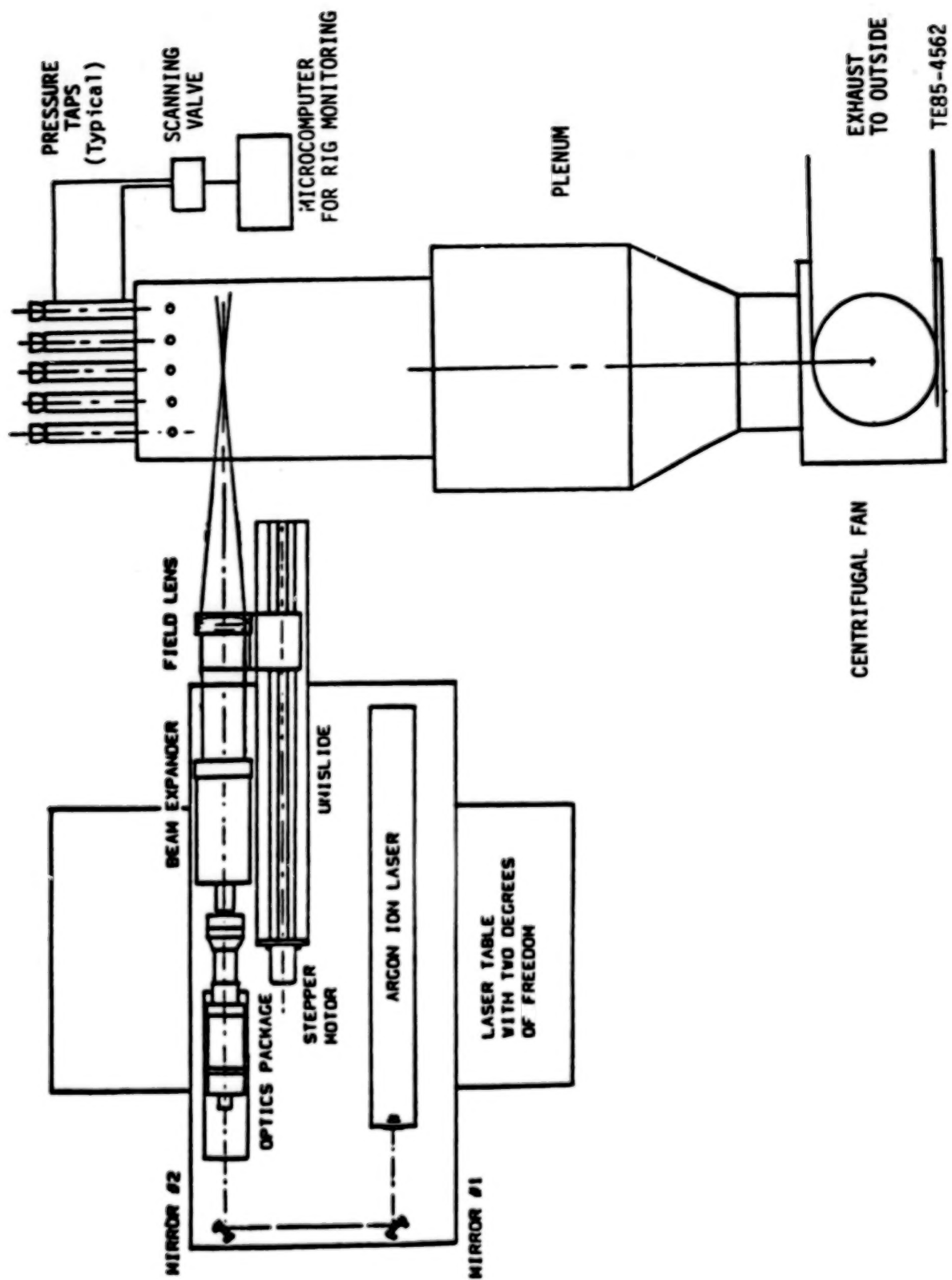


Figure 7. LDV system for flow interaction experiment.

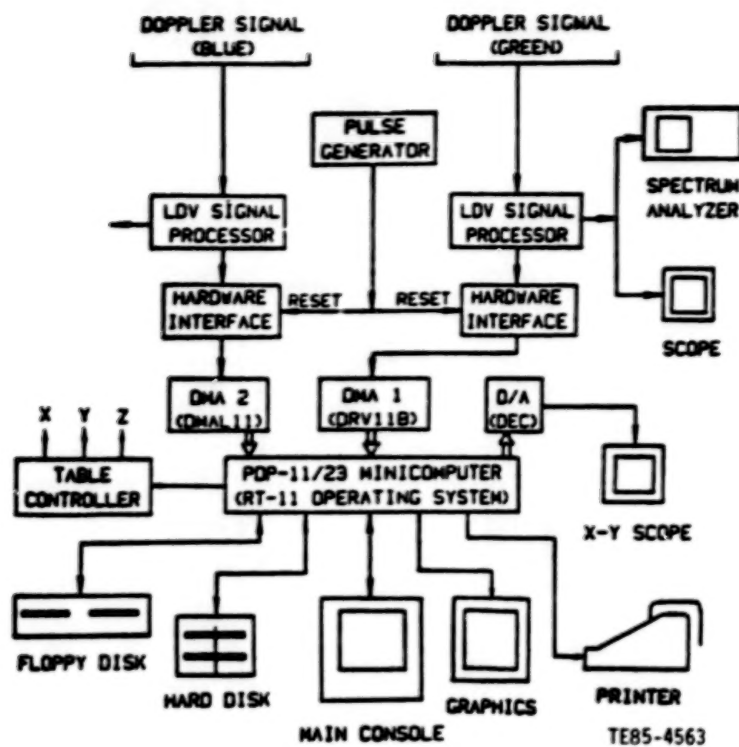


Figure 8. Data acquisition system for LDV.

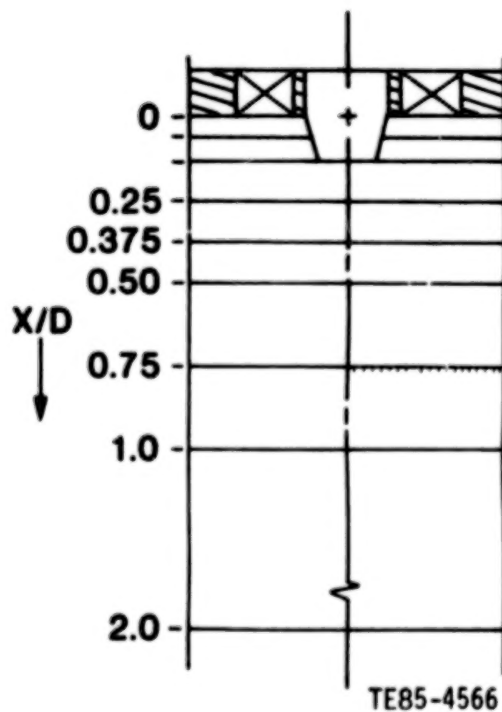


Figure 9. Experimental configuration for confined flow with liquid fuel injection and swirl.9

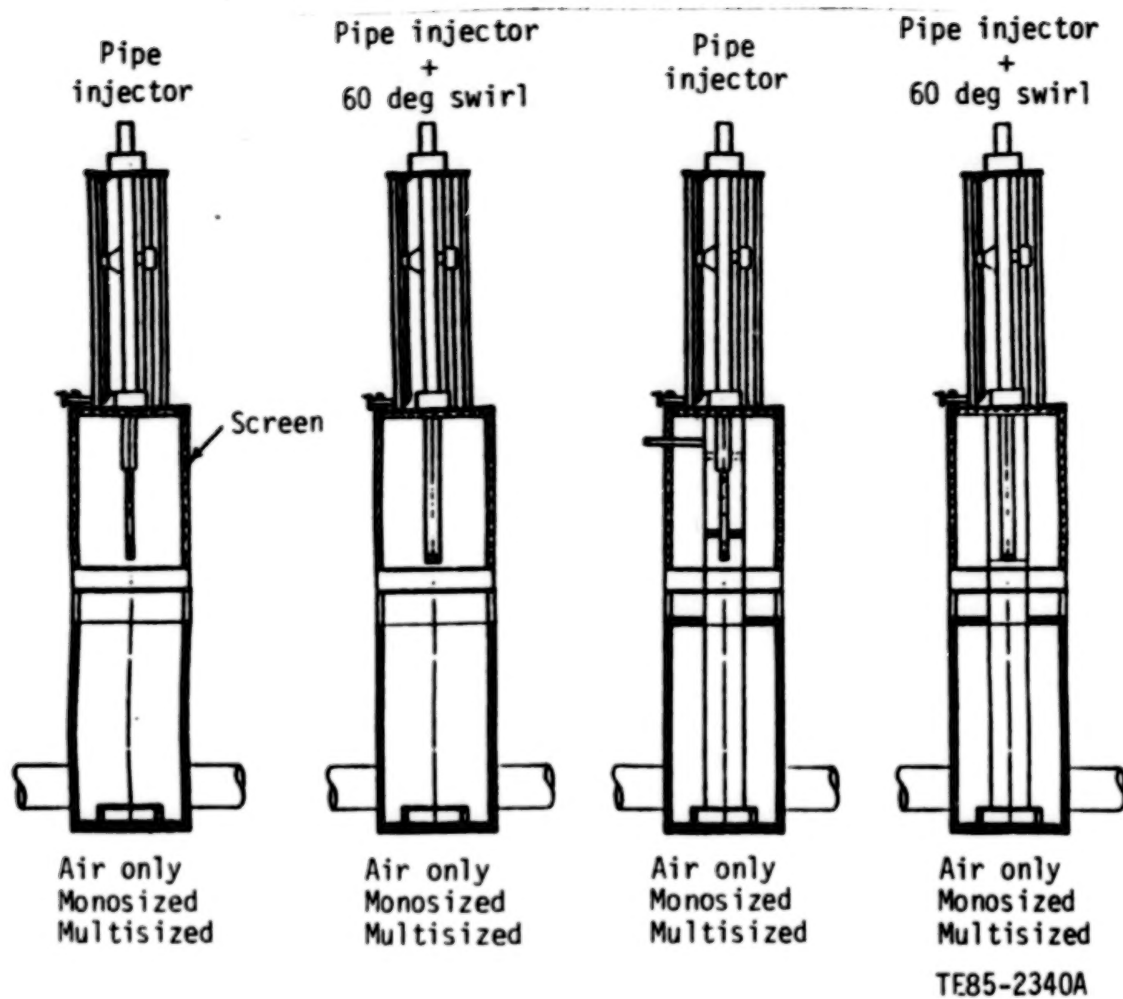
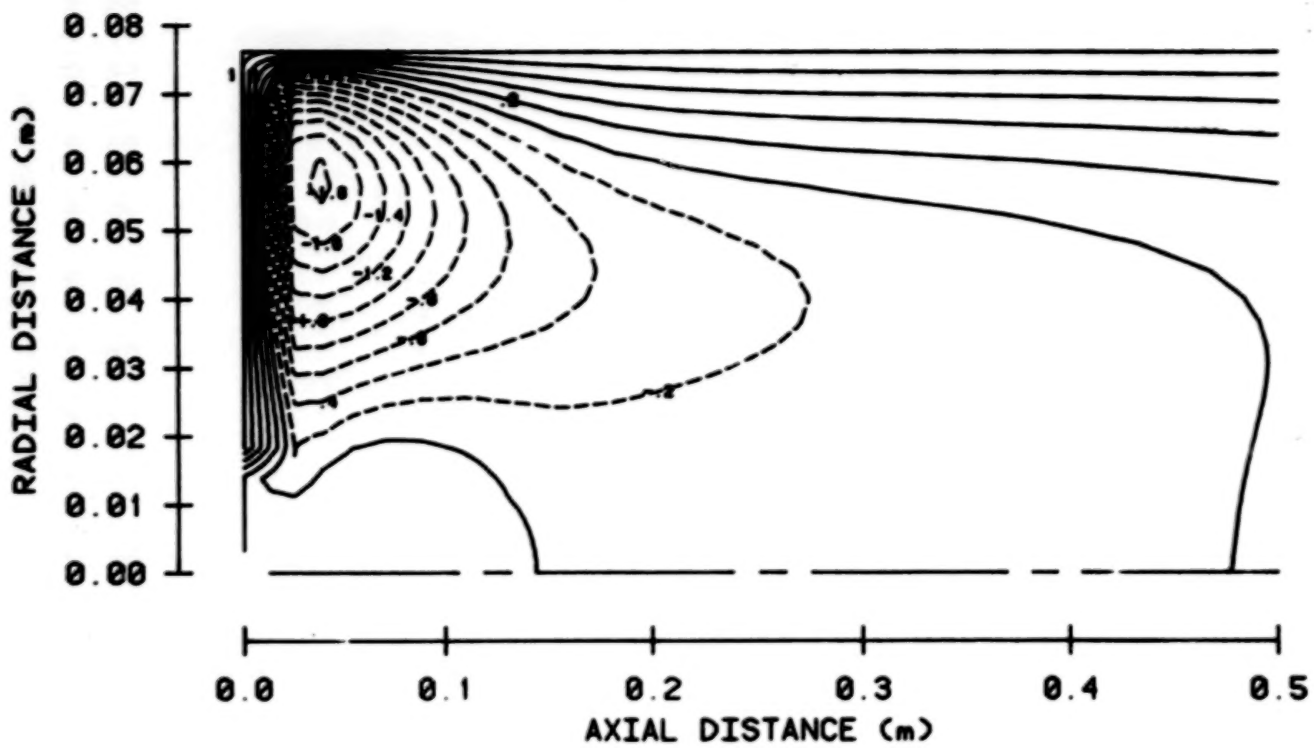


Figure 10. Experimental configurations.

GASPLT6  
FLOW STREAMLINES



GASPLT6  
VELOCITY VECTORS

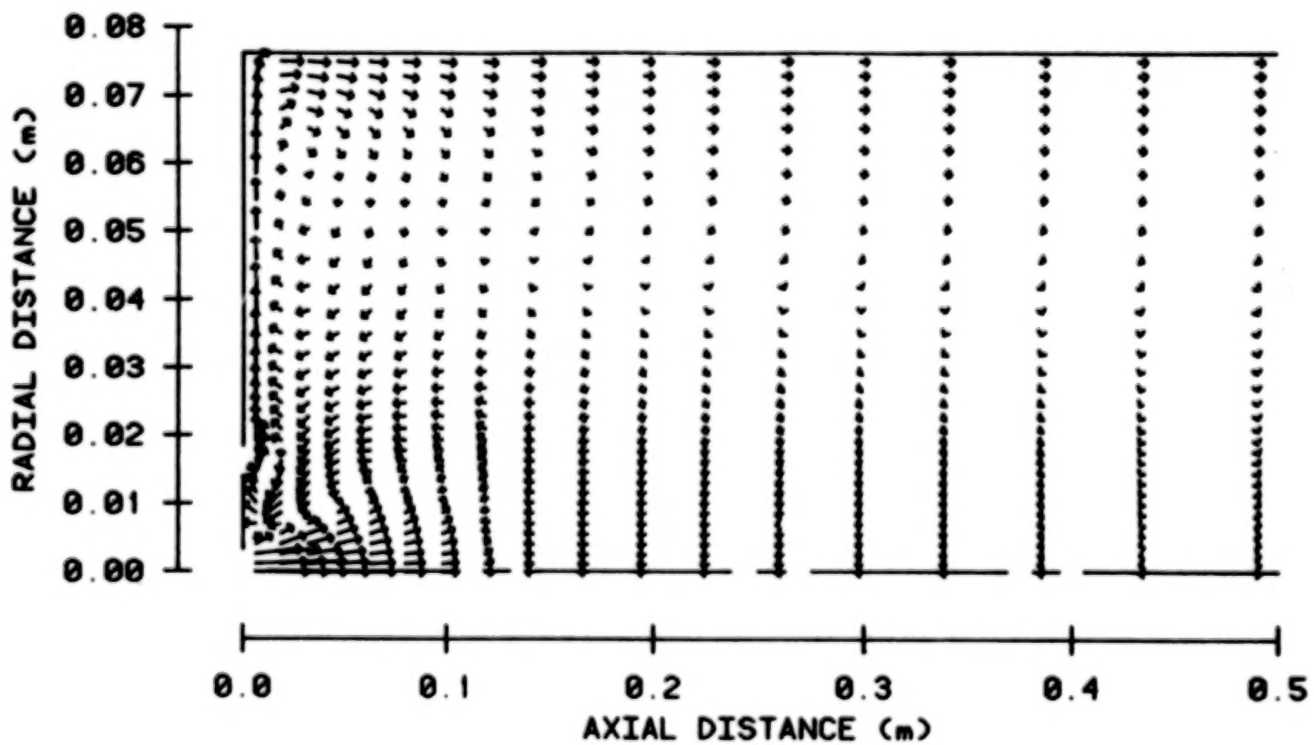
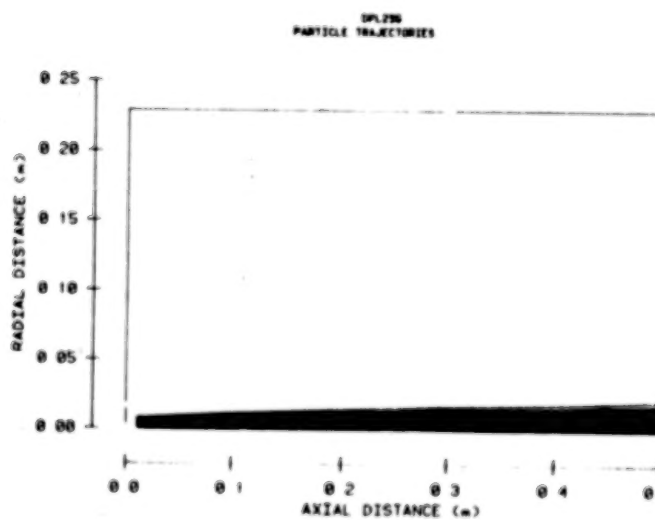
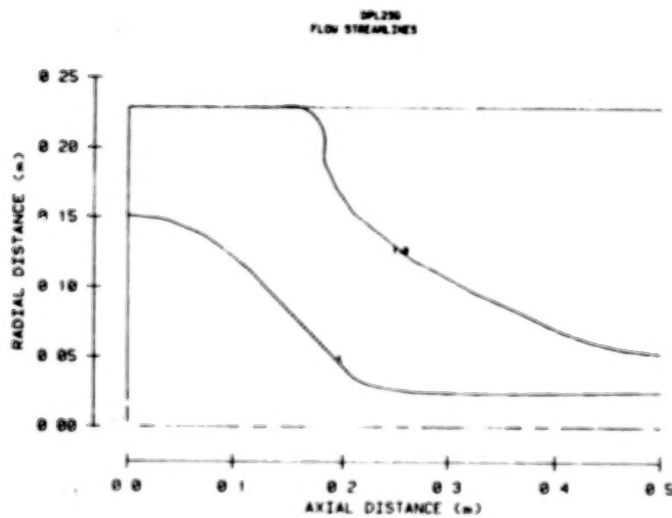
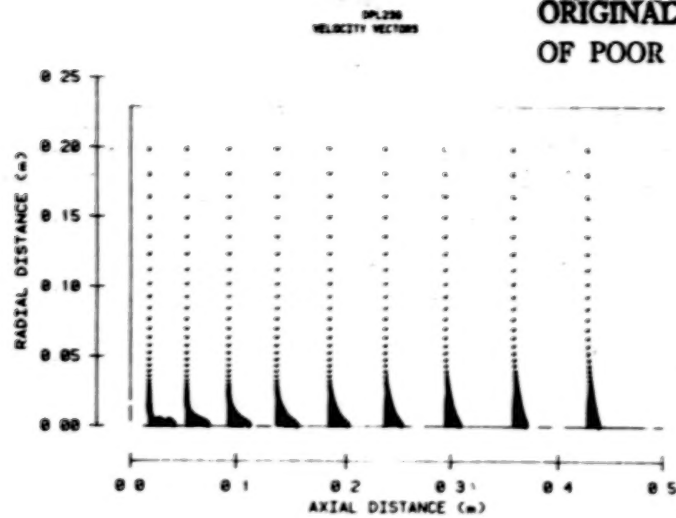


Figure 11. Air only cases at confined conditions (particles injector with 60 deg swirler).

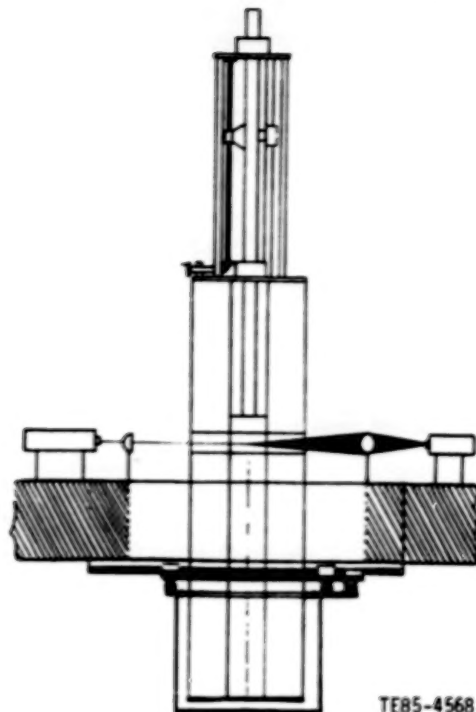
TE85-2346

ORIGINAL PAGE IS  
OF POOR QUALITY

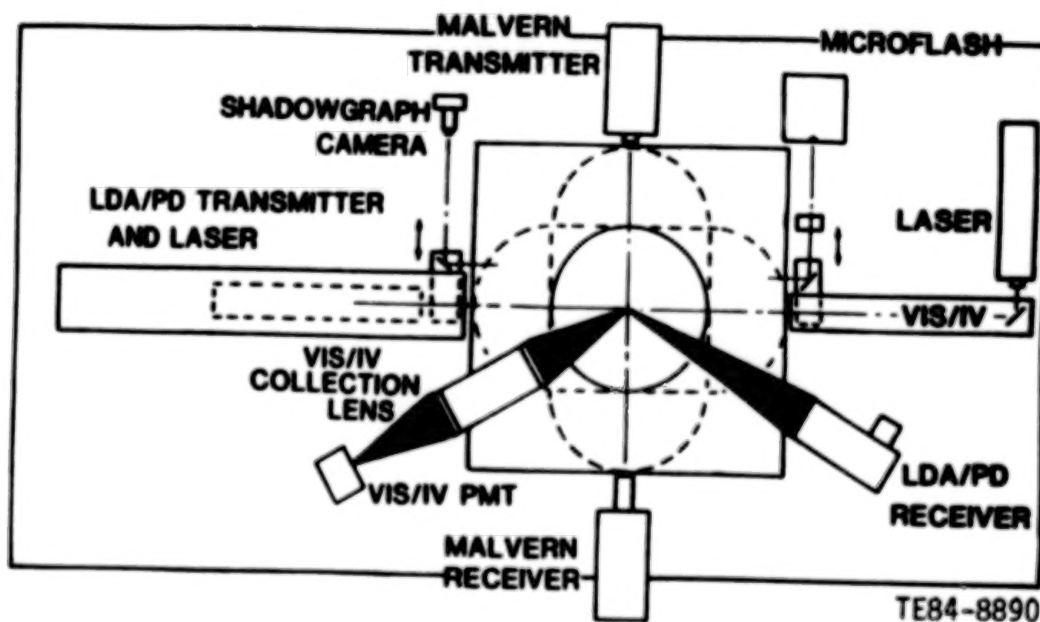


TE85-2826

Figure 12. Methanol spray dispersion at unconfined conditions  
(fuel nozzle surrounded by low velocity stream).



TE85-4568



TE84-8890

Figure 13. Flow facility and optical arrangement.

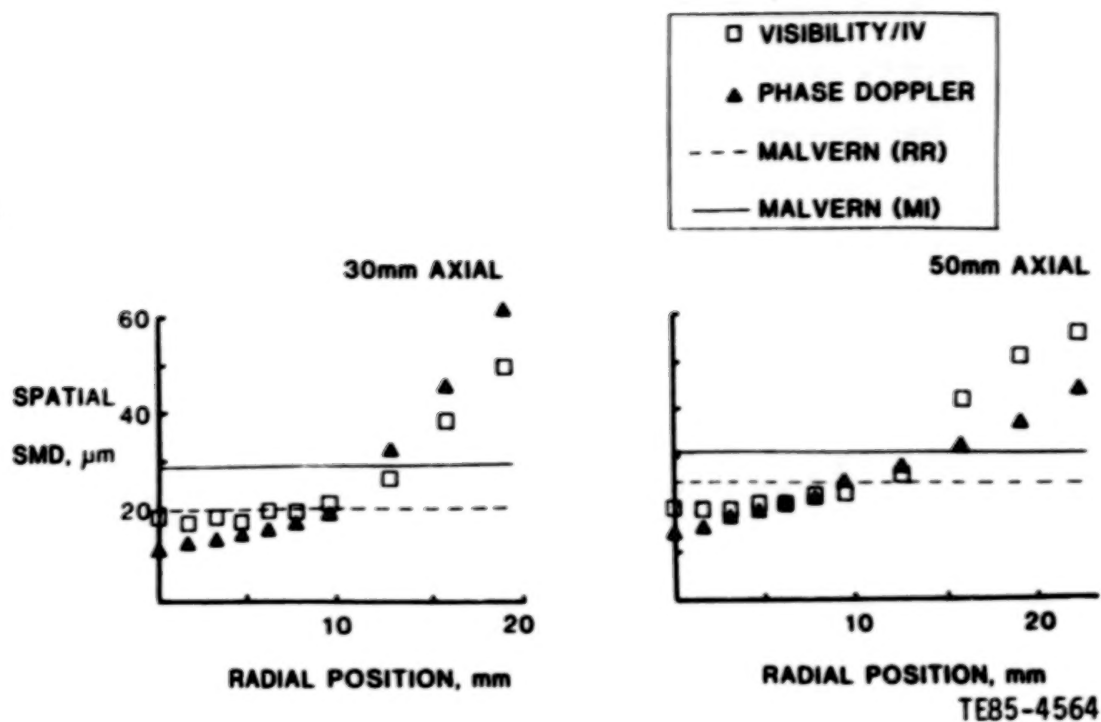


Figure 14. Radial profile of spatial SMD.

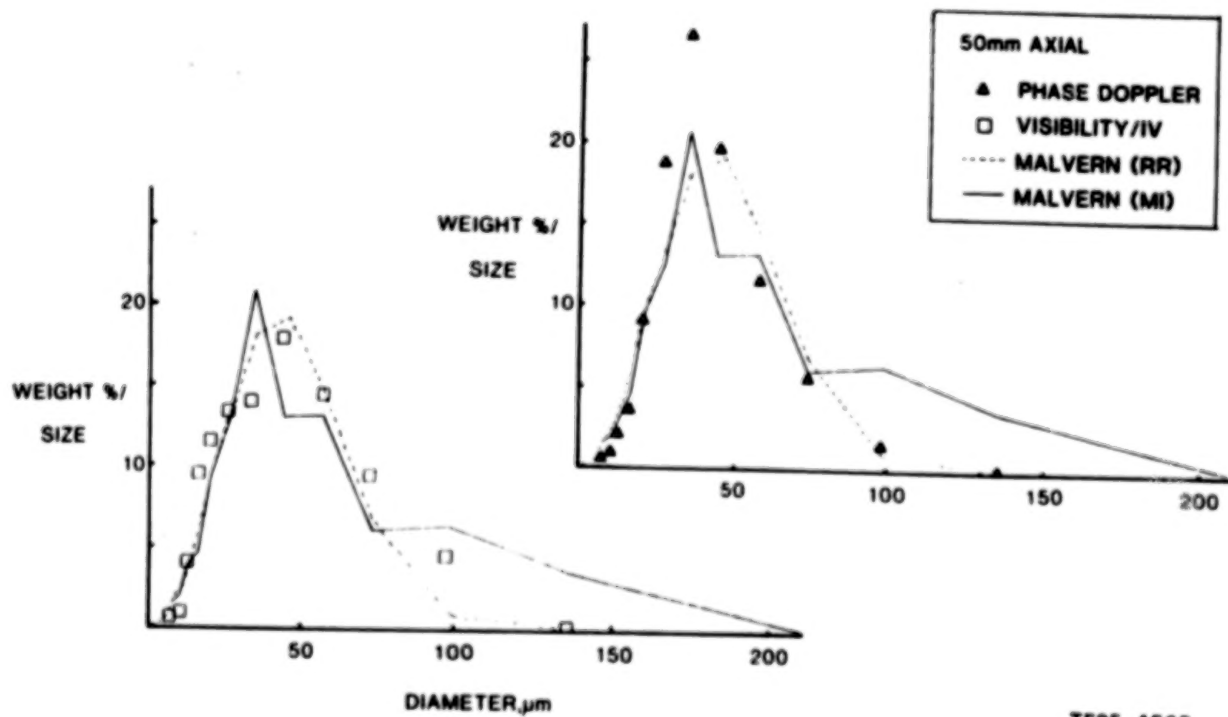


Figure 15. Mass distribution comparison.

## FUEL-INJECTOR/AIR-SWIRL CHARACTERIZATION\*

J. B. McVey and J. B. Kennedy  
United Technologies Research Center  
East Hartford, Connecticut 06108

J. C. Bennett  
University of Connecticut  
Storrs, Connecticut

## INTRODUCTION

The objectives of this program are to (1) establish an experimental data base documenting the behavior of gas turbine engine fuel injector sprays as the spray interacts with the swirling gas flow existing in the combustor dome, and (2) conduct an assessment of the validity of current analytical techniques for predicting fuel spray behavior. Emphasis is placed on the acquisition of data using injector/swirler components which closely resemble components currently in use in advanced aircraft gas turbine engines, conducting tests under conditions which simulate or closely approximate those developed in actual combustors, and conducting a well-controlled experimental effort which will comprise using a combination of low-risk experiments and experiments requiring the use of state-of-the-art diagnostic instrumentation. Analysis of the data is to be conducted using an existing, TEACH-type code which employs a stochastic analysis of the motion of the dispersed phase in the turbulent continuum flow field.

## APPROACH

The objectives of the program are to be achieved through the conduct of the following technical tasks:

1. An appropriate test configuration and the equipment and instrumentation required for documenting the two-phase flow within the configuration will be identified and assembled.
2. A sensitivity analysis will be conducted to establish which parameters should be varied in the test effort and what parameter ranges should be studied.
3. Tests will be conducted to verify the operation of the instrumentation under the conditions to be found in the data base tests. A data base will be established which will document the behavior of the two-phase flow under a number of selected conditions.
4. The acquired data will be analyzed using a TEACH-type analysis, and improvements to the physical models employed will be sought which will provide improved agreement between prediction and experiment.

\*Work done under NASA Contract NAS3-24352.

## TEST APPARATUS AND INSTRUMENTATION

The experiments will be conducted within a section in which flow representative of that in a gas turbine combustor is generated (Fig. 1). Primary airflow enters through a swirler/nozzle assembly and undergoes a sudden expansion. Secondary flow is introduced in a direction normal to the flow section axis at an appropriate downstream location (beyond the region where the fuel spray/swirl-air interaction occurs). This configuration, termed the "model combustor" configuration, is intended to establish a flow having aerodynamic characteristics (velocities, turbulence intensities, turbulence scales, swirl strength and existence of recirculation regions) which are similar to, but of a less complex nature, than those of a real gas turbine combustor, and in which the flow is suitable for use in studying spray dynamics. A photograph showing the installation of the model combustor is shown in Fig. 2.

A two-component laser velocimeter will be used to acquire velocity field data for the gas phase and dispersed phase flows. The system utilizes a 1 watt argon-ion laser, prism-based color-splitter optics, and Bragg cells to generate the probe volumes (Fig. 3). In the case where single-phase flow measurements are performed horizontal and vertical diametral traverses will be used to acquire three components of velocity. Forward scatter optics will be employed to maximize signal-to-noise ratios. In the case where two-phase flow measurements are performed a fluorescent seed material will be employed, and a single probe volume will be established using the 488 nm blue beams. One set of optics will be employed to collect the Mie-scattered signal from the dispersed phase, and the second set will be used to collect the fluorescent emission from the seed which tracks the gas flow.

A high speed particle counter will be used to acquire information on the concentration of the dispersed phase for tests conducted with monosized particles. A particle passing through the velocimeter probe volume will trigger a counter when the DC level of the received signal exceeds a threshold level. The particle count, the elapsed time, and the sampling volume cross-section will be used to obtain a particle count flux which can be converted to particle concentration using the known particle size and velocity. For the monodisperse particles, a single setting of the threshold signal level will be a suitable criterion for rejecting particles not in the sampling volume.

A single-component droplet-sizing interferometer will be used to acquire information on the size and velocity of droplets produced when using liquid fuel. The instrument gathers spatially-precise, correlated, statistical data regarding the velocities and size of droplets passing through a probe volume formed by the introduction of two laser beams. The basic hardware employed by the phase/droplet particle analyzer includes transmitting optics, receiving optics with detectors, electronic signal amplifiers, filters, signal processor, and data management system. A schematic diagram of the apparatus is given in Fig. 4.

The two-dimensional, spatial distribution of the liquid and vapor phase concentrations of the injectant will be determined using quantitative laser-induced exciplex fluorescence. This technique is based upon the single-frequency laser excitation of fluorescence which occurs at two widely separated emission bands from each of the two phases. A pulsed neodymium-YAG laser system equipped with a fourth harmonic generating crystal will be employed in this effort. This laser is capable of delivering over 50 millijoules of laser energy at a wavelength of 266 nanometers at a repetition rate of 10 Hz. A 256 x 256 photoelectric array detector will be used to record the information produced by the fluorescence process. Final computer processing of the data will result in data arrays providing values of the liquid and vapor concentration in the field of illumination at an instant of time. By combining information gathered by a large number of realizations, information on time-averaged concentrations is acquired, and a statistical evaluation of the variation about the mean can be generated. A schematic diagram showing the principal elements of the measurement system is shown in Fig. 5.

#### TEST MATRIX

An analysis of the two-phase flow field to be generated within the model combustor was conducted to determine the appropriate baseline values and ranges of parameters to be employed in the tests. The analysis was conducted using PW-TEACH (Ref. 1) which uses a stochastic calculation procedure (Ref. 2) to track the interaction of the dispersed phase with the turbulent gas eddies. Results of a typical calculation are shown in Fig. 6 where the influence of primary zone swirl angle on injectant distribution is presented. For purposes of clarity, the results of trajectory calculations for only a few classes of particles are shown, and the assumption that particles striking the wall do not rebound was employed. These results indicated that the swirler discharge flow angle should be relatively low, e.g., 30 deg, to avoid the situation where a large portion of the spray is centrifuged to the test section walls. Other factors shown to have a primary influence on spray distribution were particle diameter and specific gravity. Combustor pressure drop was predicted to have a lesser effect. Spray cone angle, injection velocity, and injectant carrier gas mass flow were found to have only minor influences.

The test matrix generated using the results of the sensitivity analysis is given in the following table:

# TEST MATRIX - DATA BASE ACQUISITION

Test No.	Type	Swirl Angle (Deg)	Pressure Drop (%)	Temp. (C)	Injectant	Instrument	Comment
1	Aero only	30	2	21	-	LV	Baseline-gas only
2		45	2	21	-	LV	High swirl
3		30	4	21	-	LV	High pressure drop
4		30	2	316	-	LV	High temperature
5	Spray only	0	0	21	30/38S	LV,C	Microspheres
6		0	0	21	35 L	LV,DSI	Baseline-Liquid
7	2-Phase, Micro-spheres	30	2	21	30/38S	LV,C	Baseline - Particles
8		30	2	21	53/62S	LV,C	Large particles
9		30	2	21	20/30S	LV,C	Small particles
10		45	2	21	30/38S	LV,C	High swirl
11	2-Phase, Liquid	30	4	21	30/38S	LV,C	High pressure drop
12		30	2	316	35 L	X,DSI	Baseline - liquid
13		30	2	316	57L	X,DSI	Large droplet
14		30	2	316	22L	X,DSI	Small droplet
15		30	2	150	35L	X,DSI	Low temperature
16		30	2	150	57L	X,DSI	Low temperature, Large droplet
17		30	2	150	22L	X,DSI	Low temperature, Small droplet

## Legend

Injectant: S = Microspheres L = Liquid Pentane  
 Instrumentation: LV = Velocimeter C = Concentration Measurement  
 X = Exciplex Fluorescence  
 DSI = Droplet Sizing Interferometer

## CURRENT STATUS

Activities are currently underway to verify the operational capabilities of the instrumentation. The verification tests for the laser velocimeter and particle concentration measurement system are being conducted using a pipe-flow test apparatus within which a two-phase flow having known characteristics will be developed (Fig. 7). The objective of the velocimeter tests will be to establish that the technique of using a fluorescent seed material is workable under the conditions of flow velocity, particle size, and particle loading to be present in the data base acquisition tests.

Tests are being conducted using two types of fluorescent seed: 1) polymer-encapsulated dye and 2) liquid dye seed. The polymer-encapsulated

dye is a proprietary material supplied by Eastman Kodak. The material has been prepared both as a dispersion in an aqueous solution, and as a dried material. The size distribution of the material in aqueous solution determined by use of a disk centrifuge technique and by transmission electron microscopy, is 0.1 to 2 microns. The dried form is more nearly monodisperse, in the size range from 2-3 microns, and the particles are roughly spherical in shape. Tests are also being conducted to establish the time response characteristics of the seed material. To be effective as a velocimetry seed, the fluorescence emission rise time and decay time must be on the order of tens of nanoseconds or less in order to follow the fringe pattern established in the sampling volume. Measurements of the fluorescence burst resulting from illumination by a pulsed laser indicate the characteristic time meets these requirements.

Liquid fluorescent dye has previously been used as a seed material for single-phase flow, but potential problems exist which must be evaluated before this approach can be applied in a two-phase flow having the characteristics of a gas turbine combustor primary zone. Tests are underway to establish that the liquid seed will not be scrubbed out of the flow by the large concentrations of particulate material that the dye coating on the large particles does not produce a velocimeter signal which would bias the results of the gas phase measurements and that micron-sized dye particles will be present in sufficient concentration at the test section site, having been injected at some far upstream location.

In related activities, efforts are underway to verify the operational capability of the exciplex fluorescence imaging system. Tests will be conducted using a single droplet test device (Fig. 8) in which the vapor cloud surrounding a vaporizing droplet can be examined. Verification of the capability of the instrument will be achieved when the vapor concentration level deduced from the measurement is found to agree with that predicted analytically for the case of the vaporization of an isolated droplet. Pentane droplets will be injected into a co-flowing heated nitrogen stream in these experiments.

#### References

1. Sturgess, Geoffrey J.: Aerothermal Modeling Program Final Report, NASA CR-168202.
2. Gosman, A. D. and Ioannides, E.: Aspects of Computer Simulation of Liquid-Fueled Combustors, AIAA 81-0323, January, 1981.

# AXISYMMETRIC MODEL COMBUSTOR CONFIGURATION

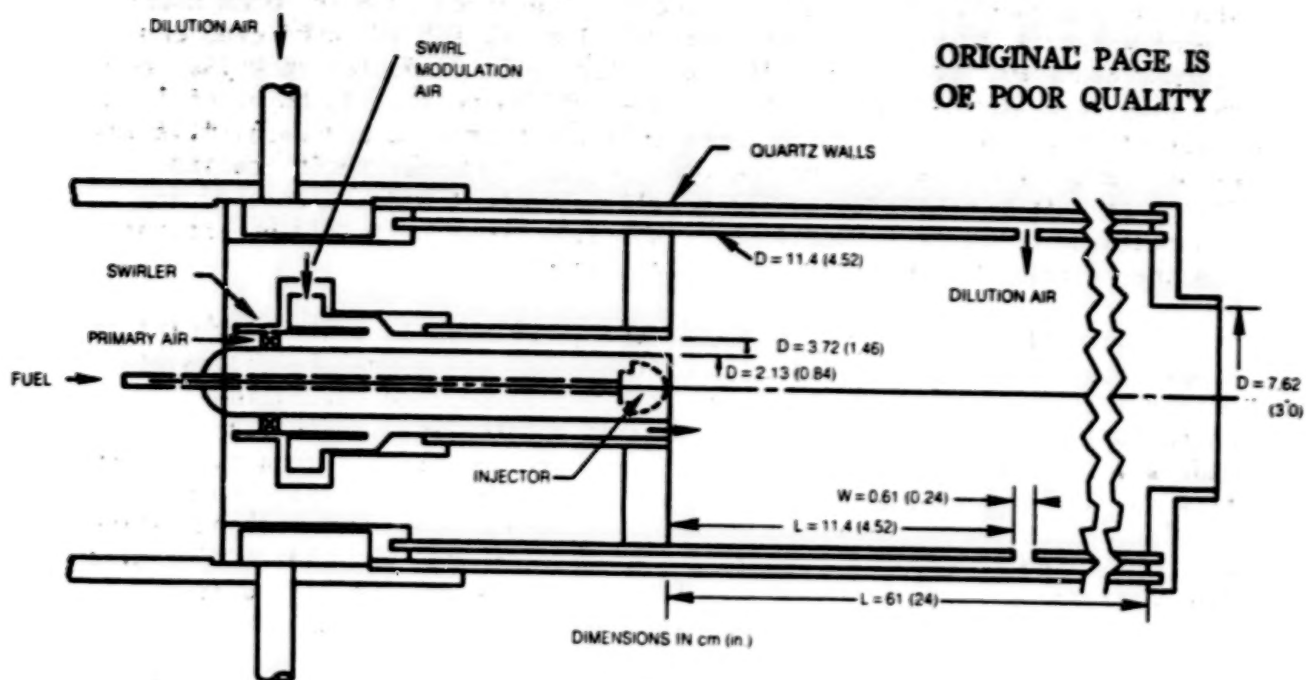


Figure 1

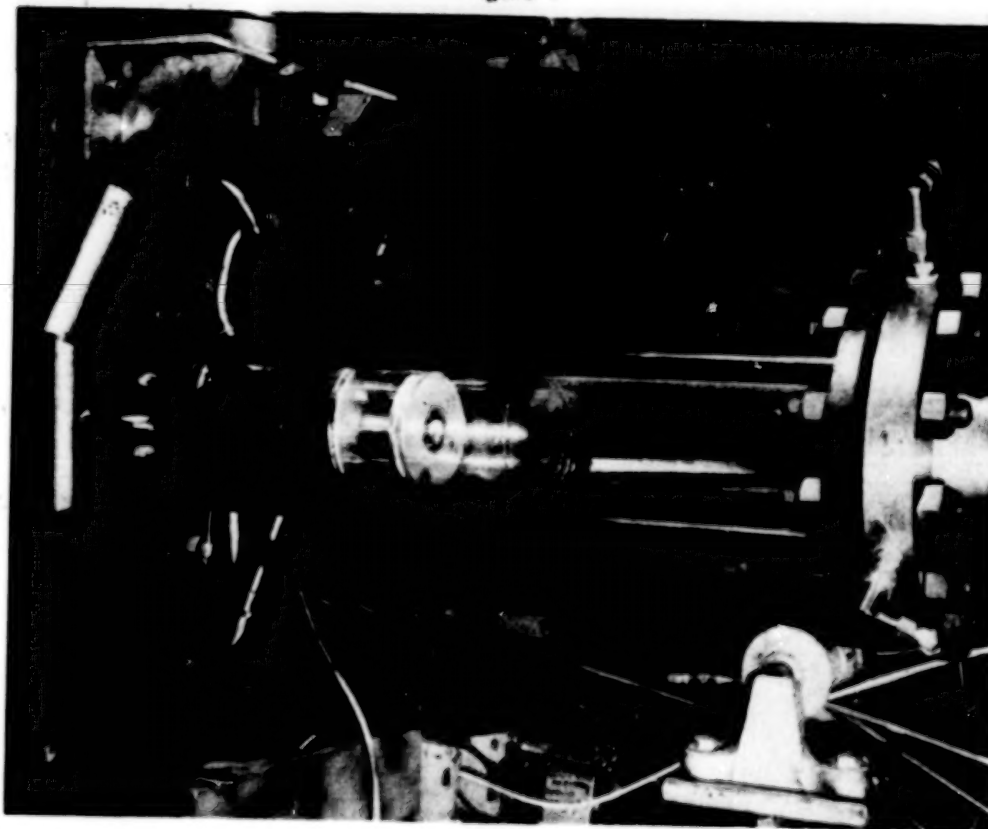


Figure 2

85-8-43-1

ORIGINAL PAGE IS  
OF POOR QUALITY

# LASER VELOCIMETER SYSTEM

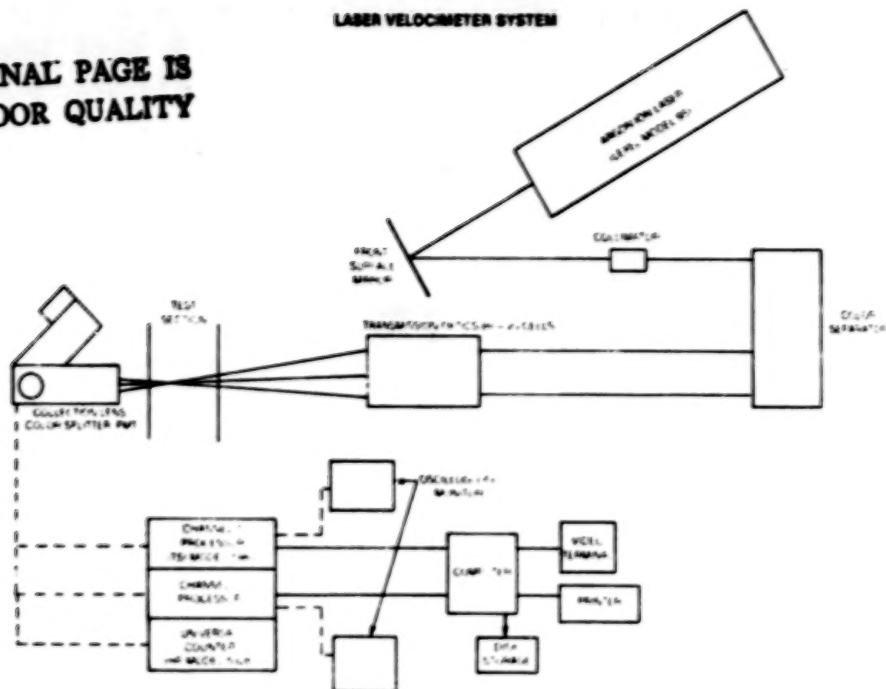


Figure 3

# PHASE/DOPPLER PARTICLE ANALYZER

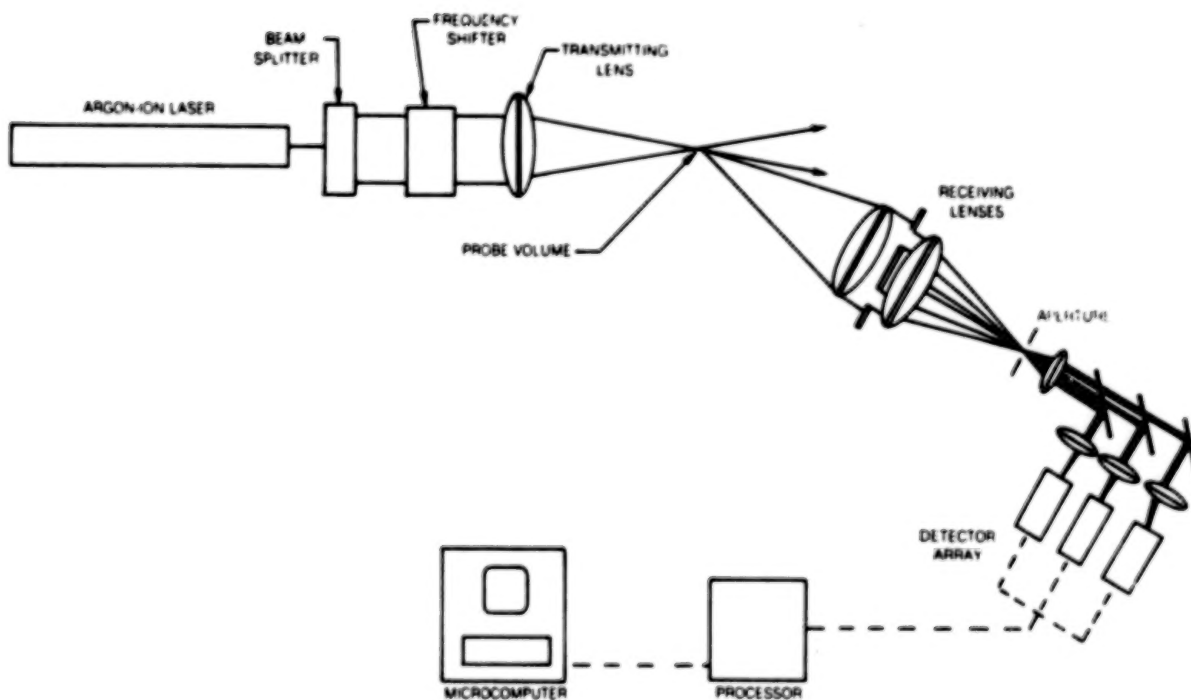


Figure 4

# EXCIPLEX FLUORESCENCE SPRAY EVALUATION SYSTEM

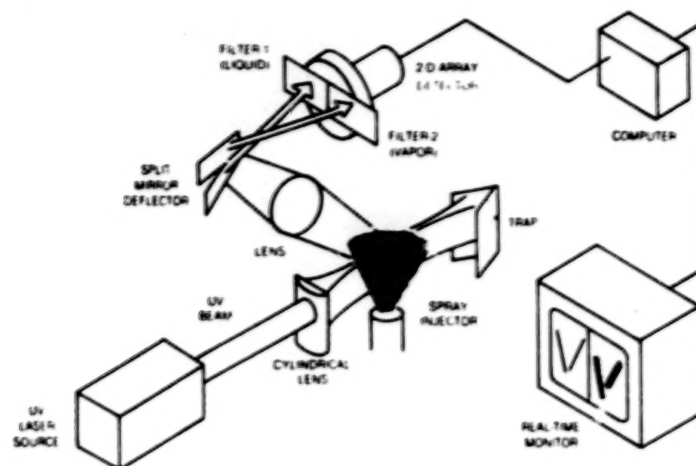
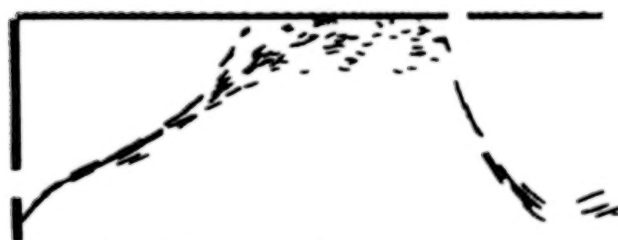


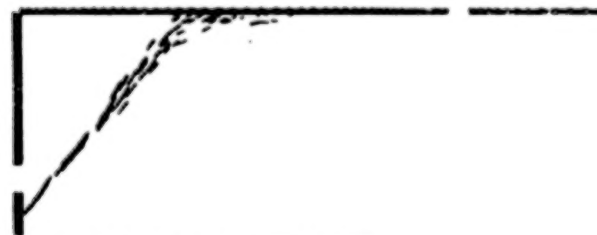
Figure 5

## EFFECT OF AIR SWIRL ON PARTICLE DISTRIBUTION

PARTICLE DIAMETER = 14 MICRONS  
PARTICLE SPECIFIC GRAVITY = 1.3



a) BASELINE — SWIRL ANGLE = 30 deg



b) INCREASE SWIRL — SWIRL ANGLE = 45 deg

Figure 6

## PIPE FLOW TEST APPARATUS

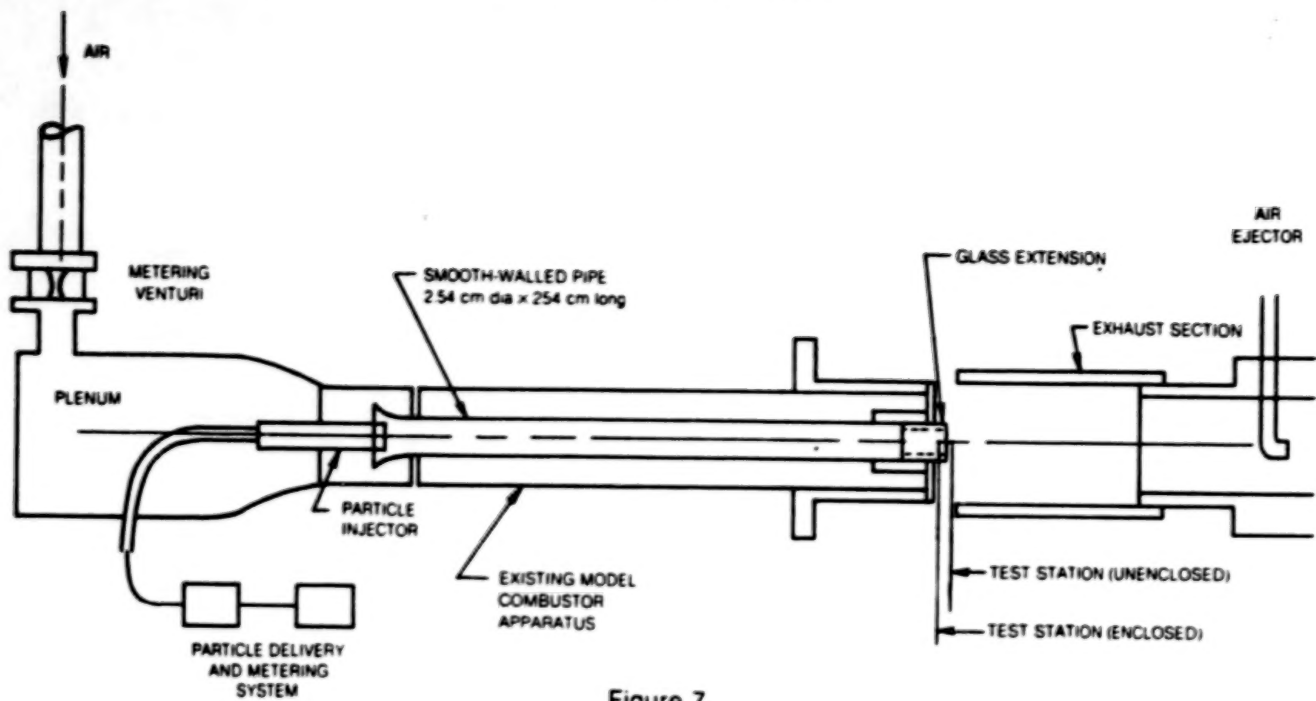


Figure 7

## SINGLE-DROPLET TEST DEVICE

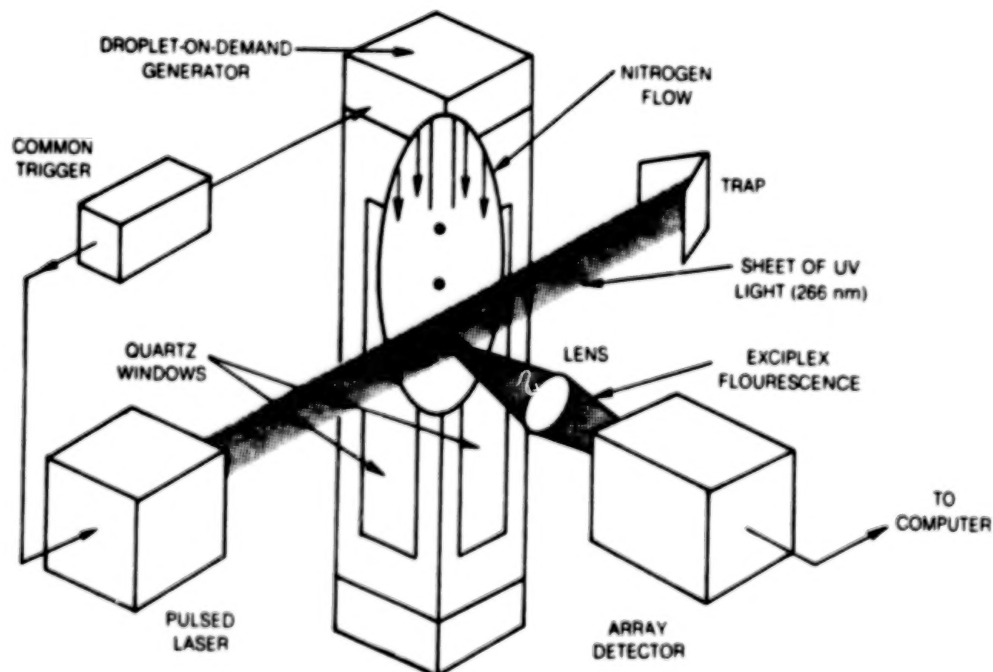


Figure 8

## EFFICIENT NUMERICAL TECHNIQUES FOR COMPLEX FLUID FLOWS\*

Suhas V. Patankar  
University of Minnesota

## INTRODUCTION

Numerical calculation methods for multi-dimensional recirculating flow have been developed over the last 15-20 years. As a result, it has become possible to predict complex flows and heat transfer in combustion chambers, gas turbines, rotating machinery, heat exchangers, and many other practical devices. As the predictive methods have become more powerful, the researchers and designers have applied them to even more challenging problems. Although the computational prediction is far less expensive than the full-scale testing of the equipment, the cost of computational run for a complex problem is still quite substantial. Therefore, attempts are continually being made for improving the accuracy and efficiency of numerical techniques so that the predictions of a given accuracy can be obtained at a modest cost.

A crucial consideration in the calculation of fluid flow is the treatment of the coupling between the velocity components and pressure as expressed by the momentum and continuity equations. A very widely used method for the coupled solution is SIMPLE. Also, its many variants have been developed in recent years. These methods provide an iterative scheme in which the momentum equations are sequentially solved and the pressure is obtained from a special equation derived from the continuity equation. Although the methods are on the whole satisfactory, they do exhibit, on occasion, slow convergence, divergence, and sensitivity to under-relaxation factors.

The aim of the present research program is the development of more efficient and reliable calculation schemes for the coupled momentum and continuity equations. The resulting schemes would significantly reduce the expense of computing complex flows such as those in combustion chambers, gas turbines, and heat exchangers.

## METHODS CHOSEN FOR STUDY

It is first realized that the coupling between the momentum and continuity equations is best handled by a simultaneous solution of their (linearized) discrete forms. For a flow at a very small Reynolds number, for which the equations are truly linear, such a direct method gives the solution instantly, without the need for iterations. For nonlinear problems, however, the direct solution of the linearized equations must be repeated many times until convergence is reached. The following methods are currently being investigated for the handling of the nonlinearity.

(1) Successive substitution

At any given iteration, the nonlinear coefficients are calculated simply from the values available from the previous iteration.

(11) Newton-Raphson method

The nonlinear terms in the discrete equations are differentiated with respect to the unknowns. Thus, the new solution is obtained as a Newton-Raphson extrapolation along the derivatives evaluated at the previous iteration. In general, this method requires the evaluation of a large number of cross derivations. The storage requirements are also correspondingly high.

\*Work done under NASA Grant NAS3-596.

(iii) The Broyden method

The expense of computing the many derivatives in the Newton-Raphson method can be reduced by employing the Broyden method described in references 1-5. The essence of the Broyden method is that the inverse of the Jacobian matrix is replaced by a suitable approximation. At each iteration, this approximate inverse is updated so as to promote convergence.

(iv) Norm minimization methods

The changes in the dependent variables predicted by the successive-substitution or Newton-Raphson methods do not always lead to convergence. Therefore, underrelaxation may be necessary. Instead of employing the underrelaxation in an arbitrary manner, the norm minimization methods seek an optimum underrelaxation so that the norm of the residual vector would be minimized.

#### TESTING OF THE METHODS

The above-mentioned methods are being applied to a number of two-dimensional problems such as the flow in a driven cavity, a sudden expansion in a duct, and the natural convection in an enclosure. The early indication is that these direct methods perform very well. Especially with methods (ii), (iii), and (iv), it has been possible to obtain solutions to highly nonlinear problems within a few (10-20) iterations. Methods like SIMPLE require about 500 iterations for the same problems.

#### REFERENCES

1. Broyden, C. G.: A Class of Methods for Solving Nonlinear Simultaneous Equations. Math. Comp., v. 19, 1965, pp. 577-593, MR 33 #6825.
2. Broyden, C. G.: A New Method of Solving Nonlinear Simultaneous Equations. Comp. J., No. 1, vol. 12, Feb. 1969, pp. 94-99.
3. Broyden, C. G.: The Convergence of an Algorithm for Solving Sparse Nonlinear Systems, Math. Comp., No. 114, v. 25, 1971, pp. 285-294.
4. Broyden, C. G.; Dennis, J. E. Jr.; and More, J. J.: On the Local and Superlinear Convergence of Quasi-Newton Methods. J. Inst. Maths. Applics., v. 12, 1983, pp. 223-245.
5. Broyden, C. G.: Quasi-Newton Methods, Optimization Methods in Electronics and Communications, ed. R. W. Cattermole and J. J. O'Reilly, Pentech Press, 1984, pp. 105-110.

## COMBUSTOR-DIFFUSER INTERACTION PROGRAM\*

R. Srinivasan and C. White  
Garrett Turbine Engine Company

## INTRODUCTION

Modern gas turbine engines for both unmanned and man-rated applications operate at high pressure and temperature levels. Advanced compressor systems for such applications produce high exit Mach numbers in excess of 0.5. With current combustor-diffuser systems, the cycle penalties and engine size negate some of the benefits from improved compressor and combustor technology. Advanced, low-pressure-loss, stable diffuser configurations are required to obtain the complete benefits of advanced compression and combustion systems.

Empirical design techniques, as used in the past, cannot be extended with accuracy to advanced technology designs. A generalized analytical model does not exist that accurately models the combustor-diffuser flowfield and is applicable to a wide variety of diffuser designs with different inlet flow conditions.

## OBJECTIVES

The objectives of the Combustor-Diffuser Interaction (CDI) Program are to:

- o Identify the mechanisms and the magnitude of aerodynamic losses in the prediffuser, dome, and shroud regions of an annular combustor-diffuser system
- o Determine the effects of geometric changes in the prediffuser, dome, and shroud wall on aerodynamic losses and loss mechanisms
- o Obtain a data base that can be used to assess advanced numerical aerodynamic computer models for predicting flowfield conditions in an annular combustor-diffuser system
- o Assess the ability of current analytical models to predict flowfield characteristics in annular combustor-diffuser systems, including pressure distributions
- o Upgrade the analytical models based on the experimental data for flowfield characteristics
- o Determine the effects of modifications to the aerodynamic models based on the combustor-diffuser system performance
- o Design and test-evaluate advanced diffuser systems to verify the accuracy of the upgraded analytical model

\*Work done under U.S. Air Force Contract F33615-84-C-2427.

## DESCRIPTION

The CDI Program consists of the following phases:

- o I - Literature Search
- o II - Baseline Configuration
- o III - Parametric Benchmark Configuration
- o IV - Performance Configuration

Phase I of the program involves a literature search of the state-of-the-art in aerodynamic models applicable to predicting the performance of a wide variety of combustor-diffuser designs. Based on this effort, an advanced analytical model will be selected.

Phase II of the program involves the design and fabrication of the baseline configuration and the acquisition of benchmark-quality data. Accurate three-dimensional (3-D) laser Doppler velocimeter (LDV) measurements will be made at several locations in the combustor-diffuser flowfield and the analytical model will be evaluated and upgraded in accordance with this experimental data.

Phase III will evaluate the effects of geometric changes to the system on the performance. In this phase, a minimum of eight geometric changes will be investigated, with benchmark-quality data obtained for each geometry. This data will be used to further refine the analytical models.

Phase IV will assess the ability of the analytical models to predict flowfields and pressure recovery characteristics for full-annular advanced combustor-diffuser configurations.

## RESULTS

Phase I efforts have been completed, resulting in collection of analytical and empirical design methodology on combustor-diffuser systems. A fully elliptic code has been selected for analyzing the combustor-diffuser interaction.

Phase II of the program is in progress. Preliminary experimental studies were made to determine the minimum sector angle needed without encountering errors due to end-wall boundary layer. Based on these tasks, a 2X sector rig was designed with a 60-degree sector angle. This design employs a straight-wall prediffuser with a dump region and combustor orientation, as shown in Figure 1. The entire rig is fabricated of Plexiglas, with provisions for installing optical-quality windows to facilitate LDV measurements. The test rig is currently in fabrication.

The 3-D LDV system to be used for benchmark testing is shown in Figure 2. This is a 3-color, 3-component system that will operate in an off-axis backscatter mode. The effective measurement volume will have a diameter of 0.06mm and a length of 0.22mm. Measurements will be made for 15 different flow rates through the inner and outer annuli. The LDV surveys will be made at several axial stations, with the near-wall measurements as close as 0.5mm from the walls. During these tests, the prediffuser inlet Mach number will be maintained at 0.35. Prior to the detailed measurements, flow visualization tests will be conducted to guide test rig modifications.

Analytical model predictions have been obtained for all of the flow conditions at which Phase II tests will be conducted. These results will be compared with the LDV data. Furthermore, a generalized nonorthogonal grid system is being developed to accurately simulate complex wall shapes.

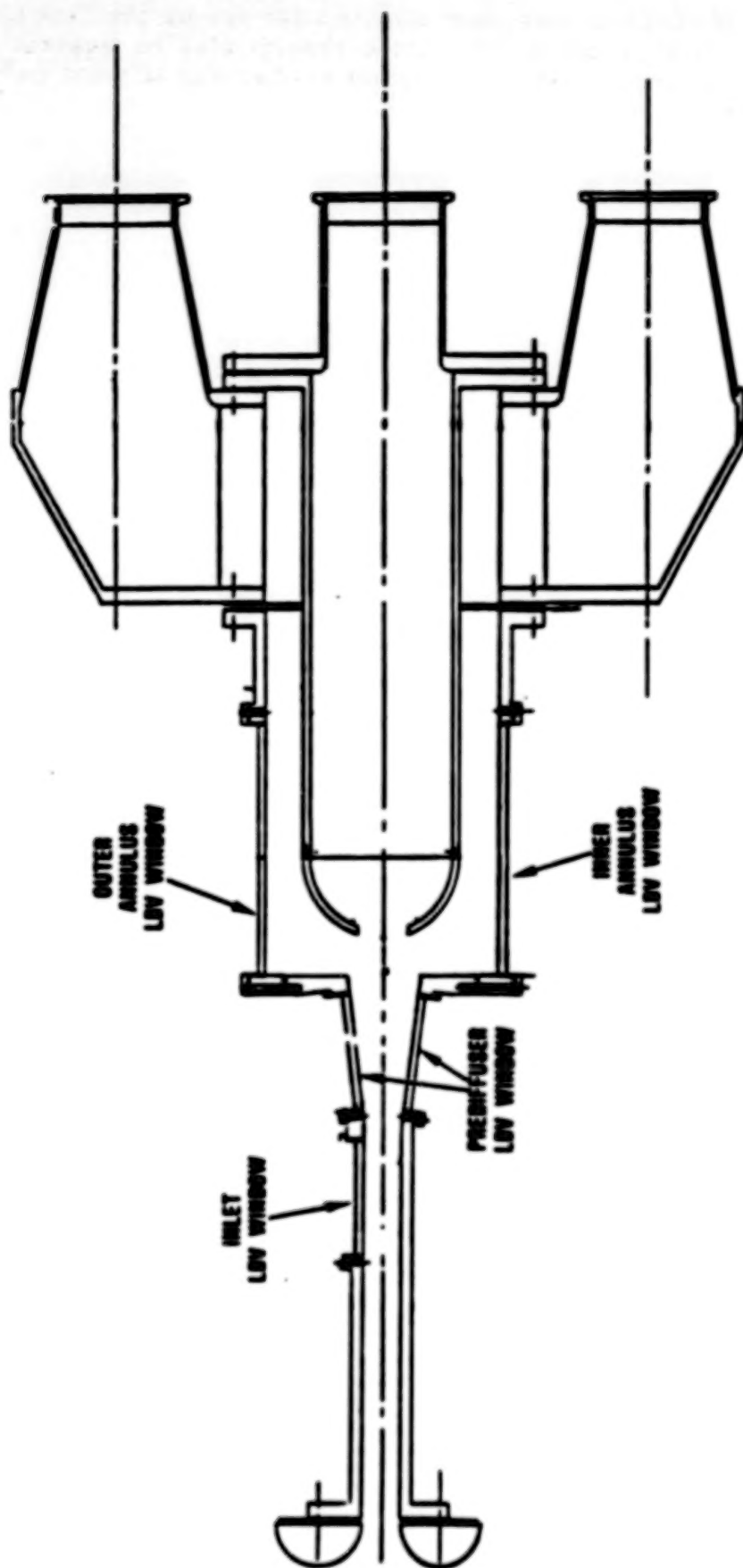


Figure 1. Schematic of CDI Test Rig.

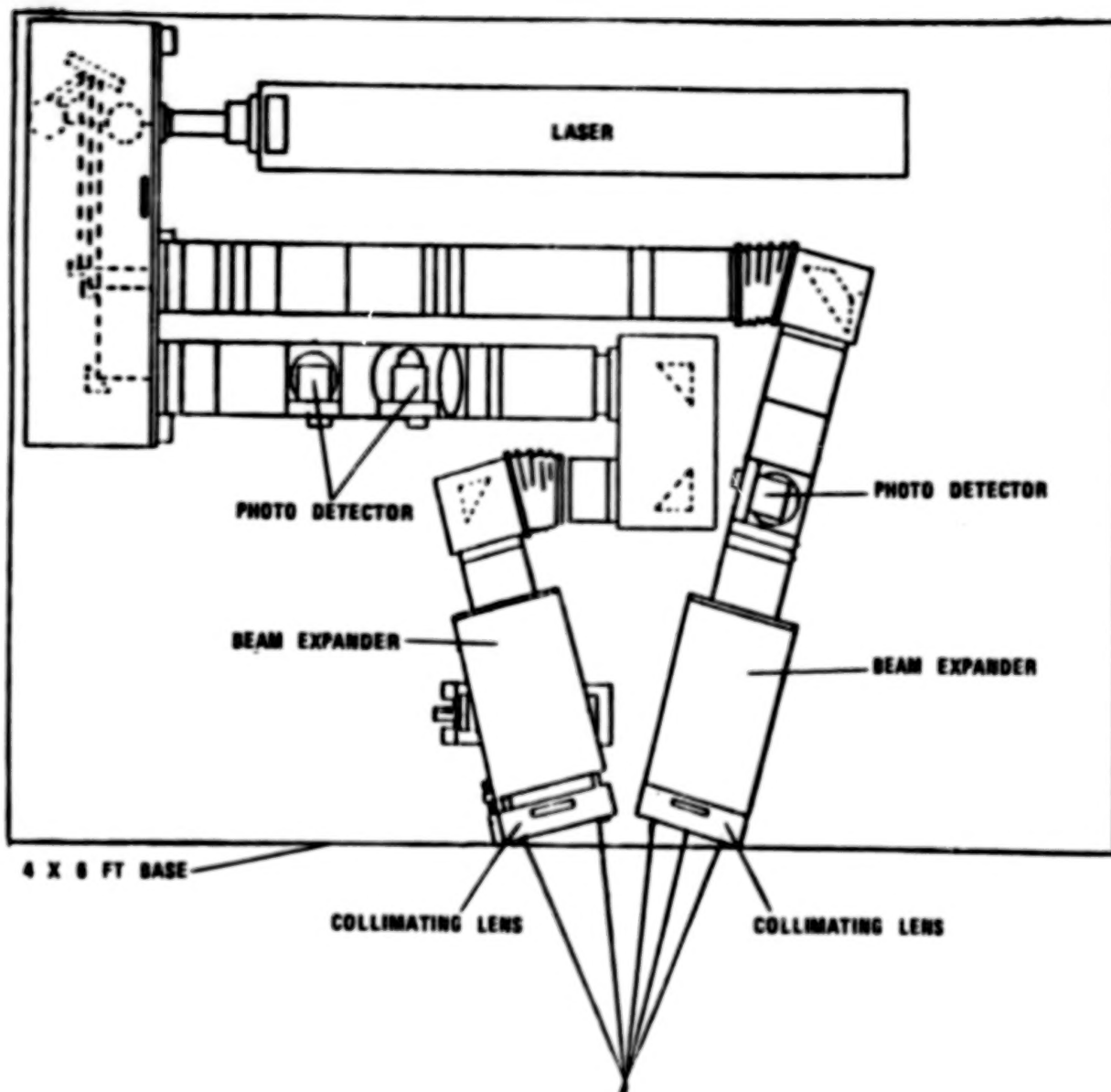


Figure 2. Layout of 3-D LDV System.

## DILUTION JET MIXING PROGRAM - PHASE III\*

R. Srinivasan, G. Myers, and C. White  
Garrett Turbine Engine Company

## INTRODUCTION

Improvements in manufacturing technology of surface coatings and other high-temperature materials have directed emphasis toward increasing combustor exit temperatures. Such increases are achieved by reducing the available dilution air, which necessitates effective use of the available dilution air to meet the combustor discharge temperature distribution requirements.

The combustor discharge temperature quality is influenced by almost all aspects of the combustor design and particularly by the dilution zone. To tailor the combustor discharge temperature pattern, the discharge temperature distribution must be characterized in terms of the dilution zone geometric and flow parameters. Such characterization requires an improved understanding of the dilution jet mixing processes.

## OBJECTIVES

The objectives of the Phase III program are to:

- o Extend the data base on mixing of a single-sided row of jets with a confined crossflow
- o Collect data base on mixing of multiple rows of jets with confined cross-flow
- o Develop empirical jet mixing correlations
- o Perform limited three-dimensional (3-D) calculations for some of these test configurations

## RESULTS

The tests were performed with uniform mainstream conditions for several orifice plate configurations. Schematics of the test section and the orifice configurations are shown in Figure 1. Temperature and pressure measurements were made in the test section at 4 axial and 11 transverse stations, using a 60-element rake probe. The measured temperature distributions for these tests are reported in Reference 1.

In addition to the experimental efforts, several 3-D numerical calculations were performed. Figure 2 shows a comparison of measured and predicted temperature distributions for the case with a double row of jets in an in-line configuration. The momentum flux ratio for this case is 26.6. The 3-D model underestimates mixing, especially in the transverse direction, with predicted peak temperature difference values higher than the data. Figure 3 shows a similar comparison of predicted and

\*Work done under NASA Contract NAS3-22110.

measured velocity distributions. The 3-D model correctly predicts the jet penetration but underestimates the jet spreading rate.

Although the 3-D model can be applied to any orifice configuration, it is not cost-effective for redesigning dilution zone configurations. For such modifications, it is desirable to develop empirical models to characterize the combustor exit temperature profile quality as a function of dilution zone geometric and flow parameters. In this program, such correlations have been developed that are applicable to single-row, double-row, and opposed-jet configurations. In addition, this model is applicable to circular as well as noncircular orifices. For opposed and double-row jets, the temperature distributions are obtained by superimposing those due to each individual row of jets. A description of the empirical model is provided in References 1 through 3.

#### CONCLUSIONS

The following conclusions are drawn by comparing the empirical model results with the test data:

- o The NASA/GTEC empirical model includes the effects of aspect ratio of discrete slots for predicting jet mixing characteristics. This model predicts the temperature field due to streamlined slots within first-order accuracy. For bluff slots, this empirical model gives an inferior agreement with the data. Additional work is needed to improve the empirical model predictions.
- o The empirical model predictions for double-row jets are obtained by superimposing the temperature field due to each individual row of jets. This superposition scheme gives good correlation with the data, especially in the regions beyond  $X/H_0 = 0.5$ . In the regions closer to the jet injection plane, the data shows non-Gaussian profiles that are not predicted by the empirical model, but even in those regions, the model is accurate for engineering calculations.
- o The empirical model accurately predicts the lateral shift of centerplanes for 45-degree slots, but does not account for the rotation of the temperature contours.
- o The modified empirical model provides a valuable first-order tool for designing gas turbine combustor dilution zones. This model can be applied to single-sided or two-sided jets, single or double rows of jets, as well as to circular and noncircular orifice configurations. The model is applicable over a wide range of geometric and flow conditions observed in gas turbine combustion systems.

#### LIST OF SYMBOLS

D	Geometric orifice diameter
$D_j$	Effective orifice diameter
$H_0$	Duct height at the jet injection plane
$H^0$	Local duct height at the survey plane
J	Momentum flux ratio, $\rho_j V_j^2 / \rho_m V_m^2$
$P_t$	Stagnation pressure
$P_s$	Static pressure
$S^s$	Orifice spacing
T	Temperature

V Velocity  
X x direction, parallel to duct axis  
Y y direction, parallel to orifice centerline (radial direction)  
Z z direction, normal to duct axis (transverse direction)  
 $\Theta$  Temperature difference ratio,  $(T_m - T)/(T_m - T_j)$   
 $\rho$  Density

#### Subscripts

j Jet property  
m Cross-flow property, average value

#### REFERENCES

1. Srinivasan, R.; Myers, G.; Coleman, E.; and White, C.; Dilution Jet Mixing Program - Phase III Report, NASA CR-174884, 1985.
2. Srinivasan, R.; Berenfeld, A.; and Mongia, H.C.; Dilution Jet Mixing Program - Phase I Report, NASA CR-168031, 1982.
3. Srinivasan, R.; Coleman, E.; and Johnson, K.; Dilution Jet Mixing Program -Phase II Report, NASA CR-174624, 1984.

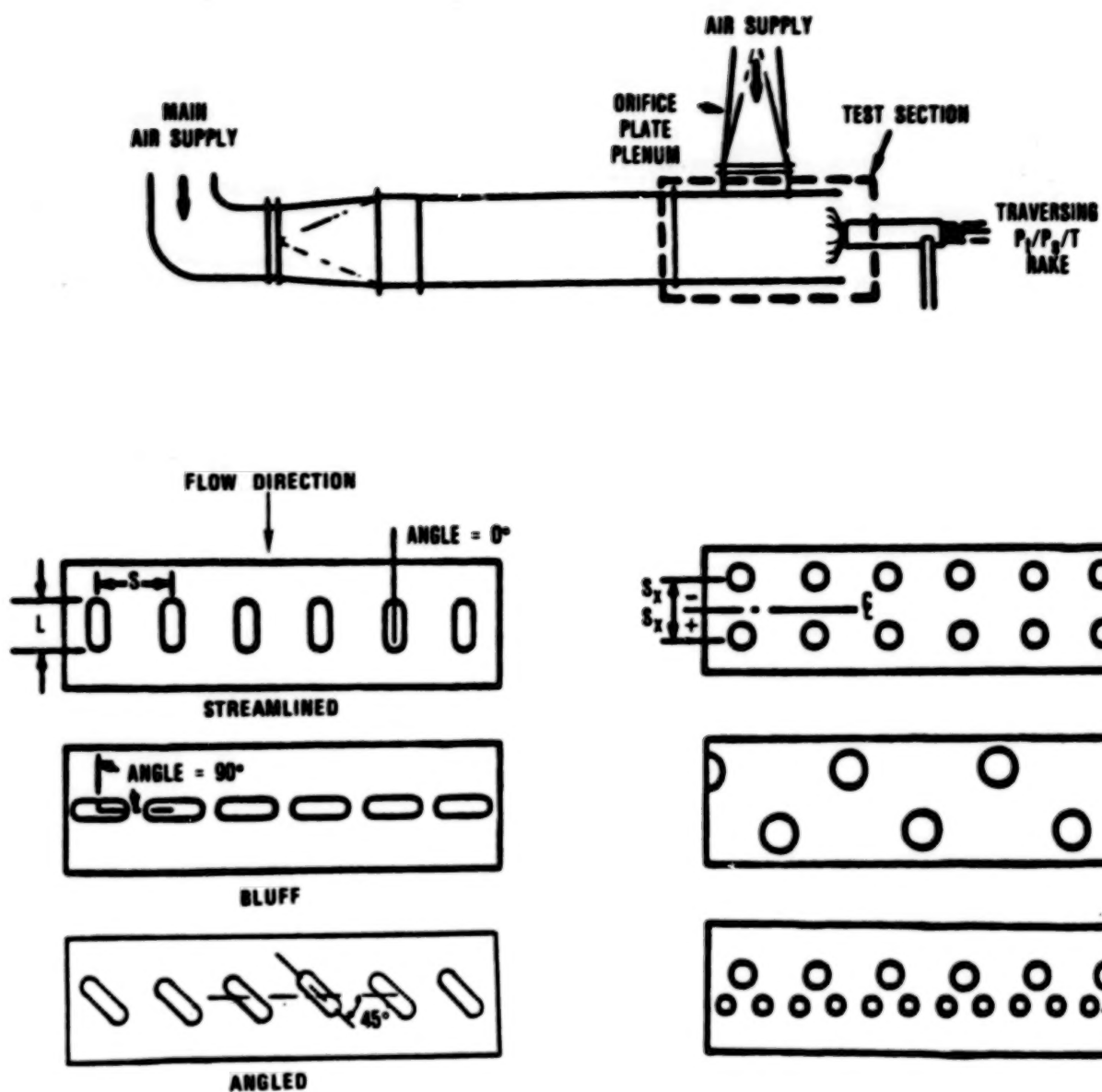


Figure 1. Dilution Jet Mixing Rig Schematic and Orifice Plates.

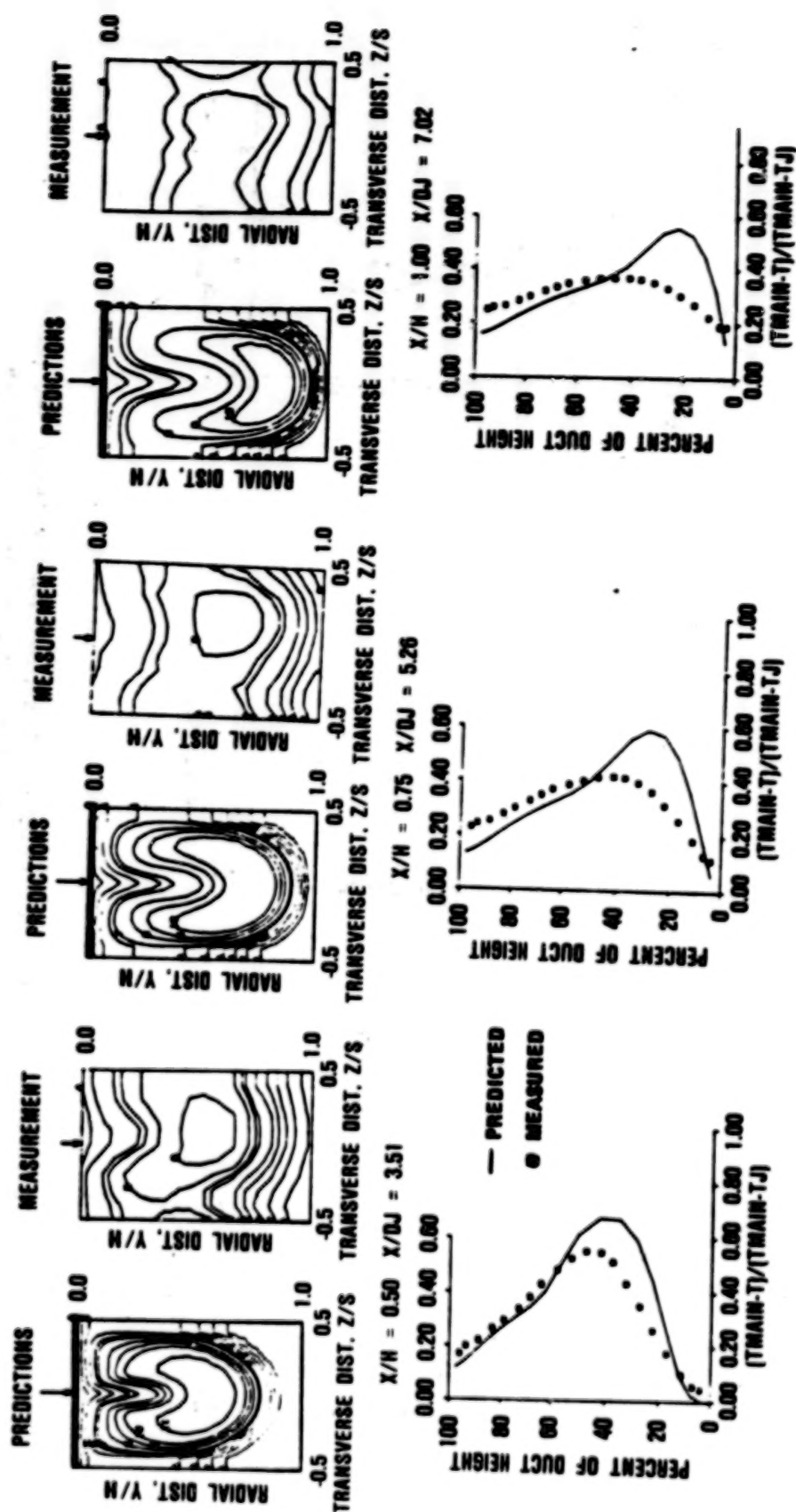


Figure 2. Comparison of Temperature Distributions Between 3-D Model Results and Data for Double Row of Jets,  $J = 26.6$ ,  $S/H = 0.5$ , Using 41 x 23 x 21 Nodes.

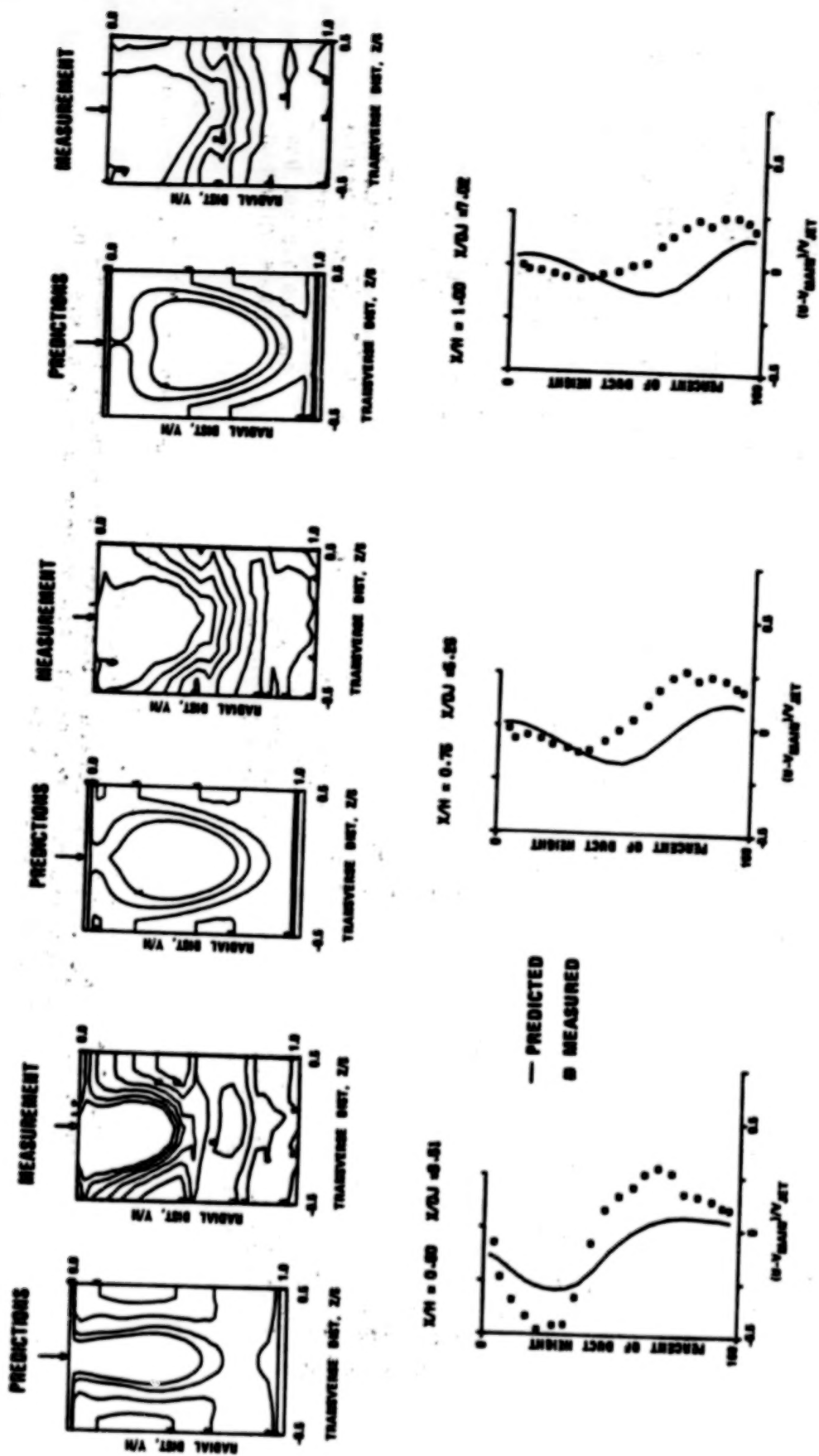


Figure 3. Comparison of Velocity Distributions Between 3-D Model Results and Data for Double Row of Jets,  $J = 26.6$ ,  $S/H = 0.5$ , Using  $41 \times 23 \times 21$  Nodes.

## ON THE MIXING OF A ROW OF JETS WITH A CONFINED CROSSFLOW

J.D. Holdeman  
 NASA Lewis Research Center  
 Cleveland, Ohio

## INTRODUCTION

Considerations in designing or tailoring temperature patterns at the exit of gas-turbine combustion chambers, necessary to maximize engine power and life, have motivated several studies of the thermal mixing characteristics of multiple jets injected into a confined crossflow (refs. 1 to 11). The objective of these studies was to identify the dominant physical mechanisms governing the mixing, to develop and extend empirical models for use as a near-term combustor design tool, and to provide a data base for the assessment and verification of three-dimensional numerical codes.

These investigations of dilution jet mixing were staged in complexity, beginning with experiments and analyses (refs. 1 to 5) that investigated the mixing characteristics of a single row of jets injected into an isothermal main-stream flow in a constant area duct. Recent experimental and analytical results (refs. 6 to 11) extended the earlier studies to investigate the role of several flow and geometric variations typical of gas-turbine combustion chambers, namely, variable temperature main stream, flow area convergence, opposed in-line and staggered injection, multiple rows of holes, and noncircular orifices.

From the data of references 1 and 2, an empirical model was developed (refs. 3 and 4) for calculating the temperature field downstream of a row of jets mixing with a confined crossflow. This model is the basis of an interactive microcomputer code which evaluates dilution-zone design alternatives (ref. 5). In this paper mean temperature profiles calculated with this routine are presented to show the effects of flow and geometric variables on the mixing of a single row of jets injected through sharp-edged orifices into a uniform flow of a different temperature in a constant area duct. In addition, this program is used to calculate profiles for opposed rows of jets with their centerlines in-line, by assuming that the confining effect of an opposite wall is equivalent to that of a plane of symmetry between opposed jets.

## FLOW FIELD DESCRIPTION

The flow schedule and the principal flow and geometric variables are shown in figure 1. The independent flow variables are the momentum flux ratio  $J$ , the density ratio  $DR$ , and the orifice discharge coefficient  $CD$ . The primary independent geometric variables are orifice size and the spacing between adjacent orifices. These are expressed in dimensionless form as the ratio of the duct height to orifice diameter  $H/D$  and as the ratio of the orifice spacing to duct height  $S/H$ . Downstream stations are defined in terms of the ratio of the distance to the duct height  $X/H$ .

The calculated temperature fields are shown in three-dimensional oblique views where the local temperature is given by the dimensionless temperature difference ratio,  $\theta = (T_m - T)/(T_m - T_j)$ . (Note that  $\theta$  is bounded by 0 and 1, with

the former representing unmixed mainstream fluid and the latter unmixed jet fluid.) Local values of this parameter are given on the abscissa in the three-dimensional plots. The ordinate Y and oblique coordinate Z are, respectively, normal to and along the orifice row, in a constant-X plane. The Z-distance shown in the oblique plots is twice the orifice spacing for each configuration. The flow and geometric variables specified as input to the empirical model were DR, J, CD, S/H, H/D, and X/H. All of the calculated profiles shown are for conditions that are within the range of the experiments against which the empirical model has been compared.

#### SUMMARY OF FLOW AND GEOMETRY EFFECTS

The calculated mean temperature profiles shown herein illustrate the effects of flow and geometric variables on the mixing. These confirm the conclusions reached previously (refs. 2 and 4) from examination of the experimental data that

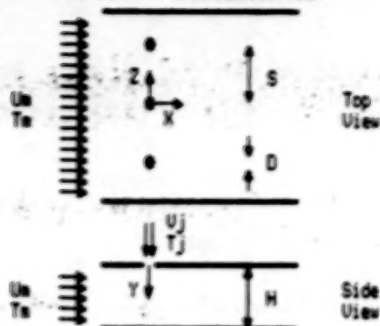
- (1) Mixing improves with downstream distance (fig. 2)
- (2) The momentum flux ratio is the most significant flow variable (fig. 3)
- (3) Variations in orifice diameter and spacing can have a significant effect on the profiles (fig. 4)
- (4) Similar distributions are obtained over a range of momentum flux ratios, independent of orifice diameter, if spacing and momentum flux ratio are coupled such that  $(S/H)(J) = \text{constant}$  (fig. 5)
- (5) Increasing the orifice diameter at constant spacing increases the magnitude of the temperature difference, but jet penetration and profile shape remain similar (fig. 6)
- (7) For opposed rows of jets with centerlines in-line, the optimum orifice spacing is one half of the appropriate value for one side injection (fig. 7).

#### REFERENCES

1. Walker, R.E.; and Kors, D.L.: Multiple Jet Study. NASA CR-121217, 1973.
2. Holdeman, J.D.; Walker, R.E.; and Kors, D.L.: Mixing of Multiple Dilution Jets with a Hot Primary Airstream for Gas Turbine Combustors. AIAA Paper 73-1249, Nov. 1973.
3. Walker, R.E.; and Eberhardt, R.G.: Multiple Jet Study Data Correlations. NASA CR-134795, 1975.
4. Holdeman, J.D.; and Walker, R.E.: Mixing of a Row of Jets with a Confined Crossflow. AIAA J., vol. 15, no. 2, Feb. 1977, pp. 243-249.
5. Holdeman, J.D.: Perspectives on the Mixing of a Row of Jets with a Confined Crossflow. AIAA Paper 83-1200, June 1983.
6. Srinivasan, R.; Berenfeld, A.; and Mongia, H.C.: Dilution Jet Mixing Program - Phase I. (Garrett 21-4302, Garrett Turbine Engine Co.; NASA Contract NAS3-22110) NASA CR-168031, 1982.

7. Srinivasan, R.; Coleman, E.; and Johnson, K.: Dilution Jet Mixing Program. (Garrett 21-4804, Garrett Turbine Engine Co.; NASA Contract NAS3-22110) NASA CR-174624, 1984.
8. Holdeman, J.D.; Srinivasan, R.; and Berenfeld, A.: Experiments in Dilution Jet Mixing. AIAA J., vol. 22, no. 10, Oct. 1984, pp. 1436-1443.
9. Holdeman, J.D.; and Srinivasan, R.: On Modeling Dilution Jet Flowfields. AIAA Paper 84-1379, June 1984.
10. Holdeman, J.D., et al.: Experiments in Dilution Jet Mixing - Effects of Multiple Rows and Non-circular Orifices. AIAA Paper 85-1104, July 1985.
11. Srinivasan, R.; Meyers, G.D.; and White, C.D.: Dilution Jet Mixing Program. (Garrett 21-5418, Garrett Turbine Engine Co.; NASA Contract NAS3-22110) NASA CR-174884, 1985.

# Flow Schematic



# Independent Variables

$DR = \rho_j / \rho_h$  density ratio  
 $J = DR (U_j / U_h)^2$  momentum flux ratio  
 $CD$  discharge coefficient  
 $S/H$  orifice spacing  
 $H/D$  orifice diameter  
 $X/H$  downstream distance

# Dependent Variables

$\theta = (T_h - T) / (T_h - T_j)$  temperature  
 $MR = m_j / m_h$  mass flow split  
 $TB = m_j / (m_h + m_j)$  equilibrium  $\theta$   
 $PF = MR (1 - \theta_{min}) / TB$  pattern factor  
 $S/D$   
 $X/D$

## Dilution Jet Mixing Flow and Geometric Variables

Figure 1

## VARIATION IN TEMPERATURE DISTRIBUTIONS WITH INCREASING ORIFICE DIAMETER

CONSTANT SPACING  $S/H = 0.5$ ,  $J = 26.4$

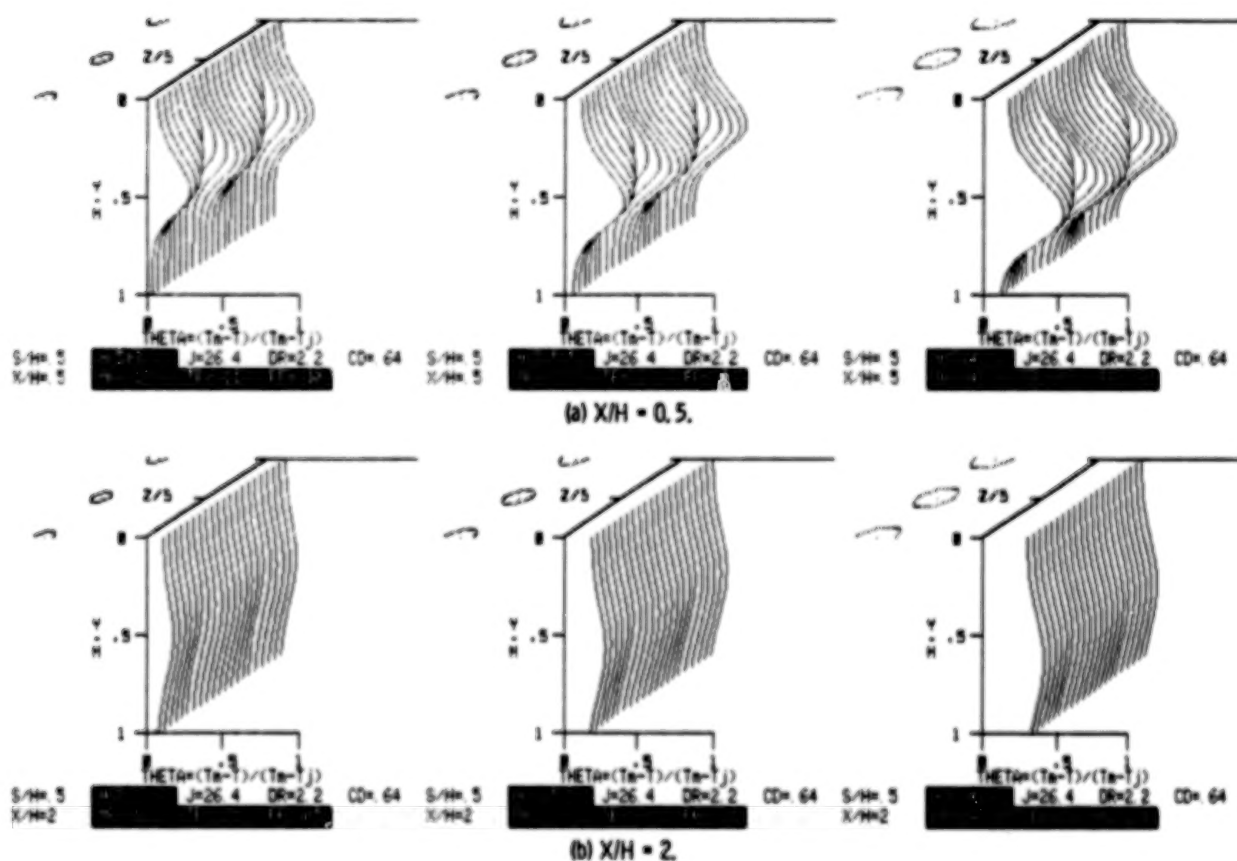


Figure 2

ORIGINAL PAGE IS  
OF POOR QUALITY

# VARIATION IN TEMPERATURE DISTRIBUTIONS WITH INCREASING MOMENTUM FLUX RATIO

$X/H = 0.5$ ;  $S/H = 0.5$ ;  $H/D = 5.66$

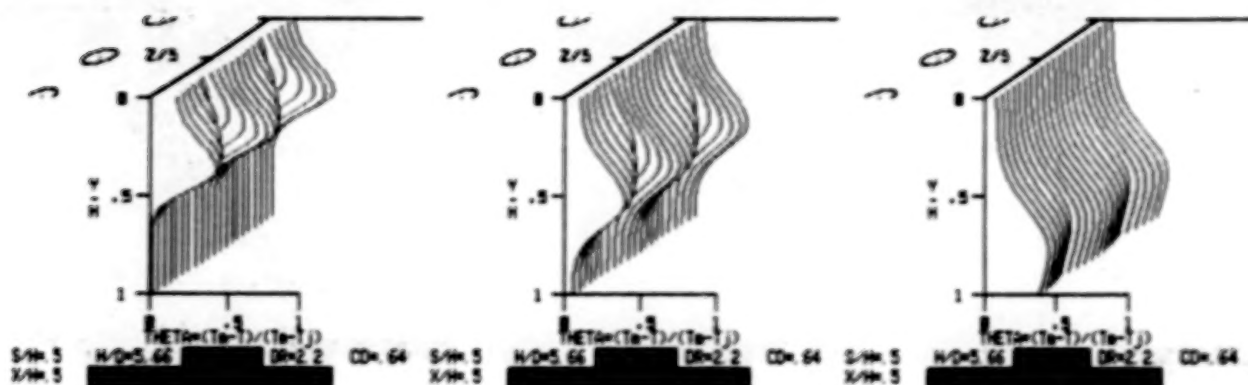


Figure 3

# VARIATION IN TEMPERATURE DISTRIBUTIONS WITH INCREASING DOWNSTREAM DISTANCE

OPPOSED JET INJECTION;  $J = 26.4$ ;  $S/H = 0.25$ ;  $H/D = 11.3$

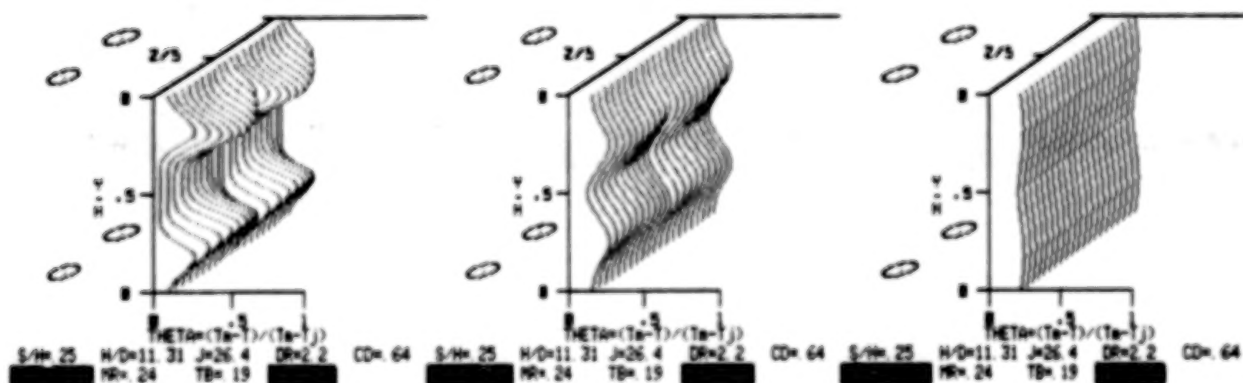
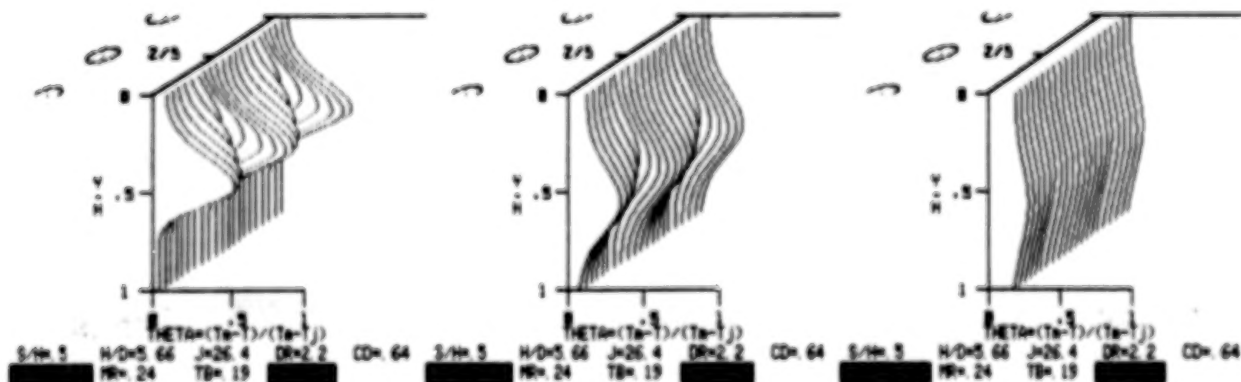


Figure 4

# VARIATION IN TEMPERATURE DISTRIBUTIONS WITH INCREASING DOWNSTREAM DISTANCE

$J = 26.4$ ;  $S/H = 0.5$ ;  $H/D = 5.66$



ORIGINAL PAGE IS  
OF POOR QUALITY

# VARIATION IN TEMPERATURE DISTRIBUTIONS WITH COUPLED SPACING AND MOMENTUM FLUX RATIO

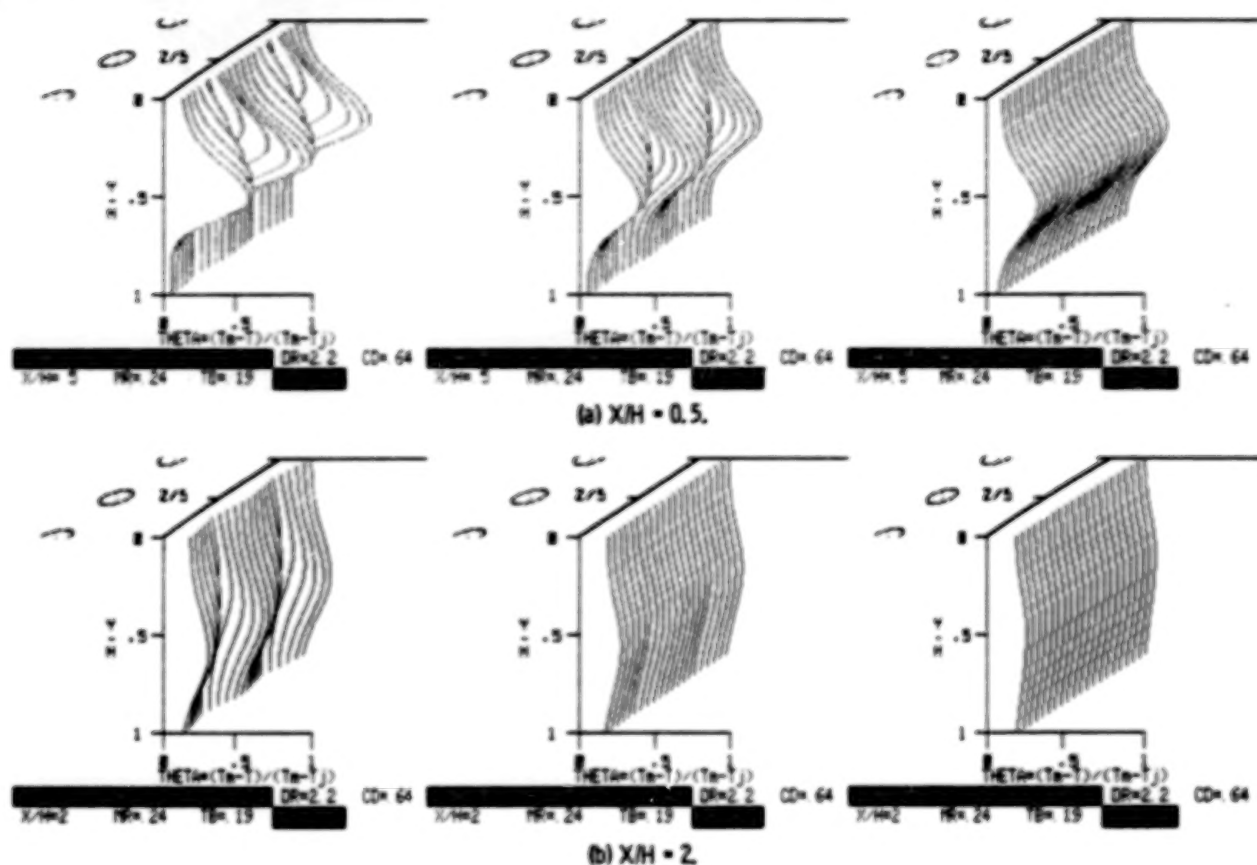


Figure 6

## VARIATION IN TEMPERATURE DISTRIBUTIONS WITH ORIFICE SPACING AND DIAMETER

CONSTANT ORIFICE AREA;  $X/H = 0.5$ ;  $J = 26.4$

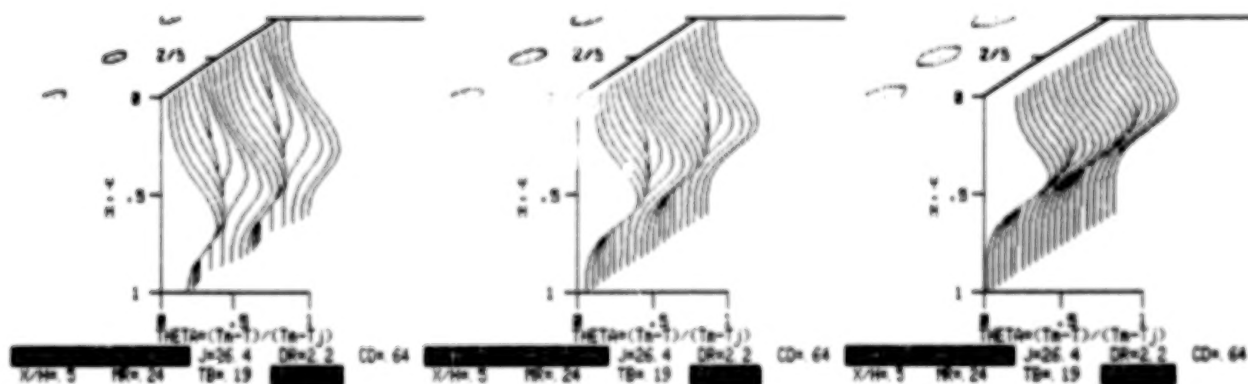


Figure 7

## HEAT TRANSFER IN A REAL ENGINE ENVIRONMENT

Herbert J. Gladden  
NASA Lewis Research Center  
Cleveland, Ohio

## INTRODUCTION

Improved performance of turbojet and turbofan engines is typically accompanied by increased cycle pressure ratio and combustor exit temperature. The continuing increase in turbine entry gas pressure and temperature as well as the high development cost puts a premium on an accurate initial aerothermal design of the turbine hot section hardware. The design goals for commercial jet engines include high cycle efficiency, increased durability of the hot section components (lower maintenance costs), and lower operating costs (increased thrust-to-weight and lower SFC). These goals are contradictory in that high cycle efficiency requires minimizing bleed air for cooling while the heat load is being increased. And durability requires the component metal temperatures and temperature gradients to be minimized. An optimum design can only be realized through an improved understanding of the flow field and the heat-transfer process in the turbine gas path.

The sophisticated computer design codes being developed have the potential of providing the designer with significantly better estimates of the flow field and the heat load on the hot-section components. These codes are evaluated and verified through low-temperature and pressure research in cascades and tunnels. However, by design, these facilities do not model all of the processes that exist in a real engine environment, and therefore, the ability of the design codes to predict the interaction of the various parameters cannot be fully evaluated.

A significant portion of the HOST project has been to develop instrumentation that can be used in a real engine environment to measure the boundary conditions of the flow field and heat-transfer process. The hot section facility (HSF) at NASA Lewis provides a "real engine" environment and convenient access for advanced instrumentation to evaluate these instruments. In addition, it provides an opportunity to study the aerothermal performance of turbine hot section components.

Several advanced instrumentation concepts developed into functional hardware under both the HOST program and independent programs were recently evaluated in the HSF. These instruments included thin-film thermocouples, two types of heat flux sensors, and a dynamic gas temperature probe. In addition, airfoil surface temperatures were measured by an infrared-film technique and by an optical pyrometer.

The thermal performance of a full-coverage film-cooled stator airfoil was also evaluated in this research program. The tests were conducted at chord-length Reynolds numbers of 0.5 to 2.5 million which correspond to typical advanced engine conditions. This corresponds to gas temperature and pressure levels up to 1500 K and 17.7 atm.

## FACILITY

The HSF has fully automated control of the research rig through an integrated system of minicomputers and programmable controllers. The major components of this facility and how they interface to provide a real engine environment are discussed in more detail in references 1 and 2.

Combustion air is provided to the facility at 10 atm through a nonvitiated preheater which modulates the air temperature between ambient and 560 K. A 20-atm mode of operation provides combustion air at pressures up to 20 atm and temperatures up to 730 K when using the heat of compression of a 2:1 compressor.

A cross-sectional schematic of the HSF cascade is shown in figure 1. The major components shown consist of a heat source (combustor), the full-annular vane row, an exhaust duct, a quench system (to lower exhaust-gas temperature), and the exhaust system. The vane row consists of 36 stator vanes separated into two groups: 10 test vanes and 26 slave vanes. The test vane and slave vane cooling airs are supplied from two separate manifolds with the flow rates to each manifold independently computer controlled.

The thermal performance of a full-coverage film-cooled vane is discussed in reference 1. The airfoil for these tests is shown in figure 2. The advanced instrumentation evaluation tests were conducted using a hollow airfoil shell with a solid surface. A typical airfoil for these tests is shown in figure 3.

## INSTRUMENTATION

The advanced instrumentation evaluated consisted of thin-film thermocouples, Gardon-type and embedded thermocouple heat flux gauges, a dual-element dynamic gas-temperature probe, and two types of infrared surface-temperature measuring devices. Thin-film thermocouples installed on a hollow shell airfoil pressure surface are shown in figure 3. The thermal elements were platinum/platinum - 10 percent rhodium (type S) sputtered on a substrate of  $Al_2O_3$ .

Two types of heat flux gauges were installed on the airfoil pressure surface: gardon-type gauges and paired thermocouple type gauges. These gauges were installed and calibrated by Pratt & Whitney Aircraft following the procedure outlined in reference 4. A step-wise procedure for installing the gardon-type gauges is depicted in figure 4.

The dual-element dynamic gas temperature probe was located at the combustor exit. The two thermal elements of the probe were platinum - 30-percent rhodium/platinum - 6-percent rhodium (type B) and were 0.076 and 0.25 mm in diameter. The probe elements are shown in figure 5, and its construction details are discussed in reference 5.

Airfoil surface temperatures can be determined by infrared radiation emitted from the hot surfaces. The two techniques described in reference 6 are based on an infrared-photography system or a photoelectric scanning system. The infrared-photography system was designed primarily for temperature measurements in stationary systems and was used for turbine-vane leading-edge region measurements. The photoelectric scanning system was developed primarily for temperature measurement in rotating systems, but during the cascade tests it was adapted to measure

temperatures on the vane trailing-edge surface. These two systems are shown schematically in figures 6 and 7.

## RESULTS AND DISCUSSION

### Thermal Scaling

During the development of an engine, the turbine components are frequently tested at lower temperature and pressure in cascades and tunnels to verify the heat-transfer design. There has been concern for the validity of these data and whether the thermal scaling laws are sufficiently satisfied between the rig tests and the actual engine. Data were taken over a wide range of temperatures and pressures to investigate the thermal scaling phenomena. The primary parameters held constant were Reynolds number and Mach number. The results are shown in figure 8. A midspan average cooling effectiveness parameter  $\phi$  for the full-coverage film-cooled vane is shown as a function of the coolant-to-gas flow ratio.

The lowest Reynolds number data taken ( $0.5 \times 10^6$ ) are presented in figure 8(a). A trend is shown by these data where the higher gas-temperature data have a lower cooling effectiveness than the lower gas-temperature data. The difference in cooling effectiveness values is about 0.02 at a coolant-to-gas flow ratio of 0.113.

The data shown in figure 8(b) represent a higher Reynolds number ( $1.25 \times 10^6$ ) and are characteristic of both engine operation (high-gas temperature) and rig tests (low-gas temperature). These data show a trend similar to the data in figure 8(a); that is, the low gas temperature data (rig tests) have a slightly higher cooling effectiveness than the higher gas temperature data (engine conditions). The difference in cooling effectiveness values is about 0.02 at a coolant-to-gas flow ratio of 0.11.

Reference 7 predicts up to a 0.04 increase in cooling effectiveness from engine conditions to lower temperature rig-test conditions. This phenomenon was shown to result from our inability to thermally scale the material thermal conductivity. This trend is shown by both Reynolds number data sets. It can be concluded from these data and reference 7 that low-temperature rig tests are somewhat optimistic in predicting the cooling performance of a design prototype operating at engine conditions.

### Infrared Temperature Measurement

A thermal image of an airfoil leading edge and pressure surface are shown in figure 9. The gray tones represent the temperature of the airfoil through its thermal energy output. The lightest regions are at high temperatures and the dark regions are cooler. The procedures for recording and interpreting thermal image is discussed in reference 6. The gray tones in the figure indicate a hot leading edge and a relatively uniform and lower temperature on the pressure surface. The pattern of dark spots on the leading edge of vane 3 are the film cooling holes. In addition, a horseshoe-vortex type thermal pattern can be seen on the hub endwall as it wraps around the leading edge of the vane.

## Heat-Transfer Coefficients

Heat-transfer coefficients were determined by repeatedly ramping the gas temperature between a low and a high temperature at several frequencies and recording the transient response of the wall temperature. A portion of typical wall and gas temperature time histories (fig. 9) illustrates the magnitude and shape of the transient input and the time response of the thin film thermocouple. Typically, the gas temperature was varied 140 K, and the wall temperature responded with a variation of 30 K. In figure 10 six repetitions of a 2-sec ramp cycle are followed by seven repetitions of a 4-sec ramp cycle. These and other ramp-cycle lengths were used to gather data at fundamental frequencies from 0.005 to 0.5 Hz (periods of 200 to 2 sec).

The amplitude ratio of the Fourier components of the wall to gas temperatures was determined from a cross-correlation of the temperature histories. The data follow a slope of  $-1/2$  and has a phase lag of about  $45^\circ$  as Dils' theory requires, justifying the use of that approximation to determine local heat-transfer coefficients. The coherence function between the gas-temperature ramp and the wall-temperature response was greater than 0.8, which indicates that there was a significant relationship. The trend of increased heat transfer with increased Reynolds number is also indicated by the data.

The experimental heat-transfer coefficients on the airfoil pressure and suction surfaces are shown in figures 10 and 12. The data are plotted as a function of the dimensionless surface distance,  $x/L$ . Also included on the figure is an analytical solution from the STAN5 boundary layer code.

Pressure surface. - The low Reynolds number data ( $0.55 \times 10^6$ ) of figure 11 show generally laminar characteristics in the midchord region with a transition to turbulent flow near the trailing edge. The steady-state experimental data from the Gardon-gauges and the paired thermocouples also show generally laminar characteristics in the midchord region with a magnitude of  $\sim 75$  percent of the transient data. The experimental data are also compared with an analytical solution that has been forced to a turbulent flow solution near the airfoil leading edge. This solution compares favorably with the steady-state heat-transfer coefficients, but it is  $\sim 75$  percent of the transient data.

The  $1.2 \times 10^6$  Reynolds number data (fig. 11) follow a trend suggesting boundary-layer transition in the midchord and trailing-edge regions. However, the heat-transfer coefficients in the leading-edge region have relatively large magnitudes, which is consistent with an augmented laminar boundary layer. The two transient measurements at  $x/L$  of 0.354 are from different vanes and show a significant difference in magnitude. Data up to an  $x/L$  of 0.354 are in an apparent transitional region indicated by the steep gradient in the heat-transfer coefficient. The steady-state experimental data from the Gardon-type and paired-thermocouple gauges generally compare with the transient experimental data. The STAN5 analysis was also forced to a turbulent flow solution near the leading edge for this Reynolds number. The results (fig. 11) show a good comparison between the analysis and the experimental data in both magnitude and trend.

Data for a Reynolds number of  $1.9 \times 10^6$  show the heat-transfer coefficients from both the transient and the steady-state measurements to have the same trend in the midchord region (fig. 11). However, the steady-state data have a larger magnitude than the transient data at this Reynolds number, which is opposite of the relation shown in the lower Reynolds number data. The analytical solution shows a good

comparison with the experimental heat-transfer coefficients when the boundary layer is forced to a turbulent flow solution near the leading edge.

Suction surface. - Experimental heat-transfer coefficients from the transient technique are shown in figure 12 for the airfoil suction surface. The analytical solution from STAN5 follows the data reasonably well for all three Reynolds numbers. However, at an  $x/L$  of 0.82, the experimental heat-transfer coefficient shows a substantial increase over the trend established by the other data. A sudden increase in heat transfer on a suction-surface trailing edge is not uncommon and may be due to secondary flow effects. In addition, the analytical solution generally underpredicts the experimental results, and the magnitude of the underprediction increases with decreasing Reynolds number.

The transient and steady-state experimental data on both the airfoil pressure surface and the transient data on the suction surface show increasing magnitude with Reynolds number as would be expected. In addition, the experimental data trends are similar to those predicted by the STAN5 boundary-layer code. Data from both transient and steady-state techniques on the pressure surface have similar magnitudes and trends. There is, however, a significant deviation in magnitude between the experimental heat-transfer coefficients and those predicted by STAN5 in the laminar and transitional regions.

#### CONCLUSIONS

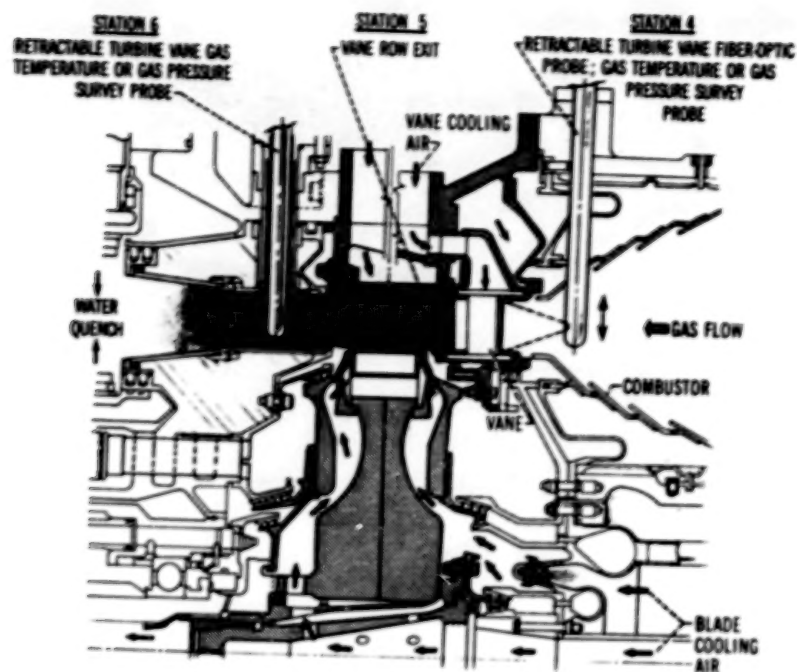
The experimental data-base for the evaluation of sophisticated computer design codes for the turbine hot section components must include data at real engine conditions. Part of the HOST program has been directed toward the development of instrumentation capable of measuring boundary conditions of the flow field and heat-transfer process in the hostile environment of the turbine. The hot section facility at the Lewis Research Center was used to demonstrate the capability of these instruments to make the required measurements. The results of thermal scaling tests show that low-temperature-and-pressure rig tests give optimistic estimates of the thermal performance of a cooling design, for high-temperature-and-pressure application. The results of measuring heat-transfer coefficients on turbine vane airfoils through dynamic data analysis show good comparison with measurements from steady-state heat-flux gauges. In addition, the data trends are predicted by the STAN5 boundary-layer code. However, the magnitude of the experimental data was not predicted by the analysis, particularly in laminar and transitional regions near the leading edge. The infrared-photography system was shown capable of providing detailed surface thermal gradients and secondary flow features on a turbine vane and endwall.

#### REFERENCES

1. Gladden, H.J.; Yeh, F.C.; and Fronek, D.L.: Heat Transfer Results and Operational Characteristics of the NASA Lewis Research Center Hot Section Cascade Test Facility. ASME Paper 85-GT-82, Mar. 1985.
2. Cochran, R.P.; Norris, J.W.; and Jones, R.E.: A High-Pressure, High-Temperature Combustor and Turbine Cooling Test Facility. ASME Paper 76-WA/GT-4, Dec. 1976.

3. Gladden, H.J.; and Proctor, M.P.: Transient Technique for Measuring Heat Transfer Coefficients on Stator Airfoils in a Jet Engine Environment. AIAA Paper 85-1471, July 1985.
4. Atkinson, W.H.; Cyr, M.A.; and Strange, R.R.: Turbine Blade and Vane Heat Flux Sensor Development, Phase I. (PWA-5914-21, Pratt & Whitney Aircraft; NASA CR-168297) August 1984
5. Elmore, D.L.; Robinson, W.W.; and Watkins, W.B.: Dynamic Gas Temperature Measurement System Final Report Volume 1 Technical Effort. (PWA/GPD-FR-17145-Vol. 1, Pratt & Whitney Aircraft, NASA CR-168267-Vol. 1) May 1983
6. Pollack, F.G.; and Cochran, R.P.: Temperature and Pressure Measurement Techniques for an Advanced Turbine Test Facility. Measurement Methods in Rotating Components of Turbomachinery, B. Lakshminarayana and P. Runstadler, Jr., eds., ASME, 1980, pp. 319-326.
7. Gladden, H.J.: Extension of Similarity Test Procedures to Cooled Engine Components with Insulating Ceramic Coatings. NASA TP-1615, 1980.

# HSF CASCADE CROSS-SECTION SCHEMATIC



CS 85-3212

Figure 1

## FULL-COVERAGE FILM COOLED VANES USED FOR THERMAL SCALING TESTS

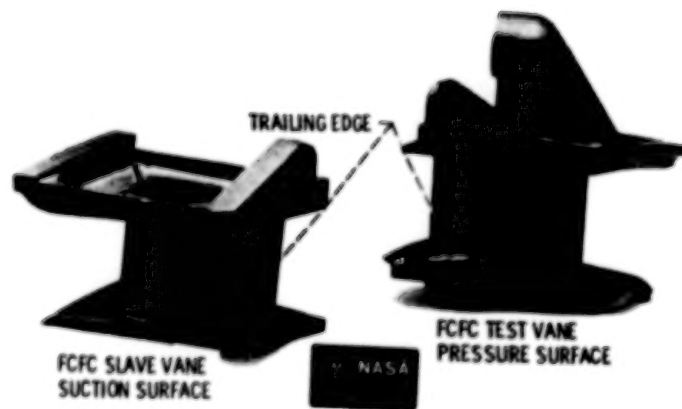
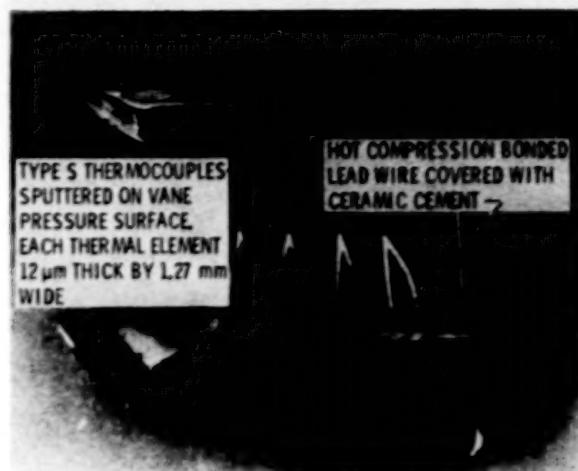


Figure 2

ORIGINAL PAGE IS  
OF POOR QUALITY

# THIN FILM THERMOCOUPLE INSTALLATION

ORIGINAL PAGE IS  
OF POOR QUALITY



CS 85-3207

Figure 3

## HEAT FLUX GAGE INSTALLATION IN VANE

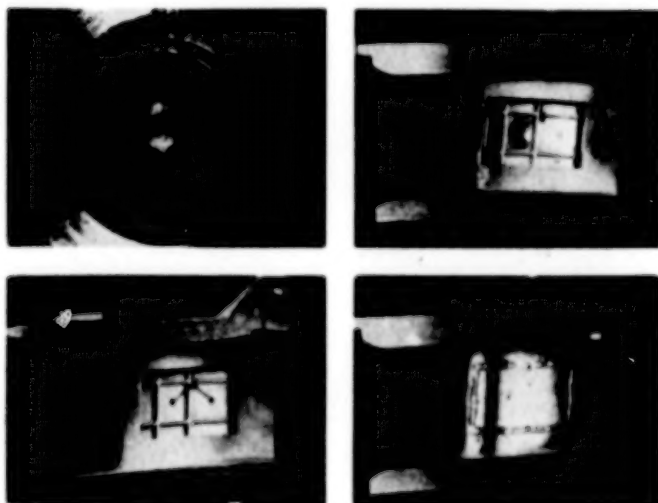


Figure 4

## DUAL-ELEMENT GAS TEMPERATURE PROBE

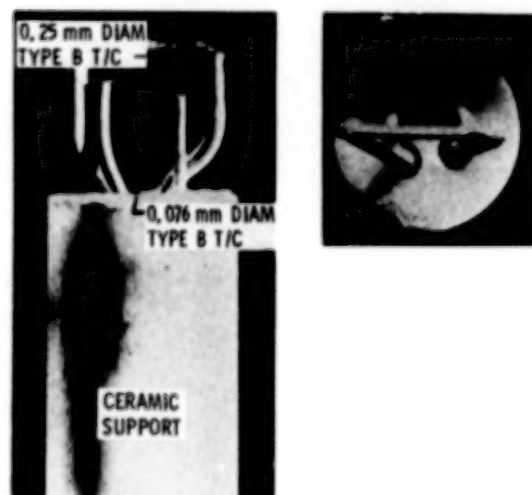


Figure 5

# PHOTOELECTRIC SCANNING SYSTEM FOR ROTATING BLADES

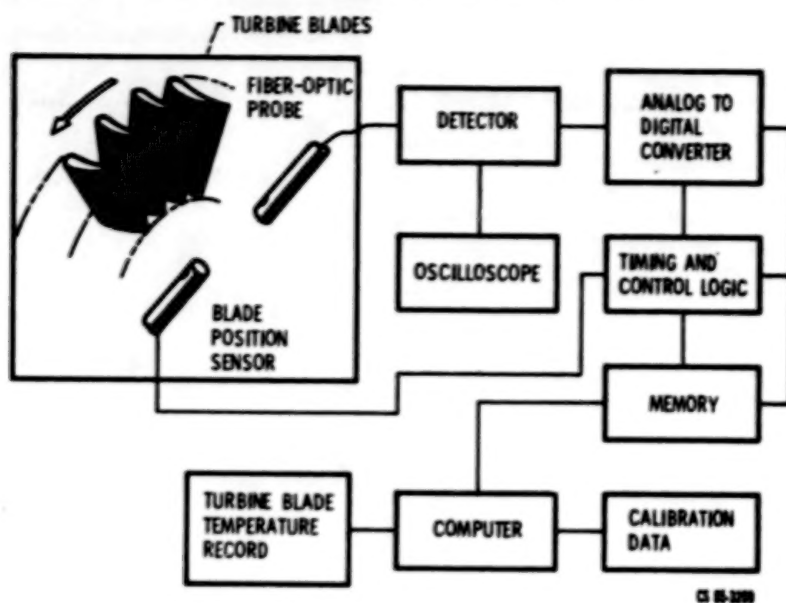


Figure 6

# PHOTOGRAPHY SYSTEM FOR STATIONARY VANES

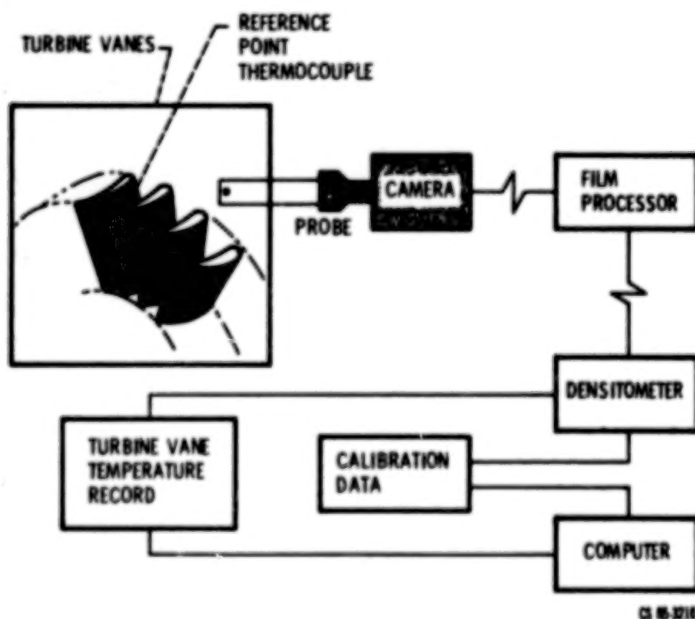


Figure 7

# THERMAL SCALING RESULTS FROM FULL-COVERAGE FILM-COOLED VANE AIRFOIL

ORIGINAL PAGE IS  
OF POOR QUALITY

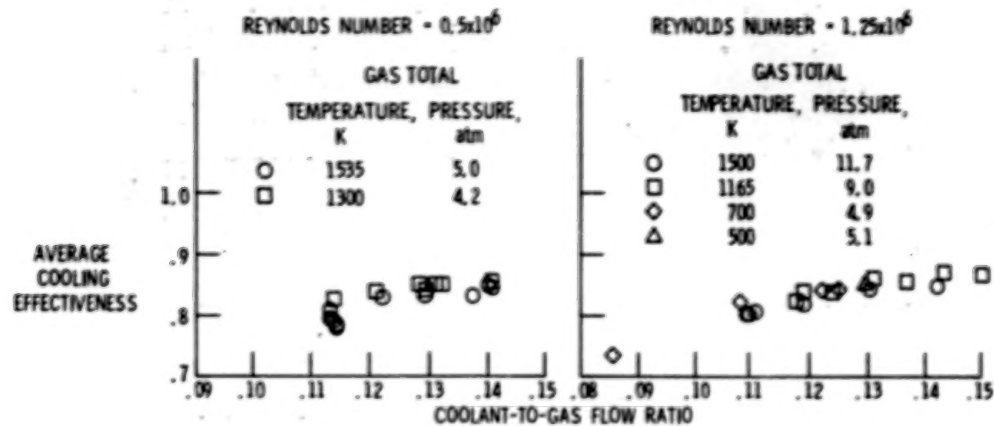


Figure 8

## FULL-COVERAGE FILM-COOLED VANE AIRFOIL THERMAL IMAGE IR PHOTOGRAPHY SYSTEM

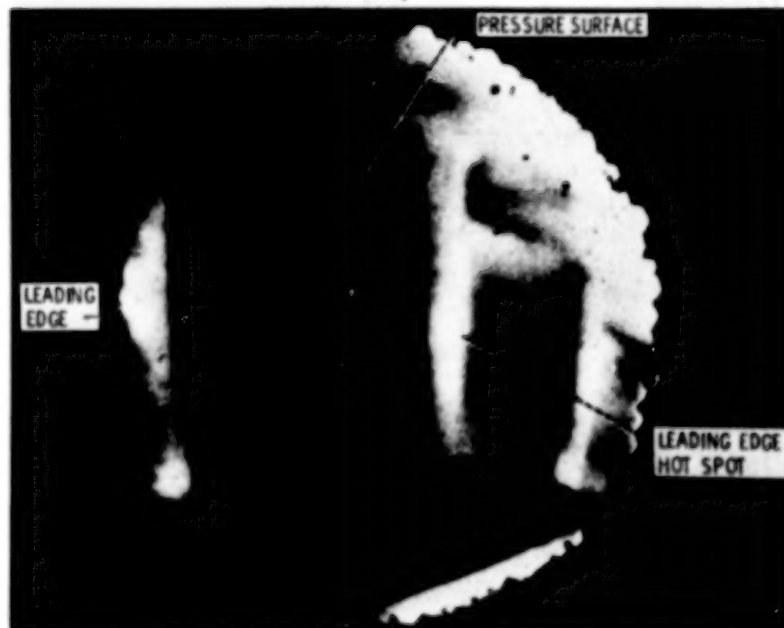


Figure 9

# TYPICAL TIME HISTORIES OF GAS AND WALL TEMPERATURES

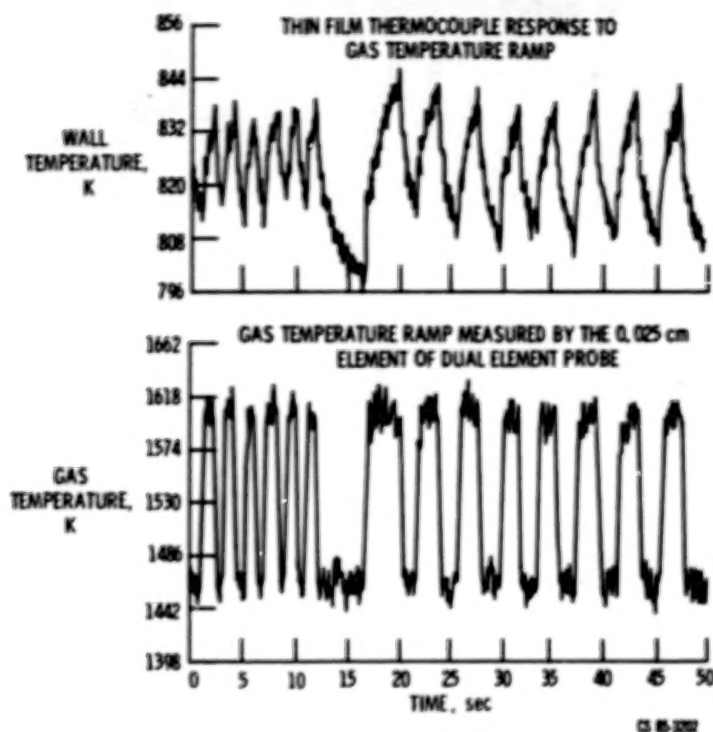


Figure 10

# EXPERIMENTAL HEAT TRANSFER COEFFICIENTS ON VANE AIRFOIL PRESSURE SURFACE

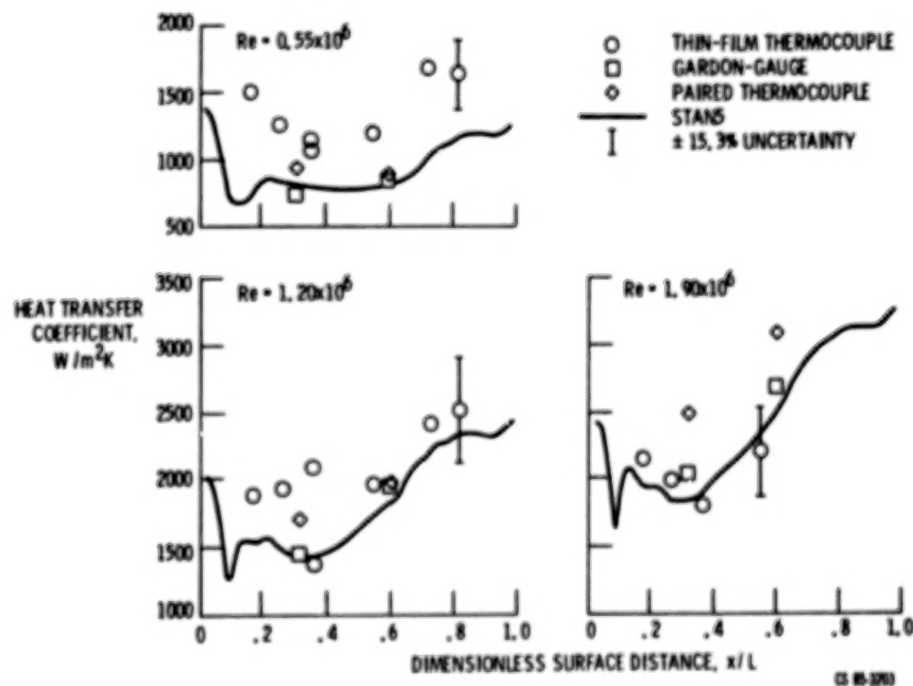


Figure 11

# EXPERIMENTAL HEAT TRANSFER COEFFICIENTS ON AIRFOIL SUCTION SURFACE

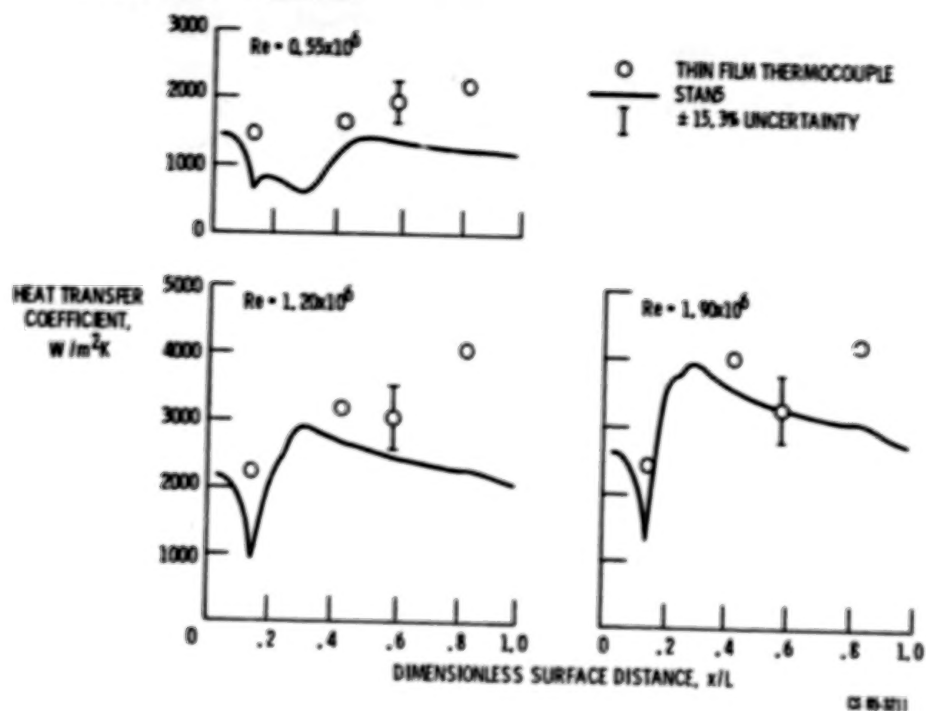


Figure 12

## FILM COOLING HEAT TRANSFER ON A TURBINE AIRFOIL\*

Larry D. Hylton  
Allison Gas Turbine Division  
General Motors Corporation

## INTRODUCTION

Recently considerable emphasis has been placed on developing more accurate analytical models for predicting hot gas side heat transfer rates to turbine airfoils. In order to achieve the durability and performance goals of new engines, cooling system designs must be carefully tailored to each application. This requires an accurate assessment of the hot gas side thermal loading. The development and verification of improved analytical models requires a systematic, closely coupled experimental and analytical program. The objectives of the current program are to develop an analytical approach, based on boundary layer theory, for predicting the effects of airfoil film cooling on downstream heat transfer rates and to verify the resulting analytical method by comparison of predictions with hot cascade data obtained under this program.

## BACKGROUND

The overall approach to attaining the stated objective has involved a series of three programs as illustrated in figure 1. The initial program, performed under Contract NAS3-22761, assessed the capability of available modeling techniques to predict non-film cooled airfoil surface heat transfer distributions, acquired experimental data as needed for model verification, and provided verified improvements in the analytical models. This effort resulted in a baseline predictive capability and was reported in CR 168015 (ref. 1) published in May 1983.

The problem of heat transfer predictions with film cooling was broken into sequential efforts with the effect of leading edge showerhead film cooling being investigated first, followed by a program to study the effects of the addition of discrete site suction and pressure surface injection. The effort on showerhead film cooling was performed under Contract NAS3-23695 and was reported in CR 174827 (ref. 2) published in July 1985. As part of that program, a five-row, simulated common plenum showerhead geometry was tested to determine differences between film and non-film cooled heat transfer coefficient distributions downstream of a leading edge, multiple hole film cooling array. Building on non-film cooling modeling improvements incorporated in a modified version of the STAN5 boundary layer code developed under Contract NAS3-22761, a program was developed to analytically model and predict differences resulting from leading edge mass injection.

A summary of the program results including experimental data and corresponding analytical predictions are shown in figures 2-5. Rather than simply form the film cooled Stanton number to non-film cooled Stanton number ratio ( $St_{FC}/St_{NFC}$ ) to isolate the effects of film cooling on downstream heat transfer, an alternate parameter referred to as Stanton number reduction (SNR) is used. SNR is defined as

$$SNR = 1 - St_{FC}/St_{NFC} \quad (1)$$

\*This work is being performed under Contract NAS3-24619

Therefore,  $SNR=0$  implies "no difference" and positive or negative values imply reduced or increased heat transfer levels respectively. Forming SNR values along the entire test surface gives the actual SNR distribution for the airfoil. In addition,  $St_{FC}/St_{NFC}$  is determined using data obtained at equivalent  $M_2$  and  $Re_2$  conditions, so SNR is approximately equal to the actual heat transfer coefficient reduction. Figures 2 and 3 illustrate the formation and type of information given by vane surface SNR distributions. All data shown in these figures were obtained at fixed operating conditions; i.e.,  $Ma_2 = 0.90$ ,  $Re_2 = 2.0 \times 10^6$ ,  $T_c/T_g = 0.82$ . Variable blowing strengths ( $P_c/P_t = 1.0, 1.30, 1.52$ , and  $1.72$ ) were set at these conditions and heat transfer data were taken. The four different surface heat transfer coefficient distributions determined from the cascade data at the four coolant to free-stream pressure ratio conditions are shown in figure 2. A value of  $P_c/P_t = 1.0$  signifies that no coolant is being ejected and  $P_c/P_t > 1.0$  signifies that coolant is being ejected. Using the results of figure 2 and the SNR definition, surface SNR distributions can be constructed. These distributions are shown in figure 3. Because each SNR distribution shows only the difference between a given film-cooled and baseline nonfilm-cooled condition, an SNR data presentation is useful for discussing phenomena unique to the film-cooled problem.

The characteristic effect of blowing strength variation is illustrated by the SNR differences shown in figure 3. These results indicate that the most significant differences occur on the suction surface between 20% and 40% of the surface distance. This region corresponds to the suction surface boundary layer transition zone. From figure 2, it can be observed that the suction surface transition origin moves forward on the airfoil as the blowing strength is increased. This results in increases in heat transfer levels (negative SNR) with increasing blowing strength as illustrated in figure 3. Smaller, but significant, increases in heat transfer occur on the pressure surface. These preturbulent increases are similar in character to the increases that would be expected to be caused by increasing the free-stream turbulence intensity from a baseline state. The discrete injection process apparently acts as a turbulence promoter.

The blowing strengths represented in figures 2 and 3 are higher than would be expected in an actual engine design, but were run to better understand the physics of the cooling process. Reducing blowing strengths to levels of interest to the turbine designer ( $< 1.10$ ) provides the results shown in figure 4. Here the area of increased heat transfer (negative SNR) is limited to the transition zone on the suction surface.

One goal of this effort was to determine whether there were any benefits to be extracted from leading edge injection in terms of recovery region surface protection. Data shown in figure 5 were obtained at variable plenum coolant to mainstream total temperature ratios ( $T_c/T_g = 0.69, 0.82$ , and  $0.89$ ) and at fixed  $Ma_2$ ,  $Re_2$ , and  $P_c/P_t$  conditions. The overall increase in SNR (i.e., decreased heat transfer) as the coolant to gas absolute temperature ratio decreased indicates the positive effect that results from diluting the hot free-stream fluid with the relatively cooler leading edge ejectant. However, as the pressure surface results indicate, the favorable thermal dilution phenomenon is offset by the adverse turbulence generation mechanism associated with the discrete injection process. The net result is that even for  $T_c/T_g = 0.69$ , SNR is still negative immediately downstream of the showerhead on the pressure surface. Figure 5 also indicates that the thermal dilution and turbulence generation mechanisms interact on the suction surface in the preturbulent zones although in the fully turbulent zones the SNR result is determined by thermal dilution strength only. These results indicate that leading edge film cooling by itself cannot be used to always offset high near recovery region heat loads even though far recovery region

loads are reduced.

Utilizing the modeling improvements made as part of this program SNR distributions were computed for the six blowing condition data sets represented in figures 3 and 4 and are shown in the figures. The comparisons shown in figure 4 indicate that with the exception of the suction surface transition zone, there is little measured and/or predicted effect due to the leading edge injection. This small effect result is significant, because the blowing levels shown ( $P_c/P_t \leq 1.10$ ) are more representative of actual design conditions than the higher blowing cases ( $P_c/P_t > 1.10$ ) shown in figure 3. For the strong blowing condition SNR predictions shown in figure 3, the proposed two parameter method predicts trends reasonably well but quantitative discrepancies exist.

SNR predictions for the variable cooling temperature blowing conditions are shown in figure 5. As illustrated in figure 5, the analytical method does a reasonable job in predicting all of the trends indicated in the data. The detailed results of the technical effort under Contract NAS3-23695 are reported in NASA CR 174827 (ref. 2) which was published in July 1985.

#### CURRENT PROGRAM

Work under NASA Contract NAS3-24619 was started in August 1985. The objectives of this program are to extend the analytical airfoil film cooling code development to include discrete site pressure and suction surface injection, with and without leading edge blowing, and to obtain relevant hot cascade data to verify the model improvements.

#### Analytical Approach

The overall approach will be to extend a base 2-D boundary layer code containing the leading edge showerhead cooling model reported in reference 2 and the multiple row film cooling model implemented in the STANCOOL code (ref. 3). Three phases have been defined to accomplish the objective of producing a tool that is acceptable in terms of qualitative/quantitative accuracy and relatively easy to incorporate within a present day turbine airfoil design system. The three phases consist of a design mode analysis phase, a method characterization phase, and a method refinement/verification phase.

The design mode analysis phase is intended to demonstrate the use of the base boundary layer method in a film-cooled turbine airfoil design system environment. This initial study will address details involved with method set-up procedures (e.g., defining initial and boundary conditions) and the qualitative behavior of the film cooling models for a relevant film-cooled airfoil design. As part of this analysis, the heat transfer distributions on the film-cooled airfoil to be tested in the hot cascade will be predicted. This initial design mode analysis phase will be followed by a detailed method characterization study. This study will determine the qualitative/quantitative attributes and deficiencies of the proposed method using measured aerodynamic and heat transfer data obtained in the experimental program. Comparisons of the data with the predictions from the design mode analysis will be made at several operating conditions. The final effort, method refinement/verification, will address modeling deficiencies discovered in the first two phases. At present, the method being proposed contains four modeling parameters that control predicted film cooling recovery region heat transfer phenomena. Two parameters are associated with the leading edge model described in Turner et al (ref. 2) and two with the full

coverage STANCOOL model (ref. 3). It is anticipated that the majority of effort in the final phase will be aimed at determining proper formulations for these parameters for incorporation in a design code. While parameter formulation for the STANCOOL code applied within a gas turbine environment has received recent attention (ref. 4-6), the two parameter leading edge model of Turner et al (ref. 2) will be further tested to demonstrate its range of applicability. Finally, when the models are combined for the case of airfoil geometries with both leading edge and downstream injection, the overall formulation must still perform satisfactorily. Using available film cooled airfoil data, it is anticipated that appropriate formulations for the four parameters can be developed to cover the range of operating conditions of interest to turbine designers.

#### Experimental Approach

The experimental phases will be an extension of the previous contract work. The hot cascade tests will utilize the same facility and cascade used in the previous contract, with the instrumented airfoil in the cascade replaced with one containing suction surface and pressure surface film cooling arrays in addition to a leading edge showerhead film cooling array. A schematic of the airfoil is shown in figure 6. The film cooled region of the airfoil will be thermally isolated from the remainder of the airfoil. Surface heat transfer measurements downstream of the suction and pressure surface hole arrays will be made using the same technique utilized in the previous contract tests. This technique, illustrated in figure 7, uses experimentally measured steady-state aerothermal boundary conditions as input for numerically solving the heat conduction equation in order to determine the airfoil internal temperature distribution. Once the internal temperature distribution is determined, a local heat transfer coefficient can be determined using the local calculated surface normal temperature gradient, measured wall and gas temperatures, and material conductivity. In addition to heat transfer measurements, the airfoil will be instrumented to obtain the surface static pressure distribution. Also as part of the experimental program, aerodynamic losses for the cascade will be measured at the exit plane by traversing a five hole cone probe across one passage at the airfoil midspan. The cascade will be operated at three levels of exit Reynolds number and two levels of exit Mach number (expansion ratio). Blowing strength and cooling strength for selected blowing configurations will be varied at these operating conditions. The tests will be conducted at constant turbulence intensity and vane-surface-to-gas-absolute temperature ratio ( $T_w/T_g$ ) levels. The test matrix should provide a significant data base for verifying the analytical models at relevant gas turbine conditions.

#### REFERENCES

1. L. D. Hylton, M. S. Mihelc, E. R. Turner, D. A. Nealy, and R. E. York, "Analytical and Experimental Evaluation of the Heat Transfer Distribution over the Surfaces of Turbine Vanes," NASA CR-168015, May 1983.
2. E. R. Turner, M. D. Wilson, L. D. Hylton, and R. M. Kaufman, "Turbine Vane External Heat Transfer," Vol I, NASA CR-174827, July 1985.
3. M. E. Crawford, W. M. Kays, and R. J. Moffat, "Full Coverage Film Cooling on Flat, Isothermal Surfaces: A Summary Report on Data and Predictions," NASA CR-3219, January 1980.
4. F. S. Stepka and R. E. Gaugler, "Comparison of Predicted and Experimental External Heat Transfer around a Film-Cooled Cylinder in Crossflow," ASME

paper 83-GT-47, 1983.

5. K. L. Miller and M. E. Crawford, "Numerical Simulations of Single, Double, and Multiple Row Film Cooling Effectiveness and Heat Transfer," ASME paper 84-GT-112, 1984.
6. C. Camci and T. Arts, "Short Duration Measurements and Numerical Simulation of Heat Transfer along the Suction Side of Film-Cooled Gas Turbine Blade," ASME paper 85-GT-111, 1985.

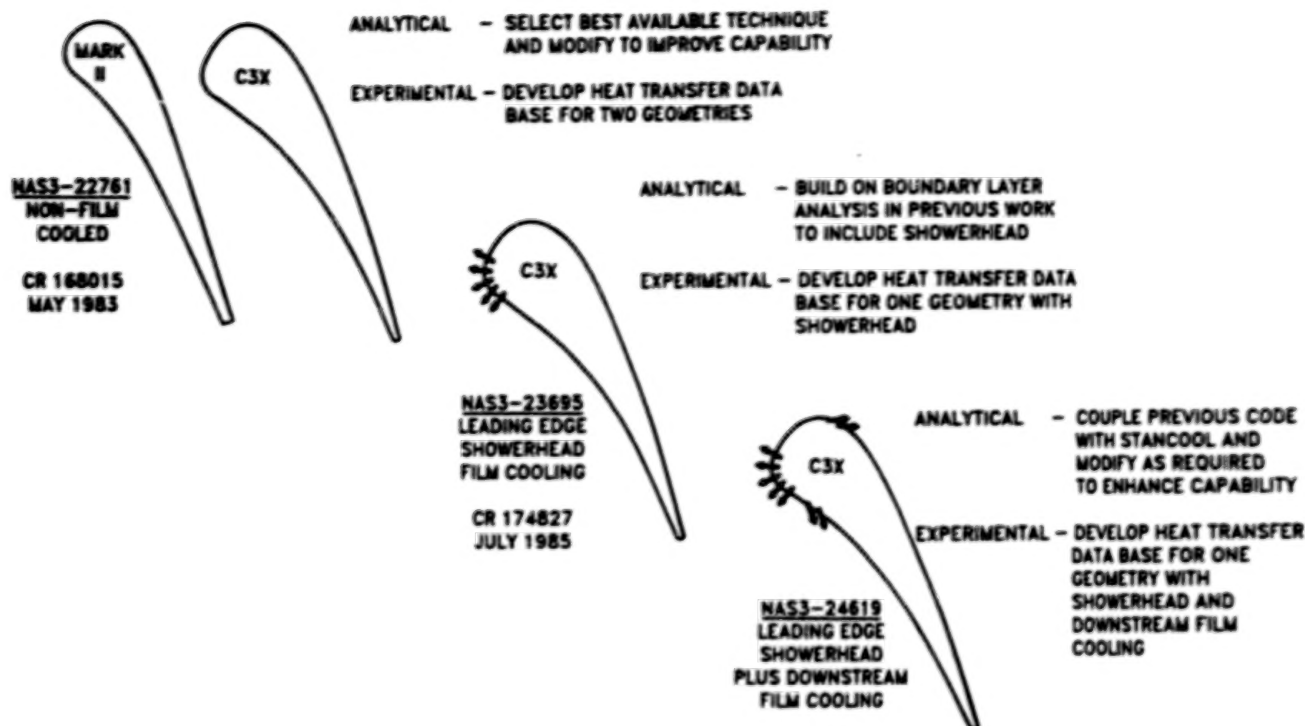


Figure 1. Overall approach

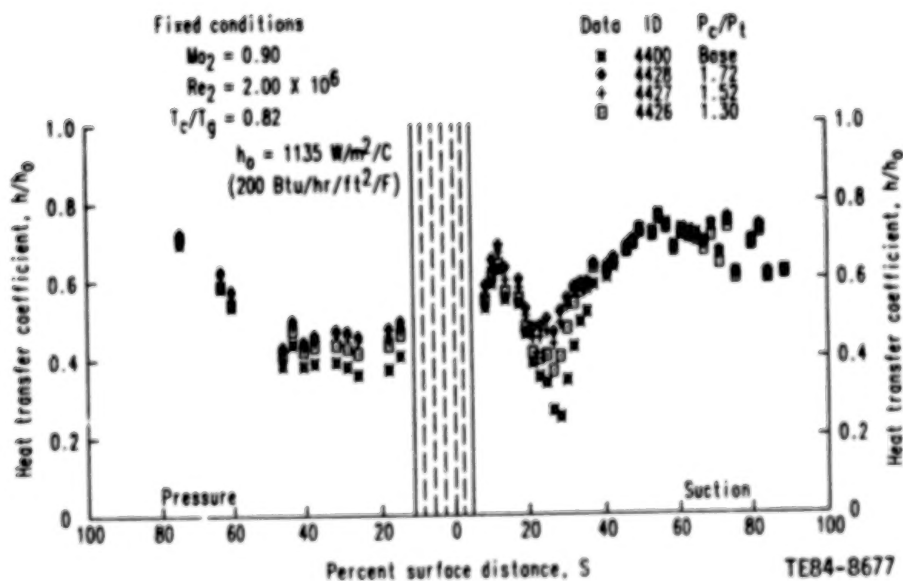


Figure 2. Measured heat transfer coefficient distribution for varying blowing strength.

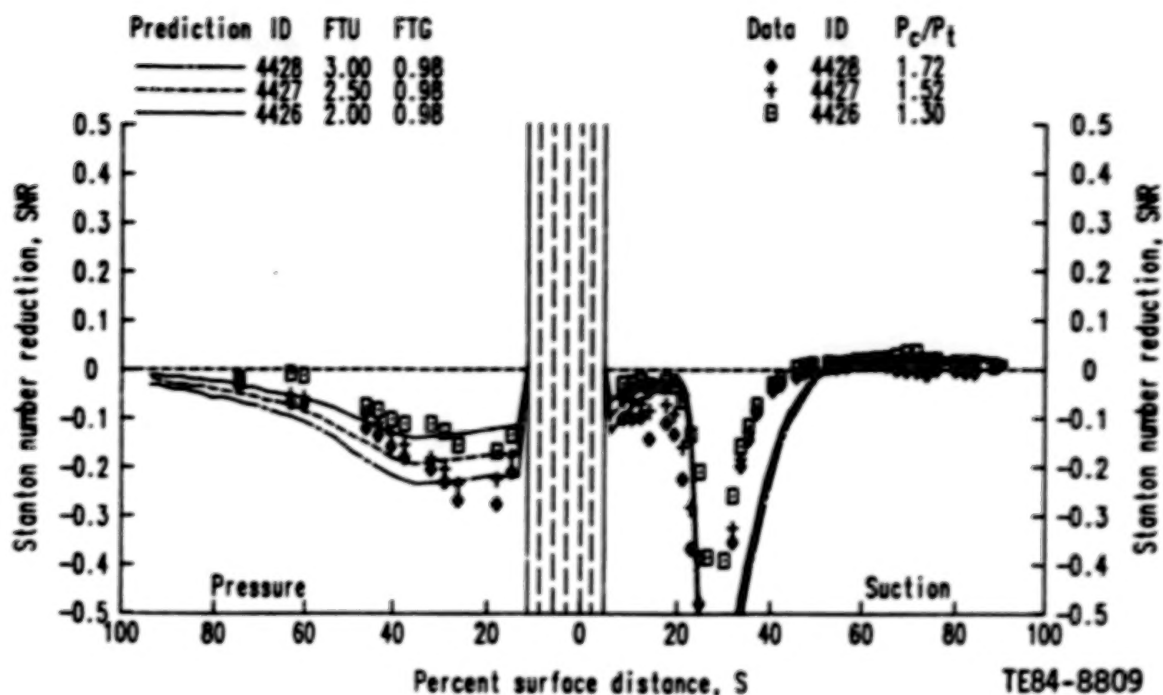


Figure 3. Measured and predicted SNR distributions for varying blowing strengths above design range.

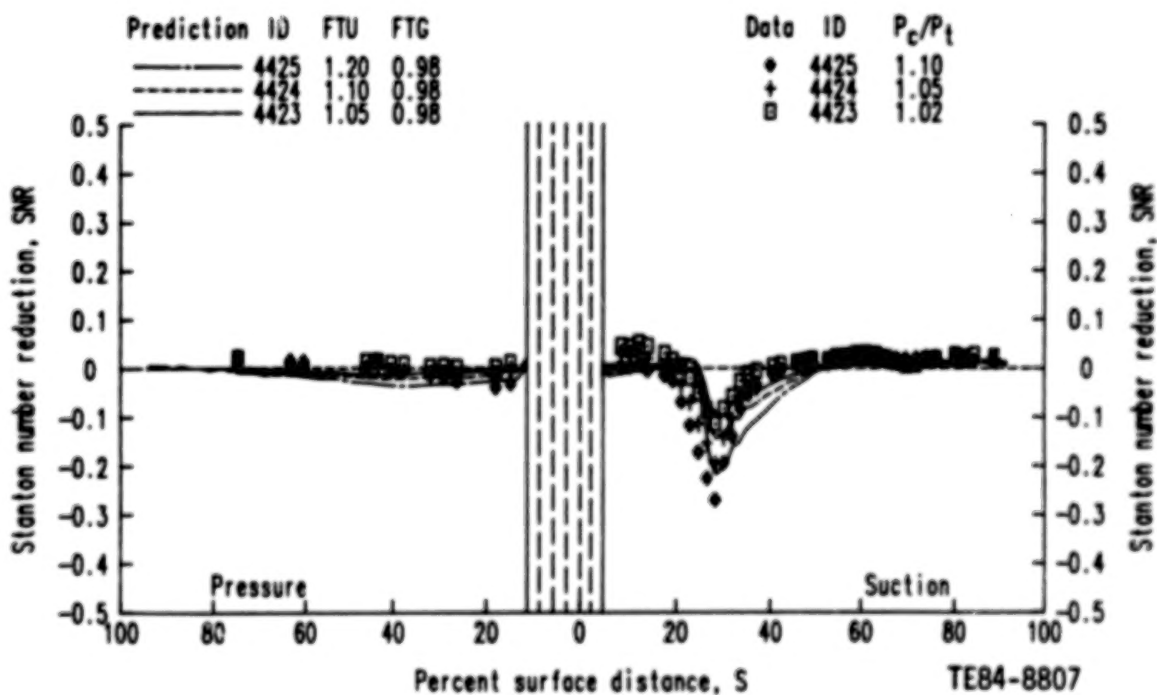


Figure 4. Measured and predicted SNR distributions for varying blowing strengths in design range.

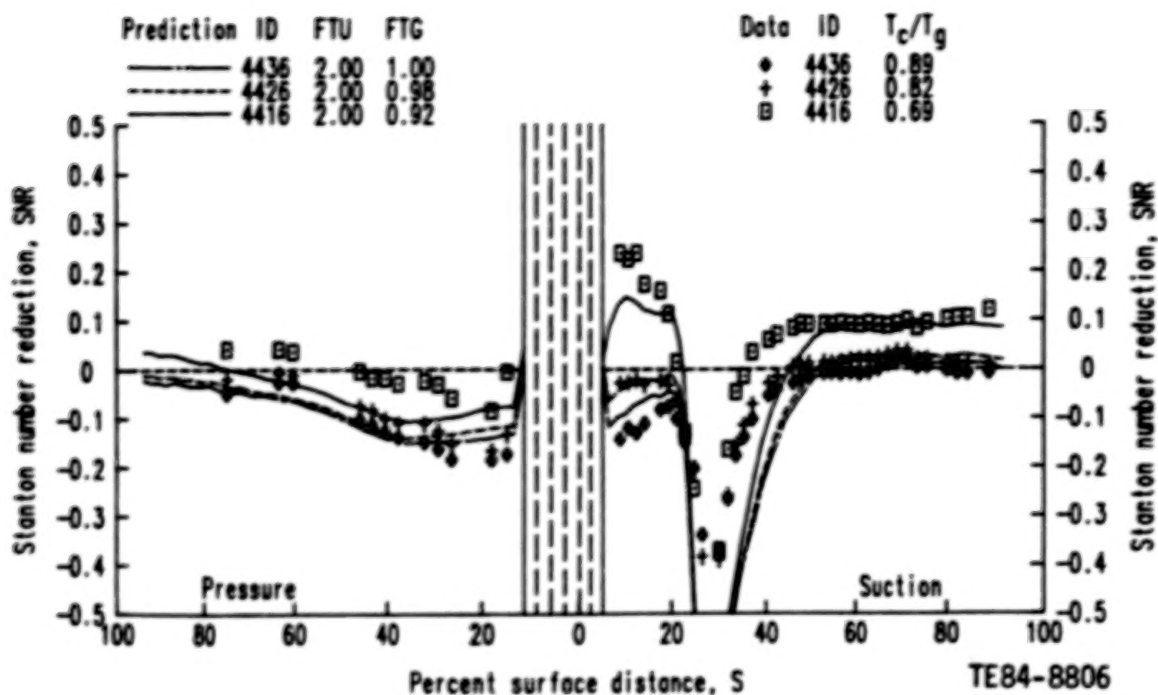


Figure 5. Measured and predicted SNR distributions for varying coolant-to-gas temperature ratio.

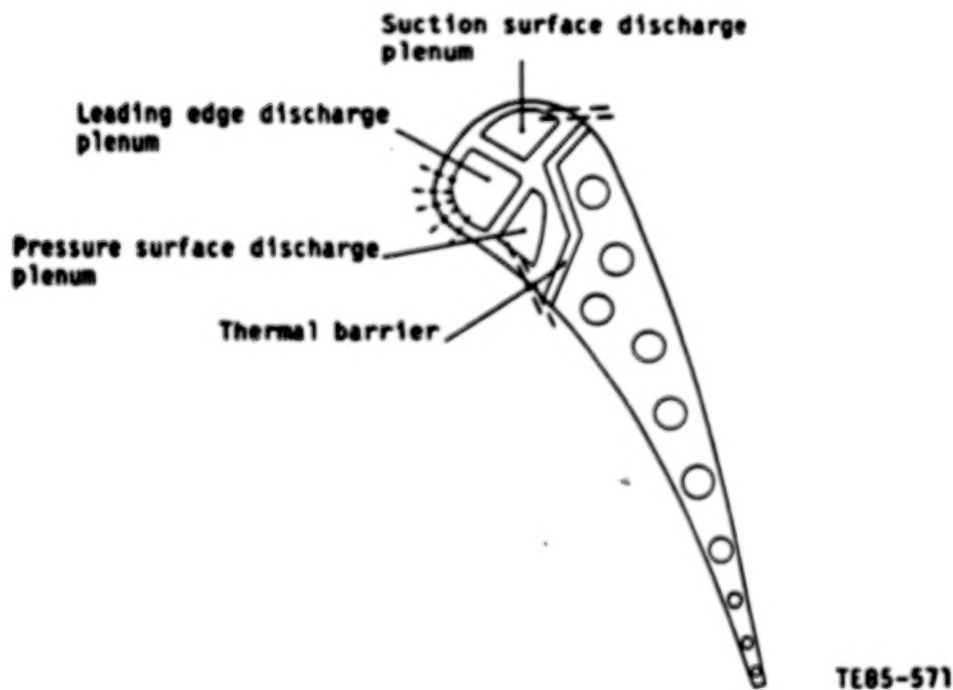


Figure 6. Schematic of airfoil with leading edge showerhead and downstream film cooling for cascade tests.

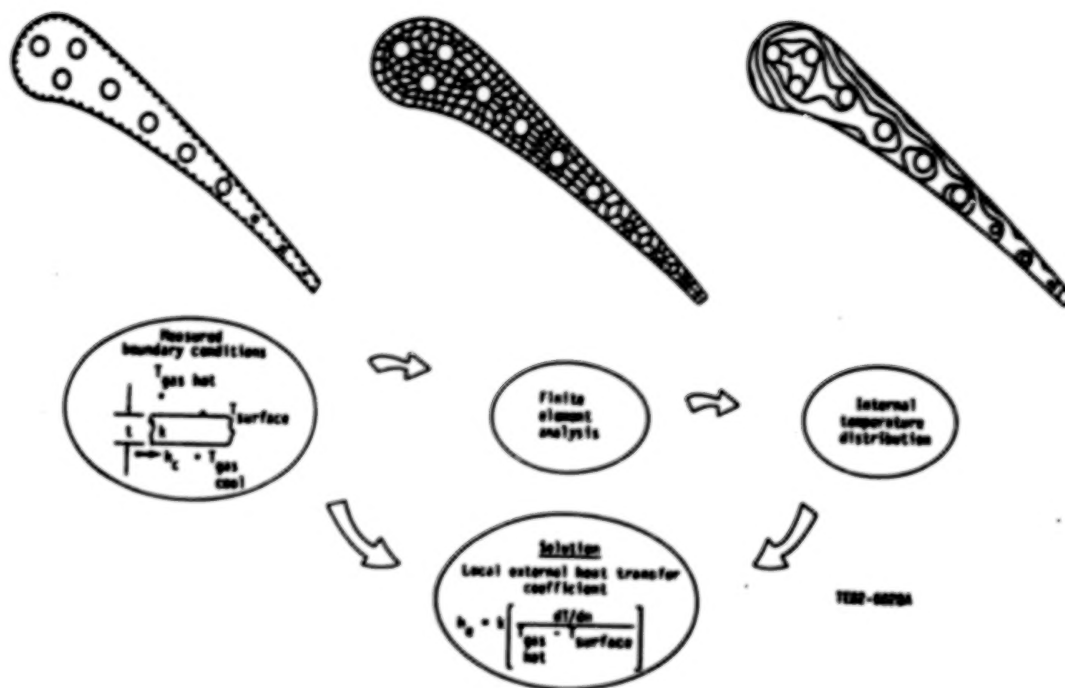


Figure 7. Heat transfer measurement technique.

## FLOW FIELD MEASUREMENTS IN A 90 DEGREE TURNING DUCT

Roger A. Crawford and Carroll E. Peters  
The University of Tennessee Space Institute  
NASA Grant NAG3-617

### INTRODUCTION

Ducted three-dimensional flows are found in many engineering applications and present a difficult challenge to computational fluid mechanics codes. The three-dimensional development of viscous shear layers has a strong influence on the complete flow field. Some of the most complex flows are found in turbine engines and rocket motor turbomachinery and associated gas ducts. These propulsion-related duct flows also contain high turbulence levels and high wall heat transfer rates. Current CFD codes do not provide satisfactory solutions for this general class of duct flows. Turbulence modeling is one of the significant short-comings, which is the result of inadequate physical understanding and inadequate experimental definition.

There are different types of turbulent flow such as boundary layers, shear flows from jets or wakes, and confined flows with high bulk turbulence. Each type must be analyzed and treated as a different flow phenomena. The turbulent boundary layer grows into the laminar or low-turbulence free-stream, and the turbulence properties have been successfully related to mean flow velocity gradients. Turbulent shear layers in jet mixing or wake flows are similar to the boundary layer flows in that the turbulent mixing zone propagates into the undisturbed free-stream. Turbulent duct flows are characterized by high turbulence in the bulk flow which interacts with solid boundaries and pressure gradients.

Combustion processes and combustor dilution flows produce a high turbulence field which passes through internal ducts and blade cascades. In this case, the wall viscous forces may increase or decrease the bulk turbulence intensity. This is a turbulent flow field for which the classic turbulence models are inadequate. Since the curved duct flow downstream of the turbine engine combustor contains high levels of turbulence, an improved understanding of this flow field is required to predict turbine cascade secondary flow development. Accurate predictions of secondary flows and turbulent intensity are required before heat transfer analysis techniques can be improved.

### OBJECTIVES AND APPROACH

The objective of this investigation is the experimental evaluation of the influence of inlet turbulence intensity on secondary flow development in a turning duct. The existing 25.1 cm square turning duct (90°) facility, developed under contract NAS-323278, Gas Flow Environment

Nonrotating 3-D Program, is being utilized to investigate the influence of bulk turbulence levels on secondary flow development. The large scale duct flow facility allows detailed mean velocity and turbulence quantities to be measured at several streamwise planes in the curved duct. Non-intrusive laser velocimetry is being used to measure the mean and fluctuating components of velocity in all three orthogonal directions. To assure that turbulence measurements are unbiased by particle lag and other effects, comparison hot wire data will be taken to validate the L/V system calibration.

The bulk turbulence is introduced into the turning duct entrance region downstream of the inlet bell by a square bar grid (fig. 1). Maximum expected turbulence intensity behind this grid has been shown to be about 10% with a nearly uniform turbulence field (ref 1.). Additional entrance length will be added to the facility to provide sufficient mixing length down stream of the grid to provide a uniform turbulence field with a boundary layer thickness of 15% tunnel half width.

One level of turbulence intensity will be demonstrated and used in the velocity surveys of the turning duct flow field. Secondary flow development and the turbulent characteristics of the near wall flow are the primary experimental objectives. The laminar- core-flow velocity survey results from the previous contract will establish the baseline flow for assessing the effects of the increased level of turbulence intensity (ref. 2.). The turbulence and mean flow velocity results must be of sufficient quality to serve as benchmark data for CFD code development.

## CURRENT STATUS AND RESULTS

The UTSI 3D LV system has been modified to improve upon the capability to reduce and analyze data in a shorter time period. This improved capability has been demonstrated and will allow increased data sample size for higher confidence in the turbulence measurements.

Additional entrance duct sections have been fabricated to provide an additional four duct widths of entrance length for a total of eight duct widths. Total pressure boundary layer surveys have confirmed a turbulent boundary layer thickness of 15-20 percent of tunnel half width at the entrance of the 90° turn. A tunnel bulk velocity of 10 m/s has been selected for the experimental conditions.

Two square-bar turbulence generator grids have been fabricated and tested for flow quality and turbulence intensity. Flow area blockages of 35 and 12 percent were evaluated for turbulence intensity generation. Hot wire data showed core levels of turbulence, two duct widths downstream of the grid, of 6 and 8 percent respectively for the two grids.

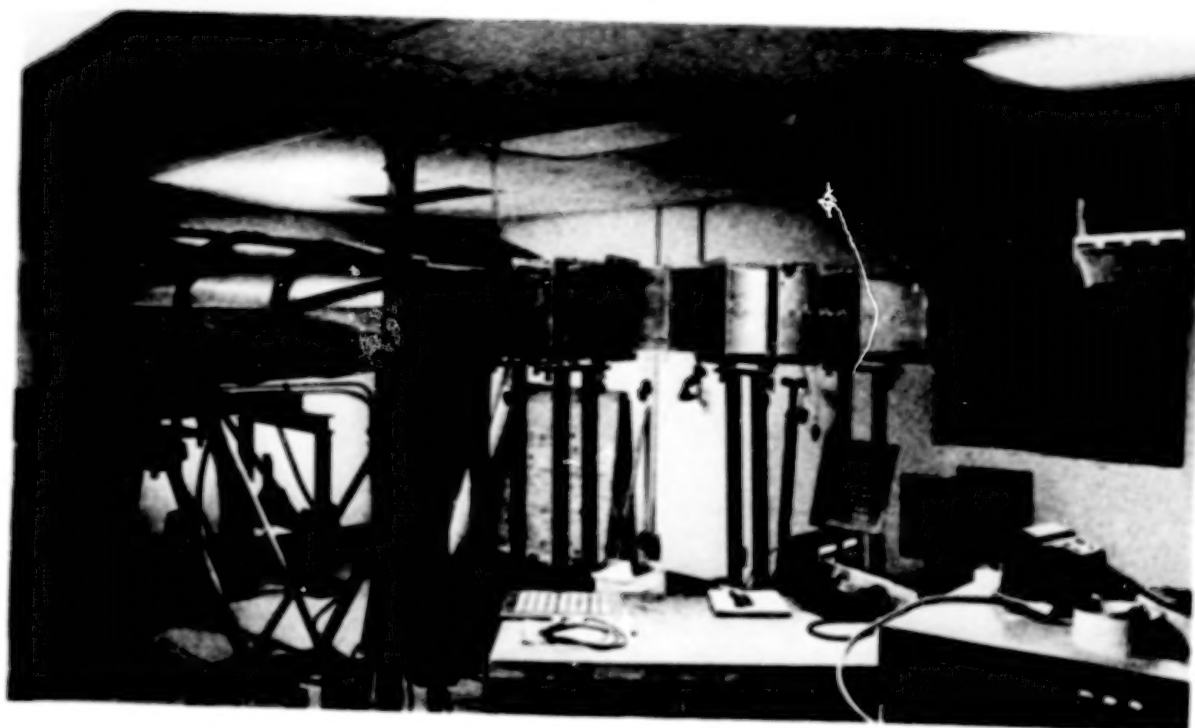
## PLANS

The detailed velocity surveys with the LV system are in progress, and six duct stations will be evaluated (entrance, 0°, 30°, 60°, 90° and exit). At each station, the flow field will be measured with and without the turbulence grid for one Reynolds number corresponding to bulk velocity of 10 m/s. These two data sets, along with the thin-turbulent-boundary-layer results from the previous investigation, will allow evaluation of the effects of both inlet boundary layer thickness

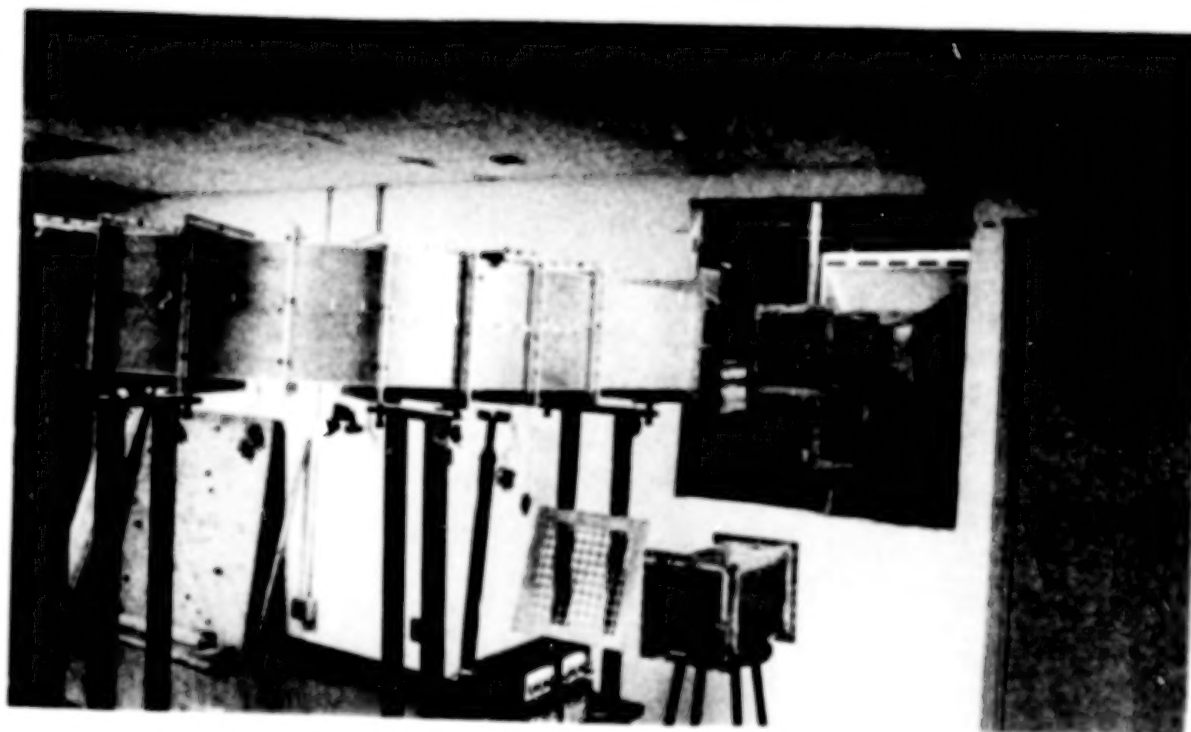
and bulk turbulence intensity. The resulting data bases will be documented in a form for use in CFD code development and validation.

#### REFERENCES

1. Cenedese, A.; Iannetta, S.; Mele, P. And Morganti, M.: Turbulence Management by means of grids. Archives of Mechanics, vol. 32, 1980, pp. 633-643.
2. Crawford, R.; Peters, C.; Steinhoff, J.; Nourinejad, J.; and Ramachandran, K.: Mean Velocity and Turbulence Measurements in a 90° Curved Duct with Thin Inlet Boundary Layer. NASA CR 174811, Sept. 1985.



a. General Facility Configuration



b. Turbulence Grid Installation

Figure 1. Curved Duct Flow Facility

MEASUREMENT OF AIRFOIL HEAT TRANSFER  
COEFFICIENTS ON A TURBINE STAGE\*

Robert P. Dring  
Michael F. Blair  
H. David Joslyn

United Technologies Research Center  
East Hartford, Connecticut 06108

## INTRODUCTION

The primary basis for heat transfer analysis of turbine airfoils is experimental data obtained in linear cascades. These data have been very valuable in identifying the major heat transfer and fluid flow features of a turbine airfoil. The question of major interest is how well all of these data translate to the rotating turbine stage. It is known from the work of Lokay and Trushin (Ref. 1) that average heat transfer coefficients on the rotor may be as much as 40 percent above the values measured on the same blades non-rotating. Recent work by Dunn and Holt (Ref. 2) supports the conclusion of Ref. 1. What is lacking is a set of data from a rotating system which is of sufficient detail as to make careful local comparisons between static cascade and rotor blade heat transfer. In addition, data is needed in a rotating system in which there is sufficient documentation of the flow field to support the computer analyses being developed today. Other important questions include the impact of both random and periodic unsteadiness on both the rotor and stator airfoil heat transfer. The random unsteadiness arises from stage inlet turbulence and wake generated turbulence and the periodic unsteadiness arises from blade passing effects. A final question is the influence, if any, of the first stator row and first stator inlet turbulence on the heat transfer of the second stator row after the flow has been passed through the rotor.

## OBJECTIVES

The first program objective is to obtain a detailed set of heat transfer coefficients along the midspan of a stator and a rotor in a rotating turbine stage (Fig. 1). These data are to be such that the rotor data can be compared directly with data taken in a static cascade. The data are to be compared to some standard analysis of blade boundary layer heat transfer which is in use today. In addition to providing this all-important comparison between rotating and stationary data, this experiment should provide important insight to the more elaborate full three-dimensional programs being proposed for future research. A second program objective is to obtain a detailed set of heat transfer coefficients along the midspan of a stator located in the wake of an upstream turbine stage. Particular focus here is on the relative circumferential location of the first and second stators. Both program objectives will be carried out at two levels of inlet turbulence. The low level will be on the order of 1 percent while the high level will be on the order of 10 percent which is more typical of combustor exit turbulence intensity. The final program

\*Work done under NASA Contract NAS3-23717.

objective is to improve the analytical capability to predict the experimental data.

## PROGRESS

During the past year the following phases of the program were completed: (1) A turbulence generating grid was designed and installed in the turbine inlet which produced the target nominal value of 10% free-stream turbulence. (2) Aerodynamic documentation of the rotor and stator midspan surface pressure distributions was obtained. (3) Midspan heat transfer data were obtained on the rotor and stator for variations in inlet turbulence, rotor-stator axial spacing, and rotor incidence. Each of these three areas will now be discussed in greater detail.

### 1. Inlet Turbulence

As part of the present contract the effects of high levels of free-stream turbulence on the heat transfer distributions through the LSRR turbine blading will be examined. These heat transfer data will be obtained for a turbine inlet turbulence intensity of approximately 10 percent. This is typical of the level of turbulence measured at the exit of aircraft gas turbine combustors. For purposes of airfoil to airfoil consistency (circumferential uniformity) and so that the present results can be compared with other data on the effects of turbulence on heat transfer, the turbulence generated for these tests is required to be spatially uniform, nearly isotropic, and temporally steady (over time scales long when compared to the turbulent fluctuations). In addition the test turbulence must be generated in a manner such that there is a reasonably high intensity through the 1 1/2 stages of the turbine, i.e., the streamwise decay of the turbulence must be similar to that in an engine.

The turbulence generator selected consisted of a nearly square array lattice of three concentric rings spaced uniformly in the radial direction with 80 radial bars evenly spaced circumferentially. Both the rings and radial bars are of nearly square 1/2 inch cross-section. The mesh spacing of the bar is 2.1 inches radially and 4.5 degrees (2.1 in. at mid-annulus) circumferentially.

Preliminary indications are that without the grid installed the inlet turbulence was approximately 0.5% at an axial location 22% of axial chord ahead of the first stator leading edge. With the grid installed, at this same axial location, the inlet turbulence intensity was typically 9.8%. The spanwise distributions at four different circumferential locations (relative to the stator leading edge) are shown in Fig. 2. The data indicate that the turbulence is spatially uniform, nearly isotropic, and temporally steady.

### 2. Aerodynamics

The aerodynamic documentation of the turbine stage indicated that all parameters were very close to data obtained during prior testing with this turbine model. As an example, the stator and rotor pressure distributions are shown in Figs. 3a and 3b for the case with the small (15%) axial gap, design flow coefficient ( $C_x/U_m=0.78$ ), and the inlet turbulence gener-

ating grid installed. Agreement with a potential two dimensional flow calculation at this midspan location is excellent. The computed surface velocity distributions are used as the input to the suction and pressure surface boundary layer calculations.

### 3. Heat Transfer

The method of fabrication of the heat transfer models was described in detail in the 1984 HOST review. Suffice it to say here that Joulean heating of a thin sheet of metal foil on the stator and rotor surfaces produces a nearly uniform surface heat flux. Conduction and radiation effects produce small departures from complete uniformity. Local airfoil surface temperatures are measured using thermocouples welded to the back of the foil and the air temperature is measured using thermocouples in the air stream. The secondary junctions to copper wire are all made on Uniform Temperature Reference blocks (Kaye Instruments, UTR-48N) and the data were recorded using a Hewlett-Packard 300 channel data acquisition unit (3497A/3498A), and an ice point reference (Kaye Instruments, K140-4). A 212 ring slip-ring unit (Wenden Co.) was used to bring heater power onto the rotor and to bring out the thermocouple data.

A low speed unheated test run indicated a max-to-min variation in absolute temperature for all thermocouples in all airfoils (rotor and stator, suction and pressure surfaces) of  $\pm 0.3^{\circ}\text{F}$ . As part of the procedure of taking the model data the temperature of the flow just upstream of the grid location was monitored at eight equally spaced circumferential locations. For these initial test cases it was decided that data would be recorded only if the outside ambient (rig inlet) conditions were such that the inlet temperature was below  $65^{\circ}\text{F}$  and that the temperature range of the eight inlet thermocouples was within approximately  $\pm 1^{\circ}\text{F}$ . These criteria were intended to assure that there would be both an adequate temperature difference between the heated surfaces and the freestream and a uniform temperature approach flow for the stator and rotor models. Preliminary examination of these data indicates that there was excellent run-to-run and day-to-day repeatability of results for nominally identical test conditions.

A sample set of rotor heat transfer distributions is presented in Figure 4. These data were all obtained with an axial rotor-stator separation of 15% chord. Data are presented for cases both with and without the turbulence grid installed for three flow coefficients ( $C_x/U_{\infty}$ ). Although the rotor inlet relative velocity ( $W_1$ ) differed widely for these three flow coefficients ( $W_1=91.4, 115.0$  and  $163.3$  ft/sec for  $C_x/U_{\infty}=0.68, 0.78$  and  $0.96$  respectively) the rotor exit relative velocity was invariant at  $W_2=176$  ft/sec. For ease of comparison the Stanton numbers of Figure 4 were computed using the nearly constant rotor exit conditions. Computation of predicted heat transfer distributions for these test cases was not completed at the time of submittal of this interim report so the data are simply connected with straight line segments.

The three sets of data in the lower portion of Figure 4 (open symbols) were obtained without the turbulence generating grid installed. A comparison of the relative levels of Stanton numbers for these three cases indicates that: (1) the heat transfer rates near the trailing edge of both the suction and pressure surfaces are independent of flow coefficient and (2) the peak stagnation region ( $S=0$ ) heat transfer obeyed the classic cylinder leading edge correlation with  $St$  inversely proportional to the square root of the Reynolds number based on nose diameter and approach relative velocity. The most distinct difference between the three low turbulence heat transfer distributions resulted near  $S \sim 1$  inch. As  $C_x/U_\infty$  increased, a region of very high local Stanton number resulted at this location. The basic cause of this spike in heat transfer is the suction surface overspeed ( $S \sim 3/4$  in.), the strength of which is a function of the flow coefficient. At  $C_x/U_\infty = 0.68$  there is only a slight overspeed followed by a favorable pressure gradient to midchord while for  $C_x/U_\infty = 0.96$  the suction surface overspeed location has by far the highest velocity on the airfoil and is followed by a very strong adverse pressure gradient. For  $C_x/U_\infty = 0.96$  the boundary layer is apparently unable to negotiate the adverse pressure gradient, separates, passes through a very short transition and reattaches as a high-speed, fully-turbulent layer. For  $C_x/U_\infty = 0.68$  the boundary layer seems to experience an extended transition length through the favorable pressure gradient to near midchord. A much subdued version of this same phenomenon can be seen on the pressure surface where the most severe overspeed ( $S \sim -1/2$  inch) occurs for  $C_x/U_\infty = 0.68$ .

A general increase in the levels of heat transfer was observed for the three cases with enhanced free-stream turbulence (solid symbols). Two of the most extreme local effects were: (1) near the suction surface overspeed where the freestream turbulence has severely increased the heat transfer and (2) at  $S \sim -2$  inches for  $C_x/U_\infty = 0.96$  where the free-stream turbulence produced a much shorter transition length.

Off-midspan data (not shown here) over the aft portion of the suction surface indicate much higher Stanton numbers near the root and tip. These enhanced heat transfer levels were almost certainly a product of the passage and tip-leakage vortex systems. It is anticipated that the flow convergence associated with these same corner vortices will cause the measured mid-span trailing edge Stanton numbers to fall well below values predicted for 2-d flow.

#### REFERENCES

1. Lokay, V. I., and Trushin, V. A.: Heat Transfer from the Gas and Flow-Passage Elements of a Rotating Gas Turbine. Heat Transfer - Soviet Research, Vol. 2., No. 4, July 1970.
2. Dunn, M.G., and Holt, J.L.: The Turbine Stage Heat Flux Measurements. Paper No. 82-1289, AIAA/ASME 18th Joint Propulsion Conference, 21-23, June, 1982, Cleveland, Ohio.

# **TURBINE STAGE AT 15% AXIAL GAP**

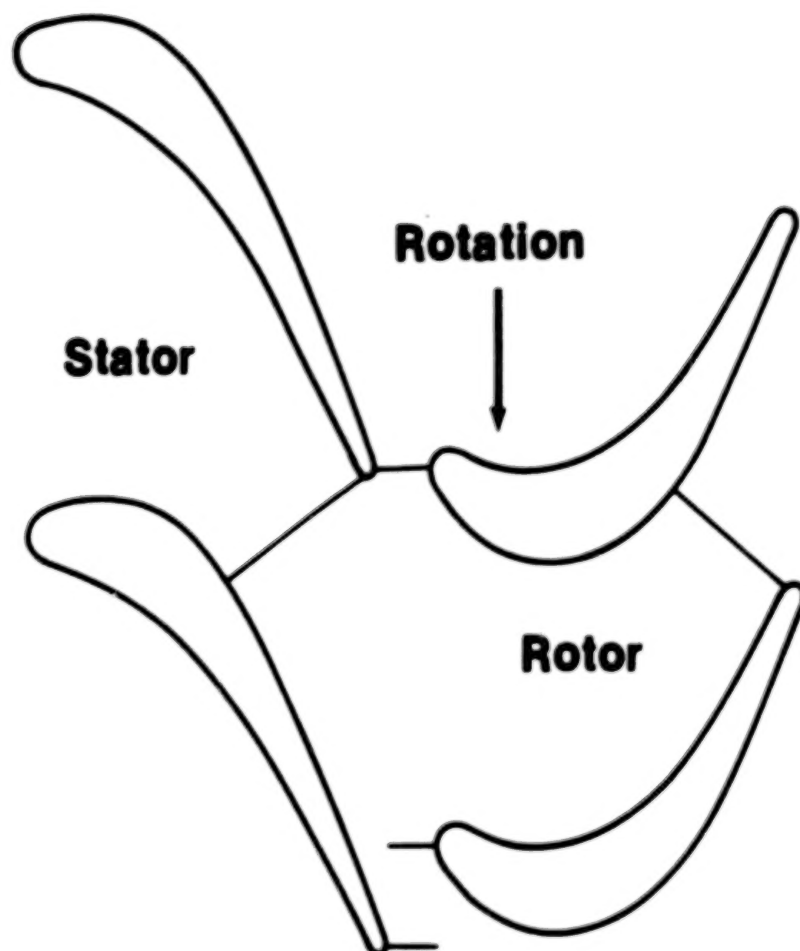


FIG. 1

## STREAMWISE TURBULENCE (RMS)

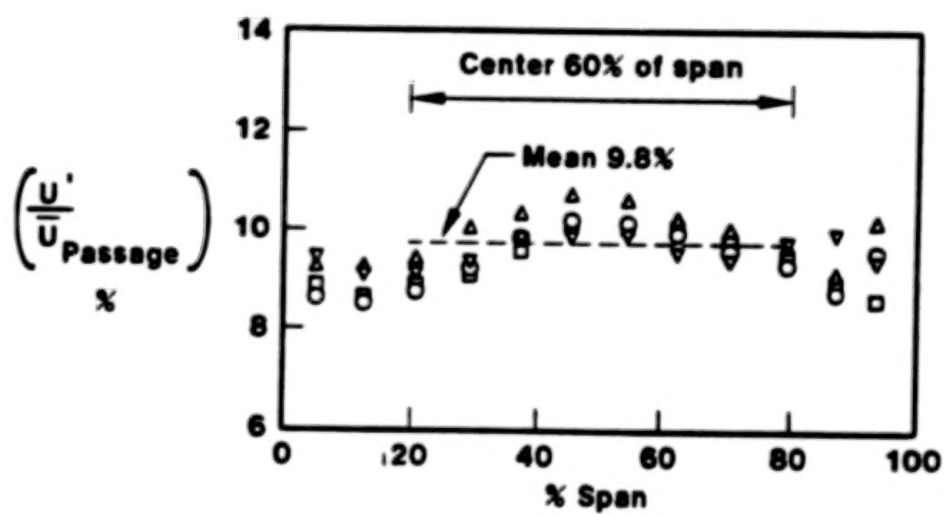


Figure 2

ORIGINAL PAGE IS  
OF POOR QUALITY

## FIRST STATOR PRESSURE DISTRIBUTION

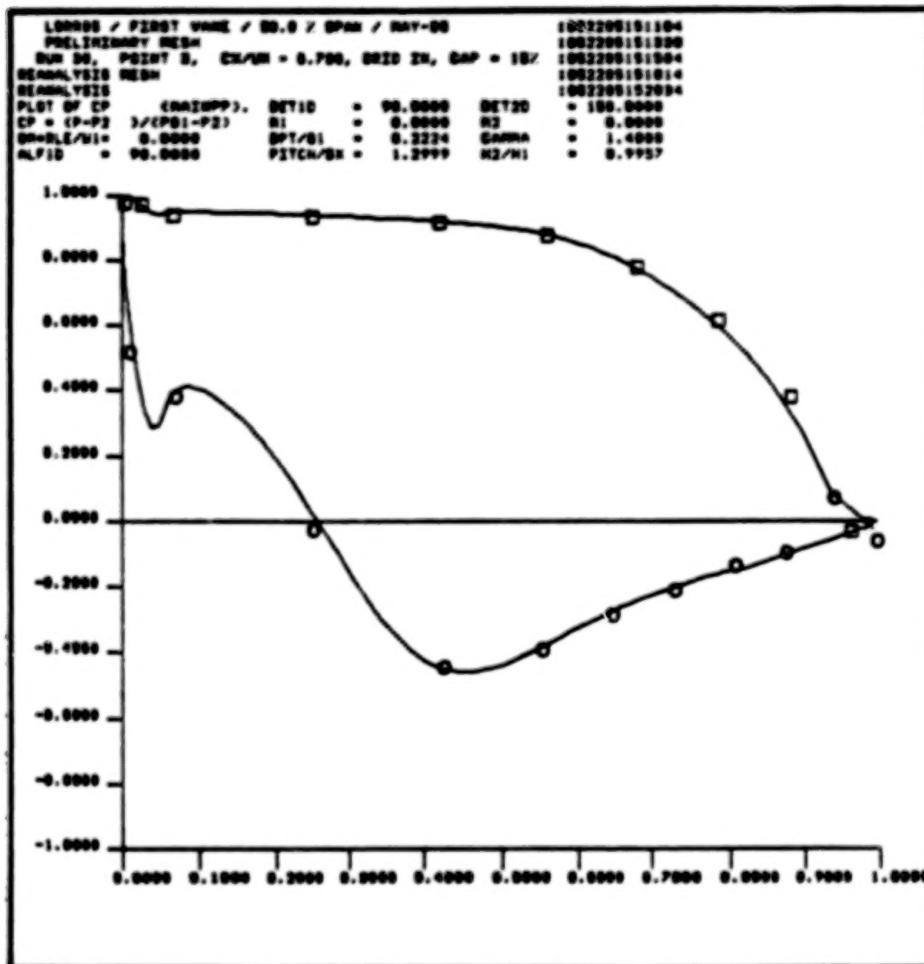


Figure 3a

ORIGINAL PAGE IS  
OF POOR QUALITY

## ROTOR PRESSURE DISTRIBUTION

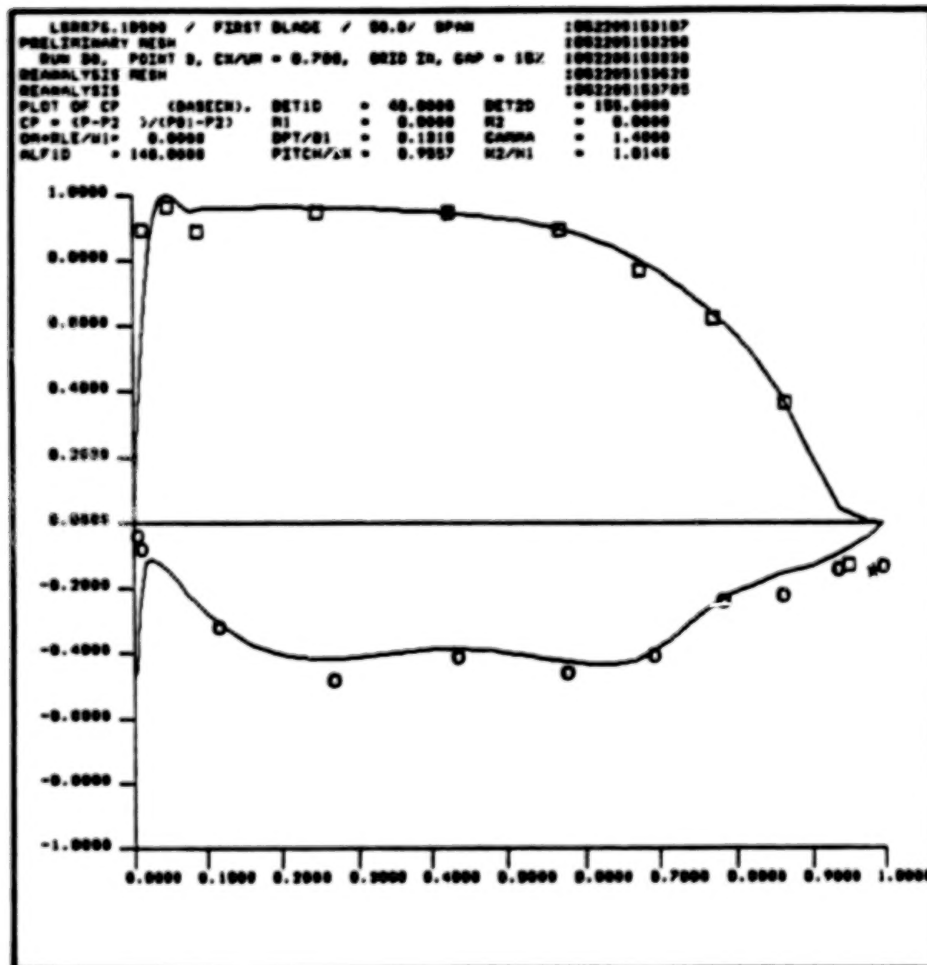


Figure 3b

# ROTOR HEAT TRANSFER DISTRIBUTIONS

Close rotor-stator spacing

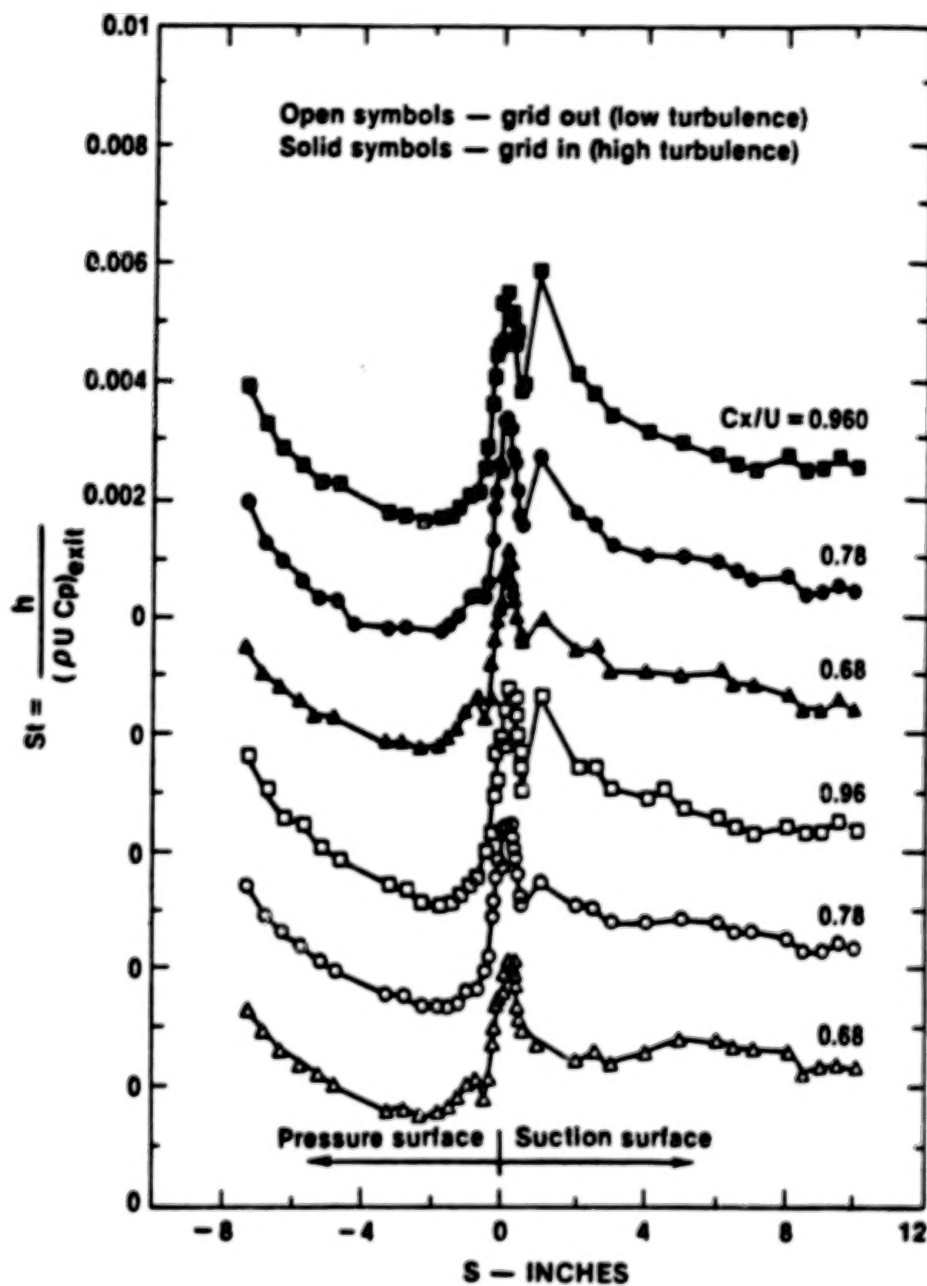


Figure 4

## HEAT TRANSFER IN THE TIP REGION OF A ROTOR BLADE SIMULATOR\*

Metzger, D.E., Chyu, M.K., and Moon, H.K.

Mechanical and Aerospace Engineering Department  
Arizona State University

## INTRODUCTION

In gas turbine engines, the tips of axial turbine blades rotate in close proximity to a stationary peripheral outer ring or shroud. Differential thermal expansion of the rotating turbine wheel and blades and the stationary outer ring causes variations in the size of the clearance gap at the blade tip. For an aircraft engine, significant variations in clearance occur at different operating conditions such as takeoff, cruise, etc. [1]; and, even with active clearance control, the gap can never be eliminated entirely.

Pressure differences between the pressure and suction sides of a blade drives a flow through the clearance gap. This flow is generally detrimental to engine performance for two primary reasons. First, the leak reduces the turbine stage efficiency, and for this reason engine designers are continually concerned with reducing the clearance gap as much as possible.

A second detrimental effect of the clearance gap flow involves the convective heat transfer between the gap flow and the blade tip. The surface area at the blade tip in contact with the hot working gas represents an individual thermal loading on the blade which, together with heat transfer to the suction and pressure side surface area, must be removed by the blade internal cooling flows. Such cooling flows impose a thermodynamic penalty on engine performance, and in this general sense the blade tip heat transfer acts to degrade engine performance.

In addition, heat transfer rates at the blade tips have been observed to be very high; and there are difficulties and uncertainties involved with cooling of the tip region. The result is that turbine blade tips have traditionally been a region very vulnerable to structural damage. This damage can have a severe effect on engine performance. Loss of material from the blade tip increases the clearance gap, increases the flow and heat transfer across the tip, and in general exacerbates the problems with resulting additional structural damage to the tip, etc. Blade tip heat transfer is therefore quite important to the issue of engine durability.

The apparent flow complexities near the tip region, the region's relatively small size, and difficulties encountered in isolating it for measurement, have in the past hindered development of a thorough understanding of convection within the leakage gap. The objective of the

\*Work done under NASA Grant NAG3-623.

current study is to acquire, through experimental and numerical modeling, an improved understanding of the nature of flow and heat transfer in the blade tip region.

#### BACKGROUND

Figures 1 and 2 depict qualitatively the gas path flowfields in the vicinity of the blade tip and clearance gap on the pressure and suction sides of the blade, respectively [2]. Clearance gaps in modern axial turbines are typically less than one percent of the blade height.

Near the pressure side of the gap, the flow is sink-like and mainstream gas is turned into the small gap. Strong secondary flows can be expected to be present in the gas path as a whole, and this can have the effect of bringing the hottest portion of the mainstream pressure side flow to the vicinity of the clearance gap, especially at the downstream portions of the blade. As the flow emerges from the suction side of the gap, it rolls into a vortex [3] as it meets the oncoming wall flow (Figure 2).

As mentioned in the preceding section, very little information exists regarding the flow and heat transfer within the clearance gaps themselves. Several studies, eg. [4], have addressed the leakage problem in terms of flow alone, in the absence of heat transfer, stimulated largely by its importance in axial compressor performance. A more recent study [5,6], used open channel flows in a water table (with flow leaking under fences or airfoil shapes) to simulate clearance gap leakage in turbine stages; but the heat transfer aspects of the problem were not addressed.

Limited heat transfer information has recently been obtained with short duration testing [7,8] which indicates that heat transfer rates as high as those present at the airfoil leading edge exist in the clearance gap. These measurements are limited in scope and as yet provide little in the way of understanding of the basic heat transfer mechanisms involved and of the variations in heat transfer associated with changes of parameters. In [7], however, results were obtained at several values of the ratio of tip surface temperature to gas temperature, and indicate that this ratio is not a dominant parameter for blade tip heat transfer. This is a common observation in turbulent forced convection which supports the choice of near unity ratios in the present study.

Another recent finding is that the sink-like character of the flow entering the clearance gap results in a thin entering boundary layer [9]. Thus pressure side boundary layer fluid is only a small percentage of the total leakage flow; and, in effect, the blade tip is exposed to the full mainstream gas temperature, as indicated schematically in Fig. 3. Also the leakage flow, viewed in a coordinate system fixed to the blade, appears identical to a conventional duct entrance flow, but with one moving wall. The present experimental approach takes this point of view.

Another recent finding exploited in the present approach is that the results of both [5] and [9] indicate that leakage through the gap

is basically an inviscid, pressure-driven flow whose magnitude can be calculated from knowledge of the airfoil loading distribution alone. Normal clearance gap heights are, in effect, small enough that the flows through the gap are uncoupled from the details of the flowfields on either side, and to render it essentially two-dimensional. Fig. 4 shows typical resulting trajectories of the leakage flow across the clearance gap.

Almost all of the very limited published work dealing with clearance gap flows involves consideration only of plain flat blade tips. Various tip geometrical treatments (Fig. 5) are of interest for their either demonstrated or potential reduction in leakage flow and/or tip heat transfer. There is an apparent total lack of information on heat transfer associated with these various tip treatments. Fig. 5(e), the grooved tip, appears to be the most common treatment in actual use, and is the focus of the present program.

Flow over the grooved tip can be categorized as flow over a rectangular cavity; and both flow and convection heat transfer in this basic geometry have been the subjects of extensive investigation for several decades, eg. [10-13]. In all cases the cavities studied have been installed in wind tunnel walls where the cavity is open to a usually well developed, zero pressure gradient flow over an otherwise smooth surface. The grooved tip differs from this situation by virtue of the confined nature of the geometry as well as by the proximity of the moving shroud. It is, in effect, a completely enclosed rectangular volume both supplied and relieved from narrow short slots at the top side corners. The degree of similarity between the heat transfer characteristics of the grooved tip and those of previous cavity studies is unclear at present.

The present project will model both the confined and moving wall aspects of the grooved blade tip. Meanwhile a preliminary study has been conducted to investigate the effect on heat transfer of confined narrow slot openings to cavities, in the absence of an adjacent moving wall [14]. There is some justification for anticipating that such stationary results may be representative of the blade tip problem as well. For example in [9], for the case of a flat ungrooved blade tip, it was found the relative motion of the shroud has a negligible effect on the blade tip heat transfer for clearance gaps with sizes usually encountered in practice.

Fig. 6 shows typical results from [14] for a confined stationary cavity in terms of local Nusselt numbers at locations on both the rib tops (1 and 2 upstream, 11 and 12 downstream) and on the cavity floor (3 through 10). This particular case is for a shallow cavity with depth to streamwise width ratio,  $D/W$ , of 0.1 for several values of clearance to width ratio. The solid symbols are values measured with the cavity present. For comparison, measured values on a corresponding flat surface ( $D=0$ ) are also shown as open symbols.

The distribution of heat transfer shown in Fig. 6 is typical. Very high heat transfer rates are present on the top surface of the upstream rib, and these have the same general magnitude and character as those measured without the cavity. Nusselt numbers drop by a factor

of from 3 to 5 on the adjacent cavity floor, and then tend to rise from front to rear on the floor. These cavity floor values are found to be in quite good agreement with previous unconfined cavity results [12] for these shallow cavities; but as the relative cavity depth is increased the confined cavity exhibits higher floor heat transfer rates than does the corresponding unconfined cavity.

Heat transfer on the top of the downstream rib is back up to its level on the top of the upstream rib. In this case, however, the highest value of  $Nu$  is on the upstream end, rather than on the downstream end as is the case for the top of the upstream rib. This behavior supports the notion that the source of the downstream gap flow is largely fluid moving downstream adjacent to the shroud, partially impinging on and flowing down the downstream rib toward the cavity floor. Thus there would be little or no separation at the downstream gap entrance as is the case in the upstream gap.

In summary, the preliminary study without relative shroud motion does indicate that the presence of a transverse cavity lowers heat transfer rates in a narrow gap entrance flow; but the effects of the adjacent moving shroud have not yet been determined. These effects will be investigated with the apparatus (now nearing completion) and planned computations described in the next section.

#### RESEARCH PLAN

In order to achieve the desired resolution of local transfer coefficients and to avoid experimental uncertainties inherent in the direct measurement of local heat transfer, the experiment for the moving-shroud situation utilizes the analogy between heat and mass transfer [15], and local mass transfer coefficients are inferred from sublimation rates on naphthalene surfaces [16]. The thermal counterpart of a naphthalene mass transfer surface is the convective heat transfer from a wall with uniform wall temperature. One of the most important advantages of using such a mass transfer system is the capability of obtaining this well-defined boundary condition which is practically difficult to establish via direct thermal methods.

Figs. 7 and 8 display schematic views of the recently completed test section. The shaded area in these figures, representing a cavity-like grooved tip, is the mass transfer-active surface cast with a thin layer of naphthalene, approximately 1.5 mm in thickness. The naphthalene sublimates as it is exposed to air flow. To ease fabrication and measurement, the test cavity is comprised of three separate aluminum flat plates, each representing the upstream wall, the cavity floor and the downstream wall, respectively. Naphthalene is cast on designated areas of these plates before the cavity is assembled. The cavity aspect ratio can be varied by either adjusting the mounting screws or changing the complete set of aluminum plates.

The moving-shroud is modeled by a flat, seamless, Neoprene belt (Belting Industry, #BIC 500) driven by a speed-adjustable, 3/4 HP, D.C. motor (Dayton Inc.). In conjunction with the motor speed controller, additional pulleys and speed-conversion sheaves are installed to provide various belt speeds as desired. The cavity can be rotated in



different orientation relative to the belt moving direction. During a test run, as shown in Fig. 8, the laboratory compressed air supply is first introduced to a plenum adjacent to the test cavity, then flows over the cavity, and subsequently discharges to the surrounding atmosphere. The entire test assembly including plenum and cavity is situated above and contacts the moving belt, with the cavity opening facing downward. Between the test assembly and the moving belt, there are several teflon pads mounted on the contacting surface of the test assembly to reduce dynamic friction and to prevent air leakage. An additional teflon plate is placed underneath and against the belt which effectively eliminates belt vibration as it moves over the test section. Preliminary tests at full anticipated belt speeds indicate that this design is very satisfactory.

To determine the local mass transfer rates, naphthalene surface profiles are measured both before and after a test run, and point by point subtraction of the two profiles gives the sublimed depth of naphthalene which is used in calculating the local mass transfer coefficient. Prior studies [17,18] indicate that the surface profile measurement procedure is tedious and time consuming; it may take more than an hour to measure approximately two hundred data points, and even longer for data reduction. Meanwhile, human error and the long measurement time may lead to significant inaccuracies. To eliminate these errors, increase precision, and reduce the time required for data acquisition, an automated, microcomputer controlled measurement system has been developed. The system provides vast improvement with regard to data accuracy as well as operational convenience. Fig. 9 shows a block diagram giving a schematic view of the entire arrangement of the measurement system. The system consists of a depth gauge along with a transducer amplifier, a digital multimeter, a two-axis, stepper-motor driven positioner, a stepper-motor controller, and a microcomputer.

The depth gauge used to measure the naphthalene surface profile is a linear variable differential transformer (LVDT, Schaevitz Engineering) capable of measuring depth change with a resolution of approximately  $2.5 \times 10^{-6}$  mm (one microinch). This resolution is two-to-three orders of magnitude smaller than the operating range of measured naphthalene sublimation. The gauge head, featuring a very light load, provides virtually traction-free operation. The LVDT is connected to an electronically compatible transducer amplifier (Schaevitz Engineering, ATA101) which supplies excitation and converts the AC signal output of the gauge to a DC voltage which can be calibrated to provide a signal of 1 volt per  $2.5 \times 10^{-3}$  mm (0.001 inch). The output of the amplifier is measured with a digital voltmeter (Fluke 8840A,  $5\frac{1}{2}$  digits) and recorded on the floppy disk of the microcomputer for further data reduction.

The two-axis positioner, produced by LinTech Inc., is used to locate the different measurement locations on a test surface. Each axis of the positioner is driven by a stepper-motor (Superior Electric, MO-63), and has the same 457.2 mm (18 inch) travel range. With the motor controller (Allen Bradley, Fastrak 4000) connected, the stepper-motor

rotates 200 steps per revolution and, combined with the pitch of lead screw, is capable of transforming each step into a linear increment of one thousands of an inch in each axis.

To ensure that the system has proper operation throughout the measurement process and to optimize the rate of data acquisition, a microcomputer (Zenith 150, IBM-PC compatible) along with a program written in BASIC language (Microsoft, GWBASIC) and IEEE-488 (National Instrument, GPIB) interfacing commands serves as a controller to the movements of stepper-motors as well as the flow of data. The bounds of measurement domain and distance of each step increment can be specified in the computer program. The computer then controls the number of steps of a stepper-motor to change location on the test surface by these specified increments during measurements. Through the IEEE-488 interface, as previously mentioned, the computer also provides space for data storage and executes data reduction procedure.

Successful execution of a local measurement in subliming mass transfer is critically dependent on precise positioning and accurate thickness change readings. Moreover, the successful measurement in which many important parameters are present and must be studied in detail requires rapid data acquisition. The computer-controlled, automated measurement system developed for the present study fulfills all of these requirements. Area-averaged results can also be obtained from the local data via numerical integration if desired. At present, the hardware has been successfully installed and tested, and the software development is nearly complete.

Although the present study primarily emphasizes an experimental approach, a numerical computation simulating the experimental study is also planned. A finite-difference program, frameworked by the SIMPLER algorithm [19], is employed for solving the prime variables, the velocity components and pressure of the Navier-Stokes equations. For turbulence modeling, a two-equation,  $k-\epsilon$  model with modifications for low-Reynolds-numbers will be used [20]. The entire computer program has been successfully developed, and is available in an IBM-3081 mainframe computer at Arizona State University. Simulations will be carried out with actual geometric and flow parameters from the experiments as inputs to the program.

## SUMMARY

The present study of heat transfer in the tip region of a rotor blade simulator is now in its initial stages. The objective is to acquire, through both experimental and computational approaches, improved understanding of the nature of the flow and convection heat transfer in the blade tip region. Such information should enable designers to make more accurate predictions of performance and durability, and should support the future development of improved blade tip cooling schemes.

## REFERENCES

1. Hennecke, D.K., "Heat Transfer Problems in Aero-Engines," Heat and Mass Transfer in Rotating Machinery, Hemisphere, Washington D.C., 1984, pp. 353-379.
2. Metzger, D.E. and Mayle, R.E., "Heat Transfer - Gas Turbine Engines," Mechanical Engineering, Vol. 105, No. 6, 1983, pp.44-52.
3. Allen, H.W., and Kofskey, M.G., "Visualization Study of Secondary Flows in Turbine Rotor Tip Regions," NACA TN 3519, 1955.
4. Lakshminarayana, B., "Methods for Predicting the Tip Clearance Effects in Axial Flow Turbomachinery," Journal of Basic Engineering, Trans. ASME, Vol. 92, 1970, pp. 467-482.
5. Booth, T.C., Dodge, P.R., and Hepworth, H.K., "Rotor-Tip Leakage: Part I - Basic Methodology," Journal of Engr. for Power, Trans. ASME, Vol. 104, 1982, pp.154-161.
6. Wadia, A.R. and Booth, T.C., "Rotor-Tip Leakage: Part II - Design Optimization Through Viscous Analysis and Experiment," Journal of Engr. for Power, Trans. ASME, Vol. 104, 1982, pp. 162-169.
7. Dunn, M.G., Rae, W.J., and Holt, J.L., "Measurement and Analysis of Heat Flux Data in a Turbine Stage: Parts I and II, ASME Papers No. 83-GT-121 and 83-GT-122, 1983.
8. Epstein, A.H., Guenette, G.R., Norton, R.J.G., and Cao Yuzhang, "Time Resolved Measurements of a Turbine Rotor Stationary Tip Casing Pressure and Heat Transfer Field," AIAA Paper No. 85-1220, 1985.
9. Mayle, R.E., and Metzger, D.E., "Heat Transfer at the Tip of and Unshrouded Turbine Blade," Proceedings of the Seventh International Heat Transfer Conference, Vol. 3, 1982, pp. 87-92.
10. Roshko, A., "Some Measurements of Flow in a Rectangular Cutout," NACA TN No. 3488, 1955.
11. Chapman, D.R., "A Theoretical Analysis of Heat Transfer in Regions of Separated Flow," NACA TN No. 3792, 1956.
12. Yamamoto, H., Seki, N. and Fukusako, S., "Forced Convection Heat Transfer on Bottom Surface of a Cavity," Journal of Heat Transfer, Trans. ASME, Vol.101, 1979, pp. 475-479.
13. Aung, W. "An Interferometric Investigation of Separated Forced Convection in Laminar Flow Past Cavities," Journal of Heat Transfer, Trans. ASME, Vol.105, 1983, pp.505-512.
14. Metzger, D.E., and Bunker, R.S., "Cavity Heat Transfer on a Transverse Grooved Wall in a Narrow Flow Channel," ASME Paper No. 85-HT-57, 1985.

15. Eckert, E.R.G., "Analogies to Heat Transfer Processes," Measurements in Heat Transfer, ed. by Eckert, E.R.G. and Goldstein, R.J., Hemisphere Publication, Washington D.C., 1976.
16. Goldstein, R.J., Chyu, M.K. and Hain, R.C., "Measurement of Local Mass Transfer on a Surface in the Region of the Base of a Protruding Cylinder with a Computer-Controlled Data Acquisition System," International Journal of Heat and Mass Transfer, Vol. 28, 1985, pp. 977-985.
17. Goldstein, R.J. and Taylor, J., "Mass Transfer in the Neighborhood of Jets Entering a Crossflow," Journal of Heat Transfer, Vol. 104, 1982, pp. 715-721.
18. Goldstein, R.J. and Karni, J., "The Effect of a Wall Boundary on Local Mass Transfer for a Cylinder in Cross-Flow," Journal of Heat Transfer, Vol. 106, 1984, pp. 260-267.
19. Partankar, S.V., Numerical Heat Transfer and Fluid Flow, Hemisphere Publication, Washington D.C., 1980.
20. Jones, W.P. and Launder, B.E., "The Prediction of Laminarization with a Two-Equation Model of Turbulence," International Journal of Heat and Mass Transfer, Vol. 15, 1972, pp. 301-313.



Fig. 1 Gap Vicinity Flow on Pressure Side

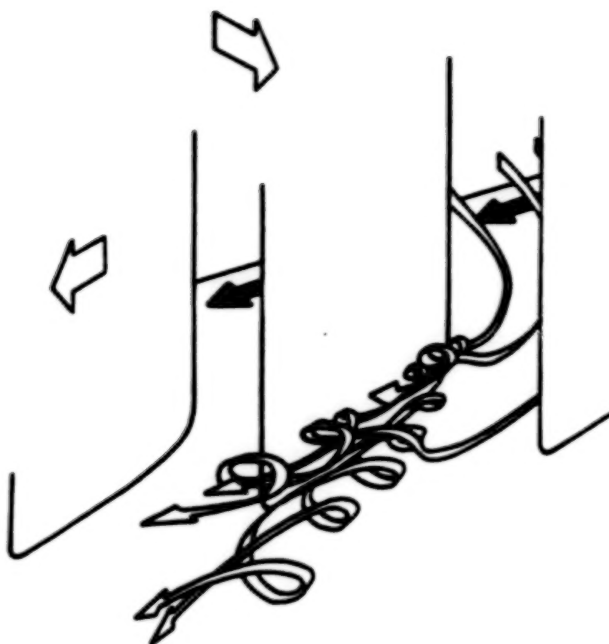


Fig. 2 Gap Vicinity Flow on Suction Side

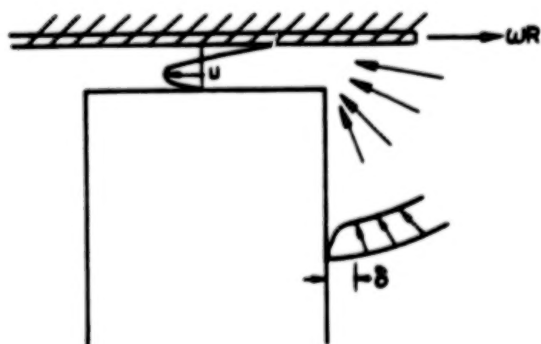


Fig. 3 Sink-like Character of Flow into the Clearance Gap

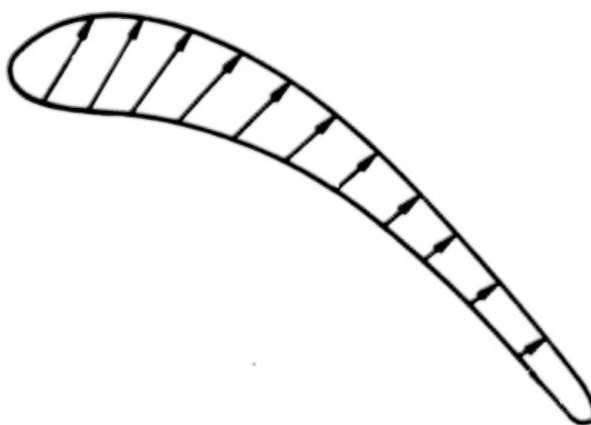


Fig. 4 Typical Clearance Gap Leak Flow Trajectories

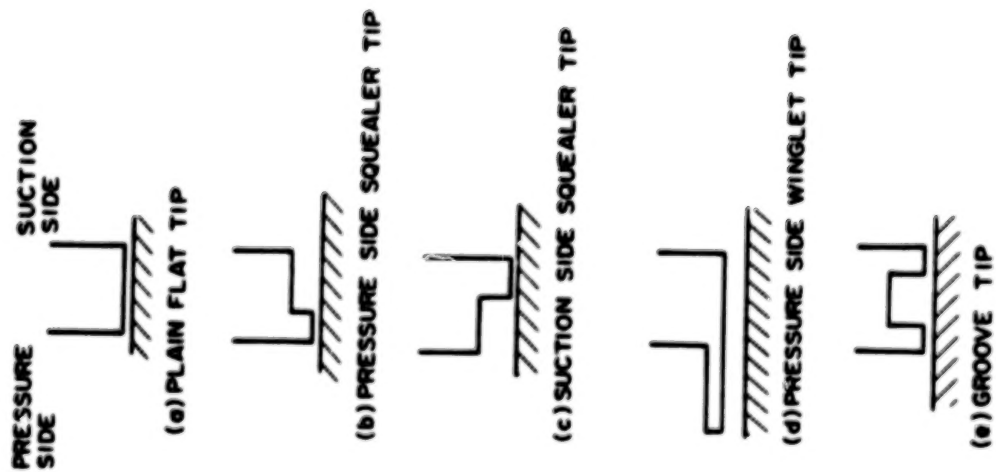


Fig. 5 Variation on Tip Geometry

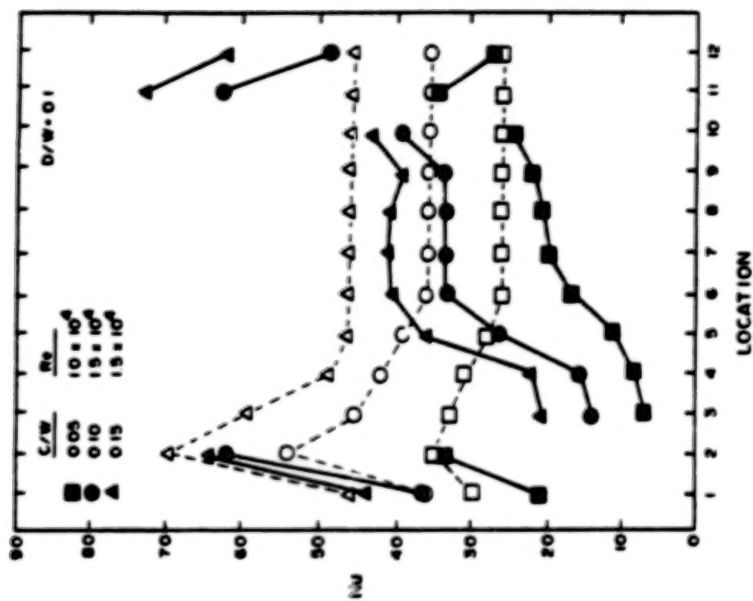


Fig. 6 Local  $Nu$  Distribution for Confined Cavities

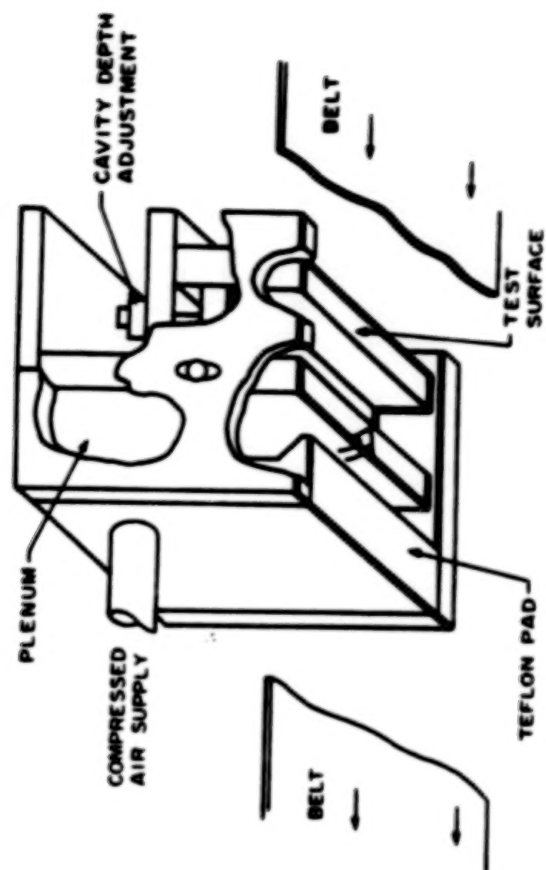


Fig. 8 Schematic View of Test Assembly

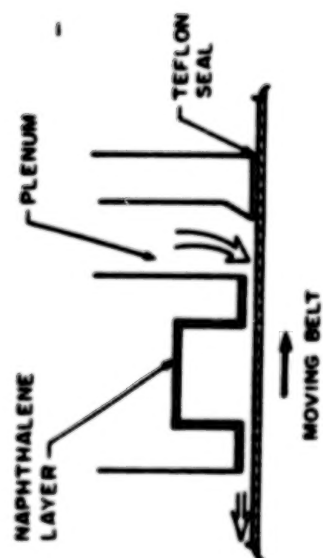


Fig. 7 Schematic View of Test Section

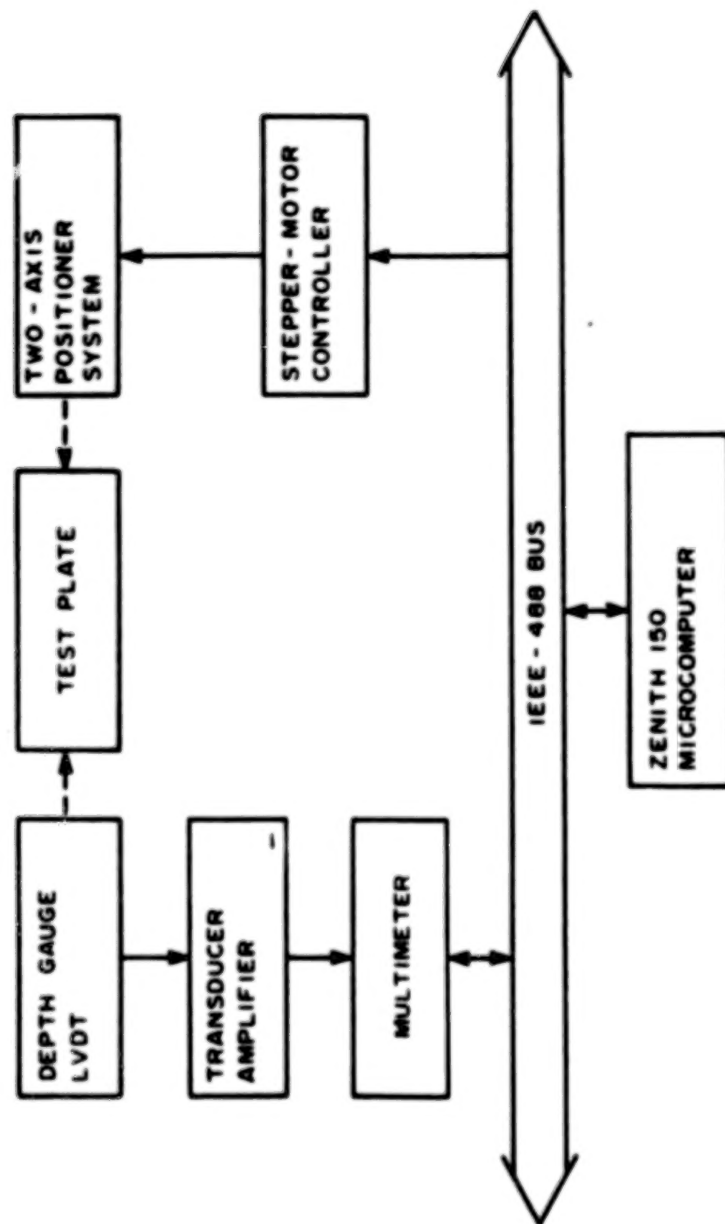


Fig. 9 Local Mass Transfer Surface Measurement System

T.J. Hajek and A.W. Higgins

United Technologies Corporation  
Pratt & Whitney

## INTRODUCTION

In current and advanced gas turbine engines, increased speeds, pressures and temperatures are used to reduce specific fuel consumption and increase thrust/weight ratios. Hence, the turbine airfoils are subjected to increased heat loads escalating the cooling requirements to satisfy life goals. The efficient use of cooling air requires that the details of local geometry and flow conditions be adequately modeled to predict local heat loads and the corresponding heat transfer coefficients.

Improved turbine airfoil local temperature and hence, life predictions can be realized by accurately accounting for the effects of rotation on internal cooling. Although the effects of rotation which give rise to Coriolis and buoyancy forces can be large, they are currently not adequately included in the heat transfer designs of blades. Experimental data is particularly needed for the higher Rayleigh and Reynolds number conditions that are characteristic of turbine airfoil cooling passages. This data is crucial for development of design correlations and computer codes as well as their verification. Accurate prediction of local heat transfer coefficients enables the designer to optimize cooling configurations to minimize both metal temperature levels and thermal gradients. Consequently, blade life and engine efficiency can be significantly improved.

## OBJECTIVE

The objective of this 36-month experimental and analytical program is to develop a heat transfer and pressure drop data base, computational fluid dynamic techniques and correlations for multi-pass rotating coolant passages with and without flow turbulators. The experimental effort is focused on the simulation of configurations and conditions expected in the blades of advanced aircraft high pressure turbines. With the use of this data base, the effects of Coriolis and buoyancy forces on the coolant side flow can be included in the design of turbine blades.

## EXPERIMENTAL MODEL

The coolant passage heat transfer model features a four-pass serpentine arrangement designed to reflect the passages within a gas turbine blade. Figure 1 shows a schematic diagram of the model with the instrumentation and wall sections indicated. Heat transfer coefficients are obtained for each wall section element. These wall elements, numbered 1 to 64, consist of a copper block backed with a thin film electrical resistance type heater and instrumented with two thermocouples. The copper wall sections are 10.7 mm x 49.3 mm (0.42 in. x 1.94 in.). Each section is thermally isolated from the adjoining section by a 1.5 mm (0.060 in.) thick divider strip of low thermal conductivity G-11 composite material. The straight radial passages have a square cross section, 12.7 mm x 12.7 mm (0.5 in. x 0.5 in.).

## DATA REDUCTION

Data acquisition/analysis consists of three general categories: equipment calibration, model heat loss measurement, and heat transfer coefficient calculations. The equipment calibration follows standard experimental procedures. Model heat loss measurements precede each test. These measurements are executed with no coolant flow and uniform wall temperature steady-state conditions; identical to the subsequent test less the coolant flow. Heat transfer coefficients are then calculated for each wall section element by applying the following procedure.

For each copper element the net energy convected to the fluid is calculated by subtracting the electrical line losses and conducted heat losses from the total energy supplied. Bulk fluid temperatures are then calculated based on an energy balance for each flowpath section as follows:

$$T_{b\text{ out}} = \frac{q_{\text{net, 4 walls}}}{mc_p} + T_{b\text{ in}}$$

where the model inlet bulk temperature is measured. Once bulk fluid temperatures are determined, heat transfer coefficients are calculated from the equation:

$$h = \frac{q_{\text{net, wall}}}{A (T_w - T_b)}$$

where  $T_b$  is the average of the inlet and exit bulk temperatures. Thus for each test case, 64 heat transfer coefficients are calculated.

Table I shows the test conditions for which data were acquired with the smooth wall model. A total of 39 tests has been conducted to isolate the effects on heat transfer of rotation rate, flow rate, coolant-to-wall temperature variations, radius length and passage angle.

## RESULTS

All of the heat transfer measurements for test conditions depicted in Table I were completed. Figures 2 and 3 show typical results for two tests conducted at the same Reynolds number but at different rotation rates. The data is plotted as the ratio of rotating to stationary heat transfer versus the streamwise position in the model. Figure 2 shows the leading and trailing walls of the passage, while Figure 3 depicts the sidewall results. As can be seen, the rotation significantly affects the heat transfer rates throughout the entire model. Augmentation factors of 300% as well as local reductions to 30% of stationary heat transfer rate values were encountered in the straight passages. Furthermore, heat transfer rates up to 5 times greater than the fully developed turbulent duct levels were seen to exist in the tip turns.

Due to the large number of data points obtained to date, comprehensive discussion of all the results is beyond the scope of this paper. Instead, the following paragraphs will focus on the first straight passage of the model. Detailed discussion of the heat transfer results along the leading and trailing surfaces of this radially outflowing leg will facilitate better understanding of the underlying physical principles.

Rotation of coolant passages introduces two forces not seen in stationary flows: Coriolis and centripetal. The Coriolis force has two major effects on internal flows. Firstly, it generates secondary flow circulations which cause the migration of low momentum sidewall fluid to the low pressure side of the channel. Secondly, it stabilizes/destabilizes the shear layer on the low/high pressure side of the passage. In the case of radially outward flow, the leading wall corresponds with the low pressure side of the passage and the trailing wall becomes the high pressure side. This trend reverses itself for radially inward flow.

#### Effect of Rotation

The high pressure side of the passage experiences a destabilization of the wall shear layers and cooler mainstream fluid will accelerate towards this wall. Increasing rotation rates will cause significant increases in heat transfer as seen in figure 4. Heat transfer rates can increase as much as 3 times the fully developed turbulent level for rotation number of  $Ro = 0.48$ .

The low pressure side of the passage is where the heated low energy fluid from the sidewalls is dumped. In addition to the fact that this already heated, relatively quiescent fluid tends to accumulate in this region, the rotation stabilizes the shear layers along this wall and further reduces the potential for heat removal. As a result, significantly lower than expected heat transfer rates were measured along the low pressure wall in a certain range of operating conditions. This result is quantified in figure 5, where the heat transfer rate is seen to drop to 40% of the fully developed level at  $Ro = 0.24$ . Heat transfer variations of this magnitude would generally affect the local blade metal temperature and thus airfoil lives.

#### Effect of Density Ratio

In general, increasing the wall temperature causes heat transfer rates to increase on both the low pressure and high pressure side of the passage for radially outward flow. Figure 6 shows the effects of  $\Delta\rho/\rho$  variations for the leading and trailing surfaces. This is believed to be a centripetal buoyancy phenomenon, whereby centripetal buoyancy forces cause the heated wall layers to oppose the mainstream flow direction. An increased turbulence level in the wall shear layer generated by these opposing forces would account for the exhibited increase in heat transfer.

#### Effect of Radius

Figure 7 isolates the effect of distance from the axis of rotation on heat transfer. For the first two element sections ( $x/D = 1.5$  and  $x/D = 4.6$ ), the heat transfer on both the leading and trailing surfaces are essentially unaffected. Moving downstream inside the passage, the heat transfer decreases on both surfaces with the smaller radius. This is most likely a result of the weakening of the centripetal buoyancy forces at the smaller radius.

#### Laminarization on the Low Pressure Surface

As mentioned previously, the large decreases in heat transfer seen on the low pressure side of the passage should be of utmost concern to turbine blade designers. The remainder of this paper will examine the cause of this deficiency. Specifically, the low pressure surface (in all three straight passages) or the leading surface in the first passage, is believed to laminarize for certain ranges of rotation rates and

density ratios. Outside of these ranges the wall shear layers become transitional and heat transfer increases.

The isolated effect of rotation number for Reynolds number of  $Re = 25,000$  is depicted in figure 5. As the rotation number increases large decreases in heat transfer occur. This minimum level attained changes in both magnitude and position with variations in the rotation number.

Figure 8 plots all the leading side data for  $\Delta T = 80^\circ F$  and  $Re = 25,000$ . The data is plotted as  $Nu_x$ ,  $x$  being the distance from the inlet, versus a rotational Raleigh number

$$Ra_x = \left( \frac{\Omega^2 R x^3 \Delta T}{\nu^2 T_b} \right) Pr$$

Note for each line of constant  $Ro$  there are three data points. Each of these correspond to one of the three test section elements downstream of the guard heaters at the inlet: elements 34, 35, and 36 in figure 1.

For the higher rotation rates,  $Ro > 0.18$ , the heat transfer, plotted as  $Nu_x$ , tends to collapse on a single curve. This curve attains a minimum around  $Nu_x = 200$  and begins a sharp upturn at  $Ra_x = 10^{11}$ . Based on the results to date, it is believed that for the lower rotation rates the data is predominantly governed by Coriolis forces while at the highest rates centripetal buoyancy dominates. There is a flow regime between these two extremes where the wall shear layer is believed to be laminar. This hypothesis is supported by the following figures.

Figure 9 plots  $Nu_x$  versus  $Ra_x$ , for high rotation,  $Ro > 0.18$ , and it includes all four temperature cases (figure 3 included only  $\Delta T = 80$ ). Two important points should be emphasized. Firstly, for  $10^{10} < Ra_x < 10^{11}$  the heat transfer is constant at  $Nu_x = 210$ . This level defines the minimum heat transfer attained for  $Re = 25,000$ . Secondly, for  $Ra_x > 10^{11}$ ,  $Nu_x$  increases significantly. This increase for large  $Ra_x$  is believed to be induced by centripetal buoyancy forces.

Consider the range of data where the heat transfer is constant at  $Nu_x = 210$  (fig. 9). If this data is compared to both the fully turbulent stationary heat transfer and to Kays (ref. 1) analytical solution for laminar flat plate heat transfer:  $Nu_x = 0.565 Pr^{1/2} Re_x^{1/2}$  (figure 10), it appears to be nearly identical to the laminar correlation, thus supporting the hypothesis that a flow regime containing laminar shear layer does exist.

These results can be further substantiated by examining the work of J. P. Johnston (ref. 2). In his rotating channel experiment at Stanford University, he discovered regions where the boundary layer on the leading wall was laminar for Reynolds numbers as high as  $Re = 15,000$ . Figure 11 schematically depicts the important characteristics of this flowfield.

On the leading side of the 7:1 aspect ratio channel, Johnston saw a nearly parabolic mean velocity profile and an absence of the bursting process normally seen at the wall in turbulent flow. On the other side of the channel, Taylor-Goertler type roll cells developed within the turbulent section of the mean velocity profile. The laminar boundary layer on the leading surface and the highly turbulent boundary

layer with bursting roll cells on the trailing surface help explain the large decreases and increases seen in heat transfer with rotation.

One of Johnston's conclusions was that the rotation induced re-laminarization was highly Reynolds number dependent. To evaluate this dependency, the present NASA data was examined at varying Reynolds numbers.

Figures 12 and 13 compare the rotating heat transfer results at  $Re = 12,500$  and  $Re = 50,000$ , respectively, to Kays correlation for laminar flow. The lower Reynolds number flow case, figure 12, matches Kays correlation at test sections 34 and 35, while the higher Reynolds number flow never reaches the laminar level; although it approaches this minimum. This data indicates that for high rotation rates the boundary layer on the leading wall is more likely to be laminar at low Reynolds number. This work compares very well with Johnston's results.

Johnston used flow visualization techniques to establish when the leading wall would laminarize. Figure 14 extends Johnston's mapping of flow regimes with rotation. The NASA data at three different Reynolds numbers is shown to complement Johnston's results. At the low Reynolds number the leading side is laminar for  $Ro = 0.24$ . At the high Reynolds number the shear layer is most likely transitional; somewhere close to but not yet laminar. At the middle Reynolds number flow,  $Re = 25,000$ , there exists extensive data to clarify where the flow becomes laminar. Remember this region existed when  $Nu_x = 210$ . This is when  $10^{10} < Ra_x < 10^{11}$ , indicating that buoyancy plays an important role in the laminarization process.

Two important results need to be highlighted:

1. The minimum level of heat transfer attained is predicted by Kays laminar flat plate correlation.
2. Centripetal buoyancy limits this laminarization process. For  $Re = 25,000$  and  $Ra_x > 10^{11}$  the leading side shear layer becomes transitional and the heat transfer increases.

#### WORK PLANNED

Currently the model is being modified to include turbulators on the leading and trailing surfaces of the straight radial passages. Two experimental programs are planned; one with turbulators aligned at an angle of  $45^\circ$  and one with turbulators normal to the axis of the passage. This testing will examine the effects of rotation on highly enhanced heat transfer coolant passages.

#### Dimensional Parameters

Reynolds number, $Re$	$\rho V d_H / \mu = V d_H / \nu = m d_H / (A \ )$
Rotation number, $Ro$	$\Omega d_H / V$
Density or Temperature ratio	$\Delta \rho / \rho \ , \ \Delta T / T$
Radius ratio	$R / d_H$
Rotational Grashof number, $Gr$	$Ro^2 Re^2 (\Delta T / T) (R / d_H)$
Nusselt number, $Nu$	$h d_H / k$

#### REFERENCES

1. W.M. Kays and M.E. Crawford, Convective Heat and Mass Transfer, Second Edition, McGraw-Hill Book Company, 1980.
2. J.P. Johnston, "The Effects of Rotation on Boundary Layer in Turbomachine Rotors", Report MD-24, Thermosciences Division, Mechanical Engineering Dept., Stanford University, May 1970.

TABLE I  
TEST CONDITIONS FOR ROTATING HEAT TRANSFER EXPERIMENTS WITH SMOOTH WALL MODEL  
Contract NAS3-23691

Test No.	$\alpha$ (deg)	Basic Dimensionless Parameters					Secondary Dimensionless Parameters		Comments
		Re	Ro	$\frac{\Delta T}{T_{IN}}$	$\frac{R}{d_H}$	$\frac{\Delta p}{P}$	$\frac{\Omega R}{V}$	Gr/Re <sup>2</sup>	
1	--	25,092	0	0.	--	0	0	0	Nonrotating
2	--	12,490	0	0.14	--	0	0	0	
3	--	49,985	0	0.14	--	0	0	0	
4	0	25,221	0.238	0.15	49	1.29	0.22	1.96	Baseline
5	0	12,591	0.227	0.15	49	1.18	0.19	0.43	Re Varied
6	0	49,627	0.253	0.15	49	1.41	0.25	8.81	
7	0	24,475	0.475	0.15	49	2.46	0.82	7.33	
8	0	24,812	0.118	0.15	49	0.64	0.05	0.46	Ro Varied
9	0	25,299	0.244	0.07	49	0.72	0.72	1.13	$\Delta T/T$ Varied
10	0	25,117	0.237	0.23	49	1.82	0.30	2.73	
101	0	25,035	0.006	0.15	49	0.04	0.00	0.00	Low Ro effects on leading wall
102	0	24,242	0.233	0.30	49	2.22	0.36	3.06	Additional point at max $\Delta T$
103	0	75,295	0.116	0.15	49	0.64	0.05	4.20	Effect of Re at Ro = 0.11
104	0	50,033	0.119	0.15	49	0.66	0.06	1.98	Effect of $\Delta T$ at Ro = 0.35
105	0	25,166	0.362	0.07	49	1.04	0.28	2.39	
106	0	24,730	0.350	0.15	49	1.84	0.45	4.22	
107	0	24,914	0.350	0.22	49	2.61	0.64	5.70	Symmetry check
108	0	25,039	0.006	0.15	49	0.04	0.0	0.00	Effect of $\Delta T$ at Ro = 0.0
109	0	24,955	0.233	0.15	49	1.23	0.20	1.79	
110	0	25,098	0.000	0.07	49	0.00	0.00	0.00	
111	0	25,098	0.000	0.23	49	0.00	0.00	0.00	Effect of $\Delta T$ at Ro = 0.18
112	0	25,082	0.000	0.31	49	0.00	0.00	0.00	
113	0	25,076	0.178	0.23	49	1.38	0.17	1.55	
114	0	24,840	0.178	0.15	49	0.97	0.12	1.06	Effect of Ro
115	0	25,131	0.183	0.08	49	0.54	0.07	0.63	
116	0	25,021	0.171	0.31	49	1.66	0.20	0.18	
117	0	25,018	0.062	0.15	49	0.34	0.01	0.13	Effect of a change; varying $\Delta T$ and Ro at Re = 25,000.
118	45	24,805	0.24	0.15	49	1.32	0.22	1.98	
119	45	24,627	0.23	0.23	49	1.77	0.29	2.52	
120	45	24,670	0.34	0.15	49	1.76	0.42	3.66	
121	45	24,605	0.32	0.12	49	2.28	0.51	4.48	
122	45	24,778	0.18	0.15	49	0.94	0.12	1.02	
123	45	24,745	0.17	0.22	49	1.26	0.15	1.30	Reversal of Rotation Direction for a change.
124	45	24,818	0.23	0.14	49	1.20	0.19	1.71	
125	45	24,907	0.22	0.22	49	1.60	0.24	2.18	
126	0	24,863	0.24	0.15	33	0.87	0.15	1.31	Radius Change
127	0	24,858	0.22	0.31	33	1.42	0.24	1.99	Effects on Centrifugal Buoyancy
128	0	24,774	0.35	0.15	33	1.19	0.31	2.57	Parameter Gr/Re <sup>2</sup>
129	0	24,886	0.33	0.33	33	2.02	0.47	4.18	

TEST SECTION ELEMENT IDENTIFICATION:  
 SIDE WALL TEST SECTION SURFACES 1-32 ARE IN PLANE  
 PERPENDICULAR TO VIEW SHOWN  
 TEST SECTION SURFACES 33-48 ARE ON " + 0" LEADING PLANE  
 TEST SECTION SURFACES (49-164) ARE ON " + 0" TRAILING PLANE  
 PRESSURE MEASUREMENT LOCATIONS 1 - 16

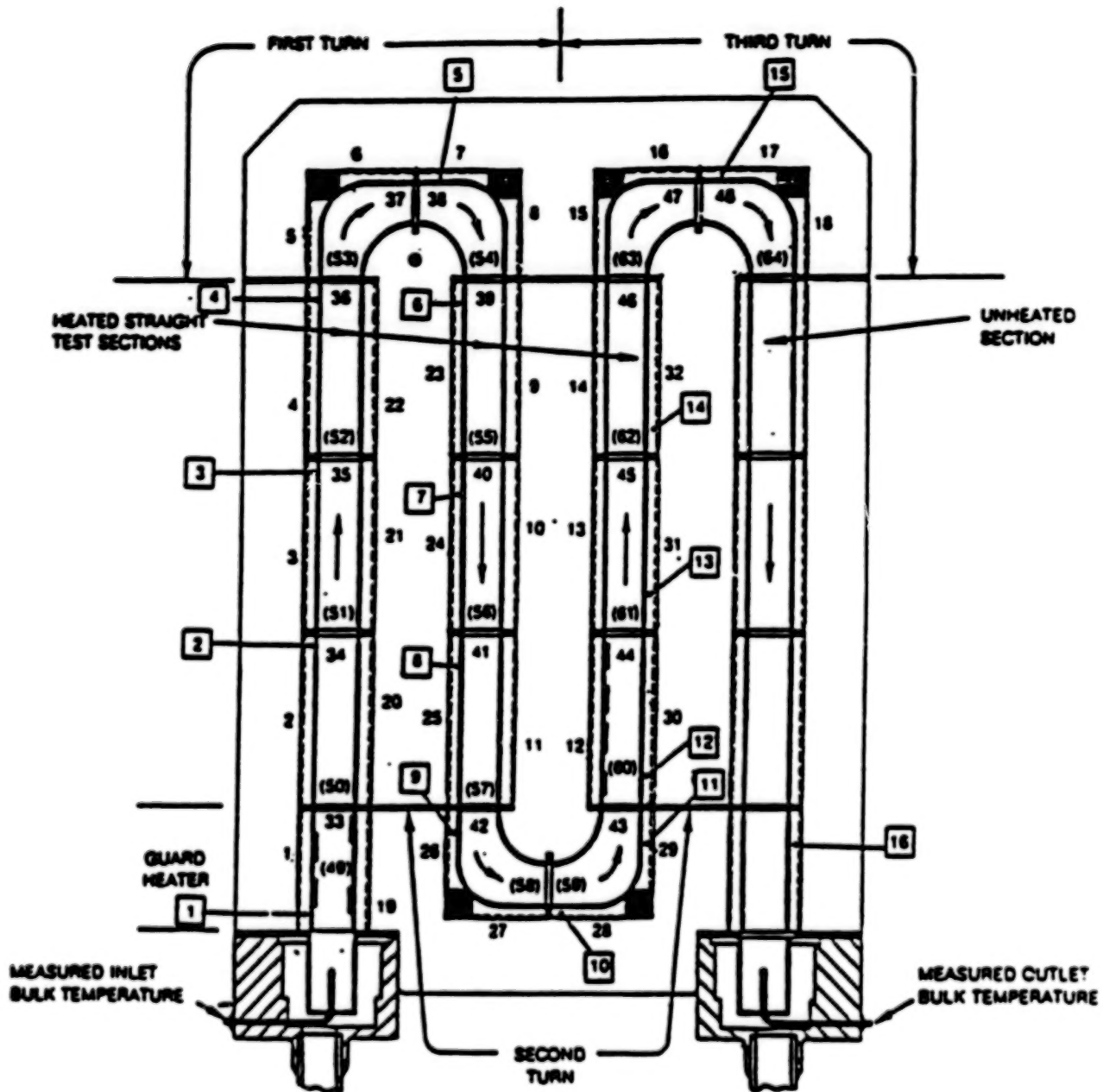


Figure 1 Instrumentation Plan for Coolant Passage Heat Transfer Model

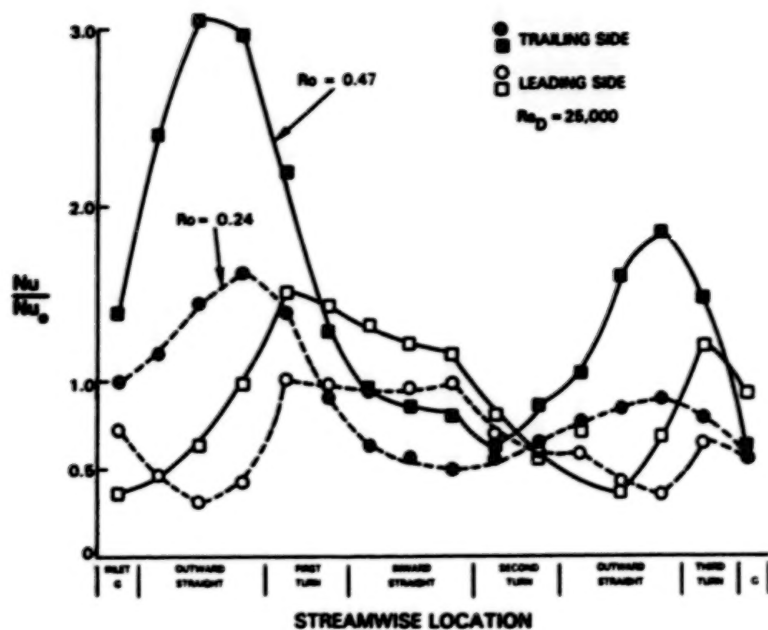


Figure 2 Leading and Trailing Surface Heat Transfer; Test Nos. 7 & 9

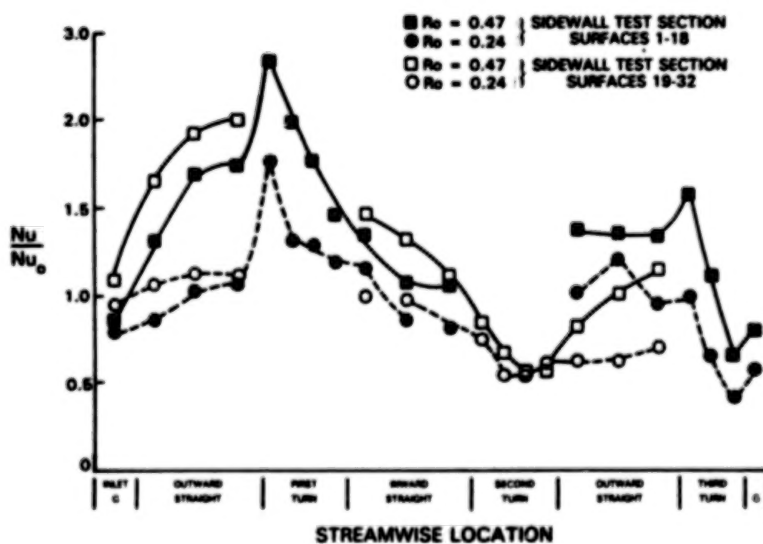


Figure 3 Sidewall Heat Transfer; Test Nos. 7 & 9

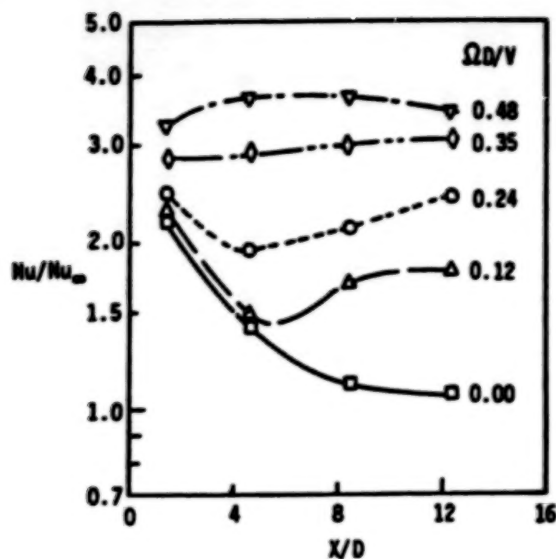


Figure 4 Effect of Rotation Number on Trailing Surface Heat Transfer  
 $Re = 25,000$ ,  $\Delta p/p = 0.11$ ,  $\bar{R}/D = 49$

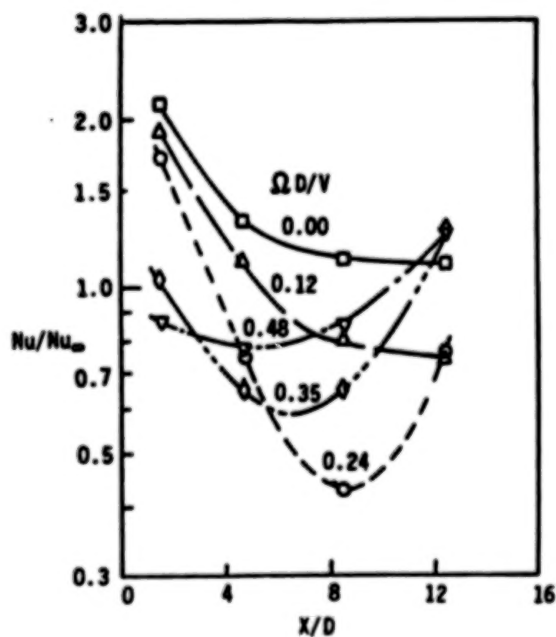


Figure 5 Effect of Rotation Number on Leading Surface Heat Transfer Ratio  
 $Re = 25,000$ ,  $\Delta p/p = 0.11$ ,  $\bar{R}/D = 49$

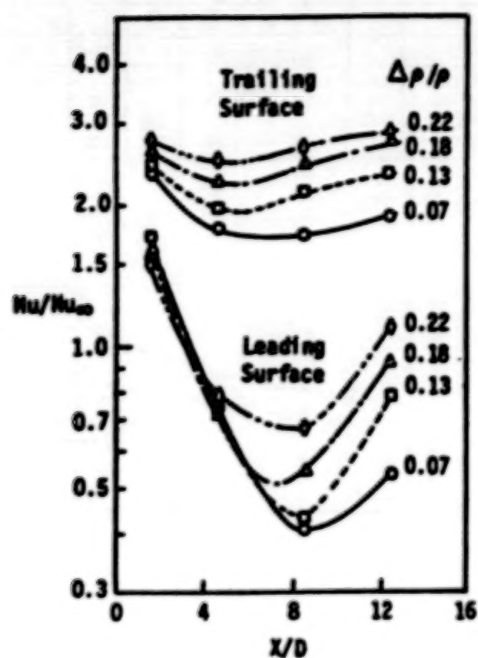


Figure 6 Effect of Wall to Bulk Density Difference  $Re = 25,000$ ,  $\Omega D/V = 0.24$ ,  $\bar{R}/D = 49$

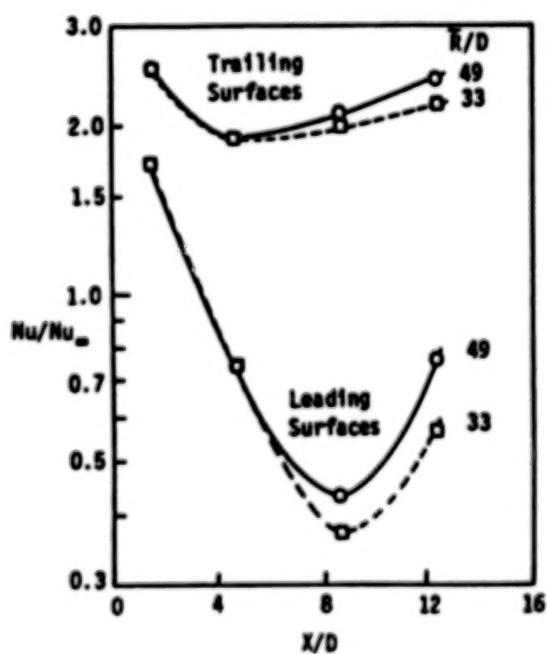


Figure 7 Effect of Model Radius on Heat Transfer Ratio Distribution;  $Re = 25,000$ ,  $\Omega D/V = 0.24$ ,  $\Delta\rho/\rho = 0.13$

LOW PRESSURE SIDE OF PASSAGE

Re ≈ 25,000

SYMBOL	○	◇	×	△	◐	◑	◒	◓	SYMBOL
ROTATION NUMBER	0.0	0.006	0.06	0.12	0.18	0.25	0.35	0.50	FLAGS
TEST NO. AT $\Delta T = 40^\circ F$	110	—	—	—	115	9	105	—	○
$\Delta T = 80^\circ F$	1	101	117	8	114	4	106	7	◐
$\Delta T = 120^\circ F$	111	—	—	—	113	10	107	—	◑
$\Delta T = 160^\circ F$	112	—	—	—	116	102	—	—	◓

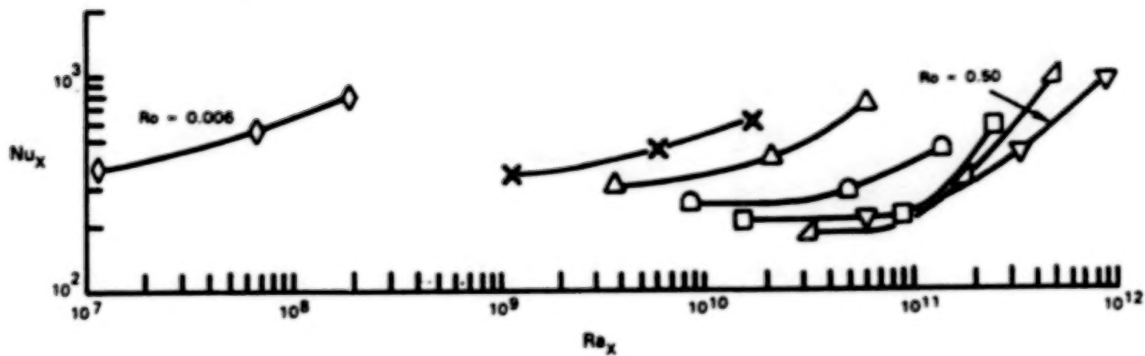


Figure 8 Leading Side Heat Transfer for 1st Passage; Radially Outward Flow

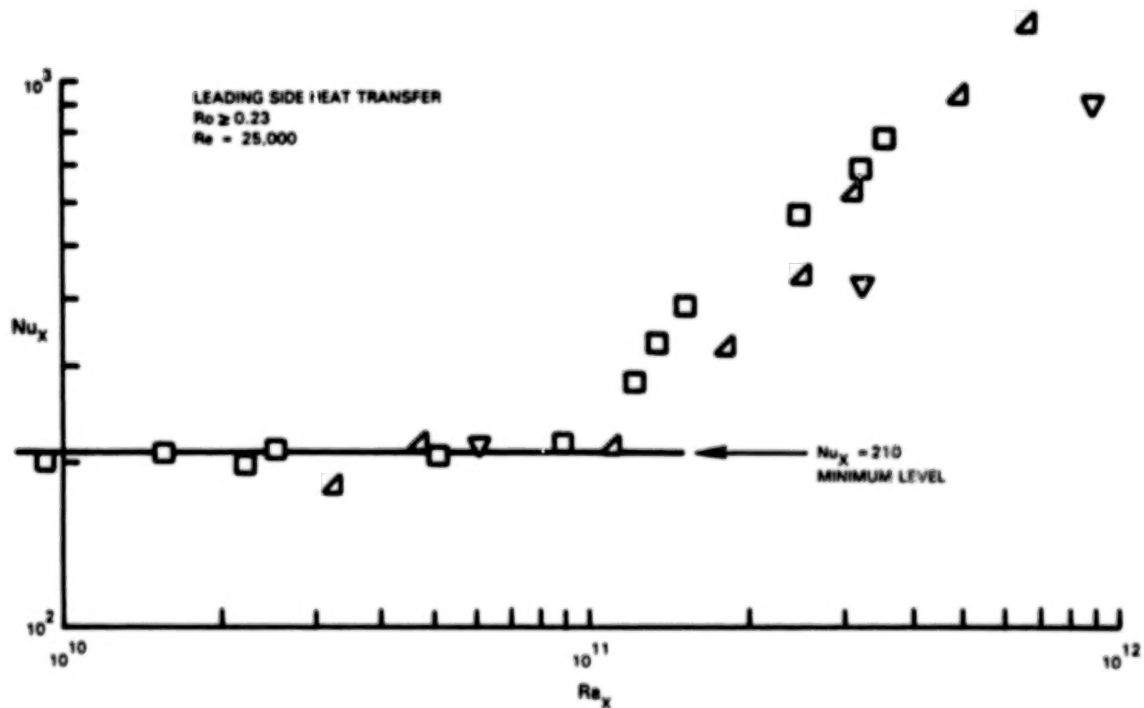


Figure 9 Leading Side Heat Transfer  $Ro \geq 0.23$ :  $Re = 25,000$

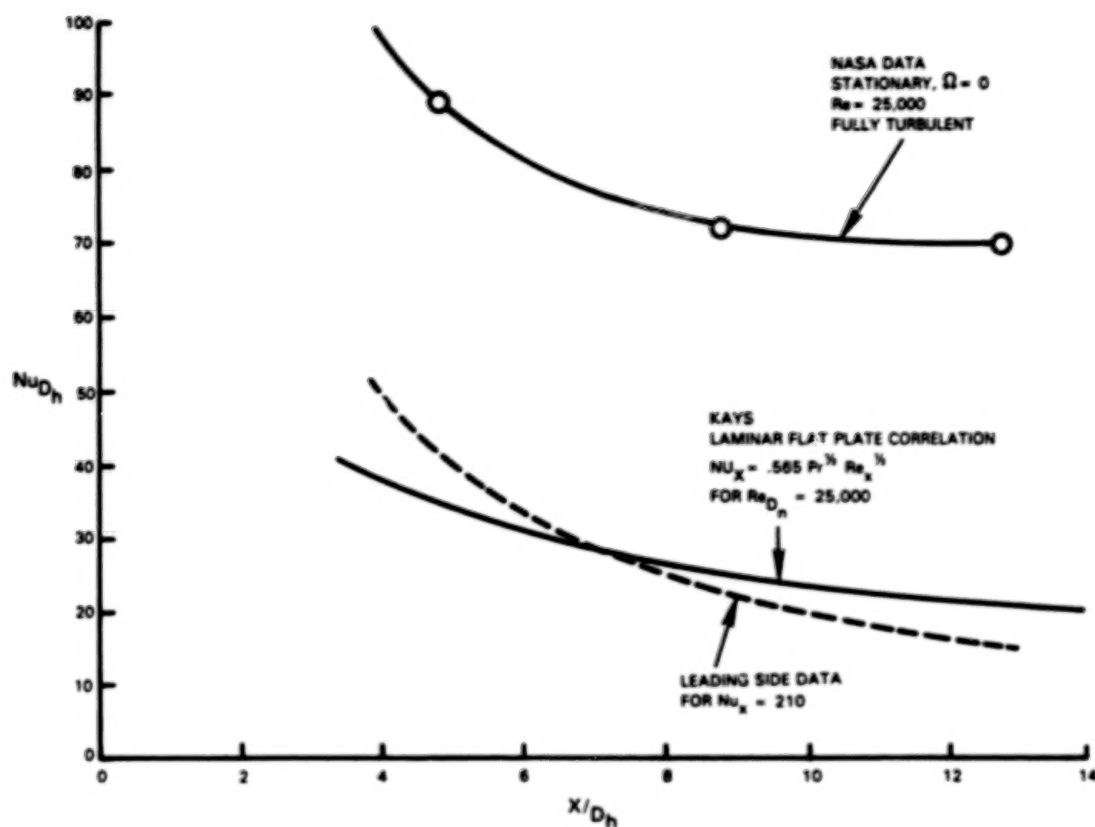


Figure 10 Leading Side Heat Transfer with Rotation Compared to Kays Laminar Heat Transfer:  $Re = 25,000$

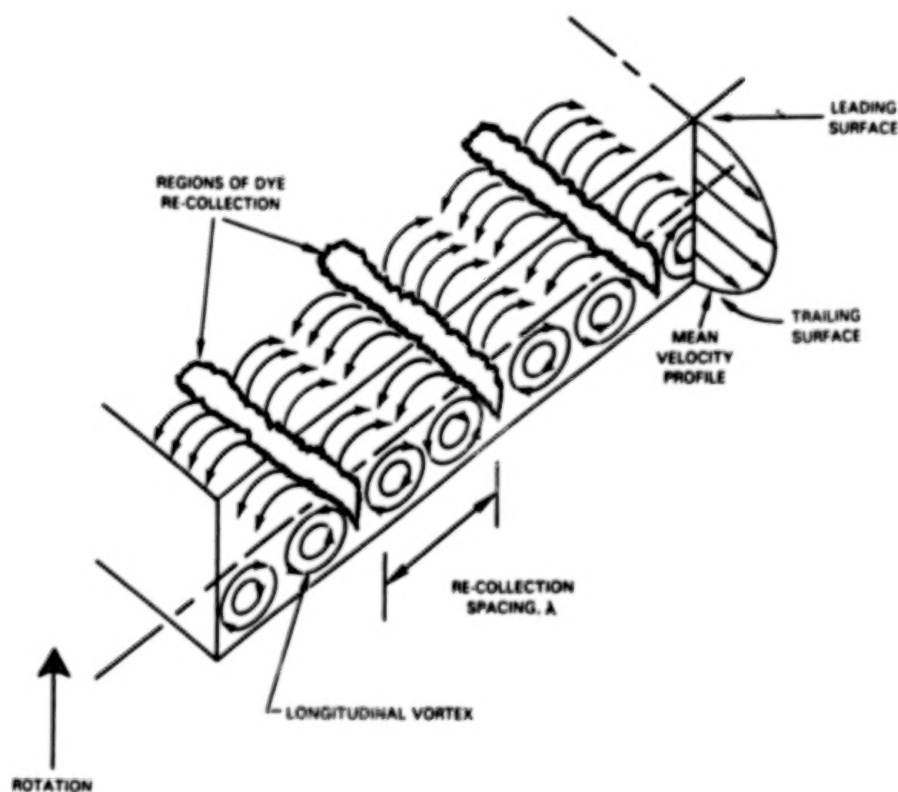


Figure 11 J. P. Johnston Flow Visualization of Rotating Channel Flow

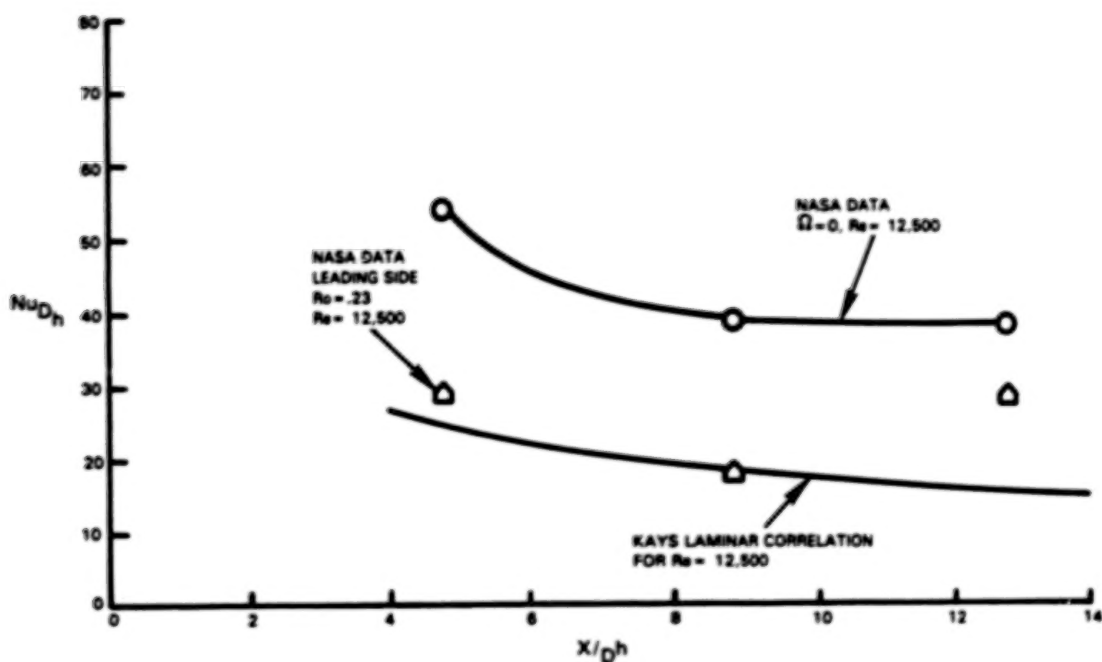


Figure 12 Leading Side Heat Transfer with Rotation Compared to Kays Laminar Heat Transfer: Re = 12,500

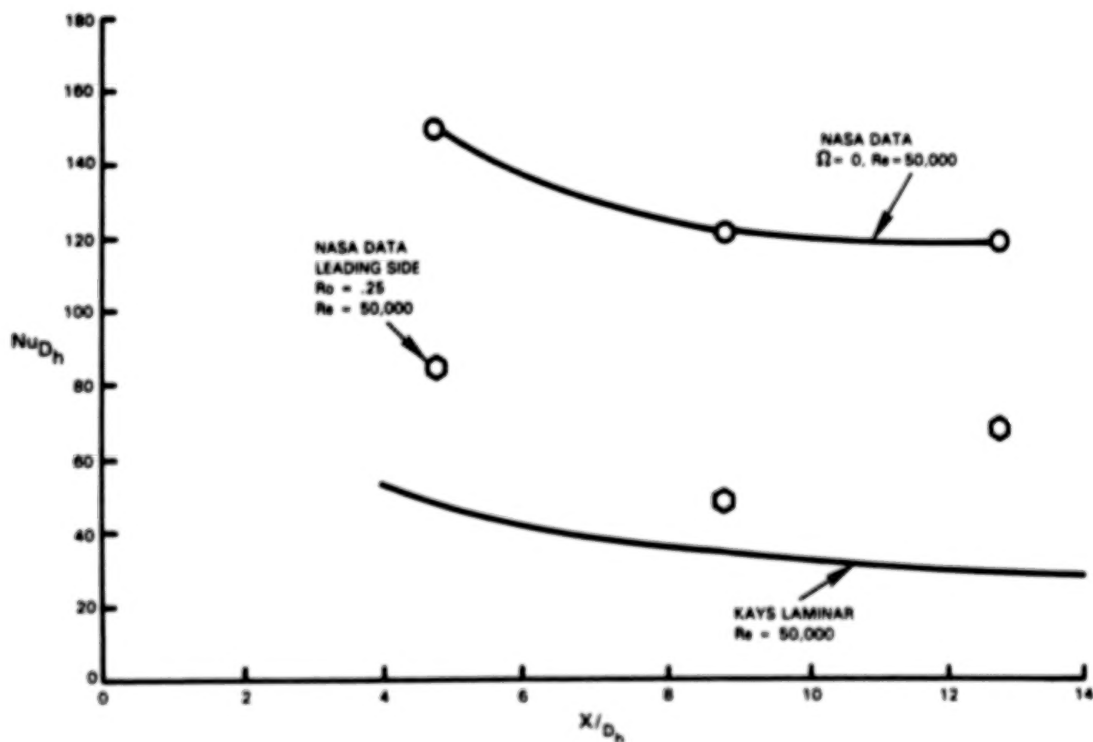


Figure 13 Leading Side Heat Transfer with Rotation Compared to Kays Laminar Heat Transfer: Re<sub>D</sub> = 50,000

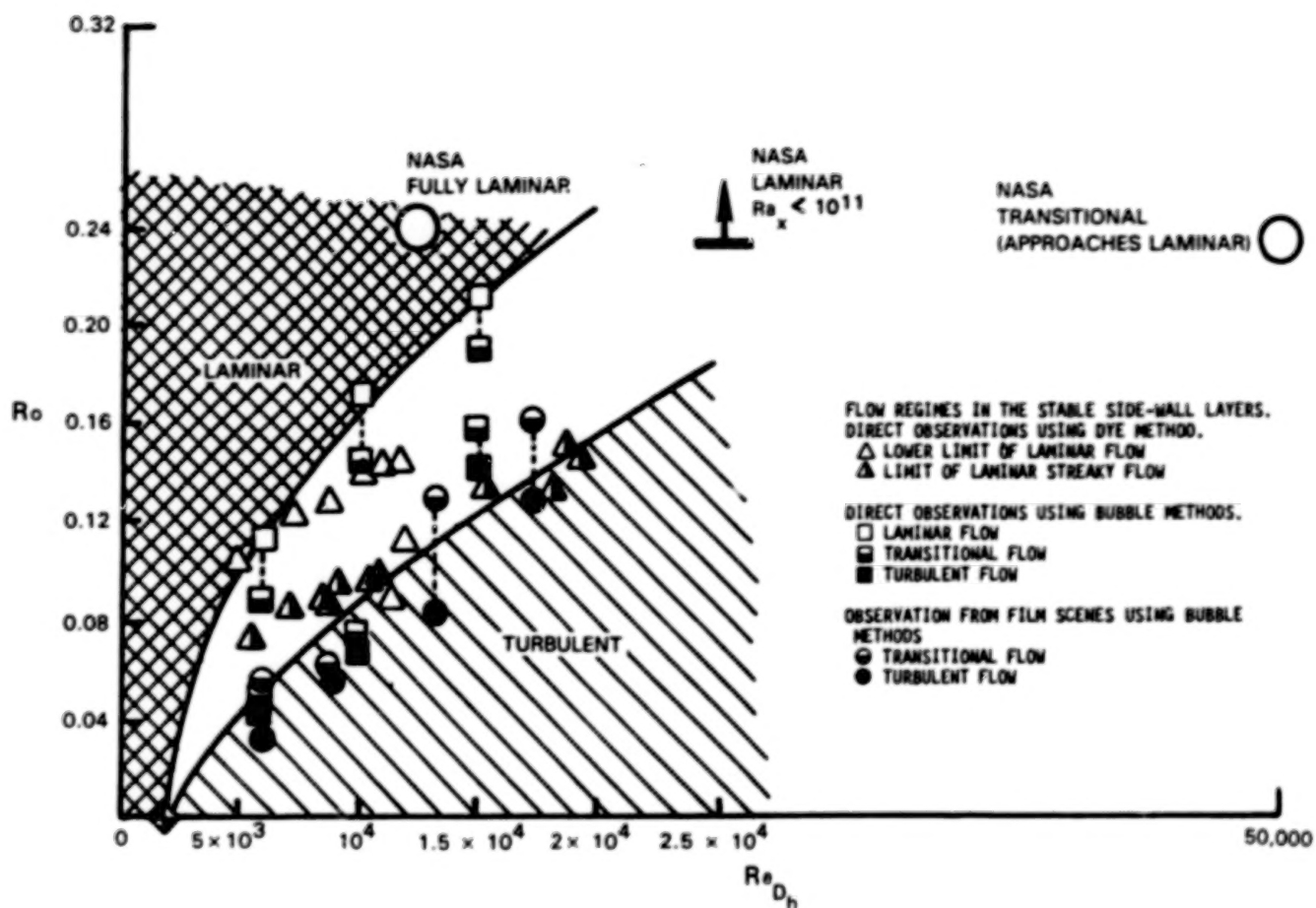


Figure 14 NASA Data Plotted on Johnston's Flow Map

## HEAT TRANSFER WITH VERY HIGH FREE-STREAM TURBULENCE\*

Robert J. Moffat  
Paul K. Maciejewski

Thermosciences Division  
Department of Mechanical Engineering  
Stanford University

## ABSTRACT

Stanton numbers as much as 350% above the accepted correlations for flat plate turbulent boundary layer heat transfer have been found in experiments on a low velocity air flow with very high turbulence (up to 50%). These effects are far larger than have been previously reported and the data do not correlate as well in boundary layer coordinates (Stanton number and Reynolds number) as they do in simpler coordinates:  $h$  vs.  $X$ . The very high relative turbulence levels were achieved by placing the test plate in different positions in the margin of a large diameter free jet. The large increases may be due to organized structures of large scale which are present in the marginal flowfield around a free jet.

## FOREWORD

Designing the cooling system for gas turbine blades and vanes requires accurate prediction of the heat transfer coefficient between the blades and the gas stream. For years the heat transfer research community has sought to provide data and models by which these predictions could be made. Academic research has, over the past twenty years, produced an impressive array of data and modeling techniques aimed at this problem. In parallel with the academic effort, industrial researchers and designers have struggled with the realities of heat transfer inside gas turbine engines. Even using the best available theories, large "safety factors" have been needed. The fact is that "unadjusted" predictions based on the best laboratory data and modeling schemes consistently underpredict engine heat transfer, by as much as 50%.

When such a state of affairs has persisted for twenty years, it is likely that something fundamental is being overlooked. Free stream turbulence is a likely candidate. It has been studied, but over this twenty year period opinions have been divided as to whether or not free stream turbulence had any effect on the already-turbulent boundary layer. It has been generally conceded that turbulence alters transition behavior, advancing it to lower Reynolds numbers, but there have been many studies which supported the notion that that was its only effect.

All of the "benchmark" heat transfer data in the literature has been from low turbulence flow fields. Turbulence has been regarded as a 'complicating factor' rather than a natural accompaniment to high energy-density systems. In fact, one of the hallmarks of careful research has been the "quality" of the flow in the tunnel - defined principally by the level of turbulence: the lower the better. Anything over 0.5% was considered a little rude, and one

\*Work done under NASA Grant NAG3-522.

had to get below 0.05% before there was any cause for celebration. When turbulence has been studied, it has almost always been "grid-generated" and, in addition, has been allowed to relax until nearly homogeneous and isotropic before its effects on heat transfer have been studied.

Meanwhile, gas turbine engines run with turbulence up to 20-30%, which is probably highly anisotropic and well laced with large coherent structures coming downstream from the combustion chamber. Dils and Follansbee (1977) measured up to 16% in the discharge of a laboratory scale combustor in a bench test. They reported increases in heat transfer of over 50% on the stagnation line of a cylinder in that flow. Recent discussions (Rohde, 1984) suggest 20 to 30% as a reasonable value for the relative turbulence near a typical first turbine nozzle ring.

This paper presents a brief look at the status of a new research program at Stanford, concerning the effects of very high turbulence - up to 50% - on heat transfer through a turbulent boundary layer. The program is following a somewhat unorthodox approach, by usual academic standards. Instead of establishing a well documented flow which contains a specified level of turbulence and studying its effect on heat transfer, the approach has been to find, by experiment, flow fields which are very aggressive in heat transfer and then try to find out what characteristics their turbulence has in common. Over a dozen different high turbulence situations have been tested in preliminary screening experiments, some of which resulted in very high heat transfer. We now seek to carefully document their heat transfer effects, and learn how they produce such high heat transfer rates. The present paper reports on the first of these significantly aggressive flow fields: the flow in the margin of a free jet.

#### SOME PREVIOUS WORK

Before looking at research laboratory data on heat transfer, it would be well to follow an old industrial dictum and "let the engine vote." Unfortunately, such votes are hard to come by: there is not much available in the open literature about heat transfer measurements on the blades and vanes of a running engine. The next nearest thing is the data available from short duration test facilities using engine components as their test sections. Figure 1 (Dunn, Rae, & Holt, 1983) shows measured distributions of heat transfer coefficient on a turbine stage in a short-duration test facility - the heat transfer coefficient is nearly constant around the entire surface of the blade. There is no evidence of a laminar or transitional region. While this is not "engine data," it is representative of what is believed to frequently occur: high uniform heat transfer around a blade or vane with no discernible laminar region, except perhaps right near the leading edge, and higher values than predicted, overall. Consigny and Richards (1982) show similar data, again from a short duration test facility, in which an increase in turbulence caused a progressive upstream march of the transition event, leaving a high and nearly uniform value of  $h$  in the turbulent region.

There have been many studies on the effects of turbulence, going well back in the heat transfer literature. Among these were Kestin (1966), Kearney, Kays, and Moffat (1970), Slanciauskas and Pedesius (1977), Brown and Burton (1978), Bradshaw and Simonich (1978), Brown and Martin (1979), and Blair (1984).

During the mid-1970's, the consensus was that the principal effect of turbulence was to re-locate the transition event. There were suggestions that strong acceleration made a turbulent boundary layer sensitive to turbulence, based mainly with experience on stagnation regions on bluff bodies. Three examples are cited in some detail because they represent the states of opinion up until the recent work began: Kearney et al (1970), Bradshaw and Simonich (1978), and Blair (1984).

Kearney et al (1970) addressed these two issues: (1) How does the local behavior of an already turbulent boundary layer respond to free stream turbulence, and (2) Does acceleration affect this response? Local effects were separated from those associated with changes in transition behavior by using a different method of data presentation, one based on purely local measures, which did not depend on the location of the virtual origin. A turbulent boundary layer was established on a smooth flat plate in a well-qualified heat transfer test section having three stream-wise parts. The first and third sections provided constant velocity flow, while the second produced a constant  $K$  acceleration. Heat transfer Stanton numbers were correlated against the enthalpy thickness Reynolds number, a purely local parameter of the boundary layer. This representation eliminated any sensitivity to the location of transition. Tests were conducted with low turbulence (about 0.7%) and with grid-generated turbulence of 3.9%. The turbulence was generated by a planar grid of round rods, 0.64 cm in diameter set on 2.54 cm centers in a square array.

The results are shown in Figure 2. There is no discernible difference between the high and low turbulence data, either in the flat plate regions or in the accelerated region. The conclusion from this study was that the already-turbulent boundary layer was not sensitive to turbulence of this nature, at this intensity.

Bradshaw and Simonich (1978) reopened the issue when they showed large increases in average heat transfer over a flat plate exposed to grid generated turbulence of up to 7%. A key feature of their experiment was the use of large grid elements of different sizes, aimed at finding the effects of scale and intensity. Figure 3 shows a sample of their results. Although not quantitatively identified, the turbulence caused large effects.

Blair (1984) published a data set which showed, for the first time, that sufficiently high free-stream turbulence could cause turbulent boundary layer behavior to persist down to very low Reynolds numbers. Low enough, in fact, that the data followed the extension of the usual turbulence correlation and intercepted the laminar behavior line. His data are illustrated in Figure 4. In addition, he showed Stanton numbers significantly higher than the low-turbulence correlation: up to 20% higher for 6% turbulence. This difference must be regarded as significant in view of his careful control of experimental uncertainty. Blair's turbulence was again grid-generated, and his papers describe its streamwise evolution through the test section. The intensities ranged from 0.25 to 7%, with length scales from 1.0 cm to 6.5 cm. The average boundary layer thickness was about 4.5 cm. The intensity decreased steadily in the streamwise direction, while the auto-correlation length scale increased. The individual variations were such that their product was nearly constant.

At about this same time, both Schultz, at Oxford, and Dunn, at Calspan, were investigating the effects of transient wake-like disturbances on turbine blade heat transfer (private communications). In both cases, small cylindrical obstructions were passed rapidly across the flow field upstream of a blade model, and time-resolved heat transfer distributions measured. Their preliminary results showed significant increases in heat transfer.

The senior author's early engineering experience with gas turbine combustion chamber development had left him with an acute awareness of the intensities and scales of turbulence in a burner outlet flowfield. It was logical to compare the disturbances produced by Schultz and Dunn to those remembered conditions and to conclude that if a relatively small wake could be so important, then the large scale, high intensity turbulence of a gas turbine combustor ought to have a very profound effect indeed. The present program grew out of these beginnings.

#### THE BASIS HYPOTHESIS OF THE PRESENT WORK

The basic hypothesis of the present work is that the heat transfer coefficient is a function of both the mean velocity of the flow, and the free-stream turbulence (without, at the moment, defining what is meant by the word turbulence). Treating turbulence as a separate variable leads to planning experiments in which the turbulence can be varied independently from the mean velocity. This viewpoint also leads to a different approach to visualizing the possible outcomes. An operating surface for  $h$  can be constructed, based on this hypothesis, using only simple physical arguments. The process is described below.

Let us first consider how surface heat transfer might respond to turbulence in the absence of any mean motion. Consider a closed box full of air, instrumented to reveal the heat transfer coefficient from its inner, bottom surface to the air inside. The mean velocity inside is zero, but there will be some low value of heat transfer coefficient. If now a distributed set of egg-beaters were started into motion, the mean velocity would remain zero but small scale "turbulence" would be developed. It seems reasonable that  $h$  would increase as the turbulence increased, slowly at first, then perhaps linearly, and finally slowly again, as it asymptotically approached some ultimate maximum value for very high turbulence.

The "zero-velocity trace" of the effect of turbulence can thus be argued to be an S-shaped curve, having zero slope at very low turbulence and at very high turbulence, and a maximum slope at some intermediate value. We expect that this same general response would be present for non-zero velocities: increasing turbulence would increase  $h$ , only slightly at low turbulence intensities but more strongly at high values.

We have ample evidence about how heat transfer behaves with zero free-stream turbulence. The "zero-turbulence trace" is simply the variation of heat transfer coefficient with position along a surface.

Most physical processes vary smoothly as their parameters are changed, and can be represented by "operating surfaces" of low mathematical order. When nothing is known except the two bounding traces, a first estimate of the operating surface can frequently be made by assuming it to be a product function of the two boundary traces.

Figure 5 shows the hypothesized distribution of  $h$  along a plate of length  $L$  for a turbulent boundary layer for a range of turbulence intensities. For this figure, the free stream velocity is assumed constant. The turbulence values could then be regarded as absolute or relative. At zero turbulence, the heat transfer coefficient shows the typical turbulent boundary layer behavior. As the turbulence gets higher,  $h$  rises toward an asymptotic value, which is the same for every position. If this asymptotic state exists, and if the turbulence can be made high enough to approach it,  $h$  would be expected to show less and less  $x$ -dependence as the turbulence increased. At very high turbulence values,  $h$  might become uniform along the surface, dominated entirely by the turbulence.

To this point we have not specified what measure is to be used to characterize turbulence intensity. The usual approach is to use one or more of the Reynolds normal stress terms. It has been suggested, e.g. by Brown and Martin (1979) that turbulence scale and frequency may also be important in this problem. The present results support this notion. There are good physical reasons for believing that both are potentially important, at least at the extremes of very large and very small scales (or very low or very high frequencies). Consider the situation of a hot-wire anemometer wire, where the turbulence scale is large compared with the boundary layer thickness. The fact that we can calibrate these wires in laminar flow and use them to measure turbulence is evidence that the boundary layer is in the same state for all frequencies of disturbances up to 100kHz. Thus, it seems that when the turbulence scale is very large compared to the boundary layer thickness (or frequencies are very low) there is little or no effect. On the other end of the spectrum, it seems unlikely that free stream turbulence would have much effect if the scale of the turbulence was an order of magnitude smaller than the natural scales within the boundary layer. If there is to be a significant effect of turbulence, it most likely will come when the scale of the turbulence is of the same order of size as the boundary layer turbulence (i.e., related to the boundary layer thickness), or a low multiple of it.

To call a flow "turbulent" doesn't say much about it except that it is unsteady in some unpredictable manner (except statistically). One important question which we hope to answer at least partially is: "What aspect of turbulence is responsible for the increase in heat transfer?" There is no a priori assurance that intensity is the appropriate descriptor, nor even intensity combined with length scale. In fact, data from the present program suggests that, even together, these are not sufficient.

Testing this hypothesis requires a flow field with very high turbulence which can be varied at will, and with length scales also variable. The shape of the hypothesized operating surface suggests that low velocity, thick boundary layers will be more strongly affected than high velocity, thin boundary layers. The flow in the margin of a large diameter, low speed, free jet meets these requirements admirably and was the first flow tested. The characteristics of a free jet, and a description of the present free jet facility are contained in the sections below.

## THE FREE JET FACILITY

The first flow studied under this program was a free jet, blowing over a flat plate. This was selected because it offers a simple flow field capable of generating very high local turbulence, with significant contributions from large scale, relatively well organized structures. Figure 6 shows the features of a free jet which made it attractive. The mean velocity is well distributed across the jet, from a maximum on the centerline to zero in the surrounding air. The relative turbulence intensity increases dramatically near the outer edge. Relative turbulence intensities of over 50%, based on local mean velocity, can easily be found and the length scales increase almost linearly with distance from the nozzle. With a variable velocity free jet facility, one can find almost any desired combination of turbulence intensity, length scale, and mean velocity.

Figure 7 shows a schematic of the free jet facility. The test plate is shown in a representative position, a few diameters off the axis of the jet and many diameters downstream from the nozzle. For most of the work so far, the test plate has been equipped with side walls, approximately as high as the plate is wide. The plate and its side walls thus form an open channel. Experience has shown that the flow tends to be "frozen" at the conditions existing at the leading edge. The presence of the plate stops entrainment from the bottom and sides. This has the effect of stopping the linear growth of the length scales, and preserving the free stream turbulence properties at those available at the entrance. The plate is shown in two positions: W, aligned with the axis of the jet, and F, aligned with a line through the virtual origin of the jet. When the plate is in the F position, the mean velocity and turbulence quantities are uniform within 1-2% along the plate - a flat plate configuration. When the plate is parallel to the axis of the jet, the W position, the situation resembles a wedge flow - the small positive incidence angle causes the velocity to increase slightly along the run of the plate. The data in the present paper were all taken in the wedge flow configuration. The mean velocity variation along the plate is still small - on the order of 5%.

The test plate is 0.5 m wide and 2.5 m long. The working surface is made of 7 plates of aluminum, each equipped with an electric heater and an array of thermocouples. Side walls on the test plate help "freeze" the flow for the whole length of the plate at the conditions existing at the leading edge of the test plate. Heat transfer is measured by energy balances on the individual segments of the test plate. The free-stream velocity and turbulence are measured with a single hot wire, about 12.5 cm above the surface of the plate, centered over the first test plate. Axial traverses have shown that the velocity increases about 5% when the plate is in the wedge-flow orientation, and about 1% when in the flat plate position. We recognize the inaccuracies of a single hot-wire under such strenuous conditions, but the results are, nevertheless, indicative of the level of turbulence. For the present it is sufficient to have accurate measurements of the increase in heat transfer and a rough measure of the turbulence, those data serve to identify an aggressive flow. Future work will study the structure of the turbulence in detail using one or more probes having orthogonal triple wire arrays, with which we have considerable experience. Turbulence length scales are now being measured using the time-delayed auto correlation of the hot wire signal. In future, the length scales will be determined from the outputs of the triple wire processor.

## QUALIFICATION OF THE APPARATUS

Figure 8 is intended to establish the credibility of data from the present experiments by demonstrating a low-turbulence baseline check and showing evidence of repeatability with high turbulence. For the baseline run, the test plate was installed in low-turbulence, closed loop wind tunnel (HMT-2, in the Thermosciences Division Heat Transfer Lab). A representative set of results are shown as the diamond shaped symbols, lying along the line representing an accepted correlation for turbulent boundary layer heat transfer in a low-turbulence situation. The agreement is within  $\pm 4\%$ . The conclusion from this series of tests was that the test plate instrumentation was functioning normally, and the results could be believed within the demonstrated accuracy.

The test plate was then removed from the tunnel and set up in the free jet facility. All of the instrumentation remained the same, and the same data interpretation program was used in reducing the free jet data. The leading edge of the plate was 5D downstream of the nozzle exit, and the 2D off the centerline. The surface of the plate was parallel to the axis of the jet. At that location, the mean velocity was 3.6 m/s and the turbulence intensity was 27%. Results are shown from two runs, taken on different days at this same location. No changes or adjustments were made between these two runs. The excellent agreement establishes that the effects reported here are repeatable.

## NEW RESULTS

Figure 9 compares typical results from the present program with a set of Blair's (1984) data and with an accepted zero free-stream turbulence boundary layer correlation from Kays and Crawford (1980). The data are plotted in conventional Stanton number versus X-Reynolds number coordinates. The RMS  $u'$  value is used as a measure of free stream turbulence. The Stanford cases are at 26% and 48% turbulence, while Blair's data are at 6%. The Stanford data at the highest turbulence show the Stanton number to be almost 350% higher than the baseline results for the same Reynolds number. This case clearly identifies the flow field in the margin of a free jet as an aggressive one as far as heat transfer is concerned. It also seems clear that the data labelled 48% comes from a "more turbulent" flow than the data labelled 26%, but relatively how much more turbulent is unknown. The present data show no sign of laminar behavior and hence no sign of transition. The heat transfer must be considered fully turbulent from the leading edge of the plate. Very high free stream turbulence eliminates the laminar region, as Blair found, but also, for these high values, increases the heat transfer at low Reynolds numbers by as much as three and one half times compared with the accepted turbulent boundary layer correlation.

Figure 10 shows cases from the present program at four different mean velocities with relative turbulence intensity held constant at 25%. The data are plotted as Stanton number versus enthalpy thickness Reynolds number, a purely local parameter - not dependent on the location of the virtual origin of the turbulent boundary layer. These data confirm that the large increases observed in Stanton number are local in nature, which agrees with Blair's conclusion but contradicts Kearney. The spread in the data for the same turbulence intensity shows that fixing the relative turbulence intensity and the enthalpy thickness Reynolds number is not sufficient to assure repeatable

results. Neither  $x$ -Reynolds number nor enthalpy thickness Reynolds number collects into one correlation the data for different mean velocities. Indeed, this may not be a boundary layer flow at all, in the usual sense of the term.

Comparing the data in Figure 10 to the line representing the established turbulent boundary layer correlation, one sees that high free stream turbulence does alter the streamwise dependence of the heat transfer, as had been anticipated: as turbulence goes up, the slope goes down. In boundary layer problems, the streamwise decay of heat transfer is typically associated with the thickening of the boundary layer. Boundary layer thickness serves as a length scale for the heat transfer problem, and is Reynolds number dependent. If the streamwise dependence of the present data is also associated with the growth of a boundary layer, this boundary layer is not Reynolds number dependent. It may be that the boundary thickness is being set by the turbulence, not by the mean velocity.

Figure 11 is a plot of the same data used in Figure 10, but plotted in terms of the heat transfer coefficient,  $h$ , versus streamwise position along the plate,  $X$ . Surprisingly, at any given  $X$ ,  $h$  is the same for all four cases within  $\pm 4\%$  even though the mean velocities vary by as much as 50%. This figure suggests that, for very high free stream turbulence, the Stanton number should be replaced by a descriptor which does not involve the mean velocity.

#### CONCLUSIONS

The flow field near the outer margin of a free jet displays very aggressive heat transfer properties. Stanton numbers as much as 350% above the usual turbulent correlations have been observed when the local relative turbulence intensity reaches 50%.

The data are not well correlated by the usual boundary layer parameters, Stanton number and Reynolds number. Data from four runs with the same relative turbulence intensity (25%) but different mean velocities (2.3 to 3.6 m/s) show the same values of  $h$  at each  $x$ -location (within  $\pm 4\%$ ). Plotting these data in terms of Stanton number and  $x$ -Reynolds number introduces considerable separation.

The failure of the usual boundary layer coordinates to collect data from the high turbulence cases into coherent groups suggests that the high turbulence has fundamentally altered the boundary layer state.

#### ACKNOWLEDGMENTS

This work is supported by the Hot Section Technology Program of NASA, through the Lewis Research Laboratory, under the terms of NASA Ngr 3-522. The program was started under the auspices of Dr. John Rohde, and is now being monitored by Dr. Raymond Gaugler. The authors appreciate their sincere interest and enthusiastic approach to research.

## NOMENCLATURE

D	Diameter of jet nozzle
F	Flat plate configuration (Fig. 7)
h	Heat transfer coefficient
K	Acceleration parameter
R	Radial position within the jet
Re(H)	Enthalpy thickness Reynolds number
Re(O)	Momentum thickness Reynolds number
Re(X)	X-Reynolds number
RMS	Root-mean-square
St	Stanton number
TKE	Turbulence kinetic energy
Tu	Turbulence
u'	Fluctuating component of x-directed velocity
U or V	Free stream velocity
U(max)	Velocity at the jet centerline, at X.
W	Wedge flow plate configuration (Fig. 7)
X	Distance downstream from the jet nozzle

## REFERENCES

- Blair, M. F. (1983), "Influence of Free-Stream Turbulence on Turbulent Boundary Layer Heat Transfer and Mean Profile Development. Part I: Experimental Data," Journal of Heat Transfer, 105: 33-41, Feb. 1983.
- Brown, A., and Burton, R. C. (1978), "The Effects of Free Stream Turbulence Intensity and Velocity Distribution on Heat Transfer to Curved Surfaces," Jn. Eng. for Power, Vol. 100, 1978, pp. 159-168.
- Brown, A., and Martin, B. W. (1979), "Factors Influencing Heat Transfer to the Pressure Surfaces of Gas Turbine Blades," International Journal of Heat and Fluid Flow, 1, No. 3, 1979.
- Consigny, H., and Richards, B. E., "Short-Duration Measurements of Heat-Transfer Rate to a Gas Turbine Rotor Blade," Jn. Eng. for Power, 104: 542-551, July 1982.
- Dils, R. R., and Follansbee, P. S., "Heat Transfer Coefficiency around Cylinders in Crossflow in Combustor Exhaust Gases," Jn. Eng. for Power, Oct. 1977, pp. 497-508.
- Dunn, M. G., Rae, W. J., and Holt, J. L., "Measurement and Analysis of Heat-Flux Data in a Turbine State. Part III: Discussion of Results and Comparison with Predictions," 28th Int'l. Gas-Turbine Conference, Phoenix, AZ, March 1983.
- Kays, W. M., and Crawford, M. E., Convective Heat and Mass Transfer, McGraw-Hill Book Co., 1980.

- Kearney, D. W., Kays, W. M., and Moffat, R. J. (1970), "The Effect of Free Stream Turbulence on Heat Transfer to a Strongly Accelerated Turbulent Boundary Layer," Proceedings of the 1970 Heat Transfer and Fluid Mechanics Institute, edited by T. Sarpkaya (Stanford University Press), pp. 3-14.
- Kestin, J. (1966), "The Effect of Free Stream Turbulence on Heat Transfer Rates," Advances in Heat Transfer, pp. 31-32.
- Simonich, J. C., and Bradshaw, P. (1978), "Effect of Free-Stream Turbulence on Heat Transfer through a Turbulent Boundary Layer," Journal of Heat Transfer, 100: 671-677, Nov. 1978.
- Slanciauskas, A., and Pedisius, A. (1977), "Effect of Free Stream Turbulence on the Heat Transfer in the Turbulent Boundary Layer," Paper FC(1)-5, Academy of Sciences of the Lithuanian USSR Institute of Physical and Technical Problems of Energetics, Kaunos, USSR.
- Wynanski, I., and Fiedler, H., "Some Measurements in a Self-Preserving Jet," J. Fluid Mech. (1969), vol. 38, part 3, pp. 577-612.

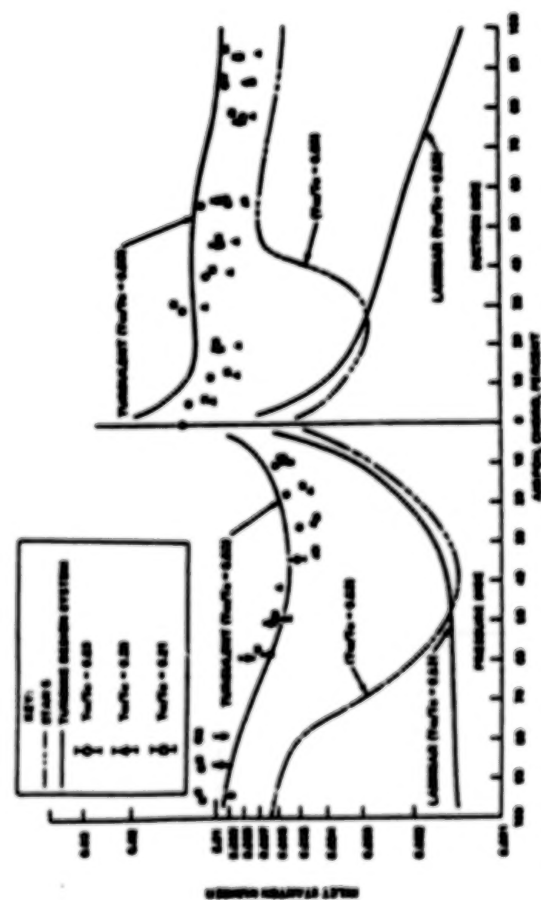


Fig.1 Heat transfer under simulated engine conditions does not always agree with predictions. [Dunn and Rae, 1983]

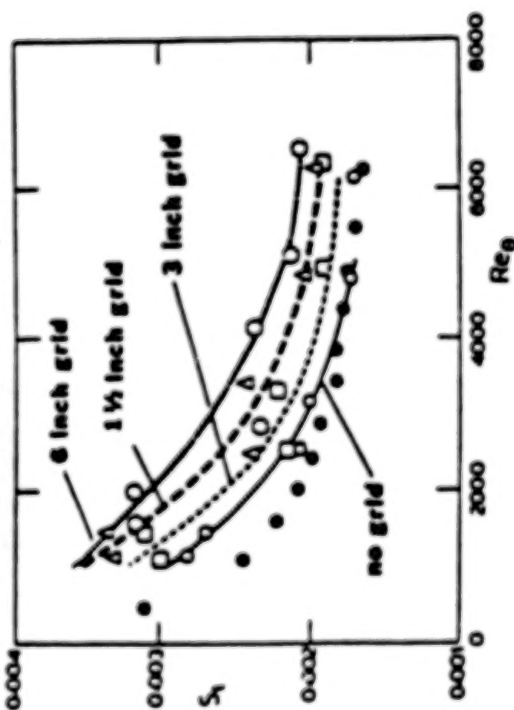


Fig.3 Large scale high intensity grid generated turbulence affects heat transfer. [Simonich and Bradshaw, 1978]

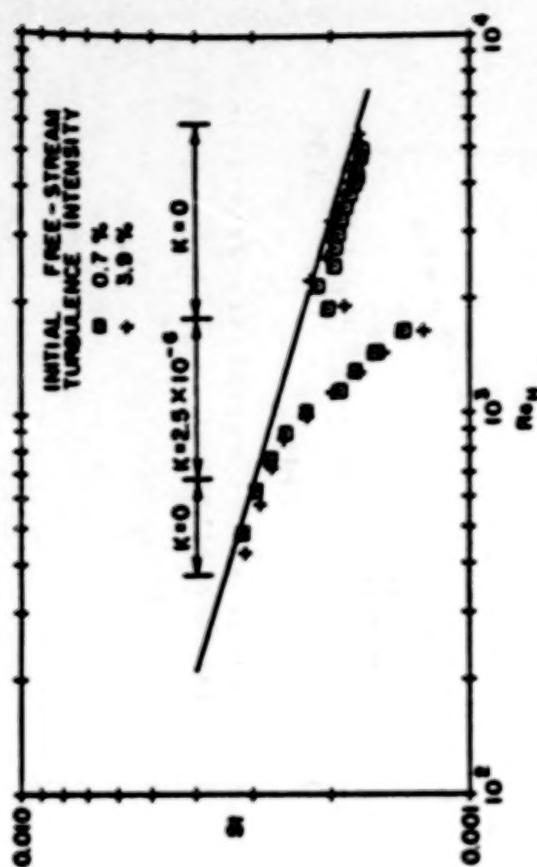


Fig.2 Moderate grid generated turbulence does not effect turbulent heat transfer. [Kearney, Kays and Moffat, 1970]

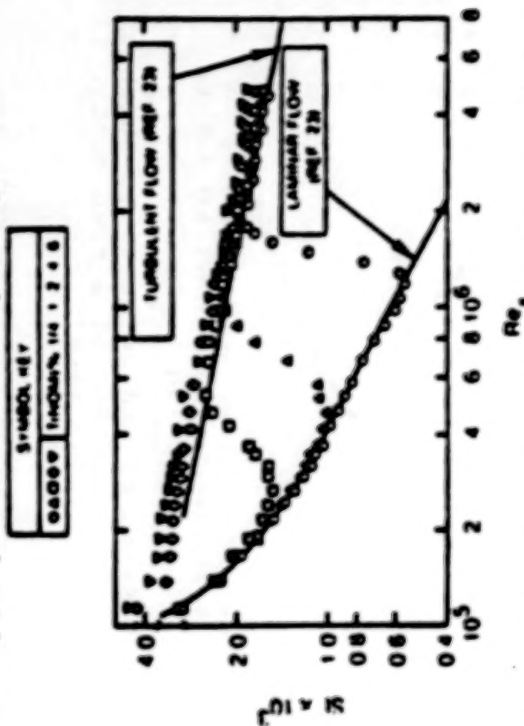


Fig.4 Grid generated turbulence eliminates laminar behavior and raises turbulent heat transfer. [Blair, 1983]

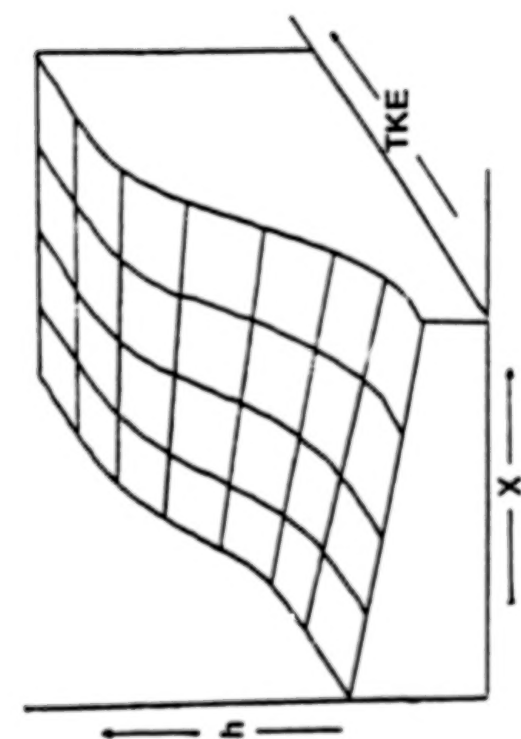


Fig.5 Proposed operating surface for  $h$  vs.  $X$  and  $Tu$ .

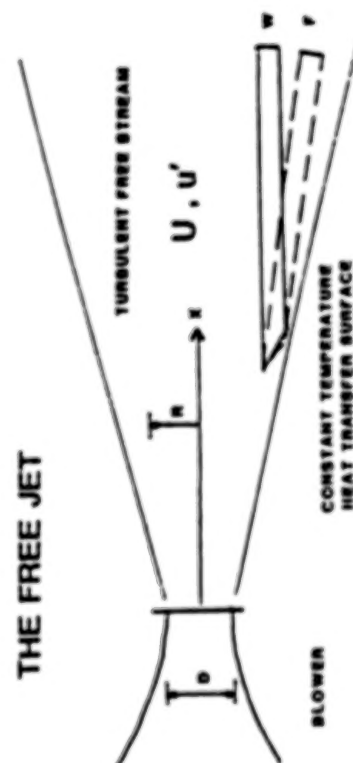


Fig.7 Schematic of the free jet facility.

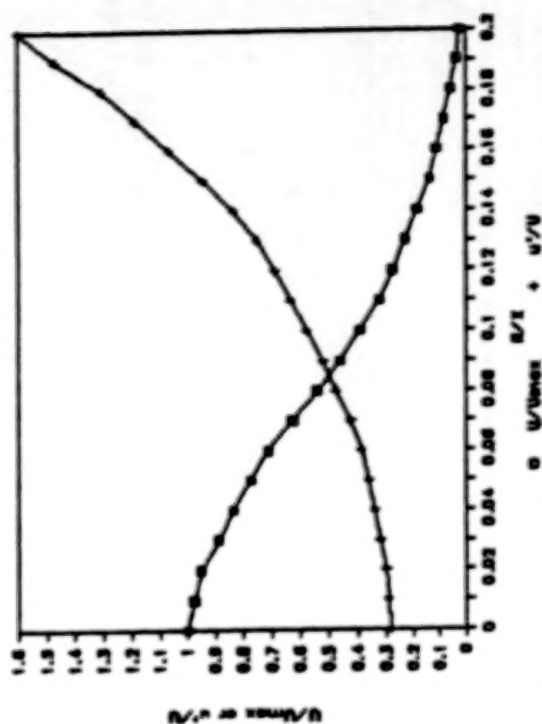


Fig.6 Mean velocity and relative turbulence intensity characteristics of a free jet. [Wyganski and Fiedler, 1969]

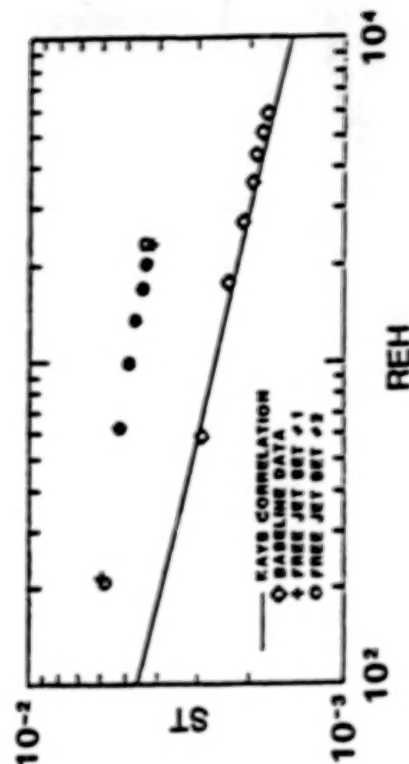


Fig.8 Baseline and repeatability data from the free jet facility.

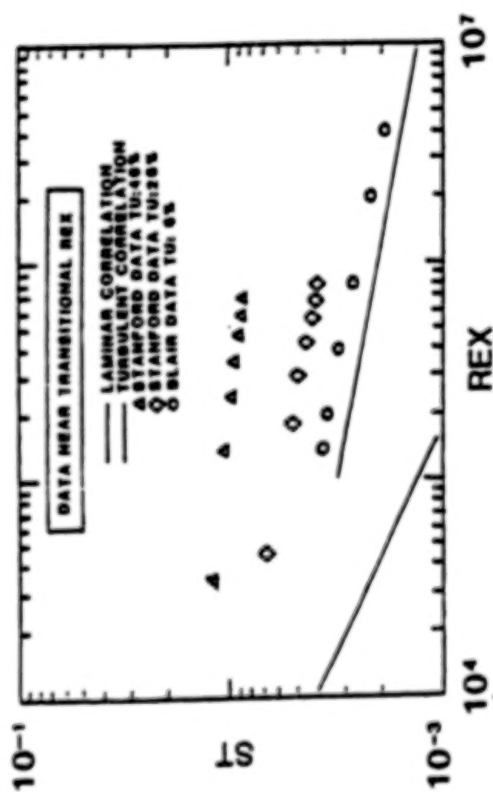


Fig.9 High turbulence causes large effects on St vs. ReX.



Fig.11 The heat transfer coefficient, h, collects the Fig.10 data better than St.

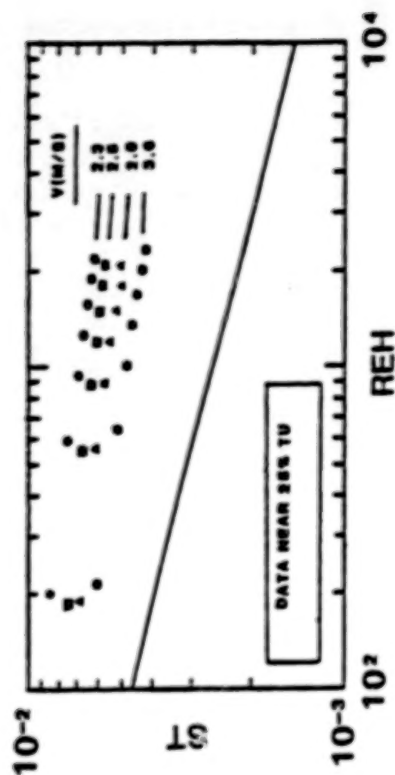


Fig.10 ReH and  $Stu$  are not a sufficient set of descriptors.

## PREDICTION OF TURBINE BLADE HEAT TRANSFER\*

Suhas V. Patankar  
University of Minnesota

## INTRODUCTION

Although numerical computation of heat transfer has been attempted for at least the last twenty years, the current capability still requires considerable improvement and refinement. The reason that it is so difficult to predict the heat transfer on turbine blades lies in the simultaneous presence of many complicating factors such as transition to turbulence, relaminarization, free-stream turbulence, rotation, curvature, unsteadiness, generation of vortices, secondary flows, and three-dimensionality. Some of these aspects are discussed in references 1-4.

The purpose of the present project is to evaluate the current state of the art and to propose appropriate turbulence models for the prediction of the turbine blade heat transfer.

## AVAILABLE EXPERIMENTAL DATA

The development of a satisfactory turbulence model is dependent on the availability of reliable and relevant experimental data. From a careful search of the literature, the experimental data given in references 5-9 are judged to be satisfactory for this purpose. The development of turbulence models will be done primarily by reference to these sets of data. Also, useful related information is available in references 10-11.

## RELEVANT TURBULENCE MODELS

The main difficulty in the correct prediction of heat transfer on a turbine blade lies in the determination of transition to turbulence. Purely empirical criteria for transition cannot properly account for the influence of free-stream turbulence, curvature, and other factors. Only the low-Reynolds number versions of the differential turbulence models have, at least in principle, the ability to "predict" the transition. In these models, the turbulence parameters are computed even in the laminar-flow region. They have very small values as long as the flow remains laminar. When the conditions are right for transition, the imbalance between the generation and dissipation of the turbulence parameters leads to a rapid growth of the predicted turbulent viscosity, and the turbulent-flow region begins. Some of the relevant low-Reynolds-number turbulence models are described in references 12-15.

Since curvature is an important aspect of the flow over a turbine blade, the turbulence model should respond to the presence of the streamline curvature. References 16-22 present turbulence models with special emphasis on curvature.

## PROPOSED WORK

It is planned to incorporate a number of low-Reynolds-number turbulence models in a general two-dimensional boundary layer calculation procedure. This will be applied to different flow conditions over turbine blades and the predictions will

\*Work done under NASA Grant NAG3-579.

compared with experimental data. The prediction activity will lead to a recommendation about a satisfactory turbulence model for turbine blade heat transfer.

#### REFERENCES

1. Graham, R. W.: Fundamental Mechanisms that Influence the Estimate of Heat Transfer to Gas Turbine Blades. ASME, 79-HT-43.
2. Priddy, W. J.; and Bayley, F. J.: Heat Transfer to Turbine Blading. 14th Int'l. Center for Heat and Mass Transfer Symposium. August 1982.
3. Metzger, D. E.: Fundamental Heat Transfer Research for Gas Turbine Engines. NASA Workshop Overview, 1982.
4. Marlin, B. W.; and Brown, A.: Factors Influencing Heat Transfer to the Pressure Surface of Gas Turbine Blades. Int. Journ. of Turb. and Jet Engines, vol. 1, 1984, pp. 247-258.
5. Hylton, L. D. et al: Analytical and Experimental Evaluation of the Heat Transfer Distribution over the Surfaces of Turbine Blades. NASA CR-168015, 1983.
6. Turner, A. B.: Local Heat Transfer Measurements on a Gas Turbine Blade. J. of Mech. Eng. Science, No. 1, vol. 13, 1971.
7. Liebert, C. H.; Gaugler, R. E.; and Gladden, H. J.: Measured and Calculated Wall Temperatures on Air Cooled Turbine Vanes with Boundary Layer Transition. ASME 83-GT-33.
8. York, R. E. et al: An Experimental Investigation of Heat Transfer to a Turbine Vane at Simulated Engine Conditions. ASME 79-GT-23.
9. Nicholson, J. H. et al: Heat Transfer Optimized Turbine Rotor Blades - An Experimental Study Using Transient Techniques. ASME 82-GT-304.
10. Danials, L. D.; and Brown, W. R.: Calculation of Heat Transfer Rates to Gas Turbine Blades. Int. J. of Heat and Mass Transfer, No. 5, vol. 24, 1981. pp. 871-879.
11. Wang, J. H.; Jen, H. F.; and Hartel, E. O.: Airfoil Heat Transfer Calculation Using Low Reynolds Number Version of a Two Eq. Turb. Model. ASME 84-GT-261.
12. Jones, W. P.; and Launder, B.E.: The Calculation of Low-Reynolds Number Phenomena with a Two-Equation Model of Turb. Int. J. of Heat and Mass Transfer, No. 6, vol. 16, 1973, pp. 1119-1130.
13. Gori, F., El Haddy, M.A.; and Spalding, D. B.: Numerical Prediction of Heat Transfer to Low Pr. Number Fluids. Numeri. Heat Transfer, vol. 2, 1979, pp. 441-454.
14. El Hadidy, M. A.; Gori, F.; and Spalding, D. B.: Further Results on the Heat Transfer to Low Pr. Number Fluids in Pipes. Numeri. Heat Transfer, vol. 5, 1982, pp. 107-117.
15. Patel, V. C.; Rosi, W.; and Scheurrer, G.: A Review and Evaluation of Turbulence Models for Near Wall and Low Reynolds Number Flows. To appear in AIAA J1.

16. Launder, B. E.; Priddin, C. H.; and Sharma, B. I." The Calculation of Turbulent B. Ls on Spinning and Curved Surfaces. J. of Fluids Eng., March 1977, pp. 231-239.
17. Rodi, W.; and Scheurer, G., Calculation of Curved Shear Layers with Two-Equation Turbulence Models. SFR 80/T.211. July 1982.
18. Chambers, T. L.; and Wilcox, D. C.: Critical Evaluation of Two-Equation Turbulence Models for Boundary Layers. AIAA Jl., No. 6, vol. 15, 1977. pp.
19. Gibson, M. M.: An Algebraic Stress and Heat-Flux Model for Turbulent Shear Flow with Streamline Curvature. Int. J. of Heat and Mass Transfer, No. 8, vol. 21, 1978, p. 1069.
20. Gibson, M. M.; and Rodi, W., A Reynolds-stress Closure Model of Turbulence Applied to the Calculation of a Highly Curved Mixing Layer. J. Fluid Mechanics, vol. 103, 1981, p. 161.
21. Gibson, M. M.; and Younis, B. A., Modeling the Curved Turbulent Wall Jet, AIAA Jl., No. 12, vol. 20, 1982, p. 1707.
22. Kline, S. J.; Cantwell, B. J.; and Lilley, G. M.: editors. 1980-1981, AFOSR-HTTM-STANFORD Conference on Complex Turbulent Flows (1980-1981).

## FLOW IN A MODEL TURBINE STATOR\*

R.C. Buggeln, S.J. Shamroth and W.R. Briley  
Scientific Research Associates, P.O. Box 498, Glastonbury, CT 06033

## INTRODUCTION

A major problem area associated with the successful design and operation of modern gas turbine engines is the engine hot section. Of particular interest in the present study is the turbine. The turbine section represents a considerable challenge as it contains significant regions of complex three-dimensional flow including both aerodynamic and heat transfer phenomena. In particular, the turbine flow field contains several features which makes its analysis a formidable problem. These include complex geometry, multiple length scales, three-dimensional effects, possible strong secondary flows, possible flow separation at off-design operation, possible transonic effects, and possibly important unsteady effects.

In considering possible approaches to this problem, three approaches are evident. These are (i) inviscid analyses, (ii) inviscid analyses with boundary layer corrections, and (iii) full Navier-Stokes analyses. In view of the complex nature of the flow, the need to predict heat transfer and flow losses, the possible appearance of separation and strong secondary flows, etc., the present effort is focusing upon a Navier-Stokes approach to the three-dimensional turbine stator problem. The advantages of a full Navier-Stokes approach are clear since when combined with a suitable turbulence model these equations represent the flow and heat transfer physics discussed previously. In particular, the Navier-Stokes equations accurately represent possible separated regions and regions of significant secondary flow. In addition, the Navier-Stokes approach allows representation of the entire flow field by a single set of equations thus avoiding problems associated with representing different regions of the flow by different equations and then matching flow regions. Although turbulence modelling remains a problem, turbulence modelling presents the same difficulties with alternate approaches, and alternate approaches cannot necessarily represent the highly complex flow physics to be found in general turbine stator flow fields.

However, application of the Navier-Stokes equations to the turbine stator problem is not an easy task. The presence of complex geometries, rapidly varying flows, strong secondary flows and the need for adequately resolving the various physical scales are items which all present their own problems. Nevertheless, with continued improvement of numerical solution techniques the Navier-Stokes approach is becoming a practical procedure for the three-dimensional turbine stator problem.

## APPROACH

The present approach solves the ensemble-averaged Navier-Stokes equations via the Linearized Block Implicit (LBI) of Briley and McDonald (Ref. 1). Boundary conditions for subsonic inflow and outflow (the usual case) set upstream stagnation pressure, upstream stagnation temperature, upstream flow angle, and downstream static pressure. Additional conditions used are density derivative on the inflow (upstream boundary), and velocity and temperature second derivatives on

\*Work done under NASA Contract NAS3-24358.

the downstream boundary. On the cascade blade no-slip conditions and a zero pressure gradient condition are applied along with either a specified temperature or a specified heat transfer rate. In applying the no-slip wall conditions, proper wall resolution is mandatory. In general, the first grid point off the wall is taken so as to place a point in the viscous sublayer. The governing equations are written in general tensor form and solved in a body-fitted coordinate system. Details of the governing equations, numerical technique, grid construction, turbulence model, etc. are given in Refs. 2-4.

Using this approach in a previously described HOST effort (Refs. 3 and 4), two- and three-dimensional calculations were made for a turbine cascade. The purpose of the first effort was two-fold; (i) demonstration of the Navier-Stokes current capability in simulating these complex flow fields, and (ii) demonstration that the Navier-Stokes approach is a practical procedure with current technology. The first goal was reached via heat transfer and pressure distribution comparisons with experimental data for two-dimensional cases and a demonstration three-dimensional laminar cascade calculation. The quantitative comparisons for the two-dimensional cases showed good agreement between calculation and measurement; a comparison between predicted and measured heat transfer on a C3X airfoil with specified transition location is shown in Fig. 1. In addition, the demonstration three-dimensional calculation showed many of the expected features such as the saddle point singularity in the endwall boundary layer as shown in Fig. 2.

In addition to providing accurate simulations, the Navier-Stokes approach, if it is to be practical, must have reasonable run times to convergence. Long run times, even if leading to accurate simulations, would severely hamper application of the Navier-Stokes procedure to practical turbine stator or rotor problems on a regular basis. Computer run time is based upon run time per time step and number of time steps to convergence. In regard to the first item, the current Navier-Stokes cascade code, BMINT/CX, requires approximately  $1.2 \times 10^{-4}$  secs/grid point/time steps on a CRAY-1 computer which for typical two-dimensional cases having 3500 grid points gives 0.4 secs/time step. A three-dimensional case of 70,000 grid points, due to additional code overhead, would require approximately 12 secs per time step. In regard to time steps to convergence selected cases showed essential convergence for engineering purpose in 70-100 time steps whereas other cases required approximately 150 time steps convergence. Both of these cases are within the constraints required for the Navier-Stokes approach to be a practical approach to the turbine blade row problem.

#### PRESENT EFFORTS

The present turbine cascade program focuses upon three efforts: (i) further code development with particular emphasis on increasing the number of grid points which can be run on a given machine, (ii) further convergence studies, and (iii) calculation of the turbulent flow through a three-dimensional turbine stator. In regard to the first objective, this will be passive to the user and will simply allow for a higher resolution calculation by utilizing out-of-core storage. The second objective would detail the convergence properties of the procedure. Results obtained in Refs. 3 and 4 indicate rapid convergence insofar as engineering predictions are concerned. Under the present effort these convergence properties are considered in more detail for a wider variety of cases.

The initial test case chosen for the convergence study was the Turner turbine cascade (Ref. 5). The convergence study calculation was run with a 'C' grid containing 113 pseudo-azimuthal grid points, and 30 pseudo-radial grid points. High wall resolution was obtained with the first point off the wall being approximately  $1.5 \times 10^{-5}$  chords from the blade surface. In regard to convergence, several criteria can be considered. These include surface pressure distribution, maximum normalized residual and pressure coefficient at the stagnation point. In regard to these factors, it should be noted that in the present calculations it is the converged steady state flow field which is the item of interest. Therefore, although the current numerical procedure solves the unsteady flow equations, it is not necessary and, in fact, is uneconomical to obtain a time-accurate solution when seeking steady state solutions. Instead, matrix preconditioning techniques are used to obtain a converged solution as rapidly as possible. In these studies, the calculation was initiated from a very simple flow field in which the velocity magnitude and static pressure were set constant throughout the flow with the velocity flow angle a function of axial location. Very simple profiles were used near the blade surface to bring the velocity to the no-slip condition.

A plot showing the maximum normalized flow residual is presented in Fig. 3. As can be seen, the maximum residual drops slightly over 4 orders of magnitude in 150 time step iterations and then levels. In general, based upon previous experience, three orders of magnitude drop in residual give convergence suitable for many engineering applications. However, in addition to monitoring the residual behavior, it is necessary to consider the flow field dependent variable behavior. Based upon experience one sensitive item is the pressure coefficient at the stagnation point where  $C_p$  is taken as  $(p - p_{ref}) / \frac{1}{2} \rho_{ref} q_{ref}^2$ . The reference quantities are taken from the inflow boundary and consequently since only total pressure, total temperature and flow angle are specified, these may vary with time. The results show the variation of stagnation point  $C_p$  with time-step iteration number. The calculation was run with an inflow Mach number of approximately 0.24; on an inviscid basis this should lead to a stagnation point  $C_p$  of approximately 1.015. The present results converge to a value of approximately 1.005 for the Navier-Stokes simulation. As can be seen in Figs. 4 and 5, the stagnation point  $C_p$  was ostensibly converged at 100 time steps although some slight oscillations occurred until 150 time steps. These results clearly indicate the rapid convergence of the present Navier-Stokes procedure and its potential for use as an engineering tool. It is expected that this type of convergence shall also be obtained for three-dimensional calculations.

In addition to these results, the present effort is aiming at the three-dimensional cascade problem for turbulent flow. A calculation shall be done for a modern turbine cascade design, the convergence properties of the procedure assessed and if possible, a comparison made between computed flow field values and values obtained by experimental measurement.

#### REFERENCES

1. Briley, W.R. and McDonald, H.: Solution of the Multidimensional Compressible Navier-Stokes Equations by a Generalized Implicit Method. *Journal of Computational Physics*, Vol. 24, pp. 372-397, 1977.
2. Shamroth, S.J., McDonald, H. and Briley, W.R.: Prediction of Cascade Flow Fields Using the Averaged Navier-Stokes Equations. *ASME Journal of Engineering for Gas Turbines and Power*, Vol. 196, pp. 383-390, 1984.
3. Yang, R.-J., Weinberg, B.C., Shamroth, S.J. and McDonald, H.: Numerical Solutions of the Navier-Stokes Equations for Two- and Three-Dimensional Turbine Cascades with Heat Transfer. NASA CR-174929. 1985.
4. Weinberg, B.C., Yang, R.-J., McDonald, H. and Shamroth, S.J.: Calculation of Two- and Three-Dimensional Transonic Cascade Flow Fields Using the Navier-Stokes Equations. ASME Paper 85-GT-66, 1985.
5. Turner, A.B.: Local Heat Transfer Measurements on a Gas Turbine Blade. *Journal of Mechanical Engineering Sciences*, Vol. 13, 1971.

# HEAT TRANSFER COEFFICIENT

CASE 144

$M_{\text{exit}} = 0.90$

$Re_{\text{exit}} = 2.43 \times 10^6$

$T_w/T_g = 0.75$

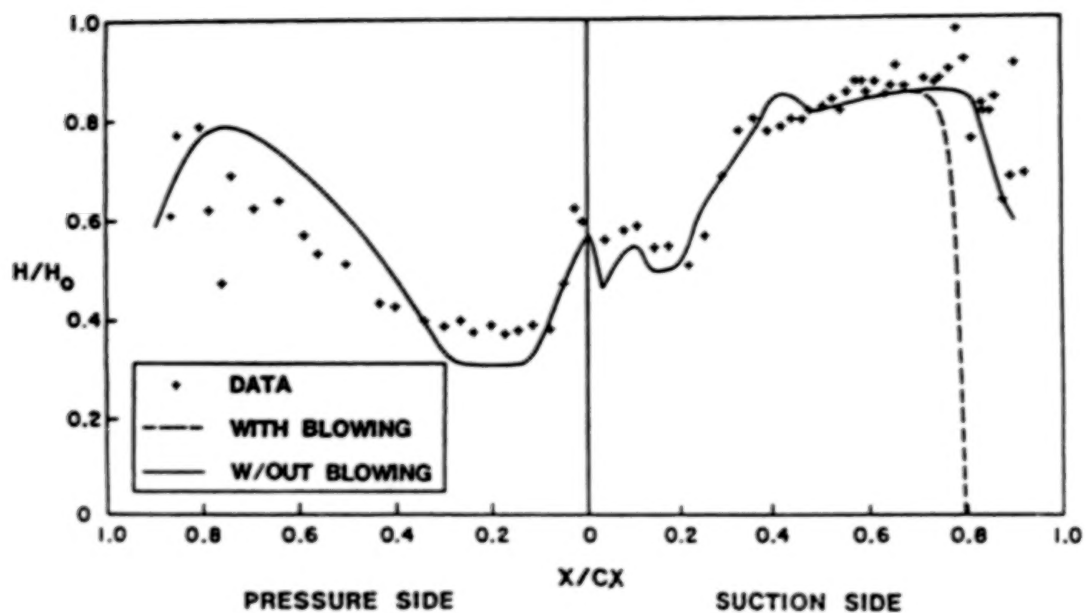
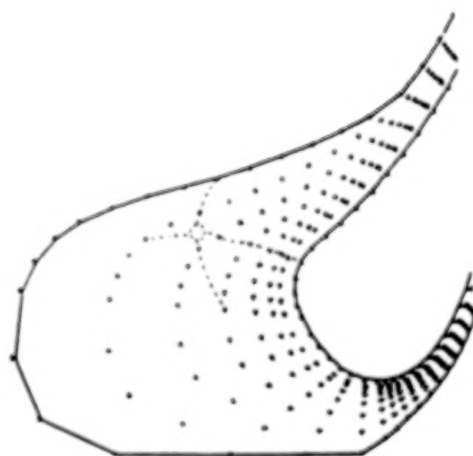
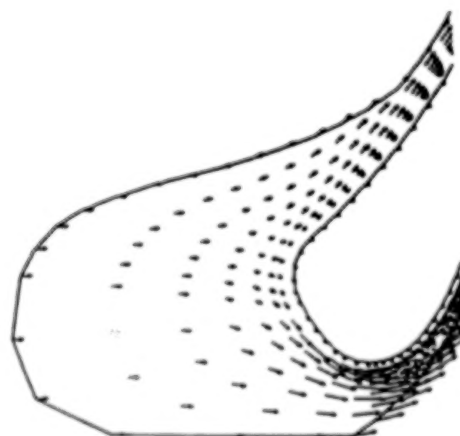


FIGURE 1



(a) VECTOR PLOT ON 0.135% SPANWISE PLANE



(b) VECTOR PLOT ON MIDSPAN PLANE

FIGURE 2

### CONVERGENCE RATE

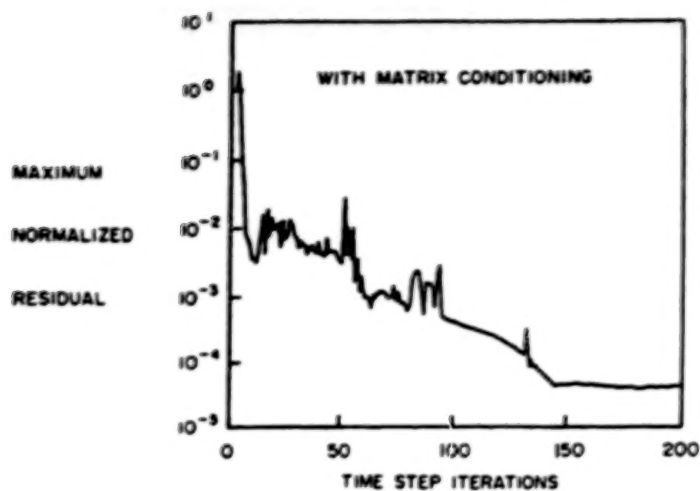


FIGURE 3

### CONVERGENCE OF PRESSURE AT STAGNATION POINT

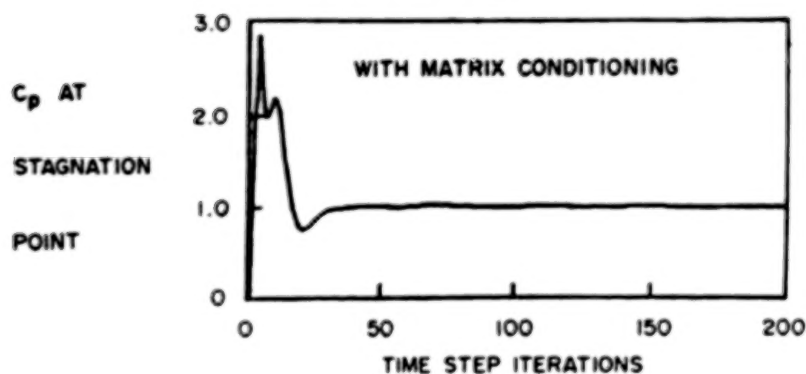


FIGURE 4

### CONVERGENCE OF PRESSURE AT STAGNATION POINT

REDUCED SCALE PLOT

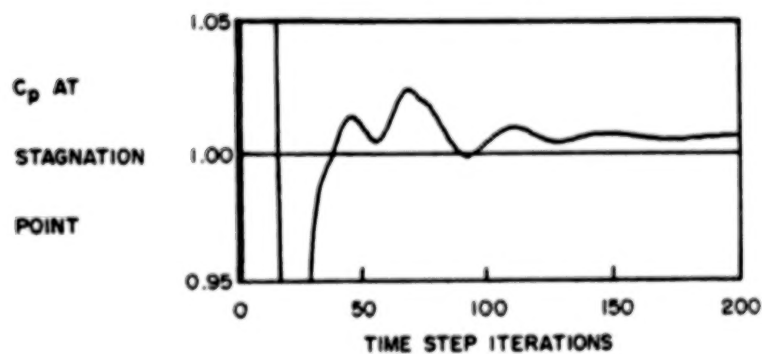


FIGURE 5

## 3D INELASTIC ANALYSIS METHODS FOR HOT SECTION COMPONENTS\*

L.T. Dame, P.C. Chen, M.S. Hartle and H.T. Huang  
General Electric Company  
Aircraft Engine Business Group

## INTRODUCTION

The objective of this research is to develop analytical tools capable of economically evaluating the cyclic time-dependent plasticity which occurs in hot section engine components in areas of strain concentration resulting from the combination of both mechanical and thermal stresses. The techniques developed must be capable of accommodating large excursions in temperatures with the associated variations in material properties including plasticity and creep.

The overall objective of this research program is to develop advanced 3-D inelastic structural/stress analysis methods and solution strategies for more accurate and yet more cost-effective analysis of combustors, turbine blades, and vanes. The approach has been to develop a matrix of formulation elements and constitutive models, three increasingly more complex formulation models and three increasingly more complex constitutive models.

The three constitutive models have been developed in conjunction with optimized iteration techniques, accelerators, and convergence criteria within a framework of dynamic time incrementing. These consist of a simple model, a classical model, and a unified model. The simple model performs time-independent inelastic analyses using a bilinear stress-strain curve and time-dependent inelastic analyses using a power-law creep equation. The second model is the classical model of Professors Walter Haisler and David Allen (Reference 1) of Texas A&M University. The third model is the unified model of Bodner, Partom, et al. (Reference 2). All models were customized for a linear variation of loads and temperatures with all material properties and constitutive models being temperature dependent.

The three formulation models developed are an eight-noded midsurface shell element, a nine-noded midsurface shell element and a twenty-noded isoparametric solid element. Both of the shell elements are obtained by "degenerating" 3D isoparametric solid elements and then imposing the necessary kinematic assumptions in connection with the small dimension of the shell thickness (References 3 and 4). The eight-noded element uses Serendipity shape functions and the nine-noded element uses Lagrange shape functions. The eight-noded element uses Gaussian quadrature for numerical integration, with nodal and surface stresses being obtained by extrapolation/mapping techniques. Lobatto quadrature is being used with the nine-noded element to effectively provide for direct recovery of the stresses and strains at the surfaces and node points. The eight-noded element has an excellent combination of accuracy and economy in the normal element aspect range encountered when modeling most hot section components. The nine-noded Lagrangian formulation overcomes the shear locking problem experienced when the

\*Work done under NASA Contract NAS3-23698.

1011-88V

element size-versus-thickness-aspect ratio becomes very large. The twenty-noded isoparametric element uses Gaussian quadrature.

A separate computer program has been developed for each combination of constitutive model-formulation model. Each program provides a functional, stand alone capability for performing cyclic nonlinear structural analysis. In addition, the analysis capabilities incorporated into each program can be abstracted in subroutine form for incorporation into other codes or to form new combinations. These programs will provide the structural analyst with a matrix of capabilities involving the constitutive models-formulation models from which he will be able to select the combination that satisfies his particular needs.

The program architecture employs state-of-the-art techniques to maximize efficiency, utility, and portability. Among these features are the following:

(i) User Friendly I/O

- o Free format data input
- o Global, local coordinate system, (Cartesian, Cylindrical, Spherical)
- o Automatic generation of nodal and elemental attributes
- o User-controlled optional print out
  - Nodal Displacements
  - Nodal Forces
  - Element Forces
  - Element Stresses and Strains

(ii) Programming Efficiency

- o Dynamic core allocation
- o Optimization of file/core utilization
- o Blocked column skyline out-of-core equation solver

(iii) Accurate and Economical Solution Techniques

- o Right-hand side pseudoforce technique

- o Accelerators for the iteration scheme
- o Convergence criteria based on both the local inelastic strain and the global displacements.

The ability to model piecewise linear load histories was also included in the finite element codes. Since the inelastic strain rate could be expected to change dramatically during a linear load history, it is important to include a dynamic time-incrementing procedure.

Three separate time step control criteria are used. These are the maximum stress increment, maximum inelastic strain increment, and maximum rate of change of the inelastic strain rate. The minimum time step calculated from the three criteria is the value actually used. Since the calculations are based on values readily available from the previous time step, little computational effort is required.

These formulation models and constitutive models have been checked out extensively against both theory and experiment. Figure 1 shows the correlation between Bodner's model in the eight-noded mid-surface shell element (MSS8) and both experiment and other predictions (Reference 5). Figures 2 through 6 illustrate the predictability of the classical (Haisler-Allen) model. Figure 7 shows a comparison of both Bodner's model and the simple model to both experiment and independent predictions (Reference 6).

These nine programs, both source (Fortran 77) and compiled have been installed and checked out on the NASA-Lewis CRAY-1 machine. The interactive deck generator has been installed on the NASA-Lewis AMDAHL machine.

Table 1 shows the lines of source code for each of the nine computer programs. These numbers do not include the interactive deck generator.

Table I. Lines of Source Code

		Elements		
		20 Noded	8 Noded	9 Noded
Constitutive Models	Simple	8300	13,800	17,900
	Haisler-Allen	9200	16,300	19,000
	Bodner	7300	13,800	17,600

Since these programs use dynamic core allocation, they can be recompiled to size for any specific machine. They are presently loaded for  $10^7$  bytes

of core. At this size, the maximum problem would be approximately 4000 nodes and 1000 elements.

#### REFERENCES

1. Allen, D.H., and Haisler, W.E., "A Theory of Thermoplastic Materials," Computers and Structures, Vol. 13, pp. 129-135, 1981.
2. Bodner, S.A., Partom, I., and Partom, Y., "Uniaxial Cyclic Loading of Elastic-Viscoplastic Material," ASME J. Appl. Mech., Vol. 46, p. 805, 1979.
3. Chang, T.Y. and Sawamiphakdi, K., "Large Deformation Analysis of Shells by Finite Element Method," Comp. and Struct., Vol. 13, pp. 331-340, 1981.
4. Chang, T.Y. and Sawamiphakdi, K., "Nonlinear Finite-Element Analysis of Shells with Large Aspect Ratio," presented at the Nonlinear Structural Analysis Workshop, NASA-Lewis Research Center, April 19 and 20, 1983.
5. Stouffer, D.C., "A Constitutive Representation for IN100," Air Force Materials Laboratory, AFMAL-TR-81-4039, 1981.
6. Bodner, S.R., "Representation of Time Dependent Mechanical Behavior of Rene' 95 by Constitutive Equations," Air Force Materials Laboratory, AFML-TX-79-4116, 1979.

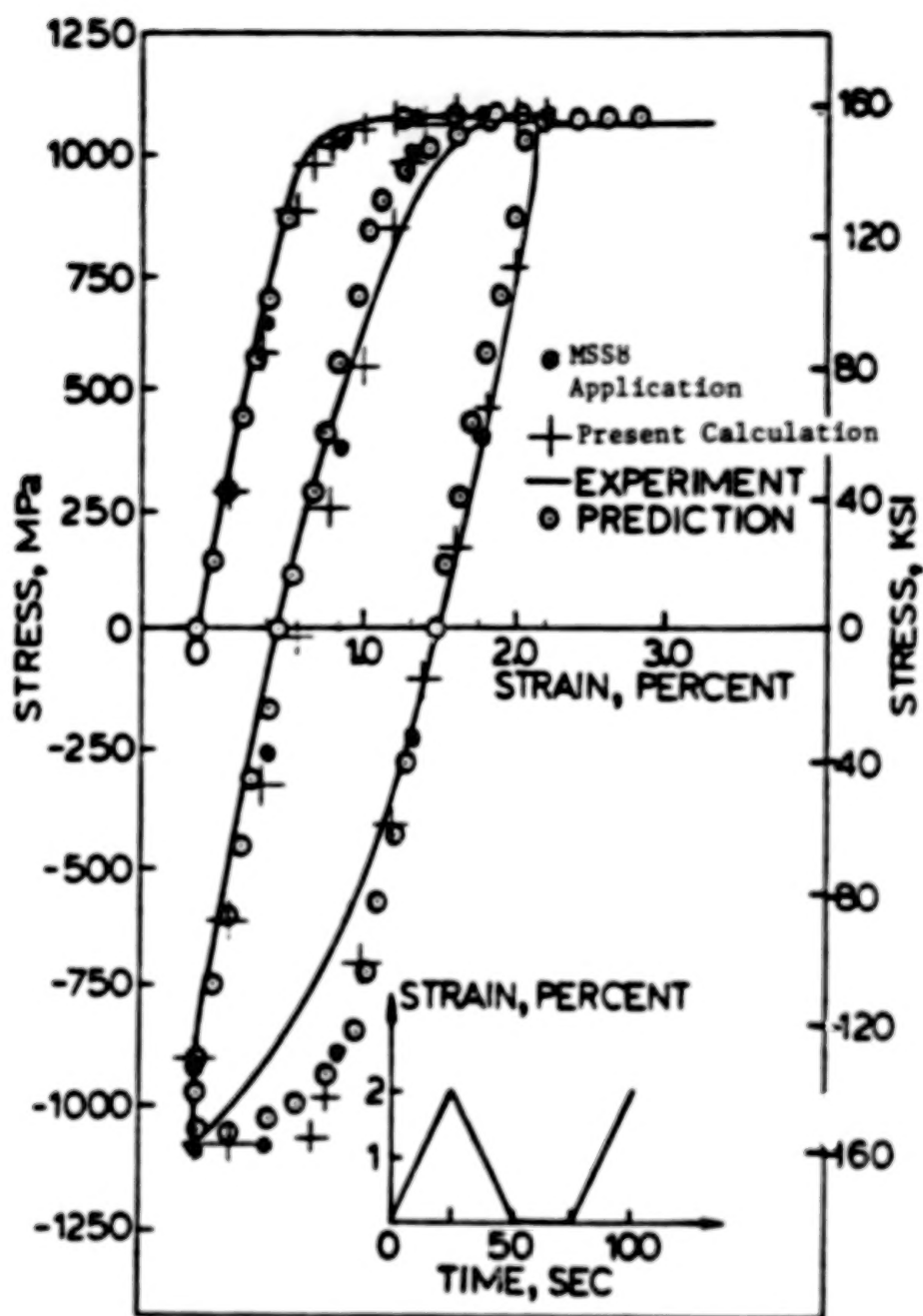


Figure 1. Displacement Controlled Cycling Results.

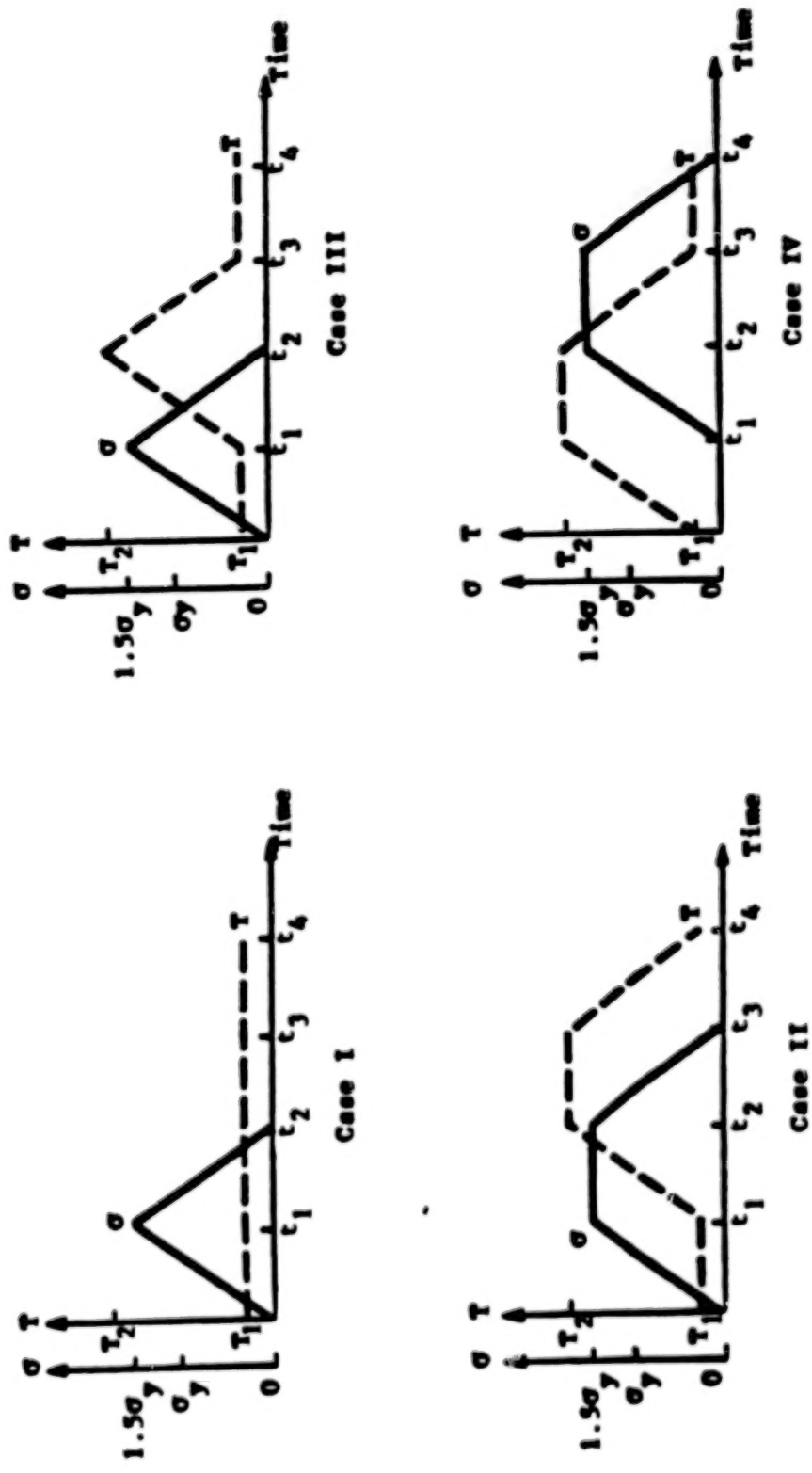


Figure 2. Load Histories for Plasticity Example.

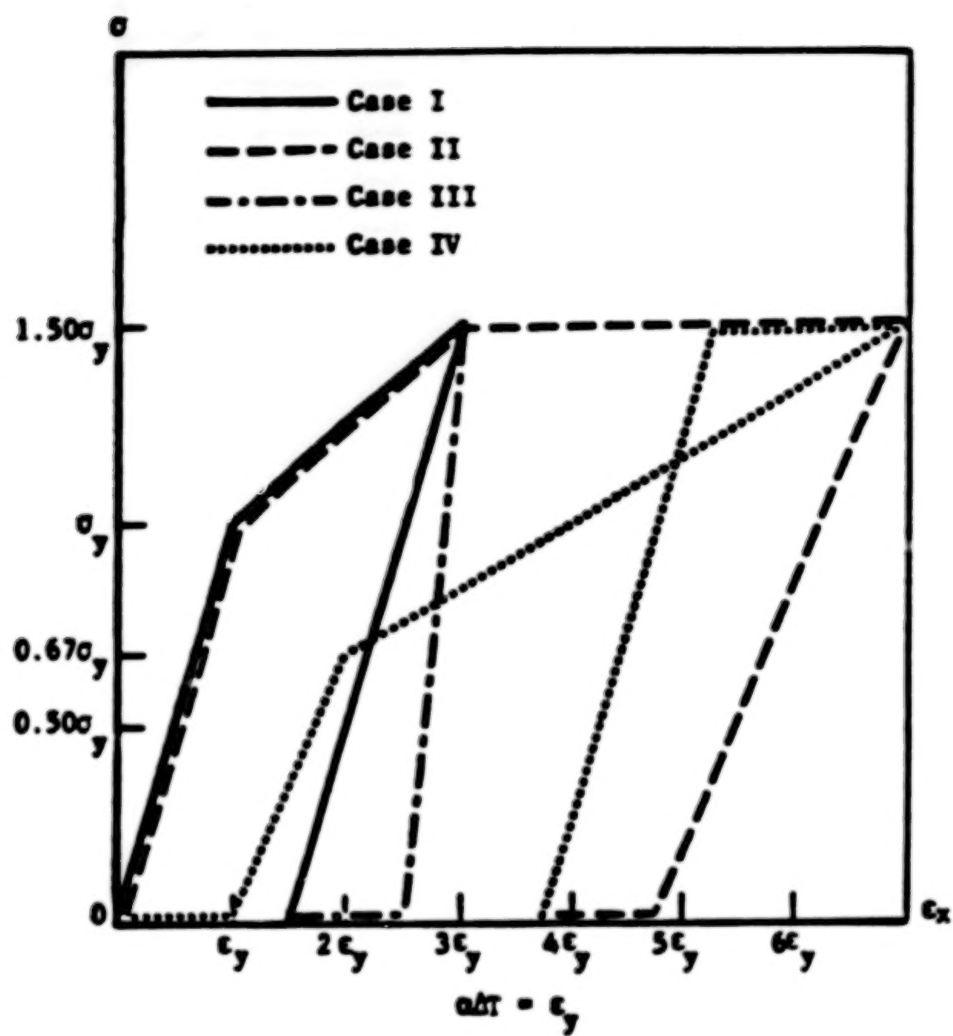


Figure 3. Results of Plasticity Example.

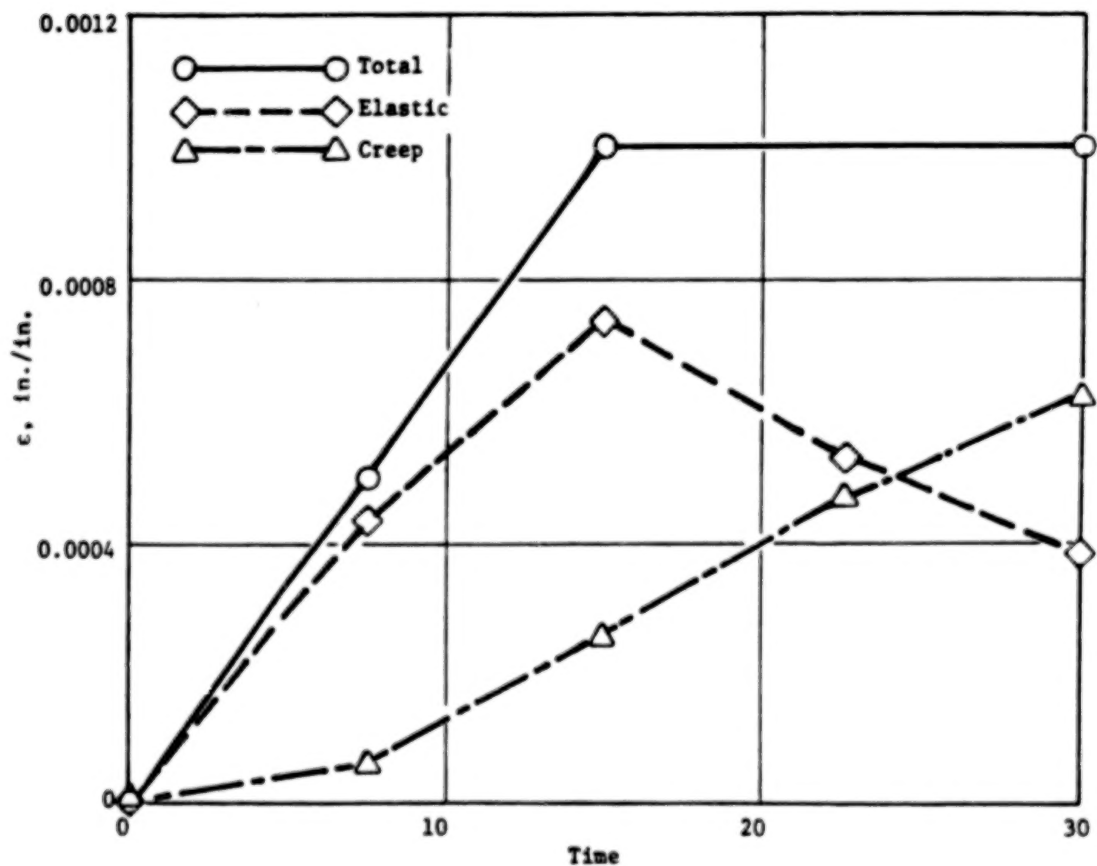
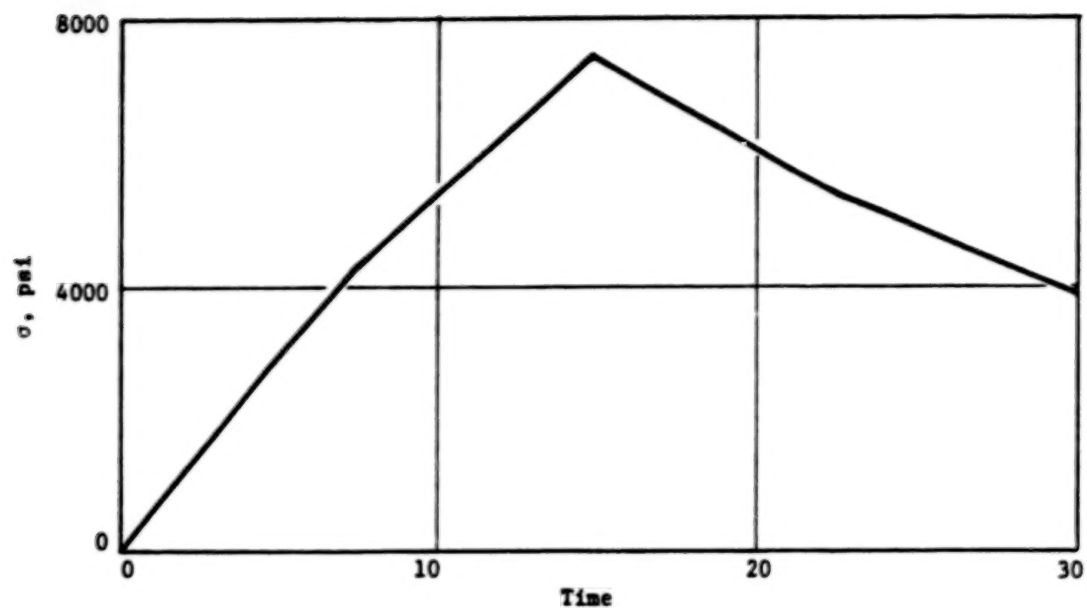


Figure 4. Strain Controlled Creep.

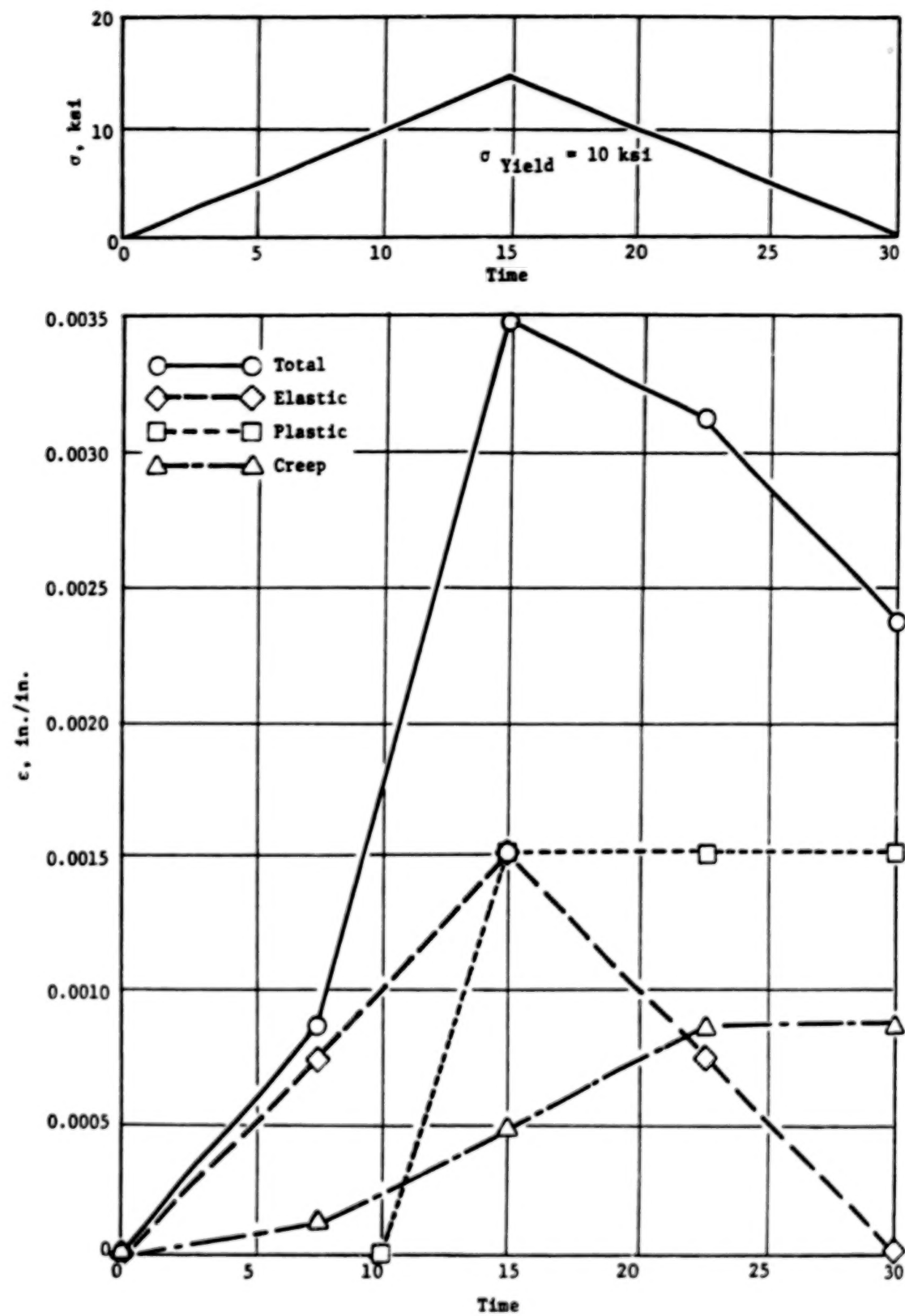


Figure 5. Stress Controlled Cycling with Combined Plasticity and Creep.

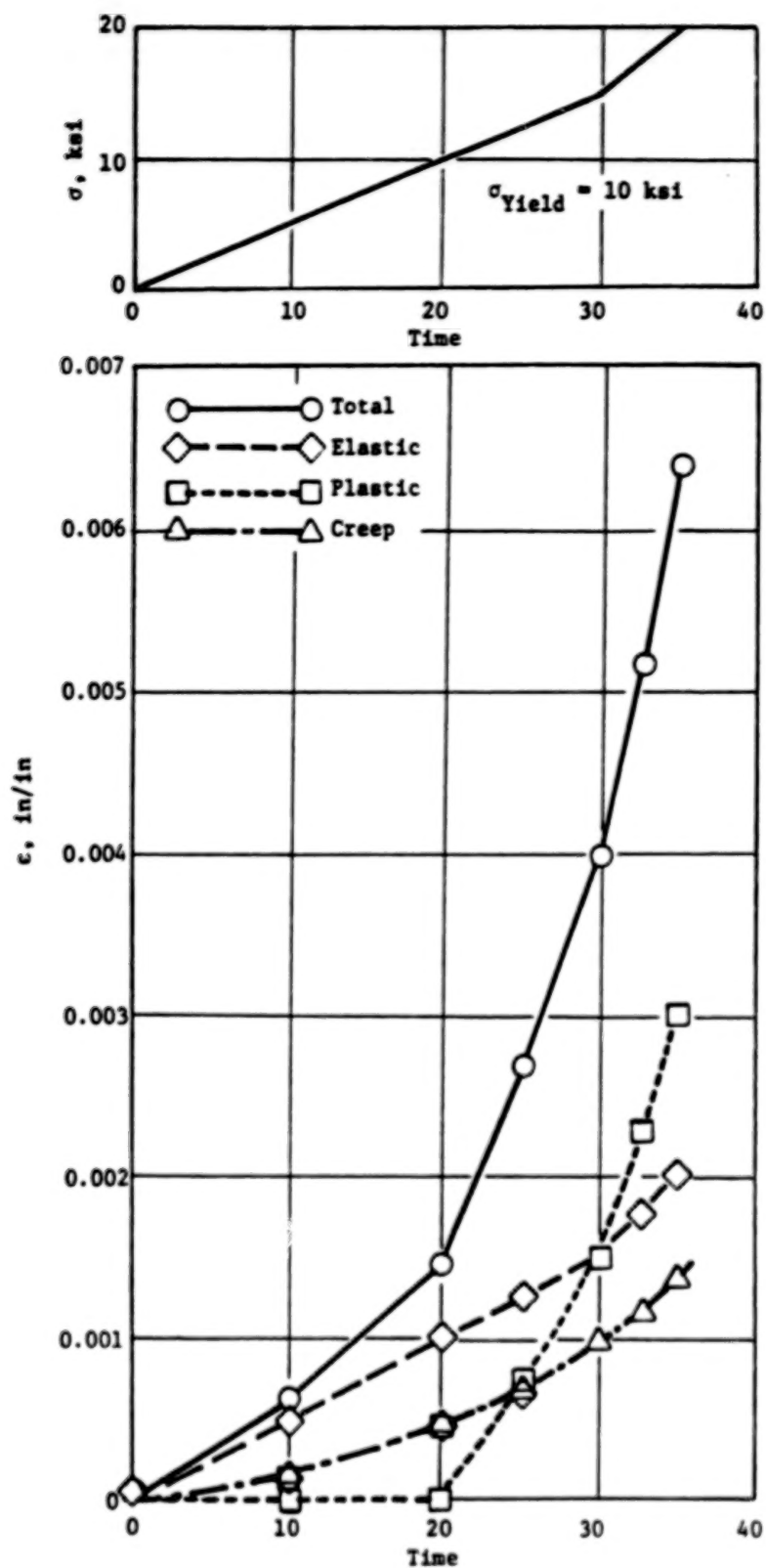


Figure 6. Stress Controlled Combined Plasticity and Creep.

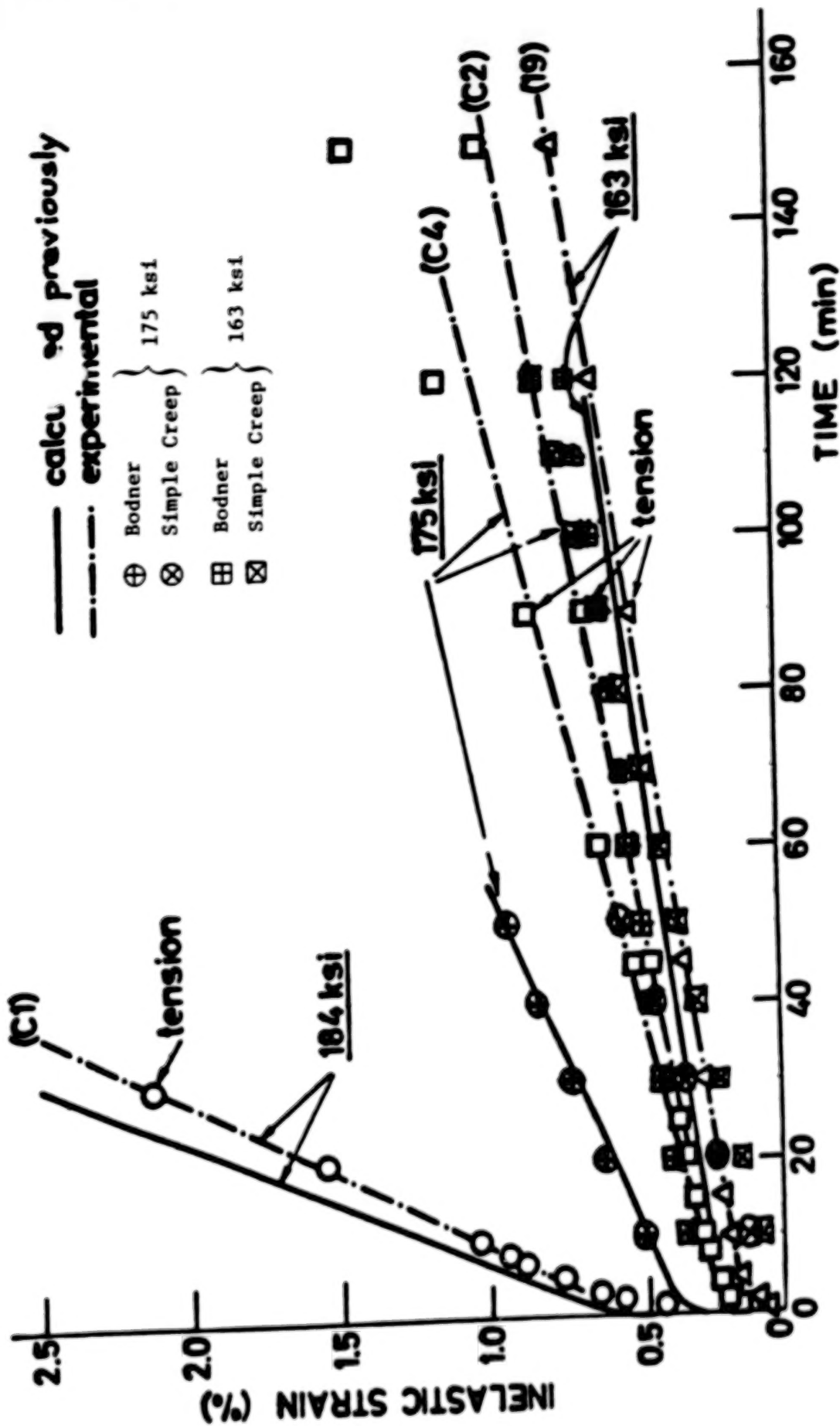


Figure 7. Comparison of Bodner Mode to Simple Creep.

### 3-D INELASTIC ANALYSIS METHODS FOR HOT SECTION COMPONENTS\*

E. S. Todd  
United Technologies Corporation  
Pratt & Whitney

The objective of this program is to produce a series of new computer codes that permit more accurate and efficient three-dimensional inelastic structural analysis of combustor liners, turbine blades, and turbine vanes. Each code embodies a progression of mathematical models for increasingly comprehensive representation of the geometrical features, loading conditions, and forms of nonlinear material response that distinguish these three groups of hot section components.

Software in the form of stand-alone codes is being developed by Pratt & Whitney (P&W) with assistance from three uniquely qualified subcontractors: MARC Analysis Research Corporation (MARC), United Technologies Research Center (UTRC), and the State University of New York at Buffalo (SUNY-B). Special finite element models are being constructed by MARC, while mechanics of materials models and constitutive models are being assembled by UTRC. Development of advanced formulation (boundary element) models is being shared by P&W and SUNY-B. Verification of the various analysis packages is being done by P&W.

The technical effort of the Inelastic Analysis Methods program is divided into two 24-month segments: a base program, and an optional program exercised at the discretion of the government. The first year (Task I) of the base program dealt with linear theory in the sense that stresses or strains and temperatures in generic modeling regions are linear functions of the spatial coordinates, and solution increments for load, temperature and/or time are extrapolated linearly from previous information. The second half of the base program (Task II), as well as the option program (Tasks IV and V), extend the models to include higher-order representations of deformations and loads in space and time and deal more effectively with collections of discontinuities such as cooling holes and coating cracks. Work on Task II (polynomial theory) has been completed, and the results are given in the Second Annual Status Report (ref. 1). Base program computer codes, hereafter referred to as MOIM (Mechanics of Materials Model), MHOST (MARC-HOST), and BEST (Boundary Element Stress Technology), have been developed and delivered to NASA-Lewis Research Center.

Three increasingly sophisticated constitutive models are employed by MOIM, MHOST, and BEST to account for inelastic material behavior (plasticity, creep) in the elevated temperature regime. The simplified model assumes a bilinear approximation of stress-strain response and glosses over the complications associated with strain rate effects, etc. The state-of-the-art model partitions time-independent (plasticity) and time-dependent (creep) in the conventional way, invoking the Von Mises yield criterion and standard (isotropic, kinematic, combined) hardening rules for the former, and a power law for the latter. Walker's viscoplasticity theory (ref. 2), which accounts for the interaction between creep/relaxation and plasticity that occurs under cyclic loading conditions, has been adopted as the advanced constitutive model.

---

\*Work done under NASA Contract NAS3-23697.

20117-884

In brief, MOMM is a stiffness method finite element code that utilizes one-, two- and three-dimensional arrays of beam elements to simulate hot section component behavior. Despite limitations of such beam model representations, the code will be useful during early phases of component design as a fast, easy to use, computationally efficient tool. All of the structural analysis types (static, buckling, vibration, dynamics), as well as the three constitutive models mentioned above, are provided by MOMM. Capabilities of the code have been tested for a variety of simple problem discretizations (ref. 1).

The MHOST code employs both shell and solid (brick) elements in a mixed method framework to provide comprehensive capabilities for investigating local (stress/strain) and global (vibration, buckling) behavior of hot section components. Over the last decade, in order to support their commercially available software, the MARC Corporation has accumulated a great deal of technical expertise creating new, improved algorithms that will significantly reduce CPU (central processing unit) time requirements for three-dimensional analyses. The MHOST code development has taken advantage of this expertise. Second generation (Task II) MHOST code is operational and has been tested with a variety of academic as well as engine-related configurations (ref. 1).

Successful assembly of the all-new BEST code was possibly the most important accomplishment of the base program effort. The challenge of extending basic theory and algorithms to encompass inelastic dynamic effects in three-space was met by combining the special skills and efforts of the research and programming teams at SUNY-B and P&W. As with MOMM and MHOST, the second version of BEST is executable and has been exercised with both small and large test cases (ref. 1). While MHOST and BEST are currently viewed as complementary, they are also competitors; and overall performance on large inelastic models will be watched with interest as the codes mature.

Experimental data from the Benchmark Notch Test program (ref. 3) are being used to verify the stress analysis capabilities of the Inelastic Methods codes. Nominal dimensions of the benchmark notch specimen are shown in figure 1. Finite element and boundary element meshes for one-quarter of the specimen gage section are shown in figure 2. Measured notch root stress-strain behavior for initial uploads of several specimens is summarized in figure 3. Correlation between the MHOST predictions and the measured strains is very good (fig. 4). Simulation of first-cycle notch root behavior with BEST has also proven to be quite accurate (fig. 5).

Work on Task IV (special functions theory) and application of the codes to representative turbine blade and vane configurations is in process, and will be described at the Fourth Annual HOST Workshop.

#### REFERENCES

1. Wilson, R. B.; Bak, M. J.; Nakazawa, S., and Banerjee, P. K.: "3-D Inelastic Analysis Methods for Hot Section Components (Base Program): Second Annual Status Report" (Draft), March 1985.
2. Walker, K. P.: "Research and Development Program for Nonlinear Structural Modeling with Advanced Time-Temperature Dependent Constitutive Relationships," NASA CR-165533, November 25, 1981.
3. Domas, P. A.; Sharpe, W. N.; Ward, M.; and Yau, J.: "Benchmark Notch Test for Life Prediction," NASA CR-165571, June 1982.

## Benchmark Notch Specimen

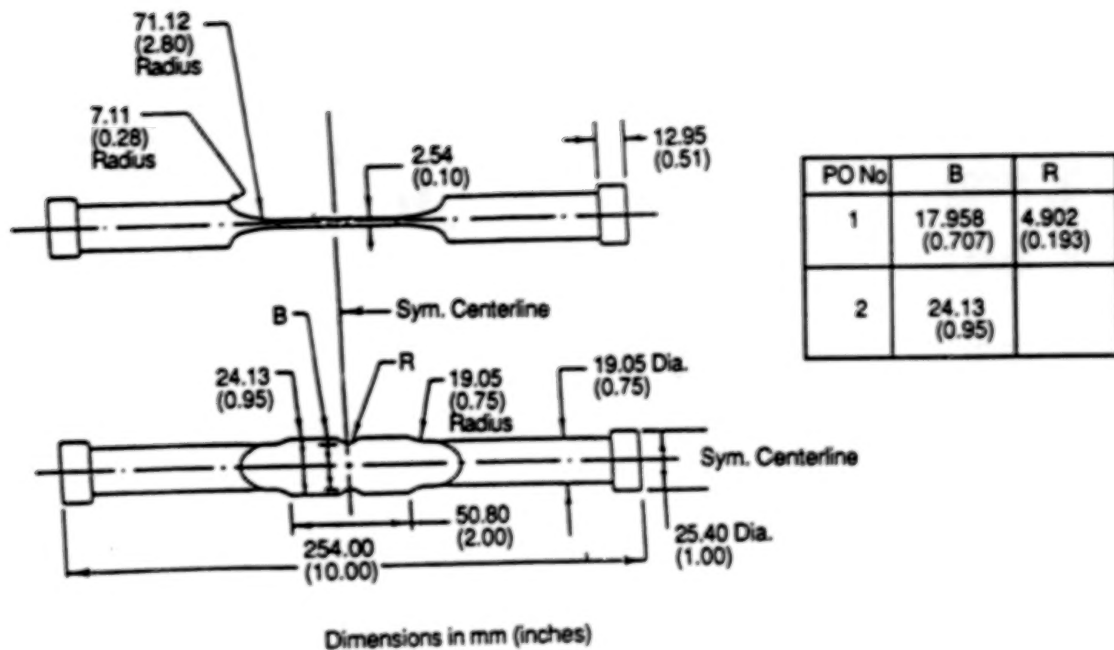


Figure 1

## Meshes Used In Benchmark Notch Analysis

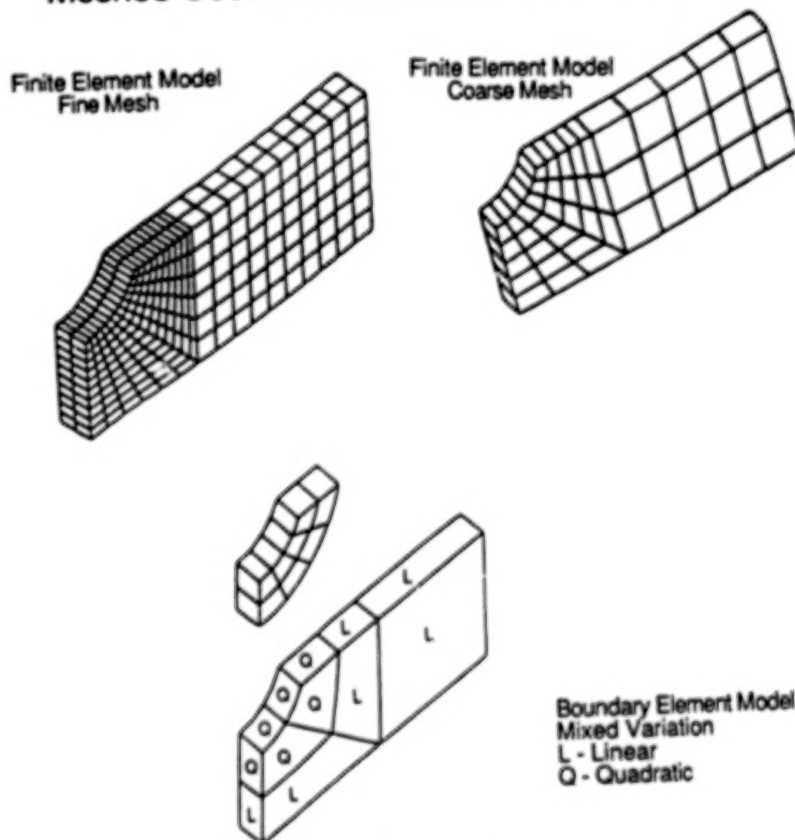


Figure 2

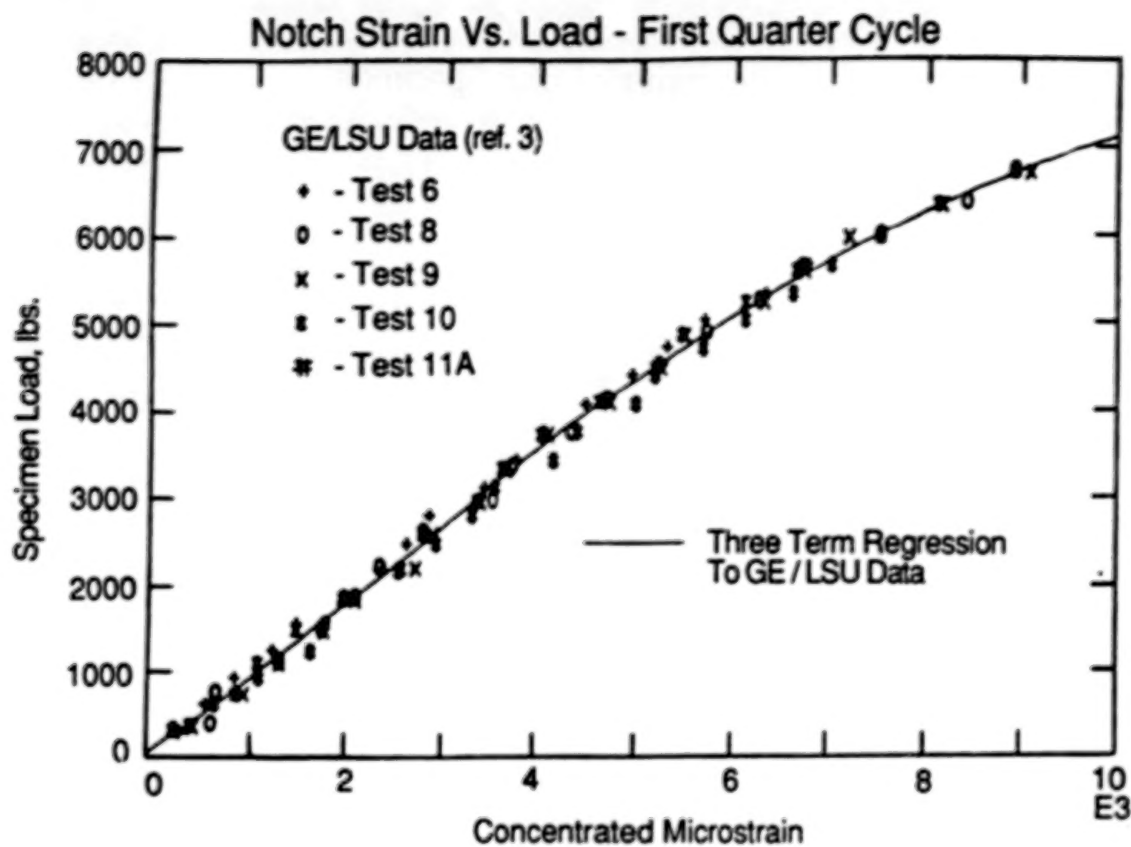


Figure 3

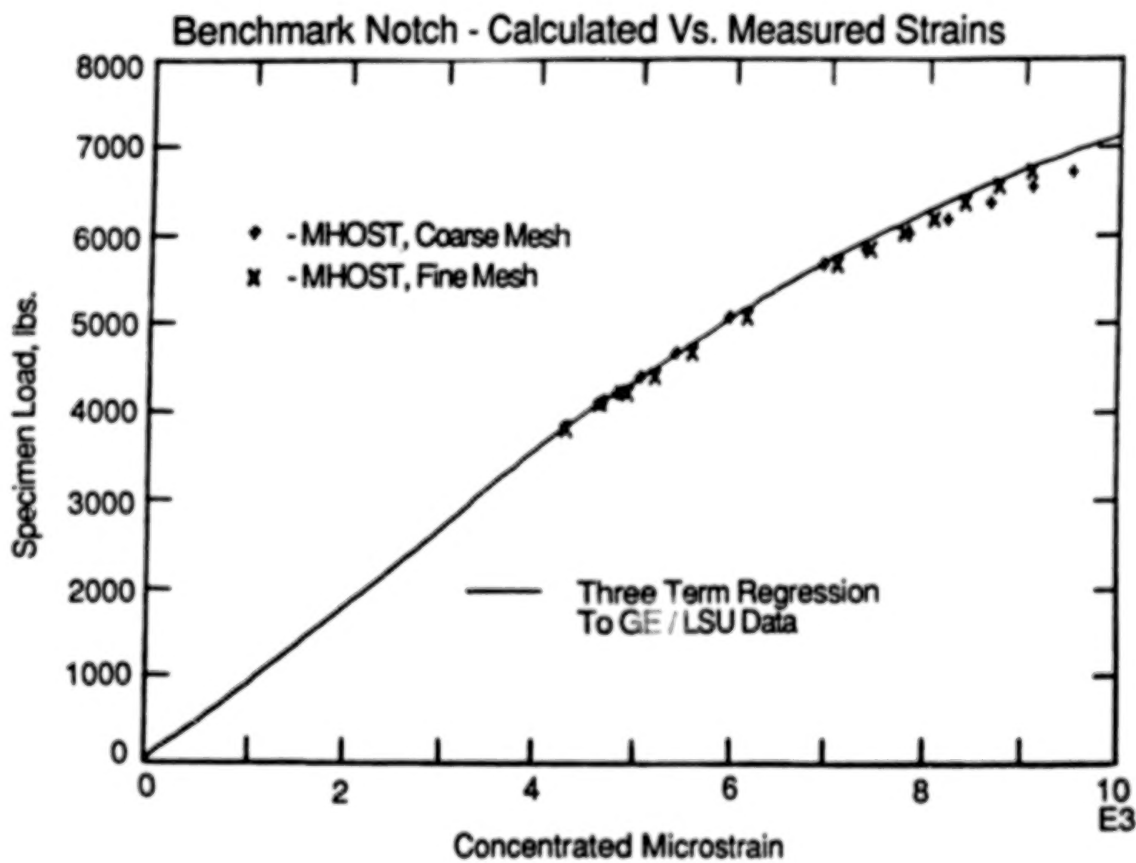


Figure 4

### Cyclic Behavior At Root Of Specimen Notch

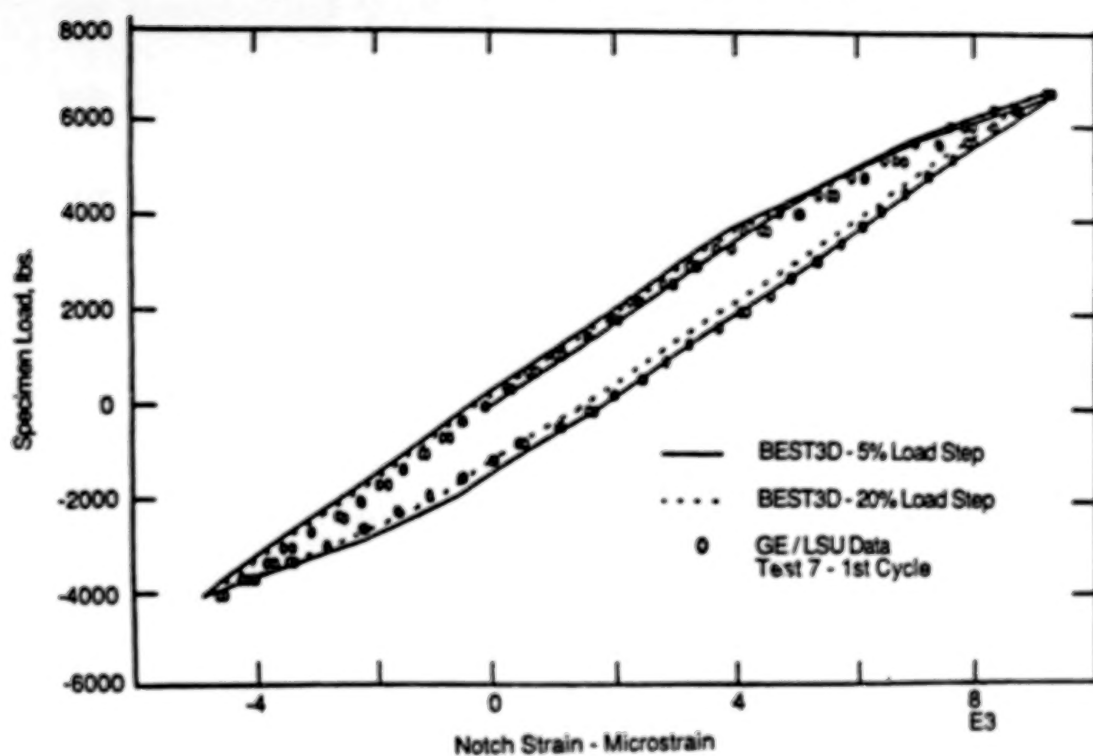


Figure 5

## COMPONENT SPECIFIC MODELING\*

R.L. McKnight and M.T. Tipton  
General Electric Company  
Aircraft Engine Business Group

## INTRODUCTION

The overall objective of this program is to develop and verify a series of interdisciplinary modeling and analysis techniques that have been specialized to address three specific hot section components. These techniques will incorporate data as well as theoretical methods from many diverse areas including cycle and performance analysis, heat transfer analysis, linear and nonlinear stress analysis, and mission analysis. Building on the proven techniques already available in these fields, the new methods developed through this contract will be integrated to provide an accurate, efficient, and unified approach to analyzing combustor burner liners, hollow air-cooled turbine blades, and air-cooled turbine vanes. For these components, the methods developed will predict temperature, deformation, stress, and strain histories throughout a complete flight mission.

The base program for the component specific modeling effort is illustrated in Figure (1). Nine separate tasks have been arranged into two parallel activities. The component specific structural modeling activity in Figure (2), is directed towards the development of the analytical techniques and methodology required in the analysis of complex hot section components. The component specific thermomechanical load mission modeling effort illustrated in Figure (3), provides for the development of approximate numerical models for engine cycle, aerodynamic, and heat transfer analyses of hot section components.

Thermomechanical Load Mission Modeling

In the thermomechanical load mission modeling portion of the program, we developed the Thermodynamic Engine Model (TEM). The TEM is complete and has been developed as a computational tool used to define mission station profiles of gas path engine flow variables and rotor speeds as a function of defined input conditions. Basic input variables for the model are mach number (M), altitude (h) power level (PL). Generated within the model for select aerodynamic stations in the combustor and high pressure gas flowpath are, gas weight flow ( $\dot{W}$ ), temperature (t), pressure (p) and the associated fan (N1) and core (N2) speeds.

The development of the TEM was presented at last years workshop so attention is directed at the capability and accuracy of the model. The accuracy of the model was evaluated relative to the steady state performance computer code (a cycle deck) of a production engine. Noting that the model is based upon multidimensional interpolation of stored data, the maximum error of

---

\*Work done under NASA Contract NAS3-23687.

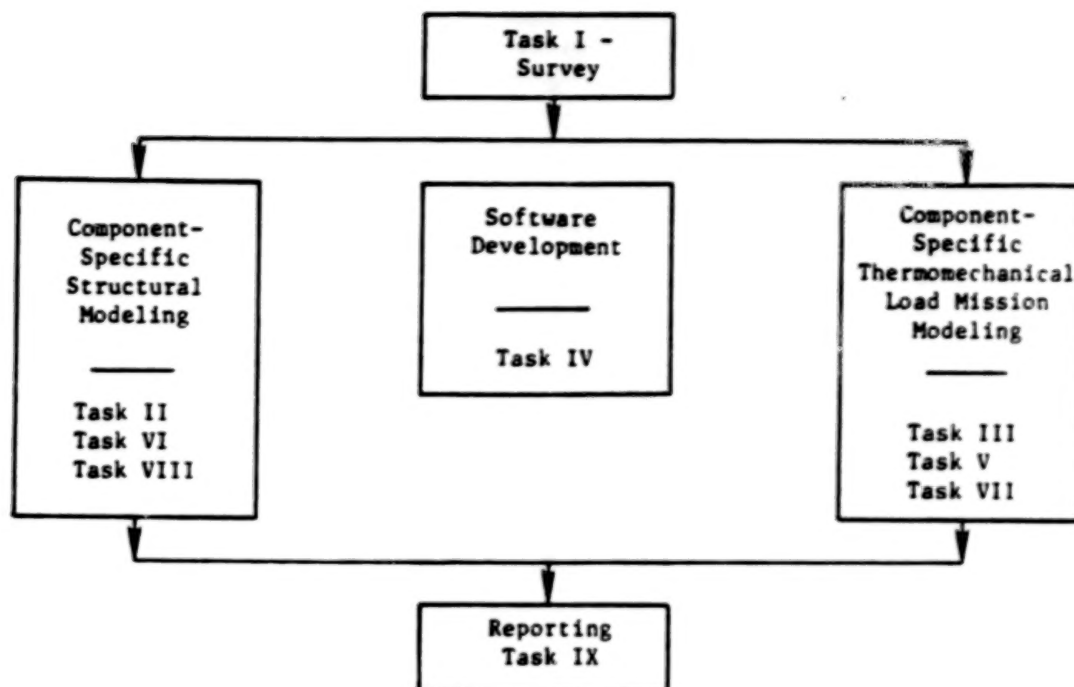


Figure 1. Component Specific Modeling Base Program.

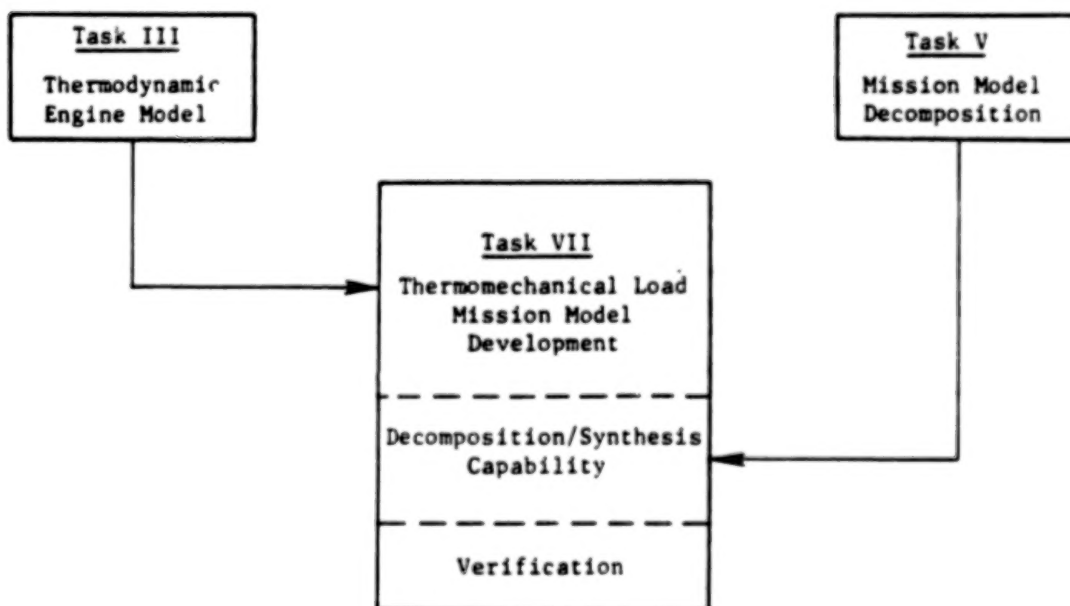


Figure 2. Component Specific Thermomechanical Load Mission Modeling.

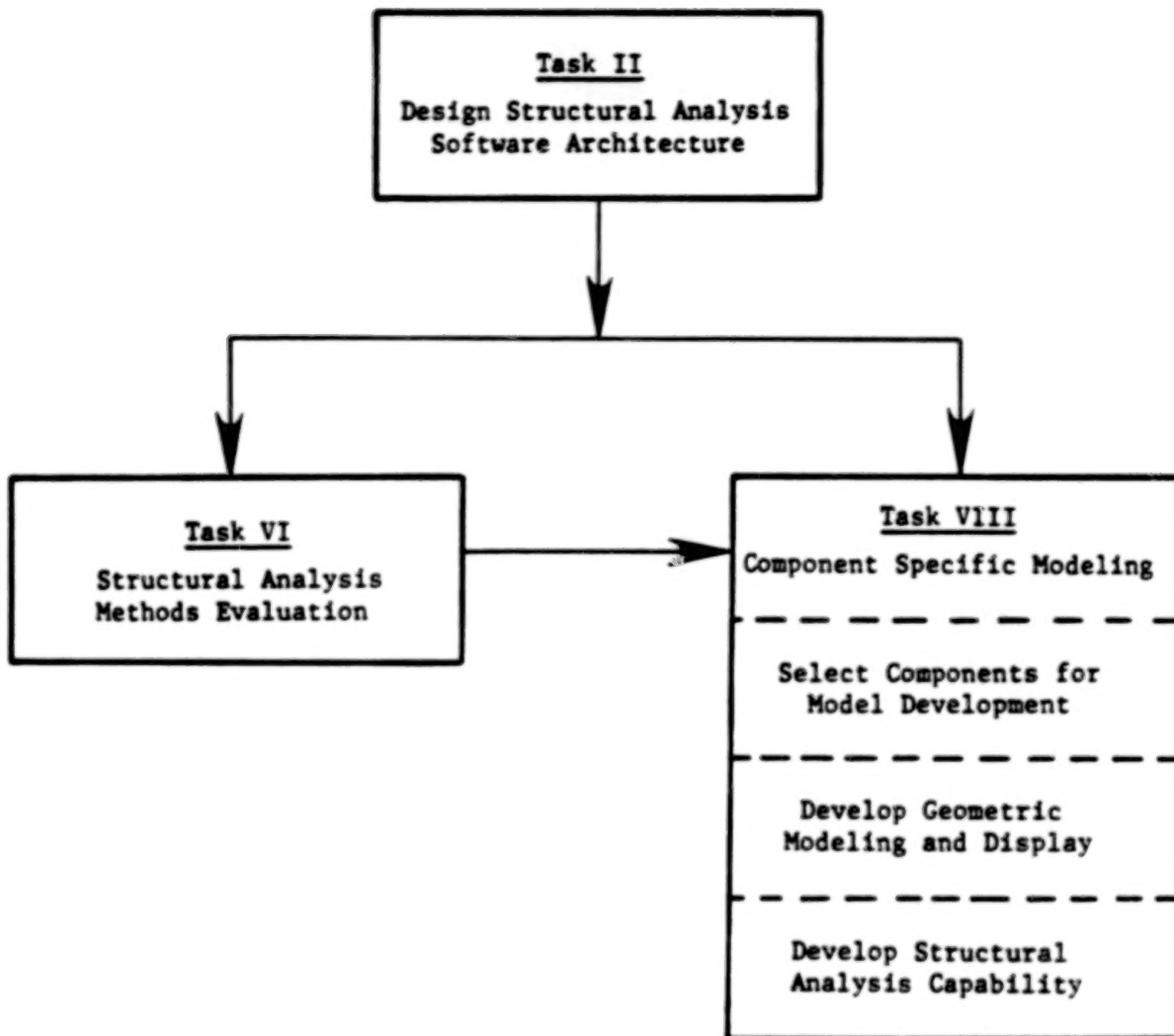


Figure 3. Component Specific Structural Modeling.

the model should occur at a position the greatest distance from known data points. Illustrated in Figure (4) is an example of a situation in which a region is bounded by four data points with the test point at its center. The region is then subdivided into four rectangles each possessing its own interpolation logic and associated error. Error curves imposed on such a figure illustrate two facts:

- (1) The error surface is approximately parabolic and attains its maximum value at the center of the region.
- (2) Each quadrant has its own error surface and discontinuities occur where they meet.

Table 1 shows a brief summary of the accuracy level achieved for the TEM. Column 2 shows the average of all test point errors. Columns 3, 4, and 5 show the value that is exceeded 2, 4 and 11 times (1%, 2%, and 5% of the 220 error values). Note that all data in this figure refers to the worst-case test points. Since the error surfaces are approximately parabolic in shape, the average error in each quadrant is approximately half of the maximum error, and the overall error is approximately half of the average error listed.

Table 1 Validation Case Error Analysis

	Error Exceeded N Times			
	Average	N = 2	N = 4	N = 11
P <sub>2</sub>	0.03%	1%	1%	1%
P <sub>3</sub>	0.23%	1.3%	1.2%	1.0%
FNIN1	0.49%	1.8%	1.8%	1.8%
XN25	0.17%	0.7%	0.6%	0.5%
T <sub>2</sub>	0.08%	5°	5°	5°
T <sub>3</sub>	2.1°	10°	10°	10°
T <sub>41</sub>	11°	47°	47°	35°

#### Component Specific Structural Modeling

The concepts and techniques developed in the NASA supported ESMOSS program have provided the basis to create an efficient modeling system for specific hot section engine components. The modeling and subsequent discretization of model geometries is component dependent and follows either a recipe or a data point/curve fit format. The capability to create geometric and discretized models of these components is well under development and examples of such are illustrated in Figure (5).

#### Finite Element Methods

This phase of the program centers on the development, implementation and evaluation of both new and existing analytical methods for the non-linear stress analysis of select hot section components. Within the structural

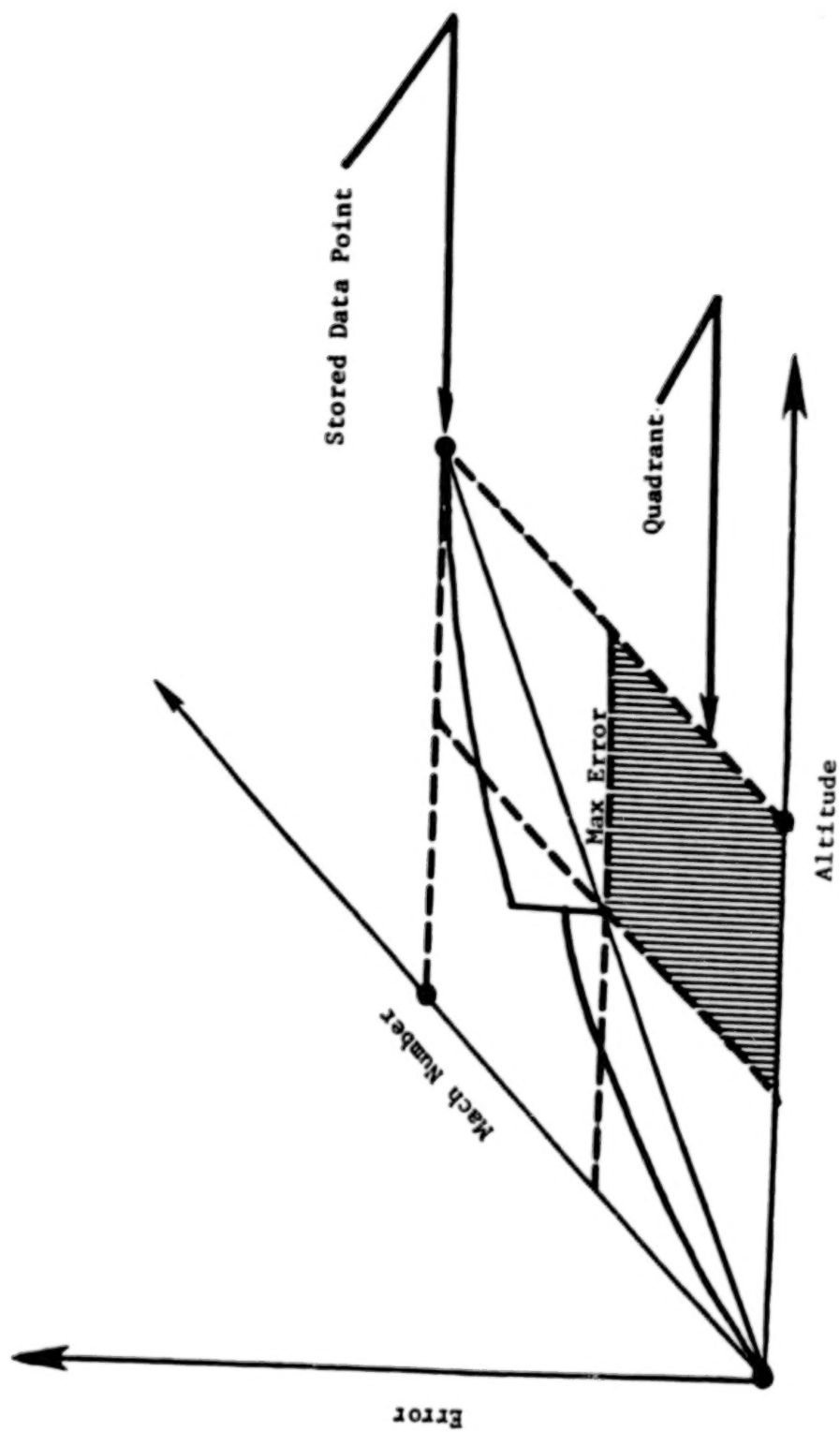
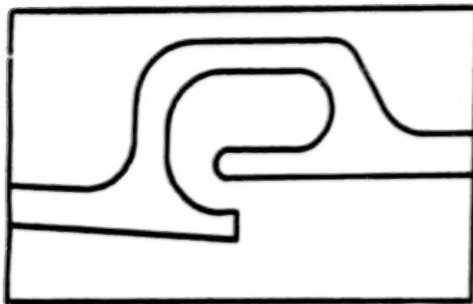
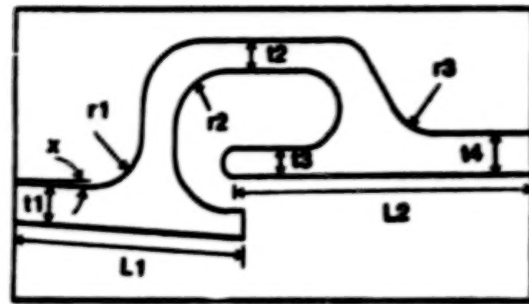


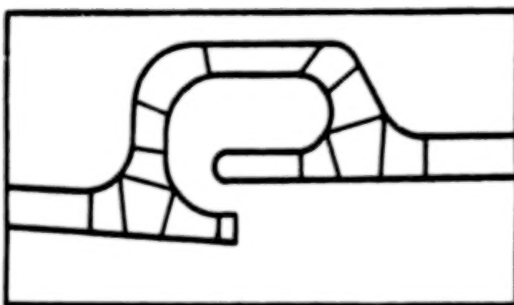
Figure 4. Quadrant Error Distribution.



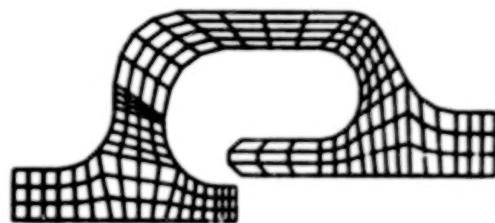
Typical Nugget



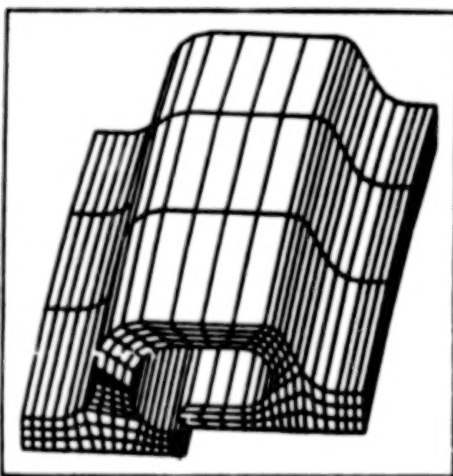
Physical Input Parameters



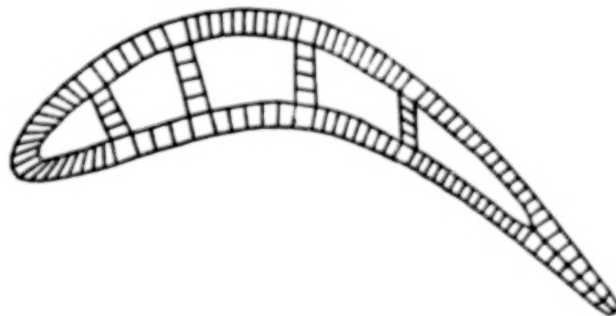
Master Region Definition



2D Model



3D Model



Turbine Blade with Cavities

Figure 5. Examples of Component Specific Structural Modeling Capabilities.

analysis software exist several new and innovative concepts. Embedded in the code are several classical solution algorithms, three constitutive models, "self-adaptive" type solution techniques, and the capability for remeshing and mesh refinement.

As noted, several classical solution techniques have been included in the code. It is intended that such a selection of solution algorithms will afford the user (and the programmer) a choice as to method of solution as well as to provide for adaptability of the code to problem definition and machine residency. Solution algorithms currently include:

(A) SESOL

- A sparse matrix solver with a skyline storage scheme.

(B) COLSOL

- A vectorized column solver.

(C) Frontal Method

- Currently under development.

In addition to our library of select solution techniques, we have included in our analysis code an alternate method for defining convergence of the numerical solution. Our current work has focused upon vector norms due to their structure, computational simplicity and potential applicability to self-adaptive solution strategies and techniques. Vector norms provide the means by which both quantitative and qualitative statements can be made between associated vectors. Noting that our current solution scheme is an iterative technique, we are looking at the convergence of a series of vectors (i.e. displacements). In such an application it is necessary to determine when a solution has been obtained as well as to determine the quality of that solution.

Convergence of the numerical solution can be determined on either the local or global level. Currently within our code we use a local or point-by-point method and the present work represents an effort to see if a global scheme has applicability.

There can be defined infinitely many norms but the three most common norms are the  $l_p$  norms,  $||\cdot||_p$  for  $P = 1, 2$ , and  $\infty$ .

$$\begin{aligned} ||\cdot||_1 &= |\bar{x}_1| + |\bar{x}_2| + |\bar{x}_3| + \dots + |\bar{x}_N| \\ ||\cdot||_2 &= \left[ |\bar{x}_1|^2 + |\bar{x}_2|^2 + |\bar{x}_3|^2 + \dots + |\bar{x}_N|^2 \right]^{1/2} \\ ||\cdot||_\infty &= \max \{ |\bar{x}_1|, |\bar{x}_2|, |\bar{x}_3|, \dots, |\bar{x}_N| \} \end{aligned}$$

The above norms are special cases of the vector norm:

$$\left( \sum_{i=1}^N (\bar{x}_i)^p \right)^{1/p}$$

To utilize the norms defined above the concept of relative and absolute error can be defined (1) for any two vectors, the absolute error can be written as:

$$E^A = \|\bar{x}_i\| - \|\bar{x}_{i-1}\|$$

And the relative error written as:

$$E^R = \frac{\|\bar{x}_i\| - \|\bar{x}_{i-1}\|}{\|\bar{x}_{i-1}\|}$$

The expression for relative error tends to be far more applicable to our needs and its structure lends itself conveniently to the formulation of convergence criteria in iterative methods. Convergence can be assumed when the magnitude of a norm, or the difference between norms of successive iterations is less than some predefined tolerance. From the above, six separate norms were defined, and then included in the code for evaluation.

$$1. \frac{\|\bar{x}_i\|_1 - \|\bar{x}_{i-1}\|_1}{\|\bar{x}_{i-1}\|_1}$$

$$2. \frac{\|\bar{x}_i\|_1 - \|\bar{x}_{i-1}\|_1}{\|\bar{x}_i\|_1}$$

$$3. \frac{\|\bar{x}_i\|_2 - \|\bar{x}_{i-1}\|_2}{\|\bar{x}_{i-1}\|_2}$$

$$4. \frac{\|\bar{x}_i\|_2 - \|\bar{x}_{i-1}\|_2}{\|\bar{x}_i\|_2}$$

$$5. \frac{\|\bar{x}_i\|_\infty - \|\bar{x}_{i-1}\|_\infty}{\|\bar{x}_{i-1}\|_\infty}$$

$$6. \frac{\|\bar{x}_i\|_\infty - \|\bar{x}_{i-1}\|_\infty}{\|\bar{x}_i\|_\infty}$$

To provide the user with a choice and offer some versatility in the modeling of non-linear material behavior, three separate material constitutive

models have been coded into the analysis program. These constitutive models are:

- (A) Haisler-Allen model
- (B) Bodner's Model
- (C) A Simplified Model

We are using remeshing and mesh refinement techniques in our self-adaptive solution strategies. Work is focused on the examination of methods and techniques required to upgrade the mesh and criteria by which this process is activated. Methods of mesh refinement could include progressive subdivision, mesh realignment and upgrade of element order. Criteria for mesh refinement may include strain energy density, elemental stress/strain gradients, inter-element stress/strain gradients and nodal stress comparisons. We are currently in the evaluation phase of the above and our strategy for proceeding in this area involves the following:

- (a) Select an analytical model with known solutions.
- (b) Analyze several meshes of different density.
- (c) Use the 20 noded brick element to evaluate remeshing criteria.

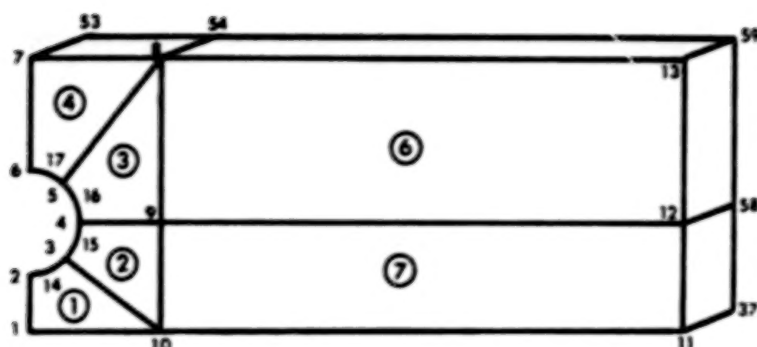
For our initial work we have selected a semi-infinite plate with a circular hole near the edge. Figure (6) shows the recipe parameters and master region definition for the problem and Figure (7) illustrates the coarse, medium and refined meshes for such a model.

For a 2D plane stress conditions, the models were fixed at the left edge and subjected to a uniform tensile stress at the right edge. Comparisons were then made as to the adequacy of computed surface stresses and inter-element stress distributions. A summary of the above appear in Figures (8) and (9).

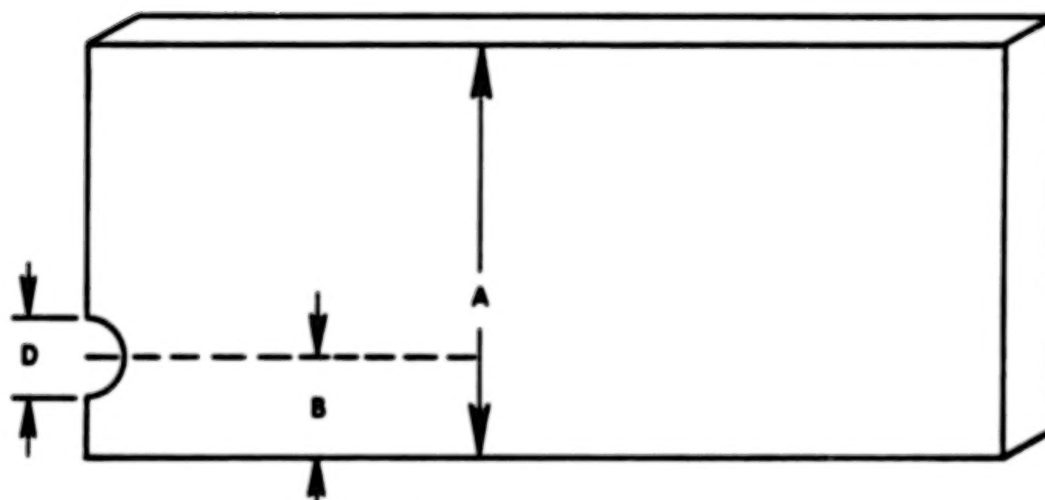
#### CONCLUSIONS

When complete, this program will provide the engineer with a total non-linear stress analysis system designed for hot section component parts. The system will enable the engineer to address the effects of mission variation and design changes on component response while demonstrating efficiency and versatility in application. The system will provide new and innovative technology in the area of non-linear high temperature stress analysis and in turn make a significant contribution to assessing hot section component durability.

# Master Region Model



## Parameters



A = Height  
 B = Relative Placement of Center  
 of Hole Relative to A  
 D = Diameter of Hole

Input: D as a Percentage of the Height  
 B as a Percentage of the Height

Note: The Hole Cannot be Placed Beyond the  
 Limits of the Beam

(Ex) Input = 20%, 23.334%  
 Set a 0.2A Hole  
 0.2334 A Center

Figure 6. Recipe Parameters and Master Region Model for Plate with Hole.

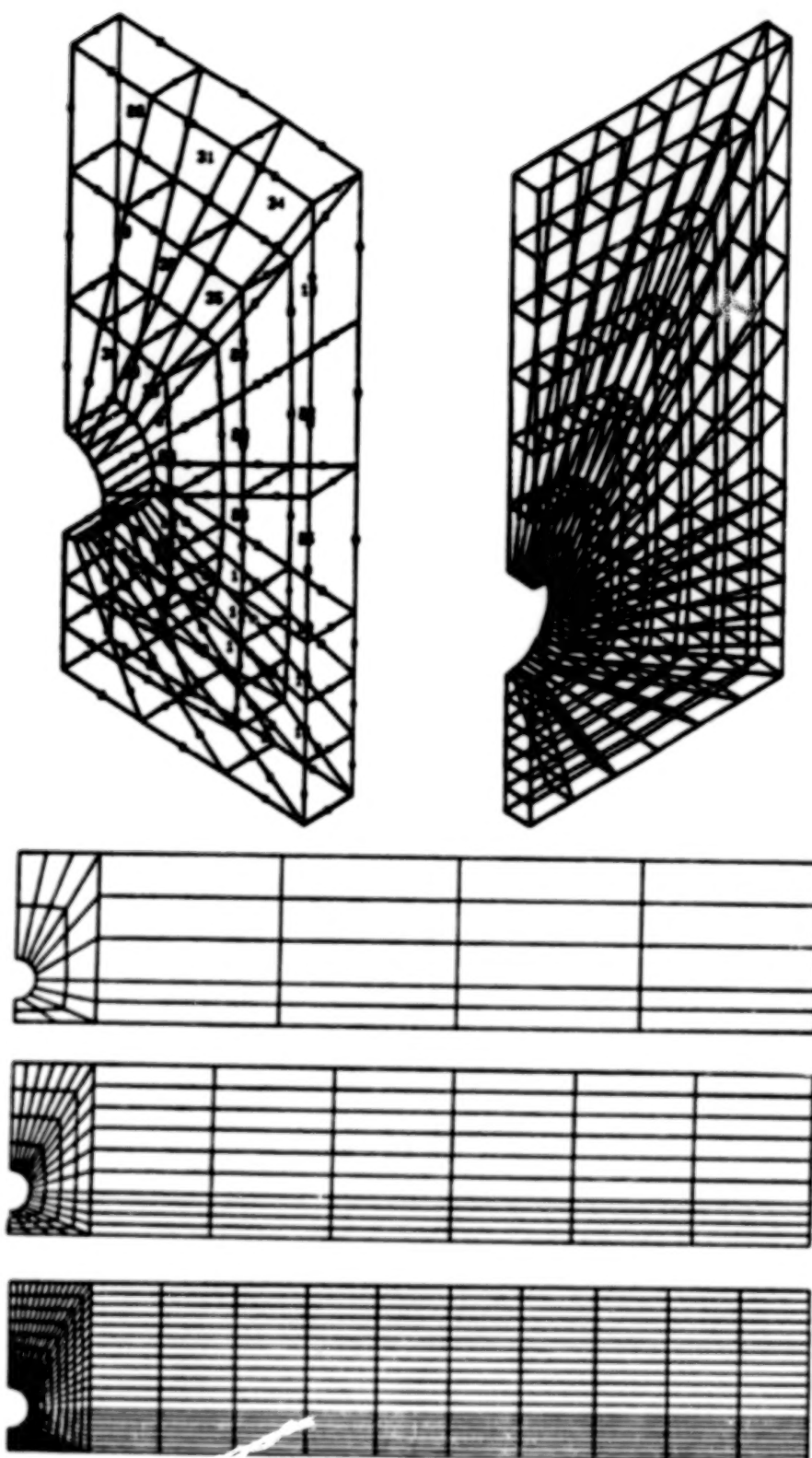


Figure 7. Discretized Mesh Geometries for Semi-Infinite Plate Model.

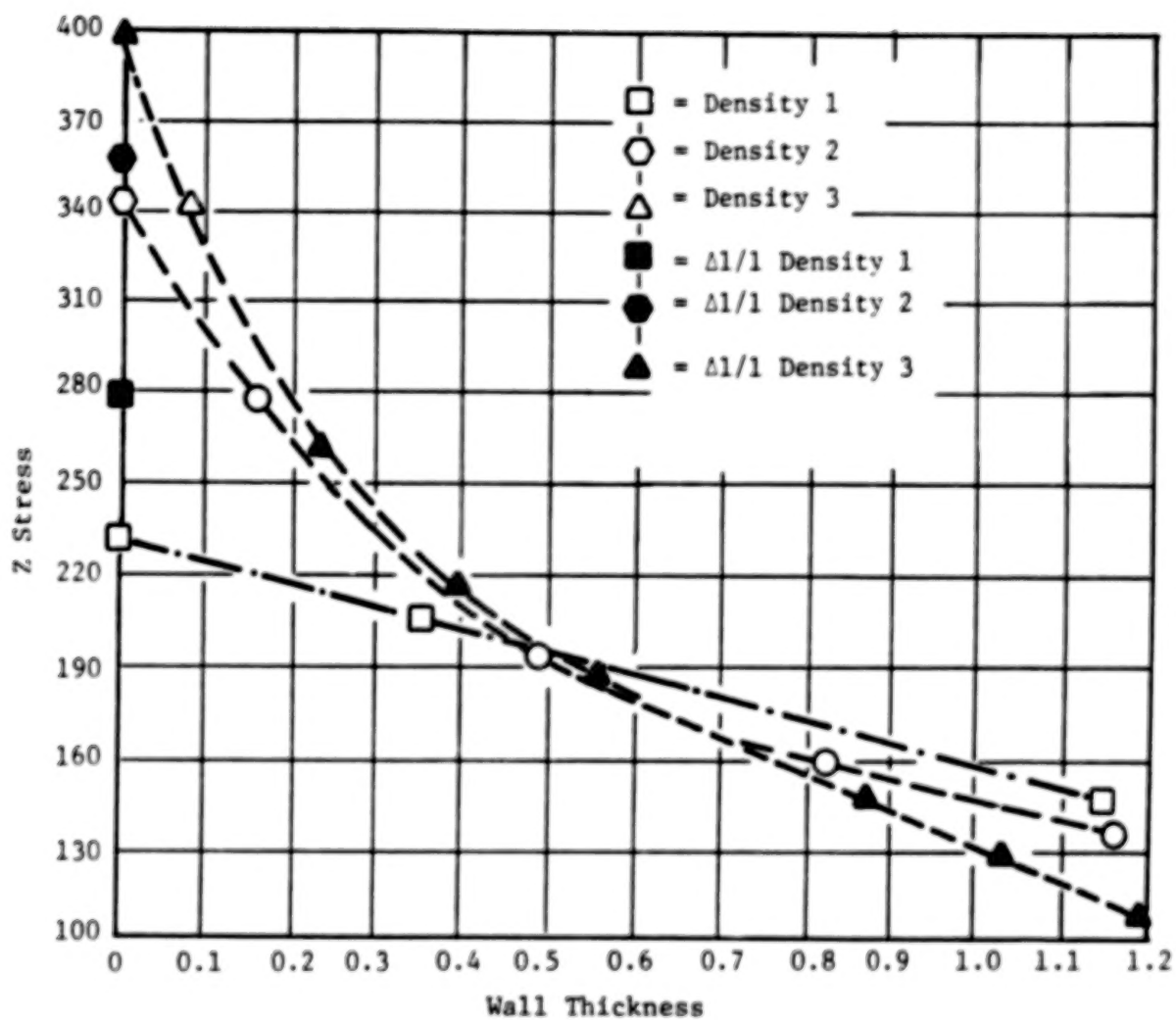
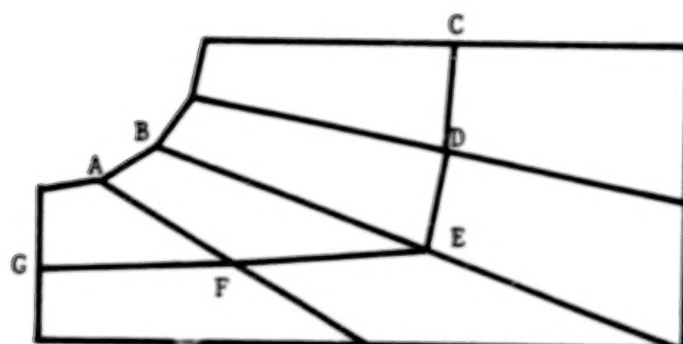


Figure 8. Effect of Mesh Density on Stress Prediction.



Points In Model	MESH (Figure 33)							
	1		2		3		4	
	$\sigma_{\text{Max}}$ Diff ksi	$\frac{\sigma_{\text{Max}} \text{ Diff}}{\sigma_{\text{Avg}}} \times 100$	$\sigma_{\text{Max}}$ Diff ksi	$\frac{\sigma_{\text{Max}} \text{ Diff}}{\sigma_{\text{Avg}}} \times 100$	$\sigma_{\text{Max}}$ Diff ksi	$\frac{\sigma_{\text{Max}} \text{ Diff}}{\sigma_{\text{Avg}}} \times 100$	$\sigma_{\text{Max}}$ Diff ksi	$\frac{\sigma_{\text{Max}} \text{ Diff}}{\sigma_{\text{Avg}}} \times 100$
A	71	42	58	30	42	20	34	15
B	46	42	38	37	26	30	20	35
C	29	38	19	26	11	15	8	11
D	46	53	28	33	16	19	11	13
E	46	41	18	16	11	9	8	7
F	83	55	29	20	12	8	7	4
G	58	33	34	20	22	12	16	9

Figure 9. Results of the Effect of Mesh Density.

EXPERIMENTAL DETERMINATION OF FLOW POTENTIAL SURFACES  
SUPPORTING A MULTIAXIAL FORMULATION OF VISCOPLASTICITY

J. R. Ellis and D. W. Robinson  
The University of Akron  
Akron, Ohio

INTRODUCTION

The form and framework of constitutive relationships for structural metals are closely tied to the concepts of a potential function and normality. For example, in elasticity the complementary energy function (or thermodynamically, the related Gibbs free energy) has the properties of a potential and the strain vector can be interpreted geometrically as lying normal to surfaces of constant complementary energy density. The existence of the complementary energy function (or its dual, the strain energy density function) is not just a theoretical contrivance but relates directly to the path independence and reversibility that is the essence of elasticity. In plasticity, the yield function plays the role of a potential and the inelastic strain increment (or rate) vector is directed normal to the yield surface. Analogously, this implies a form of path independence in plasticity, not in the complete sense as in elasticity, but in an incremental sense. In either case, it is the potential/normality structure that provides a consistent framework of a multiaxial theory. The validity of this structure has been experimentally ascertained (refs. 1-6) for a wide class of structural alloys under conditions where their mechanical behavior can be idealized as being largely time-independent, e.g., under relatively low strain rates and at low homologous temperatures.

At high homologous temperature structural metals exhibit inherently time-dependent behavior. Moreover, most important structural applications involve not only high temperature but severe temperature transients and gradients as well. Thus, time (or rate) and temperature are key variables and the development of constitutive equations unavoidably must be guided by and consistent with a general thermodynamic framework.

The thermodynamics of inelastic solids in terms of internal state variables has been discussed by several authors. In some studies (e.g., ref. 7) the internal variables are taken to be phenomenological parameters whose physical origin and associated evolutionary laws are not readily identified. Other studies (refs. 8-12) have attempted to identify internal variables with specific local microstructural rearrangements, e.g., local slip rearrangements on crystallographic planes resulting from dislocation motion and interaction. In these studies the emphasis is on rigorous local representation of rate or growth laws supplemented with an averaging procedure to obtain a macroscopic constitutive law. Consistent with either of these points of view is the assumption and adoption of a flow potential function

$$\dot{\Omega} = \dot{\Omega}(\sigma_{ij}, T, \alpha_k) \quad (1)$$

that controls the internal dissipation. Here we consider only small quasistatic

deformations and take  $\Omega$  as depending on stress  $\sigma_{ij}$ , temperature  $T$  and internal variables denoted by  $\alpha_B$  ( $B = 1, 2, \dots, n$ ). Practical theories to date have incorporated, at most, two state variables, i.e., a tensorial state variable (internal or back stress) and a scalar variable (drag or threshold stress).

The existence of a (convex) flow potential function together with the generalized normality structure:

$$\dot{\epsilon}_{ij} = \frac{\partial \Omega}{\partial \sigma_{ij}} \quad (2)$$

$$-\dot{\alpha}_B/h = \frac{\partial \Omega}{\partial \alpha_B} \quad (3)$$

where  $h$  is a scalar function of the internal state variables and  $\dot{\epsilon}_{ij}$  the inelastic strain rate, assures a positive entropy production rate as demanded by the second law of thermodynamics. Further, as discussed in references 13 and 14, this potential/normality structure also assures reasonable continuum properties in structural problems, e.g., uniqueness and important convergence properties. So again, as in the case of the classical theories discussed above, the potential/normality structure is precisely that which provides the framework of a consistent multiaxial theory. Knowledge of the form of  $\Omega$  and the demonstrated validity of the normality concept allows the forms of the flow law (eq. (2)) and the evolutionary law (eq. (3)) to be specified; this is possible only through appropriate multiaxial testing. This (exploratory) testing should be aimed at revealing the general features of behavior for classes of alloys and not take the form of detailed (characterization) tests furnishing a data base for a specific material in a specific condition. Exploratory experiments, in this sense, provide guidance to the development of a consistent theoretical framework.

Thus it is seen that  $\Omega$  plays an analogous role to the yield surface in classical plasticity. Examples of postulated forms of  $\Omega$  are given in references 9, 12, and 15-17. Experimental evidence for the existence of a flow potential function has been found in preliminary studies reported in references 18 and 19 and recently and more comprehensively in reference 20.

As discussed in references 21 and 22, flow potential surfaces are, under conditions of interest, identifiable with surfaces of constant inelastic strain rate (SCISR's). It is the direct experimental measurement of SCISR's, together with an assessment of the concept of normality, that is the subject of the research presented here. The approach is to conduct experiments under biaxial (tension-torsion) states of stress by making use of an extension (refs. 21, 23) of the probing technique used extensively in yield surface probing experiments conducted in support of the classical theory of plasticity (refs. 1-6).

In the following sections we first present the details of the experimental procedure followed in a preliminary set of experiments conducted on the representative alloy type 316 stainless steel. Although primary interest is in the determination of initial and subsequent SCISR's at high homologous temperatures (e.g.,  $\sim 0.5$ ), the preliminary tests were conducted at a lower temperatures ( $\sim 0.2$ ) largely because of

experimental convenience. Nevertheless, significant time-dependent response at the lower temperature allowed SCISR measurements to be carried out and an evaluation of the experimental technique made.

Results of the preliminary tests are presented showing three of a family of initial SCISR's, including strain rate vectors for assessing the condition of normality. Conclusions are drawn concerning the feasibility of the experimental technique, the nature of the measured SCISR's and an assessment of the normality condition. Finally, a discussion is given concerning future research.

#### EXPERIMENTAL DETAILS

As noted above, the test equipment and procedures used to determine SCISR's are similar to those used in yield surface investigations. The experiments are conducted under computer control on MTS electrohydraulic test systems. The type of specimen used is the thin-walled tube and the type of loading is tension-torsion. This approach produces stress states which are homogeneous and directly calculable from the known external loading. Prior to installation in the test system, specimens are instrumented with four rectangular strain gage rosettes. These strain gages are used to calibrate the high precision, multiaxial extensometer used in the SCISR experiments. This is accomplished by cycling the specimen within its elastic range and adjusting the outputs of the extensometer until they are identical to those of the strain gages. Further, these experiments provide values of elastic modulus (E) and shear modulus (G) which subsequently are used for control purposes. The test setup described above is shown in figure 1.

Test system control in SCISR experiments is accomplished using four independent measurements. These are total axial strain ( $\epsilon$ ) and total shear strain ( $\gamma$ ), obtained using the biaxial extensometer, and axial stress ( $\sigma$ ) and torsional stress ( $\tau$ ), obtained using a tension-torsion load cell. During individual probes, specimens are loaded radially,  $\tau/\sigma = \text{constant}$ , at predetermined stress rates. The corresponding elastic strain rates,  $\dot{\sigma}/E$  and  $\dot{\tau}/G$ , are calculated using known values of elastic moduli. During the loading, total axial strain and total shear strain are monitored by the computer. The corresponding values of total strain rate,  $\dot{\epsilon}$  and  $\dot{\gamma}$ , are obtained by making these measurements over predetermined time increments and calculating the rates. Taking total strain rate to be the sum of the elastic and inelastic components, the two inelastic strain rate components are calculated as follows:

$$\dot{\epsilon}_p = \dot{\epsilon} - \dot{\sigma}/E \quad (4)$$

$$\dot{\gamma}_p = \dot{\gamma} - \dot{\tau}/G \quad (5)$$

where  $\dot{\epsilon}_p$  is the axial component of inelastic strain rate and  $\dot{\gamma}_p$  is the torsional component. Equivalent inelastic strain rate (I) is calculated using the expression

$$I = (\dot{\epsilon}_p^2 + 1/3 \dot{\gamma}_p^2)^{1/2} \quad (6)$$

When  $I$  reaches a target value,  $100 \mu\epsilon/m$  in the subject experiments, the probe is terminated and the specimen unloaded. The same computer program allows probes to be conducted at 16 preset angles in tension-torsion stress space. The results of these tests subsequently are used to establish the locus of points corresponding to the target value of inelastic strain rate in tension-torsion stress space. The experimental approach outlined above is shown schematically in figure 2.

Regarding the material details, the material tested was type 316 stainless steel, Republic Steel heat 8092297, supplied in solution annealed condition in the form of 64 mm O.D. bar. After manufacture, the specimen was subjected to the following heat-treatment: Heat to  $1065^{\circ}\text{C}$ , hold for 30 minutes, cool at  $149^{\circ}\text{C}/\text{min}$  to  $537^{\circ}\text{C}$ , and continue cooling at a convenient rate to room temperature. This heat-treatment was performed in flowing argon to prevent specimen oxidation. An examination of the materials microstructure after the above heat-treatment showed it to be equiaxed with grain size in the range 2-4 ASTM units. A series of micro-hardness measurements made in both longitudinal and transverse senses showed that the material's hardness was reasonably uniform, the DPH values obtained being in the range 120 to 140.

#### EXPERIMENTAL RESULTS

Several techniques were used to acquire data in these experiments. One approach was to monitor the signals from the load cell and the extensometer directly using X-Y plotters and strip chart recorders. The aim here was to have a visual representation of the data as the test progressed, data in this form being particularly useful in identifying problems as they arose. The data acquisition system (DAS) was also used to check for experimental difficulties. The approach adopted was to calculate the current value of inelastic strain rate as a percentage of the target value and to print this percentage at 1 second intervals. Outputs of this form were useful in identifying "noise" problems. Also, the final values of the stress and strain were printed at the end of each probe along with the axial and torsional components of inelastic strain rate. The SCISR and strain rate vectors shown in figure 3 were constructed using data obtained in this manner.

In addition to controlling the test, the DAS was used to store the measured values of axial stress, axial strain, torsional stress and torsional strain on magnetic tape at 1 second intervals. These data subsequently were used for detailed post-test analysis of the results. As a first step in this analysis, plots of stress versus time, strain versus time, and stress versus strain were prepared for both the axial and torsional components of loading. These data were used to evaluate the performance of the control system and also the performance of the various measurement systems. Data free from experimental difficulties were reduced further as illustrated in figures 4 and 5, using results obtained in Probe (14). The curves shown in figure 4 were determined using equations (4) and (5) while the curve shown in figure 5 was determined using equation (6). As indicated in figure 5, it was possible to use curves of this type to determine SCISR's ranging from threshold to the target value of  $100 \mu\epsilon/\text{in}$ . The family of SCISR's shown in figure 6 were established in this manner for nine probes judged free from experimental difficulty.

#### CONCLUSIONS AND DISCUSSION

The following general conclusions have been drawn from the preliminary experimental results:

- The proposed experimental method for directly determining surfaces at constant inelastic strain rate (SCISR's), at a fixed inelastic state, appears feasible. This has been demonstrated, at least, in the neighborhood of the virgin state.
- The members of the family of initial SCISR's shown have the expected general shape, order, and spacing. Experimental scatter appears minimal and a reasonably regular, convex figure is defined. The elliptical figures are not too different from those predicted for a fully isotropic  $J_2$ -type material.
- Although some departure from strict normality of the strain-rate vectors to the defined  $100\mu\epsilon/m$  surface is indicated, the results strongly support the general concept of normality, or equivalently, the potential nature of  $\Omega$ .

Tests are continuing to determine flow potential surfaces (SCISR's) at high homologous temperature ( $\sim 0.5$ ) on the representative austenitic alloy type 316 stainless steel. Similar testing is planned on the class of nickel-based alloys using Hastelloy. The objective is a general understanding of the nature and behavior of SCISR's under virgin conditions and conditions subsequent to inelastic deformation (i.e., creep, plasticity, recovery, etc.). Such an understanding is prerequisite to a rational representation of multiaxial, viscoplastic behavior.

From the experimentalist's viewpoint, most difficulty in conducting these experiments results from the stringent requirements placed on the performance of the strain measurement system. In multiaxial experiments of this type attempts are made to investigate inelastic response while maintaining the material in an unchanged state. This conflicting requirement can be approximated in probing type experiments in which very small changes in inelastic stain or inelastic strain rate are used as measures of inelastic response. Clearly, strain measurements systems used for this work must be capable of detecting these small changes which in practice requires near-micro-strain resolution. Another key requirement is that the output of the instrumentation should be linear over the entire measurement range of interest and also when loading passes through zero. This is because departure from linear behavior is used ineffect as a measure of inelastic materials response. Nonlinearities resulting from the strain measurement system itself render such interpretations difficult or impossible to make. Perhaps the most limiting difficulty of all is that of crosstalk. One problem peculiar to biaxial and multiaxial experiments is that interaction or cross-talk can occur between the various forms of loading and straining. The possibility exists in tension-torsion experiments, for example, that loading in the axial sense can produce apparent torsional strains and vice versa. Clearly, crosstalk of this type precludes any meaningful investigation of normality.

In the present experiments, all of the difficulties described above were encountered to some degree. To obtain the necessary resolution, electronic gain of about  $\times 100$  was used to set up the extensometer such that  $\pm 3000\mu\epsilon \equiv \pm 10$  volts. Even though this value was relatively modest, "noise" problems were encountered with the amplifiers used for this purpose and the data generated in a number of probes was questionable as a result. Regarding linearity, post-test analysis of the data showed that the stress-time histories obtained in certain probes were nonlinear. This indicated that the integrators being used for test system control were drifting and providing less than adequate performance. Also, some difficulty was experienced with crosstalk. This was because no attempt was made to computer correct the strain signals in these preliminary experiments. The net result of these difficulties is that the directions of the strain rate vectors shown in figure 3 are somewhat open to

question. Also, the seemingly well behaved data obtained in Probe (14), figures 4 and 5, was duplicated in only eight of the remaining probes. This meant that limited data were available to construct the family of SCISR's shown in figure 6.

As the success of these experiments was seen to hinge on reliable biaxial strain measurement, an effort was initiated within the HOST program to resolve the difficulties noted above. In the case of the instrument used in the present experiments, the inductive transducers used for axial and torsional measurements are being replaced by capacitive type. The aim here is to eliminate "noise" problems in tests conducted at high homologous temperatures. It is also planned to investigate the feasibility of using a biaxial extensometer produced by MTS for the subject type of testing. Further, a third type of biaxial extensometer is being developed under contract at the Oak Ridge National Laboratory for possible use in high precision, probing type experiments.

#### REFERENCES

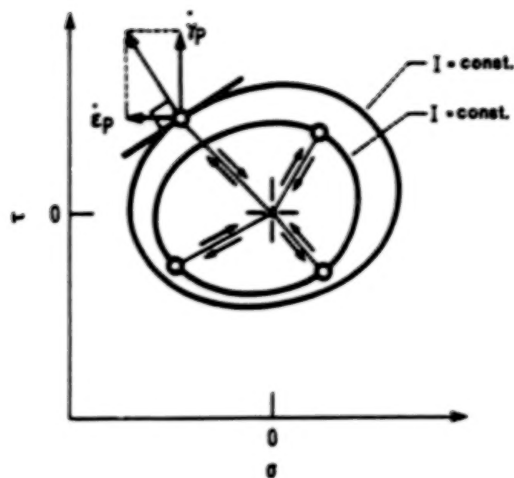
1. Bertsch, P. K. and Findley, W. N.: An Experimental Study of Subsequent Yield Surfaces - Corners, Normality, Banschinger, and Related Effects. 4th U. S. National Congress of Applied Mechanics, 1962, pp. 893-907.
2. Philips, A.: The Foundations of Thermoplasticity-Experiment and Theory. Topics in Applied Continuum Mechanics, J. L. Zemen and F. Ziegler (eds.), Springer-Verlag, Wien-New York (1974).
3. Liu, D. C. and Greenstreet, W. L.: Experimental Studies to Examine Elastic-Plastic Behavior of Metal Alloys Used in Nuclear Structures. Constitutive Equations in Viscoplasticity Computational and Engineering Aspects, ASME Publication AMD-Vol. 20, Dec. 1976, pp. 35-56.
4. Ellis, J. R.; Robinson, D. N.; and Pugh, C. E.: Behavior of Annealed Type 316 Stainless Steel Under Monotonic and Cyclic Loading at Room Temperature. J. Nucl. Eng., and Design 47, 1978, pp. 115-123.
5. Ohashi, Y. and Tanaka, E.: Plastic Deformation Behavior of Mild Steel Along Orthogonal Trilinear Strain Trajectories in Three Dimensional Vector Space of Strain Deviator. J. Eng. Mat. Tech. 103(3), October 1981, pp. 187-292.
6. Ellis, J. R.; Robinson, D. N.; and Pugh, C. E.: Time Dependence in Biaxial Yield at Room Temperature. J. Eng. Mat. and Tech., Vol. 105, October 1983, pp. 250-256.
7. Coleman, B. D. and Gurtin, M. E.: Thermodynamics with Internal State Variables. J. Chem. Phys., Vol. 47, 1967, pp. 597-613.
8. Kestin, J. and Rice, J. R.: A Critical Review of Thermo-dynamics (Stuart, E. B. et al., eds.), Mono Book Corp., Baltimore, 1970, p. 275.
9. Rice, J. R.: On the Structure of Stress-Strain Relations for Time-Dependent Plastic Deformations in Metals. J. Appl. Mech., vol. 37, no. 3, Sept. 1970, pp. 728-737.
10. Hill, R. and Rice, J. R.: Constitutive Analysis of Elastic-Plastic Crystals at Arbitrary Strain. J. Mech. Phys. Solids, vol. 20, 1972, pp. 401-413.

11. Rice, J. R.: Mechanics and Thermodynamics of Plasticity. Constitutive Equations in Plasticity, ed. A. Argon, MIT Press, 1975.
12. Ponter, A. R. S. and Leckie, F. A.: Constitutive Relationships for the Time Dependent Deformation of Metals. J. Eng. Mater. Technol., vol. 98, no. 1, 1976, pp. 47-51.
13. Ponter, A. R. S.: Convexity and Associated Continuum Properties of a Class of Constitutive Relationships: J. de Mecanique 15(4), 1976, pp. 527-542.
14. Robinson, D. W. and Swindeman, R. W.: Unified Creep-Plasticity Constitutive Equations for 2-1/4 CR-1 MO Steel at Elevated Temperature. ORNL/TM-8444, Oct. 1982.
15. Robinson, D. W. et al: Constitutive Equations for Describing High-Temperature Inelastic Behavior of Structural Alloys. Proc. of Specialists Meeting on High-Temperature Structural Design Technology of LMFBRs, IAEA Report IWGFR/11, April 1976, pp. 44-57.
16. Robinson, D. W.: Constitutive Relationships for Anisotropic High-Temperature Alloys. J. Nucl. Eng. and Des., 83, 1984, pp. 389-396.
17. Chaboche, J. L.: On the Constitutive Equations of Materials Under Monotonic or Cyclic Loadings. Rech. Aerosp., 1983, pp. 31-43.
18. Brown, G. M.: Inelastic Deformation of an Aluminum Alloy Under Combined Stress at Elevated Temperature. J. Mech. Phys. Solids 18, 1970, pp. 383-396.
19. Robinson, D. W.: On the Concept of a Flow Potential and the Stress-Strain Relations of Reactor Systems Metals. ORNL/TM 5571, 1976.
20. Oytana, C.; Delobelle, P.; and Mermet, A.: Constitutive Equations Study in Biaxial Stress Experiments. J. Eng. Materials and Tech., vol. 104, 1982, pp. 1-11.
21. Robinson, D. W.: On Thermomechanical Testing in Support of Constitutive Equation Development for High-Temperature Alloys. NASA CR 174879, May 1985.
22. Robinson, D. W. and Ellis, J. R.: High Temperature Constitutive Modeling. Turbine Hot Section Technology 1984: Proceedings of a Conference Sponsored by NASA/Lewis Research Center, NASA Conference Publication 2339, Oct. 1984.
23. Ellis, J. R. and Robinson, D. W.: Some Advances in Experimentation Supporting Development of Viscoplastic Constitutive Models. NASA CR 174855, April 1985

ORIGINAL PAGE IS  
OF POOR QUALITY



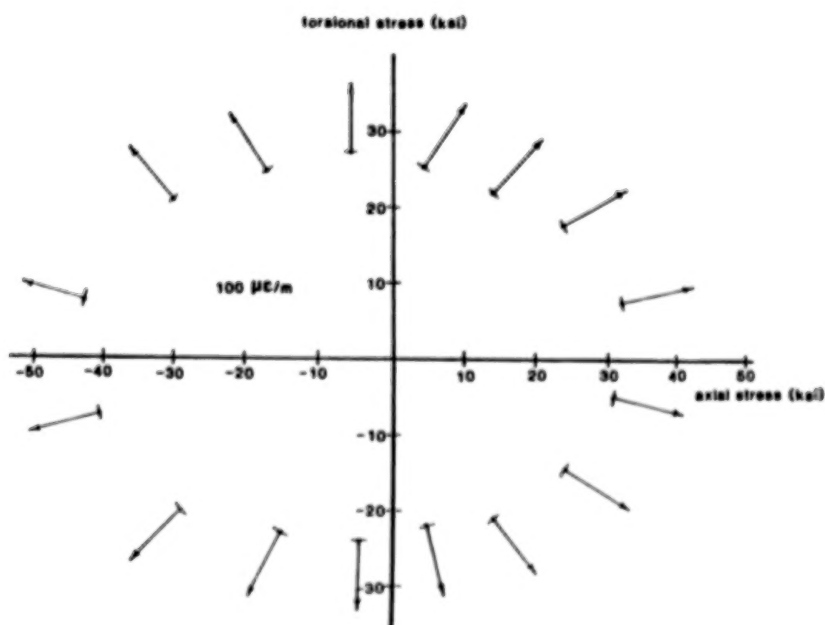
1. Experimental Setup Used in Determining Surfaces of Constant Inelastic Strain Rate (SCISRs).



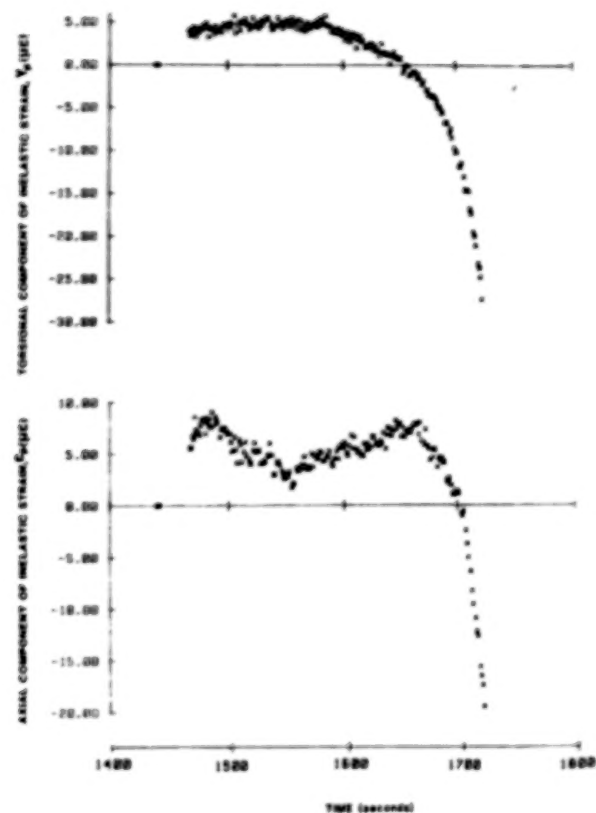
$$\begin{bmatrix} \dot{\epsilon}_p \\ \dot{\gamma}_p \end{bmatrix} = \begin{bmatrix} \dot{\epsilon} \\ \dot{\gamma} \end{bmatrix} - \begin{bmatrix} \dot{\sigma}/E \\ \dot{\tau}/G \end{bmatrix}$$

Computed                  Measured                  Controlled

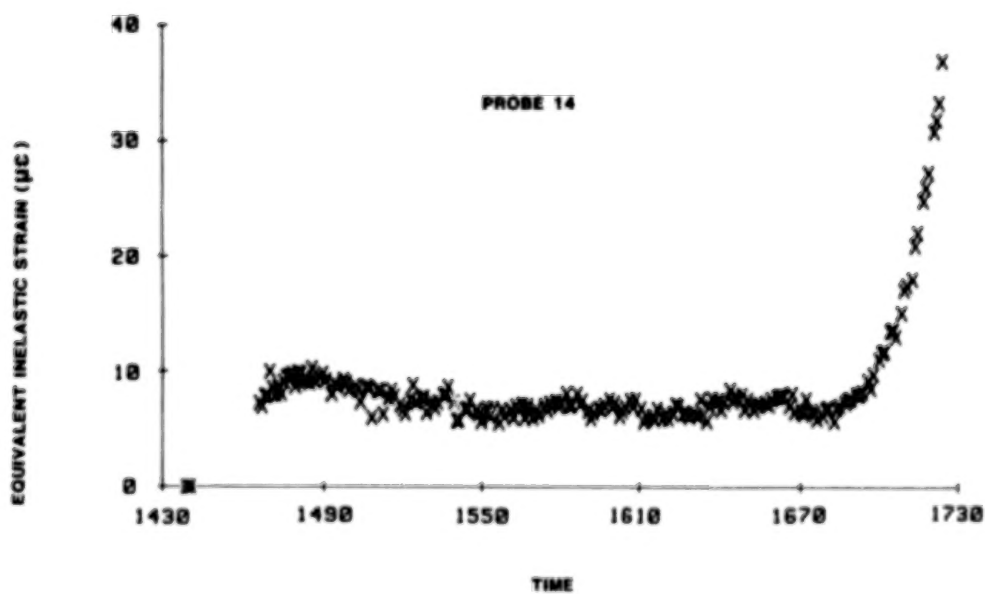
2. Approach Adopted in Determining SCISRs in Tension-Torsion Stress Space.



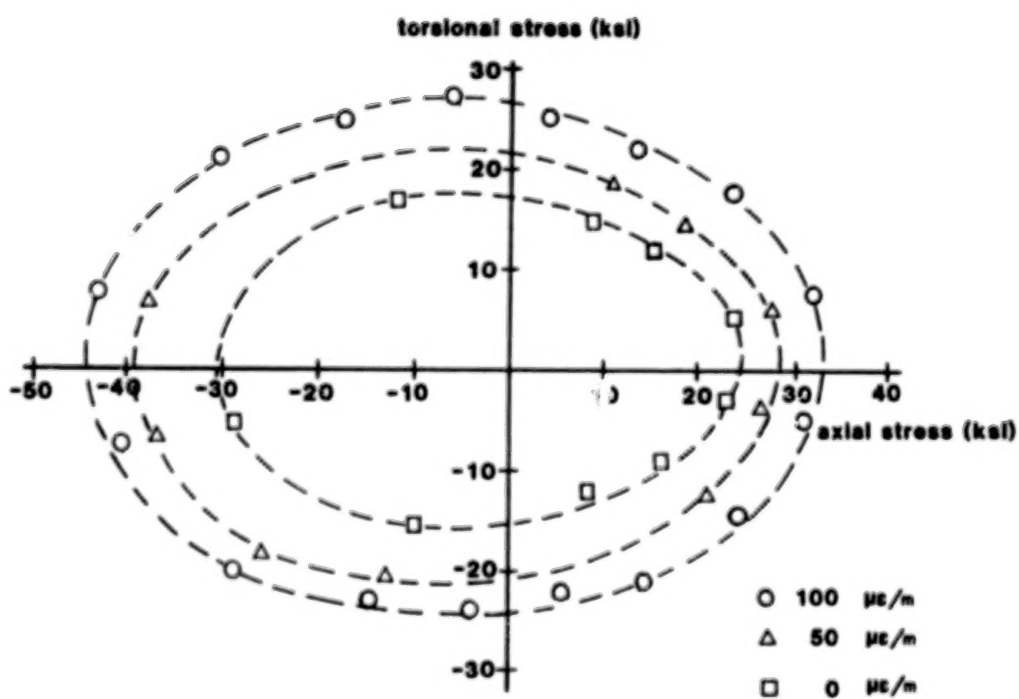
3. SCISR and Direction of the Inelastic Strain Rate Vectors: Target Value of Inelastic Strain rate = 100  $\mu\text{E}/\text{m}$ .



4. Variation of the Axial and Torsional Components of Inelastic Strain During Probe (14).



5. Variation of Equivalent Inelastic Strain with Time During Probe (14).



6. SCISRs for Inelastic Strain Rates Ranging from Threshold to 100  $\mu\epsilon/m$ .

## CONSTITUTIVE MODELING FOR SINGLE CRYSTAL SUPERALLOYS\*

Donald C. Stouffer, L. Thomas Dame<sup>†</sup> and N. Jayaraman

University of Cincinnati and \*General Electric Aircraft Engine Business Group

## INTRODUCTION

Single crystal superalloys are a two phase  $\gamma$ - $\gamma'$  alloys with a large volume fraction of  $\gamma'$ . The  $\gamma'$  precipitates have a  $L_{12}$  cubic crystal structure and are distributed in a coherent face centered cubic  $\gamma$  solid solution.

The mechanical response shows significant variation in the mechanical properties with orientation and temperature. Near 700°C the orientation dependence is most severe and a tension-compression asymmetry up to 50% has been observed in PWA 1480 (Ref. 1). The minimum creep rate typically varies by a factor up to 100 with orientation for fixed values of stress and temperature. Above 700°C the orientation dependence and tension-compression asymmetry decrease with increasing temperature. Significant strain rate dependence is observed at the higher temperatures and some cyclic hardening is also observed.

The constitutive model to be developed for the material must accurately predict the response, must be efficient in finite element calculations and should be easy to relate to experimental data so the material parameters can be reasonably determined. Specifically, the following features must be included in the model for single crystal superalloys:

- Orientation dependence
- Tension-compression asymmetry
- Temperature dependence
- Time and rate dependence

It is expected that the model should predict monotonic, fatigue and multiaxial (proportional and nonproportional) loading. At the present time the following effects are not included:

- Large strain and tertiary creep
- Slip bursts
- Coating-substrate interaction.

The current status of the work is reported in detail in Reference 2.

## CONSTITUTIVE MODELING APPROACH

A crystallographic approach to constitutive modeling is adopted. The approach is based on identifying the active slip planes and slip directions. The shear stresses are computed on each of the slip planes from the applied stress components. The slip rate is then computed on each slip system and the macroscopic inelastic strain rates are the sum of the slip in the individual slip systems.

The classical assumption of Schmid's law (slip is a function of the resolved shear stress in the slip direction) is not adequate for  $\gamma$ - $\gamma'$  alloys since it cannot explain the observed tension compression asymmetry. More recently, Lall, Chin and Pope (Ref. 3) showed the tension-compression asymmetry is controlled by cross slip which depends on the stress perpendicular to the direction of propagation of two Shockley partial dislocations. This stress tends to extend or constrict the partials and inhibit or promote cross slip, respectively.

\*Work partially supported by NASA Grant NAG3-511.

The constitutive model at the crystallographic level is based on the Bodner inelastic flow and hardening equations (Ref. 4) but is modified to incorporate the results of Lall, Chin and Pope. The formulation is valid for coupled octahedral and cube slip and has been extended in an attempt to include both the shear and diffusion mechanisms.

#### FINITE ELEMENT IMPLEMENTATION

The constitutive model was implemented in a finite element code using twenty noded isoparametric solid elements. This element was chosen since it can be used to model almost any three-dimensional geometry allowing for any orientation of the principal material axes. Order two Gaussian integration was used for stiffness generation and calculation of the body forces. The ability to represent piecewise linear load histories was also incorporated. This is particularly useful for modeling fatigue loops and other specialized load histories. Since the inelastic strain rate can change dramatically during a linear load history a dynamic time incrementing procedure is also included.

#### EXPERIMENTAL DATA

The constitutive model and finite element code (two elements) were used to predict the response of Rene N4. The experimental response at 760°C was used since the orientation dependence and tension-compression asymmetry is most severe near this value. Unfortunately, the data base is limited and the calculations were done for two specific alloys reported in the literature. At 760°C the stress-strain response in tension and compression and fatigue response was determined by Gabb, Gayda and Minor (Ref. 5) for several orientations. In another report (Ref. 6) the tensile and creep response at three orientations was reported for Rene N4 with a slightly different chemistry. Since the response characteristics of the two alloys were significantly different they were modeled independently. However, both systems were modeled to test as many properties of the constitutive theory as possible. A method has also been developed and for determining the material parameters from the experimental data.

#### CALCULATED AND EXPERIMENTAL RESULTS

The constants were determined for octahedral and cube slip systems for the data reported in Reference 5. These constants were then used to predict the tension-compression asymmetry and fatigue loops as shown in Table 1 and Figure 1, respectively. The other data set was used to model the tensile and creep response. The experimental and calculated tensile response is shown in Figure 3 and a sample creep prediction is shown in Figure 4.

#### FUTURE RESEARCH

During the next year much of the analytical effort will be spent in software development, refining the constitutive model and extending it to other temperatures. An experimental program is under way to determine response characteristics in tension, creep and fatigue at five orientations and three temperatures. Microscopy will also be included to determine the active slip systems and deformation mechanisms.

# REFERENCES

1. Shah, D. and Duhl, D., "The Effect of Orientation, Temperature and Gamma Prime Size on the Yield Strength of a Single Crystal Nickel Base Superalloy," Proc. Fifth Intern. Symp. on Superalloys, ASM, Metals Park, Ohio, 1984.
2. Dame, L.T., "Anisotropic Constitutive Model for Nickel Base Single Crystal Alloys: Development and Finite Element Implementation." Ph.D. Dissertation, Department of Aerospace Engineering, University of Cincinnati, May 1985.
3. Lall, C., Chin, S. and Pope, D., "The Orientation and Temperature Dependence of the Yield Stress of  $Ni_3(Al,Nb)$  Single Crystals," Met Trans. A, 10A, p 1323, September 1979.
4. Bodner, S., Partom, I. and Partom, Y., "Uniaxial Cyclic Loading of Elastic-Viscoplastic Materials," ASME, J. Appl. Mech., 46, p 805, 1979.
5. Gabb, T., Gayda, J. and Minor, R., "Orientation and Temperature Dependence of Some Mechanical Properties of the Single Crystal Nickel Base Superalloy Rene N4: Part II Low Cycle Fatigue." To appear Met Trans 1985.
6. Wukusick, C., "Directional Solidification Alloy Development," NADC-78136-60 Naval Air Systems Command, 1980.

TABLE 1. COMPARISON OF MONTONIC YIELD STRESSES AND CALCULATED SATURATION STRESSES WITH OCTAHEDRAL AND CUBE SLIP CONSTITUTIVE MODELS ACTIVE, RENE N4, 760°C (DATA FROM REF. 5)

ORIENTATION	TENSION OR COMPRESSION	.02% YIELD STRESS (REF [37]) (MPa)	CALCULATED SATURATION STRESS (MPa)	ERROR  (%)
[001] <sup>*</sup>	T	956	956	0
[001] <sup>*</sup>	C	-818	-819	.1
[011] <sup>*</sup>	T	748	752	.5
[011]	C	-905	-865	4.4
[111] <sup>*</sup>	T	817	827	1.3
[111]	C	-842	-828	1.7
[023]	T	695	705	1.5
[023]	C	-747	-741	.9
[236]	T	716	725	1.2
[236]	C	-714	-752	5.3
[145]	T	656	692	5.5
[145]	C	-792	-763	3.6

\* CONSTANTS WERE DERIVED USING THIS DATA

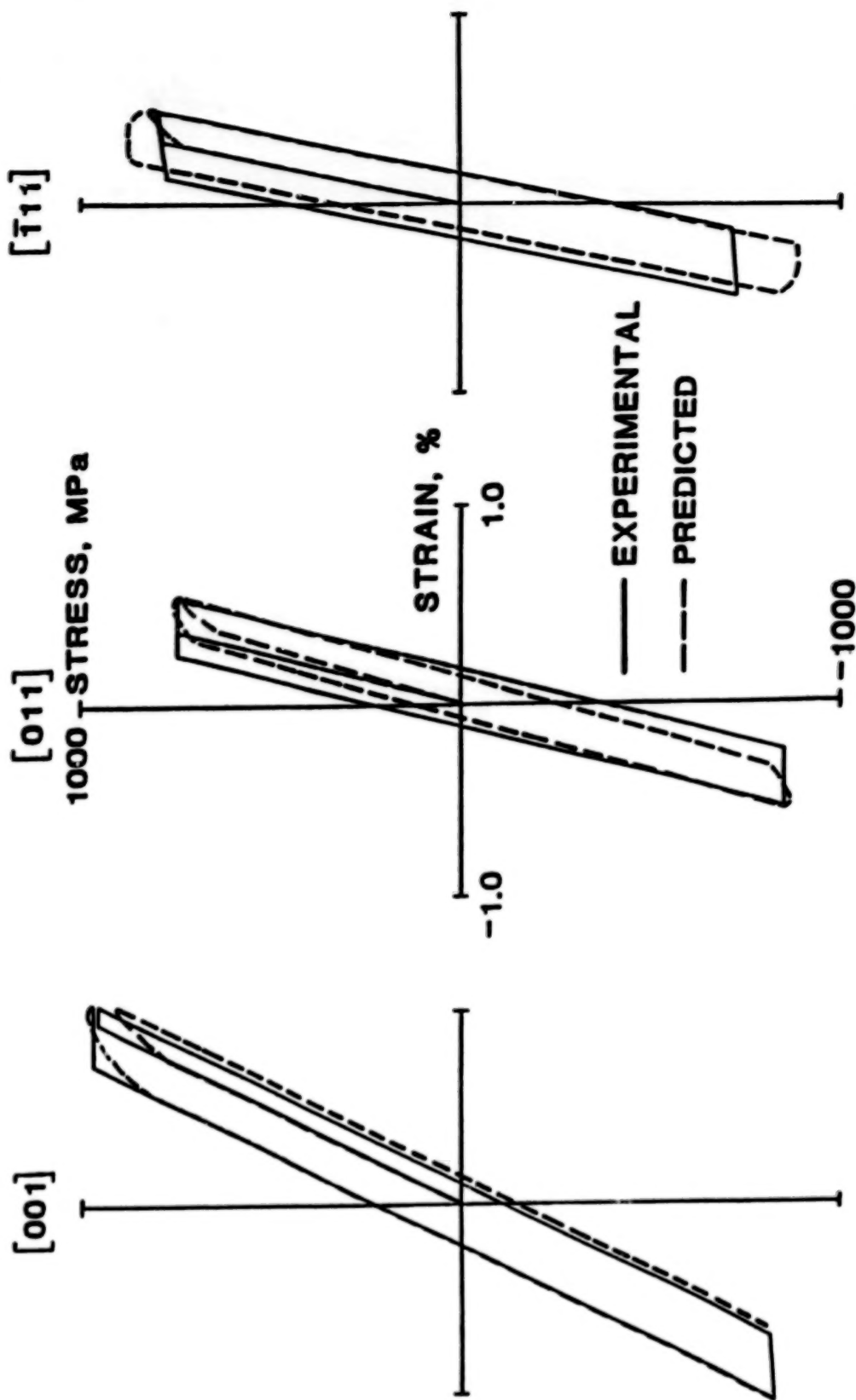


FIGURE 1 PREDICTED AND EXPERIMENTAL RESPONSE OF FIRST CYCLE FATIGUE LOOPS FOR RENE N4 AT 760°C, WITH KINEMATIC HARDENING (DATA FROM REF. 5)

FIGURE 2. PREDICTED AND EXPERIMENTAL STRESS STRAIN CURVES FOR RENE N4 VF317 AT 760°C. (DATA FROM REF. 6)

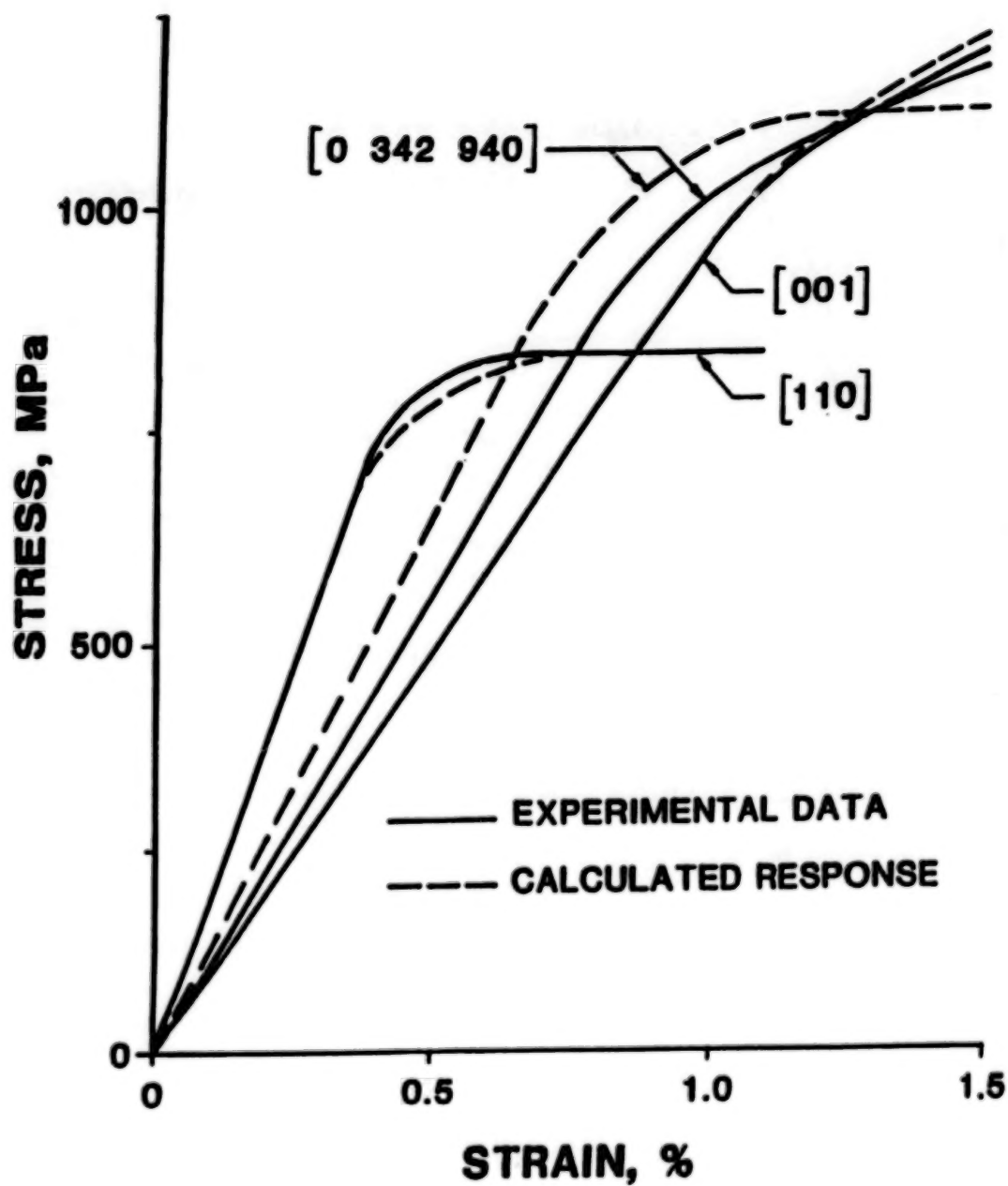
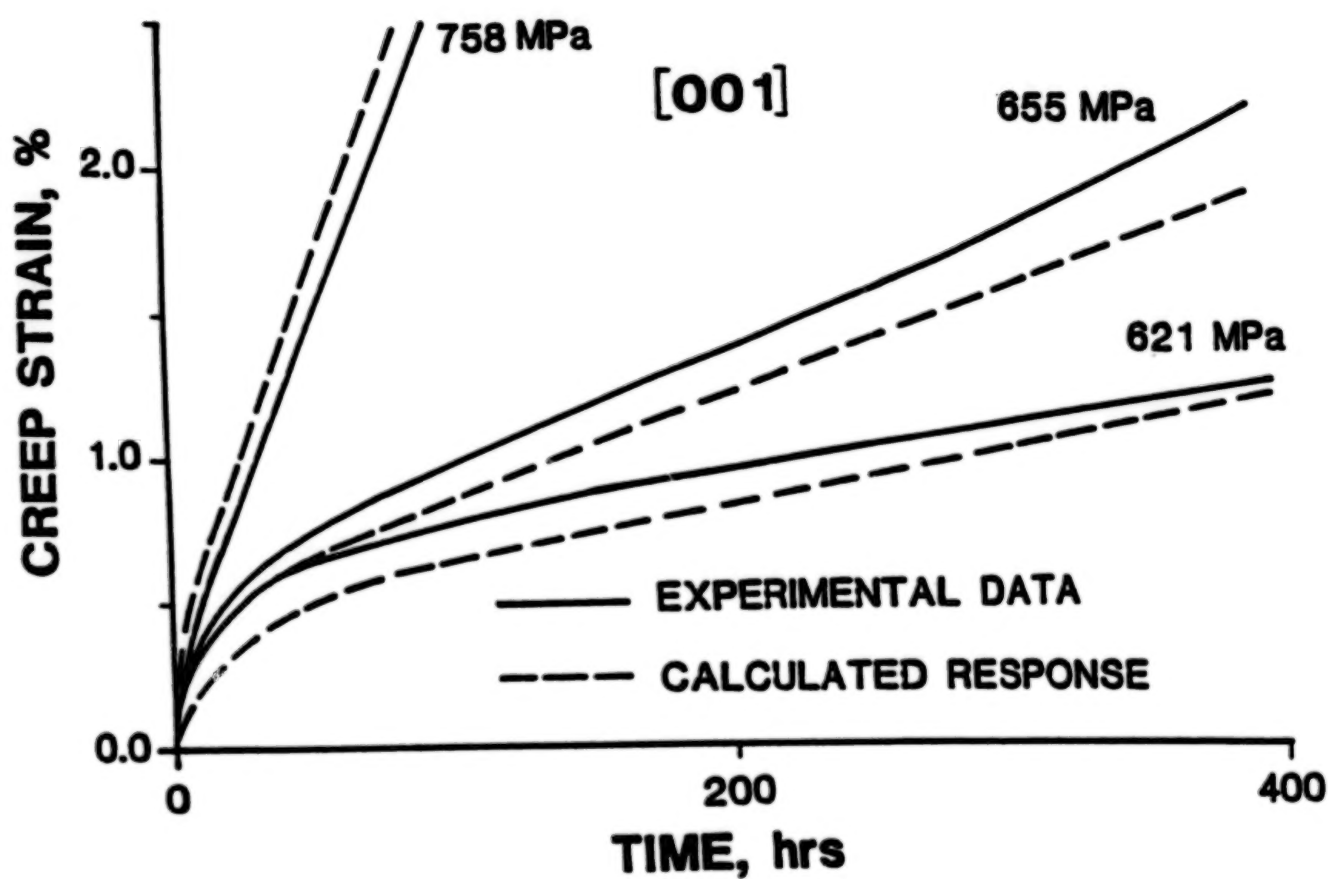


FIGURE 3. CREEP RESPONSE OF RENE N4 VF317 LOADED IN THE [001] DIRECTION AT 760°C.  
(DATA FROM REF. 6)



## CONSTITUTIVE MODELING OF SUPERALLOY SINGLE CRYSTALS WITH VERIFICATION TESTING\*

Eric Jordan  
University of Connecticut

Kevin P. Walker  
Engineering Science Software, Inc.

### INTRODUCTION

The prediction of component life is an important activity in the development of gas turbine engines. Such predictions require accurate component stress analysis. In cases involving inelastic strain at elevated temperatures these analyses are performed numerically and use constitutive equations as an essential part of the analysis. The goal of the research described in this paper is the development of constitutive equations to describe the elevated temperature stress-strain behavior of single crystal turbine blade alloys. The program involves both the development of a suitable model and verification of the model through elevated temperature tension-torsion testing. A constitutive model is derived from postulated constitutive behavior on individual crystallographic slip systems. The behavior of the the entire single crystal is then arrived at by summing up the slip on all the operative crystallographic slip systems. This type of formulation has a number of important advantages, including the prediction of orientation dependence and the ability to directly represent the constitutive behavior in terms which metallurgists use in describing the micromechanisms. Along with the model development is a biaxial test program that will generate data to determine the model constants, provide insight into the qualitative aspects of the material behavior and provide data to verify the usefulness of the constitutive model. In the remainder of the report the model will be briefly described followed by the experimental set-up and some of the experimental findings to date. Finally, several simulations of the experimental data using the model will be presented.

### BASIC MODEL FORMULATION

The inelastic anisotropic behavior of the single crystal superalloy is derived from a crystallographic slip model. In nickel-base superalloy single crystals crystallographic slip occurs on both the octahedral and cube planes, and it is necessary to incorporate both of these slip systems in the model. Indeed, as will be discussed in the simulation section, the anisotropic constitutive behavior of single crystal superalloys such as PWA 1480 cannot be modelled using only the octahedral slip system.

The constitutive behavior is assumed to be governed by the following set of equations:

\* Work done under NASA Grant NAG3-512.

$$\sigma_{ij} = Q_{ji} Q_{kl} D_{jklm} (\epsilon_{mn} - \epsilon_{mn}^P),$$

where  $Q_{ij}$  is the matrix of direction cosines between the global and crystallographic axes, and the inelastic strain rate is given by the expression:

$$\dot{\epsilon}_{ij}^P = \sum_{r=1}^{12} (\dot{\gamma}_r/2) [(i, n_r^0)(m_r^0, j) + (i, m_r^0)(n_r^0, j)] + \sum_{r=1}^6 (\dot{\xi}_r/2) [(i, n_r^c)(m_r^c, j) + (i, m_r^c)(n_r^c, j)],$$

and

$$\dot{\gamma}_r = K_r^{-p} (\pi_r - \omega_r) |\pi_r - \omega_r|^{p-1}, \quad \dot{\xi}_r = L_r^{-t} (\tau_r - \Omega_r) |\tau_r - \Omega_r|^{t-1},$$

$$\dot{\omega}_r = \rho_1 \dot{\gamma}_r - \rho_2 |\dot{\gamma}_r| \omega_r - \rho_3 |\omega_r|^{m-1} \omega_r, \quad \dot{\Omega}_r = \rho_6 \dot{\xi}_r - \rho_7 |\dot{\xi}_r| \Omega_r - \rho_8 |\Omega_r|^{n-1} \Omega_r,$$

$$\dot{K}_r = \left\{ \sum_{k=1}^M [h_{rk} - \eta_1 \{K_r - K_r^1\}] \dot{\gamma}_k \right\} - h_1 \{K_r - K_r^1\}^s,$$

$$\dot{L}_r = \left\{ \sum_{k=1}^6 [\beta_2 - \eta_2 \{L_r - L_r^0\}] \dot{\xi}_k \right\} - h_2 \{L_r - L_r^0\}^u,$$

$$h_{rk} = \beta_1 \{q + (1-q)\delta_{rk}\}, \quad K_r^1 = K_r^0 + \rho_4 \kappa_r + \rho_5 |\varphi_r|,$$

where  $\pi_r$  and  $\tau_r$  are the resolved shear stress components on the octahedral and cube planes, respectively, whilst  $\kappa_r$  represents the resolved shear stress component in the  $\langle 112 \rangle$  direction on the octahedral plane and produces a yield stress asymmetry. The term  $\varphi_r$  is the resolved shear stress on the cube plane in the direction of the octahedral slip direction and this term is also involved in the yield stress asymmetry. The terms  $\omega_r$  and  $\Omega_r$  represent the back stress components on the octahedral and cube planes, and  $K_r$  and  $L_r$  are the corresponding drag stress state variables. The constant,  $q$ , in the expression for the drag stress evolution equation allows for latent hardening in the single crystal slip systems. At 871C, no latent hardening has been detected, and we have accordingly set  $q=1$ .

The material constants for the simulations were taken to have the following values:

$$\rho_1 = 4.509 \times 10^7, \quad \rho_2 = 645, \quad \rho_3 = 9.6 \times 10^{-6}, \quad \rho_4 = 0, \quad \rho_5 = 0, \quad K_r^0 = 25775, \quad m = 1.49, \quad p = 6.69, \quad s = 1, \\ \beta_1 = 0, \quad \eta_1 = 0, \quad q = 1, \quad \rho_6 = 1.506 \times 10^7, \quad \rho_7 = 1000, \quad \rho_8 = 9.7 \times 10^5, \quad L_r^0 = 71152, \quad n = 1.05, \quad t = 7.09, \\ \beta_2 = 0, \quad \eta_2 = 0, \quad h_2 = 0, \quad u = 0, \quad D_{1111} = 31.37 \times 10^6, \quad D_{1122} = 20.84 \times 10^6, \quad D_{1212} = 21.26 \times 10^6.$$

The foregoing material constants were determined with the COPES-CONMIN general purpose optimization code, which used about one hour of computer time on an IBM PC-XT with an 8087 math coprocessor chip. This speed is due to the fact that simplified formulae are available for the inelastic strain rate in the  $\langle 001 \rangle$

direction for octahedral and cube slip.

As shown in the simulations it is necessary to include both octahedral and cube slip in the theoretical formulation in order to capture the tension-torsion biaxial behavior of single crystal superalloys such as PWA 1480.

## EXPERIMENTS AND RESULTS

The determination of model constants and model verification is being carried out using an elevated temperature (871C) tension-torsion servohydraulic test set-up developed as part of a fatigue research program (NASA NAG3-160). The maximum temperature capability of the system was increased during this program. The basic servohydraulic is a 2500 N-M, 250 KN servohydraulic tension-torsion machine differing from the commercial machines only by virtue of a University of Connecticut developed load frame made from a large die set. Force and torque are measured with a conventional strain gage load-torque cell while strain is measured by a University of Connecticut designed extensometer that utilizes high temperature noncontacting displacement probes. This extensometer, shown in Fig.1, allows testing in excess of 871C without any need to cool the extensometer. The machine is computer controlled using a DEC LSI-1123 microcomputer and software developed under this grant. The software allows a wide variety of tests to be run including tests involving a sudden change in strain rate, known (cf. reference (2)), to be useful in assessing the drag stress state variables used in the anisotropic constitutive model. The software also allows strain holds to be inserted into a strain history which is particularly useful in assessing the back stress variable (reference(3)). The material being tested is a high volume (65%) gamma-prime single crystal material, PWA 1480, graciously supplied by Pratt & Whitney.

The tests run are unique, being the first biaxial tension-torsion tests run on this type of single crystal alloy. Biaxial testing has the special advantage that orientation effects may be studied by varying the stress state as opposed to growing specimens in a wide variety of configurations as is usually done for uniaxial testing. Early experiments with this material show that at 871C (1600F) it is possible to return the material to the same deformation state by applying a few repeated cycles of almost any strain history. As a result a large number of different types of tests can be run on a single specimen. Some of the more interesting results will quickly be presented. Figure 2 shows strain rate dependence in torsion and it is qualitatively similar to tension results. When combined with tension tests these torsion results provide a powerful and easy way to determine the relative proportions of octahedral slip and cube slip, which is vital to the success of the proposed model. This will be elaborated in the next section. Many materials are known to cyclically harden to a much greater degree in non-proportional loading, reference (3), and it is important to determine if PWA 1480 exhibits this common behavior. A test series was run in which a torsional loop was taken followed by cycling with a torsion to tension strain ratio ( $\lambda$ ) of 1.5 and with tension and torsion 90 degrees out-of-phase. This type of non-proportional cycling is known to be especially effective, reference (3), in producing extra hardening. Figure 3 shows the torsional loops before and after this cycling and the loops are so similar as to be nearly indistinguishable indicating that there is no extra hardening. Finally, these

alloys are known to exhibit tension-compression yield stress asymmetry which is predicted by the proposed model, reference (4). This asymmetry should also manifest itself in biaxial tests. Figure 4 shows the asymmetry as a function of the lambda ratio ( $\lambda$ ). It is apparent that at 1600F there is little asymmetry except at the smallest lambda ratios. Because the torsion loops are very small at these lambda ratios. These findings will be rechecked in an additional experiment. If confirmed this data will provide a further test of the ability of the proposed model to predict asymmetry. Future testing will include other test temperatures and will examine the anisotropy of the back stress and drag stress through the use of two rate tests and biaxial strain hold tests.

### SIMULATIONS USING THE MODEL

The tubular specimens are oriented with the cylindrical axes along the  $\langle 001 \rangle$  crystallographic direction. When pulled in the axial direction the resolved shear stresses on the crystallographic cube planes are zero and only octahedral slip occurs. Material constants for the octahedral slip component of the constitutive model were most conveniently derived from the uniaxial data obtained at Pratt & Whitney. Figure 5 shows the experimental uniaxial data for PWA 1480 at 871C at strain rates of  $10^{-3}$ ,  $10^{-4}$  and  $10^{-5}$  per second in the  $\langle 001 \rangle$  direction and Fig. 6 shows the corresponding loops predicted with the constitutive model which agree well with the data. A check was made to ensure that the Pratt & Whitney uniaxial data, obtained from a different heat of material and with a bar instead of a tubular specimen, was comparable to the data collected in this program. The loops generated at Pratt & Whitney and at the University of Connecticut at 0.8 percent strain range and a strain rate of  $10^{-3}$  per second were practically indistinguishable. Thus, the material constants obtained from the test at Pratt & Whitney correctly predict the uniaxial data obtained at the University of Connecticut.

Figure 2 shows torsional hysteresis loops carried out at a strain rate of  $10^{-3}$ ,  $10^{-4}$  and  $5 \times 10^{-5}$  per second at a strain range of 0.6%. If only octahedral slip is included in the constitutive model the predicted loops, shown in Fig 7, are too narrow. Inclusion of cube slip in the model widens the predicted torsional loops and the predictions with combined octahedral and cube slip are shown in Fig. 8. Comparison of the data in Fig. 2 and the prediction from the combined octahedral and cube slip theory in Fig. 8 shows very good agreement. It is worth noting that  $\langle 001 \rangle$  tension data is especially suitable for the determination of the octahedral slip constitutive constants, since cube slip is inoperative for this direction under uniaxial loading conditions. Torsion tests will involve both cube slip, if operative, and octahedral slip and can be used to determine the cube slip constants once the octahedral constants have been determined from the  $\langle 001 \rangle$  uniaxial data. Comparison of the predicted torsional loops, using octahedral slip only, can be used to detect the occurrence of cube slip which is usually found only by laborious slip trace studies that are very difficult to conduct at temperatures above 593C (1100F).

### SUMMARY

A slip system based constitutive model has been formulated for PWA 1480

which represents explicitly both octahedral slip and cube slip. Tension-torsion tests on single crystal material have been run at 871C and some of the torsional results have been successfully simulated using the model. It was found that the prediction of torsion data from tension data was only successful if the correct combination of cube and octahedral slip was used. The prediction of torsion data is a useful tool in determining which slip modes are active. Future work will involve simulations of various biaxial test conditions and will also attempt to simulate tests with variable strain rates and strain holds. The results of the initial simulations are very encouraging and generation of more challenging test cases in the lab and the simulation of these more complex cases is expected to be an interesting exercise of the constitutive model development.

#### REFERENCES

1. Krempl, E., RPI Report No. RPI CS 78-5, 1978.
2. Oytana, H.S. and Sidebottom, O.M., "Constitutive Equations Study in Biaxial Stress Experiments," J. of Eng. Mat. and Tech., Trans. of ASME Ser. H, Vol. 104, Jan. 82, p. 1.
3. Lamba, H.S. and Sidebottom, O.M., "Cyclic Plasticity for Non-proportional Paths: Part I - Cyclic Hardening Experiments," J. of Eng. Mat. and Tech., Trans. of ASME Series H, Vol. 100, Jan. 78, p. 104.
4. Shah, D. and Lin, L., J. Metals, Vol. 32, No. 8, p. 62, 1980.

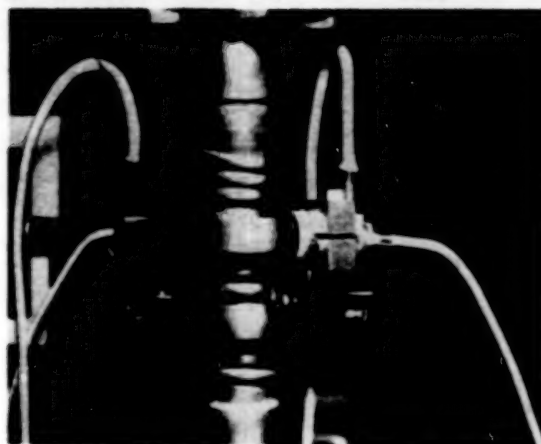


Figure 1: Single crystal specimen with extensometer and induction heater during biaxial test at 1600°F.

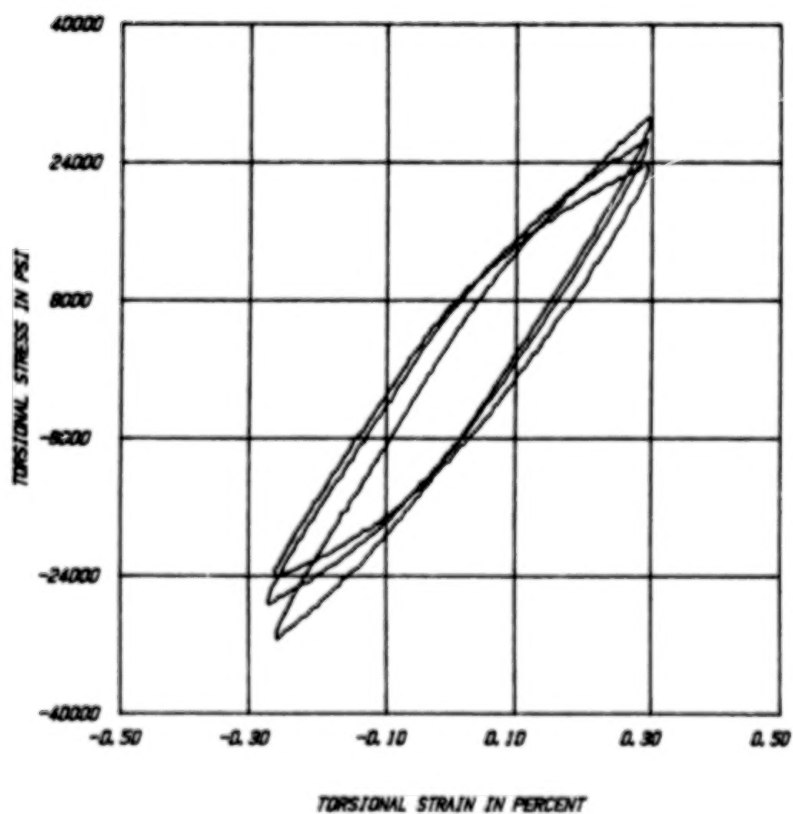


Figure 2: EXPERIMENTAL TORSIONAL LOOPS FOR PWA 1480 AT 1600°F

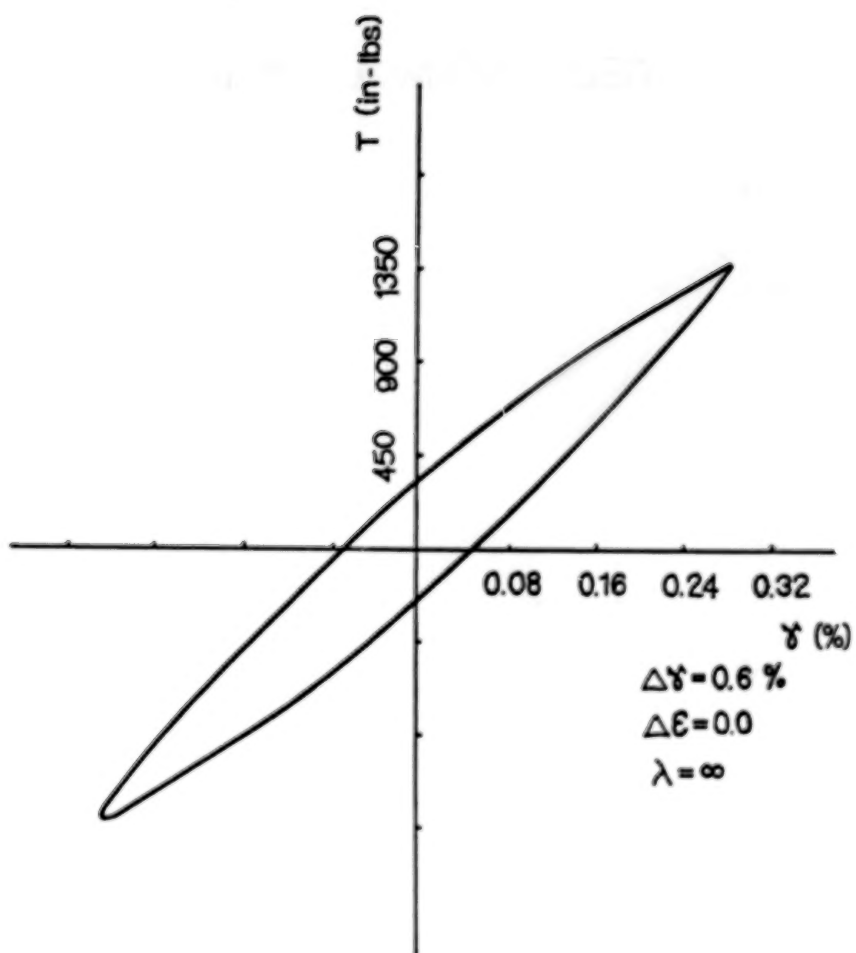
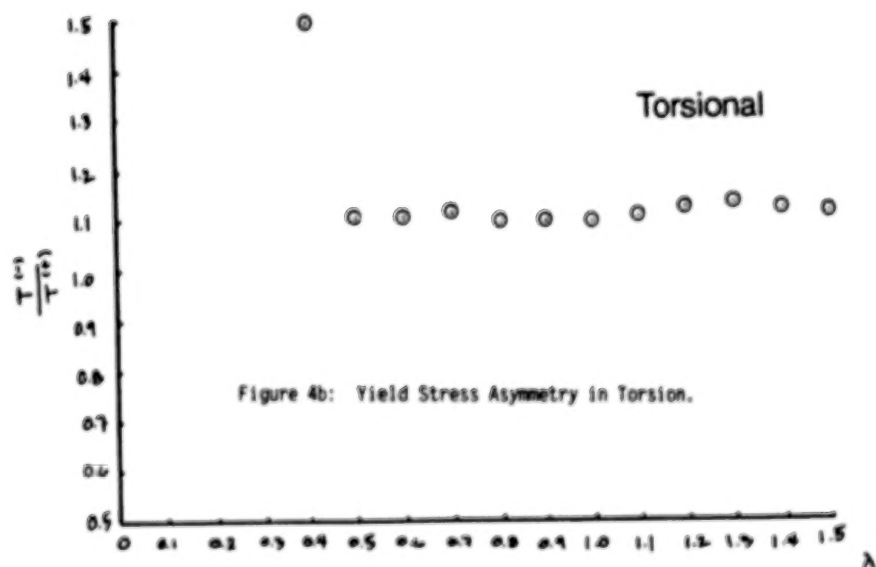
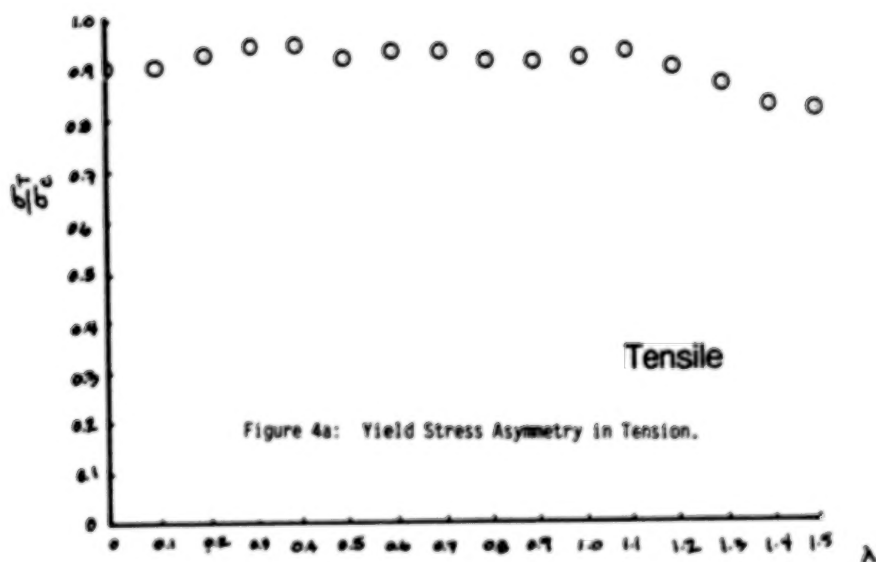


Figure 3: Torsional Loops Before and After Nonproportional Loading Cycles.

# YIELD ASYMMETRY



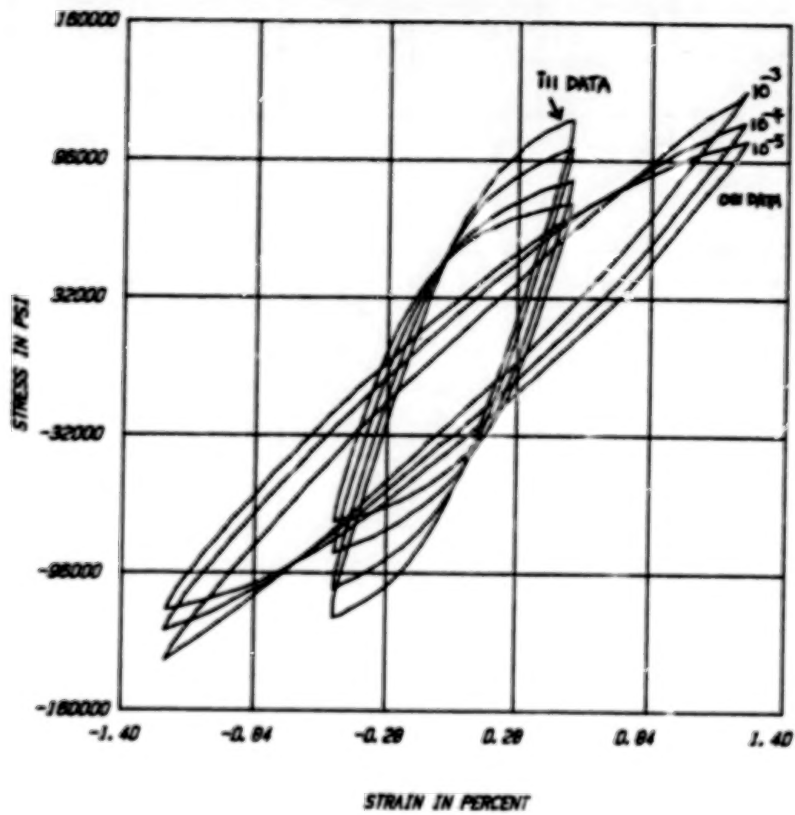


Figure 5: PWA 1480 EXPERIMENTAL HYSTERESIS LOOPS AT 1800F

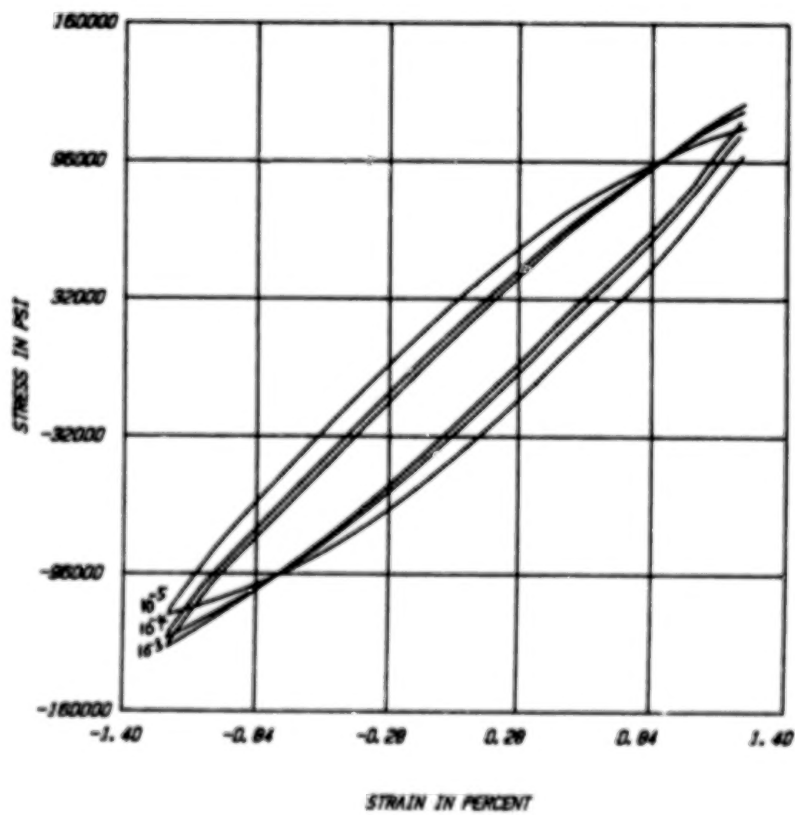


Figure 6: PREDICTED LOOPS FOR PWA 1480 AT 1800F (ODI DIRECTION)

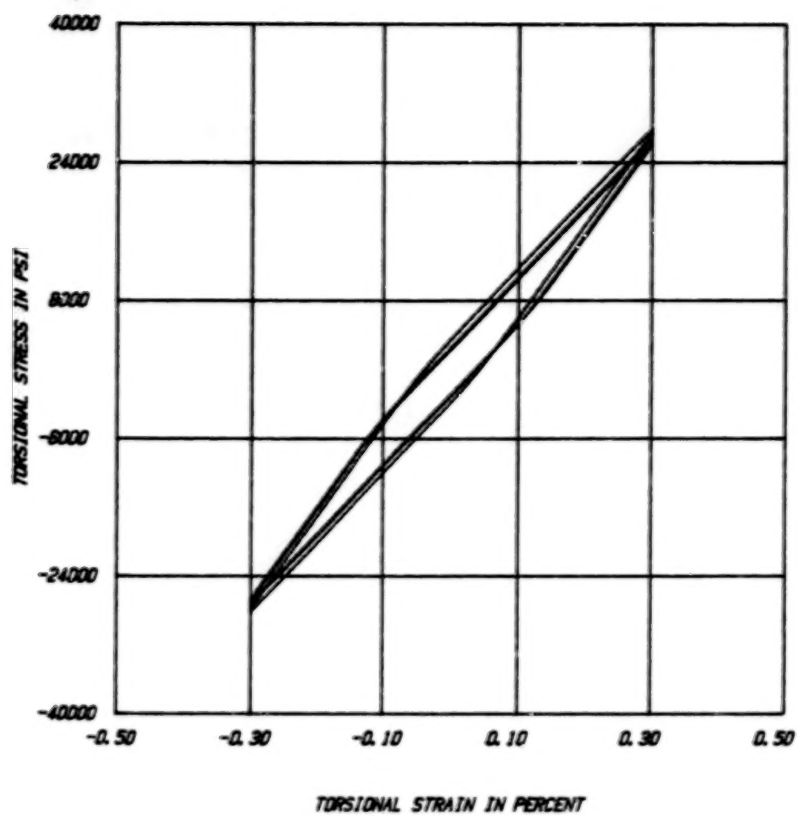


Figure 7: PREDICTED TORSIONAL LOOPS WITH OCTAHEDRAL SLIP

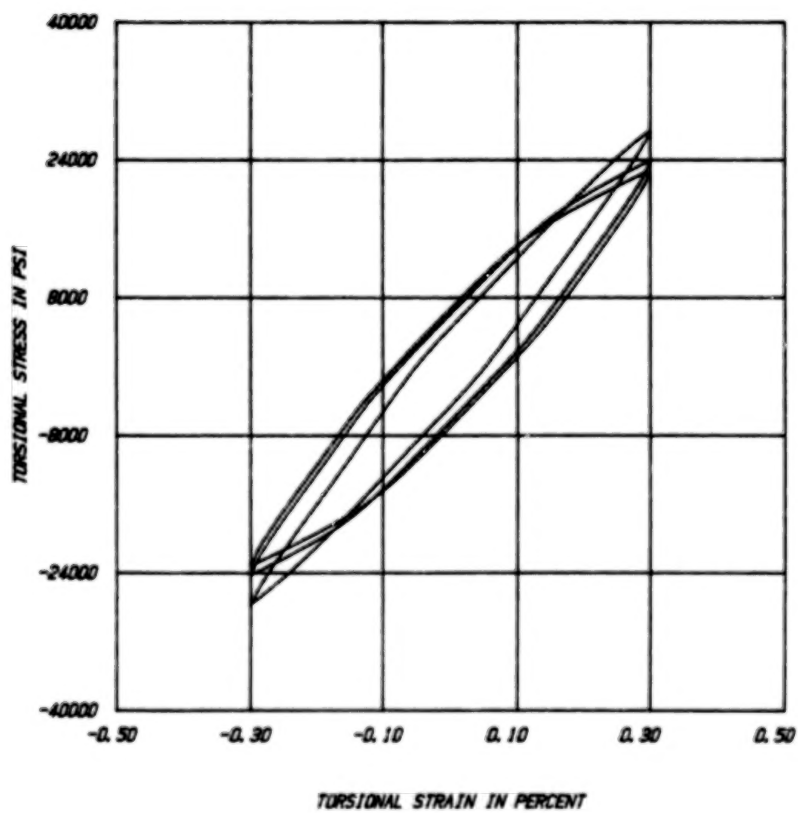


Figure 8: PREDICTED TORSIONAL LOOPS WITH OCTAHEDRAL AND CUBE SLIP

## HIGH TEMPERATURE STRESS-STRAIN ANALYSIS

Robert L. Thompson  
NASA Lewis Research Center  
Cleveland, Ohio

The objectives of the high-temperature structures program are threefold: to assist in the development of analytical tools needed to improve design analyses and procedures for the efficient and accurate prediction of the nonlinear structural response of hot-section components; to aid in the calibration, validation, and evaluation of the analytical tools by comparing predictions with experimental data; and to evaluate existing as well as advanced temperature and strain measurement instrumentation. As the analytical tools, test methods, tests, instrumentation, as well as data acquisition, management, and analysis methods are developed and evaluated, a proven, integrated analysis and experiment method will result in a more accurate prediction of the cyclic life of hot section components.

## TEST FACILITIES

The two test facilities at Lewis which support the development of the analytical tools and the evaluation of advanced instrumentation are the high-temperature structures laboratory and the structural component response test facility. Both of these facilities have the capability to conduct controlled thermomechanical cyclic experiments under computer control. Small tubular specimens will be tested in the high-temperature structures laboratory (see fig. 1) using uniaxial and biaxial test machines. Larger specimens such as flat plates, cylinders, and combustor liner segments are tested in the structural component response test facility, which consists of two rigs that operate at atmospheric pressures. Flat-plate specimens (5 by 8 in.) are tested in the bench-top quartz lamp rig (see fig. 2); large, cylindrical (~20 in. diameter) and combustor liner specimens are tested in the annular quartz lamp rig (see fig. 3). The high-temperature structures laboratory should be operational by early 1986; the bench-top quartz lamp rig and the annular quartz lamp rig are operational.

## High Temperature Laboratory

Two uniaxial test machines (load capacity,  $\pm 20$ -kip) and two biaxial test machines ( $\pm 55$ -kip load in tension/compression and 25-kip in torsional capacity) are used in the high-temperature structures laboratory for deformation testing. Each of these machines is computer controlled by an S20 Data General computer. A larger Data General computer (MV/4000) is used for data storage, management, reduction, and analysis. Five-kilowatt-radiofrequency induction heaters are used with the uniaxial machines, and 50-kW-audiofrequency induction heaters will be used with the tension/torsion test machines. Instrumentation includes high-temperature water-cooled uniaxial extensometers for measuring strains on the uniaxial test machines. Two high-temperature biaxial extensometers will be tested and evaluated on the biaxial test machines. A third high-temperature biaxial extensometer will be evaluated as part of an interagency agreement with the Oak Ridge National Laboratory. High-temperature grips for the biaxial test machines have been fabricated.

### Bench-Top Rig

The major components of the bench-top quartz lamp rig are shown in figure 2. Four quartz lamps (6 kVA) are used to heat the plate specimens. The lamps are air cooled, and the test fixture is water cooled. A manifold provides cooling air to the top surface of the test plate. The cooling air to the plate can be preheated to 400 °F. A lamp-out detection system determines when a lamp has burned out.

A dual-loop programmable controller, a microprocessor, is used to control the power to the lamps. A specified power-time history is programmed into the microprocessor, and the cooling air temperature and flow rate are appropriately set so that when combined, the desired thermal cycle is imposed on the test plate.

Thermocouples and an infrared thermovision system are used to obtain surface temperatures on the plate. There are provisions for taking 30 thermocouple measurements. A viewport, consisting of a 5-inch-diameter quartz window, provides access for obtaining an infrared thermal image. Both thermocouple and thermal image data are obtained on the cool side of the test plate. Only thermocouple data are obtained on the hot side (facing the four quartz lamps) of the test plate. The thermocouple data provide temperatures at discrete points, while the infrared system provides detailed maps of thermal information about the test specimen.

During a test run both the facilities data (pressures, flows, power, etc) and the research data (primarily temperature) are acquired for each thermal cycle using the ESCORT II data acquisition system at Lewis. These data can be stored automatically once every second on the Amdahl computer. The software, however, does allow for varying the time at which data are taken during a thermal cycle. These data can be displayed on CRT's in the control room with about a 4-sec delay time. To obtain real time readings of pertinent data, a strip chart recorder with nine channels is used.

The raw thermal images obtained from the infrared camera are stored on a VHS tape recorder, with the clock time superimposed on each image. Images of the test plate of from about 4 to about 1 in. in diameter (for finer resolution of temperatures) can be obtained with the zooming capability of the infrared system. Thirty thermal images are captured on tape every second. A computer system is then used to process, reduce, enhance, and analyze the transient temperature information. These data are also compared with the thermocouple data. Thermocouple data are used in the calibration of the infrared system.

### Bench Top Rig Test Results

Some of the salient results of tests conducted on a Hastelloy-X flat plate, with dimensions of 8 by 5 by 0.05 in., are as follows: The plate temperatures are very repeatable from cycle to cycle. A 20-second ramp time from low to peak temperature on the plate was achieved. The nominal life of the quartz lamps is 500 thermal cycles. Actual lamp life, however, varies depending on power settings (maximum or minimum), the hold times at those settings, and the ramp rates for a given thermal cycle. The infrared thermovision system provides a qualitative measure (maps) and, in some cases, a quantitative measure of transient surface temperatures. The experience, data, and other information obtained from the bench-top rig tests have benefited the installation and checkout of the annular quartz lamp rig.

## Annular Rig

Figure 3 shows the annular quartz lamp rig installation and its major components. This rig is being operated under a cooperative agreement with Pratt & Whitney Aircraft (PWA). G. Pfeifer of PWA is my coinvestigator on this project.

The quartz lamp heating system used to cyclically heat a test liner is shown in figure 4. One-hundred-twelve 6-kVA lamps configured circumferentially in 16 sectors, each having 7 lamps, are used to heat a 20-inch diameter test liner. This system, in addition to drawing up to 672 kVA of 480-V power, requires 3.5 lb/sec of ambient temperature air at 5 psig, 1.5 lb/sec of ambient temperature air at 1 psig, and 80 gal/min of specially treated water for cooling the rig.

A natural-gas and air mixture is burned in a combustor can upstream of the test section to provide preheated cooling air to the test liner. Cooling air temperatures of from 400 to 600 °F can be obtained by varying the fuel/air mixture ratio. The cooling airflow rate is variable from about 4.0 to 7.5 lb/sec at 35 psig. Both the cooling-air temperature and flow rate can be varied to obtain the desired cyclic temperatures on the test liner.

The annular rig has six 5-inch diameter viewports, three of which are spaced at 120° apart and are used to view the middle section of the test liner. The other three, also spaced at 120° apart, are used to view the upstream portion of the liner and its attachment piece. These windows are rotated 45° from the liner windows. The quartz windows are air and water cooled. Through these windows television cameras and the infrared camera are used to monitor and take temperature measurements on the liner. There are also provisions for having almost 100 thermocouples on the test liner.

The dual loop programmable controller system, the ESCORT II data acquisition system, and the infrared thermovision system, described previously for the bench-top rig application, are the same systems used for the annular rig.

For the checkout of the annular rig, a conventional combustor test liner (stacked-ring louver configuration supplied by PWA) was installed in the test section. Its purpose was to assist not only in the checkout of each of the rig systems, but also to identify potential test problems and possible integrated analysis/experimental complications and to provide some thermal cyclic data such as liner temperatures and distortions. These data were used in the preliminary structural analysis of the liner. Shown in figure 3 is the instrumented liner made of Hastelloy-X material. Seventy thermocouples provided the temperatures: 55 were used to monitor the cool-side temperatures, and 15 monitored the hot-side temperatures.

## Annular Rig Test Results

After the rig checkout steady-state and transient tests were conducted to determine the thermal response of the liner under various test conditions. Combinations of power settings, cooling airflow rates, cooling air temperatures, and ramp times were conducted. The results of these tests were used to determine the appropriate settings of the test control variables to obtain surface metal temperature profiles similar to those of an actual combustor liner. Other concerns that affected the settings of the test variables were lamp life, rig temperature, and rig durability.

Figure 5 shows the peak steady-state cool-side temperatures of the louver test liner as a function of power settings for a cooling airflow rate of 5.5 lb/sec and cooling air temperatures of 400, 500, and 600 °F. The two other cooling flow rates were 6.5 and 7.5 lb/sec. Plotted in figure 6 are the minimum temperatures for the same test conditions. The minimum and peak temperatures occur at different locations on the liner. Peak temperatures were taken from a thermocouple mounted on the louver weld. And minimum temperatures were taken from a thermocouple mounted on the louver knuckle. Over the power range plotted the peak temperatures differ by about 50° between the cooling air temperatures, whereas the minimum temperatures differ by about 100 °F.

From the steady-state data and ramp tests, not reported here, a power versus time curve was determined that simulated an actual engine mission thermal cycle. The power history for the thermal cycle is shown in figure 7. The cyclic test conditions were a coolant flow rate of 5.5 lb/sec, a coolant flow temperature of 600 °F, a minimum power of 38 percent (actual), and a maximum power of 83 percent (actual). The total thermal cycle time was 2.2 minutes. The time was broken up into a 6-sec ramp up time from minimum to maximum power, a 60-sec hold time at maximum power, a 6-sec ramp down time, and a 60-sec hold time at minimum power. This power history was programmed into the dual-loop programmable controller. The controller was run in the set-point control mode.

Figure 8 shows the temperature response to the power history of a thermocouple mounted on the hot side of the louver weld. For the 6-sec ramp up in power there was about a 25-sec time required for the liner temperature to reach equilibrium conditions, or about a 20-sec lag between the time to maximum power and stable peak liner temperatures. The 6-sec ramp down-time results in an almost mirror image of the ramp up in terms of time for the liner to reach stable minimum temperatures. The ramp up and the ramp down times simulate the ascent and descent phases of an engine mission cycle, and the hold time represents cruise conditions, where the interaction of creep and plasticity occur simultaneously.

Some typical thermocouple data are shown in figures 9 and 10. The data shown are the cool-side temperatures at maximum power of the cluster of thermocouples for the 450th thermal cycle. These data are used to plot axial and circumferential temperatures for the fourth and fifth louver liners on the liner. Examples of these types of plots are shown in figures 11 and 12. These temperatures are used in the heat-transfer/structural analysis of the liner.

The infrared thermovision system is used to obtain a more detailed map of the cool-side liner temperatures. Figure 13 is an example of the IR data obtained. Plotted are axial temperatures on the louver No. 4. Only the temperatures are shown for the maximum and minimum powers at steady-state conditions of the thermal cycle. With this system over  $10^7$  temperature measurements are obtained for each thermal cycle. Thermocouple data are also shown for comparison.

The test liner was subjected to 930 heating cycles, including the initial parametric testing. For the bulk of the tests, the cycles produced a liner hot-side surface temperature at the highest-reading thermocouple of nominally 1815 °F at 83 percent power and 1140 °F at 38 percent power. Only a few of the thermocouples failed during the tests. Thermocouple data indicated that the surface temperatures were remarkably stable and repeatable over the hundred of cycles. Temperature variation at maximum power over the hundred of cycles was generally no more than  $\pm 25$  °F. Inspection of the liner on several occasions showed minor distortion of several segment lips. The distortion was symmetric with the 16 quartz lamp zones.

Of the 112 original quartz lamps, 35 lamps were replaced. Criteria for lamp replacement were excessive darkening of the glass envelope or sagging filaments. The remaining original lamps (77 of 112) operated for 930 cycles and 52 hours, of which 23 hours were at 80 percent or greater power. Based on the cumulative failures to date, a statistical analysis predicts a lamp half life of 85 hours.

#### ANALYSIS

The liner surface temperature measurements obtained from the thermocouples and the infrared thermovision system were used first to obtain the film coefficients on the cool and hot surfaces and then to compare them with predictions. Figure 14 shows the values of the film coefficients for louver 4.

The heat-transfer analysis was performed using MARC, a general-purpose, nonlinear, finite-element heat-transfer and structural-analysis program. A two-dimensional, axisymmetric, transient, heat-transfer analysis of the louver was performed. Eight-node, heat-transfer finite elements were used in the analysis, and 107 elements and 522 nodes were used to model the louver. Figure 15 shows both predicted cool-side liner temperatures and the experimental data at maximum power (83 percent) obtained from the infrared thermovision system. The figure shows good agreement between prediction and experimental data at this power level, but at lower power levels the prediction is not quite as good. A temperature contour plot at the maximum power level is shown in figure 16. There is also good agreement between transient temperature predictions and experimental data.

The MARC program produces a tape which contains the temperature information. The temperatures (or thermal loads) are then input to the structural-analysis program. The MARC program was also used to perform the structural analysis. A two-dimensional axisymmetric transient structural analysis of the louver was performed. Eight-node-structure finite elements were used in the analysis. The stress model was identical to the heat-transfer model. Symmetric boundary conditions were assumed at the ends of the louver. Walker's viscoplastic constitutive model was used in the analysis. This viscoplastic model, and others like it, accounts for the interaction between creep and plasticity, strain rate effects, time-independent and time-dependent effects, and other effects critical to a combustor-liner analysis and design.

Figure 17 is a hysteretic plot of hoop stress versus hoop strain for a point very near the cool spot on the liner. Figure 18 is a hysteretic plot of hoop stress versus hoop strain, for a point near the weld. These data could be used to identify critical failure locations in a liner and provide for better damage or fatigue/failure predictions.

To date no strain (or displacement) measurements have been taken on a flat plate or a test liner. However, plans are underway to begin to evaluate advanced static strain measurement systems, on both contact and noncontact devices. High-temperature (1300 °F), temperature-compensating resistant strain gauges will be evaluated on tubular and flat-plate Hastelloy-X specimens. This is a cooperative effort with the Instrumentation group at Lewis. Proximity transducers will also be evaluated. In addition, a laser specklegram system developed by C. Stetson at United Technologies Research Center (UTRC) will be evaluated on the bench-top rig. This also is a cooperative effort with UTRC and the Instrumentation group at Lewis. It is these strain measurements that will be then used to validate and evaluate the structural analytical tools now being developed.

## CONCLUSIONS

The high temperature structures laboratory should be operational by early 1986. The bench-top quartz lamp rig and the annular quartz lamp rig are operational. Some preliminary tests have been conducted in both of the quartz lamp rigs. Over 900 thermal cycles were accumulated on a conventional sheet-metal louver combustor liner in the annular rig. Liner temperatures were stable and repeatable not only for each thermal cycle but from test to test. The temperature data obtained from thermocouples and the infrared camera are being analyzed and used in a preliminary heat-transfer analysis of the liner. Preliminary nonlinear, structural analyses are also being performed using as input the thermal loads obtained from the thermal analyses.

## FUTURE RESEARCH

A second conventional sheet metal louver combustor liner is being instrumented with 105 thermocouples. Testing of this liner in the annular rig should begin by early November. Plans are also to test straight cylindrical specimens. An advanced liner is scheduled to be tested in early 1986. Advanced, high-temperature strain gauges and a laser specklegram system are to be evaluated on the bench-top rig in early 1986.

## HIGH-TEMPERATURE FATIGUE AND STRUCTURES LABORATORY

ORIGINAL PAGE IS  
OF POOR QUALITY

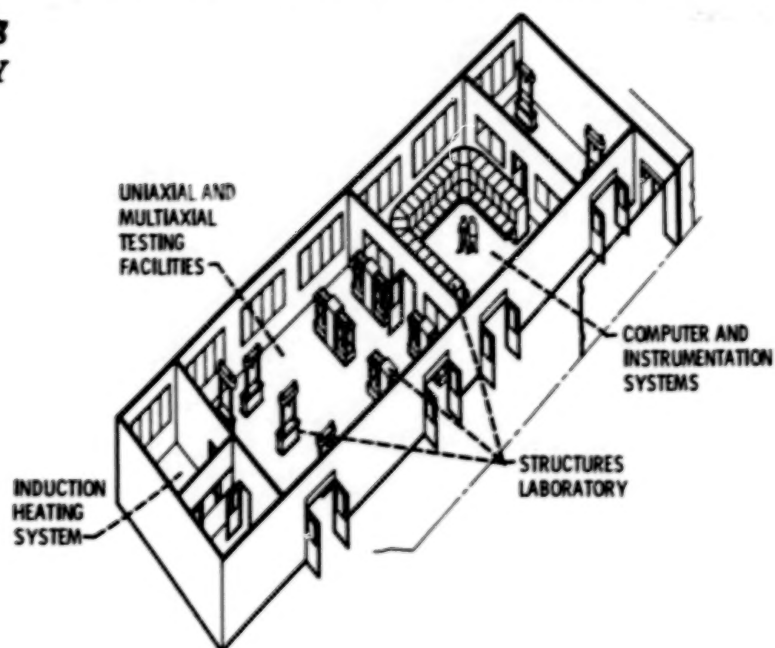


Figure 1

## BENCH-TOP QUARTZ LAMP RIG

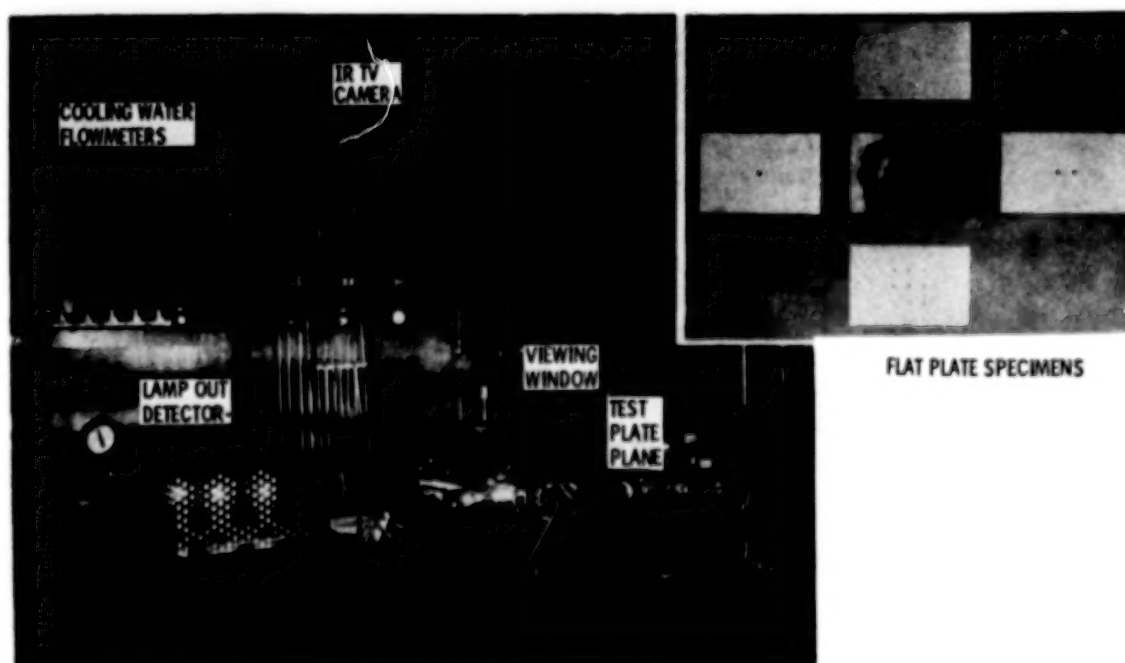


Figure 2

# ANNULAR QUARTZ LAMP RIG



Figure 3

## QUARTZ LAMP HEATING SYSTEM

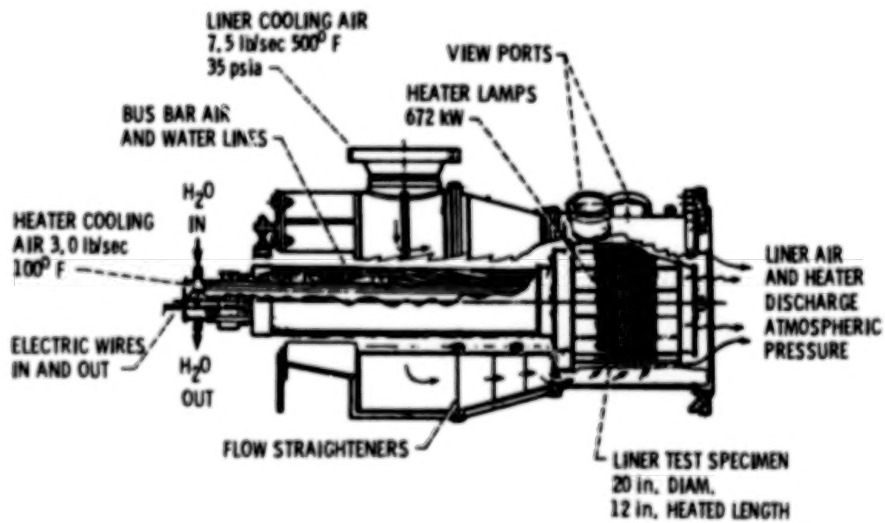


Figure 4

ORIGINAL PAGE IS  
OF POOR QUALITY

# FULL-ANNULAR LINER PEAK STEADY-STATE LINER TEMPERATURES

COOLING AIR FLOW RATE, 5.5 lb/sec

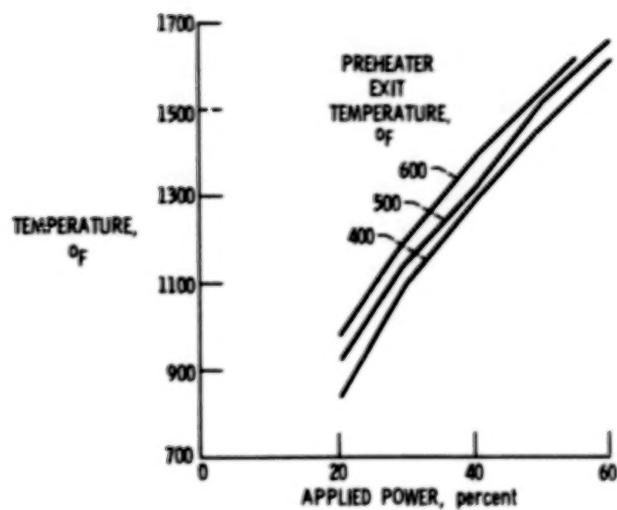


Figure 5

# FULL-ANNULAR LINER MINIMUM STEADY-STATE TEMPERATURES

COOLING FLOW RATE, 5.5 lb/sec

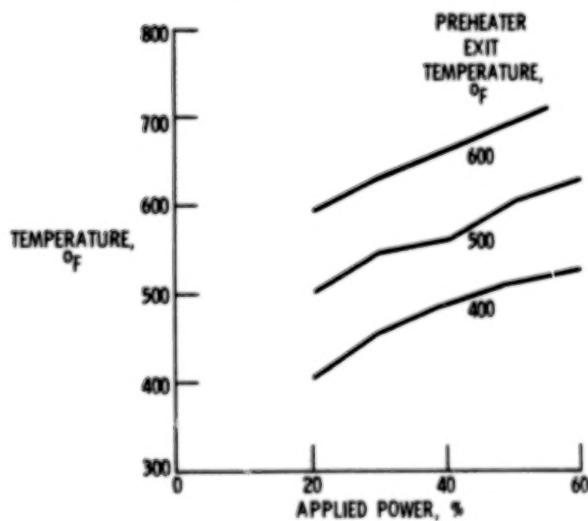


Figure 6

### POWER HISTORY FOR THERMAL CYCLE

COOLANT FLOW RATE, 5.5/sec; COOLANT FLOW TEMPERATURE, 600 °F

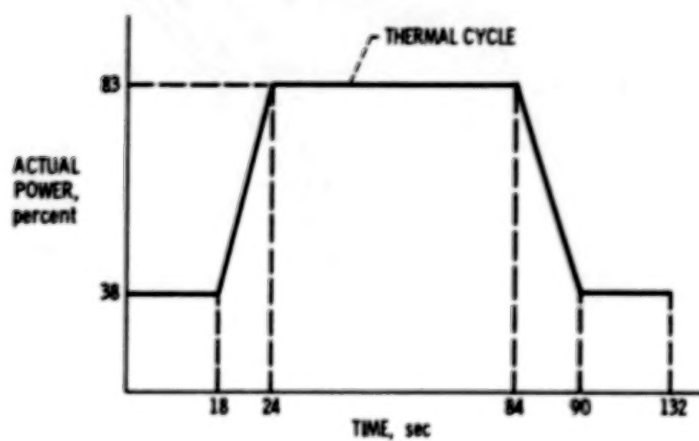


Figure 7

### MEASURED PEAK COMBUSTOR LINER TEMPERATURE

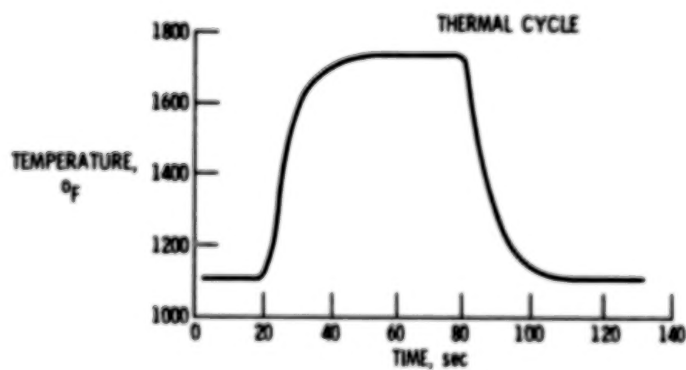


Figure 8

# TYPICAL COOL-SIDE TEMPERATURES AT MAXIMUM POWER 450 THERMAL CYCLES

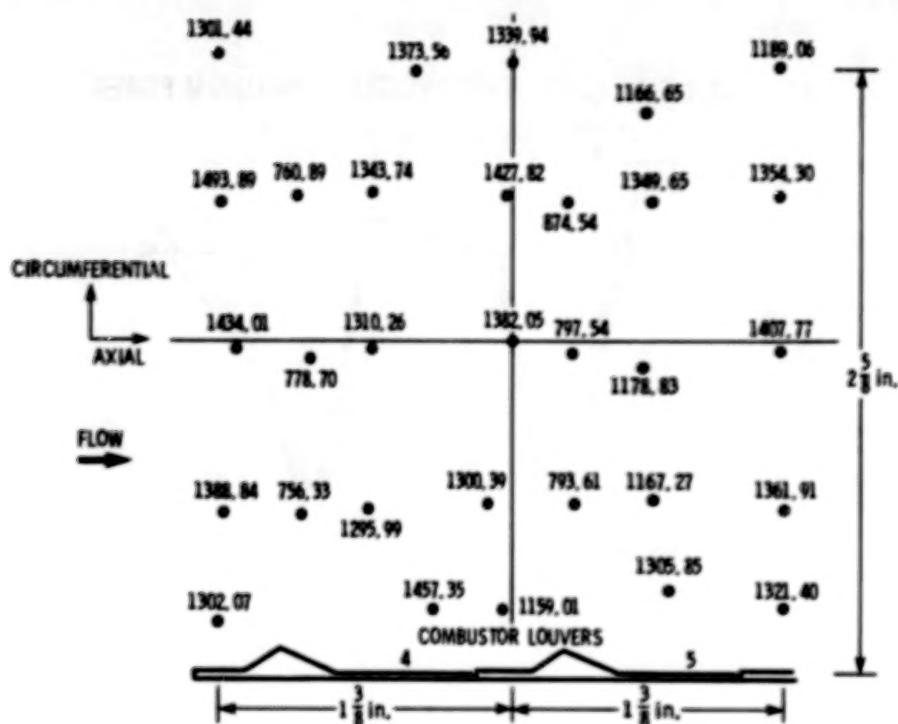


Figure 9

# TYPICAL COOL-SIDE TEMPERATURES AT MINIMUM POWER

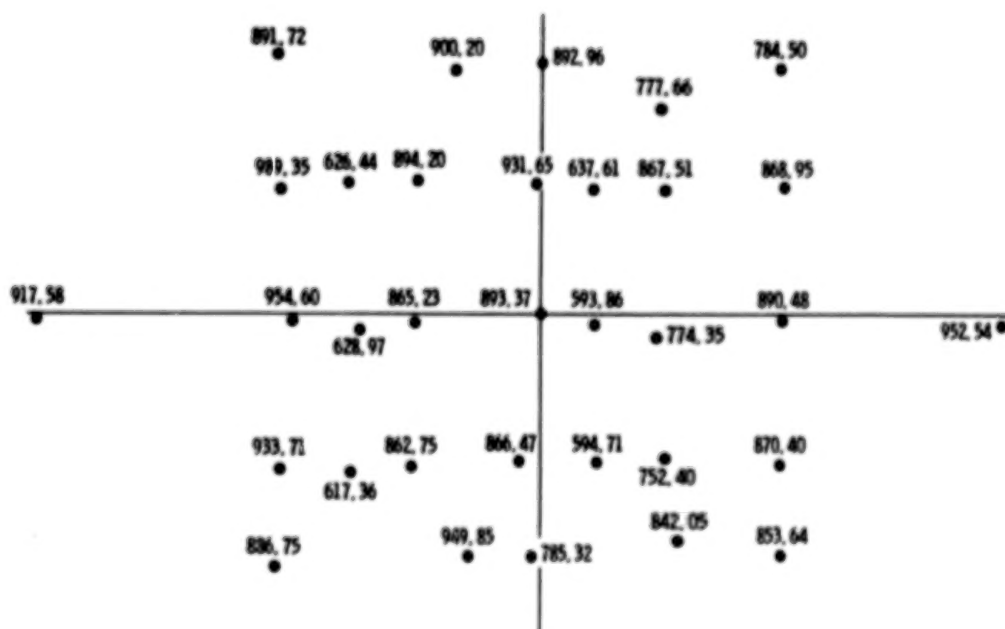


Figure 10

AXIAL COOL-SIDE LINER TEMPERATURES AT MAXIMUM POWER  
FOR THREE AXIAL LOCATIONS THERMOCOUPLE

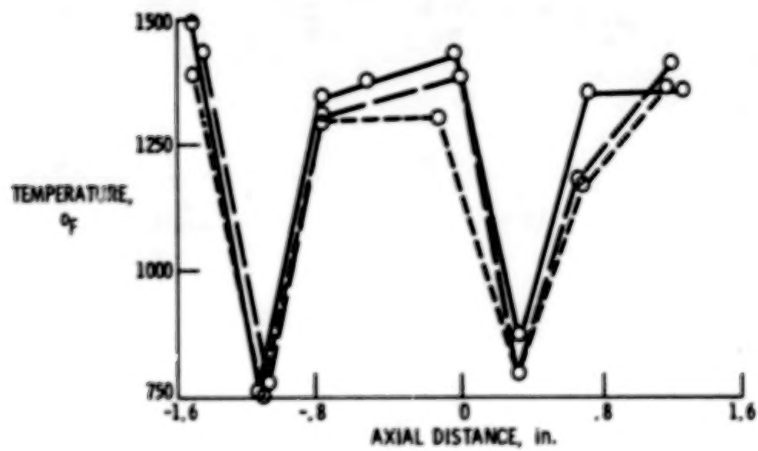


Figure 11

CIRCUMFERENTIAL COOL-SIDE LINER TEMPERATURES AT MAXIMUM POWER  
FOR THREE CIRCUMFERENTIAL THERMOCOUPLE LOCATIONS

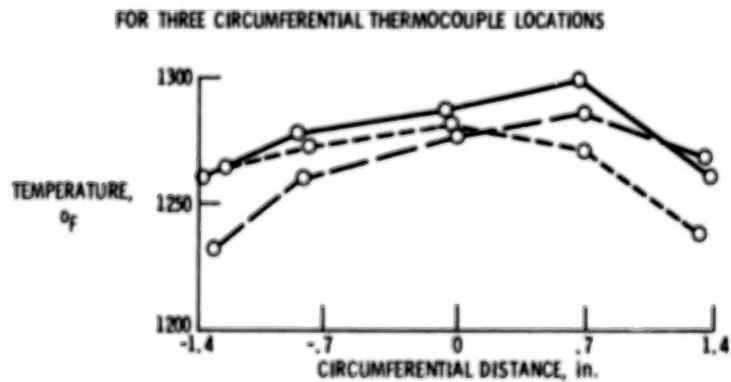


Figure 12

### MEASURED COOL-SIDE LINER TEMPERATURES

COOLING AIR FLOW RATE, 5.5 lb/sec; COOLING AIR TEMPERATURE, 600 °F

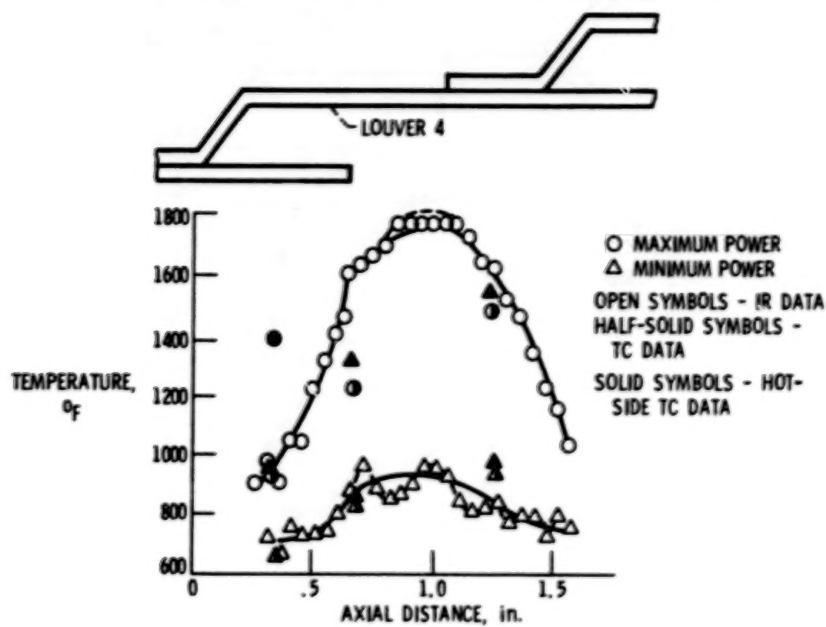


Figure 13

### THERMAL FILM COEFFICIENTS FOR LOUVER 4

NUMBERS ARE HEAT TRANSFER FILM COEFFICIENT IN  $\text{Btu/ft}^2\text{-hr} - ^\circ\text{F}$

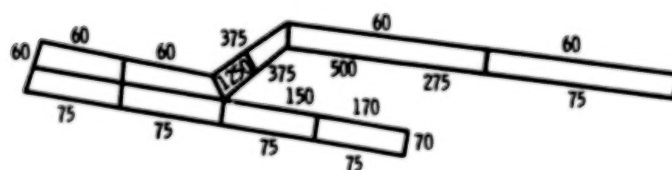


Figure 14

# COOL-SIDE LINER TEMPERATURE AT MAXIMUM POWER (83%)

COOLING AIR FLOW RATE, 5.5 lb/sec; COOLING AIR TEMPERATURE, 600 °F

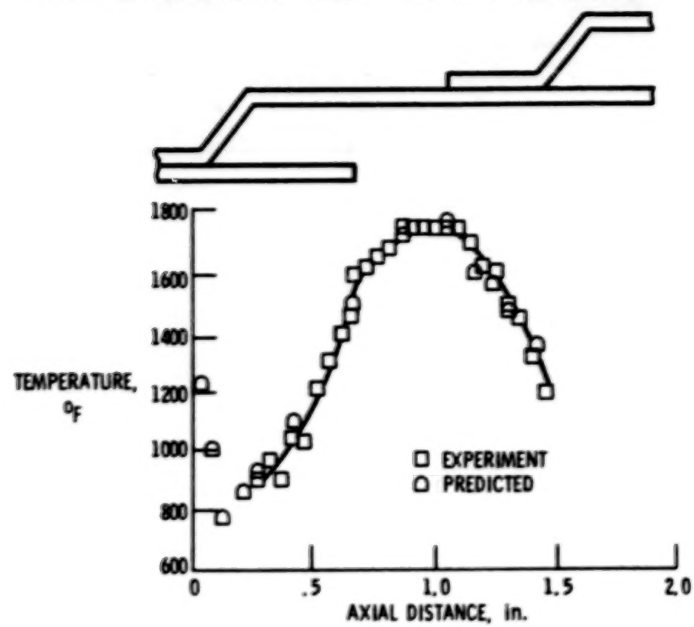


Figure 15

# PREDICTED LINER TEMPERATURES AT MAXIMUM POWER

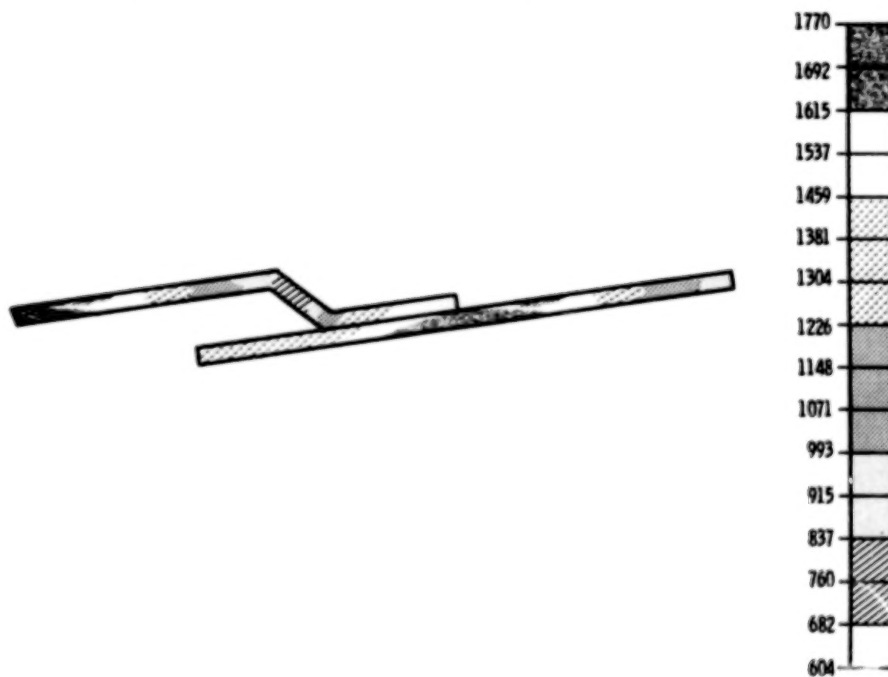
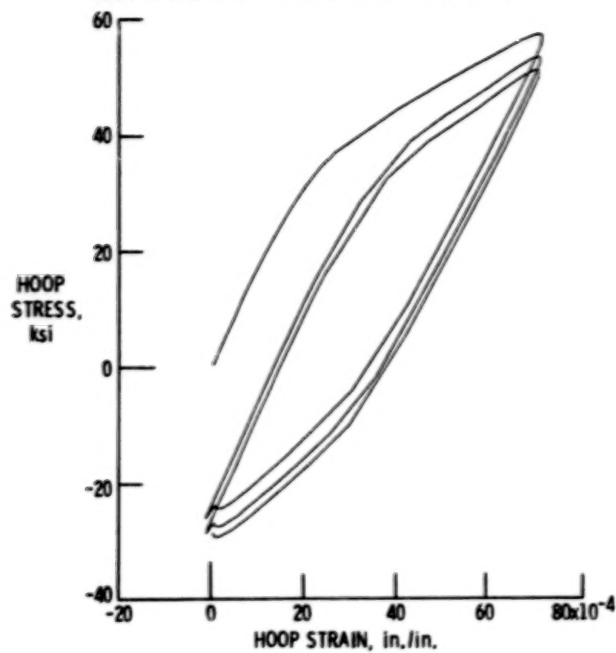


Figure 16

**THERMOMECHANICAL LOOP PREDICTED BY WALKER'S MODEL  
FOR A POINT NEAR A COOLING HOLE**



**Figure 17**

**THERMOMECHANICAL LOOP PREDICTED BY  
WALKER'S MODEL FOR A POINT AT THE WELD**

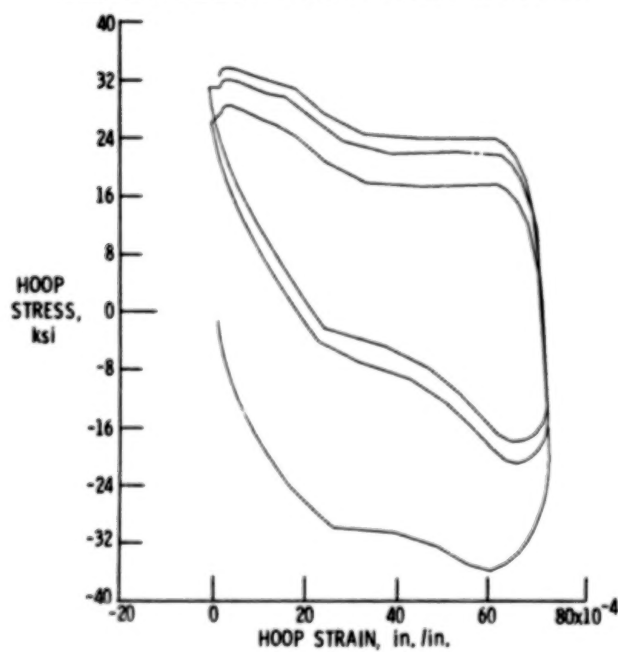


**Figure 18**

## CONSTITUTIVE MODELING FOR ISOTROPIC MATERIALS\*

Ulric S. Lindholm  
Southwest Research Institute

## INTRODUCTION

The objective of the present program is to develop a unified constitutive model for finite-element structural analysis of turbine engine hot section components. This effort constitutes a different approach for non-linear finite-element computer codes which have heretofore been based on classical inelastic methods. The unified constitutive theory to be developed will avoid the simplifying assumptions of classical theory and should more accurately represent the behavior of superalloy materials under cyclic loading conditions and high-temperature environments. This class of constitutive theory is characterized by the use of kinetic equations and internal variables with appropriate evolution equations for treating all aspects of inelastic deformation including plasticity, creep, and stress relaxation. Model development is directed toward isotropic, cast nickel-base alloys used for air-cooled turbine blades and vanes. Recent studies have shown that this approach is particularly suited for determining the cyclic behavior of superalloy-type blade and vane materials and is entirely compatible with three-dimensional inelastic finite-element formulations. More efficient and accurate inelastic analysis of hot section components--turbine blades, turbine vanes, combustor liners, and seals--fabricated from "age hardenable" isotropic superalloy materials will be realized as the result of these developments.

During the first two years of the program, extensive experimental correlations have been made with two representative unified models. The experiments are both uniaxial and biaxial at temperatures up to 1093°C (2000°F). In addition, the unified models have been adapted to the MARC finite element structural code and used for stress analysis of notched bar and turbine blade geometries.

## CONSTITUTIVE MODEL SELECTION

A literature survey was conducted to assess the state-of-the-art of time-temperature dependent elastic-viscoplastic constitutive theories which are based on the unified approach. As reported earlier (ref. 1), the review identified more than ten such unified theories which are shown to satisfy the uniqueness and stability criteria imposed by Drucker's postulate and Ponter's inequalities. These theories are compared on the basis of the types of flow law, kinetic equation, evolution equation of the internal variables, and treatment of temperature dependence.

As a result of the literature survey, the models of Bodner and Partom (ref. 2) and of Walker (ref. 3) were selected for further study. These two models are representative of the class of unified models considered in the review process but differ significantly in the choice of particular functional forms for the basic flow law, the kinetic relationship, the parameter used as a measure of hardening, and the evolution equations for the internal variables describing work hardening. Thus, a direct comparison between these two models and the experiments should illustrate well the consequences of a wide range in constitutive modeling approach. It

\*Work done under NASA Contract NAS3-23925.

is also significant that both models have already found significant application to analysis of gas turbine materials and to hot section components. Therefore, they are further along in their development and evaluation than most of the other comparable models.

### MATERIAL SELECTION

Two materials widely used in gas turbines are being evaluated with the constitutive models: PWA alloy B1900+Hf and MAR-M247. Tests completed to date have been with B1900+Hf. Casting configurations and pour and mold temperatures were selected to assure a grain size of ASTM No. 1 to 2 in the gage section and a  $\gamma'$  size of 0.9  $\mu\text{m}$  in the fully heat treated condition for the B1900+Hf.

### EVALUATION OF UNIFIED MODELS

The testing program included uniaxial and biaxial (tension-torsion) isothermal specimens in monotonic, creep, stress relaxation, and cyclic loading sequences encompassing wide variations in strain rate and temperature. Various thermo-mechanical fatigue cycles were investigated also. In each case, the measured material response was correlated with the two unified constitutive models. A small subset of the data was used to determine the constants for each model; about eight to ten constants are required. Also, definitive procedures were developed to determine each constant. The data correlations presented are based on the models with material constants determined from tensile or tensile and a few fatigue cycles. In this sense the results are predictive.

Some representative results are shown in Figures 1-4 for tensile, creep, cyclic, and TMF load histories. Over 60 different loading histories were examined with generally good correlation using both models.

Correlation of local deformation at the root of a notched round tensile specimen was not as good as for the homogeneously-stressed test specimens. This was attributed to specimen material inhomogeneity and to accuracy of the material model in the near yield (small inelastic strain) region.

### CONCLUSIONS

The results of this program provide strong evidence for the applicability of the unified constitutive equation approach to describe the strongly non-linear, time- and temperature-dependent response of metals to arbitrary load or deformation histories. As a minimum, the two models studied were correlative in that they demonstrated reasonable agreement with all the experimental data generated over a very wide range of temperature, deformation rate, and load cycle. This was accomplished with a fixed model and fixed set of material constants. In a broader sense, the models were predictive in that the functional representations and the material constants were obtained from a small subset of the total tests performed. Even better overall correlation could have been achieved if all the data were used to optimize the functions and constants in each model.

A major criticism of the unified models has been the apparent (and often real) difficulty in defining and experimentally determining the multiple material constants

employed in the models. We believe we have made significant progress in this regard. The different terms in the constitutive equations are very interactive so that it is essential to have a physical insight into the meaning of each function and its associated constants. Procedures developed delineate a deterministic method for evaluating the constitutive constants in a sequential manner from a relatively small material test data base.

While the correlative and predictive capacity of the unified models has been demonstrated, their practical application will depend on their adaptability in efficient computational algorithms when incorporated into finite element or other numerical methods for structural analysis. Preliminary use with the MARC finite element code indicates that improvement is needed in the numerical integration procedures used with these stiff, nonlinear equations. The computation time for an equivalent problem is approximately the same order of magnitude as when using classical, time-independent plasticity formulations.

#### REFERENCES

1. Lindholm, U. S.; Chan, K. S.; Bodner, S. R.; Weber, R. M.; Walker, K. P.; and Cassenti, B. N.: Constitutive Modeling for Isotropic Materials. Annual Report NASA CR-174718, 1984.
2. Bodner, S. R.; and Partom, Y.: ASME J. of Applied Mechanics, vol. 42, 1975, p. 385.
3. Walker, K. P.; NASA Contract Report NASA CR-165533, 1981.

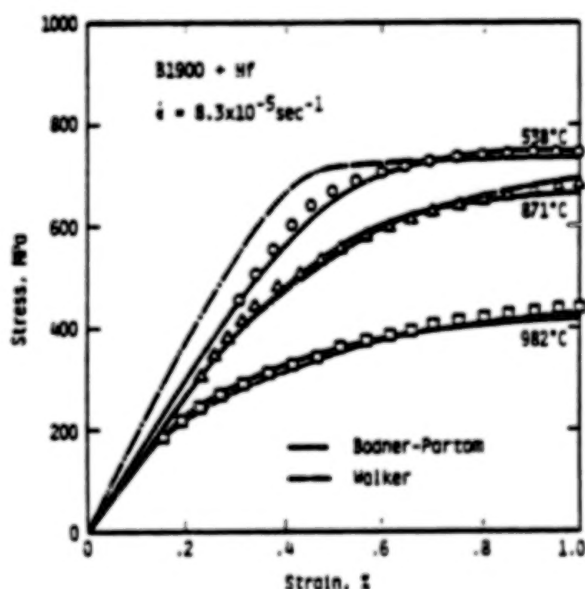


Figure 1

COMPARISON OF EXPERIMENTAL AND CALCULATED STRESS-STRAIN CURVES OF B1900+HF AT THREE TEMPERATURES

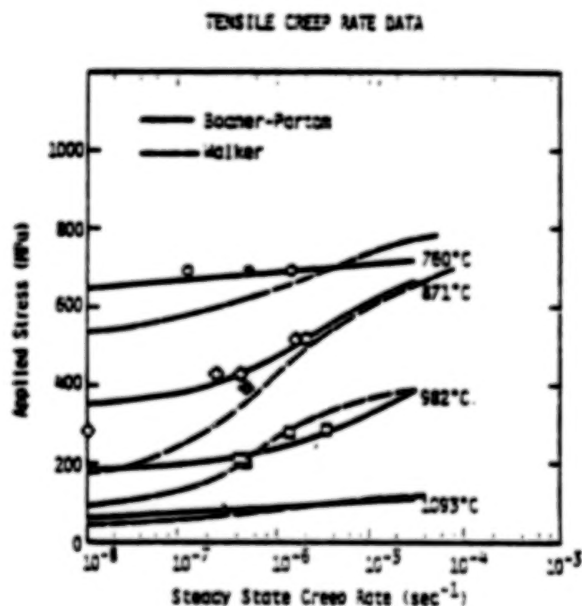


Figure 2

THE CALCULATED AND EXPERIMENTAL RESULTS OF CONSTANT LOAD CREEP TESTS

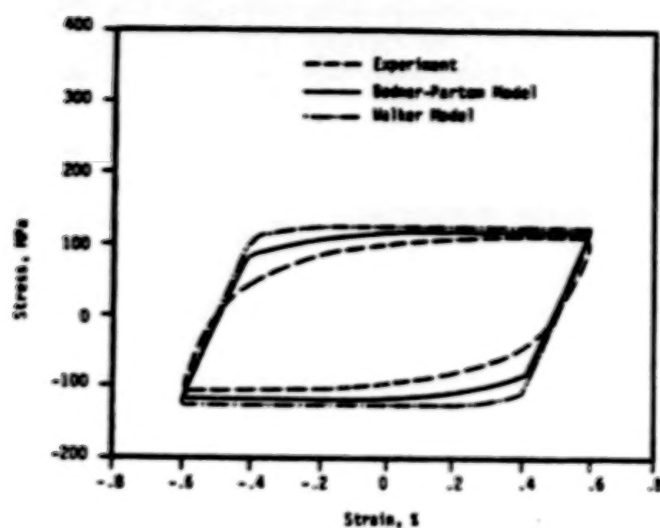


Figure 3

COMPARISON OF THE EXPERIMENTAL AND CALCULATED  
STABLE HYSTERESIS LOOPS OF B1900+Hf at 1093°C

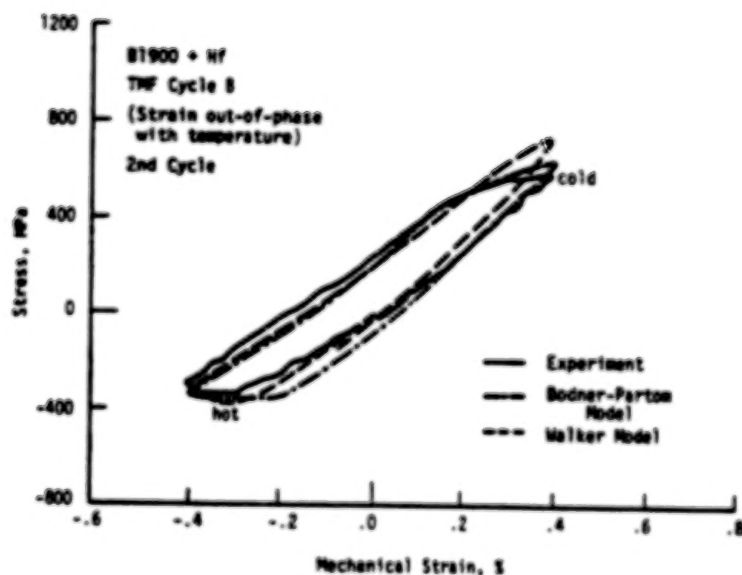


Figure 4

THERMOMECHANICAL CYCLIC DATA COMPARED WITH THE  
WALKER AND THE BODNER-PARTON MODEL PREDICTION  
FOR THE OUT-OF-PHASE TMF CYCLE

## CONSTITUTIVE MODELING FOR ISOTROPIC MATERIALS\*

V.G. Ramaswamy, R.H. Van Stone, L.T. Dame, J.H. Lafien  
General Electric Company  
Aircraft Engine Business Group

## INTRODUCTION

Accurate analysis of stress-strain behavior is of critical importance in the evaluation of life capabilities of hot section turbine engine components such as turbine blades and vanes. The constitutive equations used in the finite element analysis of such components must be capable of modeling a variety of complex behavior exhibited at high temperatures by cast superalloys. The classical separation of plasticity and creep employed in most of the finite element codes in use today is known to be deficient in modeling elevated temperature time dependent phenomena. Rate dependent, unified constitutive theories can overcome many of these difficulties and are more suitable for the analysis of the complex behavior of high temperature superalloys. However, many aspects of the unified theories had not been fully evaluated prior to the initiation of this work, and thus these theories had not been generally accepted for use in engine hardware design.

In this contract, constitutive theories were evaluated against a large uniaxial and multiaxial data base that was generated as a part of the work. Initially it was the intent to evaluate only available theories, however it was found that no available approach was satisfactory in modeling the high temperature time dependent behavior of Rene' 80 which is a cast turbine blade and vane nickel base superalloy. Additional considerations in model development included the cyclic softening behavior of Rene' 80, rate independence at lower temperatures, and the development of a new model for static recovery. The final constitutive model was implemented into a finite element computer code which was developed as a part of the contract and which was developed specifically for use with unified theories. The code was verified by a re-analysis of the Turbine Tip Durability problem which was part of the pre-HOST activities at General Electric [1]. This paper summarizes the work on the second year of the contract; the first year's work was summarized in last year's HOST Conference [2] and in the Annual Report [3]. Details of the contractual efforts are given in the final report which is currently being reviewed.

## EXPERIMENTAL PROGRAM

The experimental approach in this work was to determine the constitutive behavior of Rene' 80 under a multitude of conditions that are important in the design of gas turbine blade and vanes. This required that thin wall specimens be used as other NASA sponsored work has shown that thickness can be an important factor in material response properties [4]. Consequently, all

\*Work done under NASA Contract NAS3-23927.

specimens were designed with a thickness of 0.03 inches. Similarly, the experimental temperatures, strain ranges, strain ratios, hold times, and strain rates were established through an evaluation of the operating conditions in commercial jet engines.

In performing the experiments, the approach was to evaluate a series of transient and steady state conditions in each specimen test by using a block cycling method. This is illustrated in Figure 1 where several blocks of strain ranges are used in one experiment - all other conditions, strain rate, temperature, etc. are kept constant. By using several combinations of strain range blocks in different sequences in a single test all combinations of transient effects could be interrogated. The block length was selected to produce cyclically stable hysteresis loops by the end of each block.

All uniaxial experiments were performed at the EMTL Laboratory of the General Electric Company in Evendale, Ohio. The experimental results of each test were automatically saved in digitized form in real time by using a ETS data acquisition device. Prior to test, the number of load-strain pairs to be saved in selected hysteresis loops was determined (between 200 to 400 points). Typically 50 hysteresis loops were saved in each test. After a test, the data were permanently saved on tapes, before being loaded into mainframe computer files which were used for detailed data analyses. Final data analysis would include determining time derivatives by fitting a second order polynomial to seven consecutive data points and differentiating. These final data files could then be used in plotting data or determining constants in constitutive theories.

Similarly, the tension torsion test results were available on cassette tapes which could be used for detailed data analyses. These tests were performed at the Turbine Technology Laboratory (TTL) of the General Electric Company in Schenectady, New York under the direction of Dr. R. Williams. These tests used a development extensometer from the Instron Corporation. Additionally, a series of notched specimen test were conducted at Michigan State University under the direction of Professor J. Martin. In these tests, the notch root strains were measured using an interferometric displacement gage.

#### THEORY DEVELOPMENT

Following a detailed literature review, General Electric selected the Bodner model and a generic drag stress/back stress model for further detailed evaluations with the Rene' 80 data. The intent in the evaluations with the generic model was to perform an analysis of the Rene' 80 data to determine which functional forms in suggested back stress/drag stress models were most appropriate. Many of the results were presented in last year's paper. It was found that neither the Bodner or the generic model were very adequate for predicting the response properties of Rene' 80 at 1800°F. Consequently a new theory was developed which combined the Bodner exponential flow law with a

back stress formulation. The Bodner flow law had been found to be superior in modeling the strain rate behavior of Rene' 80, and possess the ability to predict essentially rate independent behavior at lower temperatures. These are two essential aspects of the behavior of Rene' 80. Additionally, it was found to be necessary to modify the evolution equations for the back stress to account for static recovery effects and to account for effects in the small inelastic strain regime. When these factors were included the final set of equations could be written as:

$$\dot{\epsilon}_{ij}^I = D \exp \left[ -\frac{A}{2} \left( \frac{z^2}{3K_2} \right)^n \right] \frac{(S_{ij} - \alpha_{ij})}{\sqrt{K_2}} \quad (1)$$

$$K_2 = 1/2 (S_{ij} - \alpha_{ij}) (S_{ij} - \alpha_{ij}) \quad (2)$$

$$\alpha_{ij} = \frac{G}{E} S_{ij} + (1 - \frac{G}{E}) \alpha_{ij}^I \quad (3)$$

$$\alpha_{ij}^I = f_1 \dot{\epsilon}_{ij}^I - \frac{f_1}{s} \alpha_{ij} \dot{R} \quad (4)$$

$$\dot{z} = m(z_1 - z) \dot{W}^I \quad (5)$$

$$\dot{\alpha}_s = -B(\sigma_e/\sigma_0)^r (\alpha_s - \alpha_{sat}) \quad (6)$$

where

$$\dot{R} = \sqrt{\frac{2}{3} \dot{\epsilon}_{ij}^I \dot{\epsilon}_{ij}^I}$$

$$\alpha_s(0) = \alpha_{max}, \alpha_{ij}^I(0) = 0, z(0) = z_0$$

The procedures for determining the constants in these equations have been presented previously in [2,3]. Basically the procedure involves the determination of most of the constants through the use of the monotonic strain rate dependent stress-strain curves; only the saturated value of the drag stress,  $z_1$ , is determined from cyclic tests (saturated hysteresis loops from fully reversed cyclic tests are used in this case). Verification of this method of determining the constants is presented in the form of correlations with multiaxial, hold time/relaxation, and different mean strain test data.

That these equations are very accurate is shown through comparisons with data. Figures 2, 3 and 4 show the correlation of the monotonic stress-strain data at 1400°F through 1800°F, respectively. That the theory is capable of predicting strain rate dependent as well as rate independent behavior is

apparent. Figure 5 shows a prediction of a compressive mean strain test result. Figure 5(a) shows a comparison with the first two cycles, while Figure 5(b) shows a comparison with the saturated hysteresis loop of this test. Figures 6 and 7 show that the theory can predict the stress relaxation behavior at high and low temperatures. Note that while the monotonic data at 1400°F exhibits little rate dependence there is still stress relaxation. Creep comparisons are shown in Figures 8 and 9. These predictions depend strongly on the form of the static recovery term. Note that the form that is used in the current theory is much different than those used in other unified approaches.

Multiaxial comparisons are shown in Figures 10 to 13. Figures 10 (a) and (b) show the axial and torsion comparisons, respectively, for a combined tension-torsion (in-phase) test. Figure 11 shows the data results and theory predictions from a special nonproportional test where segments of proportional cycles were used (see the insert of these two figures). Figure 11 compares results from the first segment (cycle 5), and the last segment (cycle 32) of this nonproportional loading experiment. That the predictions are accurate illustrates that the theory is good for such conditions without considering the additional hardening that has been found in some other materials. Figures 12 and 13 show that the new theory can predict 90 deg. out of phase tension/torsion experimental results at two temperatures with good accuracy.

Figures 14 and 15 show two predictions of the theory with test data from combined temperature and strain cycling tests. The predictions are shown to be reasonable considering that the predictions are based only on isothermal test data.

#### FINITE ELEMENT IMPLEMENTATION

The theory discussed in the previous section was implemented into a new 3-D finite element code which uses a 20-noded brick element. The program uses a dynamic time incrementing procedure to minimize cost while guaranteeing an accurate solution. The inelastic rate equations and state variable evolution equations are integrated using a second order Adams-Moulton predictor corrector technique. Piecewise linear load histories are modeled in order to simplify input. Further economics have been achieved by improving the stability of the initial strain method and further reducing the number of equilibrium iterations. The program was developed on an IBM PC AT and has been successfully installed on the NASA-Lewis CRAY computer.

#### SUMMARY

The experimental and analytical goals of this program were successfully accomplished. A new multiaxial constitutive model which can represent the complex nonlinear high temperature behavior of Rene' 80 was developed. The

model was extensively verified based on data at several temperatures. The TMF and nonproportional cyclic modeling capabilities of the model were demonstrated. The model was implemented in a 3-D finite element code which was installed on the NASA-Lewis CRAY.

#### REFERENCES

1. McKnight, R.L., Laflen, J.H., and Spamer, G.T. "Turbine Blade Tip Durability Analysis", NASA CR165268, February 1982.
2. Ramaswamy, V.G., Van Stone, R.H., Dame, L.T., and Laflen, J.H., "Constitutive Modeling for Isotropic Materials," NASA Conference Publication 2339, October 1984.
3. Ramaswamy, V.G., Van Stone, R.H., Dame, L.T., and Laflen, J.H., "Constitutive Modeling for Isotropic Materials", Annual Report, NASA CR17485, March 1985.

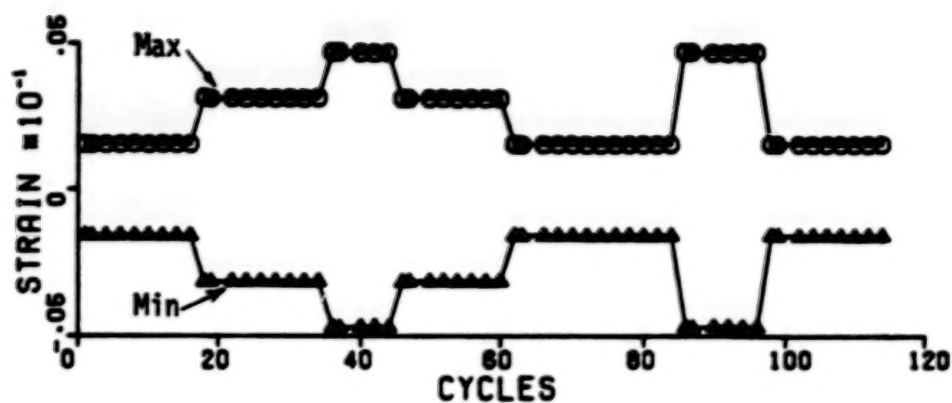


Figure 1. Typical Strain Limits Imposed During Cyclic Experiments

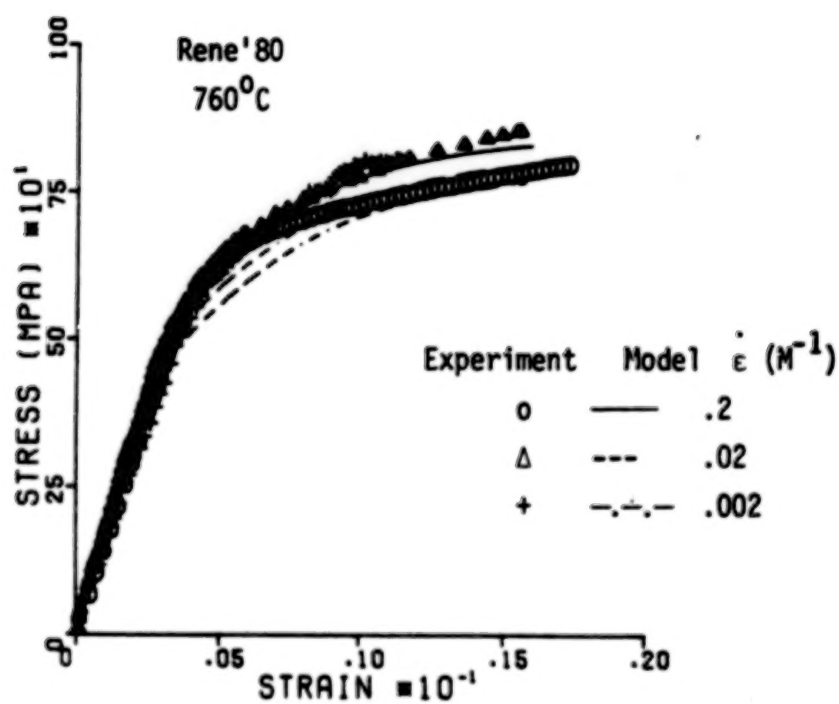


Figure 2. Monotonic Tensile Response of Rene'80 at 760°C

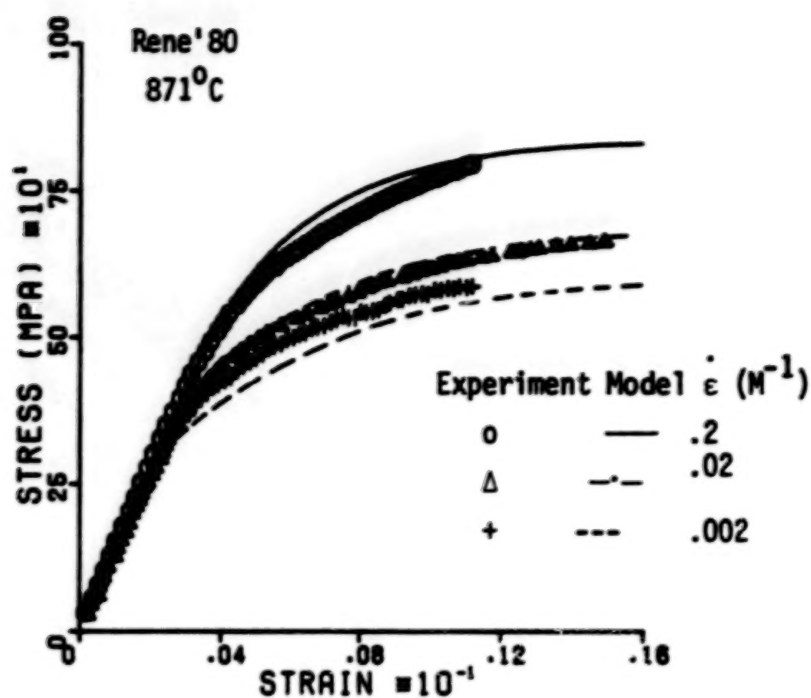


Figure 3. Monotonic Tensile Response of Rene'80 at 871°C

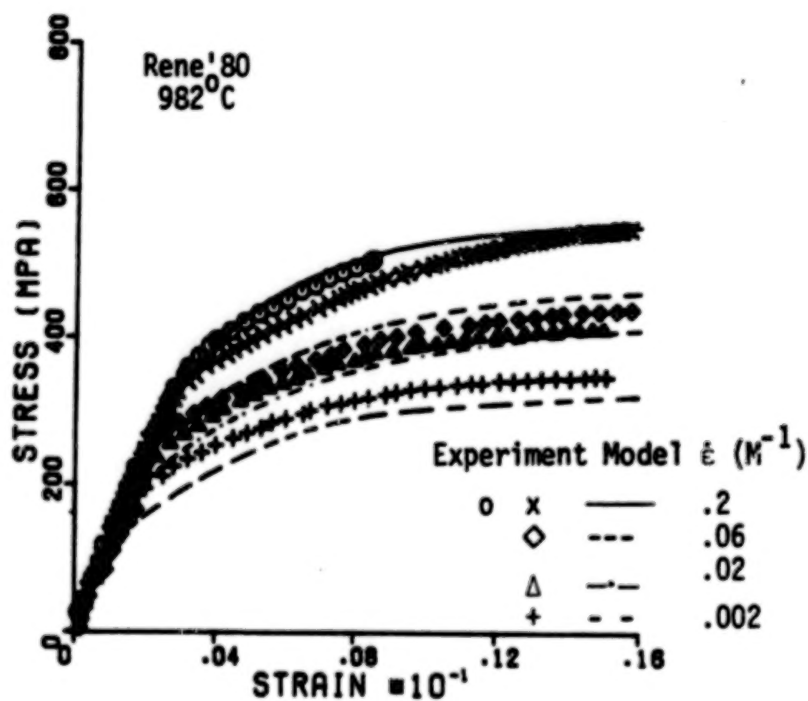
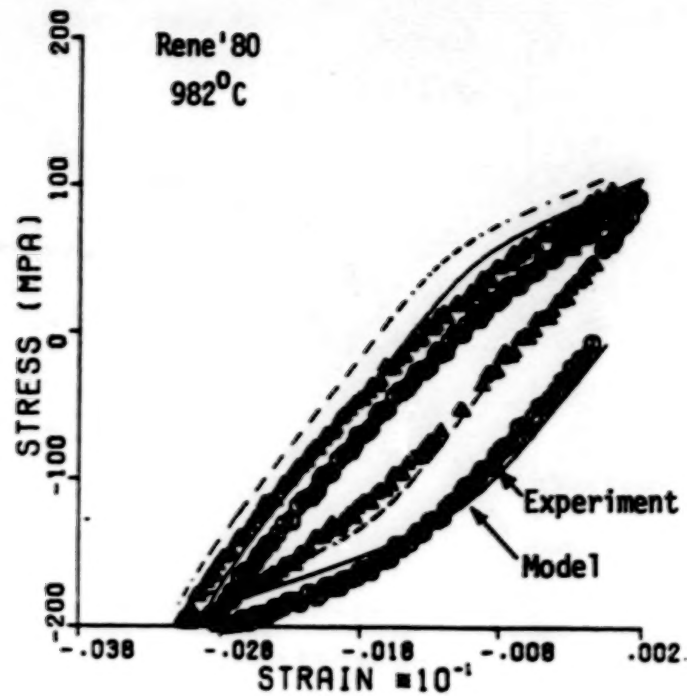
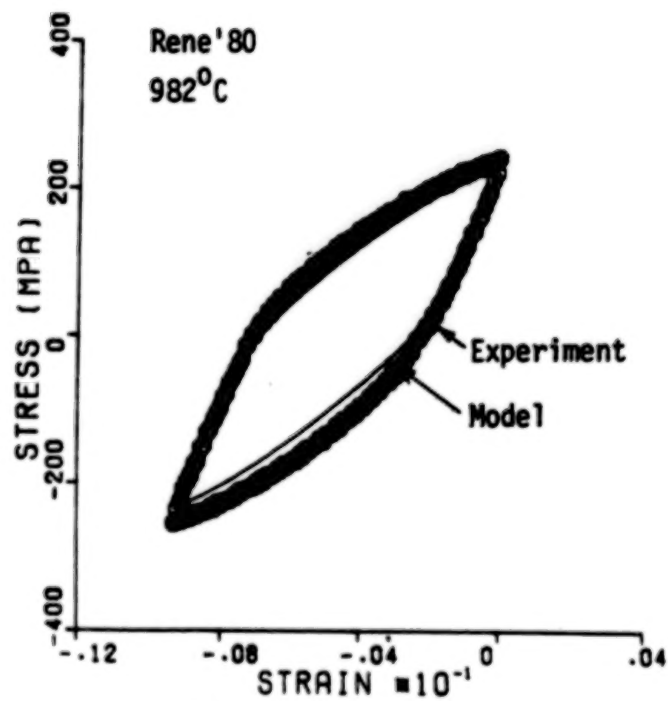


Figure 4. Monotonic Tensile Response of Rene'80 at 982°C



(a) First Two Cycles



(b) Cycle 78

Figure 5. Cyclic Response of Rene'80 with Mean Strain

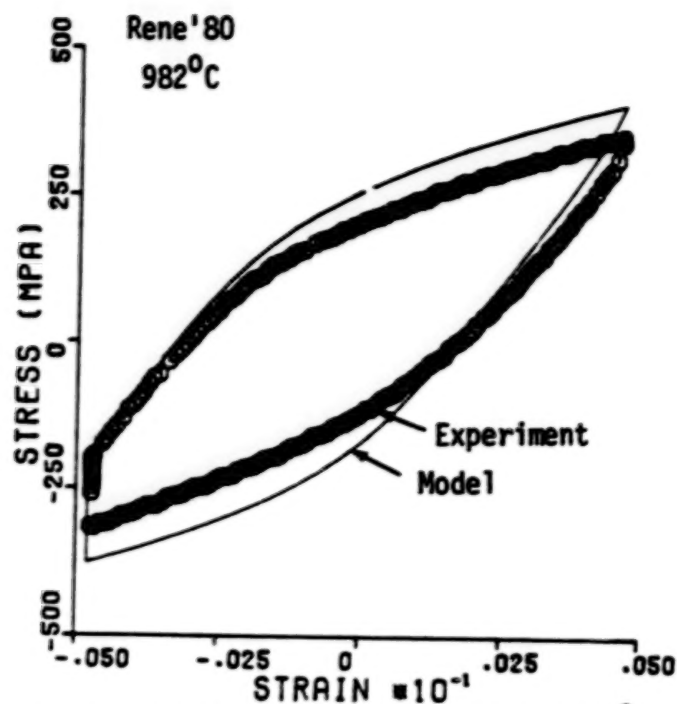


Figure 6. Stress Relaxation in Rene'80 at 982°C  
(Cycle No. 60)

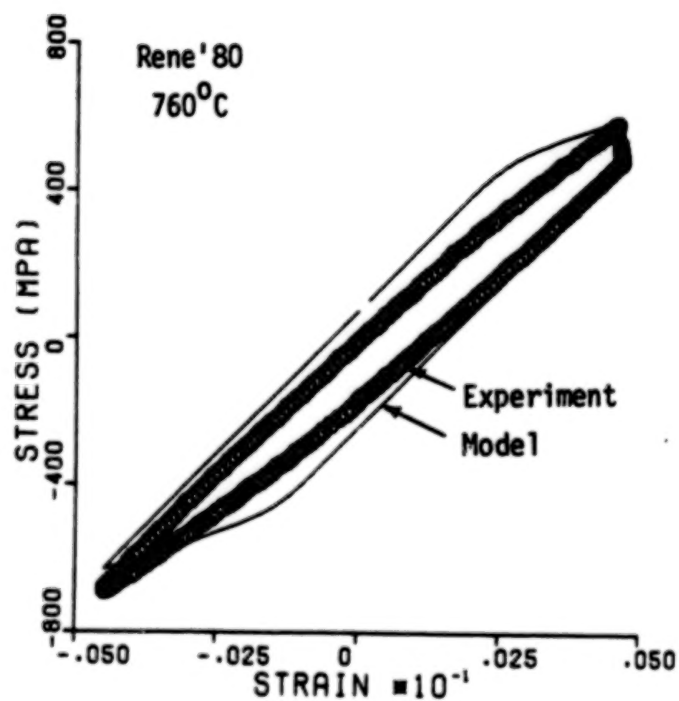


Figure 7. Stress Relaxation in Rene'80 at 760°C  
(Cycle No. 94)

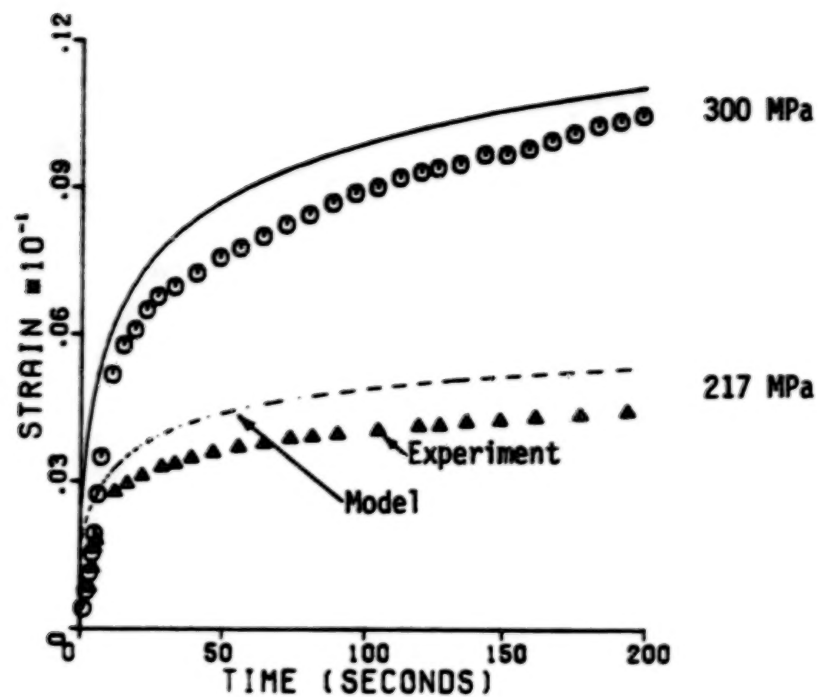


Figure 8 Creep Response of Rene'80 at 982°C

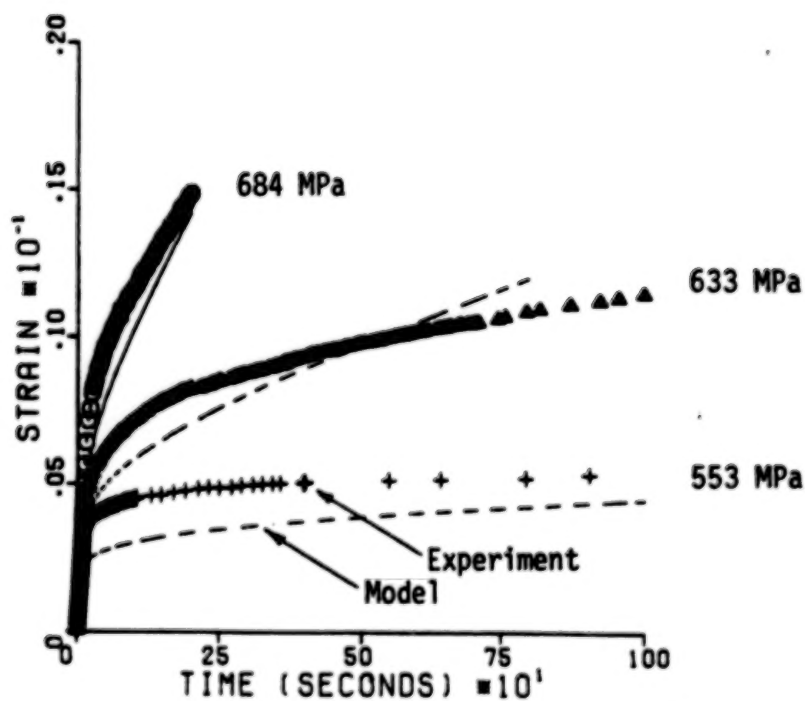
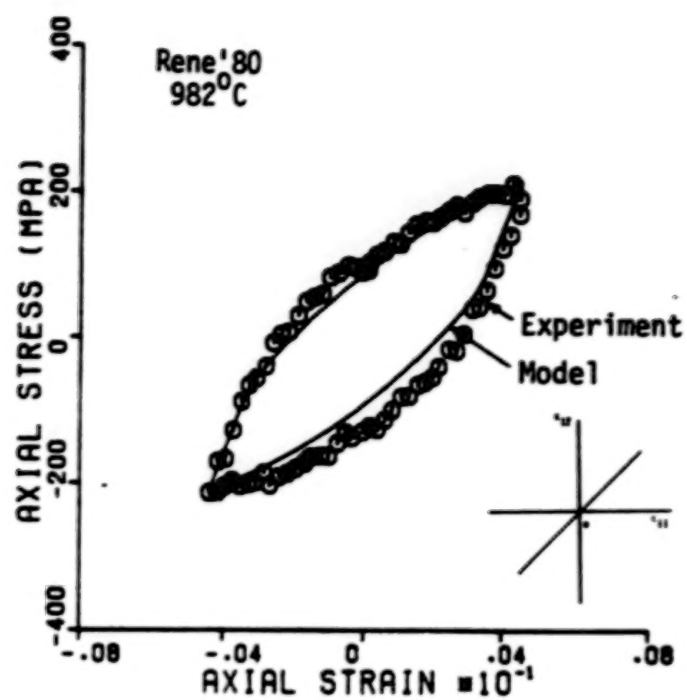
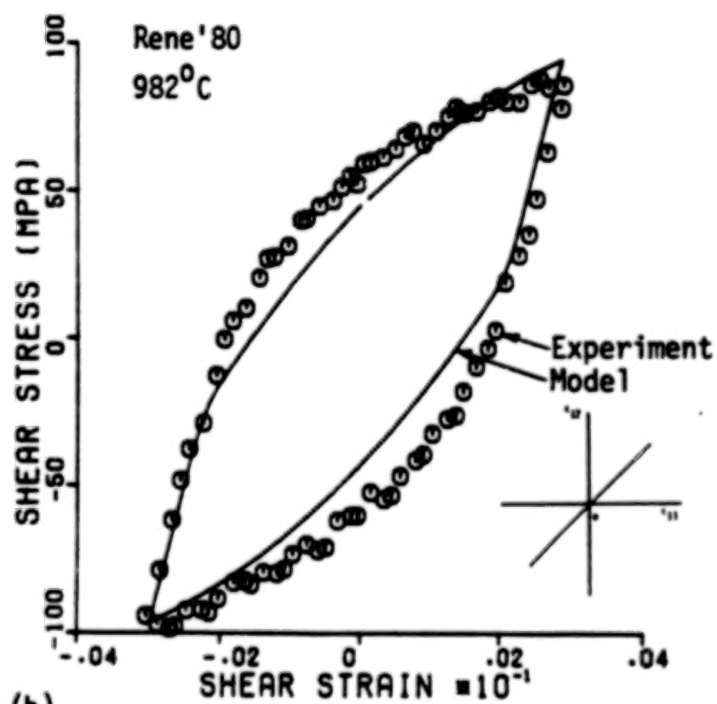


Figure 9 Creep Response of Rene'80 at 760°C



(a)



(b)

Figure 10. In phase Tension Torsion Cyclic Response of Rene'80 at 982°C,  $.002M^{-1}$

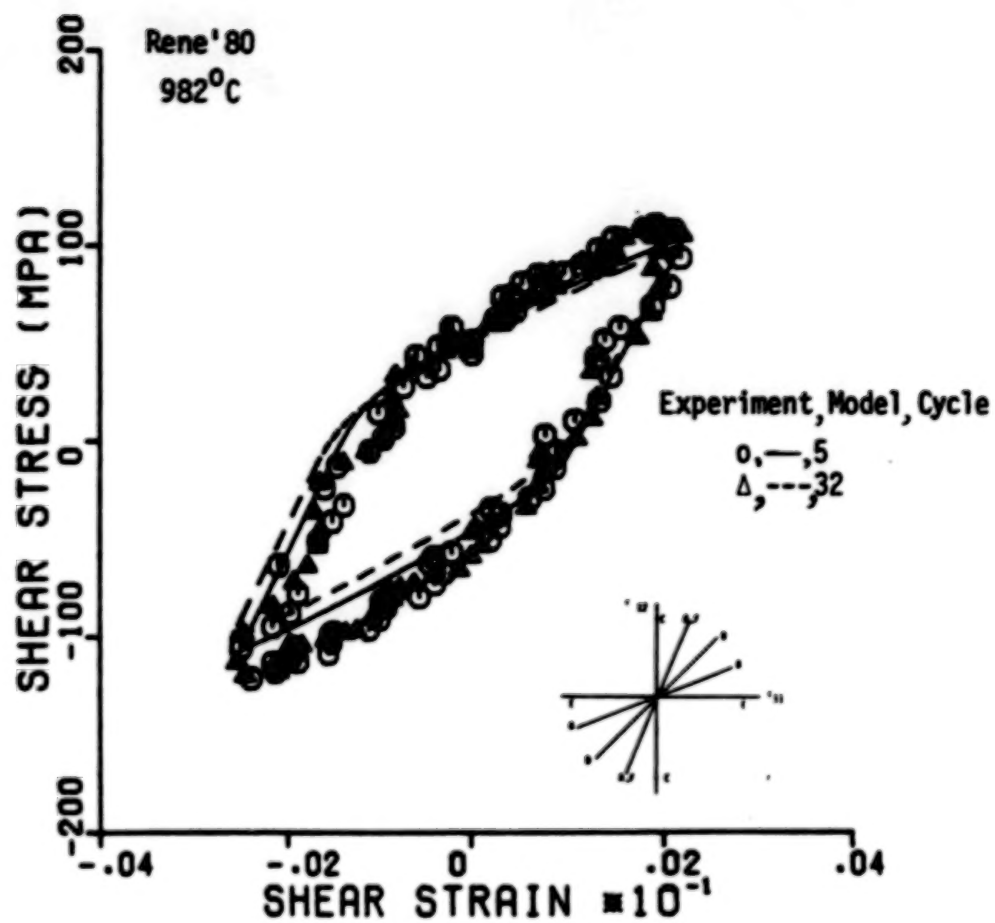


Figure 11 Comparison of Rene'80 Response Before and After Non proportional loading (Paths A,F)

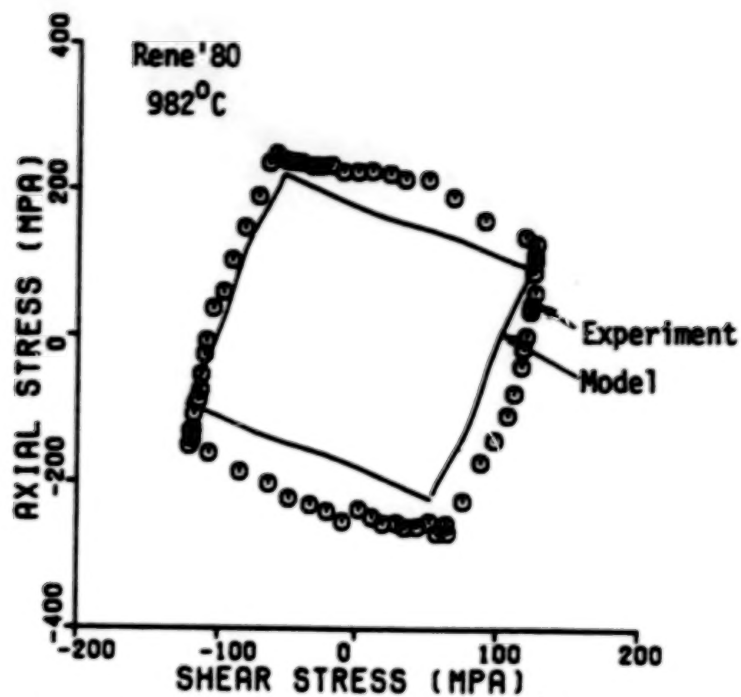


Figure 12. Rene'80 Response to 90° Out of Phase Tension/Torsion Cyclic Loading

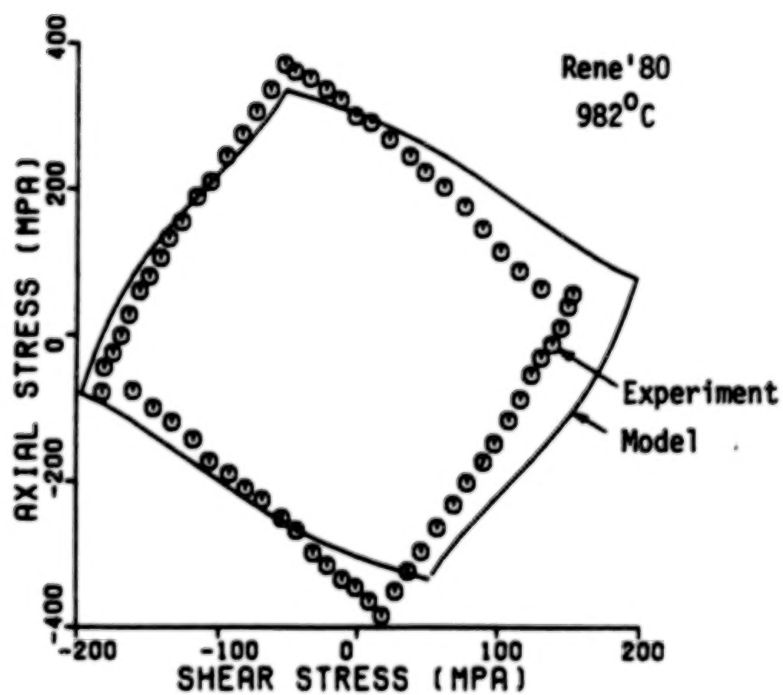


Figure 13. Rene'80 Response to 90° Out of Phase Tension/Torsion Cyclic Loading

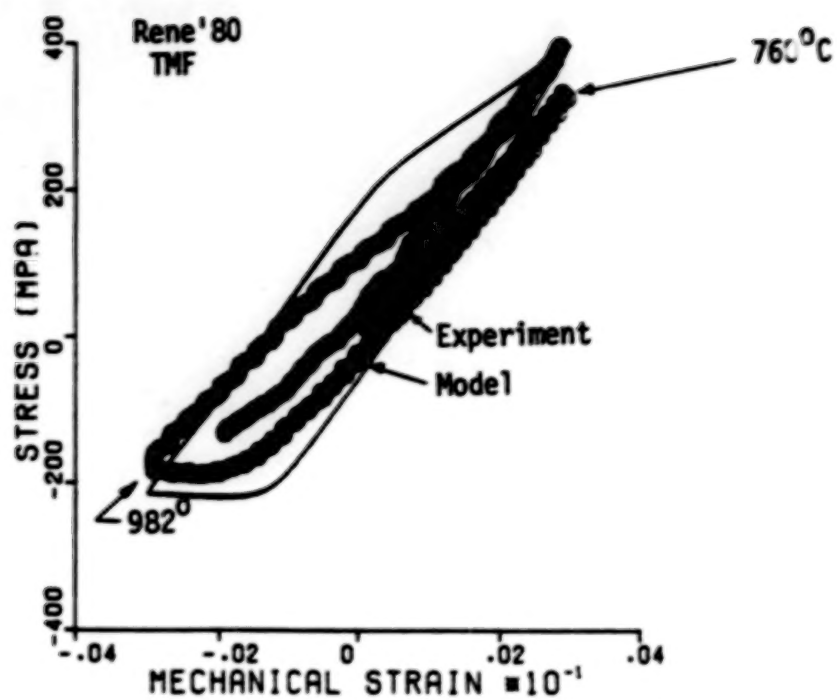


Figure 14. Rene'80 TMF Response (760°C-982°C Out of Phase)

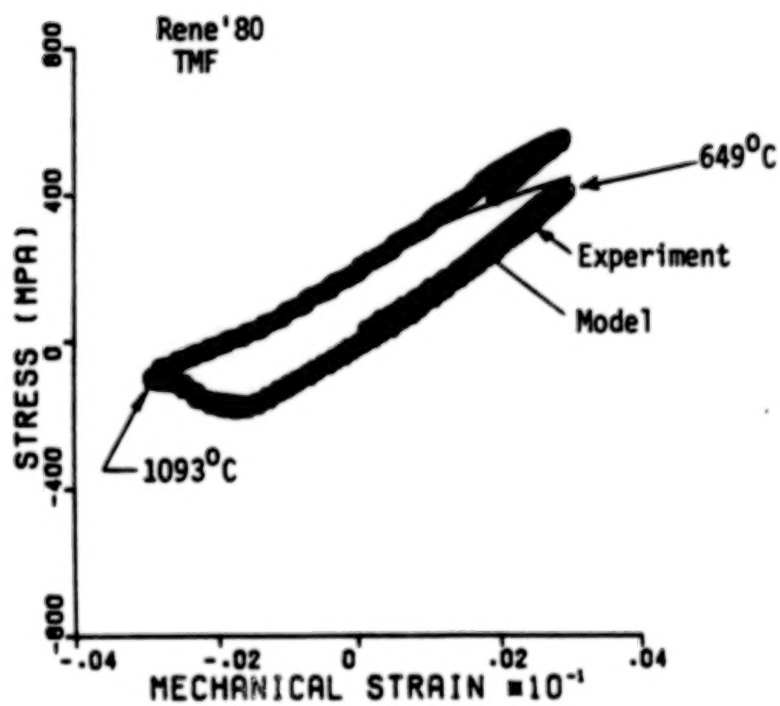


Figure 15. Rene'80 TMF Response (649°C-1093°C Out of Phase)

**CREEP FATIGUE LIFE PREDICTION FOR ENGINE HOT SECTION  
MATERIALS (ISOTROPIC) - THIRD YEAR PROGRESS REVIEW<sup>1</sup>**

Richard S. Nelson and John F. Schoendorf  
United Technologies Corporation  
Pratt & Whitney

**INTRODUCTION**

As gas turbine technology continues to advance, the need for advanced life prediction methods for hot section components is becoming more and more evident. The complex local strain and temperature histories at critical locations must be accurately interpreted to account for the effects of various damage mechanisms such as fatigue, creep, and oxidation and their possible interactions. As part of the overall NASA HOST effort, this program is designed to investigate these fundamental damage processes, identify modeling strategies, and develop practical models which can be used to guide the early design and development of new engines and to increase the durability of existing engines.

This contract is a 5-year effort comprising a 2-year base program and a 3-year option program, involving two different isotropic materials as well as two protective coating systems. The base program, which was completed during 1984, included comparison and evaluation of several popular high-temperature life prediction approaches as applied to continuously cycled isothermal specimen tests. The option program, of which one year has been completed, is designed to develop models which can account for complex cycles and loadings, such as thermomechanical cycling, cumulative damage, multiaxial stress/strain states, and environmental effects.

**REVIEW OF PROGRESS DURING BASE PROGRAM**

Approximately 150 tensile, creep, and fatigue tests were conducted during the base program using specimens made from a single heat of cast B1900+Hf material. The fatigue tests were conducted in an axial strain-controlled mode at temperatures between 538°C (1000°F) and 982°C (1800°F). Initiation life was considered to be more significant than separation life; this was defined to be the cycle at which a 0.75 cm (0.030 in.) surface crack had developed, as determined by replication of selected specimens at each test condition. These tests investigated the effects on initiation of strain range, strain rate, mean strain, and compressive and tensile dwell periods.

The base program also included a review of many different life prediction methodologies, such as correlation of macroscopic parameters (strain range, mean stress), strain range partitioning (ref. 1), rate-sensitive models (Majumdar, ref. 2), work-based models (Ostergren, ref. 3), damage accumulation (ductility exhaustion), and fracture mechanics approaches. Both desirable and undesirable features of each of these were identified and used to guide the selection of the approach having the best combination of accurate predictive capability and practical specimen data requirements. The damage model which was finally chosen and developed is based on the ductility exhaustion concept and is known as the Cyclic Damage Accumulation model. Application of this model to the data generated in the base program testing

showed very good correlation. A full description of all testing and model development conducted under the base program is contained in the second annual report (ref. 4).

#### THERMOMECHANICAL MODEL DEVELOPMENT

A significant task under the option program is the development of a damage model which is valid under conditions of thermomechanical fatigue (TMF). A total of 21 TMF specimen tests has been completed so far, covering variables such as strain range, temperature range, mean strain, cycle type, and hold times. A schematic comparison of some of the strain-temperature cycles used for these tests is shown in figure 1. It can be seen that the "dogleg" tests are identical to the base program isothermal hold tests, except that the temperature was not held constant during the strain holds. In general, the results of these specimen tests have demonstrated that TMF damage cannot always be predicted in the same manner used for isothermal tests; the model chosen must be sensitive to accumulation of damage from several different sources throughout the cycle.

The isothermal CDA model developed during the base program was applied to a selected group of the TMF specimen tests, using a rate of fatigue damage accumulation consistent with the highest temperature seen by the specimen during the test. The resulting predictions for the out-of-phase tests are shown in figure 2; note that the trend of the data is correctly predicted, but that the predictions are conservative. The same method was applied to the data from the in-phase and dogleg tests in this group, and figure 3 shows that, for these tests, the isothermal damage method does not predict the trends in the observed specimen initiation lives. Work is now continuing on a differential form of the CDA model in which the damage rate is variable and can be integrated around any arbitrary TMF cycle.

#### MULTIAXIAL STRESS STATE MODEL

Multiaxial fatigue tests are now being conducted using tubular specimens subjected to torsional loading in combination with uniaxial tension loading. Considerable effort was expended on development of the specimen, test rig and computer software codes. Collet-type grips were incorporated into the test rig to reduce the fixturing complexity and allow relaxed tolerances on the specimen grip ends which resulted in lower cost specimens.

A literature survey was conducted to identify viable approaches to predicting multiaxial effects in hot section components. Evaluation of the approaches was based on the following criteria: a demonstrated capability to predict non-proportional loading effects, use of two or more parameters to characterize multiaxial fatigue behavior, requirement for a minimal amount of multiaxial test data, and compatibility with the Cyclic Damage Accumulation model. The plastic work (ref. 5) and critical plane (ref. 6) theories were identified as having the greatest potential.

#### CUMULATIVE LOADING MODEL

During the tests conducted as part of this task, specimens have been exposed to mixed loading conditions to provide information regarding the interaction of different types of damage processes. A total of 44 such tests have been completed, including block tests (one set of conditions for the first block of cycles, followed

by a second set of conditions for the remainder), sequenced tests (alternating blocks of two different sets of conditions), and interrupted tests (fatigue cycling interrupted by periods of temperature exposure, either with or without load). The results of these tests show that some conditions obey a linear damage rule, while certain other conditions show a strong non-linear interaction. For example, figure 4 shows an interaction diagram for the block tests run with various combinations of R-ratios, and it can be seen that running a specimen at R=0 for only a fraction of the initiation life at that condition will dramatically affect the life remaining under subsequent cycling at R=-1.

As a result of these tests, it has become clear that the CDA model must be allowed to track different cyclic ductility capabilities in each portion of a test. Also, it was observed during certain tests (such as the temperature block tests) that the damage accumulation is non-linear. These changes have been incorporated into the CDA equation through the use of the concept of ductility fraction, which is defined as the fraction of the available ductility which has been consumed:

$$\text{Ductility Fraction, } f_e = \frac{\text{Ductility Exhausted}}{\text{Available Ductility}}$$

The equation used to calculate this quantity may be written as follows:

$$f_e = \int_0^N \left( \frac{1}{\bar{\epsilon}_p} \right) \left( \frac{dD}{dN} \right)_{\text{Ref}} F(\sigma_T, \Delta\sigma) dN \quad (1)$$

where:

$$F(\sigma_T, \Delta\sigma) = \left( \frac{\sigma_T}{\sigma_{TR}} \right) \left( \frac{\Delta\sigma}{\Delta\sigma_R} \right) + \left[ \left( \frac{\Delta\sigma}{\Delta\sigma_R} \right) \left( \frac{\sigma_T}{\sigma_{TR}} \right) \right]^{B'} \left[ \left( \frac{t}{t_r} \right)^{C'} - 1 \right]$$

$\bar{\epsilon}_p$	grain cyclic capability for specific test condition being predicted
$dD/dN_R$	damage rate from fully reversed testing
$\Delta\sigma$	stress range
$\sigma_T$	maximum tensile stress
$t$	1/2 cycle period
$R$	reference condition
$B', C'$	constants determined from monotonic creep tests

It can be seen that when  $f_e$  reaches 1,  $N$  will equal the predicted initiation life,  $N_i$ . Note also that the current initial ductility is now inside the integral, which permits the algorithm to switch from one loading condition to another which has a different initial ductility.

We may also rewrite equation 1 to perform the integration over  $f_e$  instead of  $N$ , and at the same time introduce a non-linear function  $G(N/N_i)$  which has the property that its integral over the interval from 0 to 1 is always 1, no matter what values are chosen for its constants:

$$N_i = \int_0^1 \left[ \frac{\bar{\epsilon} p}{\left( \frac{dN}{dN} \right)_{Ref} F(\sigma_T, \Delta\sigma)} \right] G\left(\frac{N}{N_i}\right) df_e \quad (2)$$

Several forms of the function  $G(N/N_i)$  have been evaluated, including linear and power law functions. Figure 5 shows the effect of non-linear damage accumulation on the CDA life predictions for the block loading tests, and it can be seen that in almost every case the non-linear life prediction is more accurate.

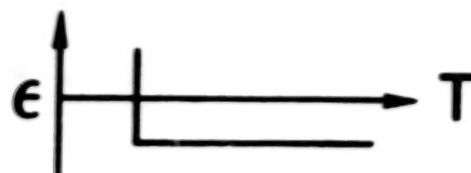
#### FUTURE TASKS

One of the important tasks to be completed in the near future is the investigation of the effects of environment on the fatigue process. Current plans call for screening tests in two types of atmospheres, inert (argon) and aggressive (high pressure oxygen), followed by further detailed tests in the environment which shows the greater effect. Other tasks include development of a life model for coated materials under creep-fatigue conditions and further investigation of the effects of mean stress on fatigue. The final task under the contract will be the application of the fully developed life prediction models to an alternative material and coating system in order to verify their applicability to alloys other than B1900+Hf.

#### REFERENCES

1. Manson, S.S.; Halford, G.R.; and Hirshberg, M.H.: Creep-Fatigue Analysis by Strain Range Partitioning. Symposium on Design for Elevated Temperature Environment, ASME, 1971, pp. 12-28.
2. Majumdar, S.; and Maiya, P.S.: A Mechanistic Model for Time Dependent Fatigue. Jour. of Materials & Technology, Vol. 102, January 1981, pp.159-167.
3. Ostergren, W.J.: A Damage Function and Associated Failure Equations for Prediction of Hold Time and Frequency Effects in Elevated Temperature, Low Cycle Fatigue. Journal of Testing and Evaluation, Vol. 4, No. 5, September 1976.
4. Moreno, V.; Nissley, D.M.; Lin, L.S.: Creep Fatigue Life Prediction for Engine Hot Section Materials (Isotropic), Second Annual Report. NASA CR-174844, December 1984.
5. Garud, Y.S.: A New Approach to the Evaluation of Fatigue Under Multiaxial Loadings. ASME Journal of Engineering Materials and Technology, Vol. 103, April 1981, pp. 118-125.
6. Kanazawa, K.; Miller, K.J.; and Brown, N.W.: Low-Cycle Fatigue Under Out-of-Phase Loading Conditions. ASME Journal of Engineering Materials and Technology, Vol. 99, No. 3, July 1977, pp. 222-228.

- "Dogleg"



- In-phase and out-of-phase

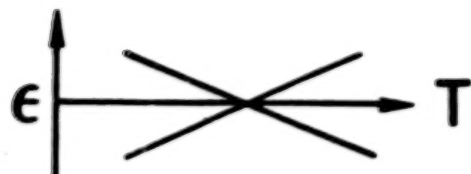


Figure 1 TMF Loading Cycles for Initial CDA Evaluation

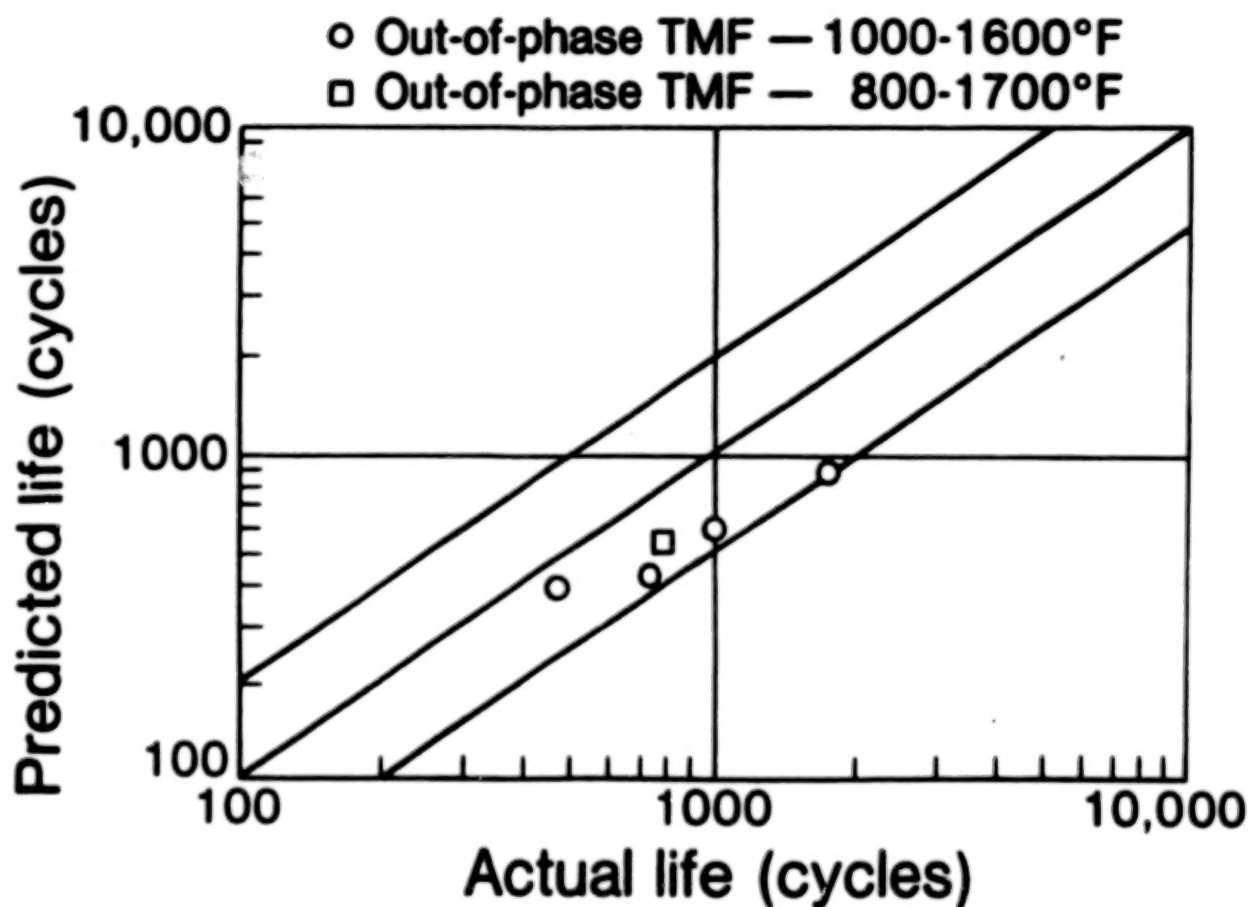


Figure 2 Prediction of Out-of-Phase TMF by CDA Model

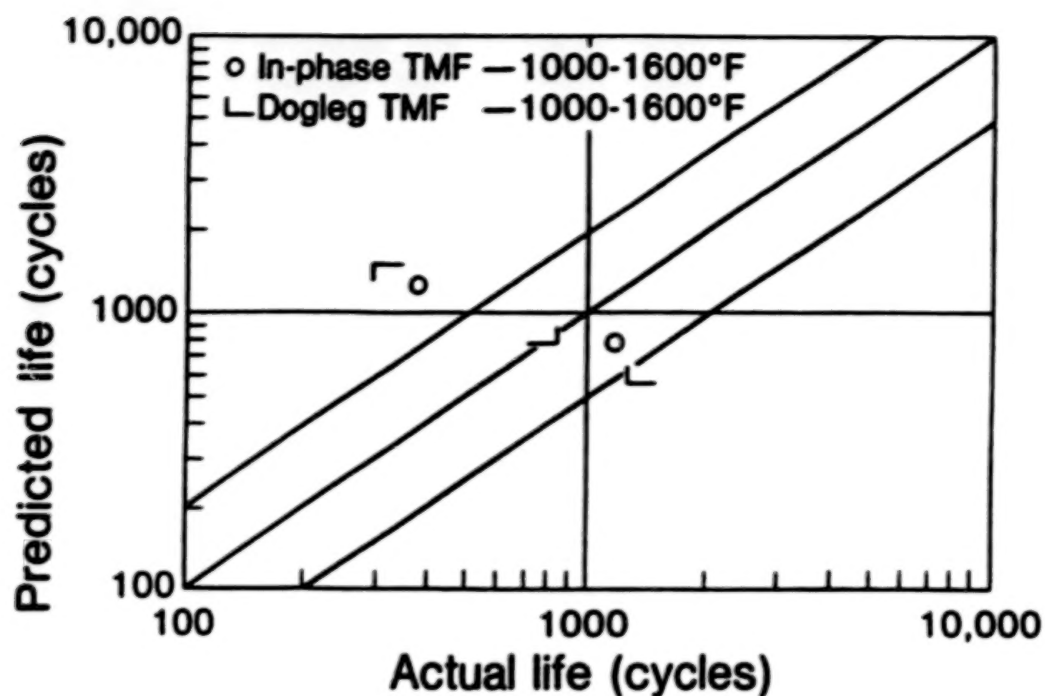


Figure 3 Prediction of In-Phase and Dogleg TMF by CDA Model

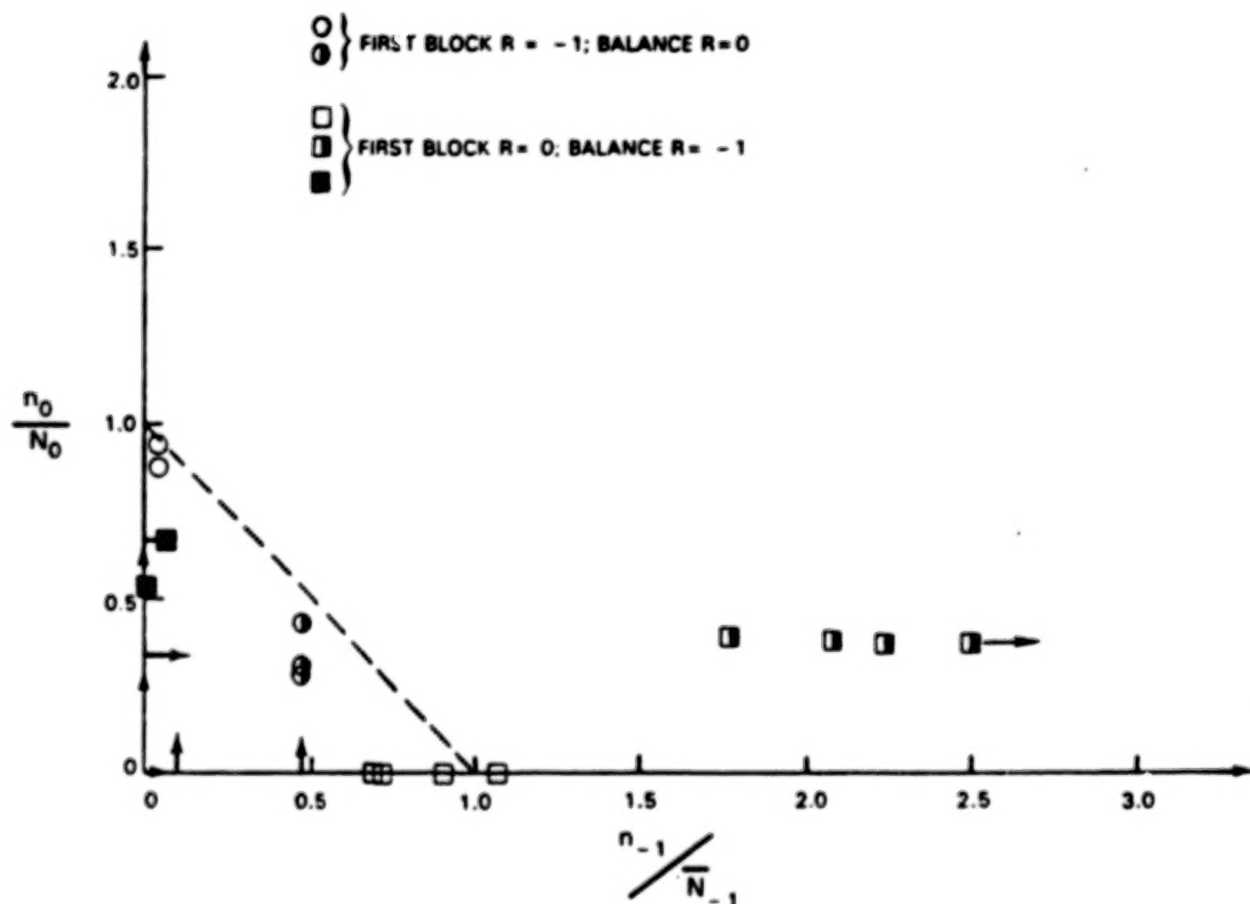


Figure 4 Interaction Diagram - Mean Stress Effects During Block Tests

- 1 ○ BLOCK TESTS -- STANDARD LINEAR DAMAGE
- 2 □ BLOCK TESTS -- NON -- LINEAR DAMAGE

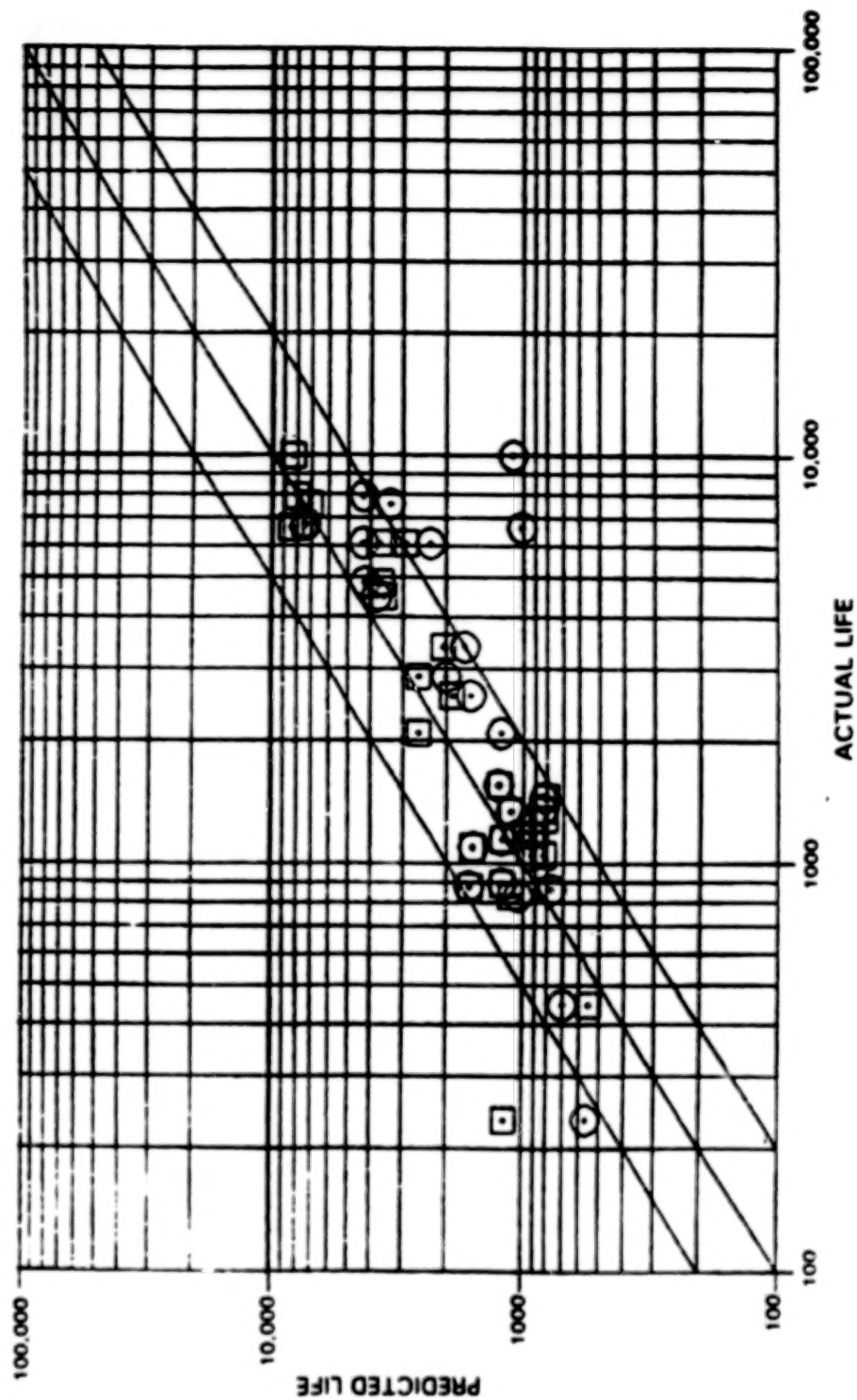


Figure 5 Effects of Non-Linear Damage Accumulation

## ELEVATED TEMPERATURE CRACK GROWTH\*

S.N. Malik, R.H. Van Stone, K.S. Kim, J.H. Laflen  
General Electric Company  
Aircraft Engine Business Group  
Cincinnati, Ohio

## INTRODUCTION

Critical gas turbine engine hot section components such as blades, vanes, and combustor liners tend to develop minute cracks during the early stages of operation. These cracks may then grow under conditions of fatigue and creep to critical size. Current methods of predicting growth rates or critical crack sizes are inadequate, which leaves only two extreme courses of action. The first is to take an optimistic view with the attendant risk of an excessive number of service failures. The second is to take a pessimistic view and accept an excessive number of "rejections for cause" at considerable expense in parts and downtime. Clearly it is very desirable to develop reliable methods of predicting crack growth rates and critical crack sizes.

To develop such methods, it is necessary to relate the processes that control crack growth in the immediate vicinity of the crack tip to parameters that can be calculated from remote quantities, such as forces, stresses, or displacements. The most likely parameters appear to be certain path-independent (P-I) integrals, several of which have already been proposed for application to high temperature inelastic problems. A thorough analytical and experimental evaluation of these parameters needs to be made which would include elevated temperature isothermal and thermomechanical fatigue, both with and without thermal gradients.

In any investigation of fatigue crack growth, the problem of crack closure should be addressed in order to develop the appropriate crack growth model. Analytically, this requires the use of gap elements in a nonlinear finite element code to predict closure loads. Such predictions must be verified experimentally through detailed measurements; the best method for measuring crack closure has not been established in previous studies.

It is the purpose of this contract (NAS3-23940) to determine the ability of currently available P-I integrals to correlate fatigue crack propagation under conditions that simulate the turbojet engine combustor liner environment. The utility of advanced fracture mechanics measurements will also be evaluated and determined during the course of the program. These goals are to be accomplished through a two year, nine task, combined experimental and analytical program. To date an appropriate specimen design, a crack displacement measurement method, and boundary condition simulation in the computational model of the specimen has been achieved. Also, the experimental testing and data acquisition is continuing. Alloy 718 has been

\*Work done under NASA Contract NAS3-23940.

selected as the analog material based on its ability to simulate high temperature behavior at lower temperatures in order to facilitate experimental measurements. Tensile and cyclic tests were run at several strain-rates so that an appropriate constitutive model could be developed. Available P-I integrals have been reviewed and the most suitable ones have been programmed into a finite element post-processor for eventual comparison with experimental data. These experimental data will include cyclic crack growth tests under thermo-mechanical conditions and, additionally, thermal gradients.

#### A REVIEW OF P-I INTEGRALS

The utility of the J integrals [1] as a parameter for predicting crack growth in the elastic-plastic regime is rather limited. The theoretical basis of the J integral does not allow the extension of its usage to nonproportional loading and unloading in the plastic regime, nor can it be utilized in the presence of a temperature gradient and material inhomogeneity. A typical example where all these limiting factors are operative would be the hot section components of a gas turbine in mission cycles.

In recent years there has been a considerable effort to modify and reformulate the J integral for applications in various areas of fracture mechanics. Consequently, a number of new path-independent (P-I) integrals have emerged in the literature. A critical review of these integrals is presented by Kim[2]. Notable among them are the Blackburn  $J^*$ [3], Kishimoto  $J$ [4, 5], Athuri  $\Delta T_p$  and  $\Delta T_p^*$ [6,7], and Ainsworth  $J_\theta$ [8] integrals. In the present program the theoretical background of these integrals has been examined with particular attention to whether or not the path-independence is maintained in the presence of nonproportional loading; unloading in the plastic regime; and a temperature gradient and material inhomogeneity. The relation among the P-I integrals, salient features and limitations were investigated. The physical meaning, the possibility of experimental measurements, and the computational ease were also examined. In view of the requirements associated with performing the tasks in this program the following conclusions were made.

- i) The  $J^*$ ,  $J$ ,  $\Delta T_p$  and  $\Delta T_p^*$  integrals maintain the path-independence under the thermomechanical cycles which will be used in the tests in this program and will be simulated numerically in subsequent tasks. Although the physical meaning of these P-I integrals needs to be further pursued, they would be the logical choices for further evaluation in this program.
- ii) The  $J_\theta$  integral is a modified version of J to include thermal strain. Therefore, it cannot be used with substantially nonproportional loading and unloading in the plastic regime. It would be worthwhile, however, to investigate the utility of operationally defined J and possibly  $J_\theta$  for the test cycles in this program.

All selected P-I integrals have been implemented in a postprocessor to the General Electric nonlinear finite element program, CYANIDE. Numerical values of the integrals will be evaluated and examined for cracks subjected to various situations such as monotonic/cyclic loadings, uniform/non-uniform temperature distributions, stationary/propagating cracks, etc. Best formulations suitable for all situations will be selected and used to correlate with the test results. The relationship between the analytical CTOD (or CMOD) displacements and the values of P-I integrals will be established to identify the displacement which must be measured to determine operational P-I integral.

#### EXPERIMENTAL PROGRAM

Alloy 718, a  $\gamma$ - $\gamma'$  nickel-base superalloy, has been selected as the analog material because over the temperature range from 800F to 1200F it shows very large changes in creep behavior. This permits the use of Alloy 718 to simulate the behavior of combustor liner materials while still performing experiments at relatively low temperatures. Tensile, creep, and cyclic constitutive tests have been performed on Alloy 718 over the temperature range from room temperature to 1200F to identify the constitutive properties to be used in finite element calculations. Tensile and cyclic tests have been performed over strain rates different by a factor of 20, and no strain rate sensitivity was observed, even at the higher temperatures where high creep rates occur. This will permit the use of classical plasticity and creep analysis in the Finite Element (FEM) analysis.

The primary specimen to be used in this study is a single edge crack (SEN) specimen with buttonhead grips. The buttonhead grips permit better load reversals and alignment, especially for compressive loads. The gage section has a rectangular cross-section with a thickness, width, and gage length of 2.54, 10.2 and 15.9mm (0.10, 0.40, and 0.625 inch) respectively. The relatively low gage length was selected to avoid buckling during the elevated temperature cycling with large plastic cyclic strains. The overall length of the specimen is 5 inch (127mm) including the cylindrical shanks and buttonheads.

The SEN tests are performed in a strain control mode with the experimental setup shown schematically in Figure 1. The controlling extensometer will be mounted at the center of the 10.2mm wide surface of the specimen. Two other displacement gages, one to monitor crack mouth opening displacement (CMOD) and one to monitor the displacement on the face opposite the crack mouth, will also be used. The purpose of the CMOD gage is to detect when crack closure occurs. A standard 12.7mm (0.5 inch) elevated temperature extensometer has been modified to have a gage length of approximately 0.76mm (0.03 inch) and significantly improved resolution of CMOD displacements.

A DC potential drop system is used to monitor crack size. The load-displacement data is periodically recorded using an ETS data acquisition system. Figure 2 shows two examples of hysteresis loops obtained from typical

tests with  $A_c = -(\epsilon_{\min} = -\epsilon_{\max})$ . Figure 2a shows an example of nominally elastic cycling and a crack depth of approximately 0.51mm (20 mils). Even at this small crack length, the CMOD is detecting closure. Also note the displacement sensitivity of the CMOD loops is twice that of the other types of loops. Figure 2b shows an example of elastic-plastic strain cycling. The CMOD loop for this cycle shows crack closure and opening at very similar values of CMOD even though the nominal stress is much different due to net section plasticity. In both cases the back face extensometer shows a bias toward negative strains indicative of bending within the gage length.

The experimental work is in progress and will measure the crack growth response of Alloy 718 under isothermal, TMF, and temperature gradient conditions. Some additional tests were performed with a 12.7mm (0.5 inch) extensometer in place of the CMOD gage to provide verification of analytical results.

#### NUMERICAL COMPUTATIONS

Numerical implementation and verification of the PI-integral post-processor program was completed and is reported in the Annual Progress Report [9]. A pre-processor program for automatic generation of finite element two-dimensional meshes for crack problems was also completed and discussed in detail in the Annual Progress Report [9]. This mesh generator program allows a gradual transitioning of the elements size from relatively coarse in the remote stress field to very refined near the crack-tip region.

Prior to performing detailed FEM analyses for crack closure, efforts were made to evaluate simplified boundary conditions which would eliminate the need for analyzing the whole specimen (including the buttonhead). In order to verify the plane stress type stress field in the gage-section of the SEN specimen, a full-specimen three-dimensional (3D) analysis using 20-noded isoparametric brick elements was made by using the 3D-CYANIDE code. It was found that in the gage section there was very little variation in through-the-thickness stresses, strains, and displacements. Therefore, a 2D plane-stress model of the "full-specimen" was developed to investigate the influence of prescribed buttonhead displacements on the displacements in the "gage-section portion" of the specimen. Figure 3 shows the full-specimen model for the 2D-CYANIDE analysis which contains 566 nodes and 1002 constant strain elements. The near crack-tip mesh refinement was validated by prescribing constant displacement boundary conditions and computing stress intensity factor ( $K_I$ ) from the post-processor J integral. For the elastic response, Figure 4 shows a comparison of computed  $K_I$  values with the Tada, Paris and Irwin handbook solution having a maximum difference of 7% for various  $a/w$  ratios. Similar comparisons made in the plastic regime using the elastic-plastic fracture mechanics handbook [10] solutions showed equally encouraging results.

The next step was to compare the computed load-displacement variation from the elastic-plastic analysis with the measured normal displacement data obtained from three 12.7mm (0.5 inch) extensometers positioned as shown in

Figure 1. Figures 5, 6 and 7 show the results obtained for an  $a/w$  ratio of 0.265. Solid lines represent test data curves for the first load cycle, whereas the circular symbols represent the computed values, and the square symbols represent test data for the second cycle. The monotonic stress-strain properties of Alloy 718 were used in the 2D-CYANIDE full-specimen analysis. It could be seen that the experimental first cycle load versus displacement data at each of the three extensometer locations compare very well with the computed values. The regions of extreme plasticity were modeled very satisfactorily by the 2D-CYANIDE analysis. Figure 8 shows  $u_y$  displacements, normal to the crack plane, near the end of gage-section. It could be seen that the  $u_y$  displacement varies approximately linearly across the gage-section width for all the seven load cases plotted in Figures 5, 6 and 7. For the larger displacement cases the  $u_y$  displacement near the back face ( $X = 0.4$  inch) developed slight deviations from linearity. The most significant implication of Figure 8 is that due to linear variation of normal displacement across the specimen width near the end of the gage-section, only two extensometers are needed to accurately predict displacement response. This simplification eliminated the need for three extensometers needed to model gross specimen displacements.

Another interesting feature of the full-specimen 2D-CYANIDE analysis was the magnitude of horizontal displacement,  $u_x$ , in the gage-section. Figure 9 shows the relationship of the  $u_y$  versus  $u_x$  displacement at each of the nine  $x$ -coordinate locations near the end of gage-section for each of the seven load values plotted in Figures 5, 6 and 7. It could be seen that  $u_x$  displacement is about 30 to 60% of the corresponding  $u_y$  displacement at the end of gage-section.

Another simplification to reduce computer cost was made by only modeling the "gage-section portion" of the SEN buttonhead specimen. This gage-section model of the specimen retains the same mesh refinement as shown in Figure 3 except that the model is extended only up to 0.3125 inch (7.94mm). It now has only 359 nodes and 634 elements. This "gage-section portion" model was prescribed with zero  $u_x$  displacement at the top edge along which  $u_y$  displacements were applied either from the extensometer data or from the "full-specimen" 2D-CYANIDE solution (shown in Figures 5, 6 and 7). The extensometer data were taken only from the back-face (Figure 6) and middle-gage (Figure 5) and were linearly extrapolated to simulate the actual data acquisition from cyclic loading tests. Figures 10 and 11 show the results of the "gage-section" portion model driven by the experimental  $u_y$  data, and by the "full-specimen" extracted data, along with the full-specimen response. It could be seen that the elastic-plastic  $K_I$  values, in Figure 10, obtained from the post-processor  $J$  integral values for the full specimen and gage-section portion models are within 5% of each other. The induced vertical load in the gage-section model is within 8% of the full-specimen model, as shown in Figure 11. The experimental data driven gage-section portion model shows excellent agreement with the full-specimen analysis. These results were obtained for upper bound crack length to be used in this program, and it is felt that these conclusions will hold good for all the lower crack lengths.

## CONCLUDING REMARKS

The work to date has shown that the 2D gage section modeling accurately simulates the behavior of the specimen as verified by experimental data. Work is continuing to simulate crack closure with the GAP-CYANIDE Finite Element Program. This effort along with the companion crack growth experiments will be used to identify path-independent integrals which predict the crack growth behavior under isothermal, TMF, and temperature gradient conditions.

## REFERENCES

1. Rice, J.R., "A Path-Independent Integral and the Approximate Analysis of Strain Concentration by Notches and Cracks," *Journal of Applied Mechanics*, Vol. 35, 1968, pp. 379-386.
2. Kim, K.S., "A Review of Path-Independent Integrals in Elastic-Plastic Fracture Mechanics," General Electric Company, 1984, NASA Contractor Report; Also presented in ASTM 18th National Symposium on Fracture Mechanics, June 1985.
3. Blackburn, W.S., Jackson, A.D., and Hellen, T.K., "An Integral Associated With the State of a Crack Tip in a Nonelastic Material," *International Journal of Fracture*, Vol. 13, 1977, pp. 183-200.
4. Kishimoto, K., Aoki, S., and Sakata, M., "On the Path-Independent Integral-J," *Engineering Fracture Mechanics*, Vol. 13, 1980, pp. 841-850.
5. Aoki, S., Kishimoto, K., and Sakata, M., "Elastic-Plastic Analysis of Cracks in Thermally-Loaded Structures," *Engineering Fracture Mechanics*, Vol. 16, 1982, pp. 405-413.
6. Atluri, S.N., "Path-Independent Integrals, in Finite Elasticity and Inelasticity, With Body Forces, Inertia, and Arbitrary Crack-Face Conditions", *Engineering Fracture Mechanics*, Vol. 16, 1982, pp. 341-364.
7. Atluri, S.N., Nishioka, T., and Nakagaki, M., "Incremental Path-Independent Integrals in Inelastic and Dynamic Fracture Mechanics," *Engineering Fracture Mechanics*, Vol. 20, 1984, pp. 209-244.
8. Ainsworth, R.A., Neale, B.K., and Price, R.H., "Fracture Behavior in the Presence of Thermal Strains," *Proceedings of Institute of Mechanical Engineers, Conference on Tolerance of Flaws in Pressurized Components*, London, 1978, pp. 171-178.

9. Yau, J.F., Kim, K.S., Malik, S.N., Van Stone, R.H., and Laflen, J.H., "Elevated Temperature Crack Growth," Annual Progress Report, General Electric Company, NASA Contractor Report, 1985.
10. Kumar, V., German, M.D., and Shih, C.F., "An Engineering Approach for Elasto-Plastic Fracture Analysis," EPRI Report NP-1931 (R.P. 1237-1), Electric Power Research Institute, Palo Alto (CA.), 1981.

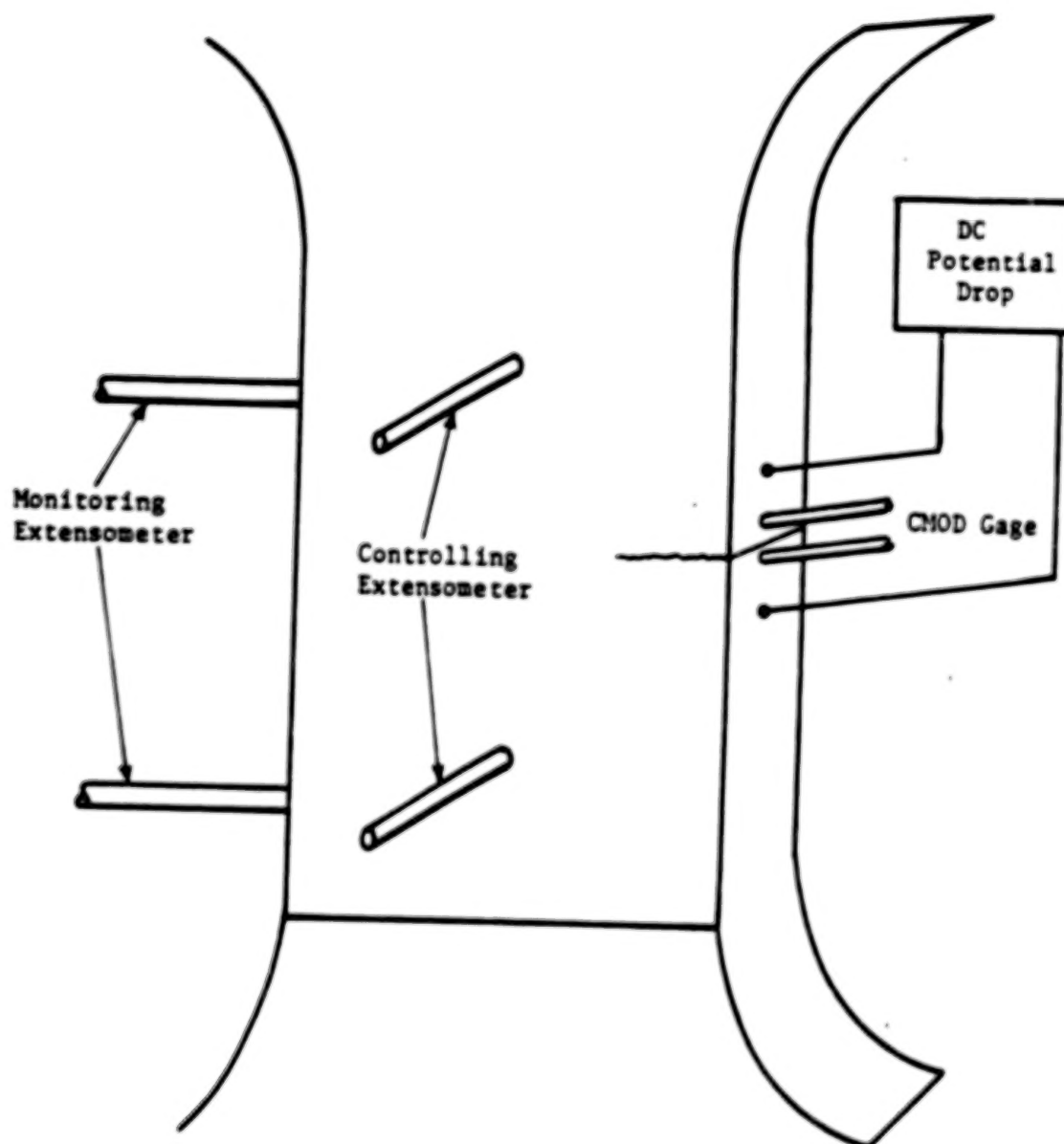


Figure 1. Schematic Drawing of SEN Test Method.

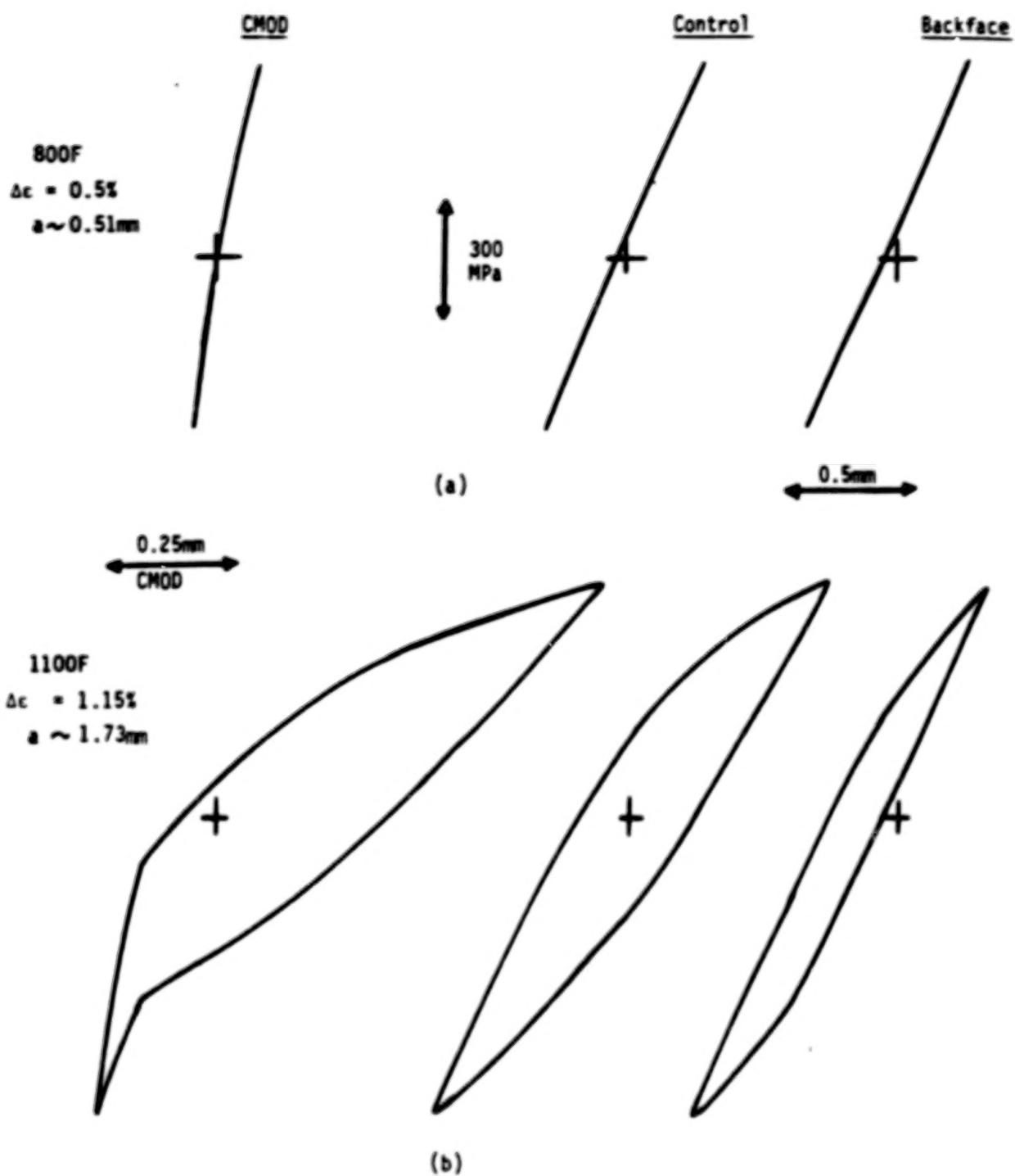


Figure 2: Examples of SEN Specimen Deflections Under  
 (a) Elastic and (b) Elastic-Plastic

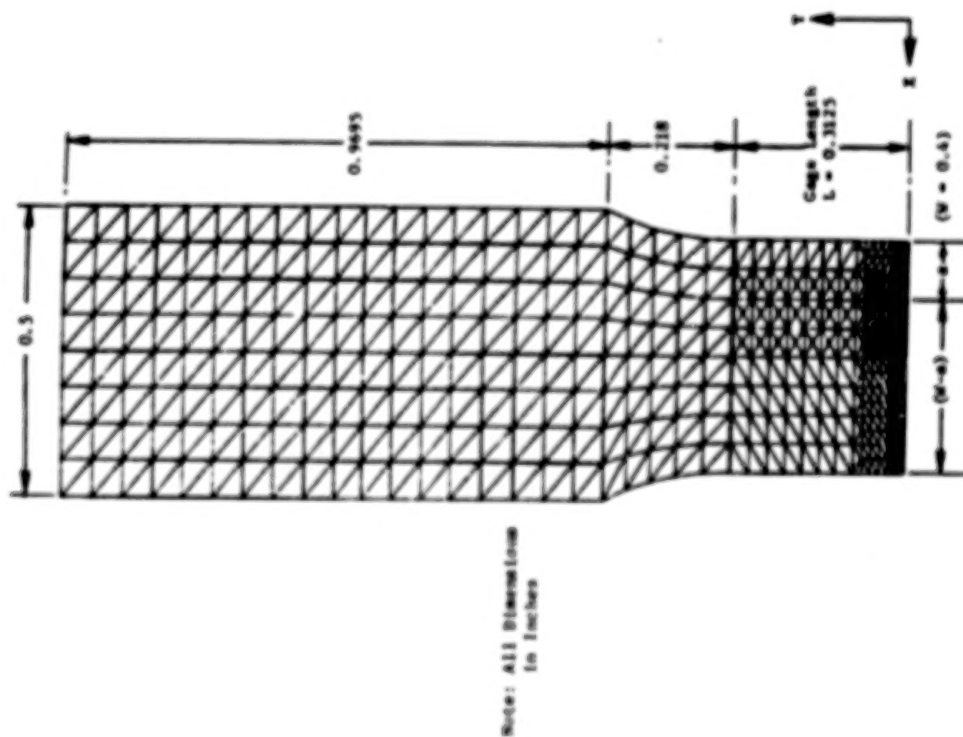


Figure 3. 2D Model of the SEM "Full Specimen" Including Gage-length and Shank Portions.

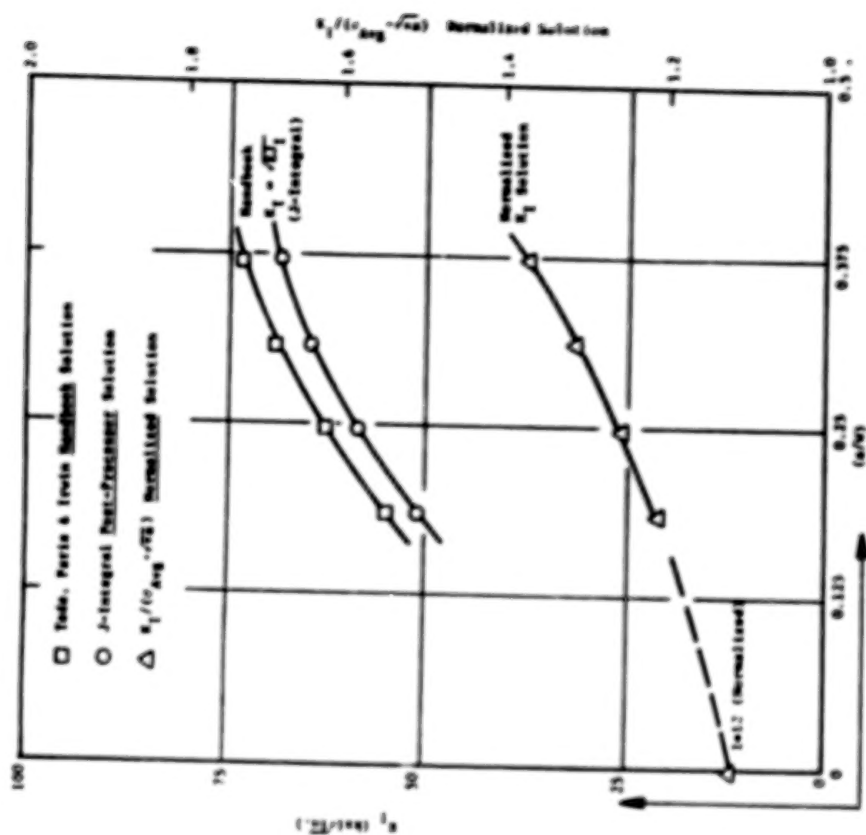


Figure 4.  $K_I$  Solution for SEM Specimen Subjected to a Uniform Normal Displacement at End of Gage Length.

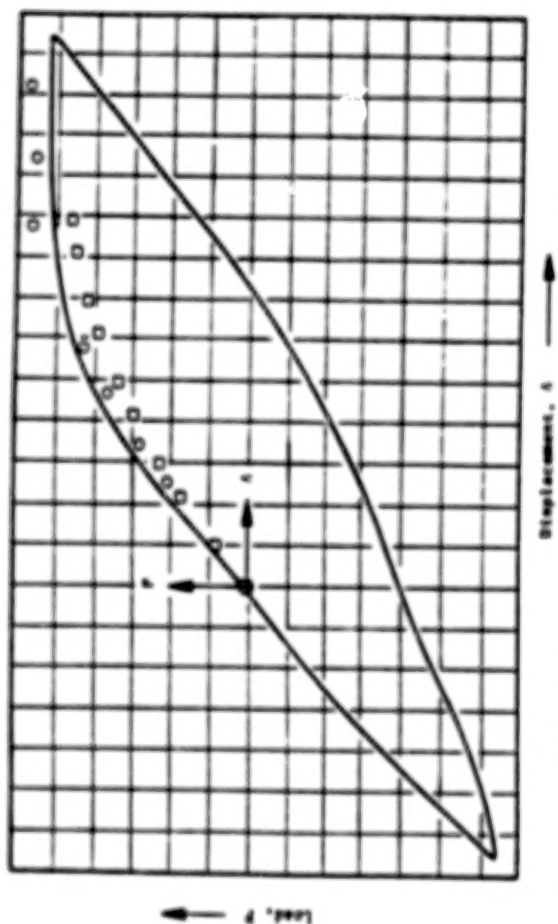


Figure 5. Load Versus Displacement Plot at Middle ( $X = 0.2$  in.) Extensometer Location in the Cage Section of the SEN Specimen at  $Y = 0.28$  inch.

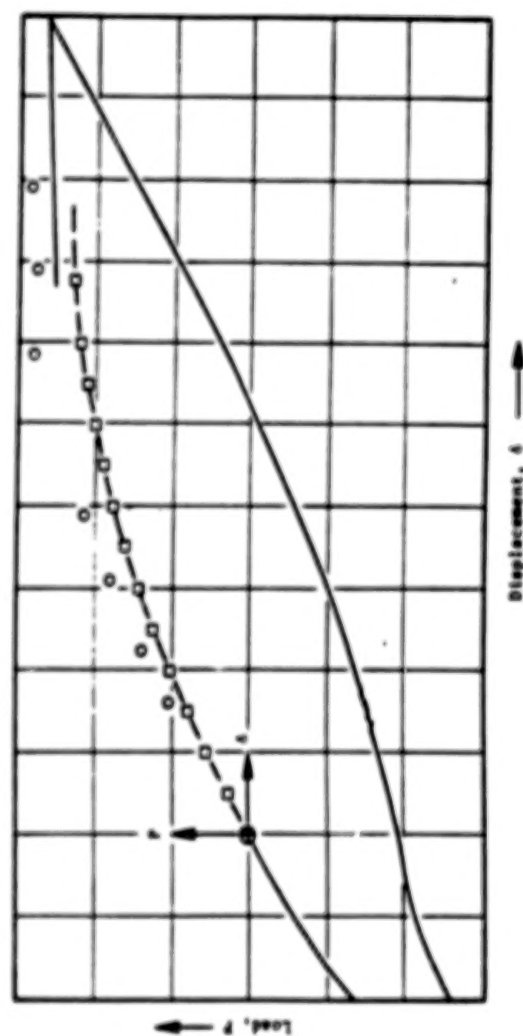


Figure 7. Load Versus Displacement Plot at Front-Face ( $X = 0.0$  in.) Extensometer Location in the Cage - Section of the SEN Specimen at  $U = 0.28$  inch.

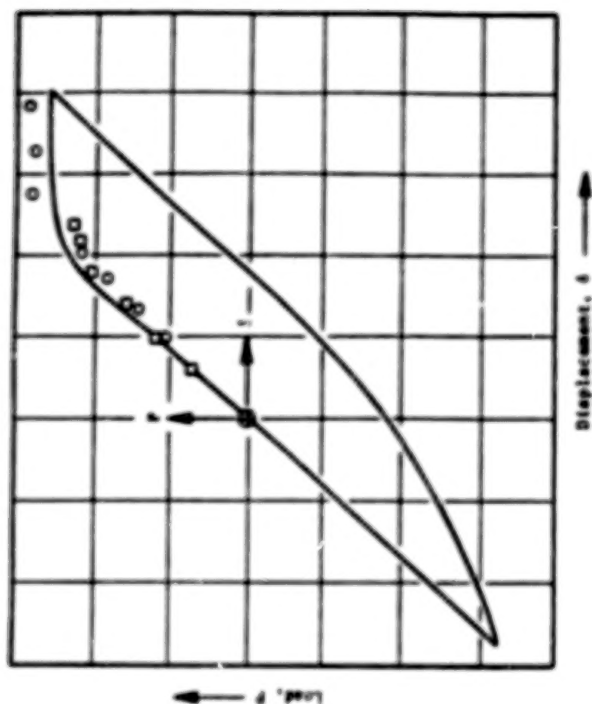


Figure 6. Load Versus Displacement Plot at Back-Face ( $X = 0.4$  in.) Extensometer Location in the Cage-Section of the SEN Specimen at  $Y = 0.28$  inch.

ORIGINAL PAGE IS  
OF POOR QUALITY

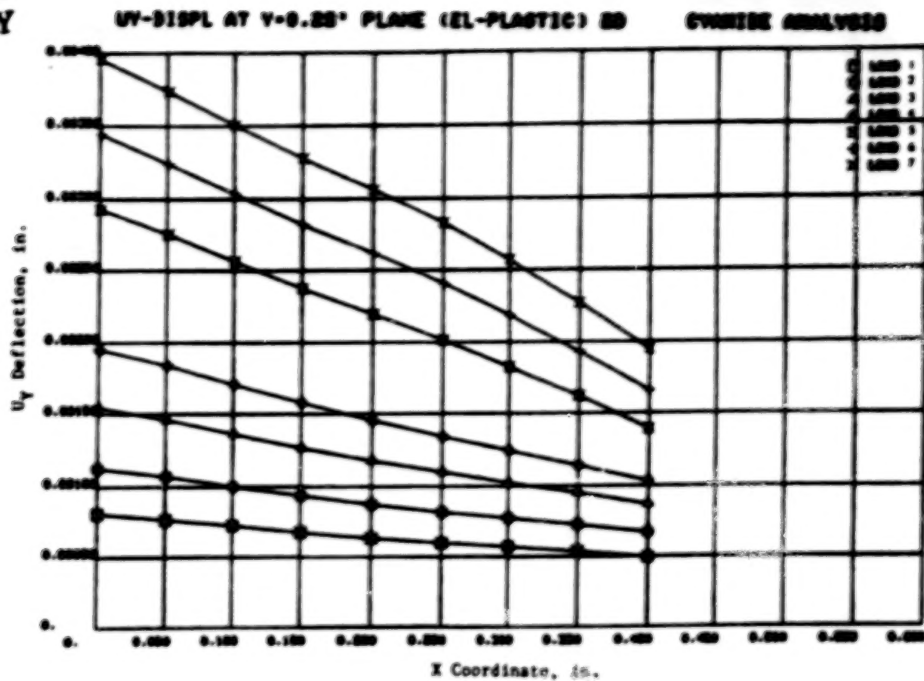


Figure 8. Normal Displacement  $U_y$  at  $Y = 0.28$  inch Plane in Cage-Section as a Function of Specimen Width for the Seven Applied Displacement Cases.

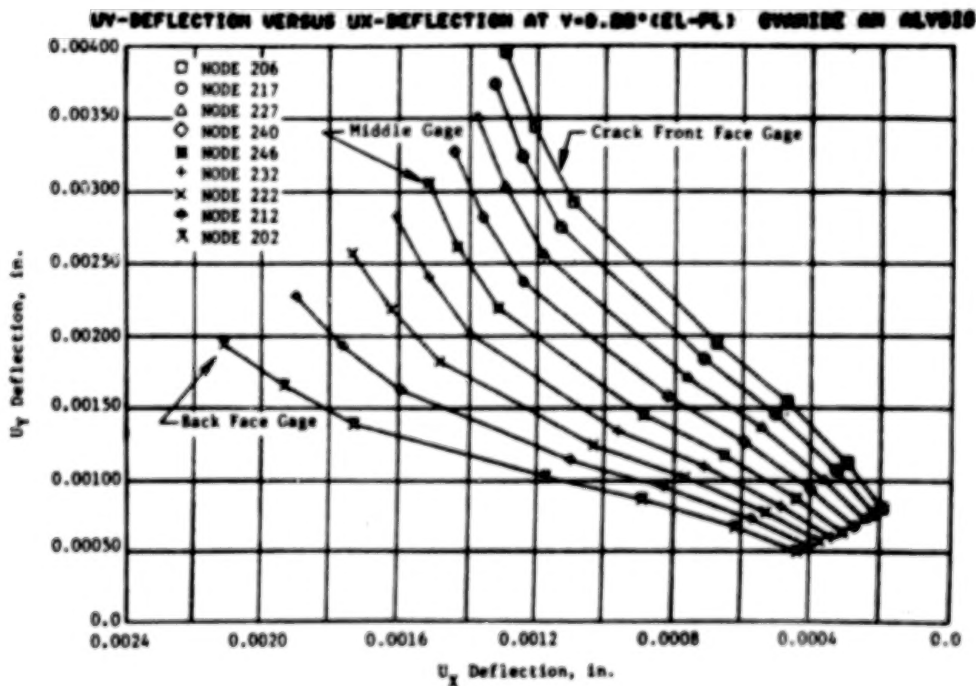


Figure 9.  $U_y$  Versus  $U_x$  Displacement Curves at Each of Nine Locations on  $Y = 0.28$  inch Plane in Cage - Section for the Seven Applied Displacement Cases.

- 2D Full-Specimen Model (Analytical)
- 2D Gage-Section Model (Analytical)
- ▲ 2D Gage-Section Model (Experimental  $u_y$  Data)

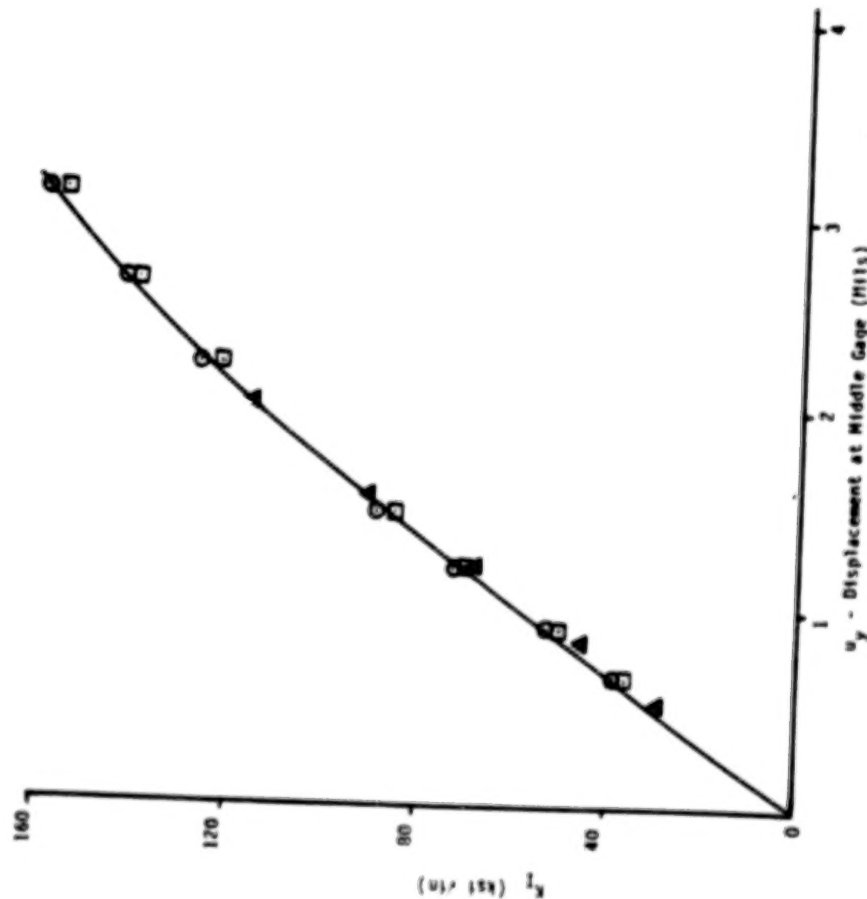


Figure 10: Vertical Displacement Boundary Condition Simulation in Terms of Elastic-Plastic Stress Intensity Factor ( $K_I = \sqrt{E\sigma_1}$ ) in the SEN Buttonhead Specimen ( $a/w = 0.265$ )

- 2D Full-Specimen Model (Analytical)
- 2D Gage-Section Model (Analytical)
- ▲ 2D Gage-Section Model (Experimental  $u_y$  Data)

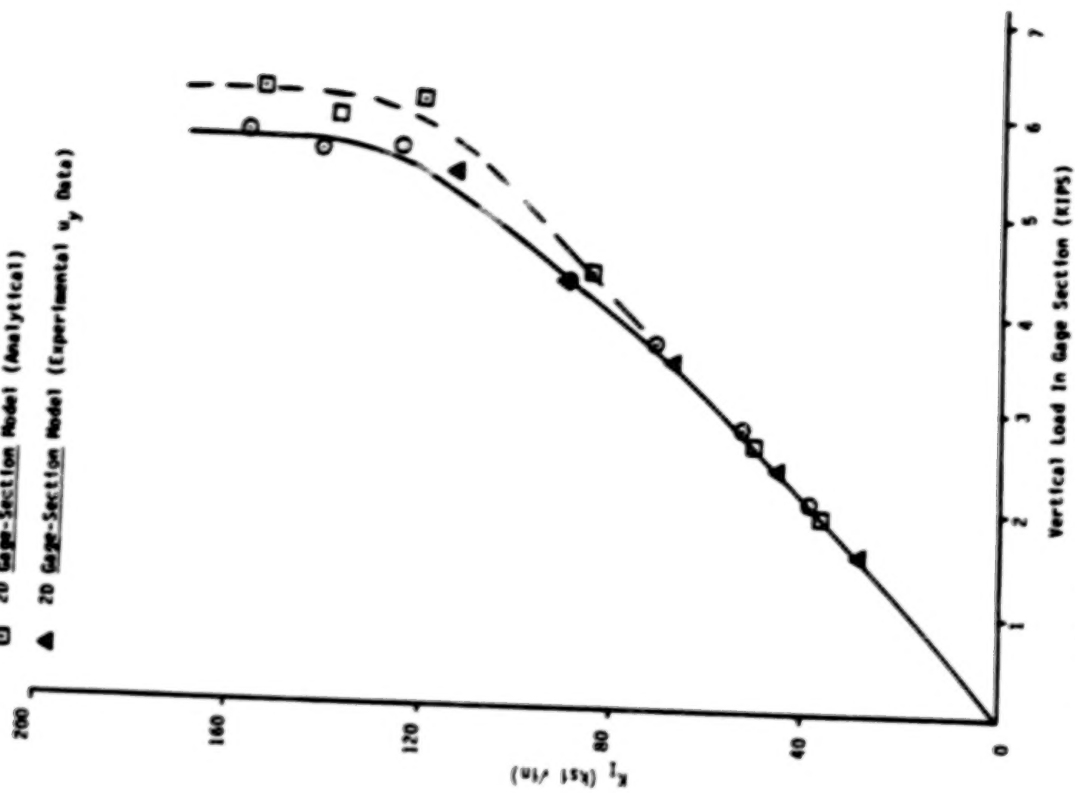


Figure 11: Stress Intensity Factor ( $K_I$ ) in the Buttonhead SEN Specimen as a Function of Vertical Displacement Boundary Condition Induced Vertical Load ( $a/w = 0.265$ )

# LIFE PREDICTION AND CONSTITUTIVE MODELS FOR ENGINE HOT SECTION ANISOTROPIC MATERIALS PROGRAM\*

G. A. Swanson  
United Technologies Corporation  
Pratt & Whitney

## INTRODUCTION

The purpose of this five-year program is to develop life prediction models for coated anisotropic materials used in gas temperature airfoils. In the base program, now underway, two single crystal alloys and two coatings are being tested. These include PWA 1480; Alloy 185; overlay coating, PWA 286; and aluminide coating, PWA 273. Constitutive models are also being developed for these materials to predict the plastic and creep strain histories of the materials in the lab tests and for actual design conditions. This nonlinear material behavior is particularly important for high temperature gas turbine applications and is basic to any life prediction system. This report will highlight some of the accomplishments of the program this year.

## SINGLE CRYSTAL CONSTITUTIVE MODEL

A literature survey was conducted to identify constitutive models and modeling approaches that are applicable to single crystal materials. Two distinct approaches were identified. The first attempts to model the anisotropic behavior by using micromechanical processes which occur during deformation as a basis for the mathematical formulation. The second approach ignores the micromechanical processes and attempts to describe the bulk behavior through macroscopic quantities which are functions of material orientation. While some of the earlier macroscopic models can be considered "fully developed", no complete micromechanical model can be considered fully developed.

Three candidate models have been identified for further evaluation. Two of these models use the macroscopic continuum approaches. These are the classical Hill model (ref. 1) and a unified viscoplastic formulation by Lee and Zaverl, et al (ref. 2). The third model uses a micromechanical approach which is currently being developed by Dr. Kevin Walker. This model is showing the most promise and, therefore, is discussed in detail in this report.

The micromechanical model is based on slip system stresses and strains and is imbedded in Walker's unified viscoplastic formulation (ref. 3). The viscoplastic constitutive formulation based on crystallographic slip theory can be written in the form:

$$\dot{\gamma}_r = K_r^{-p} (\tau_r - u_r) |\tau_r - u_r|^{p-1}$$

\*Work done under NASA Contract NAS3-23939.

where  $\dot{\gamma}_r$  is the shear strain rate resolved on a particular slip system;  $\tau_r$  is the shear stress resolved on that system; and  $\omega_r$  and  $K_r$  are evolving constants analogous to the back stress and drag stress. The term  $K_r$  accounts for the activation of slip systems other than the specific resolved one, that contribute to the shear strain.

A preliminary evaluation of this model has been made using the 982°C (1800°F) data obtained from PWA 1480. Predicted behavior differs depending on whether the model assumes activity on octahedral slip systems or on cubic slip systems, as shown in figure 1(A) through 1(C). Figure 1(A) shows the experimental cyclic hysteresis loops at 982°C (1800°F) for the  $\langle 001 \rangle$ ,  $\langle 110 \rangle$ , and  $\langle 111 \rangle$  orientations. For assumed octahedral slip, figure 1(B), the variation of peak stress response with direction is reasonable, but the theoretical hysteresis loop in the  $[001]$  direction is "fatter", i.e., displays a more inelastic response, than the corresponding experimental loop. At this strain range, viz. + 0.3 percent, the experimental  $[001]$  loop is almost behaving elastically. At higher strain ranges, the response exhibits an inelastic behavior and the loop becomes "fatter".

Figure 1(C) shows the corresponding predicted loops at a  $10^{-3}$  per second strain rate in the  $[001]$ ,  $[011]$  and  $[111]$  directions using the cube slip formula. The same constants were used here for the cube slip response as were used for the octahedral response, simply to see the variation of cube slip constitutive response with direction. The material constants are clearly inappropriate but suffice to show that no inelastic response is predicted in the  $[001]$  direction. Even for large strain ranges, no inelastic response is predicted in the  $[001]$  direction due to the fact that the resolved shear stress  $\tau_{mr}$  is zero in each of the six slip directions when the bar specimen is pulled in the  $[001]$  direction. Clearly a mixture of octahedral and cube slip will improve the correlation between the theoretical model and the experimental results.

#### COATING CONSTITUTIVE MODEL

Knowledge of coating constitutive behavior is essential to the life prediction of coated materials for a number of reasons. Coatings, as will be shown below, are very often the sites of crack initiation and, therefore, the time for a crack to initiate and progress into the substrate is very important in the overall life of the component. Secondly, the coating is effectively a structural component and its stress-strain history will affect the stress-strain history of the substrate-coating interface.

The survey of candidate constitutive models for this program was limited to isotropic formulations. Data to measure any anisotropy inherent in the actual application would be well beyond the scope of this program. Models selected for evaluation have included a classical model (ref. 4), Walker's viscoplastic formulation (ref. 3), Stowell's model (ref. 5), and Moreno's simplified version (ref. 6).

Experimental data on the aluminide coating is not yet available. The testing procedures are complex and are in the development stage. For the overlay coating some cyclic-creep relaxation data have been obtained, using both hot isostatically pressed and plasma sprayed specimens, to partially evaluate the models. Comparison of cyclic-creep relaxation data against the classical model and the Walker model is shown in figure 2. In this test the classical model matches the data almost as well as Walker's model. For longer tests and/or more complex cycles, the Walker model's better accuracy may become very important.

## LIFE PREDICTION MODEL

The selection process for life prediction models has not yet been focused to the extent of that for the constitutive models. However, an extensive list of candidates has been developed, and they generally fall into three broad classifications: 1) phenomenological models, 2) cumulative damage models, and 3) crack growth models.

In general, all of the phenomenological models have the advantage of simplicity and a rather direct relationship to data bases. A drawback, however, is that they are not very amenable to accounting for significant interaction effects when different damage mechanisms (cyclic creep, fatigue) operate either simultaneously or sequentially as a result of complex high temperature loading patterns. The cumulative damage (ref. 7-8) approaches assume that the plastic and creep components of inelastic strain cause damage which can be explicitly predicted and which define the state of the material. Damage is considered to be zero in the initial undamaged state and failure occurs when a critical level or limit is reached due to plastic, cyclic creep or monotonic creep deformations. A number of different definitions of damage and approaches for counting damage are used. Nearly all of these require use of a constitutive model to determine the portion of damage caused by a particular load condition. Life prediction models which use this approach are: Linear Time and Cycle Fraction, Ductility Exhaustion, Continuous Damage, Strain Range Partitioning, and Cyclic Damage Accumulation.

The model development will follow closely the results of low cycle fatigue and thermal mechanical fatigue tests.

## LIFE PREDICTION TESTS

From the initial test results, the importance of the coating in influencing the substrate life is demonstrated both by the metallography of the failures and the number of cycles to failure. Comparing the fracture surface photographs in figures 3 and 4, note that the diffusion coated specimens cracked almost uniformly around the circumference, whereas the overlay coated specimens developed families of thumbnail cracks around the circumference. Also, note in figure 5 that the diffusion coated specimen is more sensitive to strain range than the overlay coated specimens.

Replica data taken during thermal mechanical fatigue tests, shown in figure 6, demonstrate that cracks in the diffusion coating grow relatively quickly around the circumference and uniformly into the single crystal, while cracks in the overlay coating penetrate the coating quickly but stop at the coating-substrate interface for an "incubation" period before proceeding into the substrate. A life prediction model must account for these differences in crack initiation behavior between coatings.

Since airfoils pass through complex thermal mechanical cycles, the life prediction model must address the variation in temperature and strain through each cycle. Various thermal mechanical fatigue cycles are being tested. One interesting result is shown in figure 7. Two cycles were run with the same end points and, despite the differences in cycle shape, the lives were nearly the same. Other cycle shapes are likely to give significantly different lives.

To better understand the behavior of the coating on the substrate in a thermal mechanical fatigue cycle, a two element model was developed with one element representing the overlay coating and the other the substrate. This simple structure, uti-

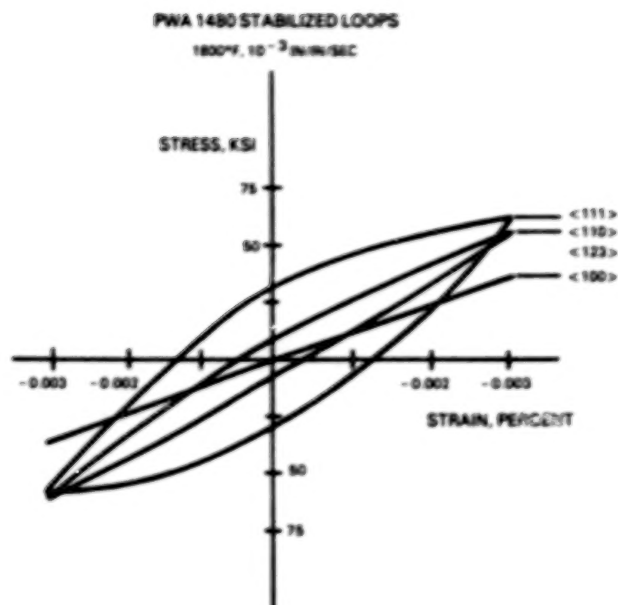
lizing the Walker constitutive model for the coating, and a simple constitutive model for the substrate, was analytically run through three cycles. As shown in figure 8, the coating mechanical strain-stress history is considerably different from that of the substrate. In each cycle the coating stress relaxes to zero stress at maximum temperature conditions due to the coating's high creep rate at these conditions. The resulting hysteresis loop should provide important parameter data for a coating cracking model.

#### FUTURE WORK

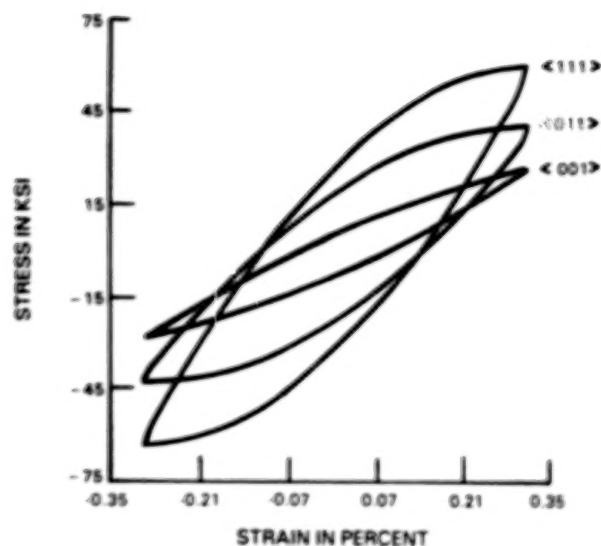
In the coming year, additional cyclic tests are planned to: 1) develop the constitutive model, 2) assist in the life prediction model formulation, and 3) evaluate constants for the models. Also, assuming Option 1 of the program is exercised, model life development will be extended to airfoil root attachment temperatures, stress levels, and notch stress concentrations.

#### REFERENCES

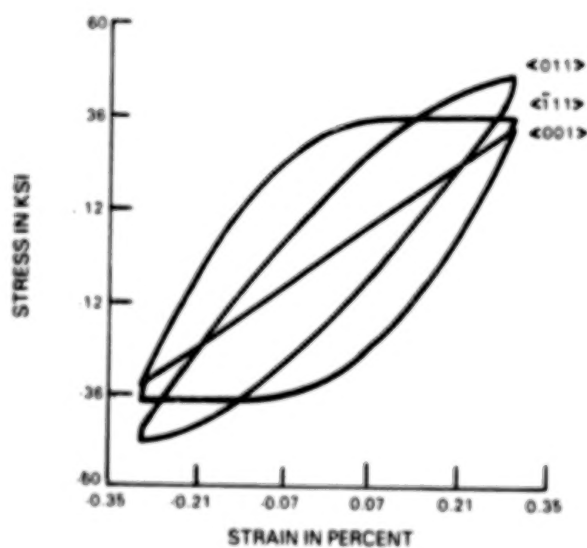
1. Hill, R.: "A Theory of the Yielding and Plastic Flow of Anisotropic Metals," Proc. Royal Society of London, Ser. A, Vol. 193, pp. 281-297, 1948.
2. Lee, D.; Zaverl, F., Jr.; Shih, C. F.; and German, M. D.: "Plasticity Theories and Structural Analysis of Anisotropic Metals," Report No. 77CRD285, General Electric Corporate Research and Development Center, Schenectady, New York, 1977.
3. Walker, K. P.: "Research and Development Program for Nonlinear Structural Modeling With Advanced Time-Temperature Dependence Constitutive Relationships," NASA CR-165533, November, 1981.
4. Kraus, H.: Creep Analysis, John Wiley & Sons, Inc., New York, Chapter 2, 1980.
5. Stowell, E. Z., et al: "Predicted Behavior of Rapidly Heated Metal in Compression," NASA TR R-59, 1960.
6. Moreno, V.: "Development of a Simplified Analytical Method for Representing Material Cyclic Response," NASA CR-168100, January, 1983.
7. Lemaitre, J.; and Chaboche, J. L.: "A Non-Linear Model for Creep Fatigue Damage Cumulation and Interaction," Mechanics of Viscoplastic Media and Bodies, J. Hult, Ed., Springer-Verlag, pp. 291-301, 1975.
8. Lemaitre, J.; and Plumtree, A.: "Application of Damage Concepts to Predict Creep Fatigue Failures," J. Eng. Materials and Technology, Vol. 10, ASME, pp. 284-292.
9. Swanson, G. A.; and Bill, R. C.: "Life Prediction and Constitutive Models for Engine Hot Section Anisotropic Materials," AIAA-85-1421, AIAA/SAE/ASME 21st Joint Propulsion Conference, Monterey, California, 1985.



(A) Experimental Hysteresis Loops for PWA 1480 at 982°C (1800°F) at  $10^{-3}$  Sec $^{-1}$  Strain Rate



(B) Octahedral Slip Predictions of Hysteresis Loops for PWA 1480 at 982°C (1800°F)



(C) Cube Slip Predictions of Hysteresis Loops for PWA 1480 at 982°C (1800°F)

Figure 1

COATING CONSTITUTIVE MODEL-DATA COMPARISON  
CYCLIC - CREEP RELAXATION TEST AT 538°C (1000°F)

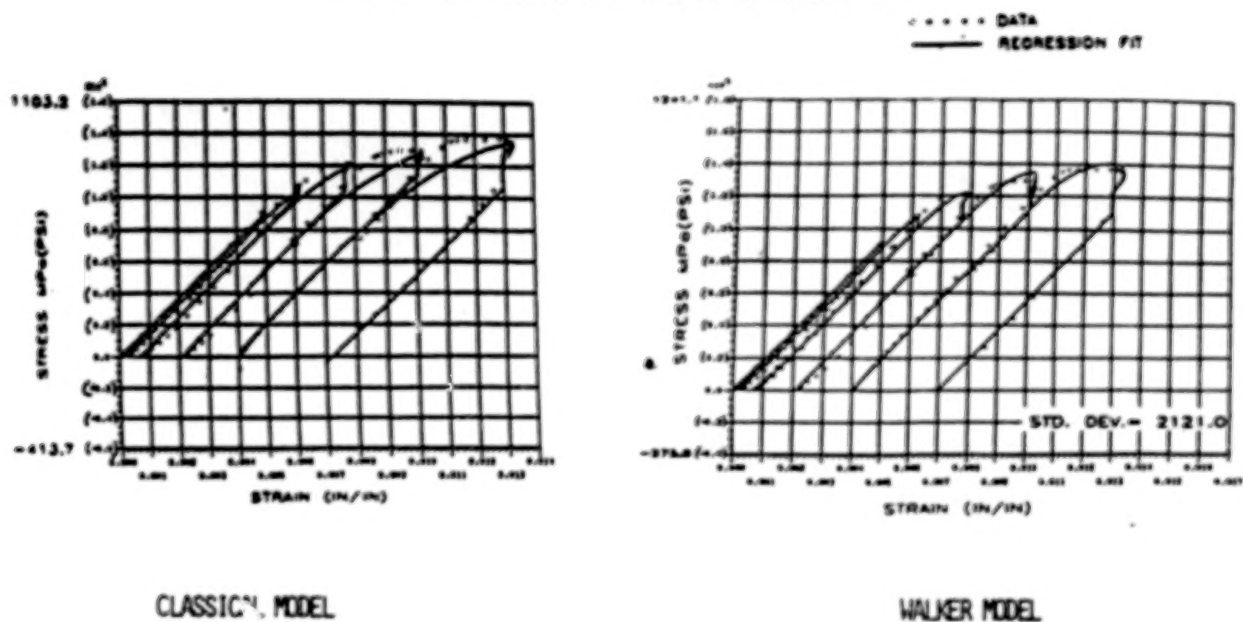
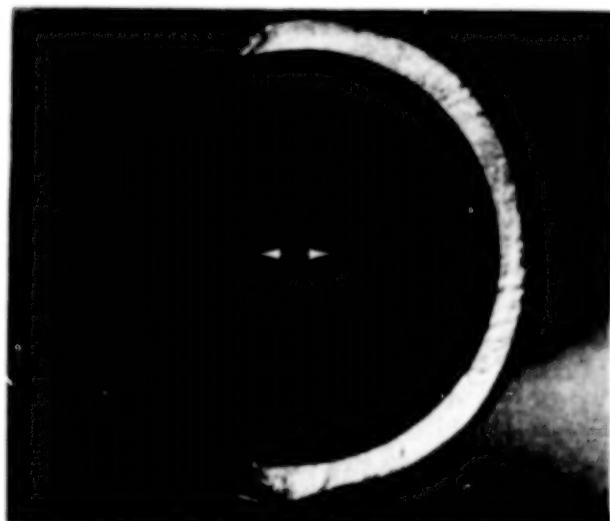
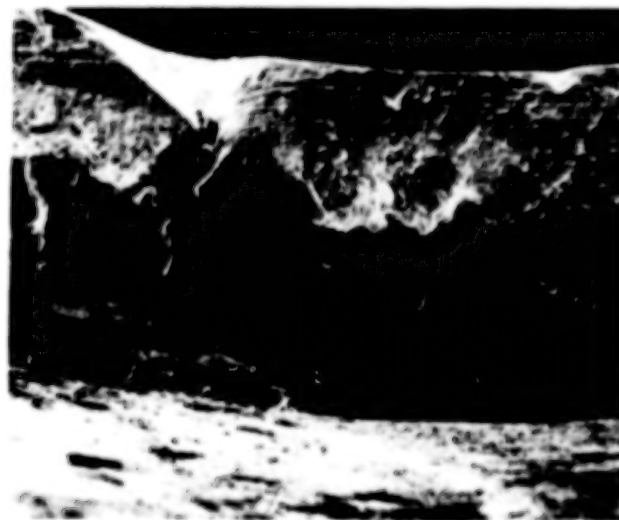


Figure 2



6X

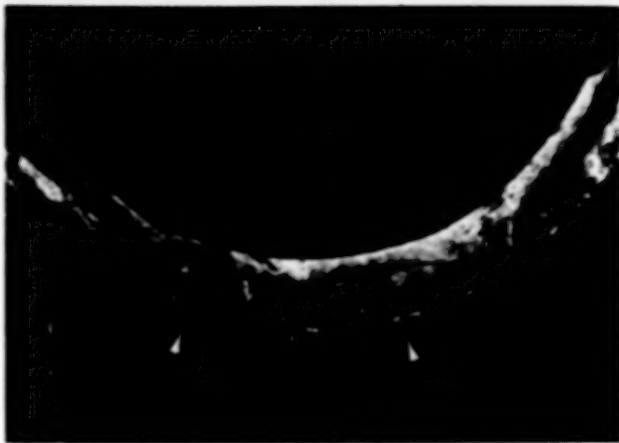
(A) Circumferential Cracking



50X

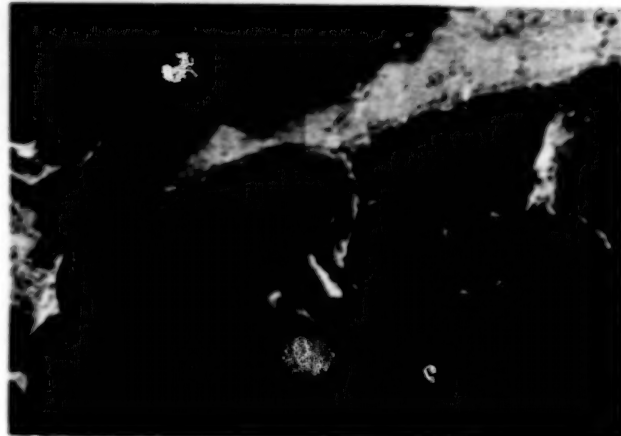
(B) Faint Fatigue Striations

Figure 3 PWA 273 Coated PWA 1480 <100>; Specimen JB-22; After Being Thermal Mechanical Fatigue Tested at 427-1038°C (800-1900°F)  $\Delta\epsilon = \pm 0.275\%$ , 1 CPM, Out-of-Phase for 3772 Cycles



10X

(A) Multiple Small Thumbnail-Like Fatigue Cracks



40X

(B) Faint Fatigue Striations

Figure 4 PWA 286 Coated PWA 1480 <100>; Specimen JB-9; After Being Thermal Mechanical Fatigue Tested at 427-1038°C (800-1900°F)  $\Delta\epsilon = +0.4\%$ , 1 CPM, Out-of-Phase for 1878 Cycles

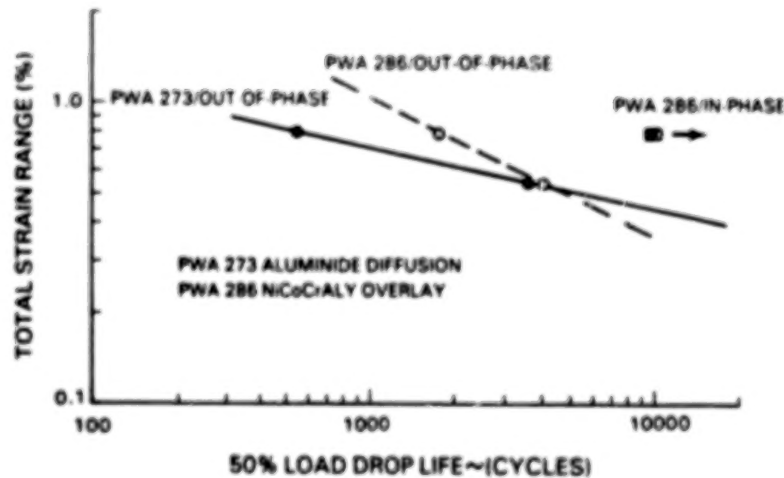


Figure 5 Thermal Mechanical Fatigue Life Vs. Strain Range for Coated PWA 1480 427-1038°C (800-1900°F)

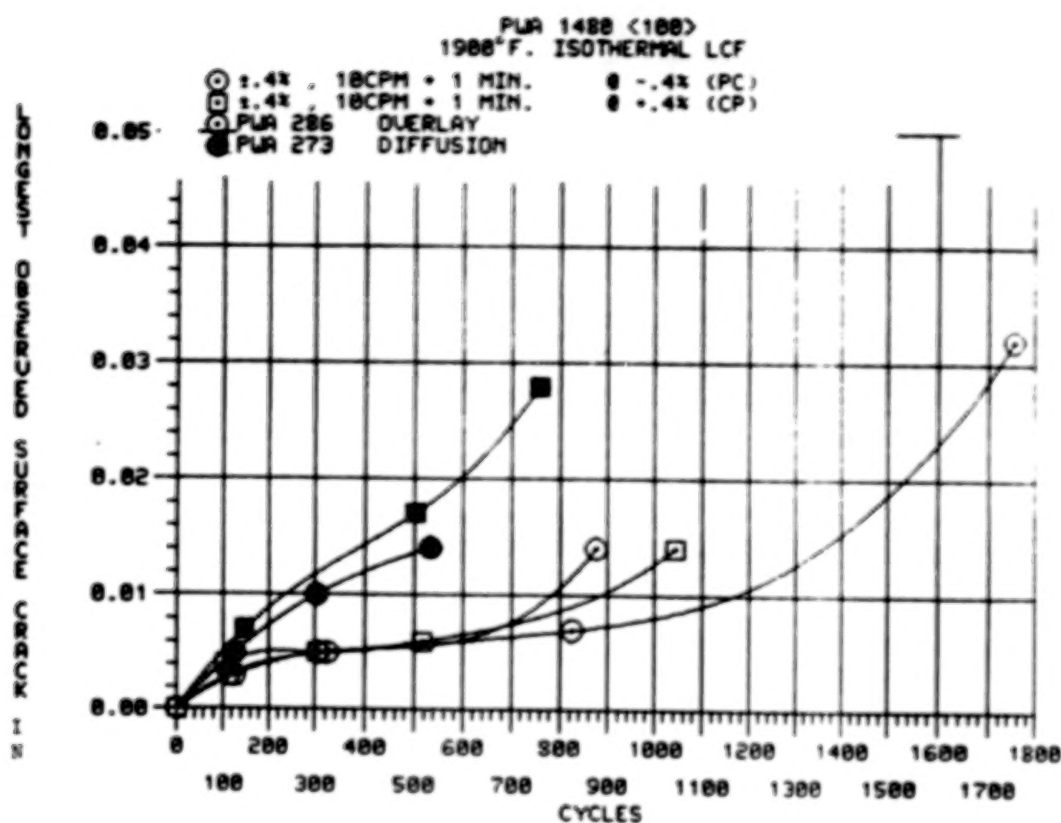


Figure 6 Comparison of Crack Growth with Diffusion and Overlay Coatings

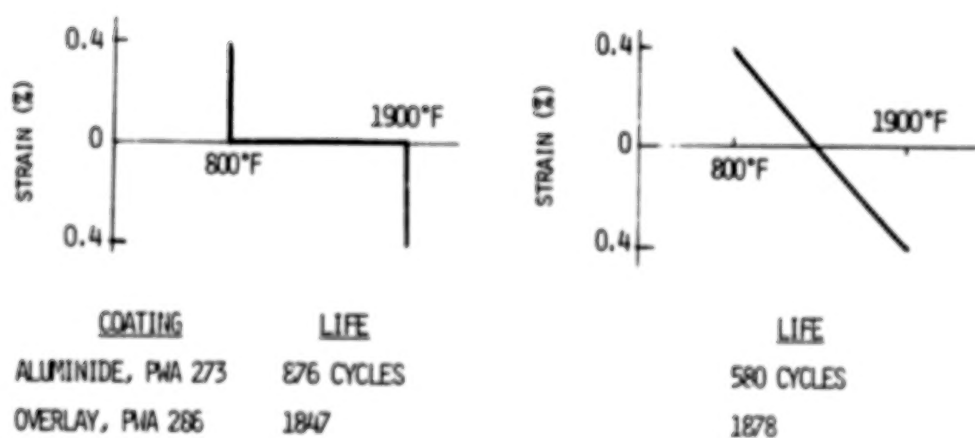


Figure 7 Coated PWA 1480 Life Comparison: Two TMF Cycle Shapes

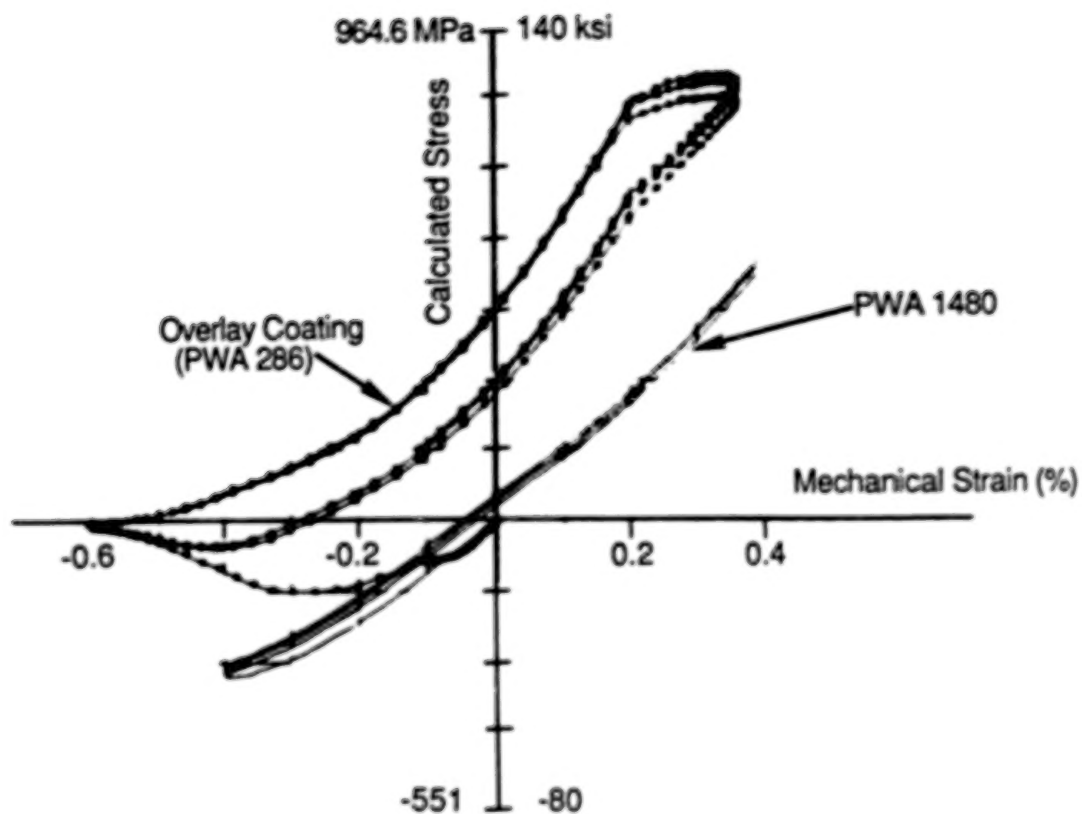


Figure 8 TMF Cycle - Coating and Substrate Stress-Strain History  
 Out of Phase Cycle  
 Temperature Range 427°C - 1038°C (800°F - 1900°F)  
 Strain Range  $\pm 0.4$  Percent

## CREEP-FATIGUE BEHAVIOR OF NiCoCrAlY COATED PWA 1480

## SUPERALLOY SINGLE CRYSTALS

R.V. Miner, J. Gayda, and M.G. Hebsur  
NASA Lewis Research Center  
Cleveland, Ohio

The present study of high-temperature fatigue and creep-fatigue behavior is part of a program to identify the basic features of the effects of temperature, creep, fatigue, and environment on the behavior of a single-crystal superalloy, a bulk coating alloy, and a coated alloy system. A system was selected which has had considerable production experience: the Ni-base superalloy, PWA 1480, and the NiCoCrAlY coating, PWA 276, inventions of the Pratt & Whitney Aircraft Company.

Isothermal behavior was studied first. A series of fatigue and creep-fatigue tests of the types commonly designated as pp, cp, pc, and cc were conducted. These tests were conducted at various constant total strain ranges. The creep-fatigue cycles employed constant stress dwells at the maximum and/or minimum load. A complete set of data is published in a NASA Technical Memorandum (ref. 1).

## MATERIALS AND PROCEDURES

## Materials

PWA 1480, which is described in the literature (refs. 2 and 3), has the following nominal composition: 10 Cr, 5 Al, 1.5 Ti, 12 Ta, 4 W, 5 Co, and the balance Ni (in weight percent). The single crystals were solution treated for 4 hr at 1290 °C before machining. Bars having their <001> planes within less than 7° of the axis were selected. After machining, the LCF specimens were coated with PWA 276 by low-pressure plasma spraying. The coating composition (in weight percent) was 20 Co, 17 Cr, 12.4 Al, 0.5 Y, and the balance Ni. The coating thickness was about 0.12 mm. After coating, the specimens were given a diffusion treatment of 1080 °C for 4 hr and then aged at 870 °C for 32 hr.

PRECEDING PAGE BLANK NOT FILMED

### Test Procedures

The testing facility used in this investigation has been described in reference 4. Fatigue tests at 0.1 Hz and creep-fatigue tests were conducted using an hourglass type specimen and diametral strain control. The extensometer was always placed across one of the  $\langle 001 \rangle$  planes nearly perpendicular to the specimen axis. Heating was produced by the passage of alternating current directly through the specimen.

After the first series of tests it was discovered that they had been conducted at 1015 °C, rather than at 1050 °C as intended. Also, it appeared that the dwell stress level affected life in the creep-fatigue cycles, but the result was somewhat confounded since the controlled dwell stresses and total strain ranges had been varied commensurately in order to minimize test times. In a second series of tests conducted at 1050 °C, total strain range and dwell stress level were varied as independently as practicable. However, life behavior in the lower temperature tests shows the same dependencies on strain and stress as in the 1050 °C tests, even though the two "independent" variables are more highly correlated.

All tests were controlled at constant total diametral strain range. However, the strains reported herein are calculated axial strains. In the creep-fatigue cycles constant stress dwells were employed. The first tests, those at 1015 °C, were controlled using an electromechanical programmer; in the 1050 °C tests a Data General S/20 computer was used. The frequency of the pp tests at both temperatures was about 0.1 Hz. The creep-fatigue tests employed about the same ramp rates as the pp tests.

### RESULTS

Some results of the 1050 and 1015 °C fatigue and creep-fatigue tests are shown in table I. Shown are the cycle type; cyclic life  $N_f$ ; the values at half life of the total axial strain range  $\Delta\epsilon_{tot}$ , inelastic axial strain range  $\Delta\epsilon_{in}$ , stress range  $\Delta\sigma$ , and maximum stress  $\sigma_{max}$ ; and the average cycle time  $t_{av}$ . Other data discussed below, such as that for the first cycle, may be found in reference 1.

#### Constitutive Behavior

The constitutive behavior of PWA 1480 at 1015 and 1050 °C for all the stress dwell creep-fatigue cycle types studied is characterized by extreme cyclic softening. Inelastic axial strain range increased with cycling for all cycle types. At  $0.5N_f$ ,  $\Delta\epsilon_{in}$  had increased an average of ~25 percent for the pp tests,

~15 percent for the cp and pc tests, but generally less than 5 percent for the cc tests. For the 1050 °C tests the decrease in  $\Delta\sigma$  at  $0.5N_f$  averaged ~10 percent for the pp and cp tests but was slightly higher for the pc tests, ~15 percent. For the cp and pc tests at 1015 °C the decrease in  $\Delta\sigma$  appeared to be smaller than for those tests at 1050 °C.

The most dramatic change with cycling in the creep-fatigue tests was the increase in creep rates. By  $0.5N_f$ , the reduction in cycle time was typically ~80 percent in the cp and pc tests and more than 95 percent in the cc tests, though the creep strain per cycle typically did not decrease during cycling. Creep strain did decrease as a fraction of the total inelastic strain range, however, and the fraction of pp strain increased. This occurred most in the 1050 °C tests.

Another interesting observation was that for the same absolute stress level, creep rates were higher in compression than in tension. This effect was observed in comparison of cp and pc tests but was most readily seen in the cc tests. Creep rates in compression were about 1.5 to 2 times higher than those in tension.

#### Life Behavior

For both the fatigue and stress dwell creep-fatigue tests conducted in this study, the life of PWA 1480 correlated well with a model including both  $\Delta\epsilon_{in}$  and  $\Delta\sigma$ . This model provides considerably better correlations than those based on  $\Delta\epsilon_{in}$  alone,  $\Delta\epsilon_{in}$  and  $\sigma_{max}$ , or  $\Delta\epsilon_{in}$  and  $t_{av}$ .

Table II is a summary of the regression analyses for all test types at either test temperature using various power law models. These various models test the basic dependencies of life on frequency, strain rate, or  $\sigma_{max}$  used in the strain-range-partitioning (ref. 5), frequency-separation (ref. 6), frequency-modified (ref. 7), and damage-rate (ref. 8) approaches.

The 1050 °C results will be examined first since they are clearer. As previously indicated, care was taken in the design of this series of tests to reduce as much as possible the correlation between the two "independent" variables in the creep-fatigue tests, total strain range, and dwell stress. The tests employed various total strain ranges but only two dwell stress levels in tension and/or compression. For this data set, even with the pp tests included,  $\Delta\sigma$  and  $\sigma_{max}$  are only 25 and 16 percent (R-values) correlated with  $\Delta\epsilon_{in}$ , respectively.

It may be seen in table II that the model  $N_f = \alpha \Delta\sigma^Y$  provides a better fit than the single variable models containing  $\Delta\epsilon$ ,  $\sigma_{\max}$ ,  $t_{av}$ , or any of the two-variable models not including  $\Delta\sigma$ . Neither the addition of  $\sigma_{\max}$  or  $t_{av}$  to  $\Delta\epsilon_{in}$  in the model provides substantial improvement. The model  $N_f = \alpha \Delta\epsilon_{in}^B \Delta\sigma^Y$  provides the best fit of all. Note also that in the models containing  $\sigma_{\max}$  or  $t_{av}$  together with  $\Delta\epsilon$ , the absolute values of the T-ratios for their coefficients are much less than 3, the usually accepted value for statistical significance. Plots of  $N_{f,obs}$  and  $N_{f,pred}$  are shown in figure 1 for the two models  $N_f = \alpha \Delta\epsilon_{in}^B$  and  $N_f = \alpha \Delta\epsilon_{in}^B \Delta\sigma^Y$ .

Also, the model  $N_f = \alpha \Delta\epsilon_{in}^B \Delta\sigma^Y$  provides the best fit for individual analyses of each cycle type. The best fit coefficients  $B$  and  $Y$  are not the same for each cycle type, as might be expected. Still, equations using the average values of  $B$  and  $Y$ ,  $-1.26$  and  $-3.08$ , provide good fits for the individual cycle types. The values of  $\alpha$  in these equations are shown in table III.

It is well demonstrated by the cc tests that  $\Delta\sigma$  is more significant than  $\sigma_{\max}$  in determining life. Three tests were conducted with  $\sigma_{\max}$  and  $\sigma_{\min}$  of about  $+200/-200$  MPa, or a  $\Delta\sigma$  of about 400 MPa. An additional 1050 °C cc test, the first listed in table III, had about the same  $\sigma_{\max}$  (210 MPa) but a larger  $\Delta\sigma$  (474 MPa). The life of this test was reduced to about 1/3 of that expected for a  $+200/-200$  MPa test with the same  $\Delta\epsilon_{in}$ . In the fourth test listed in table II it was intended to increase  $\sigma_{\max}$  but keep  $\Delta\sigma$  the same as for the first tests. Actually,  $\sigma_{\max}$  was increased about 30 percent to 257 MPa, but  $\Delta\sigma$  was also increased about 10 percent, and still life increased relative to the  $+200/-200$  MPa tests. For these cc tests alone,  $R^2$  for the model  $N_f = \alpha \Delta\epsilon_{in}^B \sigma_{\max}^Y$  is 40 percent, only slightly better than the value of 37 percent for  $N_f = \alpha \Delta\epsilon_{in}^B$ , and considerably less than the value of 76 percent for  $N_f = \alpha \Delta\epsilon_{in}^B \Delta\sigma^Y$ .

For the tests at 1015 °C the model containing  $\Delta\sigma$  alone provides no better correlation than that containing  $\Delta\epsilon_{in}$ ; however, this could be explained by the high degree of correlation between  $\Delta\sigma$  and  $\Delta\epsilon_{in}$  in these tests,  $R^2$  of 80 percent. Since  $\Delta\epsilon_{in}$  is strongly correlated with  $\Delta\sigma$ , life correlates equally well with either variable. However, as for the tests at 1050 °C,  $\sigma_{\max}$  does not provide a good correlation, nor does  $t_{av}$ , and the model  $N_f = \alpha \Delta\epsilon_{in}^B \Delta\sigma$  provides the best correlation. Figure 2 shows a comparison of the predictions of the models  $N_f = \alpha \Delta\epsilon_{in}^B$

and  $N_f = \alpha \Delta \epsilon^B \Delta \sigma^Y$ . The best fit values of  $B$  and  $Y$  for the latter model are -1.00 and -2.70. Values of  $\sigma$  which provide the best fit for each cycle type are shown in table III.

It may be seen that correlations using all the models are better for the 1015 °C data than for the 1050 °C data. This is largely because the 1015 °C data cover a greater range of the "independent" variables.

#### Failure Mode

Internal crack initiation at pores was the predominant failure mode in these tests. For the creep-fatigue tests cracking initiated at many internal pores and linked up before the final overload in 80 percent of the specimens. Others appeared to have a dominant crack which initiated near the surface, possibly at a pore, but generally the fracture faces were heavily oxidized and difficult to interpret. Fracture surfaces with this appearance were more common for the pp tests. Still, the majority of pp tests failed at multiple internal pores.

#### DISCUSSION

Except in that it permits inelastic strain, creep does not have a great effect on the cycle life of the coated single-crystal superalloy, PWA 1480. On any basis of comparison, and particularly on the basis of  $N_f = \alpha \Delta \epsilon^B \Delta \sigma^Y$  as in table III, lives for the creep-fatigue cycles are not greatly, if at all, worse than those for the pp tests. Though life may be lower for the cp cycle than for the others, it is only about 30 percent lower than the average for the other cycles. Lives for the other cycles may all be the same.

In fact, there appears to be no time-dependent process having a great effect on life. This is shown by the lack of any substantial improvement when  $t_{av}$  is included in the life models. Neither creep nor the environmental degradation have affected the coated single-crystal superalloy. The mechanisms of creep degradation in polycrystalline alloys such as grain boundary cavitation or sliding obviously cannot occur, and the environment cannot affect the internal crack propagation mode of failure.

The successful life model containing  $\Delta \epsilon_{in}$  and  $\Delta \sigma$  is unusual and may be peculiar to the coated single-crystal superalloy system studied. Crack initiation in high temperature creep-fatigue, at least for polycrystalline materials, is usually

found to be determined by  $\Delta\epsilon_{in}$  and some measure of time-dependent damage processes such as creep cavitation at grain boundaries or oxidation attack. The importance of  $\Delta\sigma$  in the life model and the internal crack initiation observed and may reflect that crack propagation is a significant portion of life in these tests. Since the cracks are protected from the atmosphere, it might be expected that the crack growth rates are relatively low, and, while crack initiation is thought to be primarily driven by  $\Delta\epsilon_{in}$ ,  $\Delta\sigma$  can be tied to crack propagation rates.

## RESULTS AND CONCLUSIONS

Fatigue tests at 0.1 Hz and cp, pc, and cc type creep-fatigue tests have been conducted on NiCoCrAlY coated specimens of a single-crystal superalloy, PWA 1480, at 1050 and about 1015 °C. The following results and conclusions were obtained:

1. Considerable cyclic softening occurred for all test cycles, evidenced particularly by rapidly increasing creep rates in the creep-fatigue tests.

2. Lives for the pp, cp, pc, and cc cycles were not greatly different; however, those for the cp cycle did appear to be lowest at both test temperatures.

3. A life model,  $N_f = a \Delta\epsilon_{in}^B \Delta\sigma^Y$ , was found to provide good correlation for all cycle types, better than models based on  $\Delta\epsilon_{in}$  alone, or  $\Delta\epsilon_{in}$  with either  $\sigma_{max}$  or  $t_{av}$ .

4. For all test types failure occurred predominantly by multiple internal cracking originating at porosity.

5. The strong correlation of life with  $\Delta\sigma$  may reflect a significant crack growth period in the life of the specimens.

6. The lack of improvement in the models when average cycle time was considered appears to reflect that neither is there a large effect of strain rate on the damage mechanisms in the single-crystal material nor any environmental effect due to the internal cracking mode of failure.

#### REFERENCES

1. Miner, R.V.; Gayda, J.; and Hebsur, M.G.: Evaluation of Development Membranes for the Mixed Reactant Iron-Chromium Redox System. NASA TM-87110, 1985.
2. Gell, M.; Duhl, D.W.; and Giamei, A.F.: The Development of Single-Crystal Superalloy Turbine Blades. Superalloys 1980, ASM, Metals Park, OH 1980, pp. 205-214.
3. Shah, D.M.; and Duhl, D.W.: The Effect of Orientation, Temperature and Gamma Prime Size on the Yield Strength of a Single Crystal Nickel Base Superalloy. Superalloys 1984, AIME, Warrendale, PA, 1984, pp. 105-114.
4. Hirshberg, M.H.: A Low Cycle Fatigue Testing Facility. Manual on Low Cycle Fatigue Testing, ASTM-STP 465, ASTM, 1969, pp. 67-86.
5. Manson, S.S.; Halford, G.R.; and Hirshberg, M.H.: Creep-Fatigue Analysis by Strain-Range Partitioning. Design for Elevated Temperature Environment, S.Y. Zamrik, ed., ASME, New York, 1971, pp. 12-24.
6. Coffin, L.F., Jr.: The Concept of Frequency Separation in Life Prediction for Time-Dependent Fatigue. Symposium on Creep-Fatigue Interaction, MPC-3, ASME, New York, pp. 349-363.
7. Ostergren, W.J.: Correlation of Hold Time Effects in Elevated Temperature Low Cycle Fatigue Using a Frequency Modified Damage Function. Symposium on Creep-Fatigue Interaction, MPC-3, ASME, New York, pp. 179-202.
8. Majumdar, S.; and Maiya, P.S.: A Damage Equation for Creep-Fatigue Interaction. Symposium on Creep-Fatigue Interaction, MPC-3, ASME, New York, pp. 323-336.

TABLE I. - LOW-CYCLE FATIGUE DATA FOR COATED PwA 1480 SINGLE CRYSTALS

[Values of  $\Delta\epsilon_{in}$ ,  $\Delta\sigma$ , and  $\sigma_{max}$  are those at half life.]

Cycle type	Cycle life, $N_f$	Total axial strain range, $\Delta\epsilon_{tot}$ , percent	Inelastic axial strain range, $\Delta\epsilon_{in}$ , percent	Stress range, $\Delta\sigma$ , MPa	Maximum stress, $\sigma_{max}$ , MPa	Average, cycle time, $t_{av}$ , min
Test temperature, 1050 °C						
pp	110	1.86	0.92	766	388	0.17
	580	1.29	.47	631	331	.17
	900	1.26	.52	571	292	.17
	950	1.05	.32	552	272	.17
	1000	1.16	.47	537	274	.17
	2900	.87	.30	416	210	.17
cp	85	2.04	1.20	655	255	1.14
	160	1.50	0.82	528	197	1.28
	300	1.53	.81	559	163	.35
	440	1.30	.69	465	206	.31
	810	1.27	.60	505	201	.50
	1150	1.12	0.52	438	201	.40
pc	195	1.62	0.85	625	376	0.60
	610	1.62	.81	639	379	.50
	930	1.42	.76	592	287	.63
	1250	1.58	.91	490	266	.60
	1410	1.54	.90	445	225	.40
	1650	1.30	.71	419	225	.40
	1700	1.12	.52	445	247	.24
cc	370	1.32	0.70	474	210	0.78
	790	1.41	.87	412	206	.64
	990	1.20	.68	403	206	.49
	1100	1.30	.74	439	257	1.45
	2110	.90	.30	400	199	.30
Test temperature, 1015 °C						
pp	174	1.81	0.62	904	457	0.14
	192	2.02	.81	941	478	.16
	2021	1.08	.38	521	275	.15
	2314	.85	.15	529	276	.15
	3900	.77	.16	438	227	.12
	7870	.05	.05	344	166	.15
cp	15	3.32	1.95	1090	429	15.3
	78	1.85	1.16	802	270	4.8
	146	1.18	.40	680	206	4.6
	218	1.51	.58	644	208	2.4
	610	.90	.30	531	345	15.0
pc	29	2.44	1.37	826	569	22.1
	54	2.01	.88	856	394	14.7
	340	1.43	.62	603	396	3.92
	730	1.10	.34	613	395	1.23
	2101	.50	.30	468	276	1.26
c	192	1.63	0.98	514	257	7.38
	724	1.37	.72	499	250	.45
	1826	.88	.30	436	218	.59

TABLE II. - FIT OF VARIOUS MODELS RELATING  $\log N_f$  FOR ALL CYCLE TYPES TO THE LOG OF SEVERAL SINGLE VARIABLES OR COMBINATIONS THEREOF

Temperature, C	Variable										s	R <sup>2</sup> , percent
	Constant		log $\Delta \epsilon_{in}$		log $\Delta \sigma$		log $\sigma_{max}$		log $t_{av}$			
	a	T	Coef- ficient	T	Coef- ficient	T	Coef- ficient	T	Coef- ficient	T		
1050	-0.792	-0.8	-1.65	-3.7							0.32	37
	12.772	6.1			-3.683	-4.8					.29	50
	5.602	2.8					-1.159	-1.4			.39	8
	3.037	22.							-0.466	-1.7	.38	12
	8.396	4.2	-1.258	-3.8	-3.077	-4.9					.23	70
	1.218	0.6	-1.578	-3.5			-0.765	-1.1			.32	40
	-1.297	-1.1	-1.927	-3.1					0.199	0.6	.33	38
1015	-1.505	-3.1	-1.762	-8.5							.34	81
	16.427	9.8			-4.958	-8.2					.33	80
	10.287	4.5					-3.091	-3.4			.60	40
	2.689	21.7							-0.654	-4.3	.53	52
	7.781	3.0	-1.003	-3.8	-2.696	-3.6					.26	90
	0.424	0.2	-1.607	-6.1			-0.63	-1.0			.34	82
	-0.706	-1.4	-1.433	-6.2					-0.251	-2.3	.30	86

TABLE III. - BEST FIT VALUES  $a$  IN THE LIFE MODELS FOR 1050 and 1015 °C

Cycle type	a	95 percent confidence limits on $a \times 10^{-8}$
1050 °C: $N_f = a \Delta \epsilon_{in}^{-1.26} \Delta \sigma^{-3.08}$		
pp	$2.25 \times 10^8$	1.8 to 2.9
cp	1.41	1.0 to 2.0
pc	3.66	2.4 to 5.5
cc	1.86	1.2 to 2.9
1015 °C: $N_f = a \Delta \epsilon_{in}^{-1.00} \Delta \sigma^{-2.70}$		
pp	$0.489 \times 10^8$	0.24 to 0.98
cp	.236	.16 to 0.35
pc	.318	.17 to 0.60
cc	.360	.11 to 1.18

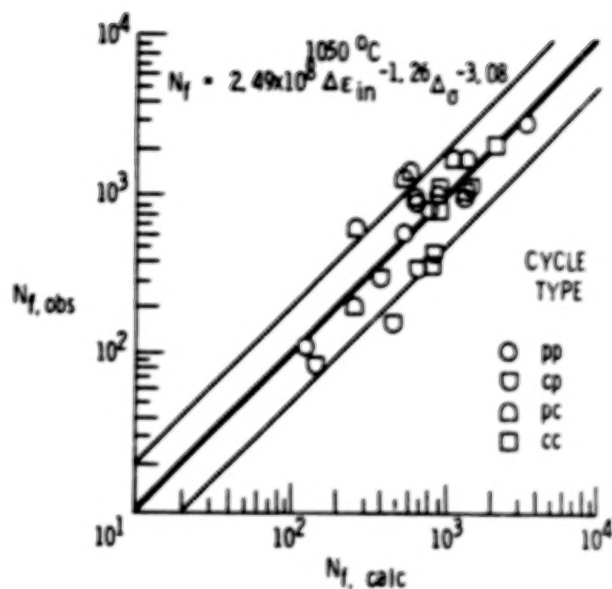
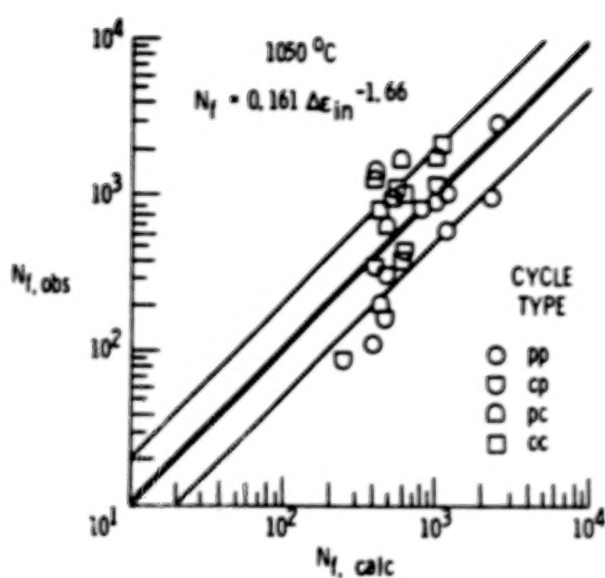


Figure 1. Observed vs. calculated cyclic life at 1050°C for life models indicated.

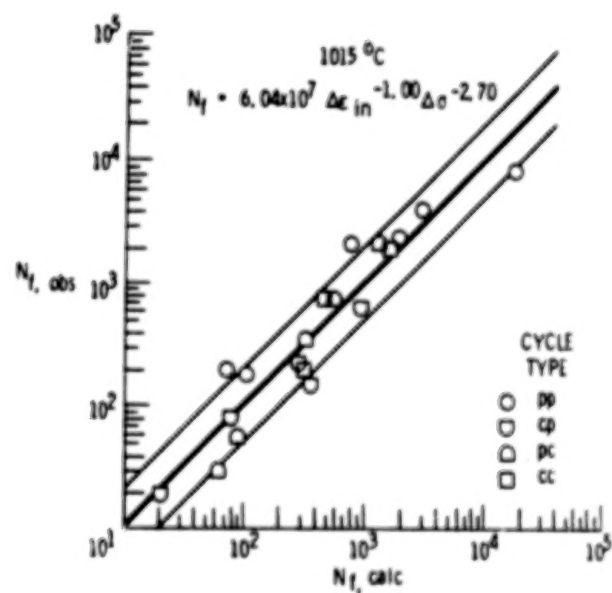
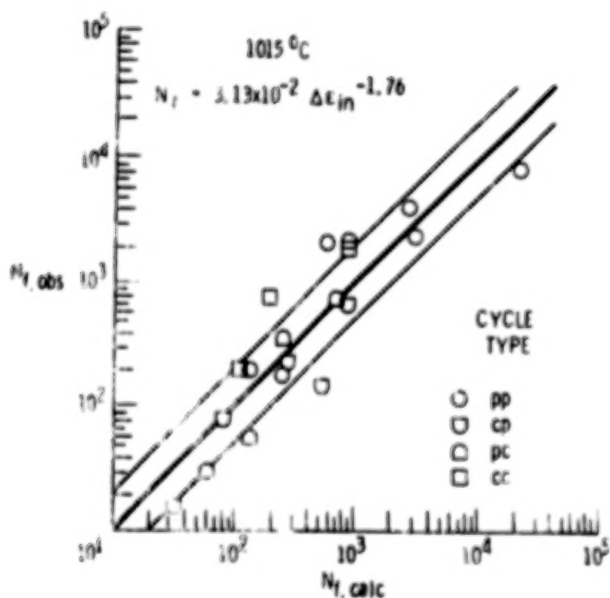


Figure 2. Observed vs. calculated cyclic life at 1015°C for life models indicated.

## LEWIS' ENHANCED LABORATORY FOR RESEARCH INTO THE FATIGUE AND CONSTITUTIVE

## BEHAVIOR OF HIGH TEMPERATURE MATERIALS

Michael A. McGaw  
NASA Lewis Research Center  
Cleveland, Ohio

Lewis' high temperature fatigue laboratory has undergone significant changes resulting in the addition of several new experimental capabilities. New materials testing systems have been installed enabling research to be conducted in multiaxial fatigue and deformation at high temperature, as well as cumulative creep-fatigue damage wherein the relative failure-life levels are widely separated. A key component of the new high-temperature fatigue and structures laboratory is a local, distributed computer system whose hardware and software architecture emphasizes a high degree of configurability, which in turn, enables the researcher to tailor a solution to the experimental problem at hand.

## AN EXPANDED LABORATORY

Significant expansion of the facility has occurred to accommodate the additions in testing systems and computer capabilities. The design convention of locating the load frames in areas separate from the control system electronics, a convention in use at Lewis for over 20 years (ref. 1), was followed, enabling separate environments to be designed for the load frames and their control electronics, as well as the computer system. Figure 1 describes the physical organization of the laboratory. The new multiaxial test systems, together with the existing uniaxial test systems, are located in the larger of the two testing areas. The second testing area houses the new HCF/LCF test systems and is located separately to isolate the remaining areas from noise produced by their operation. The centrally located control room houses the control and measurement electronics and the new computer system (fig. 2). Figure 3 details a typical uniaxial test system control console. The control room uses an elevated floor system, with all cables routed through a tray system. Both the humidity and temperature are controlled, providing an optimum environment for the operational longevity of the control electronics and computer system.

## NEW EXPERIMENTAL CAPABILITIES

## Multiaxial Capability

In response to the need for better descriptions of material behavior under complex states of stress, as seen, for example, in components used in aircraft gas turbines, an experimental capability is being developed for studying material deformation and fatigue behavior under multiaxial states of stress at elevated temperatures.

This capability consists of electromechanical servohydraulic materials test systems possessing both combined and independent axial and torsional loading abilities. Loading capacities are 50 kips axial and 20 inch-kips torsional. Figure 4 is a functional description of a typical (commercially available) system.

The control system electronics consists of two independent channels of servo-control for controlling the axial and torsional hydraulic actuators. Each system can control any axial control variable (load, strain, or stroke) asynchronously or synchronously with any torsional control variable (torque, torsional strain, or angular displacement). Conditioned analog transducer signals appear on an oscilloscope, chart recorders, or digital data displays. The data display units can be programmed to perform a number of signal processing operations and together are able to simultaneously display four channels of data. These units are equipped with RS-232 serial interfaces and can be used as computer-based data acquisition systems. Control system programming is accomplished through digitally based waveform generators. Two of the three systems use a generator able to produce phased sinusoidal and triangular command waveforms. The third system uses two independent generators (different manufacture), each able to produce arbitrary waveforms asynchronously as well as synchronously through programmable phasing. These generators possess IEEE-488 instrumentation interfaces and can be used under computer control. All three test systems are interfaced to individual satellite computer systems through a test machine interface. The test machine interface contains analog-to-digital, digital-to-analog, and discrete input-output devices to enable computer control of the test system control electronics.

High-temperature capability is attained through the use of commercially available audiofrequency furnaces. These furnaces have a power output capability of 50 kW at an operating frequency of 9.6 kHz. A commercially available PID controller is used for closed-loop temperature control. It too, is connected to the test machine interface.

Among the more difficult problems in multiaxial experimental work are specimen gripping and strain measurement. We have chosen to use commercially available hydro-collet grips because of their alignment characteristics and ease of use. Strain measurement will be accomplished through the use of commercial high-temperature extensometry as well as through the extensometry system developed by J.R. Ellis (ref. 2). The latter system is designed for very-high-resolution strain measurement, on the order of a few microstrain required for accurate identification of material behavior at the yield, an ingredient in constitutive model development. It is worth noting that the questions of gripping systems, extensometry, and specimen design are intimately related, and usually cannot be pursued independently.

#### HCF/LCF Capabilities

In response to the technological need for better understanding of the fatigue behavior of materials undergoing cumulative cyclic loadings, each having a quite different associated life level, a problem typified by gas-turbine blade service cycles, an experimental capability is being developed for studying cumulative fatigue damage accumulation.

This capability consists of being able to produce arbitrary load (or, alternatively, deformation) histories corresponding to (separation) fatigue lives over the range of 1/4 cycle to approximately  $10^7$  cycle, in wall clock times of less than 10 hr. This is achieved through the use of state-of-the-art servohydraulic materials test systems designed to NASA specifications, for wide-bandwidth (with respect to frequency and amplitude), load (deformation) history programming. Lewis has two such systems, each able to produce rated capabilities at elevated temperatures typical of turbine blade applications in gas-turbine aircraft engines. Figure 5 is a functional description of a typical system. Load ratings are 22 kips over the frequency range

of dc to 20 Hz, with a corresponding actuator piston displacement range of 0.04 in., and a load rating of 5 kips over the range of dc to 300 Hz, with a corresponding actuator piston displacement range of 0.015 in. These were the design goals, with the actual system performance exceeding these goals. During operational checkout, these machines were able to produce significant actuator piston displacement to well over 1000 Hz.

To achieve these performance characteristics, a control system consisting of five servoloops driving a unique three-servo valve, dual-faced actuator was developed. The actuator assembly uses two nozzle-flapper valves ported to the larger of the two actuator faces to control the low-frequency portions of a typical history program, driven by one control loop. The high-frequency portion of the program waveform is produced by a high performance voice-coil, slaved-spool servo valve, ported to the smaller of the two actuator faces. This valve and its actuator interface provides feedback signals of valve spool position and pressure difference across the smaller piston faces, used in two of the four servoloops controlling the high-frequency portion of the waveform. The remaining two servoloops use the high-frequency program signal as command and the desired transducer signal for feedback. The net effect of this assemblage is a uniaxial test system which has a linear response over a very wide frequency range of operation.

Data measurement can be accomplished through the use of a storage oscilloscope, a chart recorder, or the digitally based data display. This latter item is of the same type as used in the multiaxial testing systems. Command waveform programming is accomplished through the use of two digitally based arbitrary waveform generators, of the type referred to earlier, in use for one of the multiaxial testing systems. They are used in a somewhat different manner here, however, in that one generator provides the low-frequency program, and the other, the high-frequency program. The units possess ample synchronization, gate, and trigger lines and are connected to make use of these capabilities. Each system is also connected to a machine interface unit and to a unique satellite computer system.

High-temperature capability is obtained through the use of commercially available radiofrequency induction furnaces, driven by conventional PID controllers for closed-loop temperature control. These furnaces possess a 5-kW power output capability at an operating frequency of 450 kHz. The controllers are connected to the test machine interface and can be computer controlled as well.

Commercially available hydrocollet grips are being used for same reasons stated earlier: alignment characteristics and ease of use. Extensometry is a major problem: No known extensometer system exists that is capable of being used at high temperatures (to 2000 °F), with a very wide frequency response. Currently, work is going on to develop such a system, and in the interim commercially available high-temperature extensometry is being used for the low-frequency work.

An interesting capability afforded by this system's design is the ability to control, say, the low-frequency portion of a waveform program in load control, and the high-frequency portion of the waveform program in strain control. Of course, the waveform program must not require a physical behavior which cannot be achieved by the material being tested; nonetheless, provided that the material physics is compatible, such a control scenario is possible. A typical waveform which can be programmed and executed with this arrangement is a low-frequency program consisting of a ramp from zero to tension, in load control, holding for a specified period of time, then ramping back to zero, and a high-frequency program consisting of a simple sinusoid with a mean level, in strain control. In this case, the low-frequency generator is programmed to

issue either a trigger or gate signal upon reaching the hold, and the high-frequency generator is programmed either for a fixed number of output cycles or to output continuously only when gated. Such a program captures salient characteristics of histories often seen by turbine blades.

#### COMPUTER CAPABILITIES

A significant enhancement to the laboratory's capabilities has been the addition of a local, distributed digital computer system, intended to support all phases of experimental research.

The architectural design goals shaping the hardware elements of the automation effort included:

- (1) Automating the operation of each materials testing system such that each would be independent of another. This ensures that only one experiment would be lost if a failure of any sort occurred.
- (2) Establishing an environment for general non-real-time user; that is, data reduction, plotting, report writing, program development, etc.
- (3) Establishing a graceful means of allocating additional computing resources as required.

These goals are conflicting: a computing system designed for real-time use will generally not have the scheduling abilities and other resources to adequately support a multiuser development environment. The architectural solution chosen was to dedicate a set of computing resources to each materials test system, optimized for test control: the hardware must interface with the analog and digital electronics of the materials test system, and the software, comprising the operating system, must feature interrupt-driven multitasking and multiprogramming capabilities. Secondly, another set of computing resources would be required for use as a development environment. The hardware in this case should be chosen to support the needs of an operating system featuring multiuser, multiprogramming, multitasking capabilities. Finally, all systems should be interconnected in such a way that sharing of resources is possible under real-time conditions. The solution implementation at Lewis is shown in figure 6. The laboratory computer system hardware architecture is composed of fourteen 16-bit computers, each dedicated, one system per materials testing system, and one 32-bit superminicomputer. All 15 processors are connected through a high-speed (direct memory access) multiprocessor communications system and will soon be connected through serial RS-232 lines as well. Each of the 14 satellite computer systems is equipped with 256 Kbytes of main memory, a hardware floating-point unit, a battery backup unit, a disk system consisting of a 1.26-Mbyte diskette and a 5 Mbyte winchester hard disk unit, an IEEE-488 instrumentation interface, a multiprocessor communications subsystem, and a test machine interface system containing analog-to-digital, digital-to-analog, and discrete input-output interface devices. This latter system is interfaced to the control and measurement electronics of each materials test system. The 32-bit system, referred to as the host computer system, is equipped with 4 Mbytes of main memory, a hardware floating-point unit, a battery backup system, a 354-Mbyte winchester hard disk, a 800 or 1600-bit per-inch tape drive, an 800-bpi streaming tape drive, a dual 1.26-Mbyte diskette drive (for media compatibility with the satellite systems), a multiprocessor communications subsystem, an IEEE-488 instrumentation interface, and a test machine interface system. CRT-based terminals can be physically connected to any processor in the system, but soon will all be connected to the host computer, with the capability of being able to establish logical connections to any processor in the system. All printers and hard copy units are

connected to the host computer, as well as a modem and broadband network interface, enabling data communications between the laboratory system and remote personal-computer-based graphics workstations. This last item also provides access to Lewis-wide computing services, including class VI supercomputer resources.

The architectural design goals shaping the software elements of the laboratory computer system included:

- (1) Providing an efficient real-time operating system for use on the satellite processors; such an operating system should support interrupt-driven multi-programming, multitasking applications.
- (2) Providing an efficient non-real-time operating system for use on the host processing system to support multiuser, multiprogramming, multitasking applications.
- (3) Providing a strongly related user interface to both classes of systems; that is, the user should not be unduly burdened with having to learn and efficiently use two completely different operating system environments.
- (4) Providing a base for applications development: This base should include the editors, programming languages, source debuggers, etc., necessary for efficient applications development, and it should be located on the host processing system.
- (5) Providing libraries of commonly used utility routines. The libraries available should include mathematical and statistical processing, as well as graphing routines.
- (6) Providing a means of storing, retrieving and manipulating the data acquired from an experiment, as well as storing data obtained from the literature, contracts, etc. This resource should be located on the host processing system.

The solution implementation satisfying (1), (2), and (3) consists of a real-time operating system for use on the satellite processors, having interrupt driven, multi-programming, multitasking capabilities. The operating system chosen for the host processor has multiuser, multiprogramming, multitasking capabilities. A key feature in the choice of both is that the system command language processors, the user interfaces to the operating system, are essentially identical; that is, file manipulation commands, directory structures, etc., are virtually identical, permitting the user to move between the two classes of computer systems with relative ease.

The solution implementation for element d is shown in figure 7. A comprehensive set of development tools are present on the host processing system to support application development. The choice in application programming language is wide; high level languages include Ada, Pascal, Fortran-77, and BASIC. Pascal and Fortran-77 compilers producing both 16-bit and 32-bit code are available. The Ada compiler currently generates 32-bit code for use on the host processor only; a target generator for the 16-bit satellites will be available in the very near future. Assemblers are available for both the 16-bit and 32-bit machine environments. Facilities are available enabling modules to be developed in any of the above languages (except BASIC) to be called from any language. This is a vendor dependent-capability, Ada being the only language with explicitly defined facilities for including modules written in languages other than Ada. Using this facility, the libraries for statistical, mathematical, etc., use are available to a user under any language processor in the system. Graphing routines and appropriate display devices will be available shortly.

C - 5

The last design element f will be implemented shortly and consists of a database management system based on the relational model. The interface will be a structured query language (SQL). The system will reside on the host processing system.

Figure 8 describes the development cycle in use at NASA to build applications. The user develops the sources with an editor and compiles with the appropriate compiler. The choice of which implementation of the language to use, 16- or 32-bit native-code generation, is made here as well; faster execution of the compilation and resultant application in the host environment will result if the native 32-bit version is used. However, when the application is ready to be exported to the target satellite system for execution, the sources must be recompiled with the 16-bit version. Generally, the 16-bit implementation will be used for application development. Once compiled, the resulting objects are linked for execution on the host to begin initial testing. When the testing phase is completed, the user, if the 16-bit version of the language processor was used, simply relinks the objects for execution on the target satellite and exports the image. Otherwise, the sources are recompiled with the 16-bit version of the language processor and linked for execution on the target satellite and exported. The user then tests the application on the satellite system for subsequent usage. This last step is necessary since timing differences can't be easily modeled in the host processing environment.

#### REFERENCES

1. Hirschberg, M.H.: A Low-Cycle Fatigue Testing Facility. Manual on Low Cycle Fatigue Testing, ASTM-STP-465, ASTM, 1969, pp. 67-86.
2. Ellis, J.R.; and Robinson, D.N.: Some Advances in Experimentation Supporting Development of Viscoplastic Constitutive Models. NASA CR-174855, 1985.

ORIGINAL PAGE IS  
OF POOR QUALITY

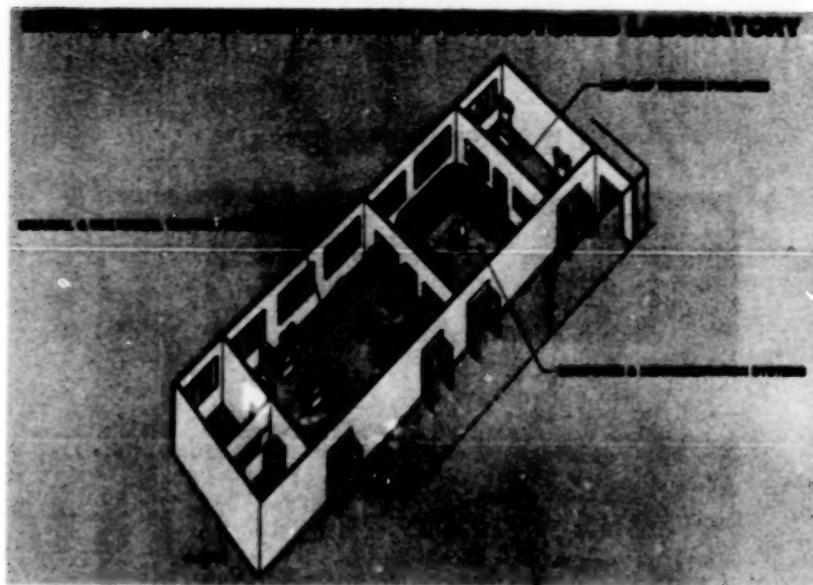


Figure 1

#### CONTROL ROOM



Figure 2

ORIGINAL PAGE IS  
OF POOR QUALITY

TEST SYSTEM CONTROL CONSOLE

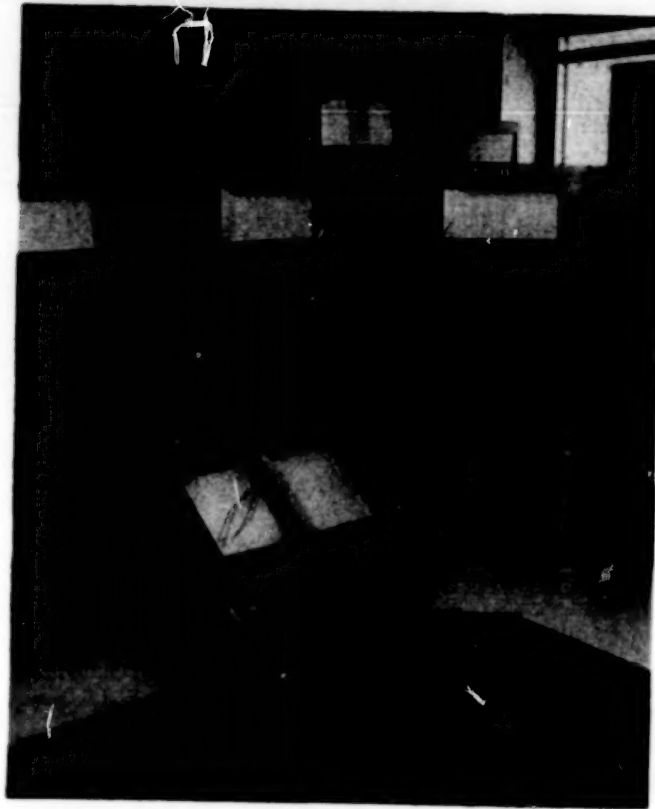


Figure 3

## AXIAL-TORSION MATERIALS TEST SYSTEM

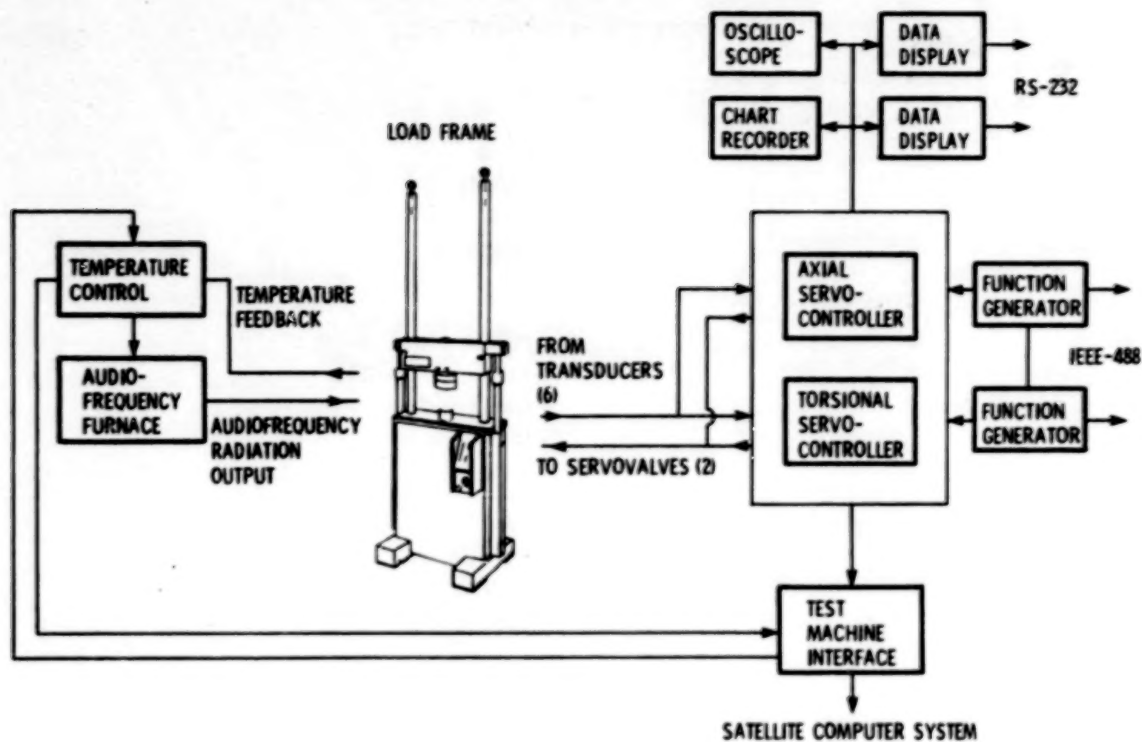


Figure 4

## HCF/LCF MATERIALS TEST SYSTEM

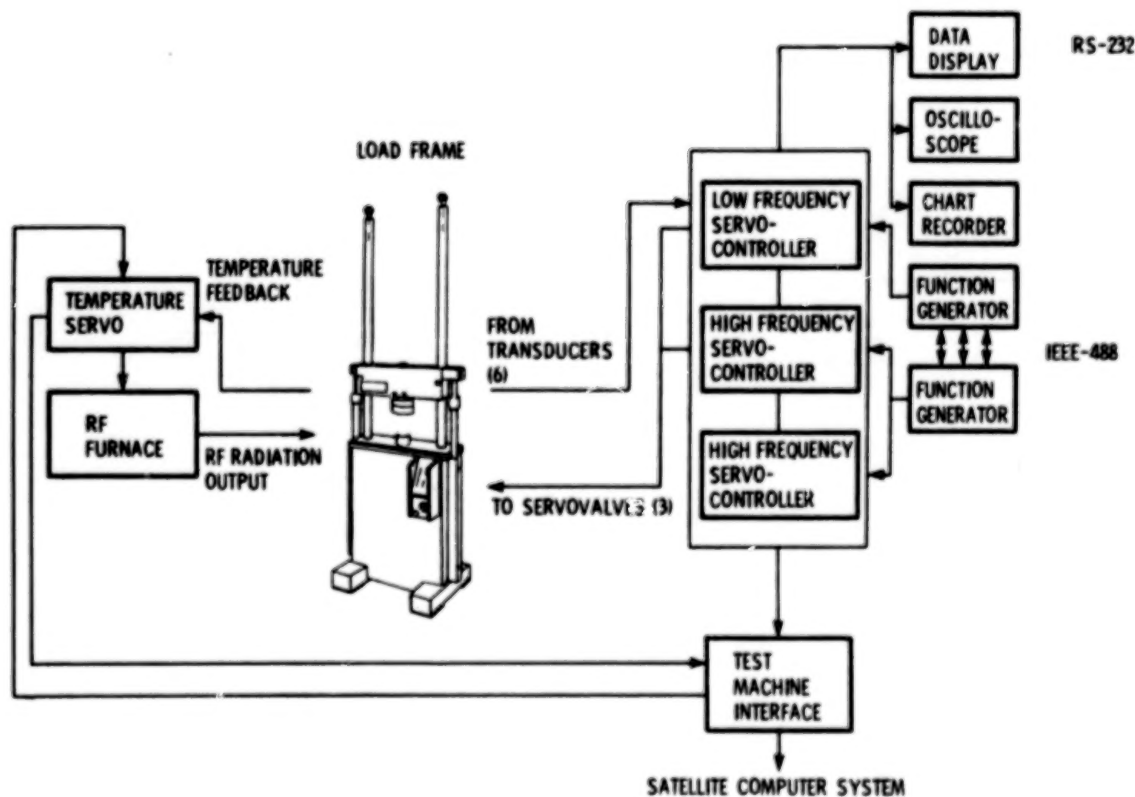


Figure 5

# PROGRAM DEVELOPMENT TOOLS

- SOURCE EDITORS
- LANGUAGE PROCESSORS
  - ADA
  - PASCAL
  - FORTRAN-77
  - BASIC
  - ASSEMBLER
- LINKER
- MISCELLANEOUS TOOLS
  - CONFIGURATION CONTROL UTILITY
  - SYMBOLIC DEBUGGERS
  - LIBRARY EDITOR
  - FILE EDITOR
  - ETC.
- LIBRARIES
  - SENSOR INPUT/OUTPUT
  - MATHEMATICS
  - STATISTICS
  - GRAPHICS

Figure 6

# HARDWARE ARCHITECTURE

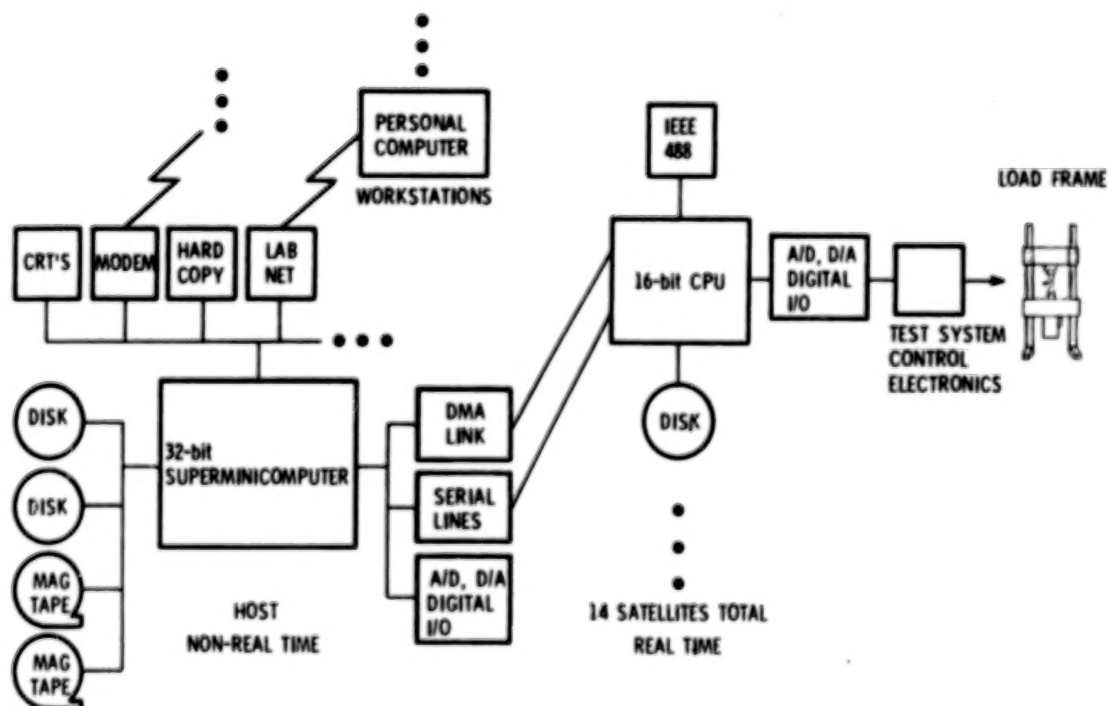


Figure 7

# PROGRAM DEVELOPMENT CYCLE

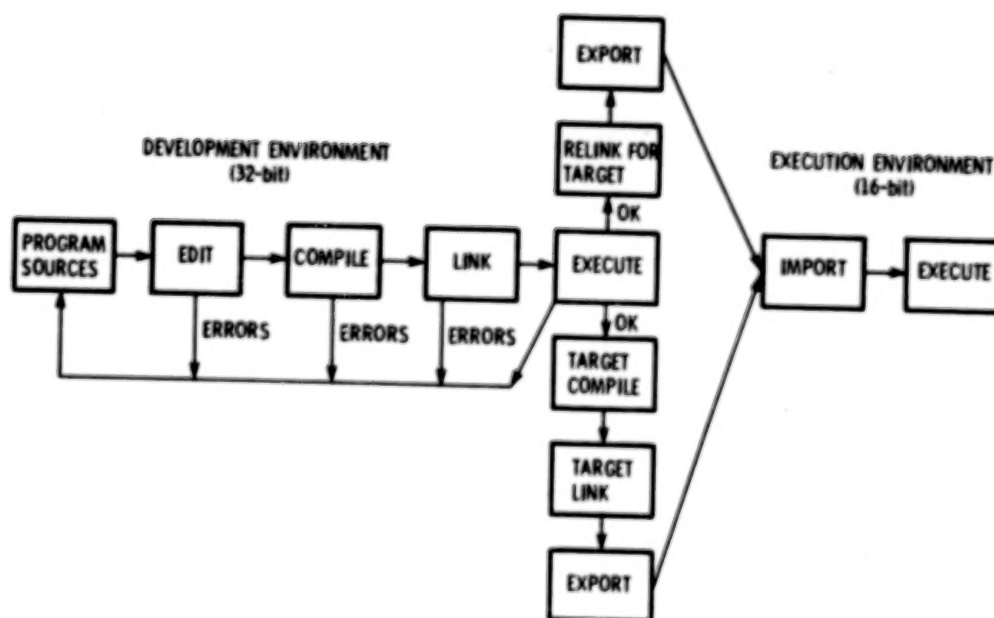


Figure 8

## TURBINE AIRFOIL DEPOSITON MODELS AND THEIR HOT CORROSION IMPLICATIONS\*

D.E. Rosner and R. Nagarajan  
Yale University

Department of Chemical Engineering  
High Temperature Chemical Reaction Engineering Laboratory

1. INTRODUCTION

Gas turbine failures associated with sea-salt ingestion and sulfur-containing fuel impurities have directed attention to alkali sulfate deposition and the consequent 'hot corrosion' of gas turbine (GT) blades under some GT operating conditions. These salts deposit and form thin, molten films which undermine the protective metal oxide coating normally found on GT blades. This research project deals with the prediction of single- and multi-component salt(-solution) deposition, flow and oxide dissolution and their effects on the lifetime of turbine blades. Our goals include rationalizing and helping to predict corrosion patterns on operational GT rotor blades and stator vanes, and ultimately providing some of the tools required to design laboratory simulators and future corrosion-resistant high-performance engines. In the program summary that follows we first review necessary background developments (Section 2) and then outline our results and tentative conclusions for single-species ( $\text{Na}_2\text{SO}_4$ (!)) condensation (Section 3), binary salt-solution ( $\text{Na}_2\text{SO}_4$ - $\text{K}_2\text{SO}_4$ ) condensation (Section 4), and burner-rig testing of alloy materials (Section 5). We conclude with a brief account of our research plans (Section 6) should follow-on funding become available.

2. THEORY OF CONDENSED LAYER FORMATION AND FLOW

The necessary first step in a complex sequence of events leading to hot corrosion failures is the deposition of alkali salts from the combustion products onto turbine blades and vanes. Our NASA-supported laboratory experiments (refs. 1, 2, 3, 4), and those carried out in collaboration with the NASA-Lewis Research Laboratories (ref. 5) have enabled further advances in salt deposition rate theory, as outlined here. A comprehensive but tractable method for predicting the rates of chemical vapor deposition (CVD) of, say, alkali sulfates from multicomponent salt-laden combustion gases has been developed, illustrated and tested in part (refs. 5, 6, 7). This theory, based on vapor diffusion through a 'chemically-frozen' (CF) gas boundary layer (BL), predicts important effects of multicomponent diffusion and thermal (Soret) diffusion (ref. 8) on dew points, CVD-rates and deposit compositions (ref. 9). A reference manual prepared for NASA-LeRC by GOKOGLU et al. (ref. 10) provides information on the structure of a CFBL computer program for the calculation of convective diffusion deposition rates, and details regarding the program input and output. Our CFBL-VD approach also applies without fundamental modifications to the deposition of pre-existing fine particles (refs. 11, 12). The inclusion of chemical reactions and/or phase change (e.g., 'mist

\*Work done under NASA Grant NAS3-590.

PRECEDING PAGE BLANK NOT FILMED

formation') within the BL is the subject of ongoing research at the Yale HTRC laboratories (refs. 13, 14, 15).

'Fluxing' of the oxide layer by the molten salt-'solvent' can occur only in the presence of dynamic processes which allow dissolution to proceed without locally saturating the liquid layer. For this reason, we have carried out studies of the dynamics of thin condensate layers, allowing for the interplay of salt arrival and run-off induced by the gas-dynamic shear-stress,  $\tau_{w,g}$ , and blade rotation (with velocity  $\Omega$ ) (fig. 1). Earlier (ref. 16), the necessary liquid layer theory was developed and used to predict steady-state laminar single-component condensate layers on smooth, non-rotating isothermal targets, with emphasis on the circular cylinder in high Reynolds number cross-flow (a common test-configuration). Subsequently, this approach has been extended to include the treatment of single-component and binary-solution condensate layers on smooth non-isothermal turbine blades (refs. 17 and 18).

Illustrative calculations have thus far been made for a test turbine (NASA TP 1018 (1977)) but most of our methods will carry over to operational engine vanes and blades (except in the vicinity of cooling holes/slots). From the inviscid stream velocity data, we compute, using efficient integral methods, the corresponding distributions of gas-side momentum-, heat-, and mass-transfer coefficients, and the distribution of blade recovery temperature (used to estimate this root-cooled temperature distribution). The corresponding local salt arrival rates and liquid-phase physical properties are then inserted into the partial differential equations (PDE's) governing the evolution of quantities of engineering interest (QOI), such as the liquid layer thickness,  $\delta_1(x,z)$  (fig. 1). The nonlinear first-order PDE's are numerically solved (by the method-of-characteristics) to obtain the condensate layer streamline pattern (fig. 2), as well as values of  $\delta_1$ , the salt arrival rate,  $\dot{m}''(x,z)$ , oxide bulk mass fraction in liquid,  $w_{o,b}(x,z)$ , and oxide dissolution rate,  $j_{o,w}''(x,z)$ . Important by-products of these calculations are estimated line- and surface-integral quantities, such as the steady-state salt inventory on the blade and relative tip and trailing edge (TE) run-off rates.

### 3. SINGLE-SPECIES CONDENSATE LAYERS ON GT BLADES

Representative calculations carried out by applying the above-mentioned formulation for  $\text{Na}_2\text{SO}_4(l)$  layers on GT rotor blades have been reported in previous HOST conferences, and summarized in Reference 17. These include the generation of solute diffusion-limited dissolution rate distributions (fig. 3) associated with solvent flow patterns of the type shown in Figure 2. Our original intention of comparing relative oxide dissolution rate (RODR) 'maps' obtained in this manner with hot corrosion rate patterns observed on blades removed from operational GT engines has been set aside due to the unavailability of high-quality operational data. Our recent efforts have been directed towards investigating certain observed 'overall' trends. For instance, limited available results for operational engines indicate that hot corrosion rates are much larger on the pressure surface of GT blades than on the suction surface. An important question, addressable via our present model, is whether this can be explained on the basis of our CVD-oxide dissolution theory, or whether it is necessary to invoke particle impaction (refs. 12 and 19) on the pressure surface. Indeed, we found that in the limiting case of transverse heat equilibration across a solid blade, when the

blade is operating under feed and stagnation conditions such that every location on the blade surface is near the local dew point, the pressure-to-suction surface dissolution rate ratio is very large, tending to infinity in the limit of zero net-deposition on the suction surface (fig. 4). Another apparent anomaly that may now be rationalized on the basis of our theory has to do with liquid deposits observed by investigators to be present on some metal surfaces that are hotter than the local dew-point. This is a less-obvious but natural consequence of flow-induced liquid 'spill-over' onto evaporation regimes of blade surfaces (fig. 5).

Our comprehensive physico-chemical/mathematical model offers the potential of economical parametric studies. We have initiated such studies to gain an understanding of how turbine blade corrosion rates might respond to changes in parameters at the disposal of designers and engine-operators, or parameters which might vary due to local environmental changes (e.g., sea-salt ingestion at higher than anticipated levels). The material leaving the blade at the TE influences downstream stage/blade condensate flow-characteristics; a study of TE salt run-off is thus necessary to understand and solve the overall problem of hot corrosion in multi-stage turbines. The parametric dependency of the TE run-off rate (with pressure level and salt seed-level the variables being changed) is displayed in Figures (6) and (7).

#### 4. BINARY CONDENSATE LAYER EFFECTS

All properties of thin liquid condensate films, including their aggressiveness as corrodants, are expected to be composition-dependent. Moreover, appreciable amounts of 'adulterants' (e.g., Ca- and Mg-compounds) are often found in GT blade deposits. This information, combined with the remarkable effect (observed at the Yale HTRC labs.) the addition of a second salt can have on the deposition rate of the primary salt (ref. 4), directed our attention toward the deposition, dynamics and dissolution rate properties of multicomponent salt layers.

Among the effects observed for binary salt solutions, perhaps the most significant are the alteration of:

- (a) deposition rates and associated dew-point temperatures,
- (b) liquid properties, including oxide solubility and associated solute diffusivity, and
- (c) freezing point of the solution (the information being extracted from the relevant thermodynamic phase diagram).

While the property effects (b) are relatively minor for physically- and chemically-similar molten salts, effects (a) and (c) can considerably broaden the 'dangerous' temperature interval ( $T_{dp} - T_{mp}$ ) within which hot corrosion is known to occur. To illustrate the consequences of the altered freezing-point we performed a preliminary steady-state analysis of the binary ( $K_2SO_4 + Na_2SO_4$ ) layer condensing on the leading edge (LE) of a root-cooled rotor blade. Figure 8 reveals that with increasing potassium levels, an increasing fraction of the condensate would become molten, eventually becoming molten over the entire LE. Figure 9 shows a typical distribution of liquid phase composition over the suction surface of a rotor blade ( $[K]/[Na] = 0.1$ ;  $\Omega = 6786$  rad/s); the primary effect of shear- and centrifugally-driven flow here is to 'shift' the condensate composition from its local 'quasi-steady' value when the liquid flow rate becomes sufficiently high.

An examination of the  $Na_2SO_4 - K_2SO_4$  binary phase-diagram suggests that

when the second component,  $K_2SO_4$ , is in sufficient excess, the solution freezing point is actually raised above that of pure  $Na_2SO_4$ . The evolution of the solution 'freezing-point locus' over the suction surface of a root-cooled rotor blade with changing values of the salt seed-ratio,  $[K]/[Na]$ , is depicted in figure 10. Upstream seeding techniques could conceivably be resorted to in order that a relatively-benign overlayer of solid sulfate 'ice' may deposit over the entire blade surface. It should also be borne in mind that increasing the amount of the second salt enhances the possibility of BL-phase change phenomena (fig. 11), which would reduce the net salt arrival rate.

#### 5. SIMULATION CRITERIA FOR HOT CORROSION RIG-TESTING

There exists at present no standard testing procedure for determining the hot corrosion resistance of turbine blade alloy materials. Economic considerations and the requirement of a controllable environment have led to the development of two general types of laboratory procedures, one involving burner rigs and the other involving furnaces. Not surprisingly, burner rig testing appears to give a more realistic simulation of service behavior. The fundamental question of which aspect(s) of the turbine environment- the convective flux of the gas-phase contaminant, the salt-contaminant dew-point and deposition rate, the thicknesses of the liquid deposit layer and the protective oxide layer, the rate of dissolution of the oxide coating, the alloy composition, etc.- is/are most crucial in determining the system corrosion characteristics remains to be settled. We offer no conclusive argument in this regard, but point out that the required operating conditions of the test rig will be quite different depending on the investigator's choice of one or more of these parameters as being corrosion rate-controlling.

In a typical simulation procedure, the seed level and pressure level are compensatingly changed to reproduce the engine alkali sulfate dew-point in the atmospheric-pressure rig (fig. 12). Our stagnation line calculations for the GT rotor blade indicate that under equivalent dew-point conditions, the Mach number of gas flow,  $Ma_\infty$ , and hence the contaminant flux rate, have to be lower in the non-pressurized rig than in the engine in order to obtain the same deposition/oxide dissolution rates, and higher in order to condense a layer of the same thickness as at the turbine stagnation-point. It should be pointed out that iso-dissolution rate profiles would diverge from iso-deposition rate profiles everywhere on the blade surface except at the stagnation-point; in order to simulate the oxide dissolution characteristics of the operational turbine blade, therefore, the rig would have to reproduce the liquid layer dynamics on the blade, as well as the gas-phase dynamics.

Thus far, we have made calculations for a particular set of 'standard' test-turbine conditions ( $P_o = 2.5565$  atm.,  $Ma_\infty = 0.4$ ,  $T_{dp,o} = 1220K$ ). Generation of such simulation-graphs encompassing a wide range of engine operating conditions could be useful in arriving at an 'international-standard' rig-testing procedure.

#### 6. CONCLUSIONS, RECOMMENDATIONS

Some interesting results of our recent studies of blade-induced alkali-salt mass-extraction from combustion gases have been:

- (1) predicted oxide dissolution rates maximize on the LE, and thereafter 'track' the salt arrival rate distribution,
- (2) computed pressure-side oxide dissolution rates are in excess of the suction-side oxide dissolution rates by many orders of magnitude for solid blades with rapid transverse heat conduction and surface temperatures not far from the local dew points,
- (3) flowing upstream condensate layers can 'spill' onto downstream regions of the blade hotter than the prevailing local dew-point; conversely, 'dry-patches' can form upstream of condensates that can flow. Streamline flow can 'shift' the condensate composition from its local 'quasi-steady' value,
- (4) rotor blade root-region addition of a second component can alter the system dew-point, freezing-point, salt deposition rate and induce BL-phase change, with obvious hot-corrosion implications, and
- (5) burner rig-testing environments are heavily dependent on the hot-corrosion simulation criteria employed; in general, equality of salt arrival rate, condensate layer thickness, and oxide dissolution rate (present work) do not lead to the same test conditions.

It is encouraging that the predictions of our model mirror 'reality' rather well- especially since, in recent years, 'hot corrosion' research seems to have moved away from seeking fundamental insights towards shorter-term empiricism. We hope that our approach of integrating a fluid-dynamical treatment of the problem with the materials-oriented philosophy of conventional corrosion research will contribute to reversing this unfortunate trend. Subject to the availability of research funding, our research plans in this area include:

- (1) improving our deliberately-simplified dissolution-model of hot-corrosion as fresh turbine data (from the field or laboratories) become available in the non-proprietary literature,
- (2) incorporating the deposition mechanisms and mixture thermodynamics of commonly encountered mixed sulfate deposits, e.g., [Ca]+[Mg]+[Na], into our CFBL-VD/ideal solution theory,
- (3) treating of transient condensate flows associated with start-up/shut-down of turbo-machinery, and
- (4) examining in closer detail the effects on localized dissolution rates of secondary flows, produced in part by surface tension gradients associated with the oxide dissolution process itself.

We believe that this program will move the turbine-community closer to a reliable means of predicting/forestalling corrosion failure of engine components caused by the deposition of molten alkali salt-solutions.

## 7. REFERENCES

1. ROSNER, D.E. and ATKINS, R.M., in Fouling and Slagging Resulting from Impurities in Combustion Gases, R.Bryers, ed., Engineering Foundation (New York) 1983, pp. 469-492
2. ROSNER, D.E. and SESHADRI, K., in Eighteenth Int. Symp. on Combustion, The Combustion Institute (Pittsburgh, PA), 1981, pp. 1385-1394
3. SESHADRI, K. and ROSNER, D.E., AIChE J., **30**, 187 (1984)
4. ROSNER, D.E. and LIANG, B., 'Laboratory Studies of the Deposition of Alkali Sulfate Vapors from Combustion Gases Using a Flash-Evaporation Technique'

- (accepted for public. in Chem. Eng. Communic.; June, 1985)
5. KOHL, F.J., SANTORO, G.J., STEARNS, C.A., FRYBURG, G.C. and ROSNER, D.E., J. Electrochem. Soc., 126, 1054 (1979)
  6. ROSNER, D.E., CHEN, B.-K., FRYBURG, G.C. and KOHL, F.J., Comb. Sci. and Tech., 20, 87 (1979)
  7. SANTORO, G.J., KOHL, F.J., STEARNS, C.A., ROSNER, D.E. and GOKOGLU, S.A., 'Experimental and Theoretical Deposition Rates from Salt-Seeded Combustion Gases of a Mach 0.3 Burner Rig', NASA TP 225 (1984); in High Temperature Corrosion, NACE-6, R.A.Rapp, ed., pp. 441-450
  8. ROSNER, D.E., J. Physicochem. Hydrodynamics, 1, 159 (1980)
  9. ROSNER, D.E. and NAGARAJAN, R., 'Transport-Induced Shifts in Condensate Dew-Point and Composition in Multicomponent Systems with Chemical Reaction', Chem. Eng. Sci., 40, 177-186 (1985)
  10. GOKOGLU, S.A., CHEN, B.-K. and ROSNER, D.E., 'Computer Program for the Calculation of Multicomponent Convective Diffusion Deposition Rates from Chemically Frozen Boundary Layer Theory', NASA CR 168329 (1984)
  11. GOKOGLU, S.A. and ROSNER, D.E., Int. J. Heat and Mass Transfer, 27, 639 (1984)
  12. ROSNER, D.E., GOKOGLU, S.A. and ISRAEL, R., in 'Fouling of Heat Exchange Surfaces', R.Bryers, ed., Engineering Foundation (New York) 1983, pp. 235-256
  13. CASTILLO, J.L. and ROSNER, D.E., 'Theory of Surface Deposition from a Unary Dilute Vapor-Containing Stream Allowing for Condensation within the Laminar Boundary Layer' (Chem. Eng. Sci., submitted 1985)
  14. CASTILLO, J.L. and ROSNER, D.E., 'Theory of Surface Deposition from a Binary Dilute Vapor-Containing Stream Allowing for Condensation within the Laminar Boundary Layer' (in preparation, 1985)
  15. CASTILLO, J.L. and ROSNER, D.E., 'Theory of Surface Deposition from Particle-Laden Dilute, Saturated Vapor-Containing Streams, Allowing for Particle Thermophoresis and Vapor Scavenging Within the Laminar Boundary Layer' (Chem. Eng. Sci., submitted, July 1985); see also: 'Nonequilibrium Theory of Surface Deposition from Particle-Laden Dilute, Condensible Vapor-Containing Streams, Allowing for Particle Thermophoresis and Vapor Scavenging Within the Laminar Boundary Layer' (prepared for submission to J. Multiphase Flow, Aug 1985)
  16. ROSNER, D.E., GUNES, D. and NAZIH-ANOUS, N., Chem. Engrg. Commun., 24, 275 (1983)
  17. ROSNER, D.E. and NAGARAJAN, R., 'Vapor Deposition and Condensate Flow on Combustion Turbine Blades: Theoretical Model to Predict/Understand Some Corrosion Rate Consequences of Molten Alkali Sulfate Deposition' (prepared for journal submission, 1985)
  18. ROSNER, D.E. and NAGARAJAN, R., 'Multicomponent Vapor Deposition and Condensate Flow on Combustion Turbine Blades: Theoretical Model to Predict/Understand Some Corrosion Rate Consequences of Mixed Alkali Sulfate Deposition' (prepared for journal submission, 1985)
  19. ISRAEL, R. and ROSNER, D.E., Aerosol Sci. and Technol., 2, 45 (1983)



# THIN CONDENSATE LAYER DYNAMICS - ROTOR BLADES

## Objectives:

- Primary Flow, and its Metal Oxide Dissolution Rate Consequences;
- Relation to observed hot corrosion patterns?

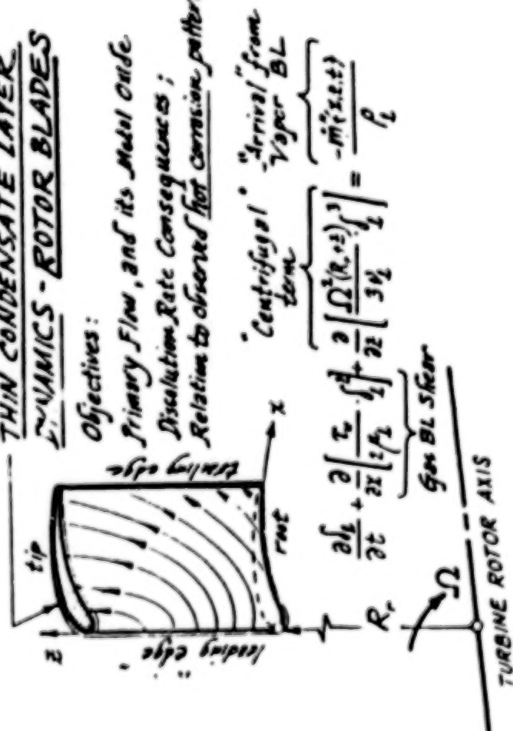


Fig. 1: Factors influencing the evolution of liquid condensate layer dynamics on a turbine rotor blade.

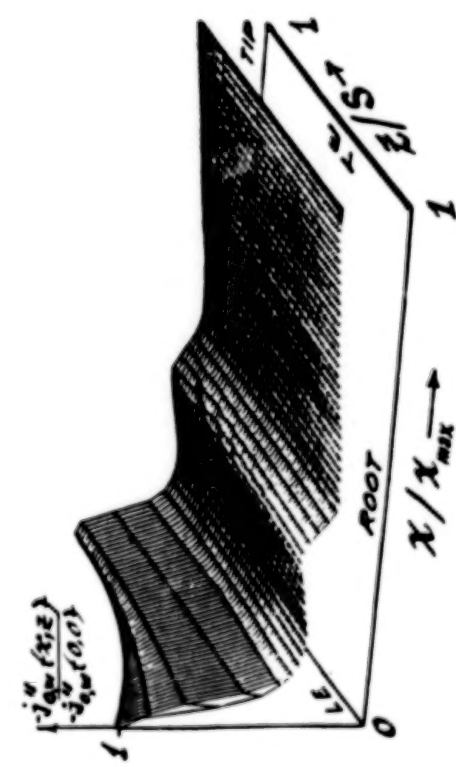


Fig. 3: Relative oxide dissolution rate distribution on suction surface of root-cooled turbine blade.

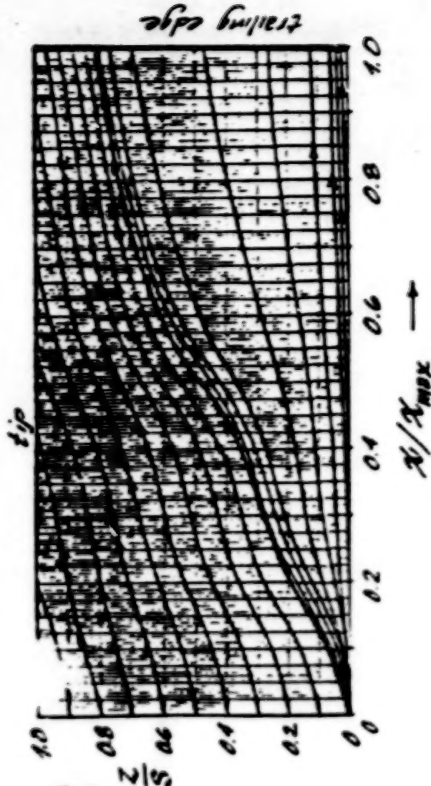


Fig. 2: Predicted streamline pattern of molten salt layer flow along suction surface of test turbine rotor blade ( $\Omega = 6786 \text{ rad/s}$ ).

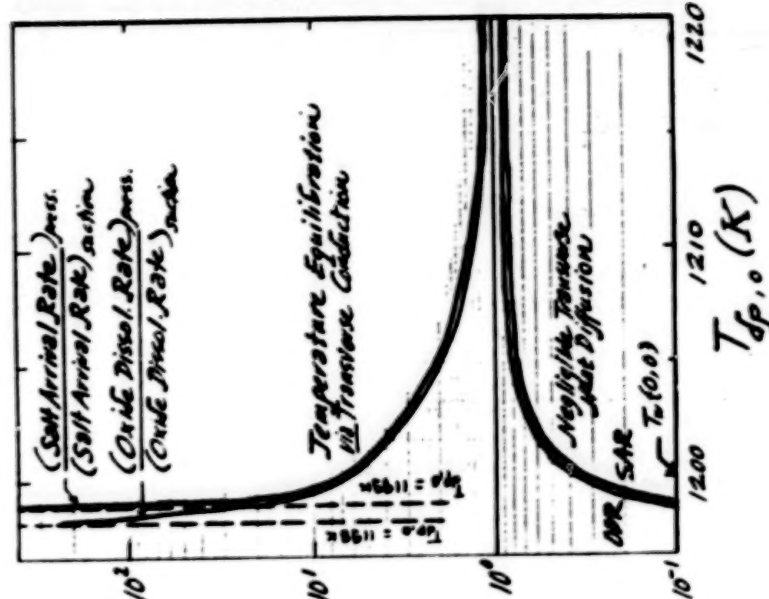


Fig. 4: Computed pressure-to-suction surface salt arrival/oxide dissolution rate ratios.

ORIGINAL PAGE IS OF POOR QUALITY

ORIGINAL PAGE IS OF POOR QUALITY

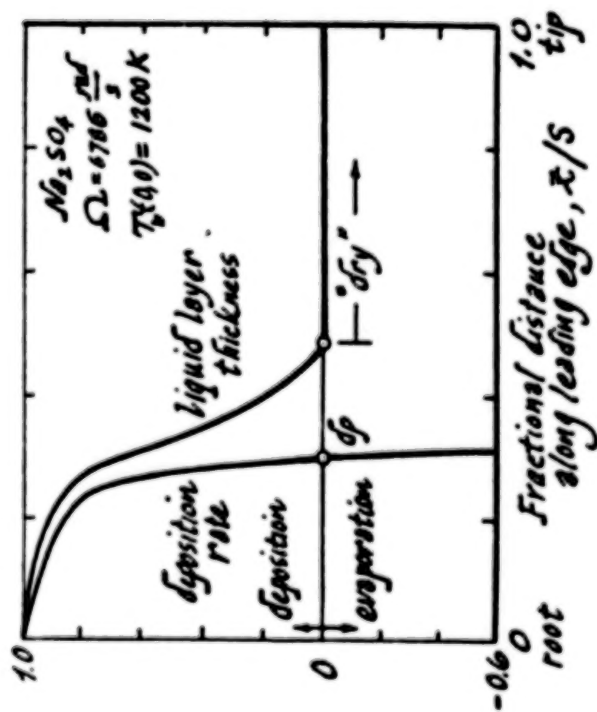


Fig. 5: Liquid layer "spill-over" onto evaporation region of rotor LE ( $\Omega = 6786 \text{ rad/s}$ ;  $T_s(0,0) = 1200 \text{ K}$ ).

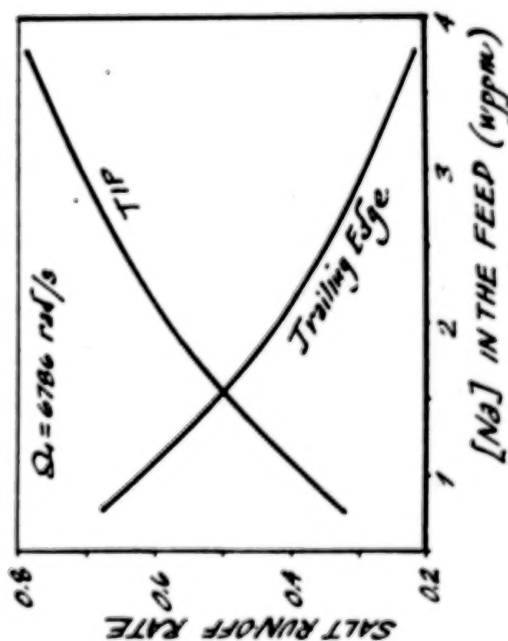


Fig. 7: Variation in salt runoff rates (TIP/TE) with salt seed level.

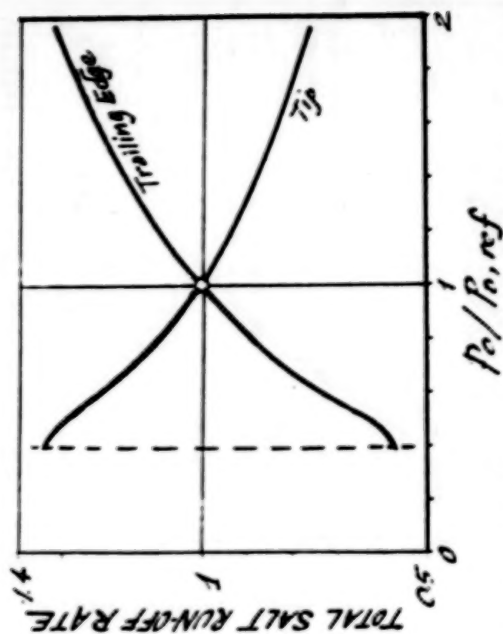


Fig. 6: Variation in salt runoff rates (TIP/TE) with stagnation pressure level.

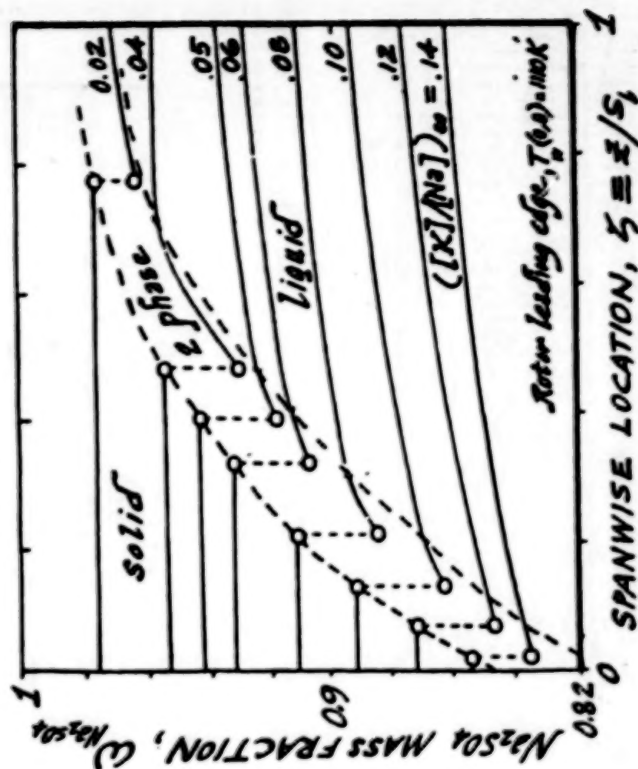


Fig. 8: Predicted distribution of condensate phase and composition of a root-cooled turbine rotor blade ( $T_s(0,0) = 1100 \text{ K}$ ) vs. mainstream potassium: sodium ratio.

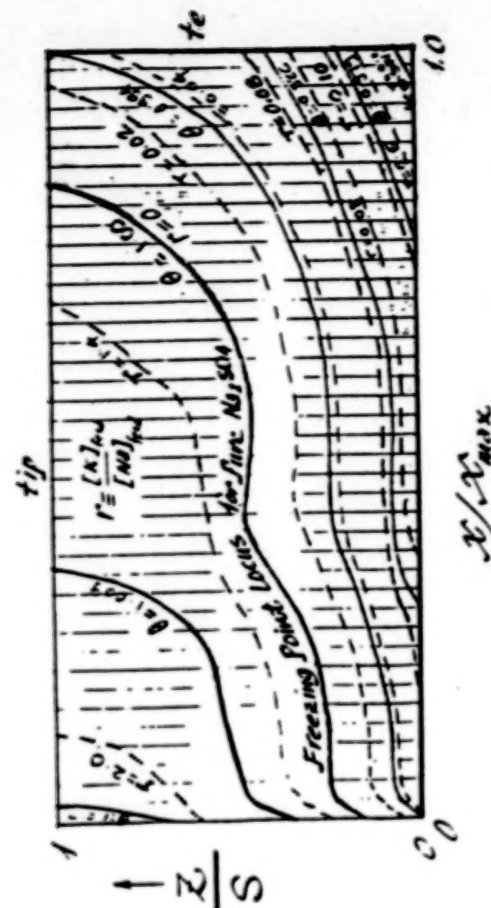


Fig. 9: Predicted distribution of liquid condensate composition on the suction surface of the rotor ( $\Omega = 6786$  rad/s;  $[K]/[Na] = 0.1$ ).

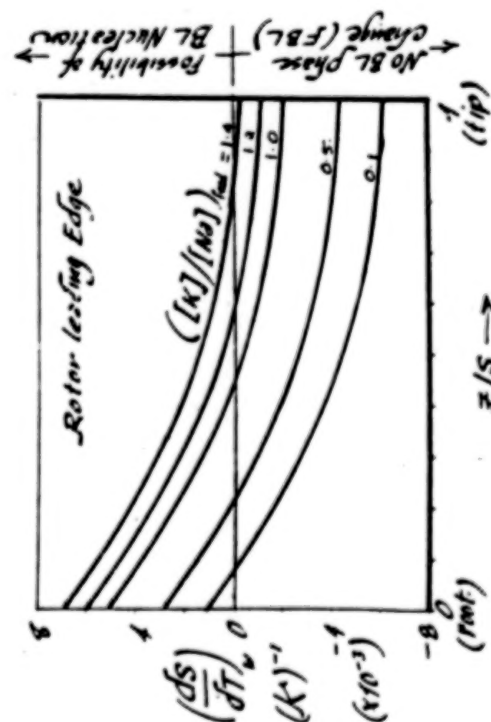


Fig. 10: Monitoring the possibility of BL-nucleation along the rotor LE as the ratio  $[K]/[Na]$  in the feed changes.

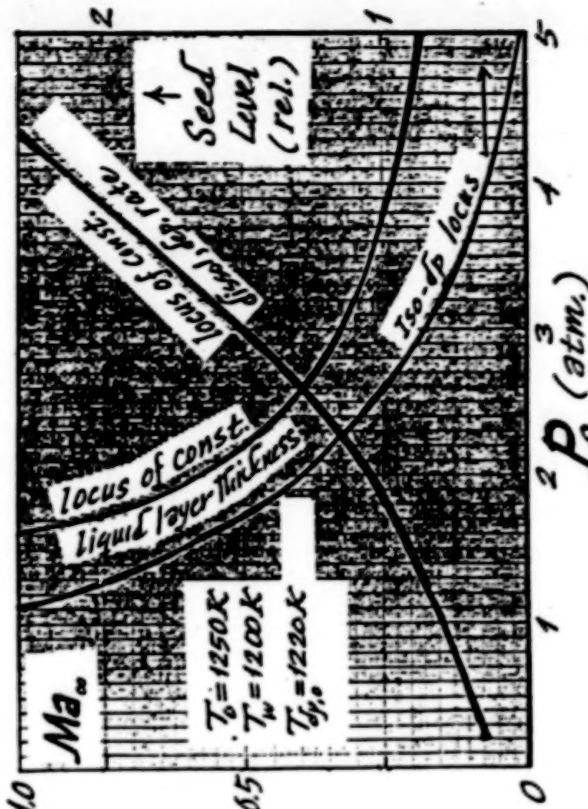


Fig. 11: Burner-rig testing under equivalent dew point conditions.

Fig. 12: Evolution of the "freezing-point locus" over the rotor suction surface with changing salt seed-ratio.

EXPERIMENTAL VERIFICATION OF VAPOR DEPOSITION RATE THEORY IN  
HIGH VELOCITY BURNER RIGS

Suleyman A. Gökoğlu\*  
Case Western Reserve University  
Department of Mechanical and Aerospace Engineering  
Cleveland, Ohio

and

Gilbert J. Santoro  
NASA Lewis Research Center  
Cleveland, Ohio

This research is motivated by gas-turbine hot-section component failures associated with accelerated "hot" corrosion to obtain a better understanding of the deposition phenomenon of corrosive species on turbine blades. A comprehensive yet tractable theoretical framework of deposition from combustion gases has been developed, covering the spectrum of various mass delivery mechanisms including vapor (refs. 1 and 2), thermophoretically enhanced small particle (ref. 3), and inertially impacting large particle (ref. 4) deposition. Rational yet simple correlations have been provided to facilitate engineering surface arrival rate predictions (refs. 5 to 7). The main objective of the program at the NASA Lewis has been the experimental verification of the corrosive vapor deposition theory in high-temperature, high-velocity environments. Toward this end, an atmospheric Mach 0.3 burner-rig apparatus has been built (fig. 1) to measure deposition rates from salt-seeded (mostly Na salts) combustion gases on an internally cooled cylindrical collector (ref. 8).

The results of the previous experiments have been reported in detail in reference 8. For sodium-salt seeded experiments there were two regions of disagreement between the deposition rate prediction of the chemically frozen boundary layer (CFBL), vapor-deposition theory and the experimentally observed deposition rates of  $\text{Na}_2\text{SO}_4$ , depending on whether the collector temperature was above or below the melting point of  $\text{Na}_2\text{SO}_4$ . Lower experimental deposition rate measurements for collector temperatures above the melting point of the deposit are attributed to the shear-driven molten deposit layer run-off from the smooth collector surface (ref. 9). Higher experimental values for collector temperatures below the melting point of the deposit, however, are explained by the presence of particles capable of inertially impacting the collector surface (cf. only Na-containing vapor species) and, subsequently, experimentally verified (refs. 10 and 11).

The elimination of particles (fig. 2) from the system was accomplished by dissolving sodium-acetate (Na source) in alcohol and mixing the alcohol solution with jet A-1 fuel in the fuel nozzle cavity before the mixture is sprayed into the combustor by the fuel nozzle. By this procedure (1) more residence time is provided

---

\*Resident senior research associate at NASA Lewis Research Center, Cleveland, Ohio 44135 U.S.A.

to the solution droplets in the combustor (as compared with an air-atomized salt-solution probe spraying further downstream of the combustor), and (2) alcohol solution droplets mixed with jet A-1 fuel burn faster (as compared with slower vaporization of water solution droplets), thereby, giving sufficient time for the complete vaporization and reaction (to equilibrium) of all sodium-containing vapor species (fig. 3). Currently the total Na content of the combustion gases, corrected for losses on combustor liner walls (i.e., as seen by the collector), is obtained from sodium-acetate/alcohol solution feed rate.

For a typical burner-rig test specimen located in the cross-stream of the combustor-exit nozzle, the prediction of convective diffusion heat and mass transfer rates is complicated by the fact that the height and the diameter of the cylindrical target are comparable to, but less than, the diameter of the circular cross-stream jet (fig. 4). Experiments exploiting the naphthalene sublimation technique and duplicating the procedure of reference 12 as adapted to our setup (figs. 5 and 6), have been successfully completed to determine the heat and mass transfer coefficients (figs. 7 and 8). These experiments accompanied by additional experimental information on the effect of cross-stream jet cooling (dilution) due to the entrainment of stagnant room-temperature air (fig. 9) have enabled us to estimate heat and mass transfer rates for such large cylindrical geometries (ref. 13).

A parallel approach has been adopted to facilitate heat and mass transfer rate prediction by using a simpler collector geometry (fig. 10). Only a segment that is 20° on both sides of the forward stagnation point of the previous cylindrical targets is being used as the collection (deposition) surface, simulating the nose region of blades. The above-mentioned naphthalene sublimation technique has been further utilized to determine the heat and mass transfer coefficient of the stagnation-point region, as well as to determine the effects of main stream turbulence on heat and mass transfer rates for our burner rig deposition experiments. The other advantage of the segmented collector is the elimination of the cross-stream jet cooling (dilution) effect.

The deposition experiments on both types of collectors are currently underway. The agreement of the corrosive-salt vapor-deposition-rate predictions, based on the experimental information obtained for our system with preliminary data for  $\text{Na}_2\text{SO}_4$  deposition experiments, is encouraging (fig. 11). More direct and precise knowledge of the sodium content of the combustion product gases in the cross-stream jet will be acquired with the installment of a sodium emission spectrometer. The availability of the high-pressure burner-rig facility will also enable us in the immediate future to study (1) the effect of pressure on deposition rates, and (2) dew point shifts.

#### REFERENCES

1. Rosner, D.E., et al.: Chemically Frozen Multicomponent Boundary Layer Theory of Salt and/or Ash Deposition Rates from Combustion Gases. Combust. Sci. Technol., vol. 20, no. 3/4, Sept. 1979, pp. 87-106.
2. Gökoğlu, S.A.; Chen, B.K.; and Rosner, D.E.: Computer Program for the Calculation of Multicomponent Convective Diffusion Deposition Rates from Chemically Frozen Boundary Layer Theory. NASA CR-168329, 1984.
3. Gökoğlu, S.A.: Thermophoretically Enhanced Deposition of Particulate Matter Across Nonisothermal Boundary Layers, Ph.D. Thesis, Yale Univ., 1983.
4. Fernandez de la Mora, J.; and Rosner, D.E.: Inertial Deposition of Particles

Revisited and Extended: Eulerian Approach to a Traditionally Lagrangian Problem. *PCH, PhysicoChem. Hydrodyn.*, vol. 2, no. 1, 1981, pp. 1-21.

5. Gökoğlu, S.A.; and Rosner, D.E.: Correlation of Thermoporetically Modified Small Particle Diffusional Deposition Rates in Forced Convection Systems with Variable Properties, Transpiration Cooling, and/or Viscous Dissipation. *Int. J. Heat Mass Trans.*, vol. 27, no. 5, May 1984, pp. 639-646.
6. Israel, R.; and Rosner, D.E.: Use of a Generalized Stokes Number to Determine the Aerodynamic Capture Efficiency of Non-Stokesian Particles from a Compressible Gas Flow. *Aerosol Sci. Technol.*, vol. 2, no. 1, 1983, pp. 45-51.
7. Rosner, D.E.; Gökoğlu, S.A.; and Israel, R.: Rational Engineering Correlations of Diffusional and Inertial Particle Deposition Behavior in Non-isothermal Forced Convection Environments. *Fouling of Heat Exchanger Surfaces*, Richard, W. Bryers, ed., Engineering Foundation, Inc., 1983, pp. 235-256.
8. Santoro, G.J., et al.: Experimental and Theoretical Deposition Rates from Salt-Seeded Combustion Gases of a Mach 0.3 Burner Rig. *NASA TF-2225*, 1984.
9. Rosner, D.E.; Günes, D.; and Wazih-Anous, W.: Aerodynamically Driven Condensate Layer Thickness Distributions on Isothermal Cylindrical Surfaces. *Chem. Eng. Commun.*, vol. 24, no. 4-6, 1983, pp. 275-287.
10. Santoro, G.J., et al.: Deposition of  $\text{Na}_2\text{SO}_4$  From Salt-Seeded Combustion Gases on a High Velocity Burner Rig. *High Temperature Corrosion in Energy Systems*. Michael F. Rothman, ed., TMS-AIME Publication, 1985, pp. 417-434.
11. Gökoğlu, S.A.; Experimental Verification of Vapor Deposition Model in Mach 0.3 Burner Rigs. *NASA CP-2339*, 1984, pp. 110-121.
12. Sparrow, E.M.; Stahl, T.J.; and Traub, P.: Heat Transfer Adjacent to the Attached End of a Cylinder in Crossflow. *Int. J. Heat Mass Trans.*, vol. 27, no. 2, Feb. 1984, pp. 233-242.
13. Gökoğlu, S.A.; and Santoro, G.J.: Determination of Convective Diffusion Heat/Mass Transfer Rates to Burner Rig Test Targets Comparable in Size to Cross-Stream Jet Diameter. To be presented at the 31st ASME International Gas Turbine Conference, Düsseldorf, Germany, June 8-12, 1986.

BURNER RIG  
SHORT EXIT NOZZLE

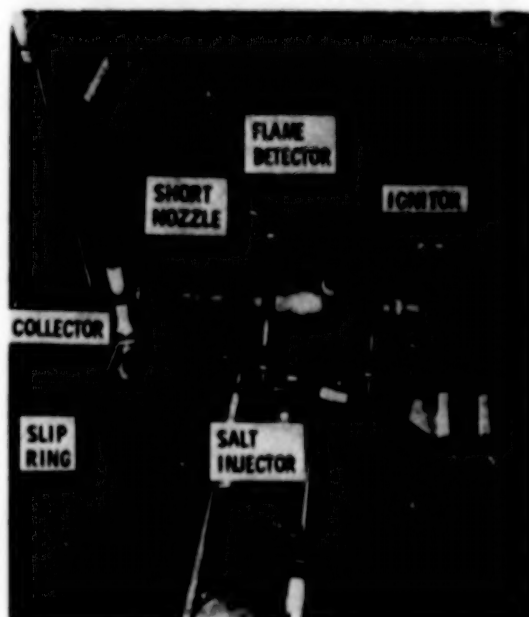
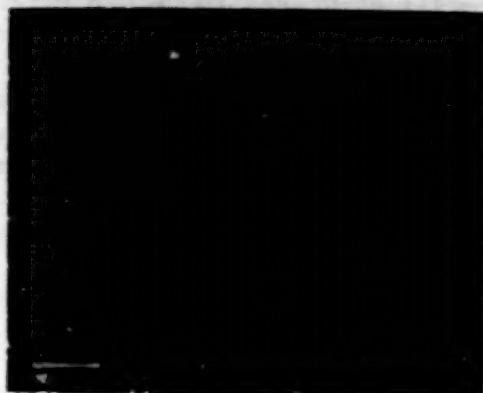


Figure 1

ORIGINAL PAGE IS  
OF POOR QUALITY

ORIGINAL PAGE IS  
OF POOR QUALITY

### NaCl PARTICLES CAPTURED



### ELEMENTS DETECTED BY EDS

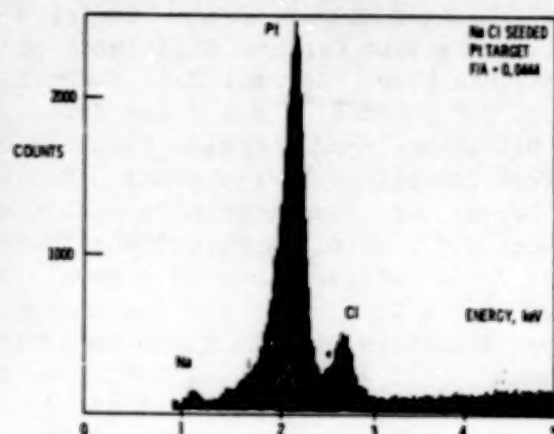


Figure 2

### Na<sub>2</sub>SO<sub>4</sub> DEPOSIT MORPHOLOGY FROM SODIUM ACETATE DOPED COMBUSTION GASES

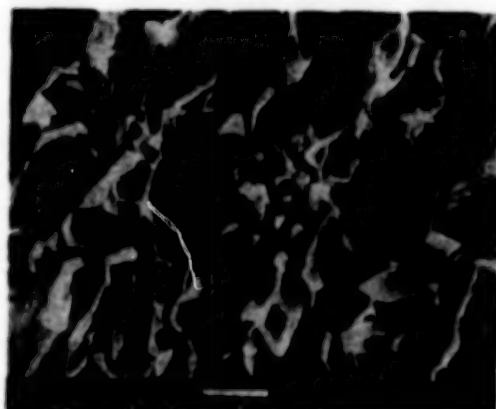
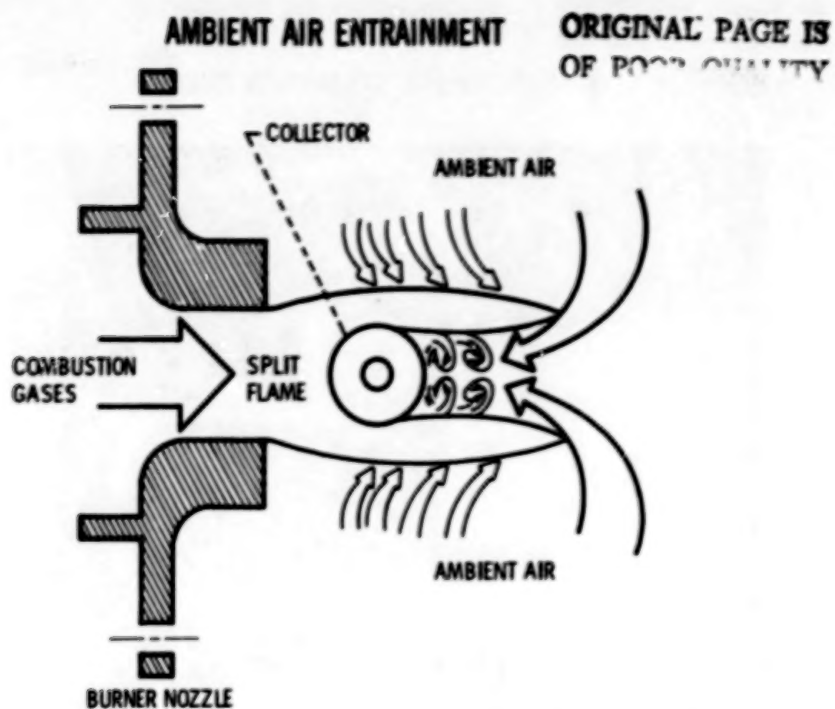


Figure 3

ORIGINAL PAGE IS  
OF POOR QUALITY



# NAPHTHALENE SUBLIMATION TUNNEL

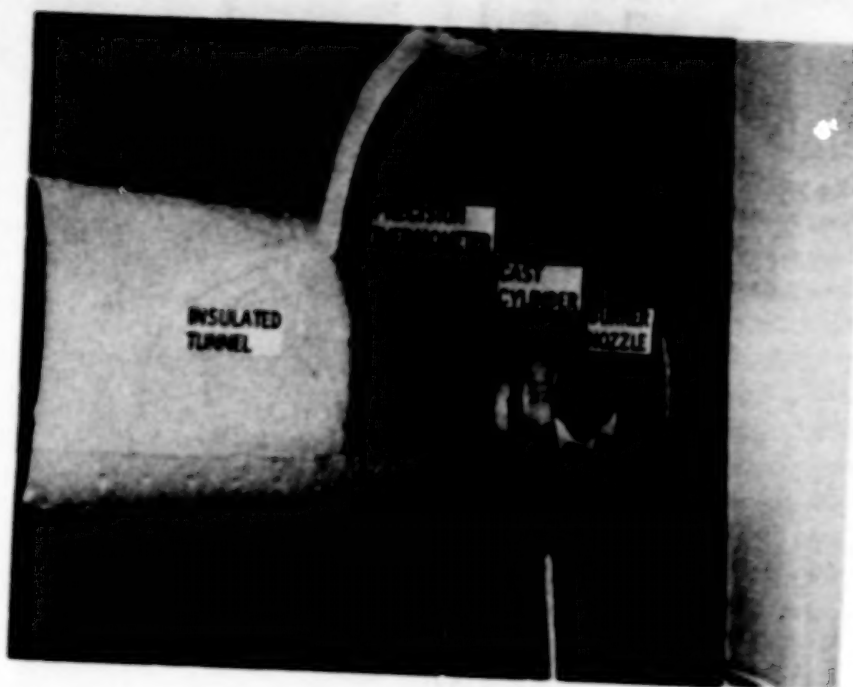


Figure 6

## MASS TRANSFER NUSSELT NUMBER VS REYNOLDS NUMBER FOR BURNER RIGS

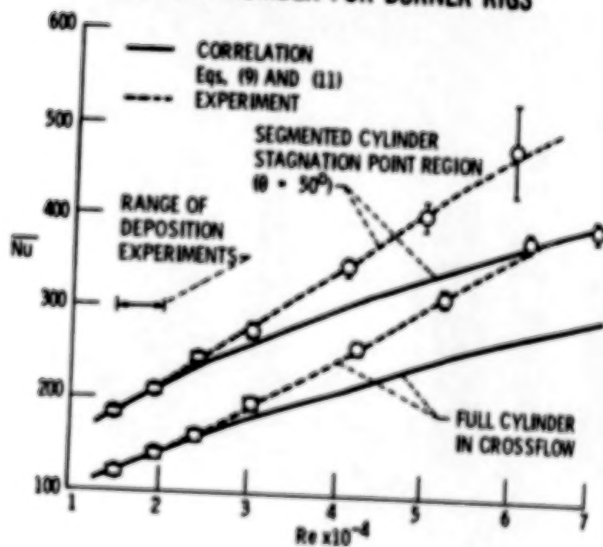


Figure 7

ORIGINAL PAGE IS  
OF POOR QUALITY

# MAIN-STREAM TURBULENCE FACTOR VS REYNOLDS NUMBER FOR BURNER RIGS

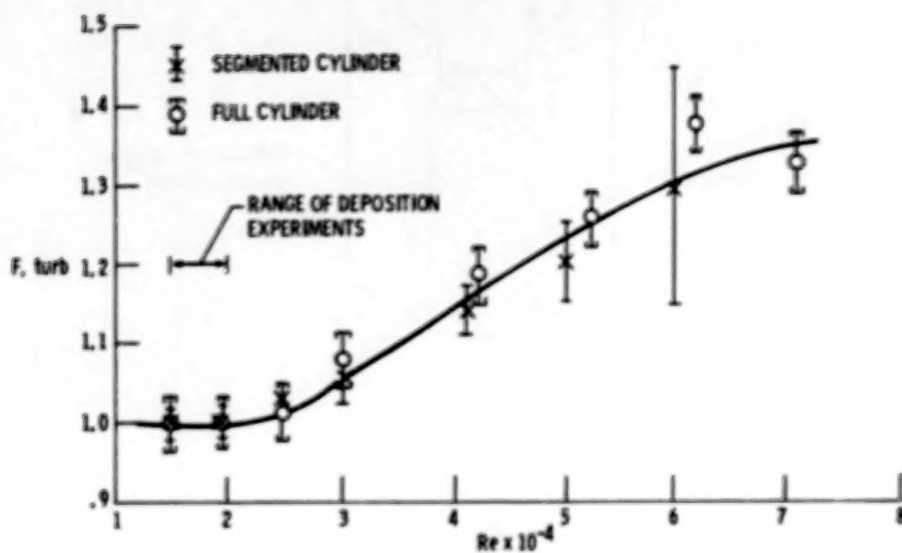


Figure 8

# MAIN-STREAM COOLING AND DILUTION EFFECT

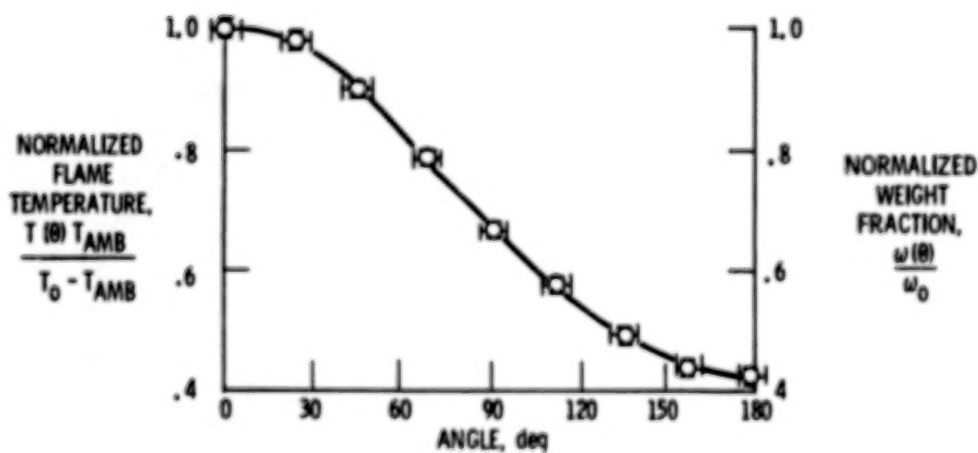
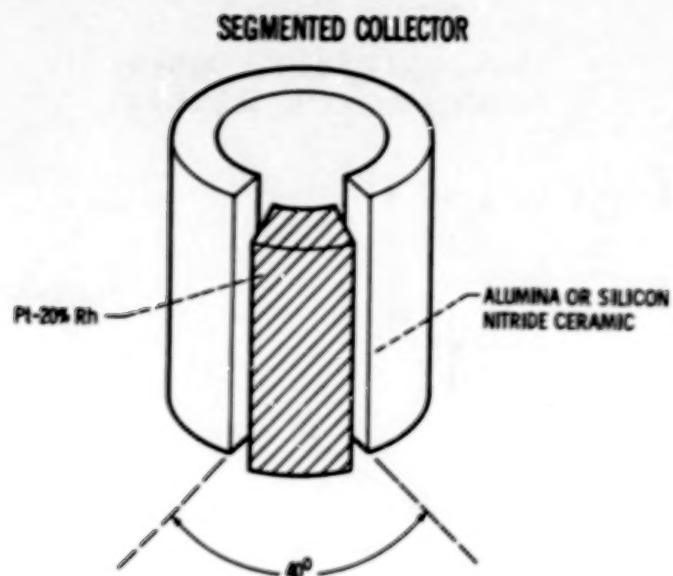
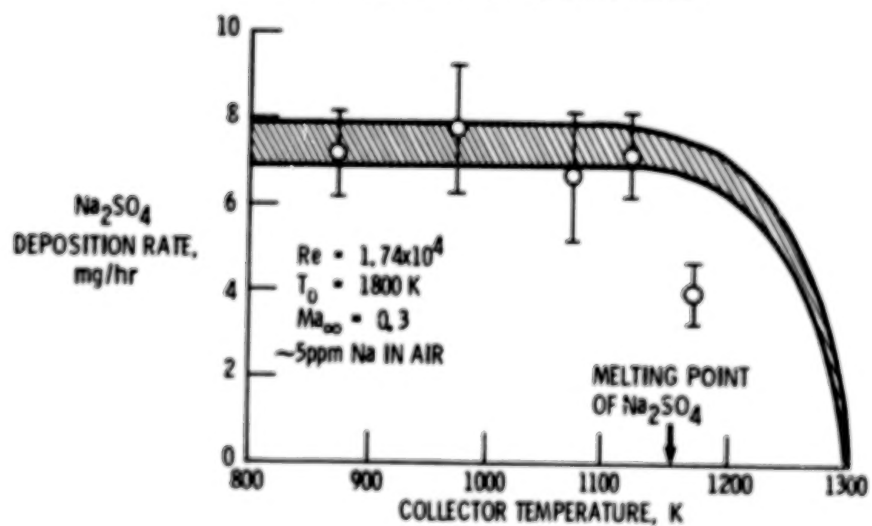


Figure 9



**Figure 10**

**PREDICTED AND EXPERIMENTAL  $\text{Na}_2\text{SO}_4$  DEPOSITION RATES FOR BURNER RIGS**



**Figure 11**

## Effects of Surface Chemistry on Hot Corrosion Life\*

R.E. Fryxell  
General Electric Company

and

G.E. Leese  
TRW Inc.

This program has as its primary objective the development of hot corrosion life prediction methodology based on a combination of laboratory test data and evaluation of field service turbine components which show evidence of hot corrosion. The laboratory program comprises burner rig testing by TRW. The discussion will summarize the results of two series of burner rig tests and outline the life prediction methodology parameters to be appraised in a final campaign of burner rig tests.

The two completed burner rig hot corrosion tests were performed under identical conditions, as given in Table 1. Specimens included U700 and Rene'80, uncoated and with the following coatings.

- o RT21 aluminide (Chromalloy American Corp.)
- o Codep aluminide (General Electric Co.)
- o Ni23Co18Cr12Al0.3Y applied by vacuum (low pressure) plasma spraying

At approximately twenty cycle intervals, specimens were visually examined, photographed, and coil inductance measurements made in a series mode at 10MHz with a multifrequency LCR meter. These measurements, which are patterned after studies at NASA-LeRC, afford a non-destructive means of following the course of metal degradation. Ultimately the inductance data bank from this program will be useful in the interpretation of the extent of oxidation/hot corrosion phenomena, in particular subtle differences between materials.

Specimens were considered to have failed when visual evidence of hot corrosion was noted in three successive inspections. Subsequent metallographic evaluation has confirmed substantial Type 1 sulfidation for all the uncoated specimens and, in most cases, coating penetration for the coated specimens.

In the first series of hot corrosion tests, duplicate as-fabricated specimens were exposed. In the second series of tests, specimens (coated alloys only) were exposed which had been preaged at 1100C under a variety of conditions to determine the effect on hot corrosion behavior caused by surface oxidation and/or interdiffusion between coating and substrate alloy. The aging conditions were:

\* Contract NAS3-23926

o	One hour cyclic, static air	100 hours
o	One hour cyclic, burner rig	100, 300, 600 hours
o	isothermal, static air	100, 300, 600 hours
o	isothermal, vacuum	100 hours

Triplicate specimens were aged; one withheld for metallographic evaluation and the remaining duplicates exposed in the hot corrosion tests.

In the baseline hot corrosion test, results in general were consistent with previous experience.

- o Uncoated U700 corroded at about twice the rate of uncoated Rene'80, paralleled by a similar difference in coil inductance changes as reported at the 1984 Workshop.
- o Coatings lives were similar on both substrates, i.e.
  - 424 to 602 hours for Codep coated specimens.
  - $\geq$  1000 hours for NiCoCrAlY coated specimens.

On the other hand the RT21 coating which is compositionally similar to Codep survived longer than Codep in this test: the coating was failed in two specimens at 697 and at 1005 hours, but not completely penetrated in two other specimens at 997 and at 1005 hours. A difference between these coatings also was apparent in the coil inductance changes as was reported at the 1984 Workshop. Detailed electron microprobe analyses failed to reveal any significant compositional differences between the two coatings and both have the structural features of inward aluminide coatings. However the RT21 coating showed some evidence of entrapment of small oxide particles in the outer 5 $\mu$ m while the Codep coating did not. Whether this difference is the cause of differences in hot corrosion lives cannot be concluded with certainty; yet it may be noted that, as will be shown, no consistent difference in life exists for specimens preaged at 1100C.

Before discussing the results of the second series of hot corrosion tests some comments are required about preaging. In furnace exposures even up to 600 hours there was frequently localized pitting but no examples of coating failure. However in burner rig preaging localized pitting was significantly more severe and approached penetration in a few instances even at 100 hours. For the longer exposures coating penetration was often observed. Since coatings on the specimens preaged in the burner rig for 300 hours or more had essentially failed during that time, their hot corrosion lives are of minimal value and will not be discussed.

Limiting the results in this manner it became clear that preaging caused substantial decreases in coatings lives relative to the baseline results cited above, particularly for the aluminides (RT21 and Codep). What is most striking (see Figure 1) is that for all three coatings life degradation is far more severe for coated U700 than for coated Rene'80. This cannot be

attributed to metal recession during the preaging which was minimal in 100 hours in air and zero in vacuum. It is interesting to note that on average the consequences of preaging in vacuum and in air appear to be similar. This suggests (as will be discussed below) that compositional changes resulting from coating/substrate interdiffusion predominate over surface oxidation in affecting subsequent hot corrosion performance.

As shown in Figure 2 coatings lives for some coating/substrate systems degrade progressively from 100 to 600 hours preoxidation; while for other systems maximum degradation has occurred in 100 hours preoxidation.

In an attempt to explain the large and consistent differences in the coated U700 and Rene'80 specimens, quantitative electron microprobe analyses of coatings were obtained on selected specimens in the as-preaged condition (prior to hot corrosion testing). Within measurement error, Codep and RT21 compositions were indistinguishable for a given preage time as were those at 100 hours oxidation whether isothermal, furnace cyclic or burner rig cyclic. Data thus consolidated are given in Table II.

- o For both aluminide and NiCoCrAlY coatings there are no apparent major differences between the U700 and Rene'80 systems.
- o For both aluminide and NiCoCrAlY coatings there are no significant differences between vacuum and air preaging, reinforcing the above comment that interdiffusion effects are far more important than surface oxidation in determining subsequent hot corrosion coating life.
- o The composition changes for the aluminide coatings are much greater (especially Al content) than for the NiCoCrAlY coating. This parallels the differences in hot corrosion life shown in Figures 1 and 2. Note also coil inductance changes (Figure 3) for cyclic oxidation preaging which parallel the lesser composition changes for the NiCoCrAlY coated specimens. Here again there is no hint as to reasons for differences in the coated U700 and Rene'80 systems.

The data in Table II represent average compositions of the coating additive layer. Another aspect to consider is the makeup of the diffusion zone (in particular for aluminide coatings) since prior experience suggests that while beta NiAl corrodes rather rapidly, the rate slows down when the diffusion zone is reached. Conceivably the makeup of the diffusion zone is equivalent in a corrosion sense for aluminide/U700 and aluminide/Rene'80 systems in the as-fabricated condition but changes in different manners (or rates) in the 1100C preaging. There are, in fact, visual differences after aging which did not exist before aging. Before aging, the diffusion zone in both systems contains a closely spaced needle like phase (sigma) in a beta matrix, oriented normal to the surface. As aging at 1100C progresses this

ORIGINAL PAGE IS  
OF POOR QUALITY

phase gradually disappears and a blocky phase (carbides) forms. The rate of this transformation is considerably faster for the U700 system and is nearly complete in 100 hours. Further investigation of these differences is planned and will be factored into life prediction modeling in the remainder of this program.

The rationale for life prediction modeling and confirmatory hot corrosion testing is as follows. Since in the mission of an aircraft engine, a small percentage of time is spent at turbine temperatures considerably higher than cruise (takeoff and thrust reverse, analogous to the 1100C aging in this program), coating/substrate interdiffusion with consequent accumulative decrease in remaining coating life can take place. A series of age treatments followed by hot corrosion tests will provide input for one element in mission analysis/life prediction. For an aircraft flying short missions, high temperature operation will accumulate faster in terms of total flying hours and hot corrosion coating life would be expected to be less based on the results discussed above. Such a correlation was qualitatively apparent in the analysis of field service turbine components performed earlier in this program, as reported at the 1984 Workshop.

It is clear that a life prediction model must include not only mission analysis and coating identification but substrate identification as well.

To have maximum opportunity to vary aging times (and test conditions) within the scope of planned tests, the remaining burner rig tests will be limited to Codep coated U700 and Codep coated Rene'80. Aging will be limited to isothermal oxidation. In the first of these tests, now underway under the conditions given in Table I, preaging times of 15 and of 25 hours are included. Evaluation will include detailed electron microprobe analyses of as-aged specimens and further consideration of possible differences in the diffusion zone between the two substrate systems. Further tests will include additional aging times and/or different salt levels.

Table I Burner Rig Operating Conditions.

Specimen Temperature -  $900^{\circ}\text{C} \pm 9^{\circ}\text{C}$

Test Cycle - 1 hour at temperature followed by 6 minutes of forced air cooling

Sodium Concentration - 0.5 ppm sodium ( $\pm 10\%$ ) in the combustion gases introduced as aqueous NaCl

Combustion Air Preheat Temperature -  $232^{\circ}\text{C} \pm 10^{\circ}\text{C}$

Specimens - Eight positioned equally on a 4.2 cm (1.64 inch) diameter circle of a holder rotating at 600 rpm

Burner Nozzle Throat Diameter - 2.54 cm (1.0 inch)

Burner Pressure - 1.0 psig

Nozzle Throat to Nearest Specimen - 4.45 cm (1.75 inch)

TABLE II Average Compositions of Coating Additive Layer as Function of Aging Time at 1100C (Weight Percent)

Aluminide	Age, Hours	*	Al	Cr	Mo	Ti	Co	Ni
Rene'80	0	2	31	5	0.6	0.7	6	52
	100 Vacuum	2	18	7	0.4	3.8	9	62
	100 Oxidation	2	18	6	0.2	3.4	9	63
U700	0	2	31	5	0.6	0.8	10	52
	100 Vacuum	1	17	7	0.6	3.1	12	61
	100 Oxidation	3	18	7	0.6	2.9	13	61
<b>NiCoCrAlY</b>								
Rene'80	0	1	13.0	20		0.2	19	43
	100 Vacuum	1	11.0	14	0.7	1.7	19	53
	100 Oxidation	2	11.3	16	0.6	1.8	17	54
	600 Oxidation	1	7.8	19	1.3	2.5	16	54
U700	0	1	12.0	20		0.4	21	44
	100 Vacuum	0			Not Analyzed			
	100 Oxidation	2	12.8	15	0.3	1.6	19	54
	300 Oxidation	1	7.4	17	1.9	2.6	19	55
	600 Oxidation	1	7.5	17	1.9	2.2	19	54

\*Entries in this column are numbers of specimens analyzed.

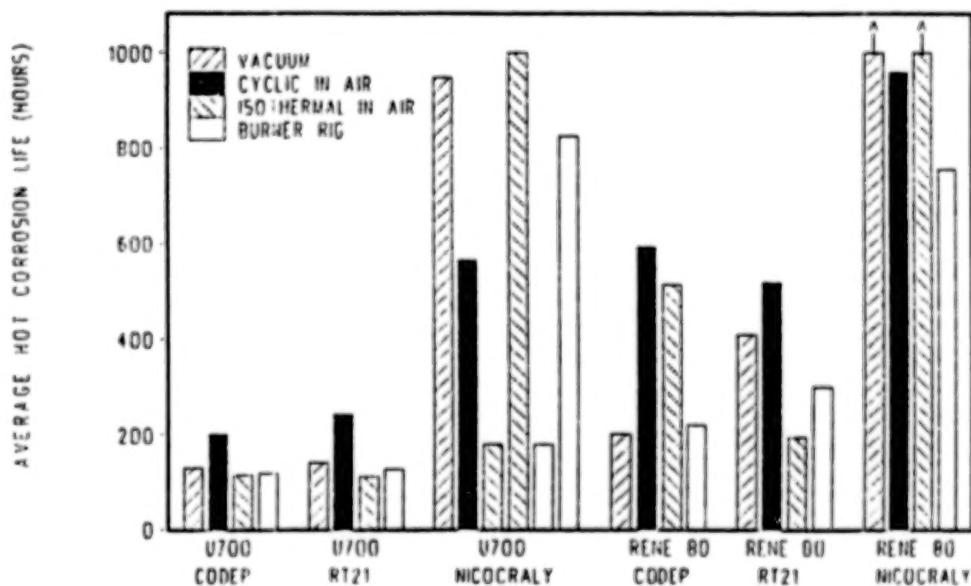


Figure 1 Hot corrosion coating life at 900C after 100 hours preaging at 1100 C. (Each bar is an average for two specimens except for NiCoCrAlY coated U700, isothermal and burner rig, for which individual results are shown).

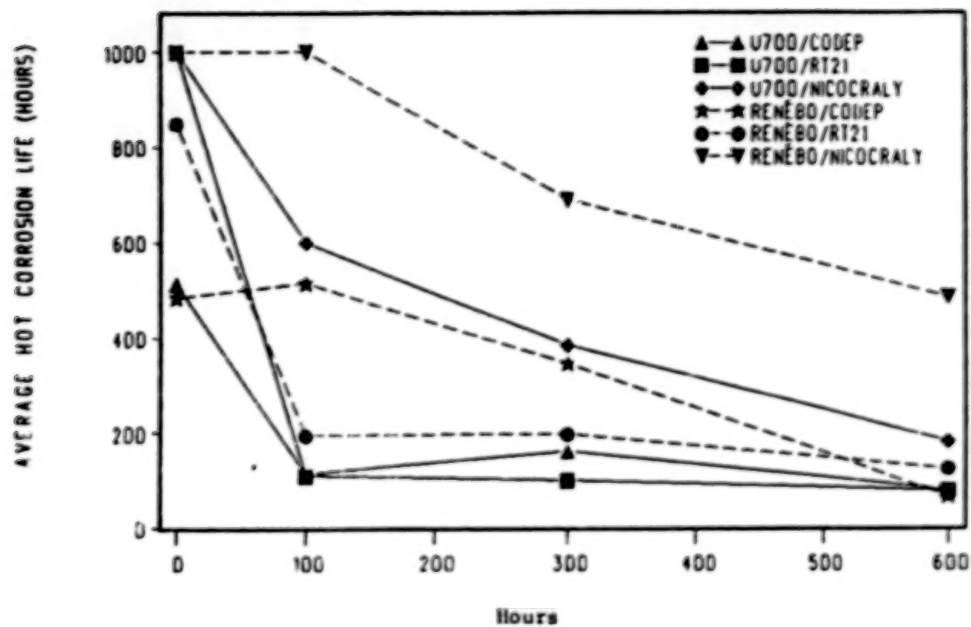


Figure 2 Hot corrosion life at 900C versus isothermal preaging time at 1100C.

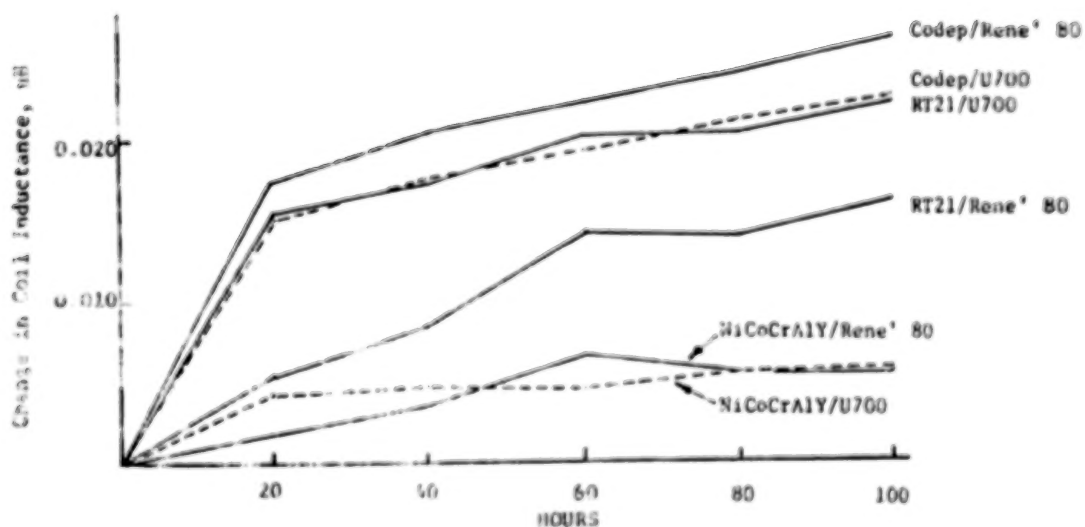


Figure 3. Changes in Coil Inductance in Static Oxidation at 1100C, Cyclic Exposure.

## COATING LIFE PREDICTION

James A. Wesbitt and Michael A. Gedwill  
NASA Lewis Research Center  
Cleveland, Ohio

Hot-section gas-turbine components typically require some form of coating for oxidation and hot-corrosion protection. These coatings are generally either aluminide coatings or MCrAlY overlay coatings, where M represents nickel, cobalt, or a combination of these two elements. Both coating types are protective as a result of the selective oxidation of aluminum to form an external, continuous  $Al_2O_3$  scale. The coatings act as a reservoir of aluminum since the aluminum content of the coating is always greater than that of the substrate. Any mechanism which reduces the aluminum content of the coating degrades the coating. Two significant forms of degradation which occur in aero gas-turbine engines are oxidation and coating-substrate interdiffusion. Coating-substrate interdiffusion involves not only the loss of the aluminum from the coating into the substrate but also the diffusion of less desirable elements to the coating surface where they may oxidize and hinder or prohibit the formation of the  $Al_2O_3$  scale. In addition, cycling of a coated component results in cracking and spalling of the  $Al_2O_3$  scale, which further accelerates coating degradation.

Efficient use of coatings requires reliable and accurate predictions of the protective life of the coating. Currently, engine inspections and component replacements are often made on a conservative basis. Consequently, there is a continuing need to improve and develop the life-prediction capability of metallic coatings in various service environments. The purpose of the present work is to develop an improved methodology for predicting metallic coating lives in an oxidizing environment and in a corrosive environment.

## APPROACH

The present investigation combines both experimental studies and numerical modeling to predict coating life in an oxidizing environment. The experimental work provides both input to and verification of two numerical models. The coatings being examined are an aluminide coating on Udimet 700 (U-700), a low-pressure plasma spray (LPPS) Ni-18Co-17Cr-24Al-0.2Y overlay coating also on U-700, and bulk deposits of the LPPS NiCoCrAlY coating. The approach taken in this study is shown schematically in figure 1.

## Experimental Testing

The experimental testing involves isothermal and cyclic furnace oxidation at 1050, 1100, and 1150 °C. In addition, Mach 0.3 cyclic burner rig testing of the aluminide and LPPS NiCoCrAlY coating (125 and 625  $\mu m$  thicknesses) on U-700 is also being undertaken at 1100 and 1150 °C. Isothermal oxidation of the coated U-700 and bulk coating yields the growth rate of the  $Al_2O_3$  scales which form on these coatings. Cyclic furnace and burner-rig oxidation yield the weight changes of the coated specimens reflecting the oxide growth and spallation which occurs during thermal

ORIGINAL PAGE IS  
OF POOR QUALITY

cycling. Analysis of the coating after an oxidation exposure includes x-ray diffraction and polarized light metallography of the retained surface oxides, observation of microstructural changes, scanning-electron microscopy, and electron microprobe analysis to measure concentration profiles across the coating and substrate. Only the experimental results for the furnace testing of the LPPS coating on U-700 will be discussed in the remainder of this paper.

#### Numerical Modeling

Two computer models are being used to predict the oxidation-limited life of the metallic coatings. A spalling model predicts the oxide growth and amount of oxide spallation which occurs during cyclic oxidation. The isothermal oxide growth rate and spall fraction  $Q_0$  (the ratio of the oxide which spalls on cooling to the total oxide present before cooling) are input to the spalling model. The spalling model predicts both the weight change of a coated specimen undergoing cyclic oxidation and the rate and total weight of metal consumption during cyclic oxidation. A diffusion model simulates the diffusional transport associated with both oxidation of the coating and coating-substrate interdiffusion. Diffusion coefficients and the rate of metal consumption predicted by the spalling model are inputs to the diffusion model. The diffusion model predicts aluminum and chromium concentration profiles in the coating and substrate and the time for which the coating is able to supply sufficient aluminum to continue forming an  $Al_2O_3$  scale. The diffusion model, therefore, predicts coating failure when there is insufficient transport of aluminum to the oxide scale.

#### CURRENT STATUS AND RESULTS

##### Experimental

Isothermal furnace oxidation testing for 100 hr at 1050, 1100, and 1150 °C is complete. Cyclic furnace testing of the coated U-700 was carried out to failure of the coating at the three test temperatures (1050, 1100, and 1150 °C). Each of the coatings on the U-700 failed prematurely due to massive spallation of the coating (fig. 2). This premature coating failure was due to excessive porosity formation at the coating-substrate interface. The coating, significantly detached from the substrate, spalled first from the cylinder ends, permitting extensive oxidation at the coating-substrate interface via the interconnected porosity.

##### Numerical Modeling

The spalling model was used to predict the rate of aluminum consumption at 1050, 1100, and 1150 °C. The spall fraction  $Q_0$ , input to the spalling model, was chosen so as to reproduce the specimen weight change during cyclic oxidation before the onset of massive coating spallation (fig. 4). The weight of aluminum consumed, as predicted by the spalling model, for each test temperature is shown in figure 5. (Parameters input to the spalling and diffusion models, except as indicated otherwise in a figure, are shown in table I.)

The diffusion model predicted the aluminum and chromium concentration profiles after cyclic oxidation at 1050, 1100, and 1150 °C. Good agreement was found between the measured and predicted profiles (figs. 6 and 7). Following this verification of its predictive ability, the diffusion model was then used to examine the effect of

various parameters (e.g., coating thickness, spall fraction  $Q_0$ , and substrate composition) on coating life. The model was also used to predict the life of the NiCoCrAlY coating on U-700 for the case where massive coating spallation had not caused premature failure (fig. 8).

#### FUTURE WORK

Current burner-rig testing should provide oxidized specimens which, although containing porosity at the coating-substrate interface, eliminate oxide formation within the porosity and the resultant premature coating failure. An accurate test of the life predictive ability of the diffusion model could then be conducted. A second diffusion model is being developed to simulate  $\gamma'$  and  $\beta$  depletion during degradation of aluminide coatings. This aluminide diffusion model should be capable of predicting coating life. Measured concentration profiles after cyclic oxidation of the aluminide coated U-700 will be compared with those predicted by the diffusion model to determine the accuracy and usefulness of the aluminide diffusion model. Predicted and measured coating lives will also be compared. The conclusion of this work should result in an improved methodology for predicting the oxidation life of both overlay and aluminide coatings.

#### DUAL CYCLE ATTACK

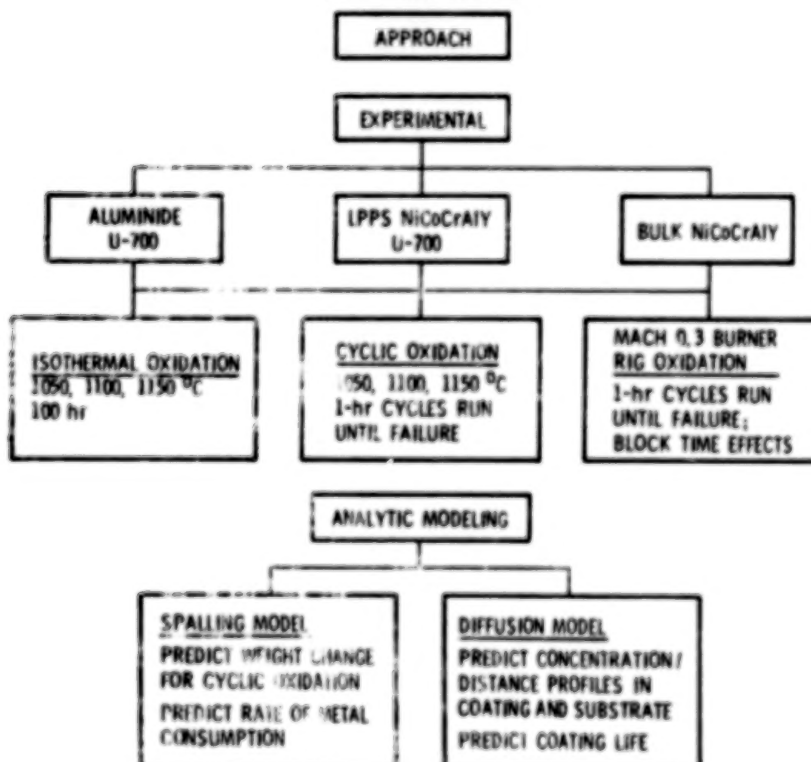
An experimental study to investigate the effect of aging in a corrosive environment (900 °C, 0.5 ppm Na) on the oxidation life of the two coatings discussed in this paper has begun. An attempt will be made to develop an empirical model to relate coating life to combined oxidation and hot-corrosion cyclic exposure.

# INPUT PARAMETERS FOR MODELS

TEMPERATURE, °C	SPALLING MODEL		DIFFUSION MODEL		
	WEIGHT CHANGE, $\Delta w$	SPALLING FRACTION, $Q_0$	COATING COMPOSITION	COATING THICKNESS, $\mu m$	SUBSTRATE COMPOSITION
1050	0.263 <sup>+0.234</sup>	0.0004	Ni-16.7Cr-24.0Al	120	Ni-15.6Cr-8.4Al
1100	.212 <sup>+0.323</sup>	0.00075 - 0.0015			
1150	.268 <sup>+0.337</sup>	0.011			

## OXIDATION-LIMITED COATING LIFE PREDICTION

OBJECTIVE: TO DEVELOP AN IMPROVED METHODOLOGY FOR PREDICTING THE OXIDATION LIFE OF METALLIC COATINGS



CS-85-3377

Figure 1

ORIGINAL PAGE IS  
OF POOR QUALITY

ORIGINAL PAGE IS  
OF POOR QUALITY

### MACROSCOPIC COATING FAILURE

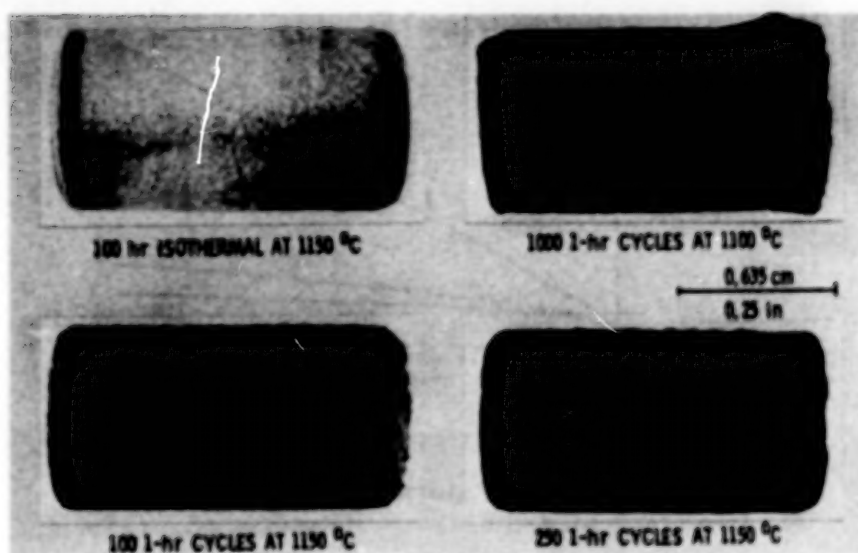


Figure 2

### MICROSCOPIC COATING FAILURE

1150 °C

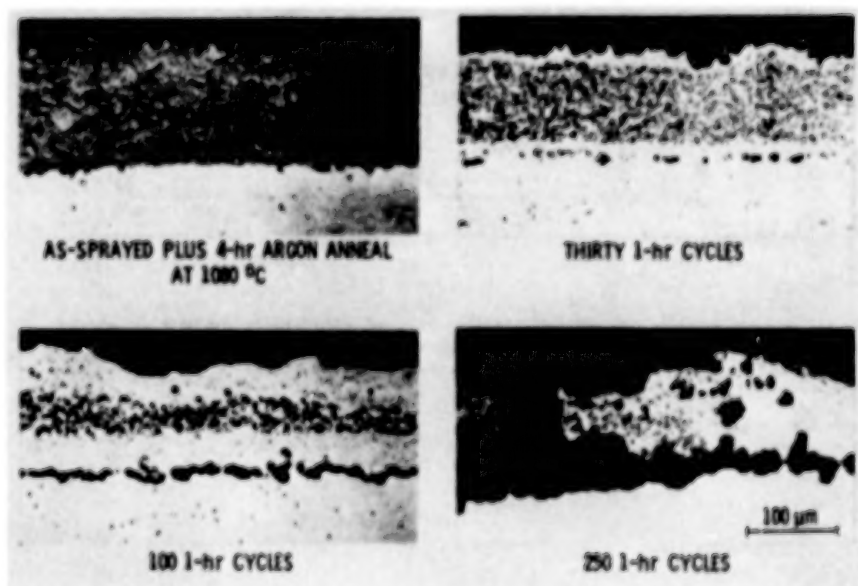


Figure 3

# ALUMINUM CONSUMPTION PREDICTED BY SPALLING MODEL

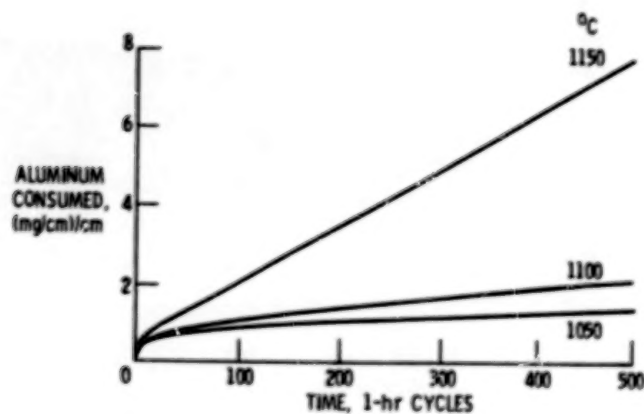


Figure 4

# WEIGHT CHANGE DURING CYCLIC OXIDATION

LPPS COATING ON U-700; 1100 °C

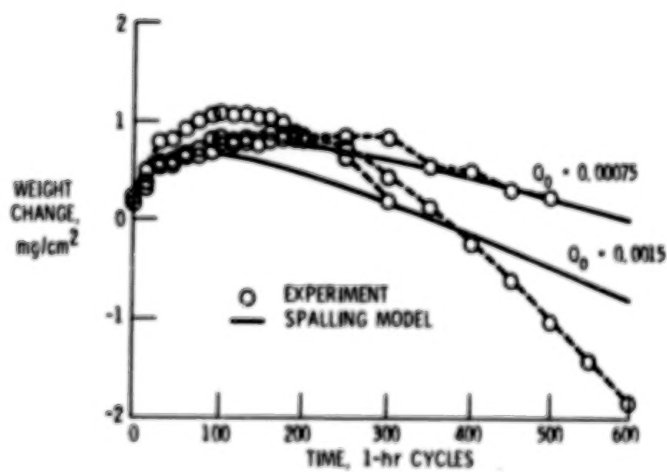


Figure 5

# MEASURED AND PREDICTED CONCENTRATION PROFILES FOR LPPS NiCoCrAlY ON U-700

1000 1/2-hr CYCLES (500 hr AT 1100 °C)

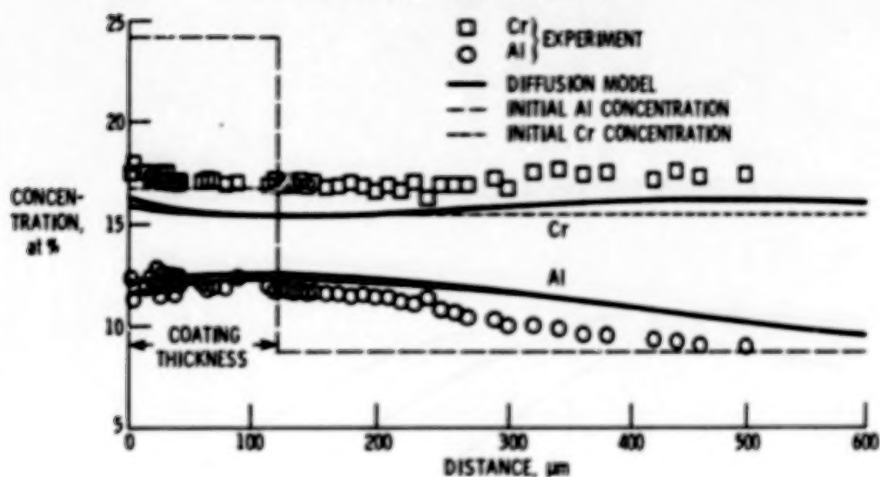


Figure 6

# MEASURED AND PREDICTED CONCENTRATION PROFILES FOR LPPS NiCoCrAlY COATING ON U-700

1000 1-hr CYCLES AT 1100 °C

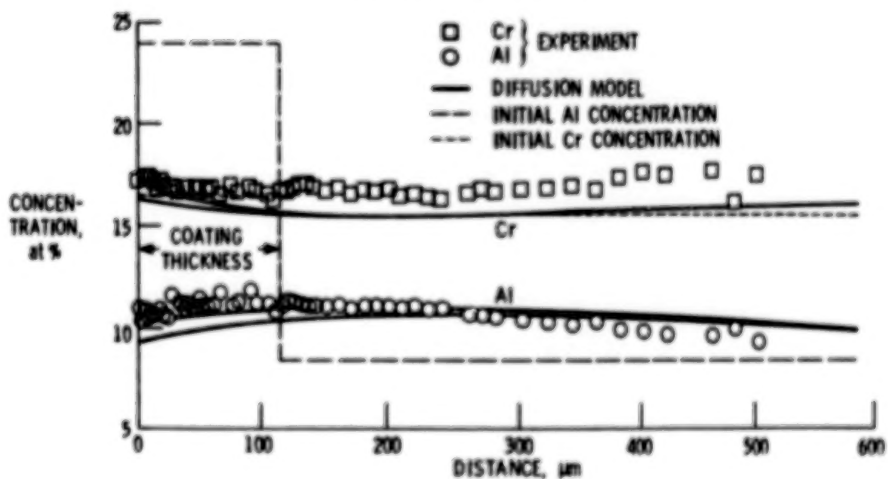
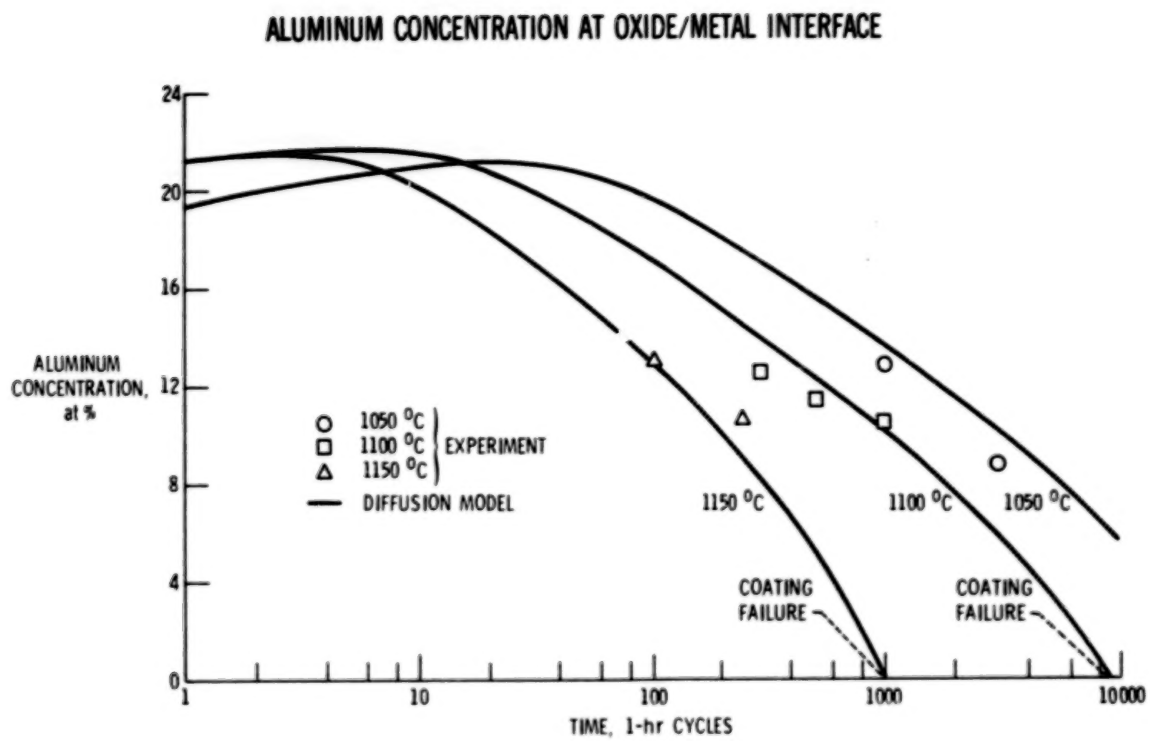


Figure 7



**Figure 8**

THERMAL EXPANSION MISMATCH AND OXIDATION IN THERMAL  
BARRIER COATINGS\*G. C. Chang and W. Phucharoen  
Cleveland State UniversityR. A. Miller  
National Aeronautics and Space Administration  
Lewis Research Center

## INTRODUCTION

Thermal barrier coatings (TBC) for advanced gas turbine blades have been under intensive development during the last several years. This is a very complex problem calling for inter-disciplinary efforts. This particular investigation is intended to help achieve a clearer understanding of the mechanical behavior of plasma-sprayed zirconia-yttria TBCs, involving a nickel-chromium-aluminum bond coat. The near-term objectives of this project is to study the stress states in a relatively simple model TBC subjected to steady-state thermal loading. The resulting thermal expansion mismatch and oxidation have been primary targets for the study.

Due to the complex nature of the problem on hand, the versatile finite element approach has been used to determine the stress states. Preliminary results obtained were discussed in reference 1. This paper describes the finite element approach and the effects of thermal expansion mismatch and oxidation. A proposed mechanism for oxidation-induced coating failure is also presented.

EXPERIMENTAL OBSERVATIONS OF  
FRACTURING OF COATINGS

Since the late 1970's, a number of researchers have reported their experimental TBC work. While some worked with simple test specimens, others ran tests of full-size engine turbine blades. Of particular interest to the present investigation is the work reported in reference 2. In this particular work, superalloy cylindrical test specimens with a radius of 0.65 cm and a length of 7.60 cm were utilized. The specimens were plasma-spray coated with the zirconia-yttria on a nickel-chromium-aluminum bond coat. Coated specimens were then individually exposed to the combustion gases of a burner rig for various periods of time before cooling took place. Most specimens went through many thermal cycles.

It was reported, in reference 2, that the coatings of all specimens tested in air at temperatures high enough to permit bond coat oxidation eventually spalled. Evidence gathered by both visual inspections and scanning electron microscope (SEM) photomicrograph indicated that such spalling was preceded by coating delamination. The TBC specimens failed within the ceramic coat just above the bond coat on cooling from high temperatures. The same photomicrography also showed the rough interface between the ceramic layer and the bond coat. Some interfaces were roughly sinusoidal with peak-to-valley and peak-to-peak dimensions up to 50-100 micrometers ( $\mu\text{m}$ ). Furthermore, oxides had been found in the bond coat adjacent to the ceramic-bond interface. Much oxides accumulated through thermal-exposure of these specimens in the air.

\*Work performed under Cooperative Research Agreement No. NCC-3-27.

These test results clearly illustrated the failure modes. They also raised the question of the quantitative nature of the stress states which may have some bearing on the TBC failure mechanism(s). This then led to the present investigation.

#### FINITE ELEMENT MODELING OF A BASIC THERMAL BARRIER COATING

Based on the above experimental observations and the need to understand the detailed distribution of stresses and strains within the TBC, it was decided that a general-purpose finite element program be used to model a cylindrical test specimen similar to that reported in reference 2. Figure 1 illustrates this modeling concept.

The cylinder is sufficiently long, as compared to its diameter, that the problem can be approximated by a two-dimensional generalized plane-strain case. Such an approximation, which can often be found in the classical theory of elasticity, implies that the strain in the axial (or  $z$ ) direction is constant for any unit slice such as the one shown in figure 1.

A wavy interface between the bond and the ceramic coat is introduced, with a period as well as peak-to-valley amplitude of  $50\text{ }\mu\text{m}$  (0.002 in.). This and other geometric dimensions of the wedge modeled are shown in figure 2.

The three materials comprising the substrate, the bond coat, and the ceramic layer, are assumed, for the time being, to be homogeneous, isotropic and linearly elastic. Each material, naturally, possesses its own temperature-dependent parameters, such as Young's modulus ( $E$ ), Poisson's ratio ( $\nu$ ), and thermal expansion coefficient ( $\alpha$ ). This greatly simplified material model represents a first step toward obtaining a detailed solution to a complex TBC problem on hand. Nevertheless, more complex models such as plasticity, viscoelasticity or creep, etc., would be incorporated in future calculations.

An overview of the advanced "TBCOC" model is given in figure 3. The model consists of 1316 nodal points and 2140 plane-strain finite elements, both triangular and quadrilateral. Particular attention has been given to the region in the vicinity of the sinusoidal interface in the discretization process. Details of that portion of the model of principal interest are shown in figures 4 to 11. Oxidized elements shown in figures 3, 8 and 9, are special types of bond coat elements. The actual modeling is done with the use of a general purpose computer program known as MARC (ref. 3) which is operational on a supercomputer (CRAY-I) at NASA Lewis Research Center.

The boundary conditions applied are fully compatible with those normally required in the theory of elasticity. More specifically, only radial displacements are allowed to occur along radial lines, OA and OB, in figures 2 and 3. Line AB is free to displace. Point O which represents the center of the unit slice or the  $z$ -axis of the cylindrical specimen, is fixed.

To validate the finite element solution, the TBCOC solution to a limiting case has been obtained. In this case, the elements in the ceramic layer and the bond coat have been assigned material properties identically the same as those of the

substrate. The finite element solution matches extremely closely with that of the analytical solution.

#### STRESS STATES RESULTING FROM THERMAL EXPANSION MISMATCH

The TBCOC computer program has been used to determine stress states for several combinations of TBC material properties. Customary units (psi, in., etc.) have been used in the calculations. The only loading applied so far is one of a uniform temperature drop throughout the model. It simulates part of the cooling-off of a TBC experiencing a temperature drop of 100°C from an assumed stress-free temperature of 700°C. Material properties for three cases are given in Table 1. It should be noted that only values of E, the Young's modulus, have changed from Cases A-2 to A-3 to A-4.

Stresses for Case A-2 are presented in figures 12-14, with corresponding strains shown in figures 15-17. The strains are of reasonable size and distribution. Stresses in the x-direction, or radial stresses, in the vicinity of the sine peak (asperity) are rather high, and are tensile in nature. Such high tensile stresses could easily initiate cracking at the asperities as the TBC cools down. It should be pointed out that these stresses correspond to a 100°C drop in temperature. An additional temperature drop would produce higher tensile stresses yet. There should be little doubt that cracking could be initiated at the asperities at some point during the cooling process. This is especially convincing when one recalls that the occurrence of such cracking may contribute to the acoustic emission observed as thermal barrier coated specimens cool (ref. 4). This is the first major observation of this work.

The stresses in the y-direction, or hoop stresses, as shown in figure 13, are in compression, as expected. These stresses are fairly uniform throughout the thickness of the coating. Shearing stresses shown in figure 14, however, maximize near the interface where failure is observed. It is inappropriate to make any conclusive remarks about these two stresses due to lack of reliable data on allowable stresses for this ceramic material at the present time.

Case A-3 employs a value of E which is half of that of Case A-2. From an elasticity viewpoint, the lower E value would allow more deformation in ceramic layer, resulting in lower stresses in all directions. This indeed occurred, as evidenced by the data shown in figures 18-20. Such is observation no. 2. It is noted that peak stresses went down by nearly 40 percent in the x-direction.

A third observation is that from an elasticity viewpoint, a softer bond coat with a lower E tends to lower stresses in the ceramic layer. This is the result by comparing figures 12-14 with 21-23. The reduction in peak stress caused by decreasing the bond coat modulus by a factor of two is on the order of 10 percent, making it much less significant than a comparable change in the modulus of the ceramic layer.

A comparison between the plane-strain finite element results and the results of more approximate calculations is in order. The stress in the y-direction in a thin ceramic coating at a planar interface is approximated by (refs. 2 and 5)

$$\sigma_y = \frac{\Delta \alpha \Delta T}{1 - \mu_c} \cdot E_c$$

where  $\Delta \alpha$  is the difference in thermal expansion coefficient between the ceramic and the substrate,  $\Delta T$  is the temperature change,  $E_c$  is the modulus of the ceramic, and  $\mu_c$  is Poisson's ratio. Using values of these properties from Table 1 and treating the substrate as if it were composed entirely of bond coat material yields

$$\begin{aligned} \sigma_y (A2) &= \sigma_y (A4) = -19.0 \text{ MPa} \\ \text{and} \\ \sigma_y (A3) &= -9.5 \text{ MPa} \end{aligned}$$

These values agree well with the peak values of

$$\begin{aligned} \sigma_y (A2) &= \sigma_y (A4) = -18 \text{ MPa (18.4 MPa)} \\ \text{and} \\ \sigma_y (A3) &= -10 \text{ MPa (-9.3 MPa)} \end{aligned}$$

given in figures 13, 19 and 22. Numbers within parentheses are taken from computer printouts and are exact values not shown by contouring.

An expression for the interfacial stress in the direction normal to the sinusoidal interface is given in equation 4 of reference 5. The expression predicts maximum stress at the peaks of the asperities and equally negative stresses in the valleys. Zero stress is predicted midway between peak and valley. Inserting the parameters in Table 1 into equation 4 of reference 5 gives

$$\begin{aligned} \sigma_x (A2) &= 16.4 \text{ MPa} \\ \sigma_x (A3) &= 9.1 \text{ MPa} \\ \sigma_x (A4) &= 13.8 \text{ MPa} \end{aligned}$$

The values reported in figures 12, 18, and 21 are

$$\begin{aligned} \sigma_x (A2) &= 18 \text{ MPa (19.6 MPa)} \\ \sigma_x (A3) &= 10 \text{ MPa (11.3 MPa)} \\ \sigma_x (A4) &= 14 \text{ MPa (15.2 MPa)} \end{aligned}$$

The above finite element results and the approximate values agree well. However, the stresses reported in at least one case, figure 21, are not sinusoidal. It appears that the approximate expressions provide a useful and quick view of maximum stresses in the x and y directions, but they are less useful in mapping out the actual stress fields. The finite element technique is also required for obtaining the corresponding strains as well as the shearing stresses and strains.

## STRESS STATES DUE TO OXIDATION

In experimental work reported in reference 2, bond coat oxidation was seen to grow with thermal cycles when the test was conducted in the air and failure was found to be correlated with this oxidation. The oxide layer appeared to grow thicker with exposure to the air at high temperatures. The net effect is equivalent to inserting an extra oxide layer between the ceramic layer and the remaining unoxidized bond material. The oxide is largely alumina which is a hard and strong material. As such, the stress state in the ceramic is expected to be severely impacted by the expanding oxide layer.

As a first attempt to model the effects of bond coat oxidation, the single layer of finite elements which border on the sinusoidal interface have been assigned the properties of alumina. These elements are shown by the dark outlines in figures 8 through 11. Oxide growth has been represented by giving these elements an artificially large thermal expansion coefficient given by

$$\alpha_a = G \times \alpha$$

where  $G$  is a growth factor. Proper choice of  $G$  rests with the need to make sure that the observed thickness of the oxide layer should be approximately equal to the product of  $\alpha_a$  and  $3 \mu\text{m}$ . For the present case  $G$  was set equal to -1000. A temperature drop of only  $0.1^\circ\text{C}$  was used to minimize thermal expansion mismatch stresses. This yielded a very modest expansion of 0.08% in the oxide layer. The resulting stresses due to this oxidation-like process are presented in figures 24-26, Case A-10.

The stresses obtained for Case A-10 are, in general, the reverse of those obtained for Cases A-2 through A-4. Stresses in the x-direction, figure 24, are compressive near the peak of the asperity and tensile above the valley. Stresses in the y-direction, figure 25, are positive near the peak of the asperity while still being negative elsewhere. Shearing stresses, figure 26, are, in general, in the opposite direction (opposite sign).

The magnitude of the above stresses are very large considering that only a very modest expansion of the oxide has been modeled. Therefore, the stress state due to oxidation can be expected to have a profound influence on the coating failure mechanism. In fact, these stresses are so large that the coating system must actually relieve much of the stresses through such processes as bond coat flow (ref. 2), ceramic microcracking, or other inelastic-like effects (ref. 6). Such efforts are not treated in the present linear analysis.

## A PROPOSED MECHANISM FOR OXIDATION-INDUCED COATING FAILURE

Based on the analytical results discussed above, a tentative mechanism may be proposed to account for the observed correlation between bond coat oxidation and coating failure. Consider the radial component of stress as indicated in figure 27. Initially, radial stresses at the peaks of the asperities are tensile. This

promotes cracking in the ceramic near the interface in that region. However, such cracks will be restrained from propagating into the region above the valley where the stresses are compressive.

As the coating oxidizes the stress in the region above the valley becomes tensile. Now the cracks may extend. This would eventually lead to delamination and spalling of the ceramic layer.

Work is underway to model the stress fields around this growing crack. Both the initial cracking and the oxidation are being taken into consideration.

#### CONCLUDING REMARKS

The present investigation represents a modest effort in combining three types of expertise: experimental material research, finite element techniques, and computer science. The authors wish to acknowledge the very significant contributions from the computer science community. Through Dr. James Guphill, of the Computer Services Division at NASA Lewis Research Center, both efficient software systems and powerful computers were brought to bear on the complex problem on hand. To ensure future success, a similar interdisciplinary approach will continue to be employed.

With the TBCOC program now operational, additional data will be generated to gain a clearer understanding of the stress states in not only the ceramic layer but also the bond coat. Shortly, TBCOC will also be used to study the effect of initial cracks in the vicinity of the asperities. Both thermal expansion and oxidation cases will soon be investigated.

The development of another computer model, known as TBCG, is well underway. This model entails a more smooth ceramic-bond interface. With the use of both computer models, a detailed study of the interface geometry will be performed within approximately six months.

The work to date has used linearly elastic material models. This may not be quite realistic. Nevertheless, this approach has made it possible to gain valuable insights into the TBC stress states under varying conditions. Results so obtained are deemed valuable in guiding experimental work as well. As a goal for the future, the present work would logically be extended into the inelastic material regime. The results from such a future cooperative endeavor between the experimentalist and the analyst may prove to be extremely useful indeed.

#### REFERENCES

1. Chang, G. C. and Phucharoen, W.: Finite Element Analysis of Thermal Barrier Coatings. NASA Workshop on Thermal Barrier Coatings, Middleburg Heights, May 1985.
2. Miller, R. A. and Lowell, C. E.: Failure Mechanism of Thermal Barrier Coatings Exposed to Elevated Temperatures. Thin Solid Films, 95, 1983, pp. 265-273.
3. Anonymous: MARC Finite Element Program User Manual, Version K-1, MARC Analysis Research Corp., 1983.

4. Berndt, Christopher C. and Miller, Robert A.: Failure Analysis of Plasma-Sprayed Thermal Barrier Coatings. NASA Technical Memorandum 83777, 1984.
5. Evans, A. G., Crumley, G. B., and Demaray, R. E.: On the Mechanical Behavior of Brittle Coatings and Layers. Oxidation of Metals, v. 20, Nos. 5/6, 1983.
6. Firestone, R. F., Logan, W. R., Adams, J. W., and Bill, R. C.: Creep of Plasma-Sprayed Zirconium Dioxide Thermal Barrier Coatings. Ceramic Engineering and Science Proceedings, 3, 1982, pp. 158-71.

TABLE 1  
MATERIAL PROPERTIES

CASE	MATERIAL	E (MPa)	$\nu$	$\rho$ (gm/cm <sup>3</sup> )	$\alpha$ (m/m/°C)
A-2	Ceramic	$0.0276 \times 10^6$	0.25	5.659	$10.01 \times 10^{-6}$
	Bond Coat	$0.1379 \times 10^6$	0.27	6.990	$15.16 \times 10^{-6}$
	Substrate	$0.1758 \times 10^6$	0.25	7.767	$13.91 \times 10^{-6}$
A-3	Ceramic	$0.0138 \times 10^6$	0.25	5.659	$10.01 \times 10^{-6}$
	Bond Coat	$0.1379 \times 10^6$	0.27	6.990	$15.16 \times 10^{-6}$
	Substrate	$0.1758 \times 10^6$	0.25	7.767	$13.91 \times 10^{-6}$
A-4	Ceramic	$0.0276 \times 10^6$	0.25	5.659	$10.01 \times 10^{-6}$
	Bond Coat	$0.0690 \times 10^6$	0.27	6.990	$15.16 \times 10^{-6}$
	Substrate	$0.1758 \times 10^6$	0.25	7.767	$13.91 \times 10^{-6}$
A-10	Ceramic	$0.0276 \times 10^6$	0.25	5.659	$10.01 \times 10^{-6}$
	Bond Coat	$0.1379 \times 10^6$	0.27	6.990	$15.16 \times 10^{-6}$
	Substrate	$0.1758 \times 10^6$	0.25	7.767	$13.91 \times 10^{-6}$
	Oxidized Layer	$0.3448 \times 10^6$	0.32	3.772	$7.79 \times 10^{-3}$

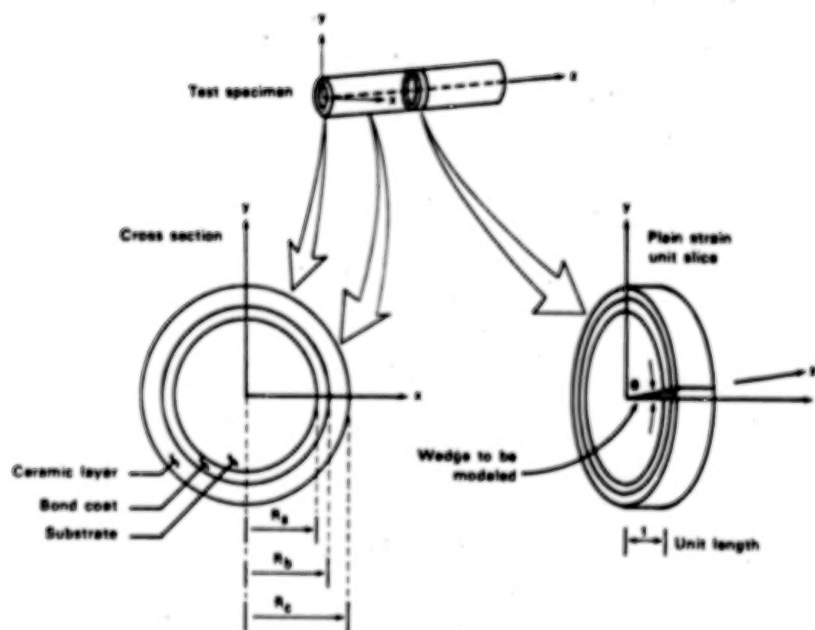


Figure 1. CYLINDRICAL TBC TEST SPECIMEN

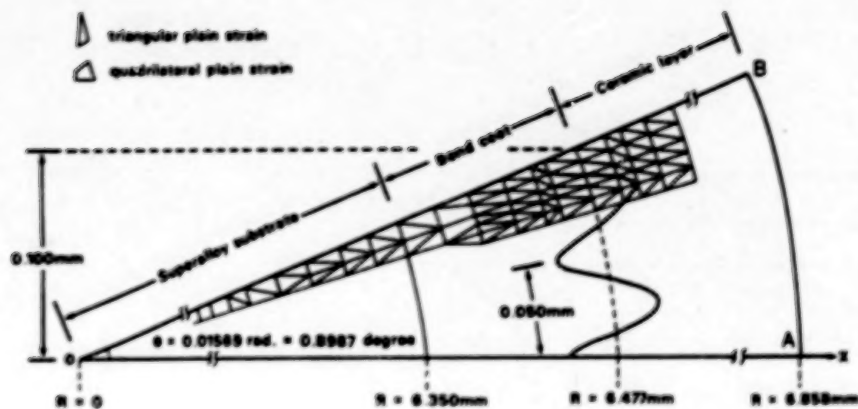


Figure 2. THE TBC FINITE ELEMENT MODEL

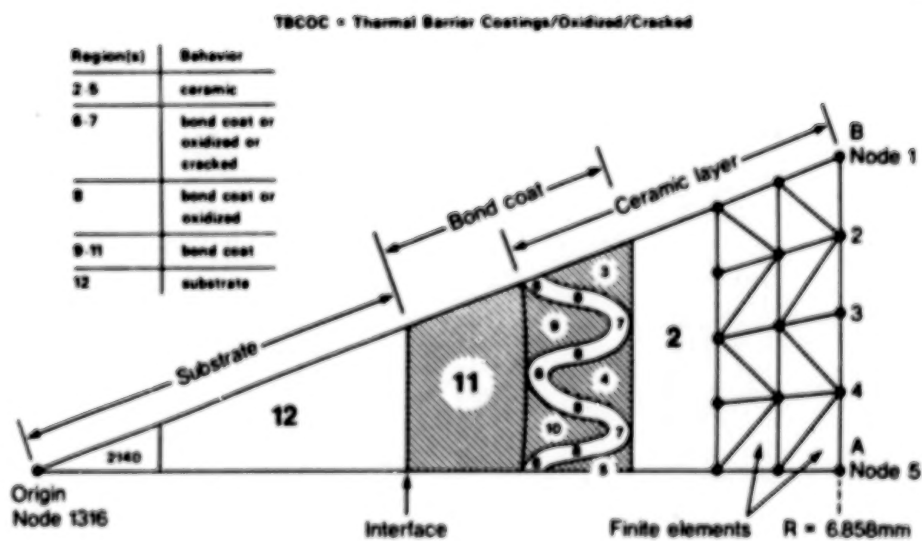


Figure 3. OVERVIEW OF THE ADVANCED TBCOC MODEL

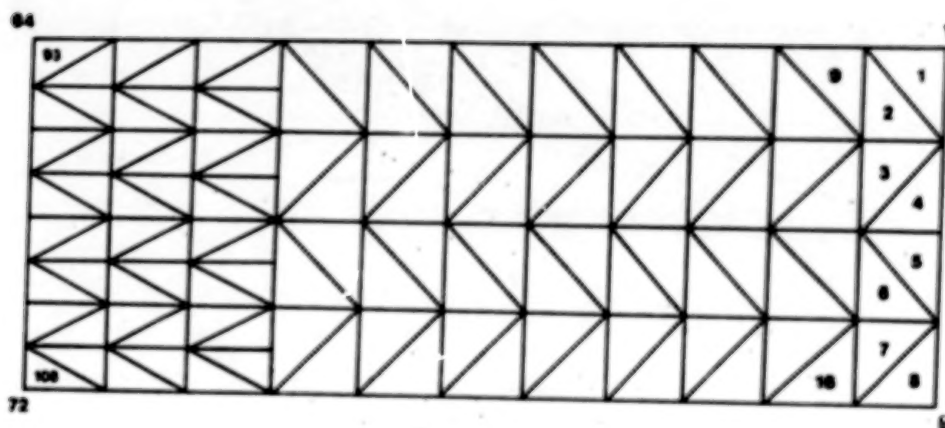


Figure 4. TBCOC MODEL (PART 1)

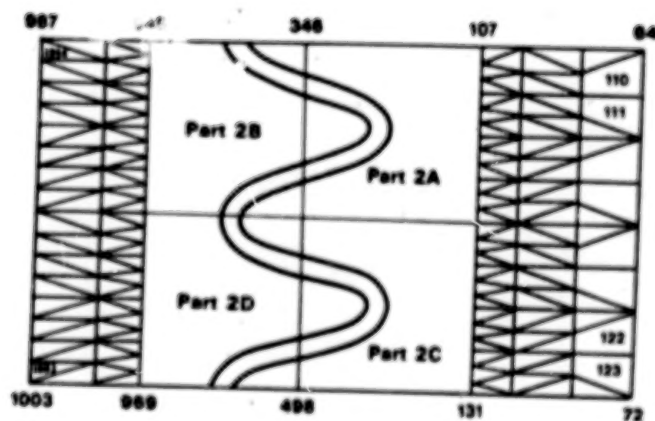


Figure 5. TBCOC MODEL (PART 2)

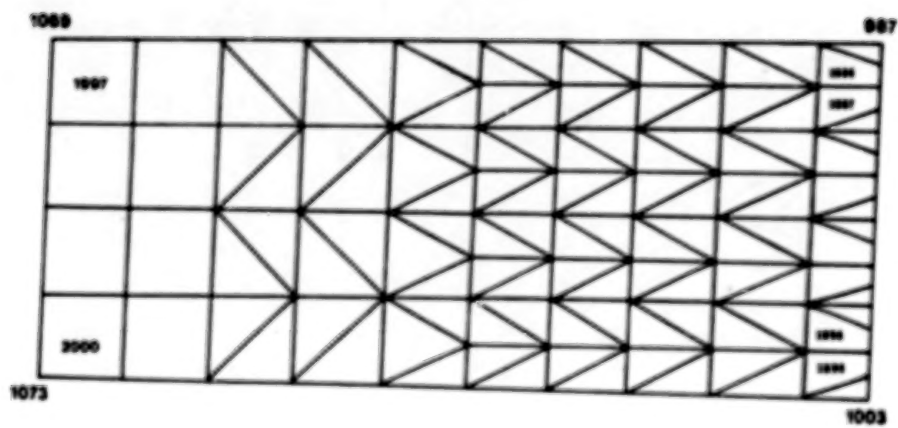


Figure 6. TBCOC MODEL (PART 3)

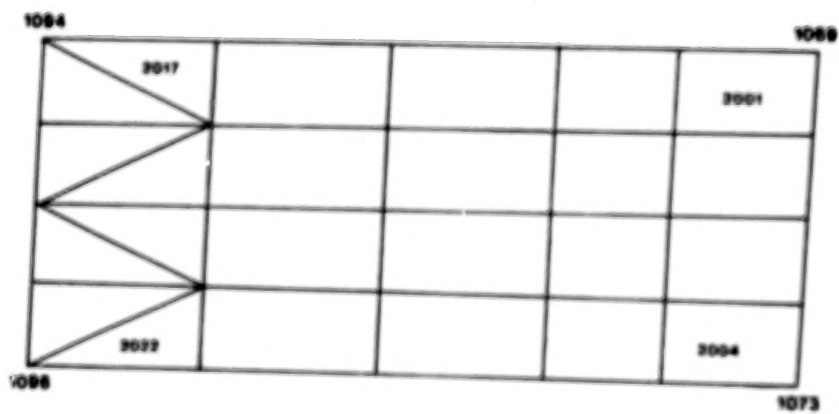


Figure 7. TBCOC MODEL (PART 4)



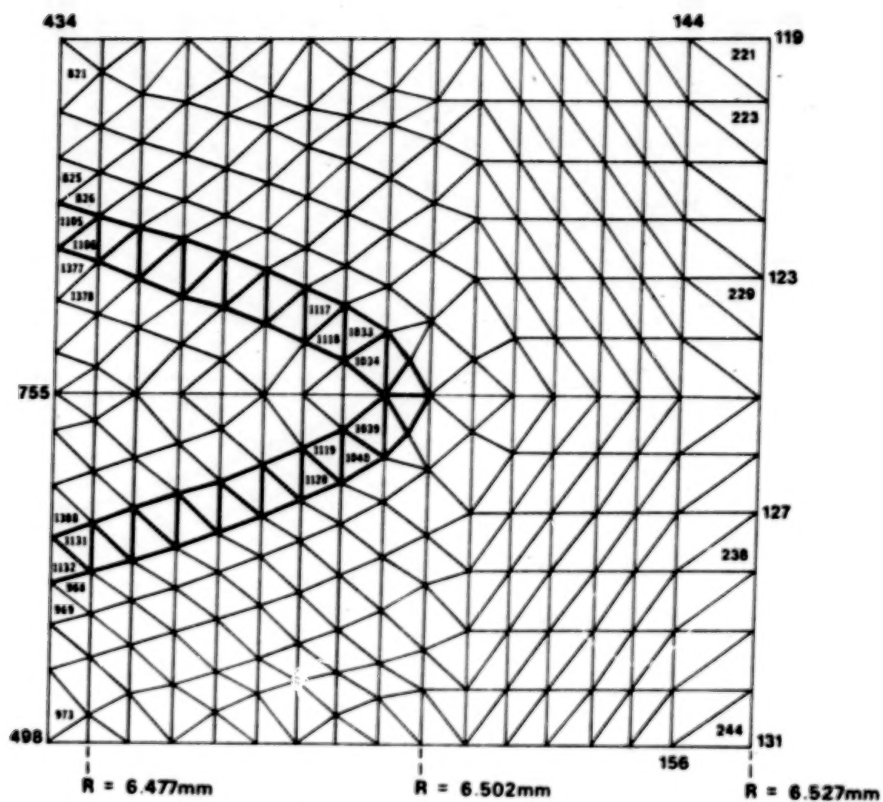


Figure 10. FINITE ELEMENT DETAILS (PART 2C)

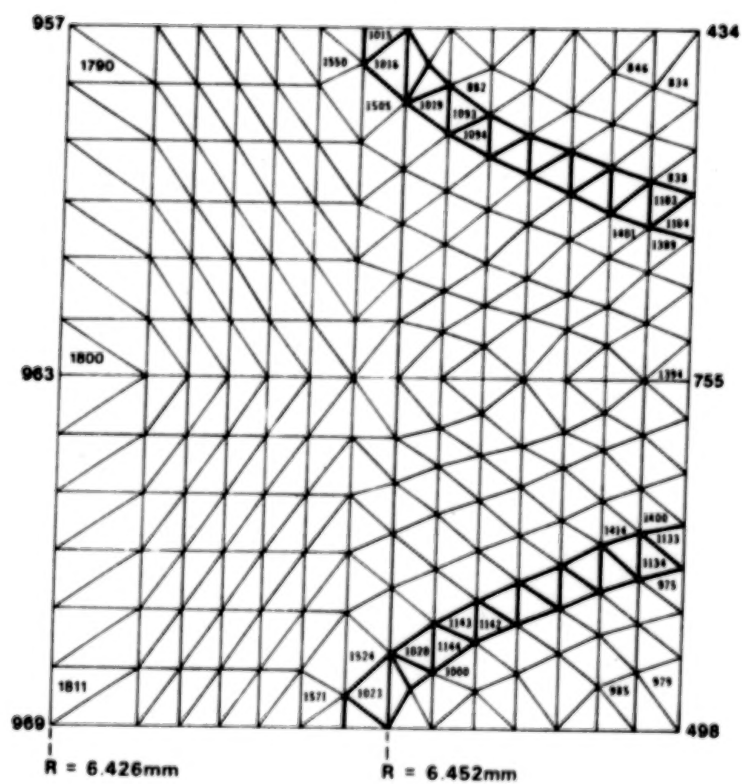


Figure 11. FINITE ELEMENT DETAILS (PART 2D)

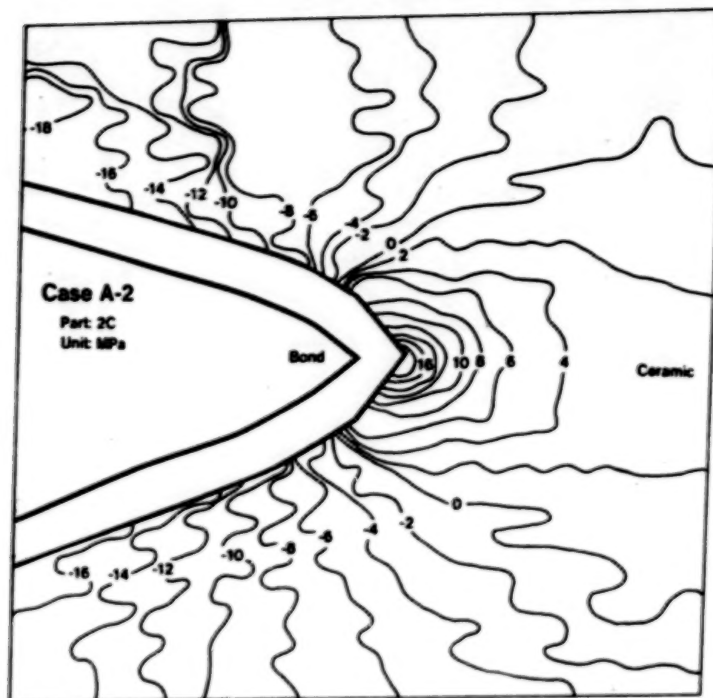


Figure 12. STRESSES IN X - DIRECTION

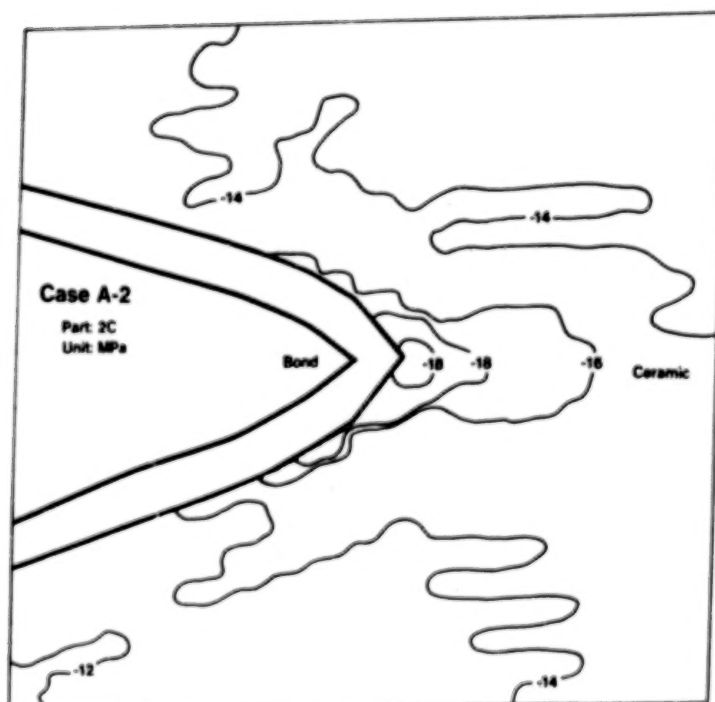


Figure 13. STRESSES IN Y - DIRECTION

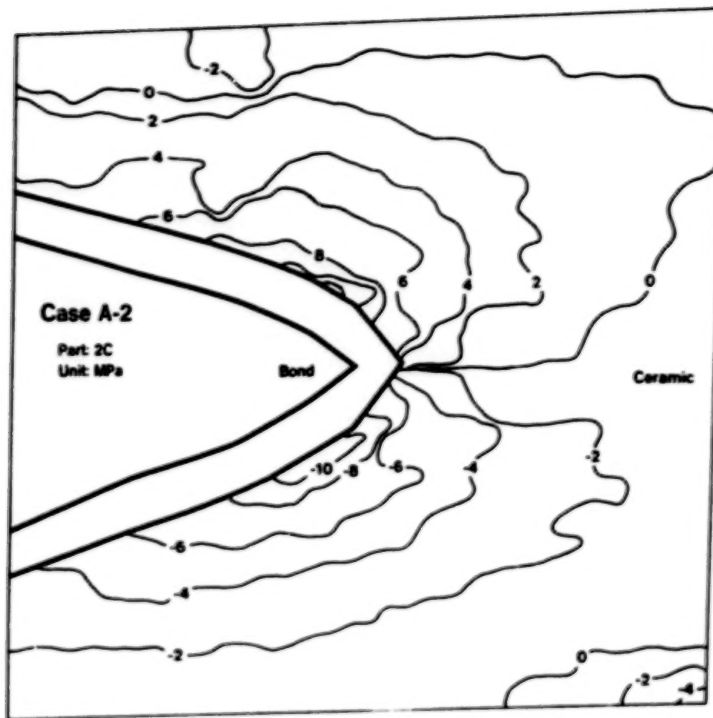


Figure 14. SHEARING STRESSES

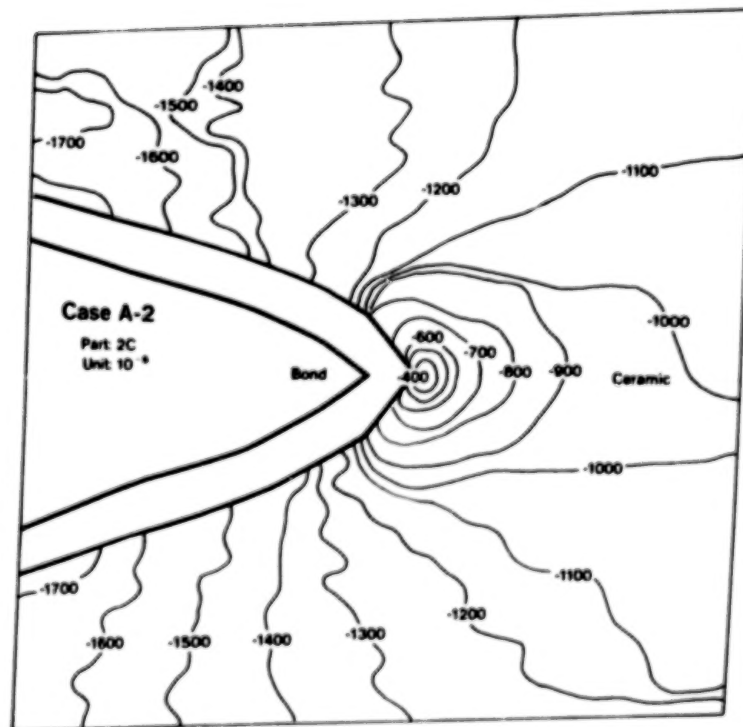


Figure 15. STRAINS IN X - DIRECTION

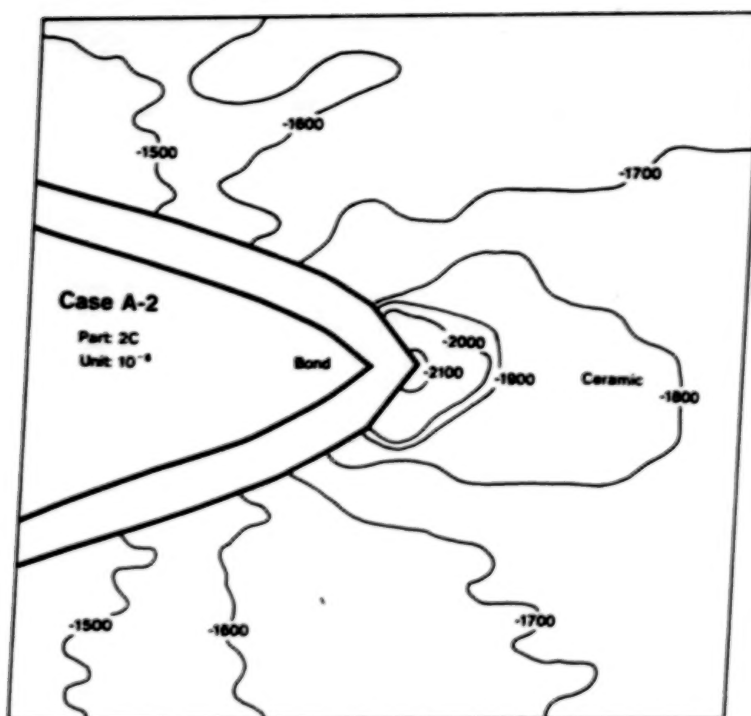


Figure 16. STRAINS IN Y - DIRECTION

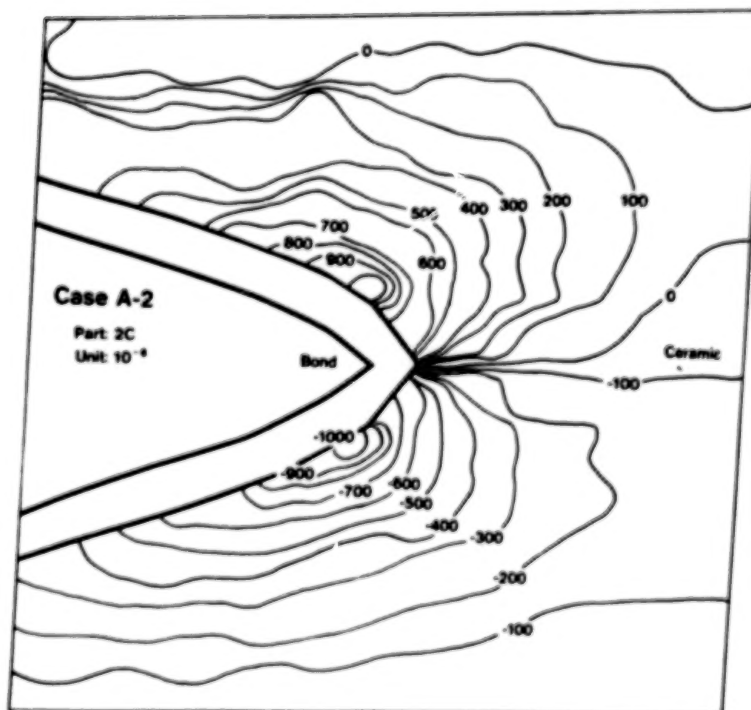


Figure 17. SHEARING STRAINS

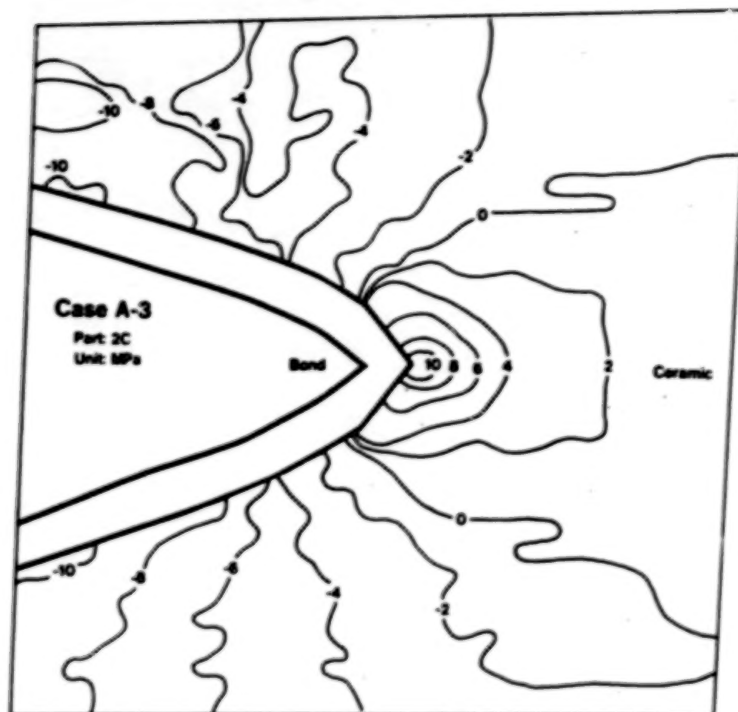


Figure 18. STRESSES IN X - DIRECTION

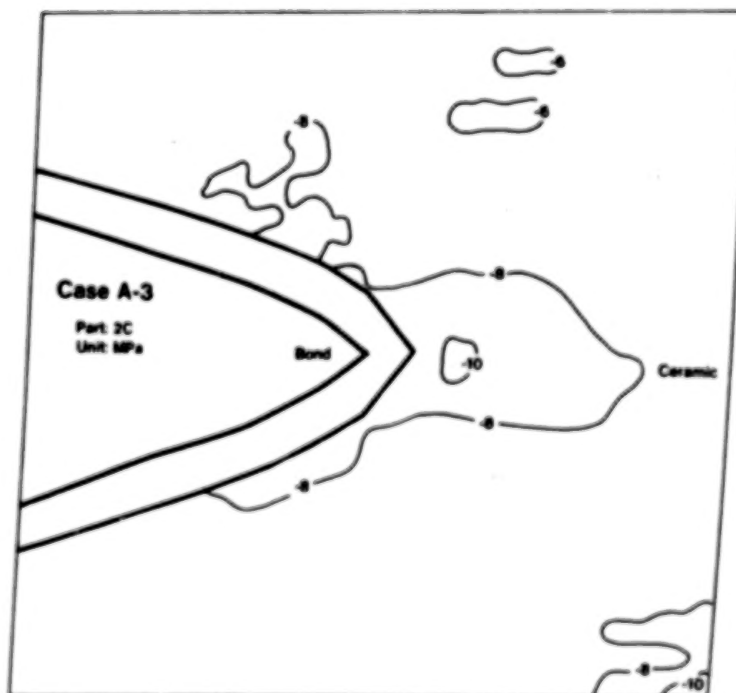


Figure 19. STRESSES IN Y - DIRECTION

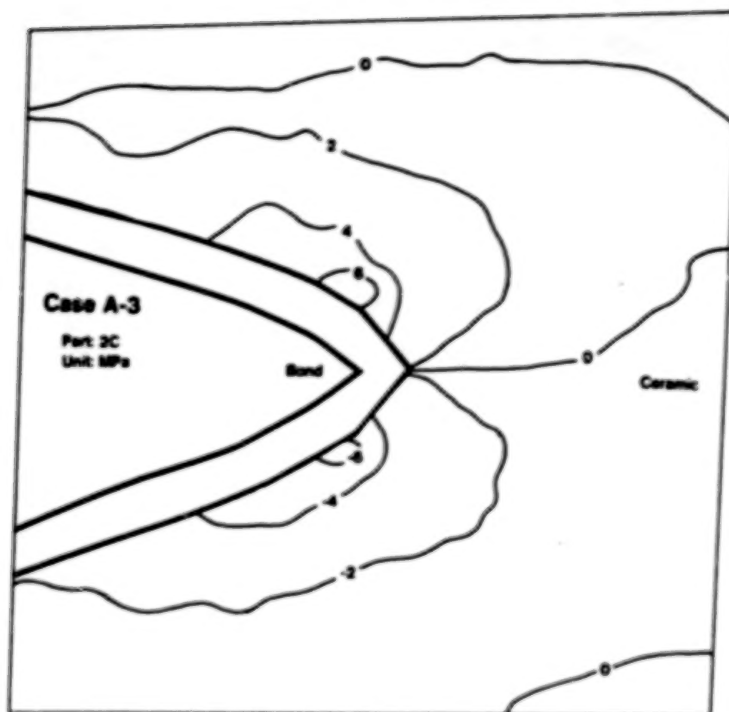


Figure 20. SHEARING STRESSES

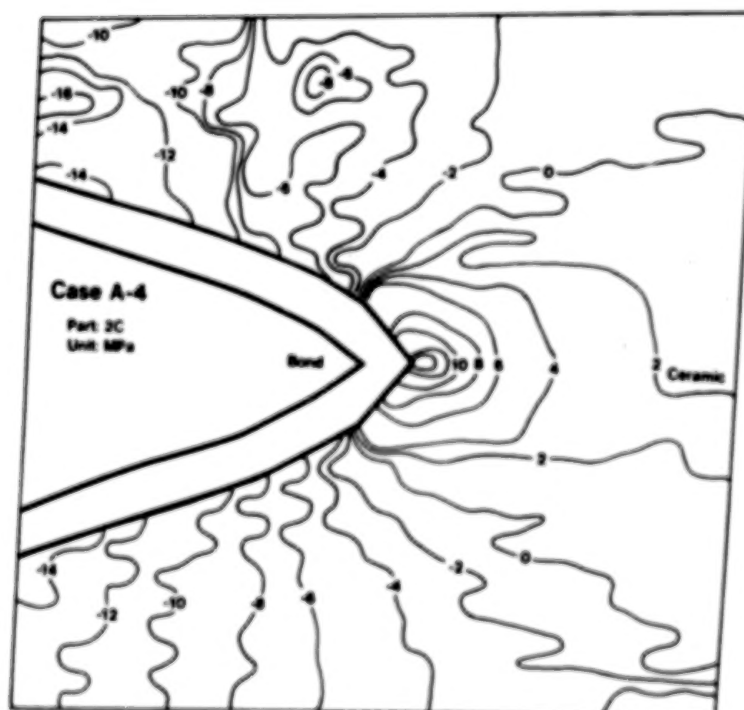


Figure 21. STRESSES IN X - DIRECTION

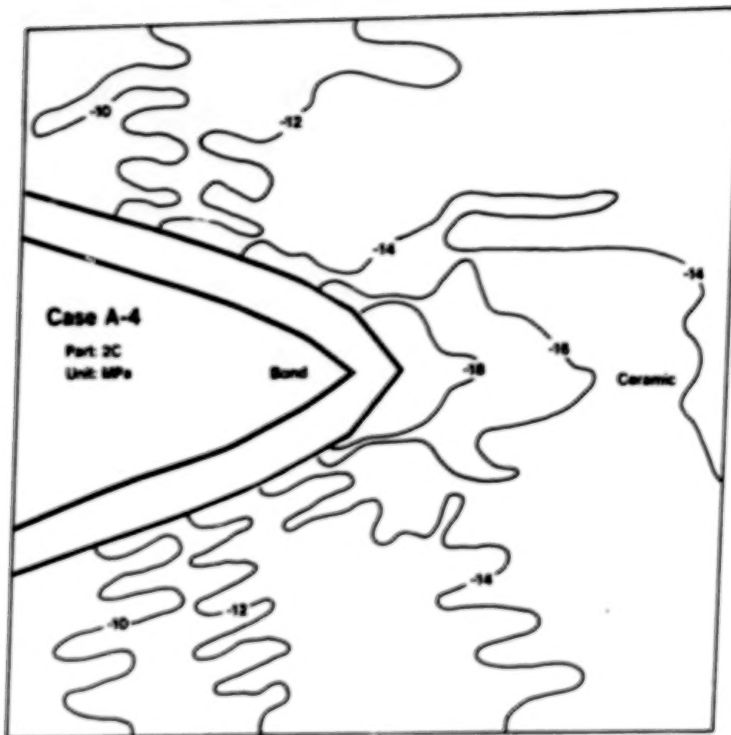


Figure 22. STRESSES IN Y - DIRECTION

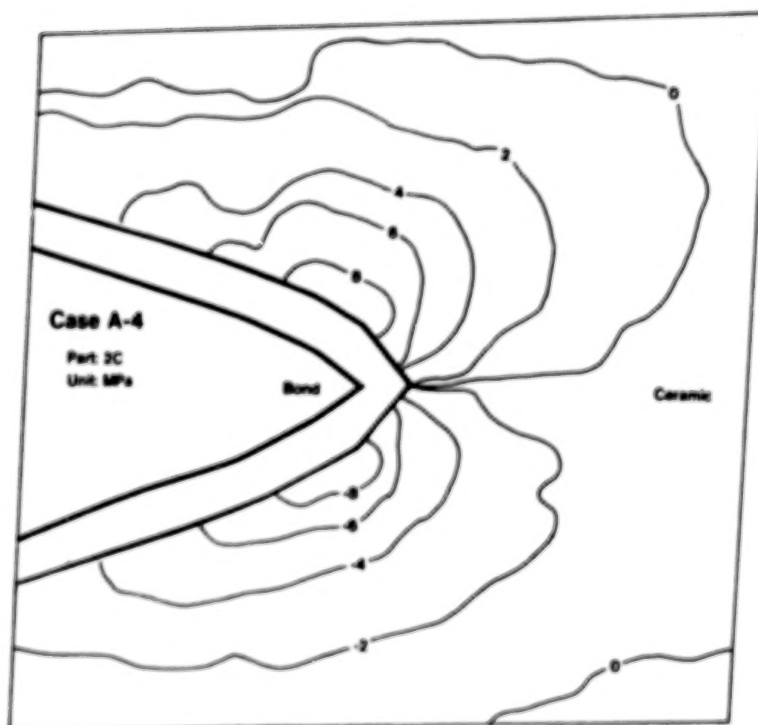
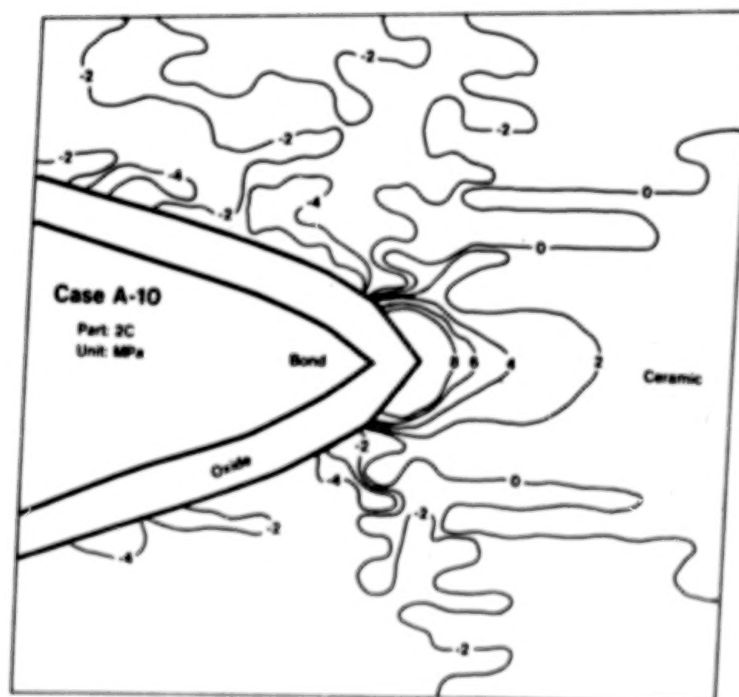
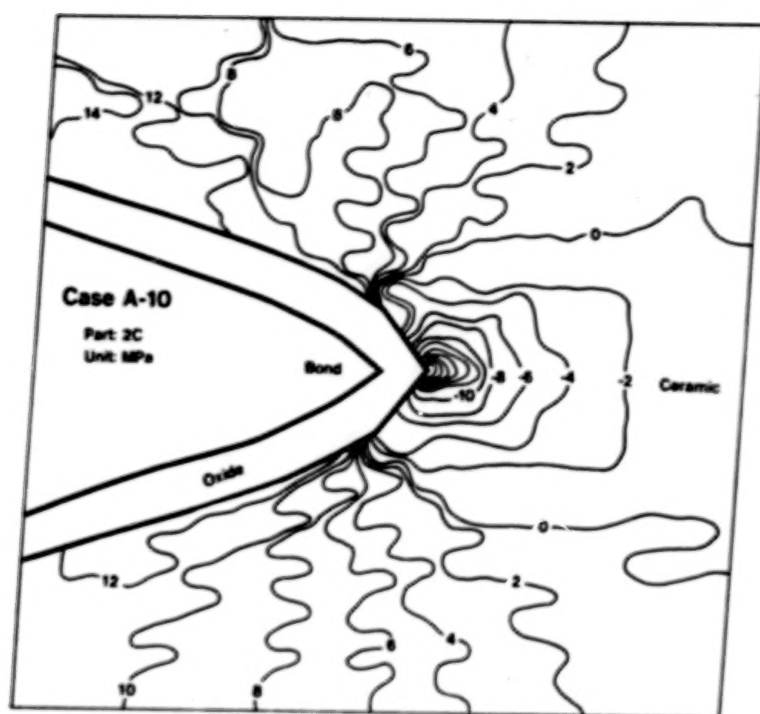


Figure 23. SHEARING STRESSES



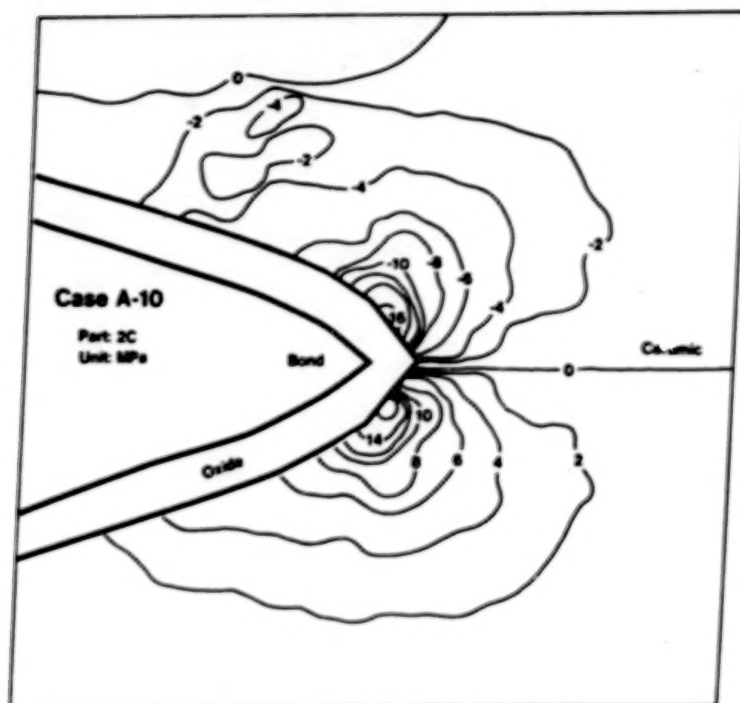
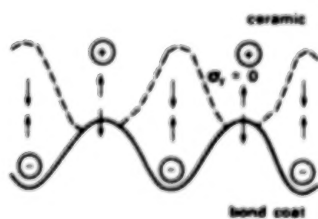


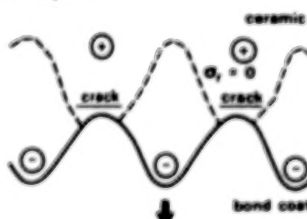
Figure 26. SHEARING STRESSES

PROPOSED MECHANISM FOR OXIDATION INDUCED THERMAL BARRIER COATING FAILURE

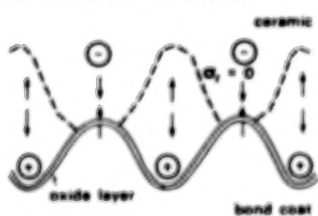
CALCULATED STRESS STATES  
Thermal Expansion Mismatch Radial Stress



PROPOSED CERAMIC RESPONSE  
Microcracking and Microcrack Coalescence at Asperities



Oxidation Growth Radial Stress



Crack Extension Leading to Spalling

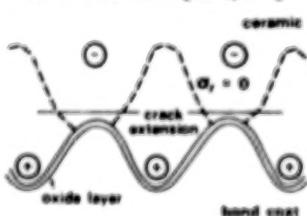


Figure 27. PROPOSED FAILURE MECHANISM

## THERMAL BARRIER COATING LIFE PREDICTION

## MODEL DEVELOPMENT

T.E. Strangman, J.F. Neumann, and A. Tasooji  
Garrett Turbine Engine Company  
Phoenix, Arizona

Thermal barrier coatings (TBC's) for turbine airfoils in high-performance engines represent an advanced materials technology with both performance and durability benefits. The foremost TBC benefit is the reduction of heat transferred into air-cooled components, which yields performance and durability benefits (fig. 1). To achieve these benefits, however, the TBC system must be reliable. Mechanistic thermomechanical and thermochemical life models are therefore required for the reliable exploitation of TBC benefits on gas turbine airfoils. Garrett's NASA HOST Program (NAS3-23945) goal is to fulfill these requirements.

This program focuses on predicting the lives of two types of strain-tolerant and oxidation-resistant TBC systems that are produced by commercial coating suppliers to the gas turbine industry (fig. 2). The plasma-sprayed TBC system, composed of a low pressure plasma sprayed (LPPS) applied oxidation resistant NiCrAlY bond coating and an air plasma sprayed yttria (8 percent) partially stabilized zirconia insulative layer, is applied by both Chromalloy (Orangeburg, New York) and Klock (Manchester, Connecticut). The second type of TBC is applied by the electron beam-physical vapor deposition (EB-PVD) process by Temescal (Berkeley, California).

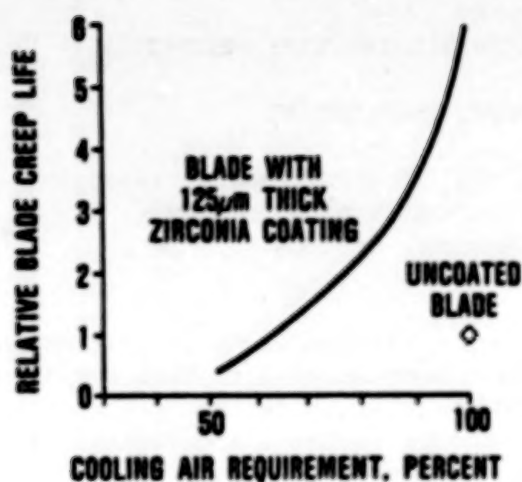
A viable model must predict TBC life on a turbine airfoil as a function of engine, mission, and materials system parameters. These parameters are incorporated into mechanical, oxidation, and salt deposition functions of TBC degradation as indicated in figure 3. The approach adopted in this program for developing a TBC life model is similar to that in use at Garrett for prediction of oxidation/hot corrosion lives of metallic coatings as a function of engine, mission, and materials system parameters (fig. 4). Similarities and differences in these models are illustrated in figure 5.

A rapid computational capability is required for preliminary design and mission analyses of TBC lives. Substructure models are being developed to facilitate the rapid computation of TBC life as indicated in figure 6. TBC life analysis will be performed for each of the critical damage modes.

Burner rig and mechanical property data are being obtained to quantify the capabilities of each of the TBC systems for each critical mode of degradation. Burner rig test data and zirconia fracture toughness data are illustrated on figures 7 and 8.

Lives of these TBC systems will be predicted for TFE731 high pressure turbine blades for factory engine test, business aircraft and maritime surveillance missions. Complementary engine validation tests are planned.

This program is now at the midpoint of Phase I. The program schedule is provided in figure 9.



GS-195-1

Figure 1. TBCs Improve Creep Life and Reduce Cooling Air Requirements for the Garrett High-Pressure Turbine Blade.

PLASMA SPRAY	ELECTRON BEAM — PHYSICAL VAPOR DEPOSITION	
APS Y <sub>2</sub> O <sub>3</sub> (8%) STABILIZED ZrO <sub>2</sub>	EB-PVD Y <sub>2</sub> O <sub>3</sub> (20%) STABILIZED ZrO <sub>2</sub>	<u>TBC</u>
LPPS Ni-31Cr-11Al-0.5Y	EB-PVD Ni-23Co-18Cr-11Al-0.3Y	<u>BASE COAT</u>
MAR-M 247 SUPERALLOY	MAR-M 247 SUPERALLOY	<u>SUBSTRATE</u>
• CHROMALLOY • KLOCK	• TEMESCAL	

GS-195-2

Figure 2. Life Prediction Models are Being Developed for Plasma-Sprayed and EB-PVD TBC Systems.

TBC  
DEGRADATION  
RATE

=  $F_1$  (MECHANICAL)

- COATING STRESSES
- TEMPERATURE
- MATERIAL SYSTEM
  - $K_{IC}$
  - FLAW SIZE
  - ELASTIC MODULUS
  - SPALLING STRAIN

+  $F_2$  (OXIDATION)

- TEMPERATURE
- CYCLE SEGMENT LENGTH
- MATERIALS SYSTEM

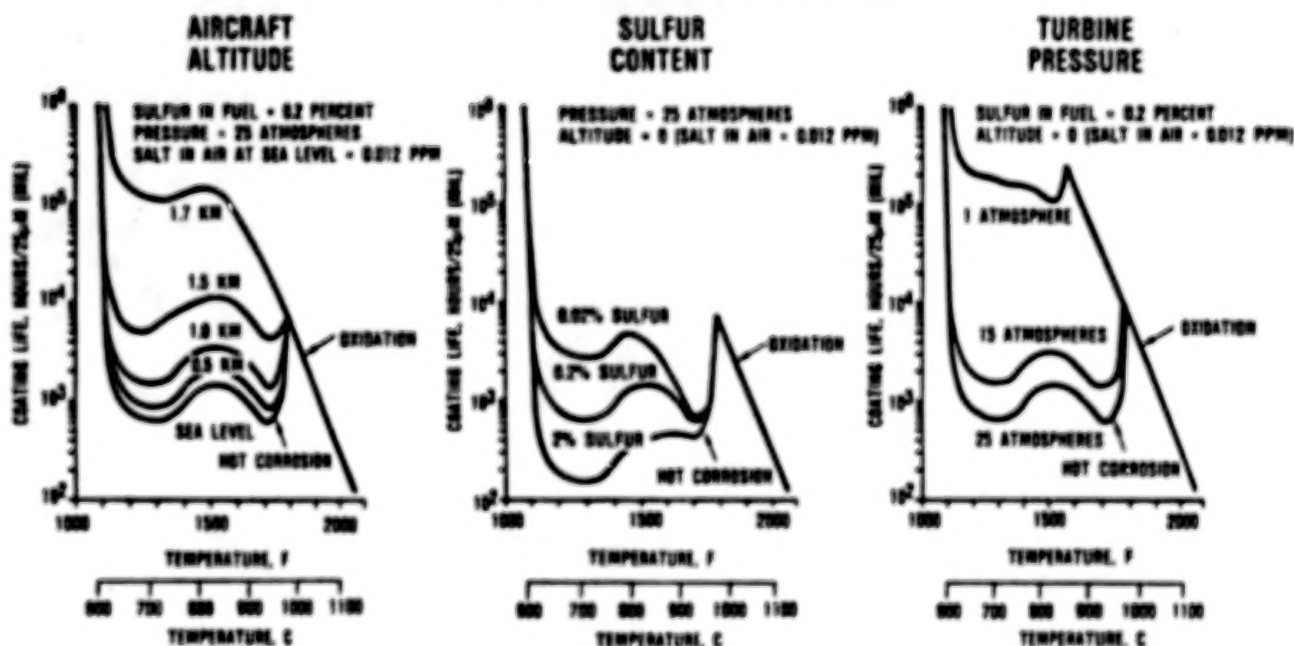
+  $F_3$  (SALT DEPOSITION)

- ALTITUDE (SALT INGESTION)
- TURBINE PRESSURE
- SALT EVAPORATION
- SALT SOLIDIFICATION
- TEMPERATURE
- GAS VELOCITY
- AIRCRAFT LOCATION
- MATERIALS SYSTEM

85-195-3

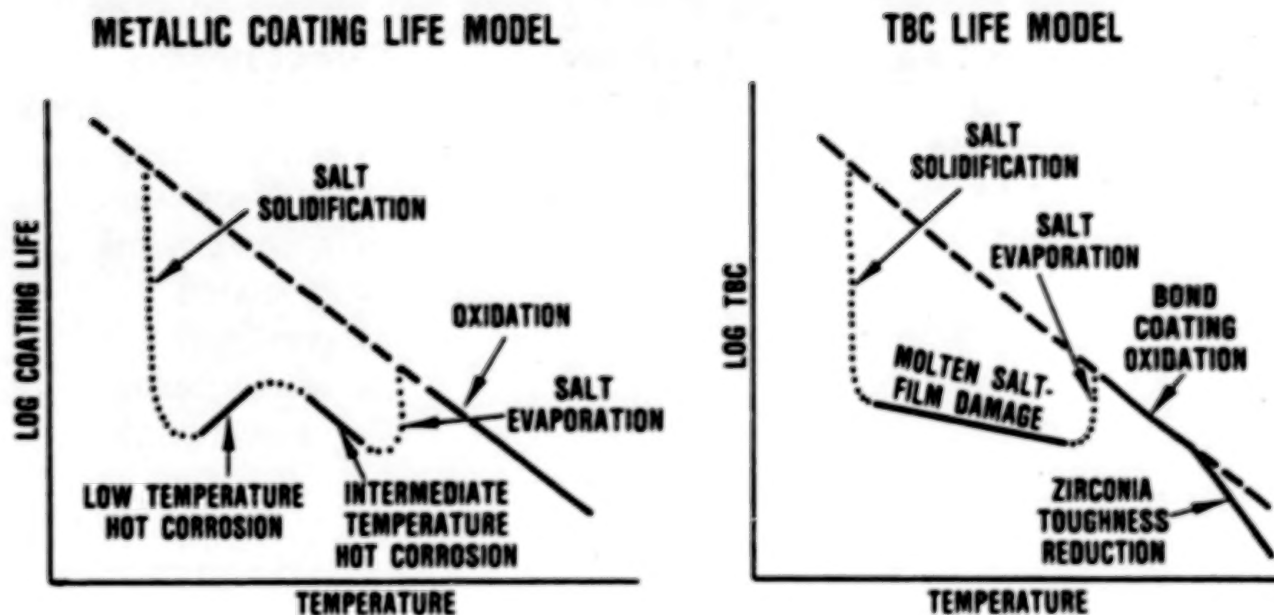
Figure 3. TBC Life is a Function of Engine, Mission and Materials System Parameters.

### ENGINE AND MISSION PARAMETERS



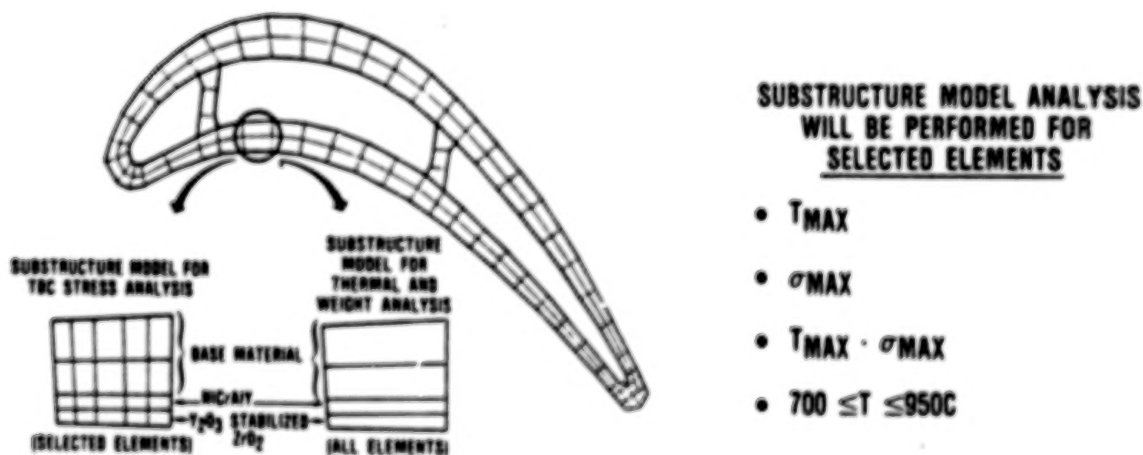
85-195-4

Figure 4. Turbine Airfoil Coating Life Predicted by Computer Model.



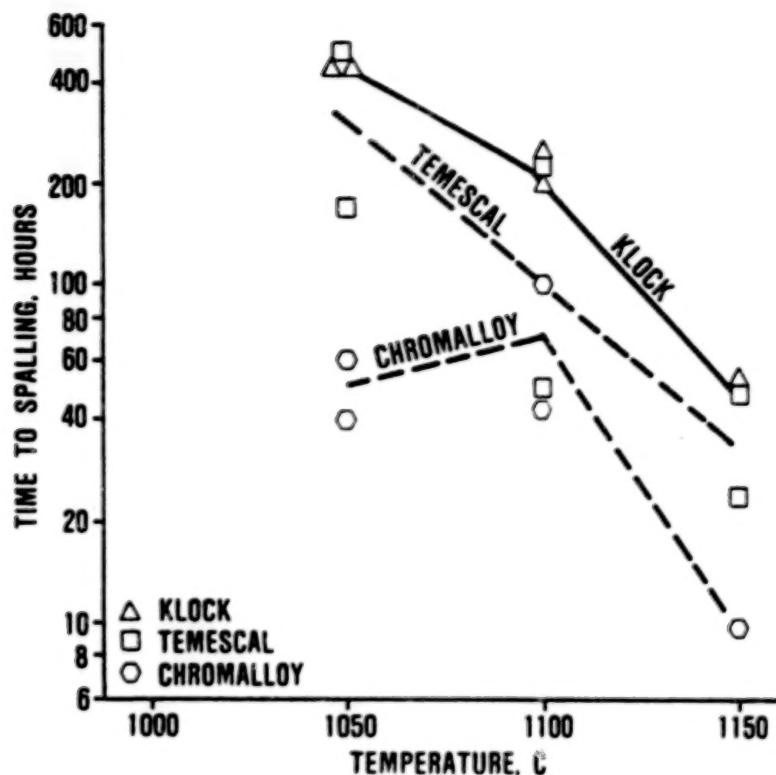
65-105-3

Figure 5. Approach to TBC Life Model Development is Facilitated by GTEC Metallic Coating Life Model.



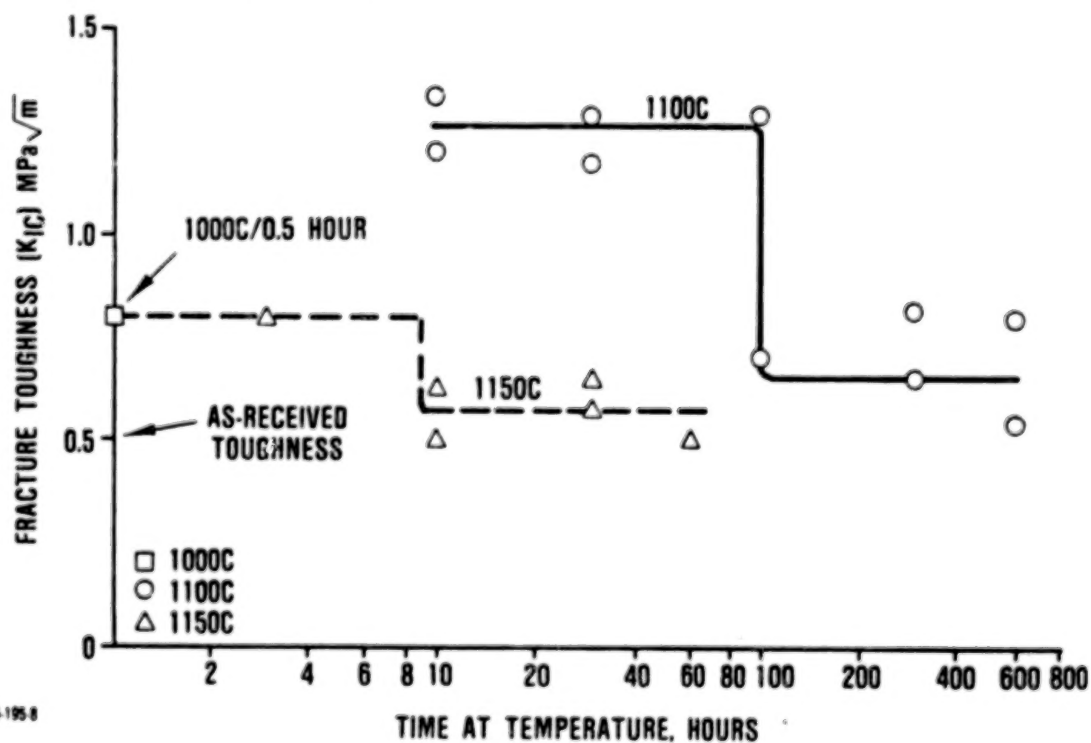
65-105-4

Figure 6. Substructure Models Facilitate the Rapid Computation of TBC Life Required for Preliminary Design and Mission Analysis.



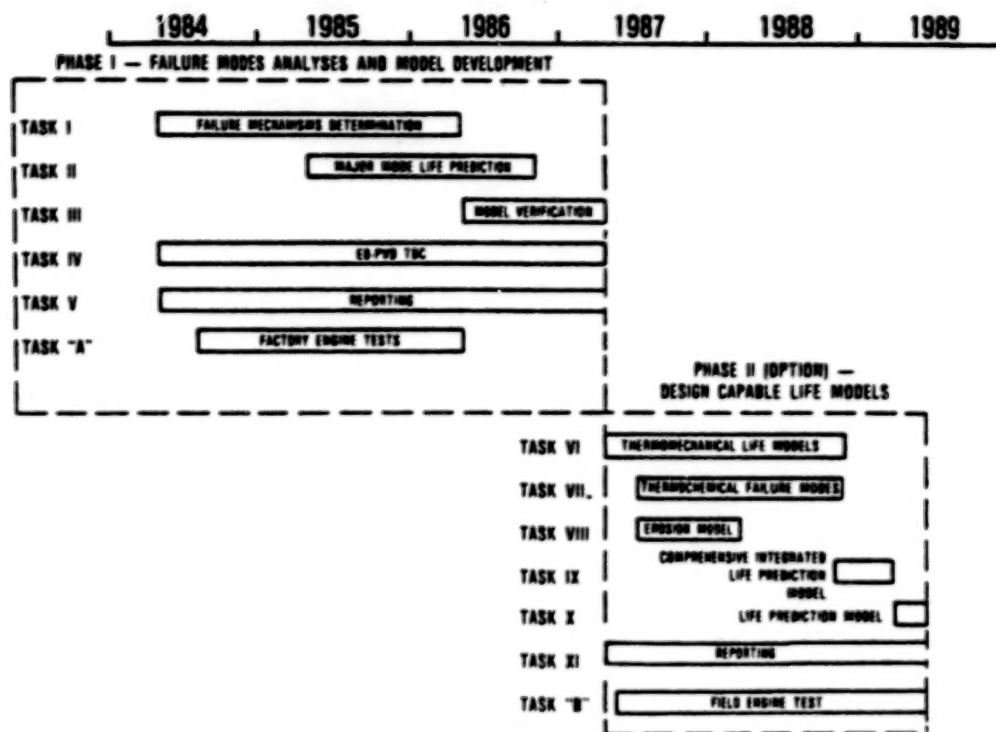
GS-1957

Figure 7. TBC Spalling in Burner Rig Test is a Function of Temperature.



GS-1958

Figure 8. Zirconia Fracture Toughness of Chromalloy Plasma-Sprayed TBC System is a Step Function of Exposure Time and Temperature.



GS-195-9

Figure 9. TBC Life Prediction Schedule.

## THERMAL BARRIER COATING LIFE PREDICTION MODEL DEVELOPMENT\*

R.V. Hillery, B.H. Pilsner, E.C. Duderstadt  
General Electric  
Aircraft Engine Business Group

The objectives of this program are to determine the predominant modes of degradation of a plasma sprayed thermal barrier coating system, and then to develop and verify life prediction models accounting for these degradation modes. The program is divided into two phases, each consisting of several tasks. The work in Phase I is aimed at identifying the relative importance of the various failure modes, and developing and verifying a life prediction model(s) for the predominant mode for a thermal barrier coating system. Two possible predominant failure mechanisms being evaluated are bond coat oxidation and bond coat creep. The work in Phase II will develop design-capable, causal, life prediction models for thermomechanical and thermochemical failure modes, and for the exceptional conditions of foreign object damage and erosion.

TBC SYSTEMS

The primary TBC system consists of a low pressure plasma-sprayed (LPPS) bond coat layer of Ni-22Cr-10Al-0.3Y, an air plasma sprayed yttria partially stabilized zirconia ( $ZrO_2$ -8% $Y_2O_3$ ) top coat, on a conventionally cast Rene '80 substrate alloy (Table 1). This bond coat composition has been demonstrated to possess good oxidation resistance and has a large data base as a TBC bond coat. The  $ZrO_2$ -8% $Y_2O_3$  top coat was chosen since numerous studies have shown that zirconia partially stabilized with 6-8 wt.%  $Y_2O_3$  is the best composition for plasma sprayed TBC's (1). The Rene '80 substrate was chosen since a large TBC data base is present for this substrate composition.

Four different TBC systems utilizing four different bond coats are being evaluated in the experiment to evaluate the effect of bond coat creep strength on TBC thermal cycle life (Table 2). These four TBC systems also utilize  $ZrO_2$ -8% $Y_2O_3$  top coats and Rene '80 substrates. TBC system #1 has the same NiCrAlY bond coat utilized in the primary TBC system. TBC systems #2, #3, and #4 have modified NiCrAlY bond coats which have received alloy additions to increase the bond coat creep strength. An aluminide overcoat is used in each of these systems (1-4) to reduce differences in oxidation resistance for the four bond coats. A comparison of the primary TBC system and its counterpart with an aluminide overcoat as the bond coat is shown in Figure 1.

THERMAL CYCLE TESTING

Thermal cycle testing is being performed in an automated Rapid Temperature Furnace (Figure 2). The thermal cycles consists of ten minutes heat up, a 45 minute exposure at 1093°C (2000°F), and 15 minutes forced air cooling. This furnace utilizes a lift which automatically cycles the specimens from the upper furnace exposure zone to the lower cooling compartment where a fan provides forced air cooling.

\*Work done under NASA Contract NAS3-23943.

## PRE-EXPOSURES IN AIR AND ARGON

In both the bond coat oxidation and bond coat creep evaluations, pre-exposures in air and argon have been utilized to evaluate the effect of bond coat oxidation on thermal cycle life. The specimens after each of the pre-exposure conditions (as-sprayed, argon, and air pre-exposures) are shown in Figure 3. The specimens pre-exposed in argon have top coats that are gray in appearance which can be attributed to oxygen deficiency, while the bond coat's silver color is indicative of the lack of significant oxidation. The specimens pre-exposed in air show that the bond coats have darkened due to oxidation, while the top coat's yellow appearance is typical of elevated temperature air exposure.

## BOND COAT OXIDATION EXPERIMENT

In the bond coat oxidation experiment, pre-exposures in air and argon for different pre-exposure times were utilized. The goal of pre-exposures in air was to develop oxide scales prior to thermal cycling, while the goal of the pre-exposures in argon was to allow the other thermally activated phenomena present in the air pre-exposures to occur without developing the oxide scale. This should allow isolation of the effects of bond coat oxidation. Pre-exposures utilized were 10, 50, 100, and 500 hours both in air and argon. The oxide scale thicknesses of the air pre-exposures are plotted as a function of pre-exposure time in Figure 4.

Unexpectedly, the specimens pre-exposed in argon failed before the specimens pre-exposed in air (Figure 5). The initial hypothesis for this unexpected result is that a phase distribution change may be occurring in the ceramic top coat. Another surprising result was the longer lives for the specimens pre-exposed in air for 10 hours. The longer lives for these specimens than for the as-sprayed specimens may be due to bond coat sintering and perhaps top coat sintering. The sintering results in less constraint for the  $\text{Al}_2\text{O}_3$  scale, while providing better top coat/bond coat adherence (improved chemical bonding).

Failure for these specimens was defined as when 10% (surface area) of the ceramic top coat has spalled (Figure 6). In all cases spalling initiated at the edges of the top coat. The failure location was the same for all pre-exposure conditions and occurred in the ceramic approximately 0.0025-0.0050 cm (0.001-0.002") from the bond coat/top coat interface.

Differences due to argon and air pre-exposures are clearly reflected in the pre-exposed, specimen microstructures (Figure 7). In all cases, a continuous  $\text{Al}_2\text{O}_3$  film formed at the bond coat/top coat interface for specimens pre-exposed in air. The effect of oxidation is also seen in the bond coat microstructure where depletion of the high Al  $\beta$  phase is observed at the bond coat/top coat interface. The effect of interdiffusion in depletion of the high Al  $\beta$  phase in the bond coat is also observed at the bond coat substrate interface. The argon pre-exposures, on the other hand, significantly retarded bond coat oxidation. The effectiveness is demonstrated by the small degree of  $\beta$  depletion (high Al phase) in the bond coat at the bond coat/top coat interface and the absence of  $\text{Al}_2\text{O}_3$  scale. These photomicrographs also show that significant interdiffusion that has occurred between the substrate and bond coat.

Differences due to argon and air pre-exposures are still reflected in the pre-exposed, specimen microstructure after thermal cycling. The microstructure of the specimen pre-exposed in argon after thermal cycling shows that very little  $\beta$  depletion has occurred in the bond coat at the bond coat/top coat interface. This is due to the argon pre-exposure and the short thermal cycle lives of these specimens (i.e. very little oxidation has occurred). This is contrasted with the microstructure of the specimens pre-exposed in air after thermal cycling where significantly more  $\beta$  depletion has occurred resulting in a larger  $\gamma$  layer at the bond coat/top coat interface. This illustrates the increased demand to continue the growth of the  $\text{Al}_2\text{O}_3$  scale. Something that may be necessary to include in our model is the effect that a changing bond coat microstructure has on TBC integrity.

Oxide scale thickness measurements after thermal cycling indicate that bond coat oxidation may be a significant contribution to the failure mechanism. The oxide scale thickness after thermal cycling for the specimens pre-exposed in air and the specimens receiving no-pre-exposure are plotted in Figure 8. The plot shows that the oxide scale is essentially the same for the specimens regardless of pre-exposure time with the exception of the 500 hr. pre-exposure. This indicates that bond coat oxidation may be important. The 500 hr. pre-exposure result indicates this 4  $\mu\text{m}$  oxide scale thickness is not large enough to cause failure if other thermally activated phenomena have not occurred. The oxide scales for the specimens pre-exposed in argon were less than 1  $\mu\text{m}$  thick.

#### BOND COAT CREEP EFFECT EXPERIMENT

As mentioned previously, the bond coat creep effect experiment utilized four bond coats all of which had received aluminide over coats to reduce differences in oxidation resistance. Again, pre-exposures in air and argon were utilized (100 hr. pre-exposures). The results for air and argon pre-exposures again show that pre-exposures in argon are more detrimental than air pre-exposures (Figure 9). Also as expected, the TBC's with the NiCrAlY bond coat, which has the lowest bond coat creep strength, also had the lowest thermal cycle life. However, the separation between the other three bond coat creep systems is not clear. These results are also true for the specimens that received no pre-exposure (Figure 10). It is believed that the bond coat creep difference between these three particular systems (2, 3, 4) is not large enough to offset the effects of other contributions to failure. A new bond coat which has been developed at GE which has a creep strength lower than the three and closer to the bond coat creep strength of NiCrAlY will be used in future testing to demonstrate this effect more definitively.

#### KEY PROPERTY DETERMINATIONS

Key property determinations of the bond coat and the top coat will also be made in this study. The methods and conditions are listed in Figure 11. Generally, conventional testing can be utilized for the bond coat materials, whereas special testing is needed for the ceramic coatings.

#### TBC LIFE PREDICTION MODEL

The failure mechanism evaluations and key property determinations will then be coupled with thermomechanical studies to develop the life prediction models. Initial studies are aimed at determining the magnitude of strains present. The work will be done utilizing a tubular LCF bar, permitting internal cooling to develop thermal gradients (Figure 12) . These initial studies will be used to set up a modified test matrix of experiments based on the initial studies to generate the thermomechanical data for the model.

1. Stecura, S. "Effects of Compositional Changes on the Performance of a Thermal Barrier Coating System," NASA TM 78976, 1979.
2. Miller, R.A., Garlick, R.G., and Smialek, J.L., "Phase Distributions in Plasma Sprayed Zirconia - Yttria," American Ceramic Society Bulletin, V.62, Dec. 1983, p. 1355-1358.

Table 1

### Baseline Thermal Barrier Coating System (Weight Percent)

- Substrate (Rene'80): **Ni-14Cr-9.5Co-5Ti-4W-4Mo-3Al-0.17C-0.3Zr-0.015B**
- Bond Coating: **Ni-22Cr-10Al-0.3Y (Low Pressure Plasma Spray)**
- Top Coating: **ZrO<sub>2</sub> - 8Y<sub>2</sub>O<sub>3</sub> (Air Plasma Spray)**

Table 2

### Bond Coat Creep Effect TBC Systems

Systems	Substrate/Bond Coating/Over Coating/Top Coating	Bond Coat Creep (Larson/Miller Parameter at 3 ksi — rupture test)
1	Rene'80/Bond Coating 1*/Aluminide/ZrO <sub>2</sub> -Y <sub>2</sub> O <sub>3</sub>	39.0
2	Rene'80/Bond Coating 2*/Aluminide/ZrO <sub>2</sub> -Y <sub>2</sub> O <sub>3</sub>	45.7
3	Rene'80/Bond Coating 3*/Aluminide/ZrO <sub>2</sub> -Y <sub>2</sub> O <sub>3</sub>	47.0
4	Rene'80/Bond Coating 4*/Aluminide/ZrO <sub>2</sub> -Y <sub>2</sub> O <sub>3</sub>	48.4

\* Ni-22Cr-10Al-0.3Y

\* Modified NiCrAlY Bond Coats

## As Sprayed TBC Microstructures

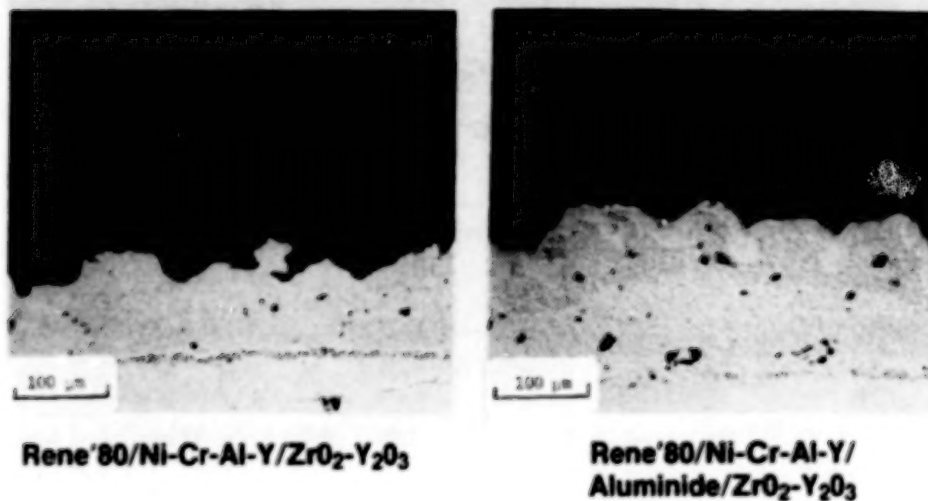


Figure 1 As-sprayed TBC microstructures



Figure 2 Rapid-temperature furnace

ORIGINAL PAGE IS  
OF POOR QUALITY

ORIGINAL PAGE IS  
OF POOR QUALITY

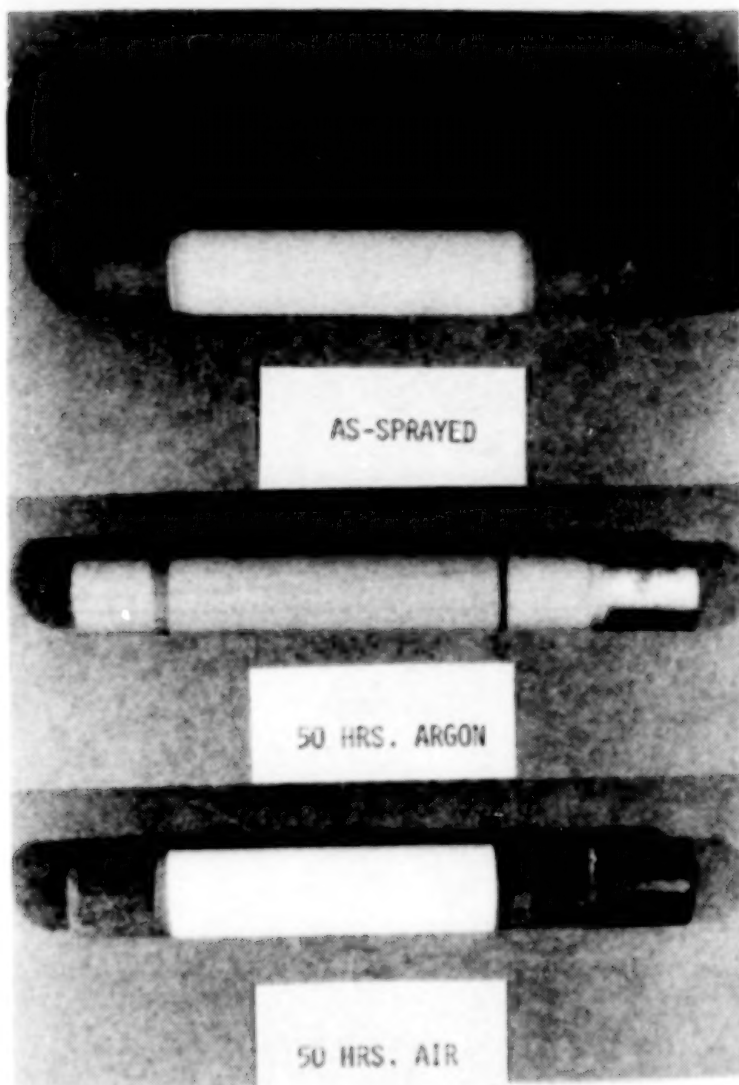


Figure 3 Specimens prior to thermal cycle testing

### Oxidizing Pre-Exposure at 2000°F

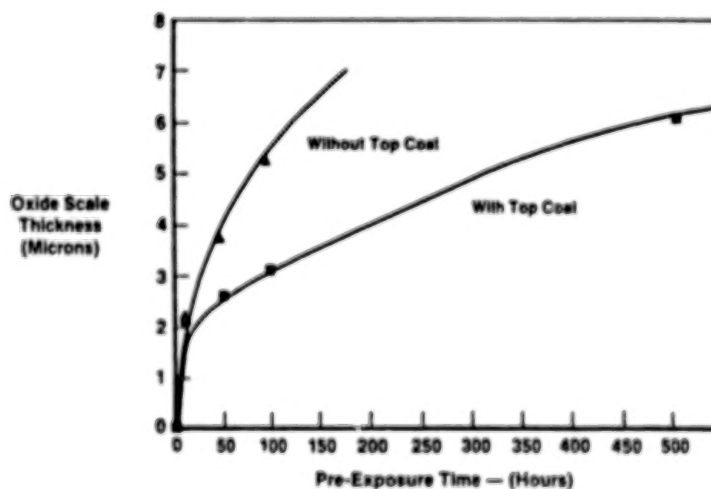


Figure 4

# **Rapid Temperature Thermal Cycle Test at 2000°F** **45 Minute Exposure — 15 Minute Cool Down**

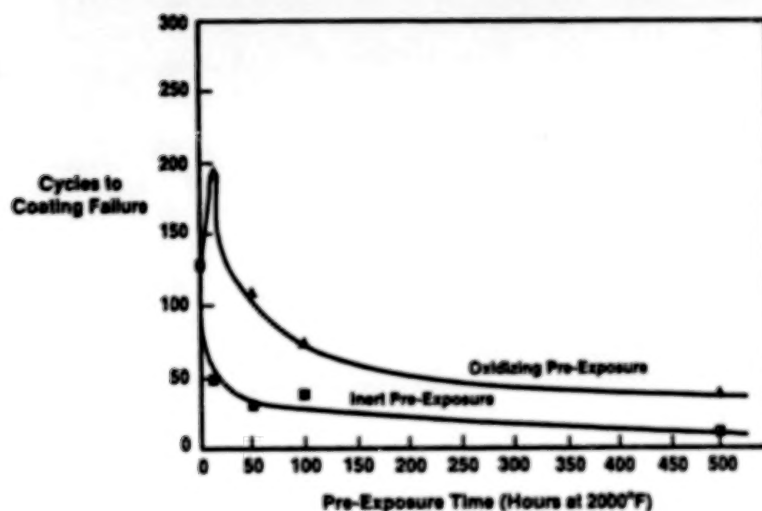


Figure 5

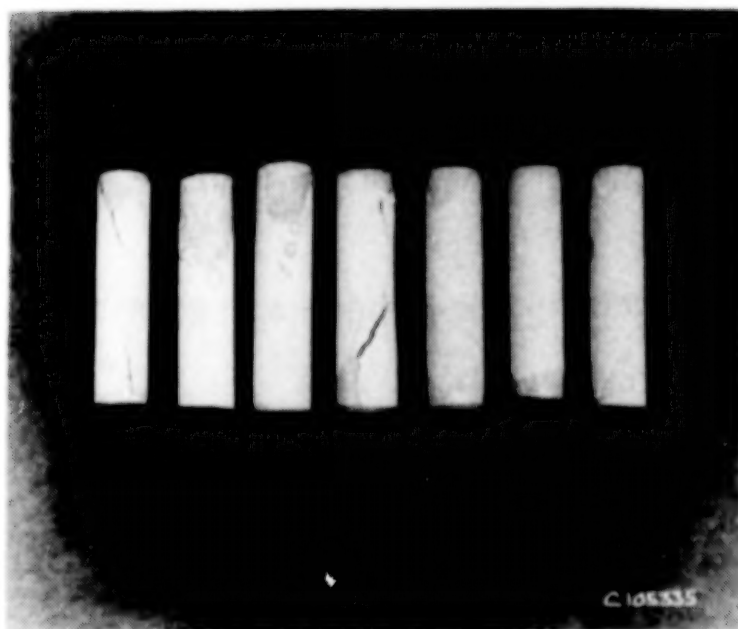


Figure 6 Failed specimens after thermal cycle testing

ORIGINAL PAGE IS  
 OF POOR QUALITY

# NiCrAlY Bond Coat

100 Hour Air Pre-Exposure



After Pre-Exposure



After Thermal Cycling

100 Hour Argon Pre-Exposure



After Pre-Exposure



After Thermal Cycling

Figure 7

ORIGINAL PAGE IS  
OF POOR QUALITY

# $\text{Al}_2\text{O}_3$ Scale Thickness at Failure After Thermal Cycle Testing (NiCrAlY Bond Coat)

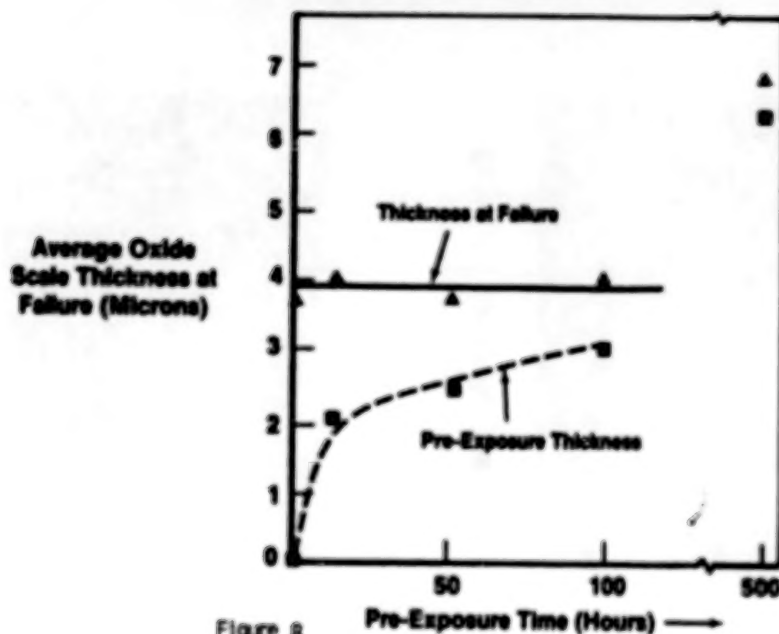


Figure 8

## 100 Hour Pre-Exposure

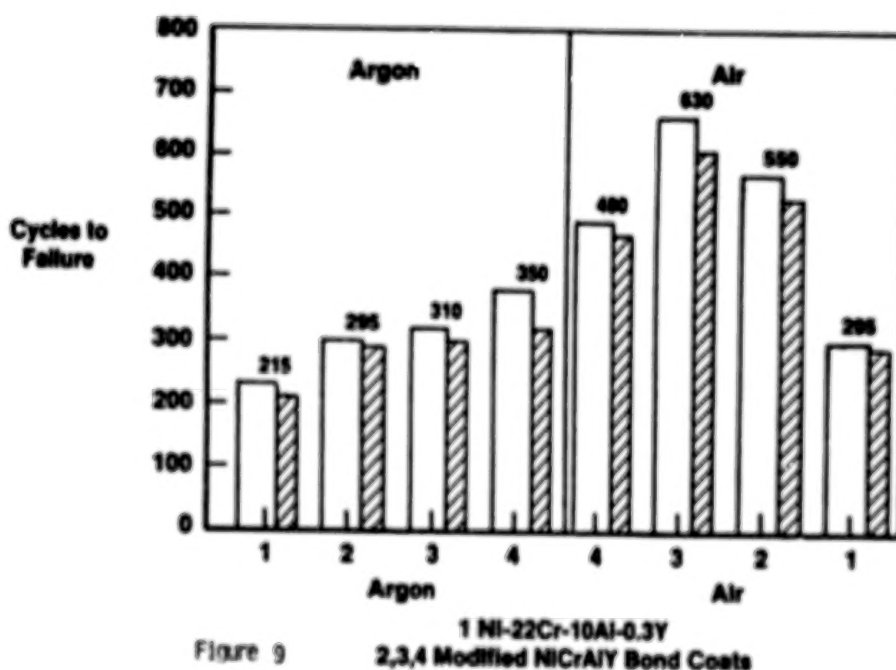


Figure 9

1 Ni-22Cr-10Al-0.3Y  
2,3,4 Modified NiCrAlY Bond Coats

## As Sprayed

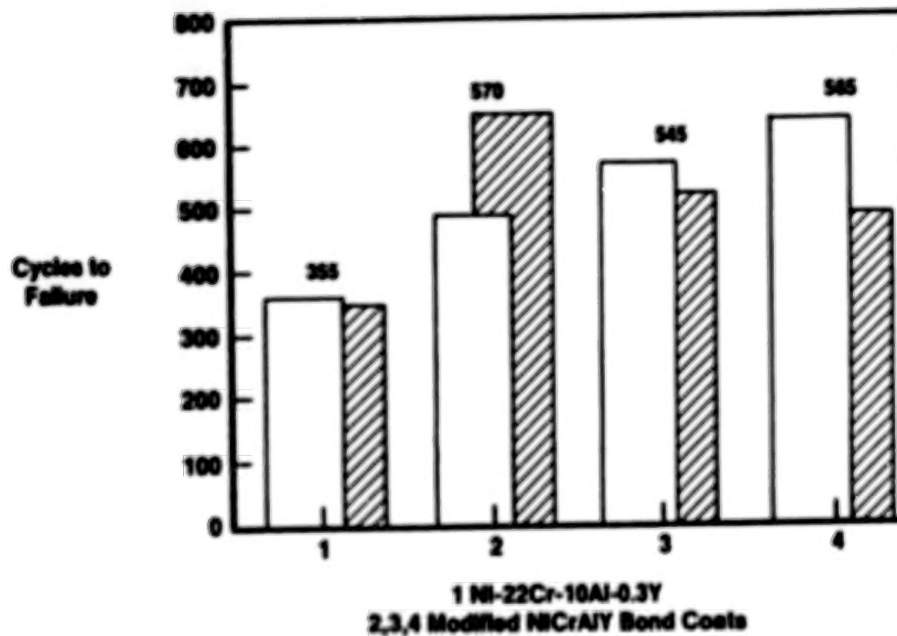


Figure 10

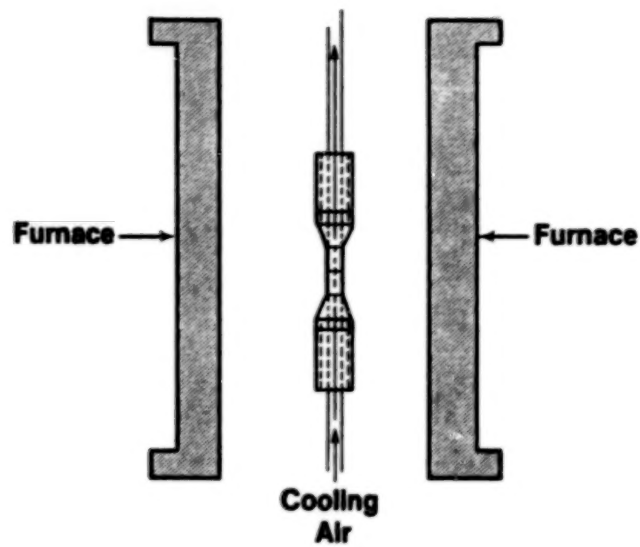
## Key Mechanical Properties

	Bond Coating	Top Coating
• Tensile Strength	Conventional	Bend
• Poisson's Ratio	Conventional	Resonance*
• Coefficient of Thermal Exposure	Conventional	Conventional
• Dynamic Modulus	Conventional	Resonance
• Temperatures R.T., 1000°F, 1800°F, 1900°F, 2000°F		

\*Also Strain Gauge at R.T.

Figure 11

## Thermomechanical Properties



**Determine Magnitude of Strains Present**  
**Utilize Test Matrix of LCF Testing**

Figure 12

## THERMAL BARRIER COATING LIFE PREDICTION MODEL DEVELOPMENT\*

J.T. DeMasi and K.D. Sheffler  
United Technologies Corporation  
Pratt & Whitney

The objective of this program is to develop an integrated life prediction model accounting for all potential life-limiting Thermal Barrier Coating (TBC) degradation and failure modes including spallation resulting from cyclic thermal stress, oxidation degradation, hot corrosion, erosion and foreign object damage (FOD). This overall program objective will be accomplished in two phases. The goal of the first phase is to determine the mechanisms and relative importance of the various degradation and failure modes, and to develop and verify the methodology to predict predominant mode failure life in turbine airfoil applications. Phase I will develop an empirically-based correlative model relating coating life to parameterically expressed driving forces such as temperature and stress. The effort in this phase consists of three tasks: Failure Mechanism Determination (Task I), Modeling (Task II), and Substantiation Testing (Task III). Phase II will experimentally verify Phase I models and develop an integrated, mechanistically-based life prediction model including all relevant failure modes. The program is currently in the final stages of Task I; predominant failure modes have been identified and a preliminary life prediction model is being developed.

The two layer TBC system being investigated, designated PWA264, is currently in commercial aircraft revenue service, on turbine vane platforms in the JT9D and 2037 engines. It is also bill-of-material on turbine vane airfoils in the advanced PW4000 and IAE V2500 engines. The TBC consists of an inner low-pressure chamber plasma sprayed NiCoCrAlY metallic bond coat (4-6 mils) and an outer air plasma-sprayed 7 w/o  $Y_2O_3$ -ZrO<sub>2</sub> (8-12 mils) ceramic layer (figure 1). The composition and structure of this coating are based in part on effort conducted under previous NASA sponsored programs (ref. 1 and 2).

## PHASE I, TASK I - FAILURE MECHANISM DETERMINATION

A review of experimental and flight service components as well as laboratory test evaluations indicates that the predominant mode of TBC failure involves thermomechanical spallation of the ceramic coating layer. This ceramic spallation involves the formation of a dominant crack in the ceramic coating parallel to and closely adjacent to the topologically complex metal ceramic interface (figure 2). This cyclic "mechanical" failure mode clearly is influenced by thermal exposure effects as shown by results of experiments conducted to study thermal pre-exposure and thermal cycle-rate effects (ref. 3-6).

## EXPERIMENTAL DESIGN AND TEST PLAN

The Task I, "Failure Mechanism Determination" investigation was designed to evaluate the relative importance of various thermomechanical and thermochemical "damage" modes, focusing on thermal stress cycling, oxidative degradation and their potential interaction. The primary experimental method used in this investigation was cyclic burner rig testing. The cyclic tests were conducted with both clean and

\*Work done under NASA Contract NAS3-23944.

381-1-407

contaminated fuels to assess the importance of hot corrosion induced ceramic spallation (ref. 7 - 10). Static furnace tests also were performed to evaluate the relative importance of oxidation and other thermal exposure effects. The test matrix (figure 3) was designed to study the influence of various "driving forces" such as temperature, thermal cycle frequency, environment, coating thickness and pre-burner rig test thermal exposure on TBC spalling life. To provide property data required for subsequently described thermal and stress analyses, physical and mechanical property tests are being conducted on monolithic ceramic and metallic specimens fabricated to simulate the composition and structure of the respective coating layers.

### CRITICAL EXPERIMENT RESULTS

All burner rig and furnace test specimens exhibited the typical ceramic spallation near the metal-ceramic interface, with a thin layer of ceramic remaining adherent after failure. Examination of the laboratory data clearly shows a strong temperature effect; comparison of these data with typical engine test conditions suggests that "cyclic content", (i.e., relative frequency and severity of engine thermal cycling) also strongly influences TBC spallation life (figure 4). Oxidation damage occurring at the ceramic-metal interface for laboratory testing was found to be somewhat greater than that found for engine exposed failures. This is attributed to the relatively high interface temperature employed in the accelerated laboratory spallation life testing.

In the laboratory tests conducted to study environmental effects, results suggest that bond coat oxidation damage at the metal-ceramic interface contributes significantly to thermomechanical cracking in the ceramic layer. Low cycle rate furnace exposure in air versus exposure in Argon clearly shows a dramatic increase of spalling life in the non-oxidizing environment (figure 5). The results of burner rig testing indicated that static thermal pre-exposure of burner rig test specimens in air causes a proportionate reduction of cyclic thermal spalling life, whereas pre-test thermal exposure in Argon does not reduce cyclic thermal spalling life (figures 6 and 7). Typical respective pre-test microstructures for air and Argon pre-exposed specimens are shown in figures 8a and b.

Laboratory testing was conducted in clean and contaminated (Na, S) fuel environments to evaluate the hot corrosion spallation resistance of the TBC. Corrodant induced failure was observed during cyclic hot corrosion testing at high corrodent levels (35 ppm  $\text{Na}_2\text{SO}_4$ ) but not for low corrodent levels (10ppm  $\text{Na}_2\text{SO}_4$ ). The failure mode, which has not been observed on engine exposed components, involved "flaking" of small patches of ceramic above the typical failure location.

Testing was also conducted to evaluate the effects of ceramic thickness on TBC spalling life. Ceramic thickness was found to have an effect on coating durability (figure 9). Thick coatings were found to decrease TBC life while thin coatings increased it as compared to the "baseline" 10 mil thick ceramic.

### PHASE I, TASK I PRELIMINARY LIFE PREDICTION MODEL DEVELOPMENT

The preliminary life prediction model currently being developed focuses on the two major damage modes identified in the laboratory testing described above. The first of these modes involves a mechanical driving force, resulting from cyclic strains and stresses caused by thermally induced and externally imposed loads. The second is an environmental driving force which appears, based on the experimental results, to be related to "oxidation damage", most probably to the in-service

growth of a NiCoCrAlY oxide scale at the metal-ceramic interface. Based on the apparently "mechanical" mode of ceramic failure, it is presumed that the growth of this oxide scale influences the intensity of the mechanical driving force. The mechanism(s) of this "interaction" are not presently understood, and no attempt is being made to incorporate interaction effects in the initial model, which will be based on linear damage summation. Interaction effects will be considered in the refined model to be developed in Task 2 of this program.

Mechanical failure of the ceramic layer is presumed to involve accumulation of fatigue "damage". Possible mechanisms for the accumulation of this damage might involve the initiation and propagation of a dominant crack in the ceramic, or possibly the subcritical growth and subsequent link-up of pre-existing microcracks in the ceramic structure. Metallographic examination of specimens removed from burner rig test prior to spallation failure presently is being conducted to identify specific mechanical damage accumulation mechanism(s).

Cyclic inelastic strain range in the ceramic layer will be used to represent the driving force for mechanical damage in the life model. Use of this parameter is based on results of mechanical (reversed bend) tests conducted on monolithic ceramic specimens having a porous, microcracked microstructure representative of the ceramic coating. These results have shown highly non-linear stress-strain behavior with significant stress-strain hysteresis in reversed loading. Finite element calculations of ceramic inelastic strain range are being conducted for each of the Task I burner rig test conditions using transient thermal data obtained from thermocouple instrumented test specimens. It is presently planned to use a relatively simple empirical relationship such as Manson-Coffin to express the functional dependence of mechanical "damage" on ceramic inelastic strain range.

Based on the observation that thermal exposure damage appears to be related to oxidation effects, the relationship between thermal damage accumulation rate and primary exposure parameters (time and temperature) will be based on the accepted parabolic and exponential forms appropriate to oxidation kinetics.

A major shortcoming of the present model is the absence of any provision for interaction between environmental and mechanical damage. The relatively coarse preliminary finite element break-up constructed to represent the substrate coating structure incorporates a planar metal-ceramic interface and predicts essentially no change of stress level with growth of an interfacial oxide scale. Thus, oxidation effects will be "forced" in the preliminary model using the linear damage summation approach. One approach which will be evaluated in an effort to incorporate interaction effects in the refined Task 2 model will involve an attempt to represent, in a relatively simple geometric form such as that employed by G. C. Chang (ref. 11), the very complex (rough) topological form of the real physical interface shown in figure 1. Other changes to the relatively simple functional forms used in the preliminary Task I model undoubtedly will be suggested by ongoing microstructural damage interpretation and by testing this preliminary model against additional burner rig verification tests to be conducted at the conclusion of Task I.

#### VERIFICATION TESTING - WORK PLANNED

To verify the preliminary Task I prediction model, additional burner rig tests will be conducted using test parameters and methods which are different from those used to generate the data on which the model is based. The test method will involve exposure of a single rotating specimen located in the center of the burner rig spindle. This will improve and simplify temperature measurement and control, and

will eliminate circumferential thermal gradients which are inherent to the multiple specimen configuration used earlier in this task. To improve the simulation of airfoil conditions the specimen will be hollow and incorporate internal cooling, thus providing a steady state thermal gradient across the TBC. Three sets of test parameters will be selected to simulate typical airfoil mission cycles.

#### REFERENCES

1. Sheffler, K.D.; Graziani, R.A.; and Sinko, G.C.: JT9D Thermal Barrier Coated Vanes. NASA CR 167964, April 1982.
2. Anderson, N.P.; and Sheffler, K.D.: Development of Strain Tolerant Thermal Barrier Coating Systems. Final Report, Contract MAS3-22548. 1982.
3. McDonald, G.; and Hendricks, R.C.: Effect of Thermal Cycling on  $ZrO_2-Y_2O_3$  Thermal Barrier Coatings. Thin Solid Film. V.73, 1980, p.491.
4. Gedwill, M.A.; Burner Rig Evaluation of Thermal Barrier Coating Systems for Nickel-Base Alloys. NASA-TM 81685, February 1981.
5. Miller, R.A.; and Lowel, C.E.: Failure Mechanisms of Thermal Barrier Coatings Exposed to Elevated Temperatures. MASA TM 82905, April 1982.
6. Miller, R.A.; Oxidation-Based Model for Thermal Barrier Coating Life. Ceramic Journal. 1984, pp. 83-87.
7. Grisaffe, S.J.; and Levine, S.R.: Proceedings of First DOE/EPRI Conference on Advanced Materials for Alternative Fuel Capable Directly Fired Heat Engines. Castine, ME. 1979, p. 680.
8. Bratton, R.J.; et. al.: Evaluation of Present Day Thermal Barrier Coatings for Industrial/Utility Applications. Thin Solid Films. 73, 1980, p. 429.
9. Hodge, P.E.; et. al.: Evaluation of the Hot Corrosion Behavior of Thermal Barrier Coatings. Thin Solid Films. 73, 1980, p. 447.
10. Bevan, C.E.; Development of Advanced Plasma Sprayed Ceramic Coatings for Industrial Gas Turbine Engines. Final Report, Contract B-A0747-A-Z. PWA 5906, July 1982.
11. Chang G.C.; and Phucharoen W.: Finite Element Analyses of Thermal Barrier Coatings. Thermal Barrier Coatings Workshop, Op. cit., May 1985, p. 111-126.

ORIGINAL PAGE IS  
OF POOR QUALITY

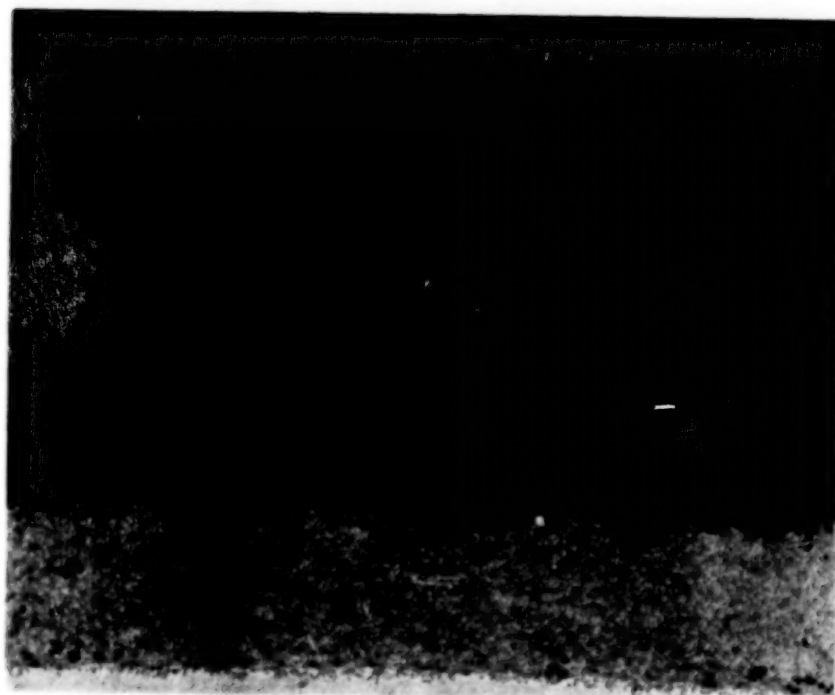


Figure 1 Light Photomicrograph Showing PWA264 Microstructure 200X



ORIGINAL PAGE IS  
OF POOR QUALITY

Figure 2 Typical Thermal Barrier Coating Failure Mode

TEMPERATURE	EXPOSURE		STATIC		CYCLIC				FRACTIONAL EXPOSURE			
	TEST		FURNACE		BURNER RIG				FURNACE		BURNER RIG	
	ATMOSPHERE		OXIDIZING	NON-OXIDIZING	OXIDIZING		HOT CORROSION		OXIDIZING	NON-OXIDIZING	OXIDIZING	HOT CORROSION
	CYCLE LENGTH				SHORT		LONG		SHORT		LONG	
	HEATING RATE				F	S	F	S	F	S	F	S
CORRODENT LEVEL					A	L	A	L	A	L	A	L
					S	O	S	O	S	O	S	O
					T	W	T	W	T	W	T	W
1650												
2000												
2100			A <sub>1</sub>	A <sub>2</sub>								
2200			B									

## CYCLIC OXIDATION BURNER RIG TEST SPECIMEN SET FOR CONDITIONS D1, D2, E &amp; F-12 SPECIMENS PER TEST

4 10 MIL VIRGIN CERAMIC ("BASELINE" COATING)

2 5 MIL VIRGIN CERAMIC

2 15 MIL VIRGIN CERAMIC

2 10 MIL AIR PRE-EXPOSED FOR APPROXIMATELY ½ ESTIMATED BURNER RIG HOT TIME LIFE

2 10 MIL Ar PRE-EXPOSED FOR APPROXIMATELY ½ ESTIMATED BURNER RIG HOT TIME LIFE

## CYCLE LENGTH

SHORT: 6 MINUTE CYCLE = 4 MINUTES IN THE FLAME + 2 MINUTES FORCE AIR COOLED

LONG: 60 MINUTE CYCLE = 57 MINUTES IN THE FLAME + 3 MINUTES FORCE AIR COOLED

## CYCLE RATE

FAST: NOMINAL 60 SECOND HEAT-UP TO MAXIMUM TEMPERATURE

SLOW: NOMINAL 180 SECOND HEAT-UP TO MAXIMUM TEMPERATURE

## CORRODENT LEVEL

LOW: 10 PPM Na<sub>2</sub> SO<sub>4</sub>HIGH: 35 PPM Na<sub>2</sub> SO<sub>4</sub>

Figure 3 Task I Test Plan To Evaluate Thermal Barrier Coating Failure Life

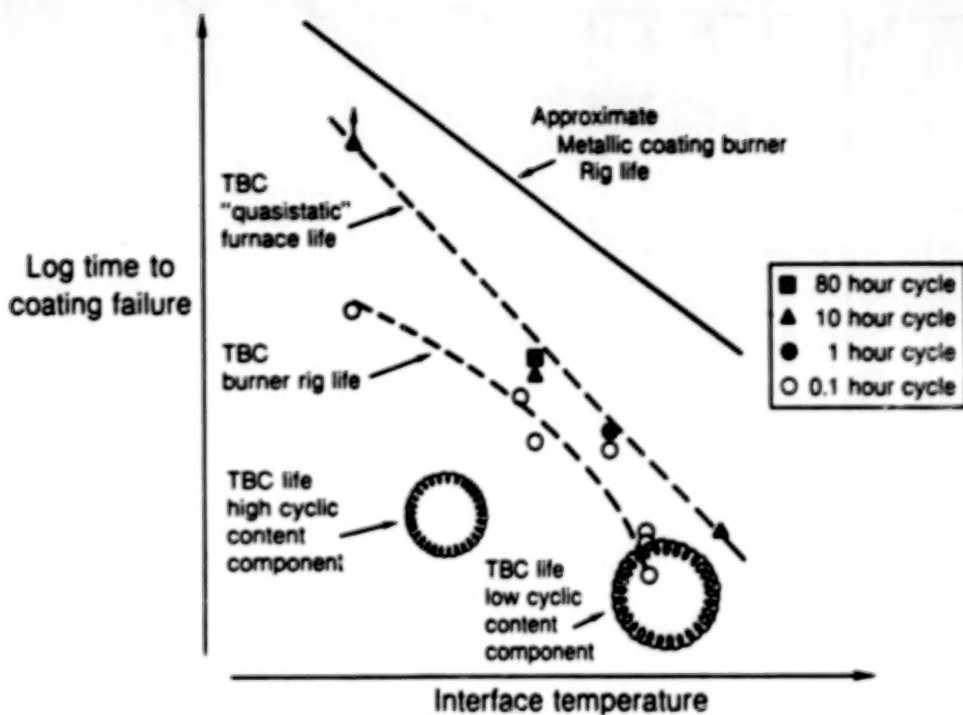


Figure 4 Test Data Showing Coating Life Dependent on Temperature, "Cyclic Content"

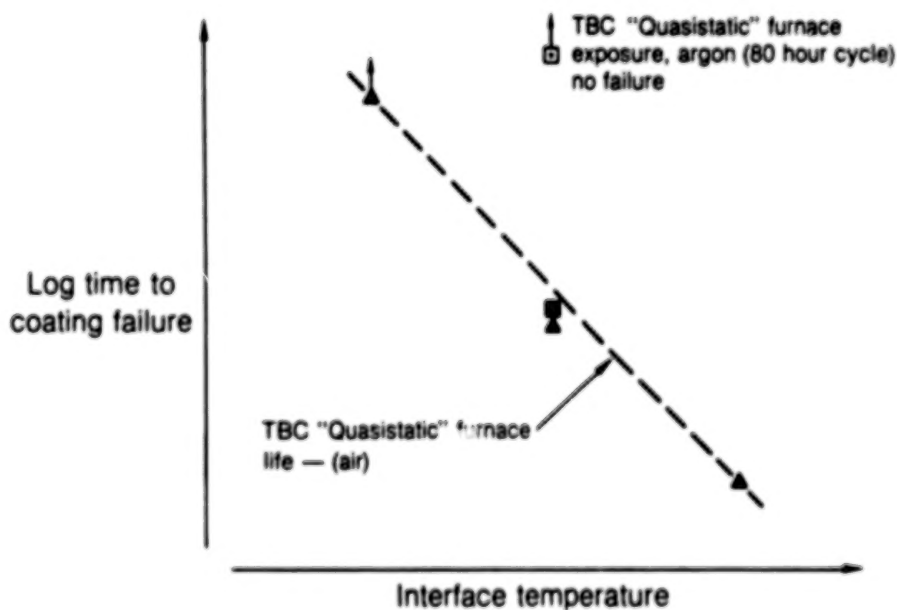


Figure 5 Test Data Showing Thermal Exposure Atmosphere Effects on Coating Durability

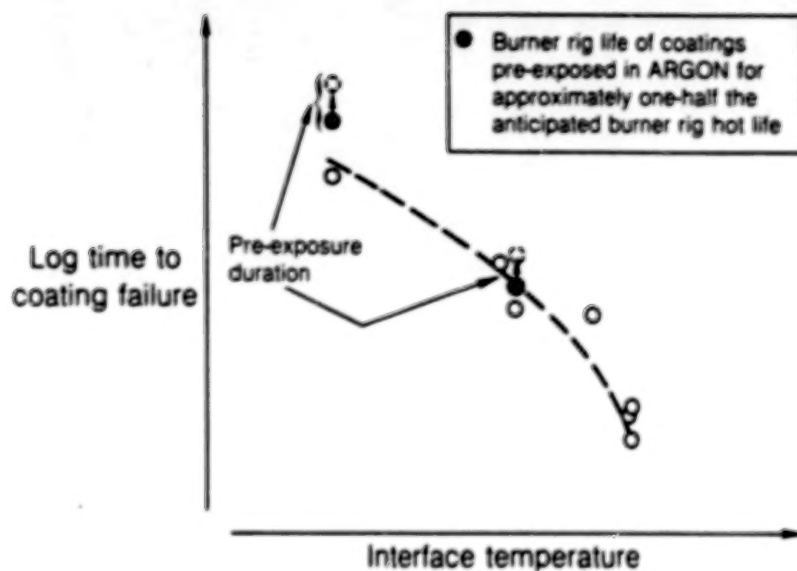


Figure 6 Test Data Showing "INERT" Pre-Exposure Does Not Effect Coating Performance

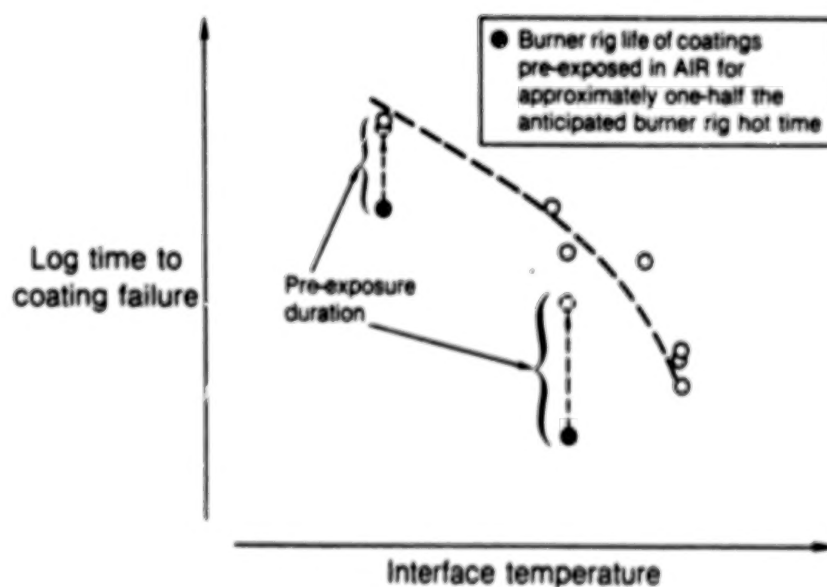
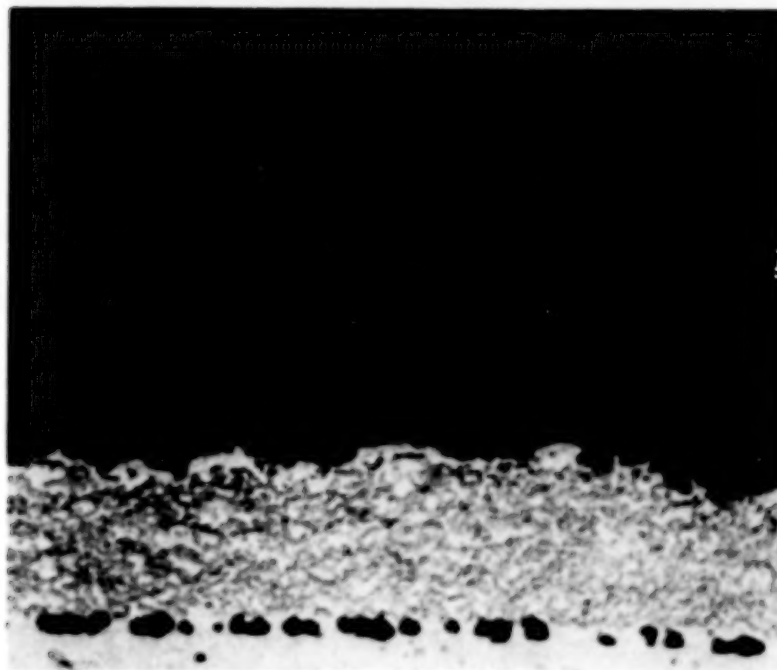
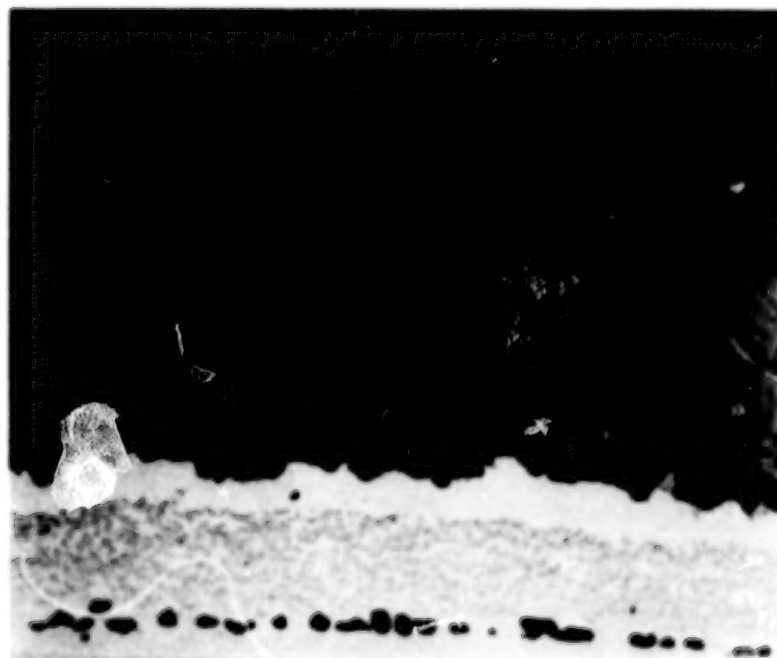


Figure 7 Test Data Showing Air Pre-Exposure Degrades Cyclic Life

ORIGINAL PAGE IS  
OF POOR QUALITY



(a)



(b)

Figure 8a and b Microstructural Variations for Pre-Test Thermal Exposure Atmospheres, (a) Argon and (b) Air

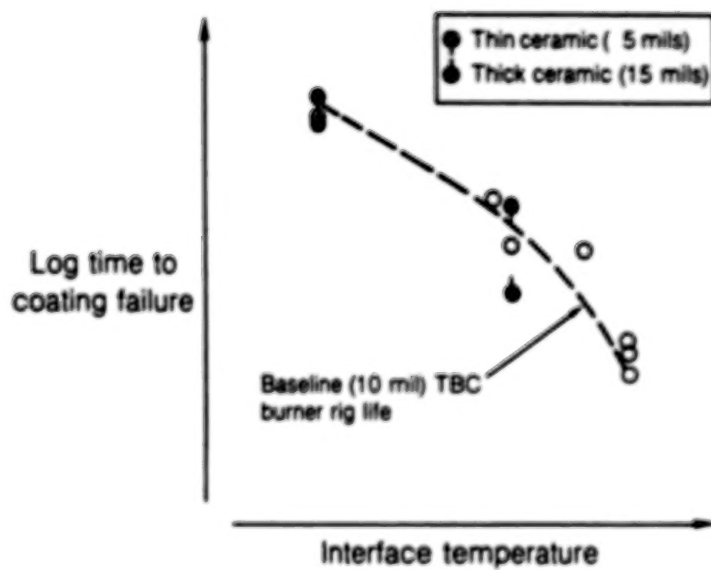


Figure 9 Test Data Showing Ceramic Thickness Effects

CONCLUDING REMARKS: FOURTH ANNUAL WORKSHOP FOR THE HOST PROJECT

Daniel E. Sokolowski  
NASA Lewis Research Center  
Cleveland, Ohio

As reported at this workshop, the HOST Project activities are well underway and are producing substantial results. Many contractor reports have become available and will continue in the future. Workshops such as this also will continue on an annual basis. The HOST Fifth Annual Workshop is tentatively scheduled for October 21-22, 1986.

The nature of the problem of durability requires not only the involvement of numerous disciplines, as discussed in the opening remarks, but also that the research itself be interdisciplinary. The HOST Project to date has been very successful. The success is due in part to unprecedented teamwork at Lewis, at the contractors, and between contractors and universities. Further, the HOST Project is recognized for the value of focused as well as interdependent research when compared with generic, independent, basic R&T activities. The problem being addressed has much influence in the advocacy and successful implementation of such a project, however.

To date, \$27.3 million has been invested in HOST. In FY 1986 another \$5.1 million will be spent. The present plan for FY 1987-89 is for a total of \$12.3 million to be spent.

Finally, I want to say "thank you" to the HOST Project Team for a job well done in conducting this workshop. In particular, I want to thank the contractor speakers; the Subproject Managers for being session chairman; my Assistant Manager, Bob Ensign; and our Project Control Assistant, Barbara DiSanto, for helping to organize and coordinate the multitude of efforts required.

END DATE JAN. 13, 1988

PRECEDING PAGE BLANK NOT FILMED